

Titre: Critical evaluation and thermodynamic modeling of phase equilibria
Title: in multicomponent oxide systems

Auteur: In-Ho Jung
Author:

Date: 2003

Type: Mémoire ou thèse / Dissertation or Thesis

Référence: Jung, I.-H. (2003). Critical evaluation and thermodynamic modeling of phase
Citation: equilibria in multicomponent oxide systems [Thèse de doctorat, École
Polytechnique de Montréal]. PolyPublie. <https://publications.polymtl.ca/7164/>

 **Document en libre accès dans PolyPublie**
Open Access document in PolyPublie

URL de PolyPublie: <https://publications.polymtl.ca/7164/>
PolyPublie URL:

**Directeurs de
recherche:**
Advisors:

Programme: Non spécifié
Program:

In compliance with the
Canadian Privacy Legislation
some supporting forms
may have been removed from
this dissertation.

While these forms may be included
in the document page count,
their removal does not represent
any loss of content from the dissertation.

UNIVERSITÉ DE MONTRÉAL

CRITICAL EVALUATION AND THERMODYNAMIC MODELING OF
PHASE EQUILIBRIA IN MULTICOMPONENT OXIDE SYSTEMS

IN-HO JUNG

DÉPARTEMENT DE GÉNIE CHIMIQUE

ÉCOLE POLYTECHNIQUE DE MONTRÉAL

THÈSE PRÉSENTÉE EN VUE DE L'OBTENTION
DU DIPLÔME DE PHILOSOPHIAE DOCTOR (Ph.D.)
(GÉNIE MÉTALLURGIQUE)

MARS 2003

© In-Ho Jung, 2003.



National Library
of Canada

Bibliothèque nationale
du Canada

Acquisitions and
Bibliographic Services

Acquisitions et
services bibliographiques

395 Wellington Street
Ottawa ON K1A 0N4
Canada

395, rue Wellington
Ottawa ON K1A 0N4
Canada

Your file Votre référence

ISBN: 0-612-86445-6

Our file Notre référence

ISBN: 0-612-86445-6

The author has granted a non-exclusive licence allowing the National Library of Canada to reproduce, loan, distribute or sell copies of this thesis in microform, paper or electronic formats.

L'auteur a accordé une licence non exclusive permettant à la Bibliothèque nationale du Canada de reproduire, prêter, distribuer ou vendre des copies de cette thèse sous la forme de microfiche/film, de reproduction sur papier ou sur format électronique.

The author retains ownership of the copyright in this thesis. Neither the thesis nor substantial extracts from it may be printed or otherwise reproduced without the author's permission.

L'auteur conserve la propriété du droit d'auteur qui protège cette thèse. Ni la thèse ni des extraits substantiels de celle-ci ne doivent être imprimés ou autrement reproduits sans son autorisation.

Canada

UNIVERSITÉ DE MONTRÉAL

ÉCOLE POLYTECHNIQUE DE MONTRÉAL

Cette thèse intitulée:

CRITICAL EVALUATION AND THERMODYNAMIC MODELING OF
PHASE EQUILIBRIA IN MULTICOMPONENT OXIDE SYSTEMS

présentée par : JUNG In-Ho

en vue de l'obtention du diplôme de : Philosophiae Doctor

a été dûment acceptée par le jury d'examen constitué de :

M. BALE Christopher W., Ph.D., président

M. PELTON Arthur D., Ph.D., membre et directeur de recherche

M. DEGTIAREV Serguei A., Ph.D., membre et co-directeur de recherche

M. GASKELL David R., Ph.D., membre

M. ERIKSSON Gunnar, Ph.D., membre

Dedication

I wish to dedicate this thesis to my family in Korea.

Acknowledgements

I would like to express my deep appreciation to Dr. Arthur D. Pelton, whose guide and enthusiastic support were of immeasurable help to me at all stages of this study. His solid financial assistance allowed me to concentrate on my research work.

I am also grateful to my co-director, Dr. Sergei Decterov, for his continual helpful advice and collaboration in my study. I enjoyed all discussions with him during my study.

I also thank Drs. David R. Gaskell, Christopher W. Bale and Gunnar Eriksson for their critical review and constructive comments. As well, I express my gratitude to Dr. Hae-Geon Lee who encouraged me to complete my study.

I am indebted to Patrice for helpful discussions, to Christian for French translation, and to Zhenya and Katherine for their assistance. I also thank to all members of the CRCT for their friendship during my study in Canada.

I also wish to thank my former Korean colleagues, Youn-Bae and Hyun-Min for their collaboration, and Pierre in NASA who introduced me an interesting geochemistry.

I very thank to my friend Yeon-Jung and Jinsoo for their love and sincere friendship.

I acknowledge the financial support during the present study by a CRD grant from the Natural Sciences and Engineering Research Council of Canada in collaboration with the following: Alcoa, Corning, Dupont, INCO, Mintek, Noranda, Norsk Hydro, Pechiney, Rio Tinto, Schott Glass, Shell, Sintef, St.-Gobain Recherche, Teck Cominco and IIS Materials.

ABSTRACT

The prediction of thermodynamic properties and phase equilibria related to liquid and solid oxides can play an important role in the development and understanding of metallurgical, ceramic and geological processes. The importance of numerical simulation of these processes is increasing, and the thermodynamic models must keep pace and be able to calculate and predict phase equilibria and thermodynamic properties of complex mixtures. The goal of this thesis is a critical evaluation and optimization of thermodynamic properties of solid and liquid oxides in order to construct accurate and extensive thermodynamic databases for the systems of industrial interest. The constructed databases can aid in understanding various industrial processes more clearly and in developing new technology in various industries.

All solid and liquid phases of 5 binary, 9 ternary and 5 multicomponent sub-systems in the $\text{CaO-MgO-Al}_2\text{O}_3\text{-SiO}_2\text{-FeO-Fe}_2\text{O}_3\text{-MnO-CrO-Cr}_2\text{O}_3\text{-CoO}$ system were critically evaluated and optimized in the course of the present study. The optimization of all systems in this study are self-consistent, and moreover are consistent with all alloy and salt databases of the FACT system (developed at Ecole Polytechnique de Montreal). From the database of model parameters of lower order (binary + ternary) subsystems, the thermodynamic properties of multicomponent solutions can be predicted with good accuracy.

All thermodynamic models for solutions used in this study were developed on the basis of their structure. In this way, the configurational entropy of solution could be properly taken into account. Thus, the number of model parameters for each solution can be minimized using physically correct thermodynamic models. The predictive ability of all models was found to be excellent.

The molten oxide was modeled by the Modified Quasichemical Model, which takes into account second-nearest-neighbor cation ordering. Extensive solid solutions such as spinel, olivine and pyroxene were modeled within the framework of the Compound Energy Formalism with consideration of their two- or three-sublattice crystal structure. Other solid solutions such as monoxide, wollastonite and so on were modeled using polynomial expansions of the excess Gibbs energy. Deoxidation equilibria in liquid Fe were also modeled using a new Associate Model developed in the present study, which takes into account the strong affinity of deoxidants to oxygen.

In particular, the spinel solution optimized in this study comprises the most extensive spinel solution database in the world, covering the Fe-Mg-Al-Cr-Co-Ni-Zn-O system, which is important for the corrosion of steel, refractories, ceramics, *etc.*

The new Associate Model can accurately describe the deoxidation phenomena of strong deoxidants such as Ca, Mg and Ba using only one temperature-independent model parameter. This is not possible with the classical Wagner Interaction Parameter Formalism. This is the first time the deoxidation equilibria of these strong deoxidants has been elucidated. The model can be applied to the deoxidation equilibria of all common deoxidant elements in liquid Fe.

In order to show the accuracy and usefulness of the thermodynamic databases developed in this study, they are applied, for example, to complex steelmaking processes: inclusion engineering, and vacuum oxygen decarburization (VOD) simulation in the stainless steelmaking process.

The newly optimized databases and thermodynamic models for oxides and liquid Fe can be incorporated with the FACT databases. The database of the model parameters can be used along with software for Gibbs energy minimization in order to calculate any type of phase diagram section, thermodynamic properties, phase equilibria, *etc.*

Consequently, they will increase the accuracy of the FACT thermodynamic databases and expand the range of applications to the industrial and natural processes significantly.

CONDENSÉ

La prédiction des propriétés thermodynamiques et des équilibres de phases pour les systèmes d'oxydes liquides et solides peut avoir un rôle important lors du développement et lors de la compréhension de procédés métallurgiques, céramiques et géologiques. La simulation numérique de ces procédés a une importance croissante et les modèles thermodynamiques doivent permettre de calculer et prédire les équilibres de phases et les propriétés thermodynamiques pour des systèmes complexes. L'objectif de cette thèse consiste en l'évaluation critique et en la modélisation des propriétés thermodynamiques de systèmes d'oxydes solides et liquides. Cela nous a amenés à développer des banques de données thermodynamiques pour des systèmes d'intérêt industriel. Ces banques de données permettent d'améliorer la compréhension de procédés industriels variés et de développer de nouvelles technologies.

Dans le Chapitre 2, nous décrivons brièvement l'importance de la modélisation thermodynamique et l'histoire de CALPHAD ("CALculation of PHase Diagrams"). Nous présentons également la procédure d'évaluation critique et de modélisation utilisée dans cette thèse. Enfin, nous décrivons brièvement le système FACT (développé à l'Ecole Polytechnique de Montréal) utilisé dans le cadre de la présente étude.

Dans le Chapitre 3, nous décrivons en détail les différents modèles thermodynamiques utilisés. Ces modèles thermodynamiques de solutions sont tous physiquement réalistes : une expression satisfaisante de l'entropie configurationnelle de la solution a été utilisée. Le nombre de paramètres requis pour chaque solution a ainsi pu être minimisé et la capacité de prédiction de chaque modèle s'est avérée excellente. Nous discutons également dans le Chapitre 3 des avantages des modèles utilisés par rapport à d'autres modèles plus anciens. Nous avons développé un nouveau Modèle d'Associés pour l'acier liquide de façon à expliquer les équilibres de désoxydation dans le fer liquide. A l'aide d'un seul paramètre (indépendant de la température), ce nouveau modèle décrit

bien les phénomènes de désoxydation pour de forts agents désoxydants tels que Ca, Mg et Ba. Pour la première fois, ces équilibres de désoxydation ont pu être expliqués car le Formalisme des Paramètres d'Interaction de Wagner n'en donnait pas une bonne description. Le nouveau modèle développé s'applique également aux équilibres de désoxydation impliquant tous les agents désoxydants classiques du fer liquide et requiert moins de paramètres que le Formalisme des Paramètres d'Interaction de Wagner.

A l'aide des modèles thermodynamiques décrits dans le Chapitre 3, nous avons modélisé les phases solides et liquides de 5 systèmes binaires, 9 systèmes ternaires et 5 systèmes multicomposants liés au système $\text{CaO-MgO-Al}_2\text{O}_3\text{-SiO}_2\text{-FeO-Fe}_2\text{O}_3\text{-MnO-CrO-Cr}_2\text{O}_3\text{-CoO}$. Les résultats sont présentés dans les Annexes I-X. En particulier, la solution solide de spinelle modélisée dans cette étude est la seule banque de données au monde de cette envergure. Elle se rapporte au système $\text{Fe-Mg-Al-Cr-Co-Ni-Zn-O}$ qui est important pour la corrosion de l'acier, des réfractaires, des céramiques, *etc.* La solution liquide d'oxydes et la solution solide de monoxyde ont été modélisées. Des solutions solides étendues de silicates telles que l'olivine, le pyroxène et la wollastonite ont également été modélisées.

Les modélisations réalisées sont toutes compatibles entre elles et sont de plus compatibles avec les banques de données d'alliages et de sels du système FACT. Les propriétés thermodynamiques des systèmes multicomposants peuvent être prédites avec une bonne précision à partir des paramètres obtenus pour les sous-systèmes d'ordre inférieur (binaires et ternaires).

Les banques de données thermodynamiques développées pour les systèmes d'oxydes et le fer liquide peuvent être incorporées aux autres banques de données de FACT. Elles peuvent être utilisées avec un logiciel de minimisation de l'énergie de Gibbs (inclus dans le système FACT) pour calculer des diagrammes de phases variés, des propriétés thermodynamiques, des équilibres de phases, *etc.* Grâce à ces banques de données, une

plus grande variété de procédés industriels et géologiques pourra être simulée à l'aide du système FACT.

De façon à montrer la fiabilité et l'utilité des banques de données développées dans cette étude, nous avons considéré à titre d'exemple des procédés complexes d'aciérage: l'ingénierie des inclusions (Annexe X) ainsi que la simulation de la décarburation par l'oxygène sous vide (DOV) mise en jeu pour des aciers inoxydables (Chapitre 4).

Les phases et systèmes évalués et modélisés dans la présente étude sont résumés ci-dessous:

Phases:

Solution liquide d'oxydes (laitier): $\text{SiO}_2\text{-CaO-MgO-AlO}_{1.5}\text{-FeO-FeO}_{1.5}\text{-MnO-CrO-CrO}_{1.5}\text{-CoO}$

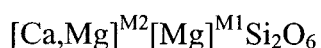
Spinelle: $(\text{Fe}^{2+}, \text{Fe}^{3+}, \text{Mg}^{2+}, \text{Al}^{3+}, \text{Cr}^{2+}, \text{Cr}^{3+}, \text{Co}^{2+}, \text{Co}^{3+})^T$



Olivine: $[\text{Ca}, \text{Mg}, \text{Fe}^{2+}, \text{Mn}^{2+}, \text{Co}^{2+}]^{\text{M2}} [\text{Ca}, \text{Mg}, \text{Fe}^{2+}, \text{Mn}^{2+}, \text{Co}^{2+}]^{\text{M1}} \text{SiO}_4$

Pyroxène: $[\text{Ca}, \text{Mg}, \text{Fe}^{2+}]^{\text{M2}} [\text{Mg}, \text{Fe}^{2+}, \text{Fe}^{3+}, \text{Al}^{3+}]^{\text{M1}} (\text{Si}, \text{Fe}^{3+}, \text{Al}^{3+})^{\text{B}} \text{Si}^{\text{A}} \text{O}_6$

(clino-, ortho-, proto-pyroxène)



(bas clino-pyroxène)

Monoxyde: $(\text{Mg}^{2+}, \text{Ca}^{2+}, \text{Fe}^{2+}, \text{Mn}^{2+}, \text{Co}^{2+}, \text{Fe}^{3+}, \text{Al}^{3+}, \text{Cr}^{3+}) (\text{O}^{2-})$

Wollastonite: $(\text{Ca}, \text{Mg}, \text{Fe}, \text{Mn}) \text{SiO}_3$

α -Ca₂SiO₄ et α' -Ca₂SiO₄: [Ca, Mg, Fe, Mn]₂SiO₄

Composés stoechiométriques unaires, binaires et ternaires: CoO (solide et liquide), Ca₃MgSi₂O₈ (merwinite), Ca₂MgSi₂O₇ (akermanite), CaMg₂Al₁₆O₂₇, Ca₂Mg₂Al₂₈O₄₆, Ca₃MgAl₄O₁₀, MnAl₂O₄ (galaxite), Mn₂Al₄Si₅O₁₈ (Mn-cordierite), Mn₃Al₂Si₂O₁₂ (spessartite), Mg₄Al₁₀Si₂Si₂₃ (sapphirine), Mg₂Al₄Si₅O₁₈ (cordierite), de même que tous les constituants des solutions solides.

Fe liquide: Equilibres de désoxydation pour Fe liquide contenant (comme solutés) Al, B, Ba, C, Ca, Ce, Cr, Hf, La, Mg, Mn, Nb, Nd, Ta, Ti, Th, Si, V et Zr.

Systèmes:

(1) Système CaO-MgO-SiO₂ (Annexe I)

Nous présentons l'évaluation critique et la modélisation des diagrammes de phases et propriétés thermodynamiques du système CaO-MgO-SiO₂ à une pression totale de 1 bar. La solution liquide d'oxydes a été modélisée à l'aide du Modèle Quasichimique Modifié, et les énergies de Gibbs des solutions solides d'olivine et de pyroxène ont été modélisées à l'aide du "Compound Energy Formalism". Nous avons obtenu un ensemble de paramètres des modèles pour toutes les phases, permettant de reproduire (dans la limite des erreurs expérimentales) l'ensemble des données thermodynamiques et d'équilibres de phases disponibles, de 25°C jusqu'aux températures du liquidus sur toute la gamme de composition. Les banques de données des paramètres peuvent être utilisées avec un logiciel de minimisation de l'énergie de Gibbs (disponible dans FACT) pour calculer n'importe quelle section d'intérêt.

(2) Système Mg-Fe-O (Annexe II)

Nous présentons l'évaluation critique et la modélisation thermodynamique des données expérimentales disponibles pour le système FeO-Fe₂O₃-MgO à une pression totale de 1 bar. Les paramètres des modèles obtenus reproduisent (dans la limite des erreurs

expérimentales) l'ensemble des données thermodynamiques et structurales ainsi que les diagrammes de phases pour le système $\text{FeO-Fe}_2\text{O}_3\text{-MgO}$. Aucun paramètre ternaire n'a été requis. Pour la phase spinelle, nous n'avons utilisé aucun paramètre du modèle pour les énergies d'interaction entre cations sur un même sous-réseau. L'utilisation d'un modèle thermodynamique approprié pour chaque phase permet de minimiser le nombre de paramètres requis et améliore la qualité de l'extrapolation dans les systèmes multicomposants à partir des paramètres binaires et ternaires. Les paramètres des modèles obtenus peuvent être utilisés avec un logiciel thermodynamique couplé à des banques de données (tel Factsage) pour calculer des équilibres de phases sous des conditions données et modéliser des procédés industriels et géologiques variés.

(3) Système $\text{MgO-FeO-Fe}_2\text{O}_3\text{-SiO}_2$ (Annexe III)

Les phases liquide et solides du système $\text{FeO-Fe}_2\text{O}_3\text{-MgO-SiO}_2$ ont un rôle important dans le domaine des céramiques, de la métallurgie et de la pétrologie. Nous présentons l'évaluation critique et la modélisation des diagrammes de phases et propriétés thermodynamiques de ce système à une pression totale de 1 bar. Nous avons obtenu des équations optimisées pour les propriétés thermodynamiques de toutes les phases, permettant de reproduire (dans la limite des erreurs expérimentales) l'ensemble des données thermodynamiques et d'équilibres de phases disponibles, de 25°C jusqu'aux températures du liquidus à toute composition et toute pression partielle d'oxygène. Les banques de données des paramètres peuvent être utilisées avec un logiciel de minimisation de l'énergie de Gibbs (disponible dans FACT) pour calculer n'importe quelle section d'intérêt.

(4) Systèmes $\text{MgO-Al}_2\text{O}_3$, $\text{CaO-MgO-Al}_2\text{O}_3$ et $\text{MgO-Al}_2\text{O}_3\text{-SiO}_2$ (Annexe IV)

Nous avons effectué l'évaluation critique de l'ensemble des diagrammes de phases et données thermodynamiques disponibles pour les systèmes $\text{MgO-Al}_2\text{O}_3$, $\text{CaO-MgO-Al}_2\text{O}_3$ et $\text{MgO-Al}_2\text{O}_3\text{-SiO}_2$. Une banque de données des paramètres des modèles a ainsi pu être obtenue. Un très petit nombre de paramètres a permis de reproduire (dans la

limite des erreurs expérimentales) la large gamme des données disponibles. La présente banque de données permet de calculer n'importe quelle section à toute composition.

(5) Systèmes MnO-Al₂O₃ et MnO-Al₂O₃-SiO₂ (Annexe V)

Nous avons effectué l'évaluation critique et la modélisation de l'ensemble des diagrammes de phases et données thermodynamiques disponibles pour le système MnO-Al₂O₃-SiO₂. Une banque de données des paramètres des modèles a ainsi pu être obtenue. Toutes les données sont reproduites dans la limite des erreurs expérimentales. A l'aide du modèle et de la banque de données développés pour l'acier liquide et à l'aide du logiciel de minimisation de l'énergie de Gibbs du système Factsage, nous avons effectué des calculs thermodynamiques appliqués au contrôle des inclusions d'un acier désoxydé par Mn/Si. Les résultats des calculs sont en bon accord avec les données expérimentales. Cela montre ainsi la capacité des banques de données thermodynamiques développées à prédire des équilibres d'intérêt pour l'ingénierie des inclusions. Lors de développements futurs, notre banque de données sera intégrée à la banque de données existant pour le système SiO₂-CaO-MgO-Al₂O₃-FeO-Fe₂O₃-TiO-TiO₂-CrO-Cr₂O₃-S.

(6) Système CaO-MnO-Al₂O₃-SiO₂ (Annexe VI)

Les propriétés thermodynamiques du système CaO-MnO-Al₂O₃-SiO₂ ont été modélisées en utilisant l'ensemble des données thermodynamiques et diagrammes de phases disponibles. Les solutions solides ont été modélisées à l'aide d'une expansion polynômiale pour les énergies de Gibbs en excès et à l'aide du "Compound Energy Formalism". Le Modèle Quasichimique Modifié a été utilisé pour le laitier liquide. Les diagrammes de phases calculés sont présentés. Les équilibres entre les inclusions et un acier à base de Mn/Si ont été calculés à l'aide du système Factsage (1), en utilisant la banque de données obtenue pour le système d'oxydes ainsi que la banque de données préalablement développée pour les solutions liquides de Fe. Ces banques de données ont pu être testées en comparant les résultats des calculs aux données expérimentales. Nous avons pu prédire des domaines de composition Mn/Si (caractérisant l'acier liquide)

permettant d'obtenir des inclusions déformables lors du tréfilage d'aciers à base de Mn/Si (impliqués dans la fabrication de pneus) et lors du laminage de l'acier Fe-36%Ni Invar. Enfin, nous discutons de l'effet sur les inclusions de laitiers de surface à base de CaO.

(7) Système Mg-Cr-Al-O (Annexe VII)

Nous avons effectué l'évaluation critique et la modélisation de l'ensemble des données thermodynamiques et diagrammes de phases disponibles pour le système $\text{MgO-Al}_2\text{O}_3\text{-CrO-Cr}_2\text{O}_3$ à une pression totale de 1 bar. Les paramètres des modèles obtenus reproduisent (dans la limite des erreurs expérimentales) l'ensemble des données de 25°C jusqu'aux températures du liquidus et pour des pressions partielles d'oxygène inférieures à 1 bar. L'évolution avec la pression partielle d'oxygène de la température de fusion de MgCr_2O_4 et du diagramme de phases $\text{MgO-Cr}_2\text{O}_3$ est expliquée pour la première fois. Les équilibres de phases peuvent être calculés à des températures, compositions et pressions partielles d'oxygène pour lesquelles aucune donnée n'est disponible.

(8) Système Fe-Co-O (Annexe VIII)

Nous avons effectué l'évaluation critique et la modélisation thermodynamique des systèmes $\text{CoO-Co}_3\text{O}_4$ et Fe-Co-O sur toute la gamme de composition et de température pour des pressions partielles d'oxygène inférieures à 100 bars. Les solutions solides de cobaltwustite et de spinelle ont été modélisées respectivement à l'aide d'une expansion polynômiale pour les énergies de Gibbs en excès et à l'aide du "Compound Energy Formalism". Le Modèle Quasichimique Modifié a été utilisé pour le laitier liquide. D'après notre étude, le diagramme de phases proposé par Muan pour le système Fe-Co-O est susceptible d'être erroné et est inconsistant avec les autres données expérimentales. Nous proposons dans cette étude de nouveaux diagrammes de phases (calculés) pour les systèmes $\text{CoO-Co}_3\text{O}_4$ et Fe-Co-O .

(9) Système Fe liquide (Annexe IX)

Un nouveau modèle de désoxydation (Modèle d'Associés) a été développé pour le fer liquide. Ce modèle est appliqué à des équilibres généraux de désoxydation pour Fe liquide contenant (comme solutés) Al, B, Ba, C, Ca, Ce, Cr, Hf, La, Mg, Mn, Nb, Nd, Ta, Ti, Th, Si, V, Zr. Les courbes de désoxydation pour Ca, Mg et Ba sont expliquées pour la première fois.

Dans l'Annexe X, nous présentons des calculs d'intérêt pour l'«ingénierie des inclusions», réalisés à partir des banques de données développées. Nous abordons différentes études de cas concernant des procédés complexes d'aciérage tels que: procédés d'injection de Ca (diagramme d'inclusions Fe-Ca-Al-O), corrosion des réfractaires, désoxydation par Mn/Si, désoxydation par Ti/Al (diagramme d'inclusions Fe-Al-Ti-O), formation de spinelle (diagramme d'inclusions Fe-Mg-Al-O), formation d'inclusions (Ti,N)(N,C), métallurgie des oxydes.

TABLE OF CONTENTS

Dedication.....	iv
Acknowledgements.....	v
Abstract.....	vi
Condensé.....	ix
Table of contents.....	xvii
List of appendices.....	xx
List of tables.....	xxi
List of figures.....	xxii
List of symbols.....	xxvii
 1: Introduction.....	 1
 2. Thermodynamic modeling.....	 3
2.1 History of CALPHAD.....	3
2.2 Critical Evaluation/Optimization.....	5
2.2.1 Procedure of Evalaution/Optimization.....	5
2.3 FactSage™.....	8
2.4 Goal of the present study.....	10
 3. Thermodynamic modeling of solid and liquid solution phases.....	 11
3.1 Liquid oxide (Slag).....	14
3.1.1 Melt structure.....	14
3.1.2 Thermodynamic models.....	16
3.1.2.1 Previous models.....	16
3.1.2.2 Present model: Modified Quasichemical Model.....	20
3.1.3 Discussion.....	23
3.2 Spinel solution.....	30

3.2.1	Crystal structure.....	30
3.2.2	Thermodynamic models.....	33
3.2.2.1	Previous models.....	33
3.2.2.2	Present model.....	42
3.2.3	Procedure of optimization and discussion.....	55
3.3	Olivine solution.....	66
3.3.1	Crystal structure.....	66
3.3.2	Thermodynamic models.....	69
3.3.2.1	Previous model.....	69
3.3.2.2	Present model.....	71
3.3.3	Discussion.....	74
3.4	Pyroxene solution.....	79
3.4.1	Crystal structure.....	79
3.4.2	Thermodynamic models.....	81
3.4.2.1	Previous model.....	81
3.4.2.2	Present model.....	84
3.4.3	Discussion.....	88
3.5	Monoxide solution.....	93
3.5.1	Crystal structure.....	93
3.5.2	Thermodynamic models.....	94
3.5.2.1	Previous model.....	94
3.5.2.2	Present model.....	95
3.6	Wollastonite solution.....	99
3.6.1	Crystal structure.....	99
3.6.2	Thermodynamic model.....	100
3.7	α -Ca ₂ SiO ₄ and α' -Ca ₂ SiO ₄ solutions.....	101
3.7.1	Crystal structure.....	101
3.7.2	Thermodynamic model.....	101
3.8	Liquid Fe solution.....	103

3.8.1	Thermodynamic model.....	103
3.8.1.1	Previous model: Classical Wagner Interaction Parameter Formalism	103
3.8.1.2	Present model: Associate Model.....	105
3.8.2	Discussion.....	108
4.	Application of the Thermodynamic Database to VOD Process Simulation in Stainless Steelmaking	117
4.1	Introduction.....	117
4.2	VOD process simulation.....	118
4.2.1	Overview of VOD process.....	118
4.2.2	VOD simulation (No consideration of refractories).....	119
4.2.3	Slag and refractories reaction.....	122
4.2.4	Summary.....	124
5.	Discussions and Conclusions.....	130
	References.....	137

LIST OF APPENDICES

- Appendix I : Article “Thermodynamic Modeling of the CaO-MgO-SiO₂ System”
- Appendix II : Article “Thermodynamic Modeling of the Fe-Mg-O System”
- Appendix III : Article “Thermodynamic Modeling of the FeO-Fe₂O₃-MgO-SiO₂ System”
- Appendix IV : Article “Critical Thermodynamic Evaluation and Optimization of the MgO-Al₂O₃, CaO-MgO-Al₂O₃ and MgO-Al₂O₃-SiO₂ Systems”
- Appendix V : Article “Thermodynamic Evaluation and Optimization of the MnO-Al₂O₃ and MnO-Al₂O₃-SiO₂ Systems and Applications to Inclusion Engineering”
- Appendix VI : Article “Critical Thermodynamic Evaluation and Optimization of the CaO-MnO-Al₂O₃-SiO₂ System and Application to Inclusion Control”
- Appendix VII : Article “Thermodynamic Modeling of the MgO-Al₂O₃-CrO-Cr₂O₃ System”
- Appendix VIII : Article “Thermodynamic Evaluation and Modeling of the Fe-Co-O System”
- Appendix IX : Article “A Thermodynamic Model for Deoxidation Equilibria in Steel”
- Appendix X : Article “Computer Applications of Thermodynamic Databases to Inclusion Engineering”
- Appendix XI : Compound Energy Model (CEF)
- Appendix XII : Interpolation Techniques

LIST OF TABLES

Table 3.1 : Comparison of the model parameters for the Fe-Mg-O and Fe-Ca-O systems obtained in previous studies using the Classical Wagner Interaction Parameter Formalism with the present study using the Associate Model.....	116
--	-----

LIST OF FIGURES

Figure 3.1 :	Schematic representation of the structure of sodium silicate glass. (After Warren and Biscoe, 1938).....	14
Figure 3.2 :	Examples of discrete silicate anions thought to exist in liquid acid silicates. (after Bockris <i>et al.</i> , 1954).....	15
Figure 3.3 :	Predicted bond fractions of free (O^{2-}), broken (O^-) and bridged (O^0) oxygen in the CaO-SiO ₂ melts from the Modified Quasichemical Model compared with measurements by XPS.....	24
Figure 3.4 :	Predicted liquidus projection of the CaO-MgO-Al ₂ O ₃ system using the Modified Quasichemical Model with no additional ternary model parameters for the slag phase. (See Appendix IV).....	25
Figure 3.5 :	Predicted phase diagram of the CaAl ₂ Si ₂ O ₈ (anorthite) – MgAl ₂ O ₄ (spinel) join in the present study compared with experimental data. (Devries and Osborn, 1957; Welch, 1956).....	26
Figure 3.6 :	Comparison of experimental liquidus projection (a), and predicted liquidus projection in the present study (b) for the CaSiO ₃ -MgSiO ₃ -Al ₂ O ₃ system.....	27
Figure 3.7 :	Comparison of experimental liquidus projection (a), and predicted liquidus projection in the present study (b) for the CaO-MgO-SiO ₂ -15wt% Al ₂ O ₃ system.....	28
Figure 3.8 :	Comparison of experimental liquidus projection (a), and predicted liquidus projection in the present study (b) for the CaO-MgO-SiO ₂ -30wt% Al ₂ O ₃ system.....	29
Figure 3.9 :	Structure of the spinel AB ₂ O ₄ unit cell. (after Navrotsky, 1994).....	32
Figure 3.10 :	The variation of the cation distribution of MgAl ₂ O ₄ . The inverse parameter is defined as the mole fraction of Al ³⁺ on tetrahedral sites. Curve is calculated from model parameters. (See Appendix IV).....	32

Figure 3.11 : Site preference energies in spinels (after O'Neill and Navrotsky, 1984)	36
Figure 3.12 : Calculated heat capacity of the Co_3O_4 spinel phase. The anomaly at about 30K is anti-ferro magnetic transition and the anomaly above 1000K is low spin–high spin transition of Co^{3+} . (See Appendix VIII for details).	54
Figure 3.13 (a) : Schematic diagram for the end-members in the Fe-Al-Mg-O spinel solution in the present model (without vacancies).	62
Figure 3.13 (b) : Schematic diagram for the end-members in the Fe-Al-Mg-Cr-O spinel solution in the present model (without vacancies and Cr^{2+}).	63
Figure 3.14 : Calculated tie-lines between spinel and the Al_2O_3 - Cr_2O_3 corundum phase. (a) FeAl_2O_4 - FeCr_2O_4 and (b) MgAl_2O_4 - MgCr_2O_4 . (See Appendix VIII).	64
Figure 3.15 : Cr^{2+} solubilities in the Fe-Cr-O system at 1600°C predicted from the present spinel model. Two arrows in the figure show the directions of solubilities of $\text{Cr}^{2+}(\text{Cr}_3\text{O}_4)$ and Fe_3O_4 .	65
Figure 3.16 : Crystal structure of olivine. (after Lumpkin and Ribbe, 1983a) M1 and M2 are octahedral sites. T is a tetrahedral site and L is “leer” or an unoccupied tetrahedral site.	67
Figure 3.17 : Structure of olivine. (after Papike, 1987) M1 and M2 are octahedral sites. T is a tetrahedral site.	68
Figure 3.18 : The relationship between the cation distribution equilibrium constant, K_d , and the ratio of ionic radii of constituent cations of the olivine solution, r_B / r_A . The A cation is bigger than B. Open circles represents predicted cation distributions.	77
Figure 3.19 : Calculated miscibility gaps in the Ca_2SiO_4 - M_2SiO_4 olivine systems. (M = Mg, Mn and Fe).	77
Figure 3.20 : Predicted miscibility gap in the $[\text{Ca}, \text{Mg}, \text{Fe}^{2+}]^{\text{M}_2}[\text{Ca}, \text{Mg}, \text{Fe}^{2+}]^{\text{M}_1}\text{SiO}_4$ olivine quadrilateral (Mg_2SiO_4 - Fe_2SiO_4 - CaMgSiO_4 - CaFeSiO_4). Experimental data from Davidson and Mukhopadhyay (1984).	78

- Figure 3.21 : Crystal structure of pyroxene. (after Papike, 1987) (a) Diopside projection on (110) plane. (b) I beam diagrams illustrating the four pyroxene structures.....80
- Figure 3.22 : Predicted pyroxene quadrilateral ($\text{Mg}_2\text{Si}_2\text{O}_6$ - $\text{Fe}_2\text{Si}_2\text{O}_6$ - $\text{CaMgSi}_2\text{O}_6$ - $\text{CaFeSi}_2\text{O}_6$) at 1200° and 900°C in this study. Noted that olivine (Oliv), tridymite (Trid) and wollastonite (Woll) appear in the quadrilateral because FeSiO_3 is not stable at normal pressures and $\text{CaFeSi}_2\text{O}_6$ is stable below about 950°C. Experimental points from Davidson and Lindsley (1985)90
- Figure 3.23 : Calculated cation distribution of $[\text{Mg}][\text{Mg}]\text{Si}_2\text{O}_6$ - $[\text{Fe}][\text{Fe}]\text{Si}_2\text{O}_6$ orthopyroxene compared with experimental data at different temperatures. Axes are mole fraction of Fe in octahedral sites M1 and M2. (See Appendix III).....91
- Figure 3.24 : Calculated optimized phase diagram of the $\text{CaMgSi}_2\text{O}_6$ - Mg_2SiO_6 pyroxene section. The thick line shows the calculated metastable miscibility gap in the $\text{CaMgSi}_2\text{O}_6$ - Mg_2SiO_6 clino-pyroxene solution. opx (ortho-pyroxene) and ppx (proto-pyroxene) also have similar miscibility gaps. (See Appendix I).....92
- Figure 3.25 : Optimized MgO - FeO - Fe_2O_3 phase diagram with $\log P_{\text{O}_2}$ (bar) isobars at 1160°C. Thick lines are calculated phase boundaries and thin lines are calculated oxygen isobars. (See Appendix II)97
- Figure 3.26 : Calculated nonstoichiometries of magnesiowustite phases with the variation of oxygen partial pressure at various temperatures and molar $\text{Mg}/(\text{Mg}+\text{Fe})$ ratios. (See Appendix II).....98
- Figure 3.27 : Crystal structure of wollastonite. (After Papike, 1987).....99
- Figure 3.28 : Comparison of the models for deoxidation equilibria of liquid Fe. (a) previous model (Classical Wagner Interaction Parameter Formalism: separate atom model) and (b) new model (Associate Model).....112

- Figure 3.29 : Assessed deoxidation equilibria in previous studies using the Classical Wagner Interaction Parameter Formalism. (a) Itoh *et al.*(1997): ‘3’ and JSPS (1988): ‘1’ (b) Seo and Kim (2001) and (c) Cho and Suito (1994) and Ohta and Suito (1997): ‘Eq.[7]’. Neither model can explain the entire region by one equation (need different set of model parameters depending on composition range).....113
- Figure 3.30 : Total dissolved oxygen and total dissolved Ca contents of liquid Fe in equilibrium with solid CaO. Lines calculated from database with the Associate Model. Dashed line calculated from the Classical Wagner Formalism with parameters of JSPS (1988). See Appendix IX.....114
- Figure 3.31 : Total dissolved oxygen and total dissolved Mg contents of liquid Fe in equilibrium with solid MgO. Lines calculated from the Associate Model. See Appendix IX.....114
- Figure 3.32 : Total dissolved oxygen and total dissolved Ba contents of liquid Fe in equilibrium with solid BaO. Lines calculated from the Associate Model. See Appendix IX.....115
- Figure 4.1 : The calculated amount of solid and slag phases formed during the VOD process at 1650°C for 120 tonnes stainless steel. The specific process conditions are from real plant data at ALZ in Belgium.....125
- Figure 4.2 : The calculated slag composition during the VOD process at 1650°C for 120 tonnes stainless steel126
- Figure 4.3 : The calculated composition of liquid stainless steel during the VOD process at 1650°C for 120 tonnes stainless steel.....127
- Figure 4.4 : The change of the phases at equilibrium during the dissolution of refractories at 1650°C. In the simulation, the slag is taken from the final reduction slag in Figures 4.1 and 4.2 and additions of small amounts of refractory are made incrementally, with equilibrium being recalculated after each addition. The overall refractories composition is 58MgO + 6.5Al₂O₃ + 21Cr₂O₃ + 13.5FeO (in wt%), composed of spinel and

periclase phases. The formation of periclase and spinel phases in the figure means that the slag has become saturated in these phases and so the rate of corrosion should decrease markedly.....128

Figure 4.5 : The calculated change of slag composition during the dissolution of refractories at 1650°C. The shaded square means the position of average slag composition analyzed in ALZ after the VOD process. (See text for details).....129

LIST OF SYMBOLS

C_p	Heat capacity (J/mol·K)
f_i	Activity coefficient of i relative to the infinite dilution standard state
G_i°	Standard molar Gibbs energy of i
G^m	Molar Gibbs energy of solution
g_i°	Molar Gibbs energy of component i .
G_{ij}	Molar Gibbs energy of “ ij ” component
G^E	Molar excess Gibbs energy
ΔG^{ex}	Site exchange energy
ΔG^{red}	Redox Gibbs energy
ΔG_{dis}	Gibbs energy of disordering
$\Delta g_{\text{M}^*\text{O}}^\circ$	Gibbs energy for the association reaction of M^*O from M and O
$\Delta H_{298.15}^\circ$	Enthalpy at 298.15 K
H_i°	Standard enthalpy of i
ΔH_{int}	Interchange enthalpy between sublattices
ΔH_{dis}	Enthalpy of disordering
${}^c I_{AB}$	Inversion reaction model parameters for a reaction: $G_{CAB} - G_{CBA}$
I_{AB}^c	Inversion reaction model parameters for a reaction: $G_{ABC} - G_{BAC}$
I_{ij}	Inversion model parameters for a reaction: $G_{jj} + G_{ji} - 2G_{ij}$
L	Excess interaction parameter expanded as Redlich-Kister polynomials
$L_{ij;k}$	Interaction energies between cations i and j on one sublattice when the other sublattice is occupied only by k cations.
M	M species dissolved in liquid Fe
n_i	Numbers of moles of i
n_{ij}	Number of moles of i - j bonds in one mole of solution
P	Number of sites on each sublattice (Reciprocal Ionic Solution Model)

Q	Number of sites on each sublattice (Reciprocal Ionic Solution Model)
q_{AB}^{ij}	Excess interaction parameter between A and B on i and j sublattice respectively
$q_{AB:C}$	Ternary interaction parameter of the Modified Quachemical Model (Influence of C on the formation of A-B pairs)
r_{ij}	Numbers of moles of “ ij ”
$r_{A^{n+}}$	Cationic radius of A^{n+}
S_i^o	Standard entropy of i
$S_{298.15}^o$	Entropy at 298.15 K
ΔS^{conf}	Molar configurational entropy of solution
ΔS_{dis}	Entropy of disordering
T	Absolute temperature (K)
T_{unquen}	Cation distribution is unquenchable above this temperature
T_{froz}	Cation distribution is frozen below this temperature
W_{IJ}	Molar energy of formation of cell “ IJ ”
x	Extent of disordering (disorder parameter)
X_i	Mole fraction of i in solution
X_{ij}	Mole fraction of i - j pairs
y	Mole fraction of the species on a particular sublattice
Y_i^A	Site fraction of i species in A sublattice
Z_i	Cordination numbers of i
α	Model parameter in O'Neill and Navrotsky's (1984) spinel model
α_{AB}	Excess interaction parameter in A-B solution
β	Model parameter in O'Neill and Navrotsky's (1984) spinel model
γ_i^o	Henrian activity coefficient of i at infinite dilution
γ_i	Activity coefficient of i in solution

$\varepsilon_{II,SS}$	Interaction energy between “II” and “SS” cells
ε_i^j	First-order interaction parameter between i and j in solution
ρ_i^j	Second-order interaction parameter between i and j in solution
$\rho_i^{i,j}$	Second-order cross-interaction parameter between i and j in solution
ω_{ij}	Binary excess interaction parameter (temperature-independent) for the formation of i - j pairs in the Modified Quachemical Model
η_{ij}	Binary excess interaction parameter (temperature-dependent) for the formation of i - j pairs in the Modified Quachemical Model
Δ_{ij}	Exchange reaction model parameters for a reaction: $G_{ii} + G_{jj} - G_{ij} - G_{ji}$
Δ_{ijk}	Exchange reaction model parameters for a reaction: $G_{jj} + G_{ik} - G_{ij} - G_{jk}$
Δ_{AB}^C	Exchange reaction model parameters for a reaction: $G_{AAC} + G_{BBC} - G_{ABC} - G_{BAC}$
ξ_{ij}	Fraction of subgroup ij

1. Introduction

The oxide system containing CaO, MgO, Al₂O₃, SiO₂, FeO, Fe₂O₃, MnO, CrO, Cr₂O₃, CoO, *etc.* is of great importance in the fields of metallurgy, ceramics and geology. The phases appearing in this system are: liquid oxide (slag), extensive solid solutions such as spinel, olivine, pyroxene, monoxide, *etc.*, and numerous stoichiometric compounds. In industrial and natural processes, oxide phases are often present along with gas, alloy phases, *etc.* These chemical processes are often difficult to understand due to their complexity. In order to solve practical problems and to understand the complex phenomena in these processes, therefore, a large body of experimental data has been acquired over the years at great expense.

Over the last three decades, computational thermodynamics has progressed apace with the progress of computer power. With the advances in computational thermodynamics, more and more applications to industrial processes are being carried out. A crucial and necessary requirement for accurate thermodynamic calculations in complex systems is the availability of accurate thermodynamic databases. The Center for Research in Computational Thermochemistry (CRCT) at Ecole Polytechnique has developed accurate and extensive databases for oxides, salts and alloys, as well as the FactSageTM thermodynamic computational software, over the last 25 years.

The goal of the present study is to extend the present FactSage oxide databases to wider applications in industrial and natural processes. For the development of the databases, the ‘critical thermodynamic evaluation/optimization’ technique is used. In the thermodynamic optimization of a chemical system, all available thermodynamic and phase equilibrium data are evaluated simultaneously in order to obtain one set of model equations for the Gibbs energies of all phases as functions of temperature and composition. From these equations, all of the thermodynamic properties and the phase diagrams can be back-calculated. In this way, all the experimental data are rendered self-consistent and

consistent with thermodynamic principles. Thermodynamic property data, such as activity data, can aid in the evaluation of the phase diagrams, and phase diagram measurements can be used to deduce thermodynamic properties. Discrepancies in the available data can often be resolved, and interpolations and extrapolations can be made in a thermodynamically correct manner.

In the present study, 5 binary, 9 ternary and 5 multicomponent sub-systems in the CaO-MgO-Al₂O₃-SiO₂-FeO-Fe₂O₃-MnO-CrO-Cr₂O₃-CoO system are optimized. All solid and liquid phases containing these components, such as liquid oxide, spinel, olivine, pyroxene, monoxide, wollastonite, *etc.*, are optimized using thermodynamic models based on their solution structure. All thermodynamic models used in this study show high predictive capacity in multicomponent systems. The thermodynamic models for each liquid and solid phase will be discussed in Chapter 3. The optimized results of each sub-system will be presented in Appendices I to VIII.

A new Associate Model has been developed in the course of the present work in order to model deoxidation phenomena in liquid Fe. In particular, the new model can easily explain the deoxidation phenomena of strong deoxidants such as Ca, Mg and Ba, which cannot be explained by the classical Wagner Interaction Parameter Formalism. The model can be applied to deoxidation equilibria of all common deoxidants in liquid Fe. The new model and optimized results will be discussed in Appendix IX.

Finally, in order to show the accuracy and applicability of the present optimized databases, two examples are given which are very sensitive to the accuracy of the thermodynamic databases: inclusion engineering (Appendix X) and vacuum oxygen decarburization (VOD) process simulation (Chapter 4) in steelmaking processes.

2. Thermodynamic modeling

2.1 History of CALPHAD

CALPHAD is an acronym for the CALculation of PHase Diagrams. It can perhaps be better described as: “*The Computer Coupling of Phase Diagrams and Thermochemistry.*”

Phase diagrams are used by scientists and engineers to understand thermodynamic phase equilibria. However, in many cases, there are difficulties in constructing and interpreting phase diagrams, especially for ternary and higher-order systems. Furthermore, almost all real materials are multicomponent in nature, and phase diagrams for these systems are not well-known. Thus, with the advance of computing technology, an attempt to construct multicomponent thermodynamic databases began in the late 1960's in order to understand the phase equilibria and thermodynamic properties of multicomponent systems.

All types of thermodynamic information such as phase diagrams, phase equilibria, activities, *etc.* are critically evaluated and optimized simultaneously, using proper thermodynamic models in order to construct multicomponent databases. This is the CALPHAD technique. In order to explain the thermochemistry of materials, many new thermodynamic models for complex phases with complex structures have also been developed. From the resultant databases of model parameters for lower order (binary + ternary) subsystems, the thermodynamic properties of multicomponent solutions can be predicted with good accuracy.

Several research groups performing thermodynamic modeling using the CALPHAD method have been formed worldwide. The Thermo-Calc group (Thermo-Calc, 2002) at KTH in Sweden, the THERMODATA group (THERMODATA, 2002) in France,

Thermotech Inc. (Thermotech, 2002) in the UK, and thermochemical group at NIST (NIST, 2002) in the USA, the FACT group (FactSage, 2002) (led by A. Pelton and C. Bale in cooperation with G. Eriksson at GTT Technology in Germany) at Ecole Polytechnique in Canada, the MTDATA group (MTDATA, 2002) at NPL in the UK and the IRSID group (led by H. Gaye) in France may be mentioned among others. Furthermore, the Scientific Group Thermodata Europe (SGTE, 2002) has been organized as a consortium of research groups to accelerate the development of alloy databases. The commercial databases and thermochemical software developed by these groups have been applied to interpreting and understanding complex systems academically and industrially. Based on these thermodynamic databases, kinetic processes are recently also being simulated using programs such as DICTRA (ThermoCalc, 2002) for multicomponent diffusion in alloys.

Recently, new approaches to thermodynamic modeling have been conducted with the aid of faster computing systems. Among these are first principle calculations. The first principle calculation technique starts from the fundamental physics of atoms composing a lattice. This technique is used to examine the fundamental chemistry of materials such as what structure is stable at a certain temperature and pressure. However, these techniques are still in the initial stages and cannot yet be applied quantitatively to complex systems. Therefore, combinations of first principle calculations and the CALPHAD technique are currently popular.

In conclusion, the CALPHAD technique is still the best choice for the development of thermodynamic databases for applications to complex industrial processes.

2.2 Critical Evaluation/Optimization

In a thermodynamic “optimization” of a system, all available thermodynamic and phase-equilibrium data are evaluated simultaneously in order to obtain one set of model equations for the Gibbs energies of all phases as functions of temperature and composition. From these equations, all of the thermodynamic properties and the phase diagrams can be back-calculated. In this way, the data are rendered self-consistent and consistent with thermodynamic principles. Thermodynamic property data, such as activity data, can aid in the evaluation of the phase diagram, and phase diagram measurements can be used to deduce thermodynamic properties. Discrepancies in the available data can often be resolved, and interpolations and extrapolations can be made in a thermodynamically correct manner. A small set of model parameters is obtained. This is ideal for computer storage and calculation of properties and phase diagrams.

2.2.1 Procedure of Evaluation/Optimization

- 1) Define the system of interest.
- 2) Collect all available literature:
 - Thermodynamic data: Phase equilibria (phase diagrams, two- or three-phase equilibria among solids/liquid/gas), calorimetric data (heat capacity, enthalpy of formation and enthalpy of mixing), vapour pressures (Knudsen cell, Langmuir method), chemical potentials (emf), activities, *etc.*
 - Structural data: Cation distributions between sublattices, lattice parameters, *etc.*
 - Physical properties such as magnetism, conductivity, *etc.* may sometimes aid in the evaluation of the system.
 - Also, if enough data are not available to define the thermodynamic properties of the system, useful data may be available from a higher-order system of which the system of interest is a sub-system.

- 3) Choose the appropriate thermodynamic model based upon the structure of the phase:
This is very crucial to the construction of an accurate multicomponent database because only a good physical model based on the structure of the phase, can yield good predictions of multicomponent solution properties from lower-order (binary + ternary) model parameters.

- 4) Critical evaluation of experimental data:

The quality of the literature data must be evaluated before doing the optimization. Often, the experimental data in one article are different from others by more than the experimental error limits. Moreover, although two articles report different types of experimental data, they can be compared using thermodynamic functions and may turn out not to be consistent with each other. Therefore, all articles should be evaluated critically based on the experimental techniques, sample preparation and analytical methods. All possible experimental errors should be considered during the evaluation.

Sometimes, when it is difficult to evaluate the accuracy of thermodynamic data solely from the description of the experimental technique, the accuracy of the data can also be judged during the optimization of the entire system. In certain cases, the accuracy of the experimental data in lower-order systems can be evaluated from the experimental data in higher-order systems by extrapolation.

- 5) Optimization of model parameters for the system:

Once the initial evaluation of experimental data is completed, one can start the optimization of the selected model parameters for each model based on the reliable experimental data. Usually, in this stage, optimization software (based for example on a least-square regression code) can be used for the optimization of the system.

Optimization of model parameters should be continued until back-calculation reproduces the reliable experimental results within experimental error limits.

In the case of the ternary and multicomponent oxide systems examined in the present study, the initial prediction from the models using only the binary model parameters was generally good, so that at most a few small ternary parameters were required. Hence, the optimization of the ternary and higher-order systems could be performed by trial and error without requiring optimization software.

6) Back-calculation of all thermodynamic data and phase diagrams of interest:

From the thermodynamic models, using the optimized model parameters, any type of thermodynamic calculations can be made. For the calculations, the FactSageTM (FactSage, 2002) thermochemical software was used in the present study.

2.3 FactSage™

FactSage (FactSage, 2002; Bale *et al.*, 2002) is the fusion of the FACT-Win/F*A*C*T and ChemSage/SOLGASMIX (Eriksson and Hack, 1990) thermochemical packages that were founded over 25 years ago. The FactSage package runs on a PC operating under Microsoft Windows and consists of a series of information, database, calculation and manipulation modules that enable one to access and manipulate databases for pure substances and solutions. With the various modules one can perform a wide variety of thermochemical calculations of interest to chemical and physical metallurgists, chemical engineers, corrosion engineers, inorganic chemists, geochemists, ceramists, electrochemists, environmentalists, *etc.* Currently, FactSage is installed in well over 200 universities around the world where it is used as a research tool and educational aid. Also well over 200 industrial users from various fields use FactSage to solve technical problems and perform research and development for industrial processes.

FACT databases

- 1) Compound (pure substance) database: over 4,400 compounds for solid, liquid, gaseous and aqueous phases.
- 2) Solution databases:
 - 120 non-ideal multicomponent phases for solid and liquid oxide, sulfide and salt phases and solid and liquid alloys
 - Recently, the Steel database (updated from the SGTE alloy database) containing over 60 non-ideal multicomponent alloy and carbonitride phases for 14 components.

The FACT solution database contains consistently assessed and critically evaluated thermodynamic data for $\text{SiO}_2\text{-CaO-Al}_2\text{O}_3\text{-MgO-FeO-MnO-CrO-Cr}_2\text{O}_3\text{-TiO}_2\text{-Ti}_2\text{O}_3\text{-NiO-CoO-Cu}_2\text{O-Na}_2\text{O-K}_2\text{O-ZrO}_2\text{-B}_2\text{O}_3\text{-PbO-ZnO}$ melts/glasses with dilute solutes S-

SO₄-PO₄-CO₃-F-Cl-I-OH-H₂O. Many solid oxide solutions of these components are also stored: monoxide, spinel, perovskite, pseudobrookite, melilite, olivine, wollastonite, etc. Most solid and molten salt solutions of the system Li, Na, K, Rb, Cs, Mg, Ca/F, Cl, Br, I, SO₄, CO₃, OH, NO₃ are also available as well as liquid sulfides (mattes) Fe-Ni-Co-Cr-Cu-Pb-Zn-As-S, several alloys such as dilute liquid steel, Pitzer parameters for concentrated aqueous solutions, etc. The FACT solution databases are being constantly extended and updated through a large internationally-funded research program.

2.4 Goal of the present study

The goal of the present study is to construct thermodynamically consistent databases for industrially important oxide systems for the Industrial Consortium Project funded by 16 companies worldwide: (CRD grant from the Natural Sciences and Engineering Research Council of Canada in collaboration with INCO, Noranda, Rio Tinto, Teck Cominco, Alcoa, Dupont, Shell, Corning, Pechiney, Norsk Hydro, Sintef, Schott Glas, St.-Gobain Recherche, Mintek and IIS Materials.)

Numerous binary, ternary and multicomponent sub-systems (including all solid and liquid phases) in the $\text{CaO-MgO-Al}_2\text{O}_3\text{-SiO}_2\text{-FeO-Fe}_2\text{O}_3\text{-MnO-CrO-Cr}_2\text{O}_3\text{-CoO}$ system were critically evaluated and optimized during the course of the present study. All oxide systems were optimized to be self-consistent and consistent with the alloy and salt databases of FACT. In this way, the optimized database can be incorporated with the existing FACT databases in order to increase the accuracy and range of applications.

3. Thermodynamic modeling of solid and liquid solution phases

In order to describe the thermodynamic properties of complex solid or liquid solutions, a certain sophisticated thermodynamic model, correctly based on the actual structure of the solution, is necessary. Only in this way can the contribution of the configurational entropy to the Gibbs energy of the solution be properly taken into account. A proper physical model can describe the thermodynamic properties of the solution with only a small number of model parameters. Only when the model is properly based on the real structure of the solution can it have high predictive ability (for predicting properties of multicomponent solutions from model parameters of lower-order systems.)

Basic equations

The standard Gibbs energy of a pure i component is written as:

$$G_i^\circ = H_i^\circ - TS_i^\circ \quad (3.0.1)$$

where G_i° , H_i° and S_i° are the standard Gibbs energy, enthalpy and entropy of i , respectively, and T is the absolute temperature.

When components A and B are mixed to form a solution, the Gibbs energy of solution becomes dependent on interactions between A and B.

For example, the Gibbs energy of an ideal solution can be written as:

$$G^m = (g_A^\circ n_A + g_B^\circ n_B) - T\Delta S^{\text{conf}} \quad (3.0.2)$$

$$\Delta S^{\text{conf}} = -RT(n_A \ln X_A + n_B \ln X_B) \quad (3.0.3)$$

where G^m is the molar Gibbs energy of solution and g_i° is the molar Gibbs energy of component i . ΔS^{conf} is the molar configurational entropy of solution. The ideal solution model assumes no interaction between A and B in solution. However, in the general case, the interactions between components are not zero, so the Gibbs energy of solution can be written as:

$$G^m = (g_A^\circ n_A + g_B^\circ n_B) - T\Delta S^{\text{conf}} + G^E - T\Delta S^{\text{non-conf}} \quad (3.0.4)$$

where G^E is a mixing enthalpy often expanded as a polynomial in the mole fractions:

$$G^E = \sum_{i,j} q_{AB}^{ij} X_A^i X_B^j \quad (3.0.5)$$

where the excess interaction parameters q_{AB}^{ij} ($= a + bT + cT^2 + \dots$) can be also dependent on temperature. When only q_{AB}^{11} is used to describe the thermodynamic properties of a solution, it is called a “regular” solution. When the q_{AB}^{ij} are dependent on temperature the non-configurational entropy of solution $\Delta S^{\text{non-conf}}$ is non-zero.

Model development

Although the thermodynamic properties of binary solutions may often be adequately reproduced using a polynomial expansion for the excess Gibbs energy as in equation 3.0.5, the properties of ternary or higher-order systems are generally poorly predicted from such simple polynomial-based models. This results from the failure of the model to properly describe the configurational entropy of the solution. When the configurational entropy is not well described by the model, many large arbitrary temperature- and composition-dependent excess model parameters are usually required,

and the non-configurational entropy terms of the model becomes very large. This results in poor predictive ability.

Therefore, one of the most important factors in the development of a model for a given solution is how well the model can describe the configurational entropy of the solution without the addition of large arbitrary model parameters. That is, the real structure of the solution must be taken into account in the model.

In the present study, solutions such as liquid oxide, spinel, olivine, pyroxene and monoxide, *etc.* are described using different thermodynamic models, based on the solution structures. The details of each solution structure and the dedicated model used in the present study are described in the following section. The differences between the present models and previous models are also discussed.

3.1 Liquid oxide (Slag)

3.1.1 Melt structure

Silicate slags are built up of Si atoms which are surrounded by 4 oxygen atoms arranged in the form of a tetrahedron. These SiO_4 tetrahedra are joined together in chains or rings by bridging oxygens (BO). Cations such as Na^+ , Ca^{2+} , Mg^{2+} , Mn^{2+} , Fe^{2+} , *etc.* tend to break these bridging oxygens and form non-bridging oxygens (NBO), O^- , and free oxygen ions, O^{2-} . Silicate melts contain various 3-dimensionally interconnected anion units such as SiO_2 , $\text{Si}_2\text{O}_5^{2-}$, $\text{Si}_2\text{O}_6^{4-}$, $\text{Si}_2\text{O}_7^{2-}$ and SiO_4^{4-} which coexist in the melt. The degree of depolymerization of a silicate melt is often expressed by the ratio (NBO/T). (T is the number of tetrahedrally coordinated atoms such as Si). The physical properties of the melts such as viscosity, thermal conductivity *etc.* are very dependent on the (NBO/T) ratio. Figures 3.1 and 3.2 show the schematic structure of silicate melts.

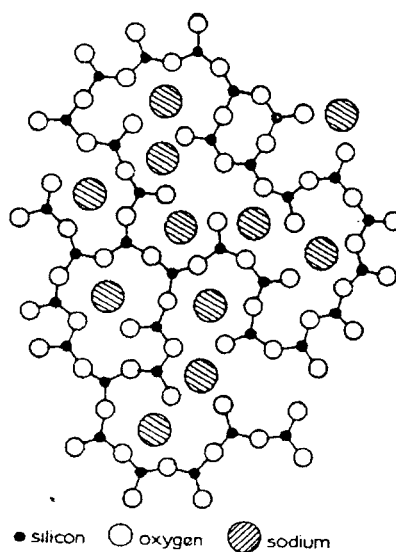


Figure 3.1 : Schematic representation of the structure of sodium silicate glass. (After Warren and Bischoe, 1938)

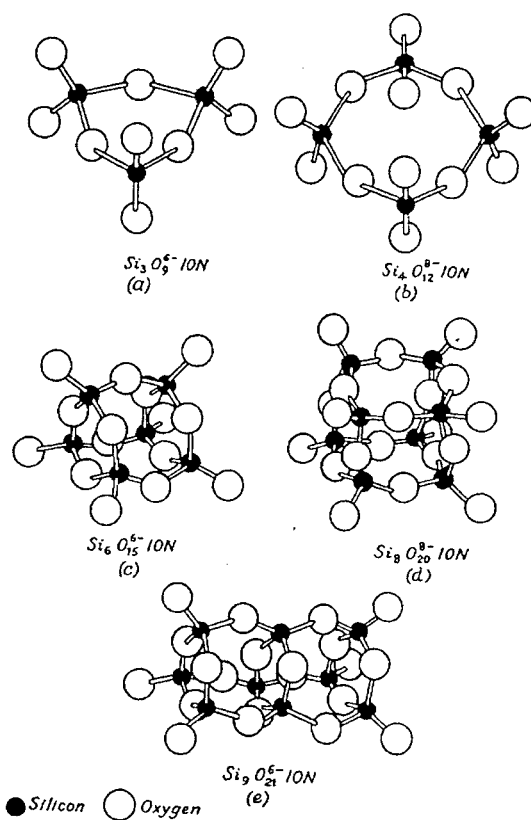


Figure 3.2 : Examples of discrete silicate anions thought to exist in liquid acid silicates.
 (after Bockris *et al.*, 1954)

3.1.2 Thermodynamic models

3.1.2.1 Previous models

Reciprocal Ionic Liquid Model

The Reciprocal Ionic Liquid Model was developed by Hillert, Jansson, Sundman and Agren (1985). This model supposes the two sublattices in the liquid. For example, in the CaO-MgO-SiO₂ system (Huang *et al.*, 1995), the liquid structure is formulated as:



where P and Q indicate the number of sites on each sublattice, which can vary with composition in order to maintain electroneutrality.

$$P = 4y_{\text{SiO}_4^{4-}} + y_{\text{O}^{2-}} \quad (3.1.2)$$

$$Q = 2y_{\text{Ca}^{2+}} + 2y_{\text{Mg}^{2+}} = 2 \quad (3.1.3)$$

where y is the site fraction; *i.e.*, the fraction of the species on a particular sublattice. The Gibbs energy of the liquid for one mole of formula unit is given by:

$$\begin{aligned} G^m = & y_{\text{Ca}^{2+}} y_{\text{SiO}_4^{4-}} G_{(\text{Ca}^{2+})_4 (\text{SiO}_4^{4-})_2} + y_{\text{Mg}^{2+}} y_{\text{SiO}_4^{4-}} G_{(\text{Mg}^{2+})_4 (\text{SiO}_4^{4-})_2} \\ & + y_{\text{Ca}^{2+}} y_{\text{O}^{2-}} G_{(\text{Ca}^{2+})_2 (\text{O}^{2-})_2} + y_{\text{Mg}^{2+}} y_{\text{O}^{2-}} G_{(\text{Mg}^{2+})_2 (\text{O}^{2-})_2} \\ & + Q y_{\text{SiO}_2^0} G_{\text{SiO}_2^0} \\ & + PRT(y_{\text{Ca}^{2+}} \ln y_{\text{Ca}^{2+}} + y_{\text{Mg}^{2+}} \ln y_{\text{Mg}^{2+}}) \\ & + QRT(y_{\text{SiO}_4^{4-}} \ln y_{\text{SiO}_4^{4-}} + y_{\text{O}^{2-}} \ln y_{\text{O}^{2-}} + y_{\text{SiO}_2^0} \ln y_{\text{SiO}_2^0}) + G^E \end{aligned} \quad (3.1.4)$$

where the G_{ij} parameters refer to one mole of formula unit of various stoichiometric compositions, $G_{\text{SiO}_2^0}$ is the Gibbs energy of liquid SiO_2 , and G^E is the excess Gibbs energy:

$$G^E = \sum_i \sum_j \sum_k y_i y_j y_k L_{i,j,k} + \sum_i \sum_k \sum_l y_i y_k y_l L_{i,k,l} \quad (3.1.5)$$

$$+ y_{\text{Ca}^{2+}} y_{\text{Mg}^{2+}} y_{\text{O}^{2-}} y_{\text{SiO}_4^{4-}} L_{\text{Ca}^{2+}, \text{Mg}^{2+}, \text{O}^{2-}, \text{SiO}_4^{4-}}$$

where i and j are species on P sites and k and l are species on Q sites. The L parameters are expanded as Redlich-Kister polynomials:

$$L_{i,j,k} = \sum_m^m L_{i,j,k} (y_i - y_j)^m \quad \text{and} \quad L_{i,k,l} = \sum_m^m L_{i,k,l} (y_k - y_l)^m \quad (3.1.6)$$

The Ionic Liquid Model has been applied to several systems (Huang *et al.*, 1995; Hallstedt 1990, 1992, 1995). However, as mentioned by Hallstedt (1995), often the ionic species defined in the binary systems are not enough to reproduce the properties of ternary systems, so certain modifications of the structural formulae must often be made. That is, often the model has poor predictive ability for ternary or higher-order systems. This is because the structure is not properly taken into account in the model. The assumption of two sublattices is “artificial.” Therefore, this results in difficulties in the development of multicomponent liquid oxide databases.

Cell model

Kapoor and Froberg (1973) applied their “cell” model to the ternary system CaO-FeO-SiO_2 . They envisaged that mixing occurs by formation of three ‘asymmetric cells’ obtained by a reaction between ‘symmetric cells’ of the metallic oxides and silica. For the CaO-SiO_2 system, the formation energy for the asymmetric cell is denoted W_{IS} ,

where the subscripts I and S denote the combination of ‘symmetric’ cells from CaO and SiO₂. In addition, interactions between the various symmetric and asymmetric cells were considered such that

$$\varepsilon_{II,SS} = 2\varepsilon_{IS,SS} \quad (3.1.7)$$

where $\varepsilon_{II,SS}$ represents the interaction between the symmetric CaO and SiO₂ cells and $\varepsilon_{IS,SS}$ represents the interaction between the asymmetric cell formed between CaO and SiO₂ and the symmetric silica cell. This was expanded with the addition of FeO so that the two further asymmetric cells are formed with energies W_{JS} and W_{IJ} , where J represents the FeO cell, and the additional interaction energies between the cells were related in the following way:

$$\varepsilon_{IJ,SS} = \varepsilon_{IS,SS} + \varepsilon_{JS,SS} \quad (3.1.8)$$

where $\varepsilon_{JS,SS}$ is the interaction energy between the asymmetric cell formed between FeO and SiO₂ and the silica cell. It was further assumed that interaction terms were negligibly small in comparison to the cell formation energies and that $\varepsilon_{IS,SS}/kT$ and $\varepsilon_{JS,SS}/kT$ were small compared to unity. Based on these assumptions they were able to define the Gibbs energy of mixing in a system such as CaO-FeO-SiO₂ as:

$$\begin{aligned} \frac{\Delta G^m}{RT} = & -\frac{3N_S}{2} \ln N_S - \frac{(1-N_S)}{2} \ln(1-N_S) - N_I \ln N_I - N_J \ln N_J \\ & + (N_I - R_{IS} - R_{IJ}) \ln(N_I - R_{IS} - R_{IJ}) \\ & + (N_J - R_{JS} - R_{IJ}) \ln(N_J - R_{JS} - R_{IJ}) \\ & + (N_S - R_{IS} - R_{JS}) \ln(N_S - R_{IS} - R_{JS}) \\ & + 2R_{IS} \ln R_{IS} + 2R_{JS} \ln R_{JS} + 2R_{IJ} \ln R_{IJ} \\ & + \frac{2W_{IS}R_{IS}}{RT} + \frac{2W_{JS}R_{JS}}{RT} + \frac{2W_{IJ}R_{IJ}}{RT} + \frac{2\varepsilon(1-N_S)(N_S - R_{IS} - R_{JS})}{RT} \end{aligned} \quad (3.1.9)$$

where

$$N_i = \frac{n_i}{\sum_i n_i + 2n_s} \text{ and } N_s = \frac{n_s}{\sum_i n_i + 2n_s} \quad (3.1.10)$$

where i represents either CaO or FeO and n_i and n_s are the numbers of moles of CaO, FeO and SiO₂. The interaction parameter ε is given by:

$$\varepsilon = \frac{\sum_i n_i \varepsilon_{IS,SS}}{\sum_i n_i} \quad (3.1.11)$$

and the various values of $R_{ij,S}$ are equal to:

$$R_{ij} = \frac{r_{ij}}{\sum_i n_i + 2n_s} \quad (3.1.12)$$

$$(N_I - R_{IS} - R_{IJ})(N_J - R_{JS} - R_{IJ}) = R_{IJ}^2 \exp\left(-\frac{2W_{IJ}}{RT}\right) \quad (3.1.13)$$

$$(N_I - R_{IS} - R_{IJ})(N_S - R_{IS} - R_{JS}) = R_{IS}^2 \exp\left(-\frac{2W_{IS}}{RT}\right) \exp\left(-\frac{2\varepsilon(1 - N_s)}{RT}\right) \quad (3.1.14)$$

$$(N_J - R_{JS} - R_{IJ})(N_S - R_{IS} - R_{JS}) = R_{JS}^2 \exp\left(-\frac{2W_{JS}}{RT}\right) \exp\left(-\frac{2\varepsilon(1 - N_s)}{RT}\right) \quad (3.1.15)$$

where the r_{ij} are the numbers of moles of the different asymmetric cell types. In equation (3.1.9), it can be seen that the first five lines correspond to the configurational entropy term. This is no longer ideal because of preferential formation of the various asymmetrical cells and the system effectively becomes ordered. Such ordering is a feature of ionic systems and will also be discussed in the next section on the

quasichemical model. Gaye and Welfringer (1984) extended the cell model to multicomponent systems.

3.1.2.2 Present model: Modified Quasichemical Model

The Modified Quasichemical Model for short-range ordering has been developed by Pelton and Blander (1984, 1986). Recently, the model has been summarized (Pelton *et al.*, 2000; Pelton and Chartrand, 2001).

For a binary system, consider the formation of two 1-2 pair bonds from a 1-1 and a 2-2 pair:

$$(1-1) + (2-2) = 2(1-2) \quad (3.1.16)$$

Let the molar Gibbs energy change for this reaction be $\Delta g_{12} = (\omega - \eta T)$. Let the coordination numbers of 1 and 2 atoms or molecules be Z_1 and Z_2 . The total number of bonds emanating from an i atom, ion or molecule is $Z_i X_i$. Hence, mass balance equations can be written as

$$Z_1 X_1 = 2n_{11} + n_{12} \quad Z_2 X_2 = 2n_{22} + n_{12} \quad (3.1.17)$$

where n_{ij} is the number of i - j bonds in one mole of solution. Equivalent fractions may be defined as

$$Y_1 = 1 - Y_2 = \frac{Z_1 X_1}{Z_1 X_1 + Z_2 X_2} \quad (3.1.18)$$

where the total number of pairs in one mole of solution is $(Z_1 X_1 + Z_2 X_2)/2$. Letting X_{ij} be the fraction of i - j pairs in solution, Equation (3.1.17) may be written as

$$2Y_1 = 2X_{11} + X_{12} \quad 2Y_2 = 2X_{22} + X_{12} \quad (3.1.19)$$

The molar enthalpy and excess entropy of mixing are assumed to be directly related to the number of 1-2 pairs:

$$\Delta H - TS^{\text{non-conf}} = (Z_1 X_1 + Z_2 X_2) X_{12} (\omega - \eta T) / 4 \quad (3.1.20)$$

An approximate expression for the configurational entropy of mixing is given by a one-dimensional Ising model:

$$\begin{aligned} \Delta S^{\text{conf}} = & -R(X_1 \ln X_1 + X_2 \ln X_2) - \frac{R}{2} (Z_1 X_1 + Z_2 X_2) [X_{11} \ln(X_{11}/Y_1^2) \\ & + X_{22} \ln(X_{22}/Y_2^2) + X_{12} \ln(X_{12}/2Y_1 Y_2)] \end{aligned} \quad (3.1.21)$$

Thus, the Gibbs energy of solution can be written as:

$$G^m = (g_1^o X_1 + g_2^o X_2) + \Delta H - TS^{\text{non-conf}} - T\Delta S^{\text{conf}} \quad (3.1.22)$$

The equilibrium distribution is calculated by minimizing G^m with respect to X_{12} at constant composition. This results in a quasichemical equilibrium constant for reaction (3.1.16):

$$\frac{X_{12}^2}{X_{11} X_{22}} = 4 \exp\left(-\frac{\omega - \eta T}{RT}\right) \quad (3.1.23)$$

When $(\omega - \eta T) = 0$ the solution of Equations (3.1.18) and (3.1.19) gives a random distribution with $X_{11} = Y_1^2$, $X_{22} = Y_2^2$ and $X_{12} = 2Y_1 Y_2$, and equation (3.1.21) reduces

to the ideal Raoultian entropy of mixing. When $(\omega - \eta T)$ becomes very negative, 1-2 pairs predominate and the plot of $\Delta H - TS^{\text{non-conf}}$ versus composition becomes V-shaped and ΔS^{conf} becomes m-shaped with minima at $Y_1 = Y_2 = 1/2$. When $(\omega - \eta T)$ is positive, (1-1) and (2-2) pairs predominate. The quasichemical model can thus also treat such clustering which accompanies positive deviations from ideality. The $(\omega - \eta T)$ parameter is usually expanded as a polynomial in the equivalent fractions.

The Modified Quasichemical Model has been applied to the molten slag phase in the present study. In a binary silicate melt, $\text{AO}_x\text{-SiO}_2$ ($A = \text{Ca, Mg, Na, Fe, Mn, ...}$), the tendency to short-range ordering can be identified with the tendency to form SiO_4^{4-} ions, or with the break-up of the silicate network and the resultant formation of second-nearest-neighbor A-Si pairs. At the orthosilicate composition, $\text{A}_{2/x}\text{SiO}_4$, a completely ordered solution can be considered to consist of only A^{2x+} cations and SiO_4^{4-} anions. This is equivalent to saying that there are only A-Si pairs and no A-A or Si-Si pairs. An Si-Si pair can be considered to be joined by a doubly-bonded (bridged) oxygen and an A-A pair is a pair of cations separated by an O^{2-} ion. Hence the quasichemical reaction is applied for second-nearest-neighbor pairs:



and this is identical to the well-known equilibrium between free, broken (singly-bonded) and bridged (doubly-bonded) oxygens:



For optimizing a given binary $\text{AO}_x\text{-SiO}_2$ system, the model parameters of the Gibbs energy of the quasichemical reaction, Δg_{ASi} are optimized, using a minimum number of parameters, in order to reproduce all reliable phase diagram data and thermodynamic data in the system.

3.1.3 Discussion

The Modified Quasichemical Model appears to reflect the actual structure of liquid silicate solutions. For example, the concentrations of the different types of oxygen as functions of concentration in the CaO-SiO_2 system, calculated from the optimized model parameters, are plotted in Figure 3.3. As can be seen in the figure, the calculated fractions of the different types of oxygen are in excellent agreement with experimental data obtained by X-ray Photoelectron Spectroscopy (XPS). (Park and Rhee, 2001).

Figure 3.4 shows the predicted phase diagram of the ternary $\text{CaO-MgO-Al}_2\text{O}_3$ system calculated using the Modified Quasichemical Model for the slag phase using only optimized binary model parameters without any additional ternary model parameters. The Gibbs energies of the three ternary compounds were optimized to reproduce the phase equilibria. The predicted phase diagram is in excellent agreement with the experimental phase diagram as will be discussed in Appendix IV. In the majority of cases, the thermodynamic properties of ternary oxide melts are well described without any additional ternary parameters, or using one or two very small ternary model parameters.

Figures 3.5 to 3.8 show the predicted quaternary phase diagram of the $\text{CaO-MgO-Al}_2\text{O}_3\text{-SiO}_2$ system. No model parameters were used for the quaternary system. That is, the thermodynamic properties of the quaternary liquid phase were predicted from the model using only the binary and ternary parameters obtained in the present study. In all

cases, the predicted diagrams and thermodynamic properties such as activities are in excellent agreement with experimental data.

In conclusion, the thermodynamic model used for the molten oxide phase, in the present study, the Modified Quasichemical Model, adequately represents the actual structure of liquid slags and also has very high predictive ability for multicomponent systems.

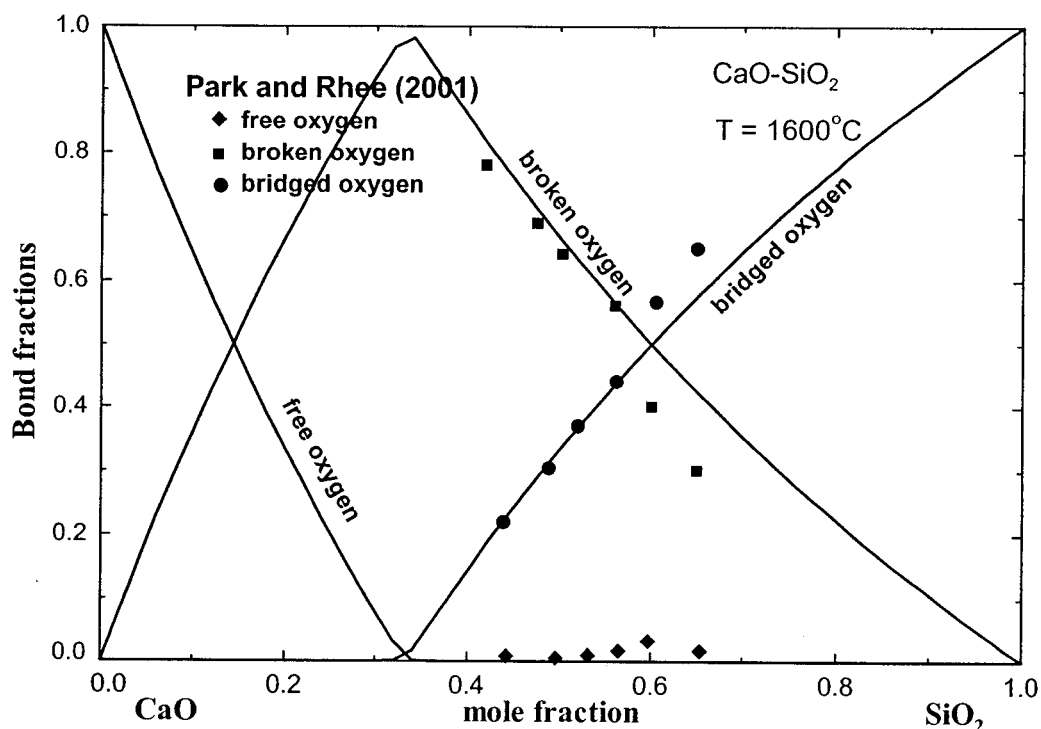


Figure 3.3 : Predicted bond fractions of free (O^{2-}), broken (O^-) and bridged (O^0) oxygen in the CaO-SiO₂ melts from the Modified Quasichemical Model compared with measurements by XPS.

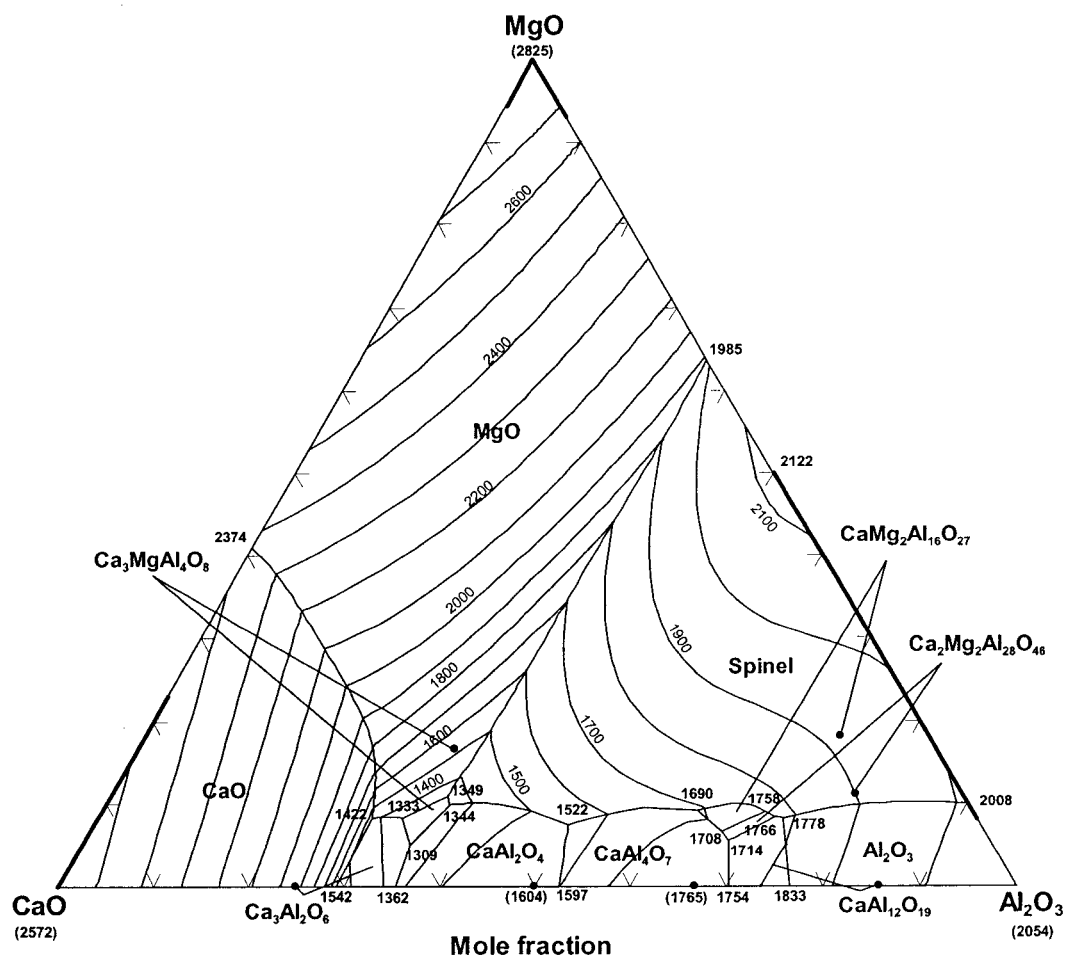


Figure 3.4 : Predicted liquidus projection of the CaO-MgO-Al₂O₃ system using the Modified Quasichemical Model with no additional ternary model parameters for the slag phase. (See Appendix IV)

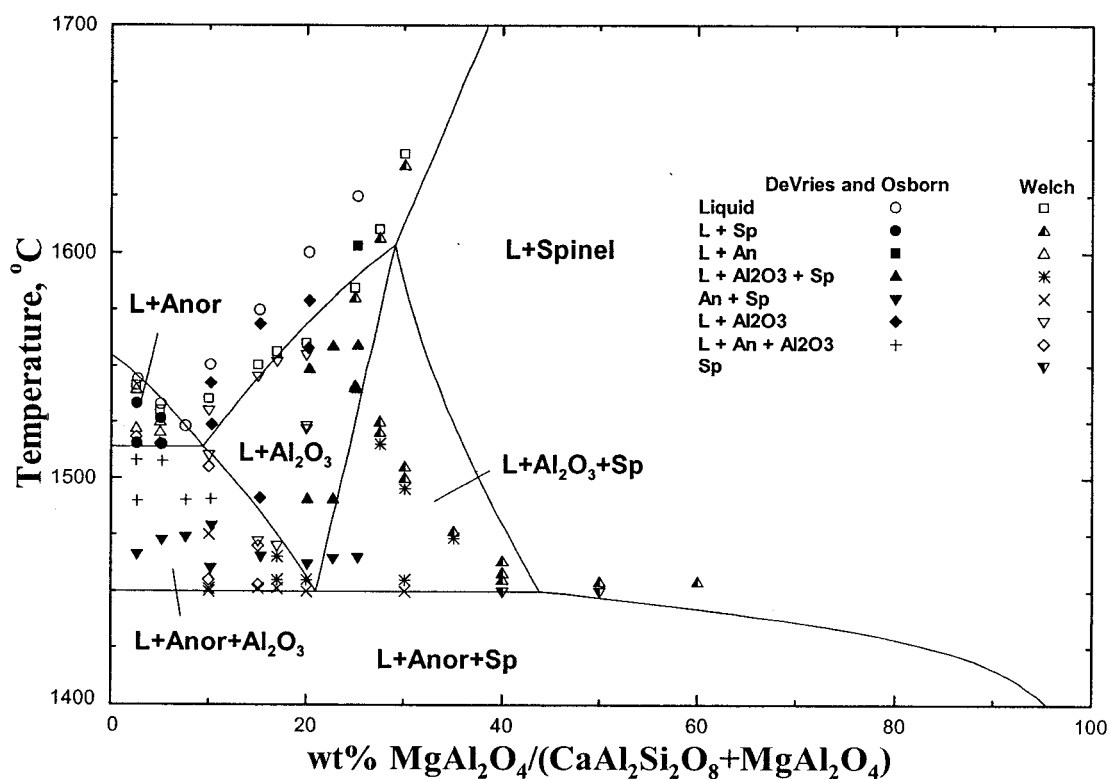


Figure 3.5 : Predicted phase diagram of the $\text{CaAl}_2\text{Si}_2\text{O}_8$ (anorthite) – MgAl_2O_4 (spinel) join in the present study compared with experimental data. (Devries and Osborn, 1957; Welch, 1956)

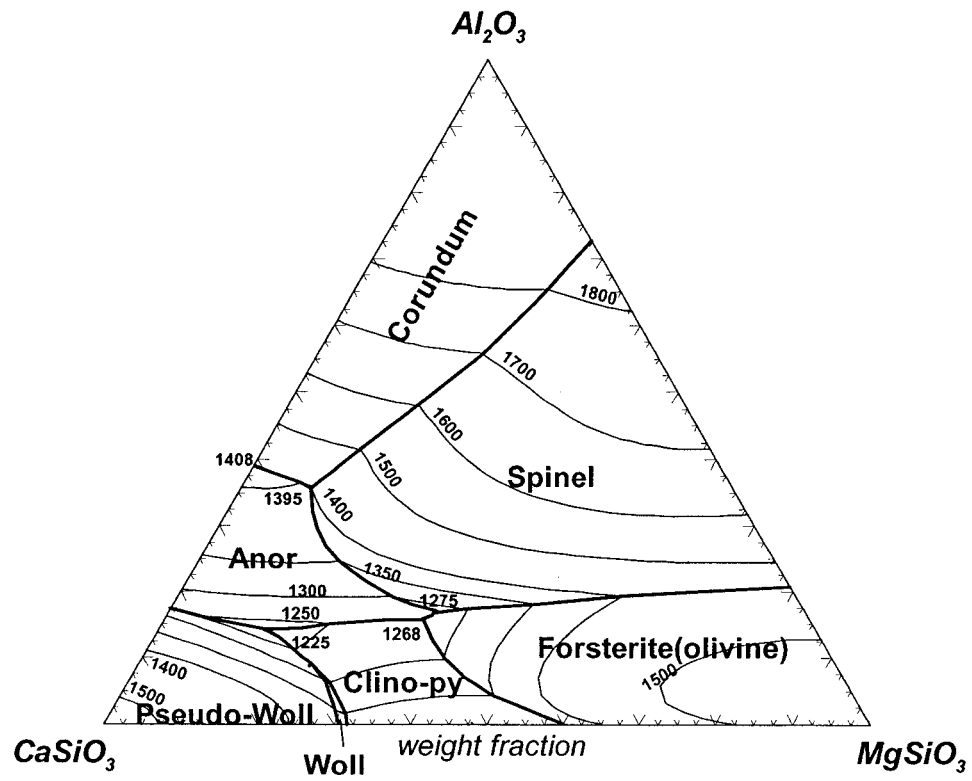
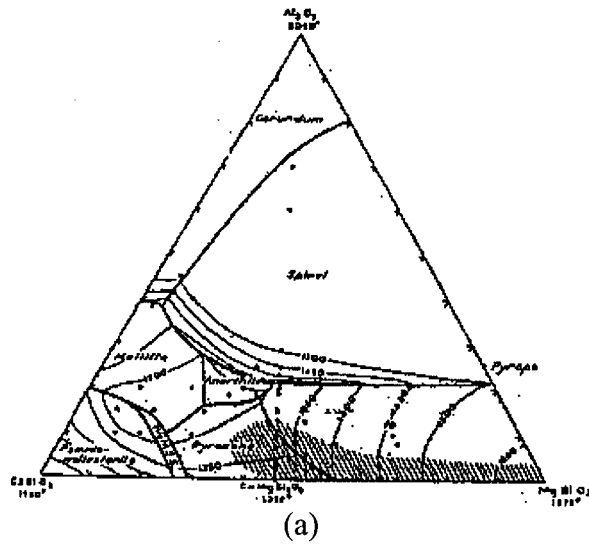


Figure 3.6 : Comparison of experimental liquidus projection (a), and predicted liquidus projection in the present study (b) for the CaSiO_3 - MgSiO_3 - Al_2O_3 system.

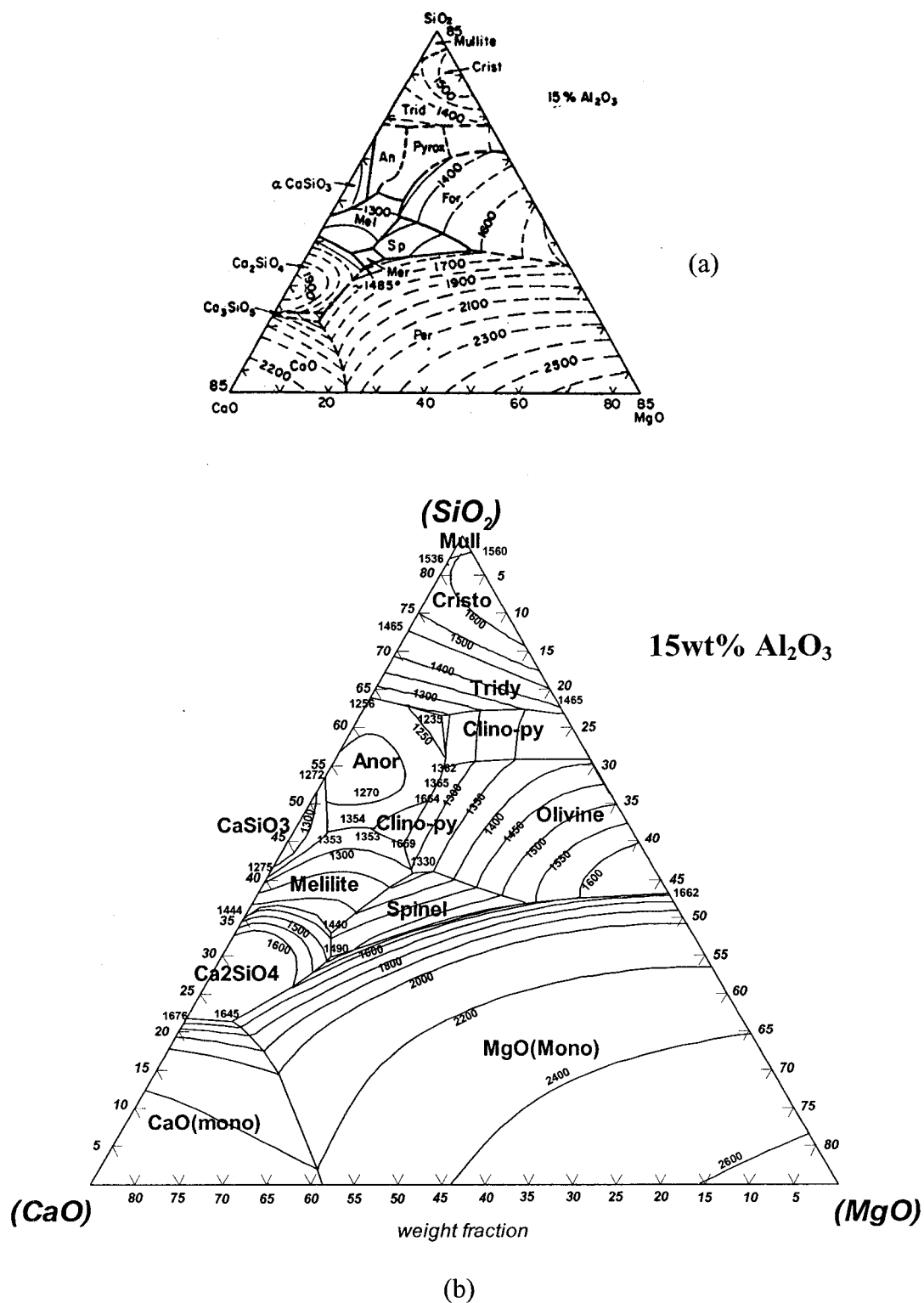


Figure 3.7 : Comparison of experimental liquidus projection (a), and predicted liquidus projection in the present study (b) for the CaO-MgO-SiO₂-15wt% Al₂O₃ system.

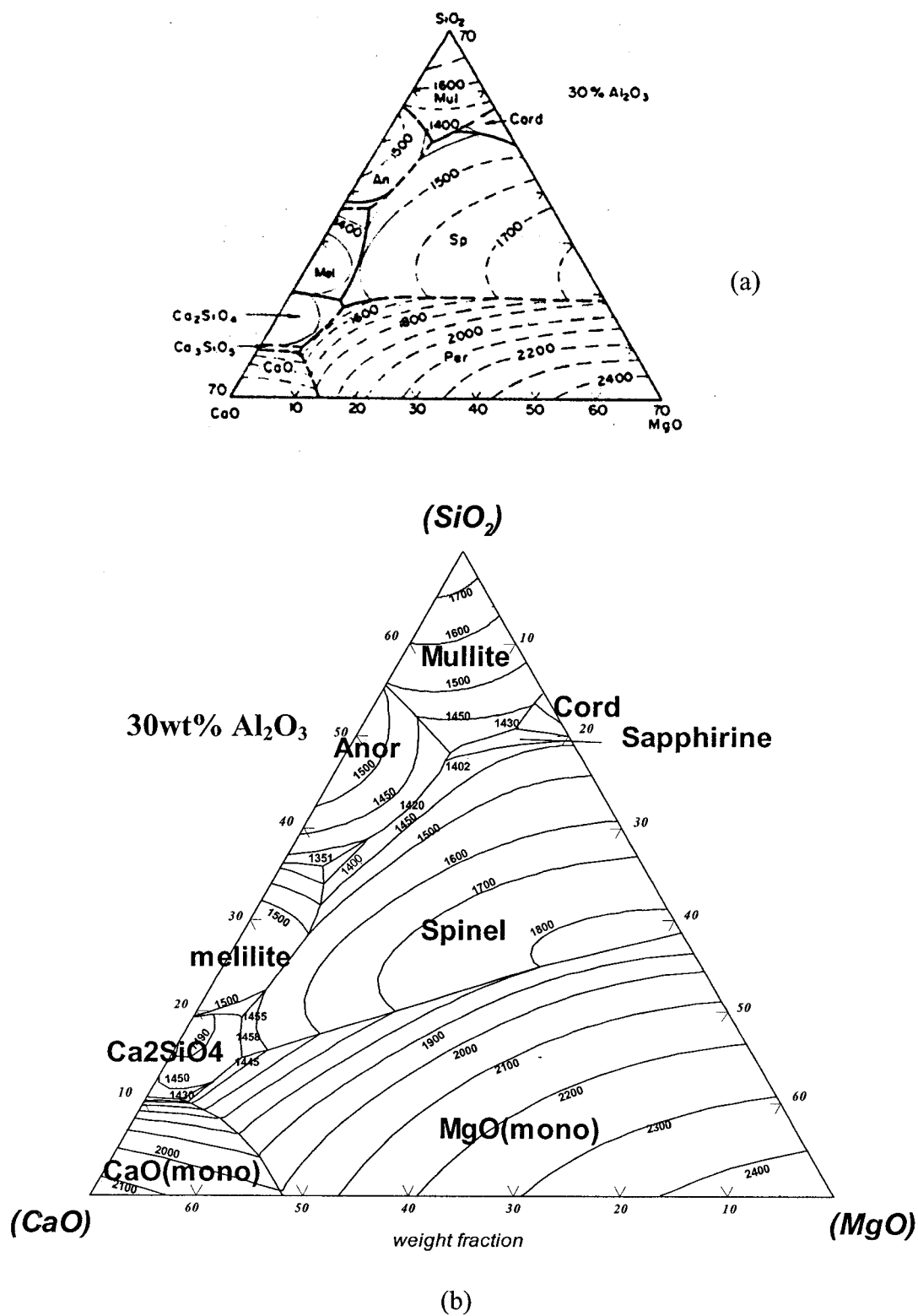


Figure 3.8 : Comparison of experimental liquidus projection (a), and predicted liquidus projection in the present study (b) for the $\text{CaO-MgO-SiO}_2\text{-}30\text{wt}\% \text{Al}_2\text{O}_3$ system.

3.2 Spinel solution

3.2.1 Crystal structure

The majority of spinel compounds belong to the space group $Fd3m$. Figure 3.9 shows the schematic structure of spinel. In this AB_2X_4 compound, A atoms are located in the 8 tetrahedral positions (represented as small filled circles in the figure), B atoms in the 16 octahedral positions (half filled circles) and oxygen atoms in the 32 positions indicated by open circles. The unit cell contains 32 oxygens and, therefore, eight AB_2O_4 formula units. The lattice parameter corresponding to oxide spinels is approximately 0.8-0.9 nm. A simple spinel contains two different cations in the ratio 2:1. If the more abundant (B) of these cations resides on octahedral sites, the spinel is called fully normal. If it is split evenly between the octahedral and tetrahedral sites, the spinel is called fully inverse. Generally, both cations in a simple spinel are present on both tetrahedral and octahedral sublattices, and the spinel is called mixed.

In general, oxide spinels AB_2O_4 are thermodynamically very stable at 1 bar total pressure. Well-known spinels are $MgAl_2O_4$ (spinel), Fe_3O_4 (magnetite), $FeAl_2O_4$ (hercynite), $MgFe_2O_4$ (magnesium ferrite), $MgCr_2O_4$ (magnesium chromite), $FeCr_2O_4$ (iron chromite), $MnAl_2O_4$ (galaxite), $CoAl_2O_4$, $NiAl_2O_4$, $ZnAl_2O_4$, $NiFe_2O_4$, *etc.* Some silicate spinels, Mg_2SiO_4 , Fe_2SiO_4 , Co_2SiO_4 and Ni_2SiO_4 are formed under high pressure because the olivine structure (A_2SiO_4) transforms to the spinel structure at high pressure. Oxide spinels often dissolve γ - A_2O_3 oxides such as γ - Al_2O_3 , γ - Fe_2O_3 , γ - Cr_2O_3 and so on. This results in the introductions of vacancies on octahedral sites and often in wide ranges of solid solution.

The spinel structure exhibits unique characteristics of cation distributions (order/disorder). Usually the cation distribution between the tetrahedral and octahedral sites is unquenchable above a certain temperature (unquenchable temperature, T_{unquen})

because the ordering-disordering process is too fast to be quenched. On the other hand, it does not reach an equilibrium distribution below a certain temperature (frozen temperature, T_{froz}) because the ordering-disordering process becomes too slow. In the case of MgAl_2O_4 (Figure 3.10), for example, the cation distribution becomes frozen in as the samples are cooled below $T_{\text{frozen}} \sim 973$ K, this temperature being estimated from the results of Redfern *et al.* as seen in Figure 3.10. Furthermore, above a temperature of $T_{\text{unquen}} \sim 1200$ K, the high temperature cation distribution cannot be retained by quenching, this temperature being estimated very roughly from the results of Wood *et al.*, which appear to level off above this temperature. Hence, above ~ 1200 K the cation distribution can only be determined by *in situ* measurements. For details, see Appendix IV.

Certain spinels are ferro- or antiferro-magnetic. This must also be considered in the thermodynamic modeling of spinel solutions. Fe_3O_4 and MgFe_2O_4 are ferromagnetic, with a critical Curie temperature. FeAl_2O_4 is anti-ferromagnetic with a Néel temperature. Sharp peaks in the measured heat capacity C_p occur at these temperatures indicating 2nd order transitions. In some cases such as CoAl_2O_4 , MgCr_2O_4 , FeCr_2O_4 , *etc.*, other peaks (anomalies) also appear in the measured C_p . These peaks are due to complex effects of crystal structure change (Jahn-Teller effect) and/or changes of electron structure (high spin - low spin transition) of the transition metal.

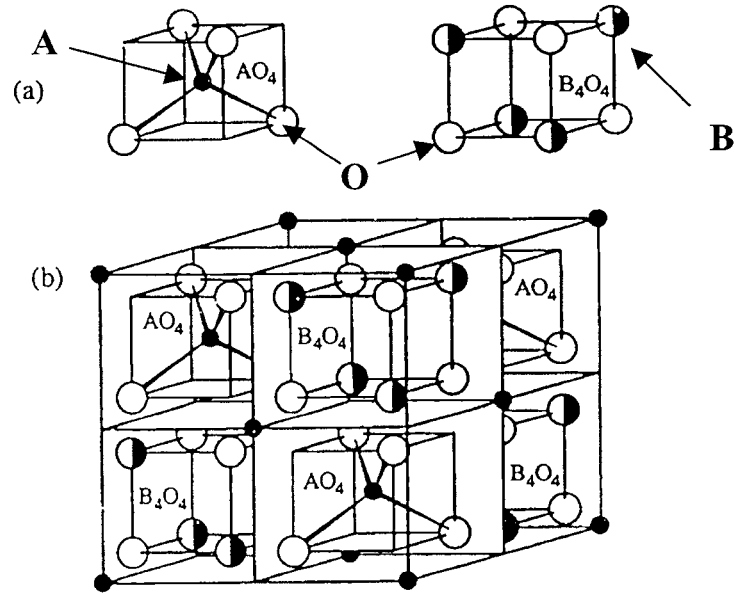


Figure 3.9 : Structure of the spinel AB_2O_4 unit cell. (after Navrotsky, 1994)

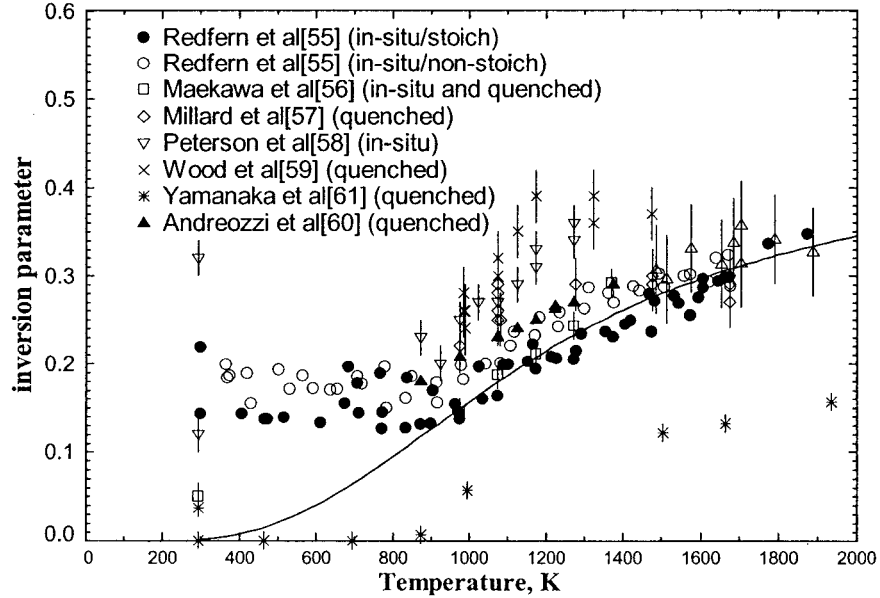


Figure 3.10 : The variation of the cation distribution of $MgAl_2O_4$. The inverse parameter is defined as the mole fraction of Al^{3+} on tetrahedral sites. Curve is calculated from model parameters. (See Appendix IV)

3.2.2 Thermodynamic model

3.2.2.1 Previous models

Navrotsky and Kleppa (1967), and O'Neill and Navrotsky (1983, 1984)

A simple thermodynamic treatment of cation distributions in simple spinels, $(A_{1-x}B_x)^T[A_xB_{2-x}]^O O_4$, is formulated as follows (Navrotsky and Kleppa, 1967). T and O represent tetrahedral and octahedral sites respectively. The enthalpy of disordering is assumed to be the extent of disordering, x , multiplied by an interchange energy, ΔH_{int} . The latter may be thought of as the enthalpy associated with the reaction



and is assumed to be independent of the degree of disorder. Then

$$\Delta H_{\text{dis}} = x\Delta H_{\text{int}} = H(x = x) - H(x = 0) \quad (3.2.2)$$

The entropy of disordering is assumed to be just the configurational entropy

$$\Delta S_{\text{dis}} = S_C = -R[x\ln x + (1-x)\ln(1-x) + x\ln(x/2) + (2-x)\ln(1-x/2)] \quad (3.2.3)$$

S_C varies with the degree of disorder, x . It varies from 0 at $x = 0$ and increases and reaches the highest entropy for a random distribution ($x = 2/3$) and decreases with further increase of x . At $x = 1$ (pure inverse spinel), the configurational entropy is $-2R\ln(1/2)$. The Gibbs energy of disordering is then

$$\Delta G_{\text{dis}} = x\Delta H_{\text{int}} - RT[x\ln x + (1-x)\ln(1-x) + x\ln(x/2) + (2-x)\ln(1-x/2)] \quad (3.2.4)$$

and, at the equilibrium state, $(dG_{\text{dis}}/dx) = 0$,

$$-RT \ln \left[\frac{x^2}{(1-x)(2-x)} \right] = \Delta H_{\text{int}} \quad (3.2.5)$$

From cation distributions observed in spinels, a series of values of interchange enthalpies can be calculated and a set of octahedral site preference energies for cations in the spinel structure can be obtained.

This simple model can be refined in two ways. Lattice energy arguments suggest that the interchange energy should depend on the degree of disorder:

$$x\Delta H_{\text{int}} = \alpha + \beta x \quad (3.2.6)$$

and there may be non-configurational contributions to the entropy of disordering. Then, as suggested by O'Neill and Navrotsky (1983, 1984),

$$\Delta G_{\text{dis}} = x(\alpha + \beta x) - T(\Delta S_{\text{C}} + \Delta S_{\text{non-C}}) \quad (3.2.7)$$

In general, experimental data are too sparse to determine both the non-configurational entropy ($\Delta S_{\text{non-C}}$) terms and the dependence of enthalpy on the degree of disordering, and O'Neill and Navrotsky chose to ignore $\Delta S_{\text{non-C}}$ as being smaller in magnitude. At equilibrium $(dG_{\text{dis}}/dx) = 0$, and neglecting the non-configurational entropy,

$$-RT \ln \left[\frac{x^2}{(1-x)(2-x)} \right] = \alpha + 2\beta x \quad (3.2.8)$$

The coefficients α and β are generally of approximately comparable magnitude and opposite sign. The effects of crystal field stabilization energies are implicitly included in

this model, since they can be accommodated in α . The coefficients α and β will depend mainly on the differences in radii and charge of the two ions, but these coefficients must be determined empirically from observed cation distributions.

O'Neill and Navrotsky (1984) applied this model to spinel solid solutions. After examining data for a number of spinels, they concluded that the value of the coefficient β depended mainly on the charge type, with $\beta \sim -20\text{kJ/mol}$ for 2-3 spinels (AB_2O_4 where A^{2+} and B^{3+}) and $\beta \sim -60\text{kJ/mol}$ for 2-4 spinels (A_2BO_4 where A^{2+} and B^{4+}). Assuming these constant values of β , a series of values of α , which maintain a meaning of cation site preference energies, could be calculated and are shown in Figure 3.11. For a spinel solid solution at any given temperature, the cation distribution is calculated by solving a set of equilibrium equations involving several pairs of cations.

Several general conclusions can be drawn: (1) The enthalpy and entropy of mixing depend strongly on temperature because the degree of order is temperature dependent. (2) The lattice parameter can vary rather nonlinearly with composition, especially at low temperature for end-members with different cation distributions. A sigmoid variation of lattice parameter with composition is commonly seen in solid solutions between a normal and an inverse spinel. (3) The calculated entropies of mixing can be quite asymmetric, especially for the mixing of a normal and an inverse spinel. This results in significantly asymmetric Gibbs energies of mixing, not because one invokes Margules parameters and asymmetry in the enthalpies and vibrational entropies of mixing, but because the configurational entropy term itself departs from symmetrical behavior. At low temperature this asymmetry is pronounced and a miscibility gap between a largely normal and a largely inverse spinel develops.

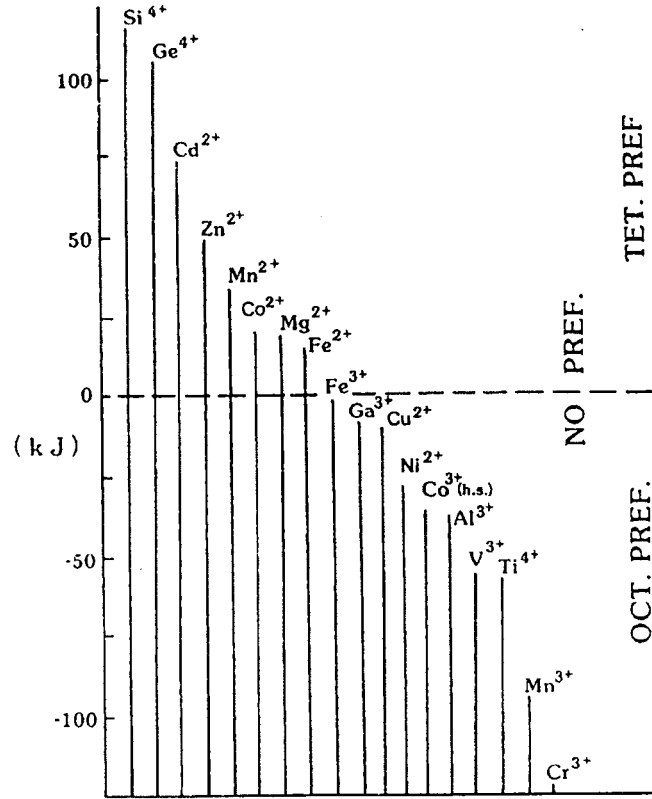
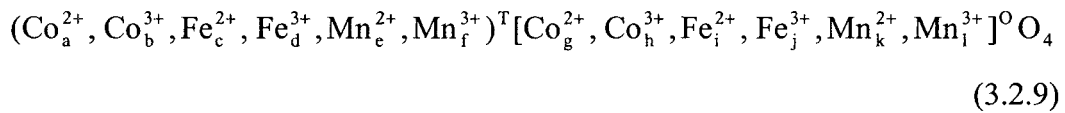


Figure 3.11 : Site preference energies in spinels (after O'Neill and Navrotsky, 1984)

Pelton (1979, 1994)

Pelton and colleagues (Pelton *et al.*, 1979 and Subramanian *et al.*, 1994) developed a spinel model for $(\text{Co}_x\text{Fe}_y\text{Mn}_{1-x-y})_3\text{O}_4$ spinels using site-exchange equilibria between tetrahedral and octahedral sites and redox reactions. (Note: This is NOT the model used for the spinel solutions in the present study.)



where T and O represent tetrahedral and octahedral sites.

Site, charge and mass balances yield:

$$a + b + c + d + e + f = 1 \quad (3.2.10)$$

$$g + h + i + j + k + l = 2 \quad (3.2.11)$$

$$2 \cdot (a + c + e + g + i + k) + 3 \cdot (b + d + f + h + j + l) = 8 \quad (3.2.12)$$

$$e + f + k + l = x_{\text{Mn}_3\text{O}_4} = 1 - x - y \quad (3.2.13)$$

$$a + b + g + h = x_{\text{Co}_3\text{O}_4} = x \quad (3.2.14)$$

$x_{\text{Mn}_3\text{O}_4}$ and $x_{\text{Co}_3\text{O}_4}$ are the overall mole fractions of Mn_3O_4 and Co_3O_4 . Seven independent internal equilibria can be formulated:

$$\text{Fe}_A^{2+} + \text{Fe}_B^{3+} = \text{Fe}_B^{2+} + \text{Fe}_A^{3+} \quad \Delta G_{\text{FeFe}}^{\text{ex}} = -RT \ln\left(\frac{i \cdot d}{c \cdot j}\right) \quad (3.2.15)$$

$$\text{Mn}_A^{2+} + \text{Mn}_B^{3+} = \text{Mn}_B^{2+} + \text{Mn}_A^{3+} \quad \Delta G_{\text{MnMn}}^{\text{ex}} = -RT \ln\left(\frac{k \cdot f}{e \cdot l}\right) \quad (3.2.16)$$

$$\text{Fe}_A^{2+} + \text{Mn}_B^{3+} = \text{Fe}_B^{2+} + \text{Mn}_A^{3+} \quad \Delta G_{\text{FeMn}}^{\text{ex}} = -RT \ln\left(\frac{i \cdot f}{c \cdot l}\right) \quad (3.2.17)$$

$$\text{Co}_A^{2+} + \text{Co}_B^{3+} = \text{Co}_B^{2+} + \text{Co}_A^{3+} \quad \Delta G_{\text{CoCo}}^{\text{ex}} = -RT \ln\left(\frac{g \cdot b}{a \cdot h}\right) \quad (3.2.18)$$

$$\text{Co}_A^{2+} + \text{Mn}_B^{3+} = \text{Co}_B^{2+} + \text{Mn}_A^{3+} \quad \Delta G_{\text{CoMn}}^{\text{ex}} = -RT \ln\left(\frac{g \cdot f}{a \cdot l}\right) \quad (3.2.19)$$

$$\text{Fe}_B^{2+} + \text{Mn}_B^{3+} = \text{Fe}_B^{3+} + \text{Mn}_B^{2+} \quad \Delta G_{\text{FeMn}}^{\text{red}} = -RT \ln\left(\frac{i \cdot l}{j \cdot k}\right) \quad (3.2.20)$$

$$\text{Fe}_B^{3+} + \text{Co}_B^{2+} = \text{Co}_B^{3+} + \text{Fe}_B^{2+} \quad \Delta G_{\text{FeCo}}^{\text{red}} = -RT \ln\left(\frac{h \cdot i}{j \cdot g}\right) \quad (3.2.21)$$

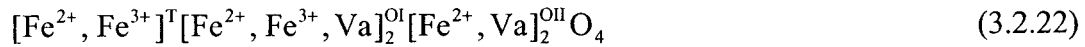
Equations (3.2.15)-(3.2.19) are site-exchange equilibria, while equations (3.2.20)-(3.2.21) are redox reactions on the octahedral sub-lattice. Other equilibria, such as redox

reactions on the tetrahedral sublattice, can be obtained by linear combinations of these equations.

Site exchange energies, ΔG^{ex} , have been estimated from crystal field theory and from an assessment of thermodynamic and spectroscopic data. Redox Gibbs energies, ΔG^{red} , have been estimated from thermodynamic data. Therefore, by solving the above seven internal equilibria along with the five charge and mass balances equations, the equilibrium state of the spinel at any given composition can be calculated.

KTH model (Hillert *et al.* 1988; Sundman 1991)

A three sublattice spinel model was proposed using the Compound Energy Formalism (CEF) (see Appendix XI) (Hillert *et al.*, 1988). For example, Fe_3O_4 is structurally formulated as:



with a tetrahedral and two octahedral sublattices. The third sublattice is used for the description of small deviations of Fe_3O_4 spinel towards excess iron in equilibrium with wustite and with liquid oxide at high temperature, while the second sublattice is used for the description of the well-known solubility of $\gamma\text{-Fe}_2\text{O}_3$. Then the Gibbs energy expression in the CEF is straightforward with 12 end-member G_{ijk} model parameters.

$$G^{\text{m}} = \sum_i \sum_j \sum_k Y_i^{\text{T}} Y_j^{\text{OI}} Y_k^{\text{OII}} G_{ijk} - TS_{\text{C}} + G^{\text{E}} \quad (3.2.23)$$

where Y_i^{T} , Y_j^{OI} and Y_k^{OII} represent the site fractions of constituents i , j and k on the tetrahedral and the I and II octahedral sublattices, G_{ijk} is the Gibbs energy of an “end-member $[\text{i}]^{\text{T}}[\text{j}]_2^{\text{OI}}[\text{k}]_2^{\text{OII}}\text{O}_4$ ” where the 3 sublattices are occupied solely by i , j , and k

species, and S_C is the configurational entropy assuming random mixing on each sublattice:

$$S_C = -R \left(\sum_i Y_i^T \ln Y_i^T + 2 \sum_j Y_j^{OI} \ln Y_j^{OI} + 2 \sum_k Y_k^{OII} \ln Y_k^{OII} \right) \quad (3.2.24)$$

There are several different ways to establish the Gibbs energies of end-members in equation (3.2.23). First stoichiometric magnetite is considered. Then, there are four parameters G_{ijVa} where i and j are Fe^{2+} and/or Fe^{3+} . At equilibrium, the following equation describes the ordering:

$$0.5(G_{Fe^{2+}Fe^{2+}Va} + G_{Fe^{2+}Fe^{3+}Va} - 2G_{Fe^{3+}Fe^{2+}Va}) + Y_{Fe^{2+}}^T (G_{Fe^{2+}Fe^{3+}Va} + G_{Fe^{3+}Fe^{2+}Va} - G_{Fe^{2+}Fe^{2+}Va} - G_{Fe^{3+}Fe^{3+}Va}) = RT \ln \frac{Y_{Fe^{3+}}^T Y_{Fe^{3+}}^T}{Y_{Fe^{3+}}^T Y_{Fe^{2+}}^T} \quad (3.2.25)$$

From the cation distribution data, one finds that the right-hand-side of equation (3.2.25) can be described by a temperature dependent function that is independent of the order. This means that a second term can be set to zero.

$$G_{Fe^{2+}Fe^{3+}Va} - G_{Fe^{3+}Fe^{3+}Va} = G_{Fe^{2+}Fe^{2+}Va} - G_{Fe^{3+}Fe^{2+}Va} \quad (3.2.26)$$

The authors interpreted the above relation as meaning that the energy for an exchange from an Fe^{2+} to an Fe^{3+} ion in the tetrahedral sublattice is independent of whether the octahedral sublattice is filled with Fe^{2+} or Fe^{3+} . It is further assumed that:

$$G_{Fe^{3+}Fe^{2+}Va} = G_{Fe^{2+}Fe^{3+}Va} \quad (3.2.27)$$

For extension to nonstoichiometric spinels (towards higher oxygen contents), relations similar to equation (3.2.26) are applied:

$$G_{\text{Fe}^{2+}\text{VaVa}} - G_{\text{Fe}^{3+}\text{VaVa}} = G_{\text{Fe}^{2+}\text{Fe}^{2+}\text{Va}} - G_{\text{Fe}^{3+}\text{Fe}^{2+}\text{Va}} \quad (3.2.28)$$

$$G_{\text{Fe}^{2+}\text{VaVa}} - G_{\text{Fe}^{2+}\text{Fe}^{3+}\text{Va}} = G_{\text{Fe}^{2+}\text{VaVa}} - G_{\text{Fe}^{3+}\text{Fe}^{3+}\text{Va}} \quad (3.2.29)$$

The model parameter $G_{\text{Fe}^{2+}\text{VaVa}}$ describes the tendency to form vacancies. The deviation towards lower oxygen content can be obtained by the following relations.

$$\begin{aligned} G_{\text{Fe}^{2+}\text{Fe}^{2+}\text{Fe}^{2+}} - G_{\text{Fe}^{2+}\text{Fe}^{2+}\text{Va}} &= G_{\text{Fe}^{2+}\text{Fe}^{3+}\text{Fe}^{2+}} - G_{\text{Fe}^{2+}\text{Fe}^{3+}\text{Va}} = G_{\text{Fe}^{2+}\text{VaFe}^{2+}} - G_{\text{Fe}^{2+}\text{VaVa}} \\ &= G_{\text{Fe}^{3+}\text{Fe}^{2+}\text{Fe}^{2+}} - G_{\text{Fe}^{3+}\text{Fe}^{2+}\text{Va}} = G_{\text{Fe}^{3+}\text{Fe}^{3+}\text{Fe}^{2+}} - G_{\text{Fe}^{3+}\text{Fe}^{3+}\text{Va}} = G_{\text{Fe}^{3+}\text{VaFe}^{2+}} - G_{\text{Fe}^{3+}\text{VaVa}} \end{aligned} \quad (3.2.30)$$

$G_{\text{Fe}^{2+}\text{Fe}^{2+}\text{Fe}^{2+}}$ is chosen to be a model parameter.

Then, four independent Gibbs energy parameters, $G_{\text{Fe}^{2+}\text{VaVa}}$, $G_{\text{Fe}^{2+}\text{Fe}^{2+}\text{Va}}$, $G_{\text{Fe}^{2+}\text{Fe}^{3+}\text{Va}}$ and $G_{\text{Fe}^{2+}\text{Fe}^{2+}\text{Fe}^{2+}}$ are selected and all other Gibbs energies are calculated from the above relations. Also, the magnetic contribution to the Gibbs energy of the spinel solution is described using the magnetic formalism suggested by Inden (1975) for “bcc” iron, although the spinel has the “fcc” structure.

Hallstedt (1992) used a similar model to describe the thermodynamic properties of MgAl_2O_4 spinel:

$$[\text{Mg}^{2+}, \text{Al}^{3+}]^{\text{T}} [\text{Mg}^{2+}, \text{Al}^{3+}, \text{Va}]_2^{\text{OI}} [\text{Mg}^{2+}, \text{Va}]_2^{\text{OH}} \text{O}_4 \quad (3.2.31)$$

It should be noted that the reference state is important in these models. As mentioned by Hallstedt (1992), for example, when combining the previously developed database for the Fe-O spinel solution (by Sundman, 1991) with his database for the $\text{MgO-Al}_2\text{O}_3$

spinel solution, the charge reference states used in the two studies was different, which caused difficulties in combining the databases. In principle, therefore, separate optimization of each spinel system using different charge reference states causes inconsistency between the optimized databases when it is attempted to combine them.

Taylor and Dinsdale (1991, 1993)

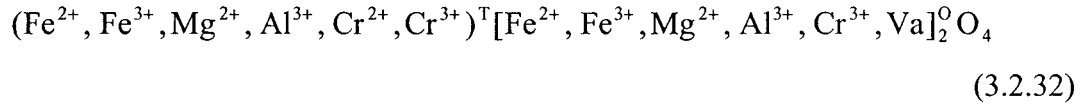
Taylor and Dinsdale proposed a two-sublattice spinel model in the framework of the Compound Energy Formalism (CEF) (see Appendix XI). They applied the model to the Fe-Cr-O and Ni-Cr-O systems: $(\text{Fe}^{2+}, \text{Fe}^{3+}, \text{Cr}^{2+}, \text{Cr}^{3+})^T [\text{Fe}^{2+}, \text{Fe}^{3+}, \text{Cr}^{3+}, \text{Va}]_2^{\text{O}} \text{O}_4$ and $(\text{Ni}^{2+}, \text{Cr}^{2+}, \text{Cr}^{3+})^T [\text{Ni}^{2+}, \text{Cr}^{3+}, \text{Va}]_2^{\text{O}} \text{O}_4$.

However, the Gibbs energies of several end-members were arbitrarily fixed in their model. This can result in arbitrary, and incorrect predictions of the properties of multicomponent spinels as shown by Decterov *et al* (2001). That is, rather than optimizing the G_{ij} parameters directly, one should optimize linear combinations of the G_{ij} which have physical significance as discussed in the following section.

3.2.2.2 Present model

Model description

A two-sublattice spinel model (Decterov *et al.*, 2001) in the framework of the Compound Energy Formalism (CEF) (see Appendix XI) (Hillert *et al.*, 1988) is used in the present study to describe the Gibbs energy of spinel solutions in the Fe-Al-Mg-Cr-Co-Ni-Zn-O system. For example, the model for the Fe-Al-Mg-Cr-O system is described below. The spinel solution in the Fe-Al-Mg-Cr-O system can be structurally formulated as:



where ions enclosed in parentheses occupy the same (tetrahedral or octahedral) sublattice, and Va represents vacancies.

In the present model, all cations except Cr^{2+} are assumed to enter both tetrahedral and octahedral sites. The assumption that divalent chromium (Cr^{2+}) can only exist on tetrahedral sites is generally accepted in the literature (See Appendix VII). The Gibbs energy of the spinel solution is expressed, in the CEF, as

$$G^m = \sum_i \sum_j Y_i^{\text{T}} Y_j^{\text{O}} G_{ij} - TS_{\text{C}} + G^{\text{E}} \quad (3.2.33)$$

where Y_i^{T} and Y_j^{O} represent the site fractions of constituents i and j on the tetrahedral and the octahedral sublattices, G_{ij} is the Gibbs energy of an “end member $[i]^{\text{T}}[j]_2^{\text{O}}\text{O}_4$ ” in which T and O sites are occupied only by i and j cations respectively, S_{C} is the configurational entropy assuming random mixing on each sublattice:

$$S_C = -R(\sum_i Y_i^T \ln Y_i^T + 2\sum_j Y_j^T \ln Y_j^T) \quad (3.2.34)$$

and G^E is the excess Gibbs energy:

$$G^E = \sum_i \sum_j \sum_k Y_i^T Y_j^T Y_k^O L_{ij;k} + \sum_i \sum_j \sum_k Y_k^T Y_i^O Y_j^O L_{k;ij} \quad (3.2.35)$$

where $L_{ij;k}$ and $L_{k;ij}$ are the interaction energies between cations i and j on one sublattice when the other sublattice is occupied only by k cations. The interaction energies, $L_{ij;k}$ and $L_{k;ij}$ are internally set in the model as follows:

$$L_{ij;k} = L_{ij;s} = \dots \quad (3.2.36)$$

$$L_{k;ij} = L_{s;ij} = \dots \quad (3.2.37)$$

That is, the interaction between i and j on a sublattice is assumed to be the same, independent of which cation resides on the other sublattice.

There are 36 Gibbs energies G_{ij} of end-members of the model to be determined in equation (3.2.33). These are the primary model parameters. However, from the experimental data alone it is not possible to determine the Gibbs energies of all end-members. Certain logical and physically meaningful assumptions should be made to fix the values of these Gibbs energies properly. In the present model, physically meaningful linear combinations of the G_{ij} are used as the actual optimized parameters. For a fully normal spinel, for example, $G_{AB} = G^o(\text{AB}_2\text{O}_4)$, the (measurable) Gibbs energy of pure normal AB_2O_4 . In this case, G_{AB} is used directly as an optimized parameter. Energies Δ_{AB} of site exchange reactions:

$$\Delta_{AB} = G_{AA} + G_{BB} - G_{AB} - G_{BA} \quad (3.2.38)$$

are also used as optimized parameters. These are expected generally to have values of about 40kJ/mol from the study by O'Neill and Navrotsky (1984) (described in the section 3.2.3). "Inversion parameters" I_{AB} :

$$I_{AB} = G_{BB} + G_{BA} - 2G_{AB} \quad (3.2.39)$$

are indicators of the tendency towards the formation of an inverse spinel structure.

Non-stoichiometry in many spinels is due to the formation of vacancies on octahedral sites. For example, non-stoichiometry in MgAl_2O_4 can be considered as a solution of $\gamma\text{-Al}_2\text{O}_3$, $(\text{Al}^{3+})(\text{Al}_{5/6}^{3+}\text{Va}_{1/6})_2\text{O}_4$, in MgAl_2O_4 . Therefore, assuming a random mixture of Al^{3+} and vacancies on the octahedral sites, the Gibbs energy of $\gamma\text{-Al}_2\text{O}_3$ is given by:

$$\begin{aligned} 8G^\circ(\gamma\text{-Al}_2\text{O}_3) &= G_{AV} + 5G_{AA} + 2RT(5\ln 5/6 + \ln 1/6) \\ &= G_{AV} + 5G_{AA} + 2RT(5\ln 5 - 6\ln 6) \end{aligned} \quad (3.2.40)$$

where A and V represent Al^{3+} and vacancies respectively. Thus, the Gibbs energies of $\gamma\text{-M}_2\text{O}_3$, $G^\circ(\gamma\text{-M}_2\text{O}_3)$, were used as optimized parameters to reproduce the solubilities of M_2O_3 in spinel solutions.

In the case of the solubility of Cr^{2+} (Cr_3O_4), because Cr^{2+} can only exist on tetrahedral sites, certain site exchange reactions of reasonable reciprocal systems were used for the model parameters in the present model as discussed below.

In addition, other site exchange reaction model parameters (Δ) can be used to describe the properties of binary spinel solutions. These exchange energies are expected generally to have small values and are often set to zero.

The model parameters in the present spinel model are described below in detail for the Fe-Al-Mg-Cr-O system: $(\text{Fe}^{2+}, \text{Fe}^{3+}, \text{Mg}^{2+}, \text{Al}^{3+}, \text{Cr}^{2+}, \text{Cr}^{3+})^T [\text{Fe}^{2+}, \text{Fe}^{3+}, \text{Mg}^{2+}, \text{Al}^{3+}, \text{Cr}^{3+}, \text{Va}]_2^{\text{O}} \text{O}_4$. For convenience, alphabetic symbols are used to represent each cation: $\text{Fe}^{2+} = \text{F}$, $\text{Fe}^{3+} = \text{E}$, $\text{Mg}^{2+} = \text{M}$, $\text{Al}^{3+} = \text{A}$, $\text{Cr}^{2+} = \text{C}$, $\text{Cr}^{3+} = \text{G}$, $\text{Va} = \text{V}$.

Optimized model parameters

End-member Gibbs energy determined

Stoichiometric Fe_3O_4

$$G_{\text{FE}} \quad G_{\text{FE}} \quad (3.2.41)$$

$$G_{\text{EF}}^{\circ} = G_{\text{FE}} \quad G_{\text{EF}}^{\circ} \quad (3.2.42)$$

$$I_{\text{FE}} = G_{\text{EE}} + G_{\text{EF}} - 2G_{\text{FE}} \quad G_{\text{EE}}^{\circ} \quad (3.2.43)$$

$$\Delta_{\text{FE}} = G_{\text{EE}} + G_{\text{FF}} - G_{\text{FE}} - G_{\text{EF}} \quad G_{\text{FF}} \quad (3.2.44)$$

$\gamma\text{-Fe}_2\text{O}_3$

$$8G^{\circ}(\gamma\text{-Fe}_2\text{O}_3) = G_{\text{EV}} + 5G_{\text{EE}} + 2RT(5\ln 5 - 6\ln 6) \quad G_{\text{EV}} \quad (3.2.45)$$

Stoichiometric FeAl_2O_4

$$G_{\text{FA}} \quad G_{\text{FA}} \quad (3.2.46)$$

$$I_{\text{FA}} = G_{\text{AA}} + G_{\text{AF}} - 2G_{\text{FA}} \quad \left. \begin{array}{l} G_{\text{AF}} \\ G_{\text{AA}} \end{array} \right\} \quad (3.2.47)$$

$$\Delta_{\text{FA}} = G_{\text{AA}} + G_{\text{FF}} - G_{\text{FA}} - G_{\text{AF}} \quad G_{\text{AA}} \quad (3.2.48)$$

$\gamma\text{-Al}_2\text{O}_3$

$$8G^\circ(\gamma - \text{Al}_2\text{O}_3) = G_{\text{AV}} + 5G_{\text{AA}} + 2RT(5\ln 5 - 6\ln 6) \quad G_{\text{AV}} \quad (3.2.49)$$

Stoichiometric MgAl_2O_4

$$G_{\text{MA}} \quad G_{\text{MA}} \quad (3.2.50)$$

$$I_{\text{MA}} = G_{\text{AA}} + G_{\text{AM}} - 2G_{\text{MA}} \quad G_{\text{AM}} \quad (3.2.51)$$

$$\Delta_{\text{MA}} = G_{\text{AA}} + G_{\text{MM}} - G_{\text{MA}} - G_{\text{AM}} \quad G_{\text{MM}} \quad (3.2.52)$$

Stoichiometric MgFe_2O_4

$$G_{\text{ME}} \quad G_{\text{ME}} \quad (3.2.53)$$

$$I_{\text{ME}} = G_{\text{EE}} + G_{\text{EM}} - 2G_{\text{ME}} \quad G_{\text{EM}} \quad (3.2.54)$$

Solution Fe-Al-Mg-O-Va

$$\Delta_{\text{FME}} = G_{\text{MM}} + G_{\text{FE}} - G_{\text{FM}} - G_{\text{ME}} \quad G_{\text{FM}} \quad (3.2.55)$$

$$\Delta_{\text{MFE}} = G_{\text{FF}} + G_{\text{ME}} - G_{\text{MF}} - G_{\text{FE}} \quad G_{\text{MF}} \quad (3.2.56)$$

$$\Delta_{\text{FEA}} = G_{\text{EE}} + G_{\text{FA}} - G_{\text{FE}} - G_{\text{EA}} \quad G_{\text{EA}} \quad (3.2.57)$$

$$\Delta_{\text{EA}} = G_{\text{AA}} + G_{\text{EE}} - G_{\text{EA}} - G_{\text{AE}} \quad G_{\text{AE}} \quad (3.2.58)$$

$$\Delta_{\text{EFV}} = G_{\text{FF}} + G_{\text{EV}} - G_{\text{EF}} - G_{\text{FV}} \quad G_{\text{FV}} \quad (3.2.59)$$

$$\Delta_{\text{AMV}} = G_{\text{MM}} + G_{\text{AV}} - G_{\text{FM}} - G_{\text{MV}} \quad G_{\text{MV}} \quad (3.2.60)$$

Stoichiometric MgCr_2O_4

$$G_{\text{MG}} \quad G_{\text{MG}} \quad (3.2.61)$$

$$I_{\text{MG}} = G_{\text{GG}} + G_{\text{GM}} - 2G_{\text{MG}} \quad \left. \begin{array}{l} G_{\text{GG}}^\circ \\ G_{\text{GM}} \end{array} \right\} \quad (3.2.62)$$

$$\Delta_{\text{MG}} = G_{\text{GG}} + G_{\text{MM}} - G_{\text{MG}} - G_{\text{GM}} \quad \left. \begin{array}{l} G_{\text{GG}}^\circ \\ G_{\text{GM}} \end{array} \right\} \quad (3.2.63)$$

Stoichiometric FeCr_2O_4

$$G_{\text{FG}} \quad G_{\text{FG}} \quad (3.2.64)$$

$$I_{\text{FG}} = G_{\text{GG}} + G_{\text{GF}} - 2G_{\text{FG}} \quad G_{\text{GF}} \quad (3.2.65)$$

 $\gamma\text{-Cr}_2\text{O}_3$

$$8G^\circ(\gamma\text{-Cr}_2\text{O}_3) = G_{\text{GV}} + 5G_{\text{GG}} + 2RT(5\ln 5 - 6\ln 6) \quad G_{\text{GV}} \quad (3.2.66)$$

Solution $\text{Fe-Al-Mg-O-Cr}^{3+}$

$$\Delta_{\text{MEG}} = G_{\text{EE}} + G_{\text{MG}} - G_{\text{ME}} - G_{\text{EG}} \quad G_{\text{EG}} \quad (3.2.67)$$

$$\Delta_{\text{EG}} = G_{\text{GG}} + G_{\text{EE}} - G_{\text{EG}} - G_{\text{GE}} \quad G_{\text{GE}} \quad (3.2.68)$$

$$\Delta_{\text{MAG}} = G_{\text{AA}} + G_{\text{MG}} - G_{\text{MA}} - G_{\text{AG}} \quad G_{\text{AG}} \quad (3.2.69)$$

$$\Delta_{\text{AG}} = G_{\text{GG}} + G_{\text{AA}} - G_{\text{AG}} - G_{\text{GA}} \quad G_{\text{GA}} \quad (3.2.70)$$

Stoichiometric Cr_3O_4

$$G_{\text{CG}} \quad G_{\text{CG}} \quad (3.2.71)$$

Addition of Cr^{2+} in tetrahedral sites: all model parameters set to zero

$$\Delta_{\text{CE}} = G_{\text{CE}} + G_{\text{FG}} - G_{\text{CG}} - G_{\text{FE}} \quad G_{\text{CE}} \quad (3.2.72)$$

$$\Delta_{\text{CA}} = G_{\text{CA}} + G_{\text{FE}} - G_{\text{FA}} - G_{\text{CE}} \quad G_{\text{CA}} \quad (3.2.73)$$

$$\Delta_{\text{CV}} = G_{\text{CV}} + G_{\text{MG}} - G_{\text{CG}} - G_{\text{MV}} \quad G_{\text{CV}} \quad (3.2.74)$$

$$\Delta_{\text{CM}} = G_{\text{CM}} + G_{\text{MG}} - G_{\text{CG}} - G_{\text{MM}} \quad G_{\text{CM}} \quad (3.2.75)$$

$$\Delta_{\text{CF}} = G_{\text{CF}} + G_{\text{FG}} - G_{\text{CG}} - G_{\text{FE}} \quad G_{\text{CF}} \quad (3.2.76)$$

The influence of magnetism on the thermodynamic properties of spinel solutions is also modeled in the present model. The phenomenological approach proposed by Hillert and Jarl (1978) for the fcc structure is used to describe the magnetic contribution to the thermodynamic functions. Details are described by Decterov *et al.* (2001).

This study is the first to model spinel solutions with a large numbers of elements over wide compositional ranges. For the development of such a large spinel database, the order of the optimizations is critical to maintaining internal consistency. The thermodynamic optimization of spinel solutions also involves several other interesting aspects as will be discussed below.

Evaluation of experimental data

Since spinels exhibit unique characteristics of cation distributions and difficulties in the preparation of samples, the following aspects should be considered during the evaluation of the experimental data.

1) Sample preparation

There are many difficulties in the preparation of stoichiometric spinel samples. For example, stoichiometric MgFe_2O_4 is only stable at very high oxygen pressure. Also, it may have a slight solubility of MgO or a considerable solubility of $\gamma\text{-Fe}_2\text{O}_3$ and it can easily form solid solutions with Fe_3O_4 . Thus, depending on the oxygen partial pressure, temperature and impurities during the sample preparation, the final products can deviate somewhat from the desired stoichiometric MgFe_2O_4 spinel. Therefore, during the evaluation of experimental data in the present study, the sample preparation techniques were examined very carefully based on several aspects: (1) Oxygen partial pressure in sample preparation, (2) Synthetic temperature, (3) Stoichiometric/non-stoichiometric (impurities), (4) Lattice parameter of final products.

2) Cation distribution (order-disorder)

The spinel structure becomes more disordered with increasing temperature and converges to a fully disordered state at infinitely high temperature. Cation distributions have been measured by several different spectroscopic techniques such as neutron powder diffraction, NMR, ESR, XRD, Mossbauer, saturation magnetization (SM), thermopower-conductivity measurements, *etc.* The best technique depends on the spinel system. For example, Mossbauer spectroscopy is unable to resolve Fe^{2+} and Fe^{3+} cations on the octahedral sites because the rate of electron hopping is faster than the precession of the iron nucleus ($\sim 10^{-7}$ seconds). (O'Neill and Navrotsky, 1984) Thus, the cation distribution of Fe_3O_4 is measurable only by a thermopower technique. XRD is more accurate than Mossbauer spectroscopy for MgFe_2O_4 . MgCr_2O_4 and FeCr_2O_4 have almost a fully normal spinel structure, so the cation distributions are not determined accurately by any technique.

Spinel has unique characteristics of cation distribution as has been discussed in section 3.2.1. As can be seen in Figure 3.10 for MgAl_2O_4 , for example, the cation distribution measured by Wood *et al.* for the quenched samples shows a constant cation distribution as temperature increases above 1200 K. From this result, T_{unquen} could be estimated to be about 1200 K for MgAl_2O_4 . From the results of Redfern *et al.*, T_{froz} could be estimated to be about 973 K for MgAl_2O_4 as can also be seen from Figure 3.10. Usually T_{unquen} and T_{froz} for spinels were found to be in the ranges 1200 to 1400K and 600 to 1000K, respectively.

Accurate cation distributions can be measured at high temperatures by an *in situ* technique to overcome the problem of unquenchability. Therefore, during the evaluation of experimental data, *in situ* measurements are preferred to quenching measurements. However, even using an *in situ* technique, the equilibrium cation distribution below T_{froz} cannot be measured. Even for *in situ* measurements, sample preparation is important because impurities (deviation from stoichiometric composition) in the sample can cause

serious error in measurements in cation distributions. For example, as can be seen from the results by Redfern *et al.* in Figure 3.10, the impurities (solubilities of $\gamma\text{-Al}_2\text{O}_3$; open symbols in the figure) results in the increase of disorder. (See Appendix IV for details)

3) Enthalpy measurements

Because spinels have unique characteristics of cation distribution, special care must be taken in interpreting the result of enthalpy measurements. Enthalpy (heat content) is usually measured by dropping a sample from a given temperature (T) to room temperature (298 K). During the measurement, the cation distribution (C·D) may not be in the equilibrium state because of the T_{unquen} and T_{froz} problems discussed above. Therefore, the measured enthalpy difference, ΔH_{mea} , should be interpreted differently according to three temperature zones:

$$T < T_{\text{froz}}$$

$$\Delta H_{\text{mea}} = H_T(\text{C} \cdot \text{D at } T_{\text{frozen}}) - H_{298}(\text{C} \cdot \text{D at } T_{\text{frozen}}) \quad (3.2.77)$$

$$T_{\text{froz}} < T < T_{\text{unquen}}$$

$$\Delta H_{\text{mea}} = H_T(\text{C} \cdot \text{D at } T) - H_{298}(\text{C} \cdot \text{D at } T) \quad (3.2.78)$$

$$T > T_{\text{unquen}}$$

$$\Delta H_{\text{mea}} = H_T(\text{C} \cdot \text{D at } T) - H_{298}(\text{C} \cdot \text{D at } T_{\text{unquen}}) \quad (3.2.79)$$

where $H_T(\text{C} \cdot \text{D at } T')$ means the enthalpy at T' of a sample with the equilibrium cation distribution of a sample at T' .

4) Enthalpy associated with the redistribution of cations

Navrotsky (1986) measured the enthalpies associated with cation redistribution using a special experimental technique. She performed certain batch experiments to measure

this. First she prepared a sample at high temperature (T_H) and dropped it to room temperature. Then, she took this sample, and dropped it from room temperature to 973K (Transposed-temperature-drop calorimetry), and measured enthalpy change (1st measurement). Next, she quenched the sample from 973 K to 298 K and then used the same sample for a second drop from room temperature to 973 K and measured another enthalpy (2nd measurement). From the difference of the measured enthalpies, the enthalpy of cation redistribution could be calculated. She assumed that the heat capacity is independent of the cation distribution.

a) Preliminary stage:

Sample at T_H -> quenching -> sample ($H_{298}(C \cdot D \text{ at } T_H)$) when $T_{\text{froz}} < T_H < T_{\text{unquen}}$

(or -> sample ($H_{298}(C \cdot D \text{ at } T_{\text{unquen}})$) when $T_H > T_{\text{unquen}}$. Thus, $T_H = T_{\text{unquen}}$)

b) 1st measurement: sample ($H_{298}(C \cdot D \text{ at } T_H)$) -> dropping

-> sample ($H_{973}(C \cdot D \text{ at } 973K)$):

$$\Delta H_{\text{mea}(1)} = H_{973}(C \cdot D \text{ at } 973K) - H_{298}(C \cdot D \text{ at } T_H)$$

c) Equilibration stage: sample ($H_{973}(C \cdot D \text{ at } 973K)$) -> equilibration and quenching

-> sample ($H_{298}(C \cdot D \text{ at } 973K)$):

d) 2nd measurement: sample ($H_{298}(C \cdot D \text{ at } 973K)$) -> dropping

-> sample ($H_{973}(C \cdot D \text{ at } 973K)$):

$$\Delta H_{\text{mea}(2)} = H_{973}(C \cdot D \text{ at } 973K) - H_{298}(C \cdot D \text{ at } 973K)$$

e) Finally, the difference between first and second measurements:

$$\Delta H_{\text{cation redistribution}} = \Delta H_{\text{mea}(2)} - \Delta H_{\text{mea}(1)} = H_{298}(C \cdot D \text{ at } T_H) - H_{298}(C \cdot D \text{ at } 973K)$$

In order to calculate values for comparison with her results, the following relations can be written. In the present study, the model also assumes that heat capacity is independent of cation distribution.

$$\begin{aligned}
H_{298}(C \cdot D \text{ at } T_H) - H_{298}(C \cdot D \text{ at } 973K) &= H_{T_H}(C \cdot D \text{ at } T_H) - H_{T_H}(C \cdot D \text{ at } 973K) \\
&= [H_{T_H}(C \cdot D \text{ at } T_H) - H_{973}(C \cdot D \text{ at } 973K)] - [H_{T_H}(C \cdot D \text{ at } 973) - H_{973}(C \cdot D \text{ at } 973)]
\end{aligned}
\tag{3.2.80}$$

Then, the first part of equation (3.2.78) can be calculated from the equilibrium state and the second part can be calculated just from the C_p expression with no consideration of cation redistribution.

5) Gibbs energy measurements and enthalpies of mixing

Cation distribution may also affect Gibbs energy measurements. Because Gibbs energies of spinels are usually measured by *in situ* techniques such as emf, vapor pressure, two- or three-phase equilibration, *etc*, the cation distributions are in an equilibrium state during the measurement if the experiment is performed at a temperature above T_{froz} . Also because enthalpies of mixing are usually measured near 1000K, which is slightly higher than T_{froz} , the measured values can be directly compared with the values obtained from equilibrium calculations.

6) Magnetism and anomalies appearing in C_p .

Spinel such as Fe_3O_4 and MgFe_2O_4 can be ferro-magnetic (strictly speaking, they are often ferri-magnetic) and FeAl_2O_4 can be anti-ferromagnetic. In order to model the contribution of magnetism to the Gibbs energy (and heat capacity), the structure factor (fcc = 0.28), critical temperature (Curie or Néel temperature) and Bohr magneton number (β) of magnetic materials must be determined in the phenomenological magnetic model of Hillert and Jarl (1978). Curie temperatures and Néel temperatures are the critical temperatures for ferro- and antiferro-magnetism, respectively. Usually the critical temperature is nearly independent of the cation distribution except in the case of MgFe_2O_4 for which the Curie temperature decreases slightly with an increase of disorder.

The magnetic transition is most apparent in the heat capacity (C_p) measurements. In some spinels such as MgCr_2O_4 , FeCr_2O_4 and NiCr_2O_4 , the peak in C_p resulting from the magnetic transition is too sharp and high to be modeled by the present magnetic equation proposed by Hillert and Jarl (1978). Because the transition occurs at very low temperatures ($< 50\text{K}$), however, the magnetic contribution to the Gibbs energy can simply be directly added to the entropy at 298K ($S_{298.15}^\circ$) for these spinels without explicitly introducing magnetism in the spinel model. Moreover, in the case of these spinels, certain electronic transitions (transitions from low-spin to high-spin of transition metal M^{3+}) and structural changes (Jahn-Teller effect) of the spinel also cause anomalies in the C_p curve. These anomalies usually occur below 100K. No model has been developed to describe these effects yet. In this study, the influence of the anomalies to C_p are also simply integrated into $S_{298.15}^\circ$ in order to avoid complexity. However, in the case of Co_3O_4 (Figure 3.12), the electron transition from low-spin to high-spin of Co^{3+} has been measured above 1000K. In this case, the electron transition effects are directly added to the C_p expression of Co_3O_4 .

In the case of ferro-magnetism, where the Curie temperature is above 298K, the magnetic properties of spinels were well modeled in the present study.

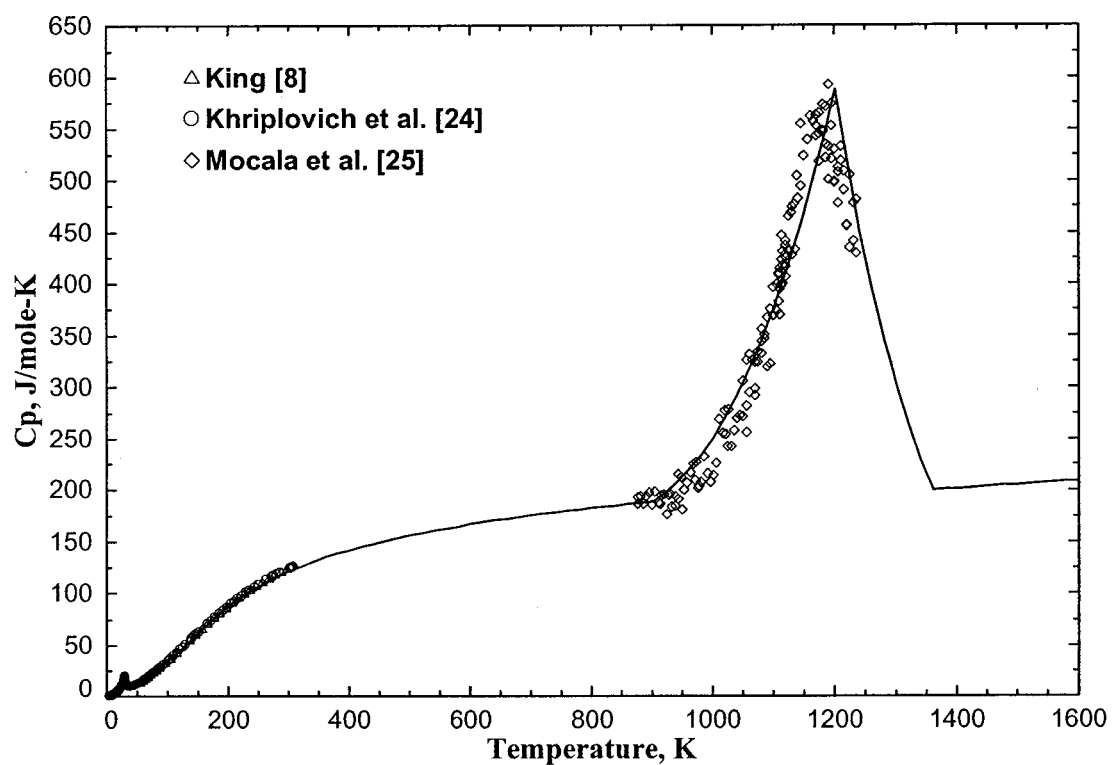


Figure 3.12 : Calculated heat capacity of the Co_3O_4 spinel phase. The anomaly at about 30K is anti-ferro magnetic transition and the anomaly above 1000K is low spin–high spin transition of Co^{3+} . (See Appendix VIII for details)

3.2.3 Procedure of Optimization and Discussion

In general, the thermodynamic properties of stoichiometric spinels are optimized in a first step and then the spinel solutions are optimized. Even stoichiometric spinel is not a simple compound because it has cation distributions dependent on temperature. Therefore, strictly speaking, a stoichiometric spinel itself is also a spinel solution. In the modeling, the structural and thermodynamic properties of stoichiometric spinel are described by Gibbs energies of four end-members correlated with the chosen model parameters.

a) Stoichiometric spinel

Usually the heat capacity, C_p , of a compound may be separated into a lattice part and a magnetic part in thermodynamic modeling.

$$C_p(T) = C_p^{\text{lattice}}(T) + C_p^{\text{magnetic}}(T) \quad (3.2.81)$$

When a compound exhibits ferro- or antiferro-magnetism, the magnetic part is non-zero.

In the present model, $C_p^{\text{lattice}}(T)$ of the normal structure and the inverse structure are assumed to be the same. That is, $C_p^{\text{lattice}}(T)$ is assumed to be independent of cation distribution.

$$C_p^{\text{lattice}}(T) = C_p^{\text{lattice}}(T) \text{ of normal spinel} = C_p^{\text{lattice}}(T) \text{ of inverse spinel} \quad (3.2.82)$$

With this assumption, C_p of a hypothetical pure normal compound end-member $(A^{2+})[B^{3+}]_2O_4$ is taken to be equal to the measured C_p of the real (mixed) spinel.

b) Closed circle spinel solution structure

As illustrated in Figure 3.13, the stoichiometric spinels were optimized in the order: Fe_3O_4 , FeAl_2O_4 , MgAl_2O_4 , MgFe_2O_4 , MgCr_2O_4 and FeCr_2O_4 . The four stoichiometric spinels form a closed circle spinel solution system, which is an inherent characteristics of the present spinel model as well as the previous models (KTH and Taylor and Dinsdale).

As noted in Figure 3.13, however, in the optimization for the last stoichiometric spinel in each circle structures, such as MgFe_2O_4 and FeCr_2O_4 , only one parameter, I_{ij} , remains for fitting the experimental data of the stoichiometric spinel. The Δ_{ij} parameter is automatically determined from the other three previously optimized Gibbs energies of end-members immediately after fixing the I_{ij} parameter. This is an inherent constraint of the present model due to the closed circle structure of spinel solutions. One I_{ij} parameter may not be enough to describe the structural and thermodynamic properties of the last stoichiometric spinel. In this event, all parameters of the other stoichiometric spinels should be re-optimized in an iterative procedure until the thermodynamic properties of all four stoichiometric spinels are properly reproduced within experimental uncertainty. For example, in the case of the Fe_3O_4 - FeAl_2O_4 - MgAl_2O_4 - MgFe_2O_4 circle, during the optimization of spinels such as Fe_3O_4 , FeAl_2O_4 and MgAl_2O_4 , the range of flexibility I_{ij} and Δ_{ij} parameters were checked and if necessary these parameters were re-optimized in order to describe the measured thermodynamic properties of all stoichiometric spinels simultaneously.

Even though the properties of all four stoichiometric spinels are well reproduced using certain sets of model parameters, this may not mean that all I_{ij} and Δ_{ij} parameters determined in the optimization are proper or reasonable for the entire closed circle of spinel solutions. Only after the set of optimized model parameters has been shown to accurately predict multi-component equilibria in the entire closed spinel circle, can the

parameters be considered as properly optimized. If the prediction is not good enough, the parameters should be optimized yet again.

c) Using the model parameters recommended by O'Neill and Navrotsky (1984)

As mentioned by Decterov *et al.* (2001), the present model can be reduced to the model suggested by O'Neill and Navrotsky (1984) for stoichiometric spinels. The following relations between the model parameters of the two models can be found:

$$\Delta_{ij} = -2\beta \quad (3.2.83)$$

$$I_{ij} = 2(\alpha_{ij} + \beta) \quad (3.2.84)$$

where α_{ij} and β are the model parameters of O'Neill and Navrotsky. (See section 3.2.2.1) In particular, O'Neill and Navrotsky, after modeling many stoichiometric AB_2O_4 spinels, found that the average value of the β parameter is about -20kJ/mol. In the course of the present study, it was found that most Δ_{ij} parameters for stoichiometric spinels (Δ_{MA} , Δ_{ME} , Δ_{AE} , *etc.*) had values close to 40kJ/mol ($= -2\beta$). This seems to be a characteristics of site exchange reactions in these spinels. Therefore, in most of cases, if possible, the Δ_{ij} parameters for stoichiometric spinels were fixed to be 40kJ/mol in the present study.

Since $MgCr_2O_4$ and $FeCr_2O_4$ are virtually pure normal spinels, their cation distributions can not be accurately determined by any spectroscopic technique. Therefore, it may be difficult to optimize the I_{ij} and Δ_{ij} parameters of these stoichiometric spinels. In this study, the values of the I_{MG} and Δ_{MG} parameters were taken from the values recommended by O'Neill and Navrotsky (1984) based on the site preference energies of cations. Since $FeCr_2O_4$ is the last spinel in the spinel circle Fe_3O_4 - $MgFe_2O_4$ - $MgCr_2O_4$ - $FeCr_2O_4$, there is only one I_{FG} parameter left. Δ_{FG} can be determined from the I_{MG} parameter. Thus, when the I_{FG} parameter is taken from O'Neill and Navrotsky, Δ_{FG} becomes different from the value recommended by O'Neill and Navrotsky, and vice

versa. Therefore, in the case of FeCr_2O_4 , only one model parameter can be taken from O'Neill and Navrotsky. During the modeling, it was found that when Δ_{FG} was set to be the same as the value proposed by O'Neill and Navrotsky, the predictive ability of the model became better than when I_{FG} was set equal to the value proposed by O'Neill and Navrotsky. In the modeling, therefore, the value of the I_{FG} parameter which satisfies $\Delta_{\text{FG}} = 40 \text{ kJ/mol}$ was used. Similarly, in all other cases when the cation distribution data is not well known, the I and Δ parameters were fixed in this way.

d) Non-stoichiometry through dissolution of $\gamma\text{-Al}_2\text{O}_3$

Once the optimization of the stoichiometric spinel solution is completed, the oxygen non-stoichiometry (vacancies) can be modeled. The solubilities of vacancies can be modeled through the Gibbs energy of $\gamma\text{-Al}_2\text{O}_3$ ($A=\text{Fe, Al, Cr}$) and other parameters such as Δ_{EFV} and Δ_{AMV} . For example, the solubility of Al_2O_3 in MgAl_2O_4 spinel depends on the Gibbs energy of $\gamma\text{-Al}_2\text{O}_3$ and Δ_{AMV} . However, since the present study deals with the general spinel solution database containing Mg, Co, Ni, Fe and Zn, the Gibbs energy of $\gamma\text{-Al}_2\text{O}_3$ must be determined to be consistent with the observed solubilities limits of Al_2O_3 in all aluminate spinels such as MgAl_2O_4 , CoAl_2O_4 , NiAl_2O_4 , FeAl_2O_4 and ZnAl_2O_4 simultaneously. This is one more constraint in developing a general database for spinel solutions.

e) Parallel binary spinel solutions

Next, the binary spinel solutions such as $\text{MgAl}_2\text{O}_4\text{-MgFe}_2\text{O}_4$, $\text{MgFe}_2\text{O}_4\text{-Fe}_3\text{O}_4$, $\text{MgAl}_2\text{O}_4\text{-MgCr}_2\text{O}_4$, $\text{MgCr}_2\text{O}_4\text{-MgFe}_2\text{O}_4$, *etc.* can be optimized based on the results of simple stoichiometric spinels. The parameters in equations (3.2.55)-(3.2.58) and (3.2.67)-(3.2.70) are used to describe the thermodynamic properties of binary spinel solutions. In this stage, the phase equilibria between the spinel solutions and other solutions such as corundum and monoxide should be taken into account in order to optimize the parameters. It should be noted that the thermodynamic properties of 'parallel binary solutions' in the closed circle structure are influenced by the same

solution model parameters. (As can be seen in the Figure 13, ‘parallel binary solutions’ means two binary solutions which are parallel to each other in the square of the closed spinel structure. That is, for example in the $\text{Fe}_3\text{O}_4\text{-FeAl}_2\text{O}_4\text{-MgAl}_2\text{O}_4\text{-MgFe}_2\text{O}_4$, the binary $\text{MgAl}_2\text{O}_4\text{-MgFe}_2\text{O}_4$ and $\text{FeAl}_2\text{O}_4\text{-Fe}_3\text{O}_4$ solutions are parallel binary solutions as are the binary $\text{MgFe}_2\text{O}_4\text{-Fe}_3\text{O}_4$ and $\text{MgAl}_2\text{O}_4\text{-FeAl}_2\text{O}_4$ solutions.) For example, Δ_{FEA} and Δ_{EA} can influence both $\text{Fe}_3\text{O}_4\text{-FeAl}_2\text{O}_4$ and $\text{MgFe}_2\text{O}_4\text{-MgAl}_2\text{O}_4$ solutions simultaneously, and Δ_{MFE} and Δ_{FME} can influence both $\text{Fe}_3\text{O}_4\text{-MgFe}_2\text{O}_4$ and $\text{MgAl}_2\text{O}_4\text{-MgFe}_2\text{O}_4$ solutions simultaneously. This is yet another constraint on the present thermodynamic model.

The thermodynamic properties of parallel binary solutions in the circle $\text{FeAl}_2\text{O}_4\text{-MgAl}_2\text{O}_4\text{-MgCr}_2\text{O}_4\text{-FeCr}_2\text{O}_4$ show this correlation very well. Figure 3.14 shows the tie-line measurements between the $\text{Al}_2\text{O}_3\text{-Cr}_2\text{O}_3$ corundum solution and the spinel $\text{MgAl}_2\text{O}_4\text{-MgCr}_2\text{O}_4$ and $\text{FeAl}_2\text{O}_4\text{-FeCr}_2\text{O}_4$ solutions respectively. Two model parameters (Δ_{MAG} and Δ_{AG}) are reserved for the adjustment of solution properties for these spinel solutions. Δ_{MAG} can alter the solution properties of both $\text{MgAl}_2\text{O}_4\text{-MgCr}_2\text{O}_4$ and $\text{FeAl}_2\text{O}_4\text{-FeCr}_2\text{O}_4$ binary solutions by affecting G_{AG} . Furthermore, since the amount of $(\text{G})[\text{A}]_2\text{O}_4$ is almost negligible due to the very low concentration of Cr^{3+} on tetrahedral sites, the effect of the Δ_{AG} parameter on G_{GA} in the spinel solution is very weak. Therefore, the Δ_{MAG} parameter was used to reproduce the data for the binary spinel solutions $\text{MgAl}_2\text{O}_4\text{-MgCr}_2\text{O}_4$ and $\text{FeAl}_2\text{O}_4\text{-FeCr}_2\text{O}_4$. In addition, a small $L_{\text{i,A,G}}$ interaction parameter was also used.

Certainly, thermodynamically, the correlation between parallel binary solutions can be thought of as resulting from the interaction of two cations which are common in parallel solutions. During the present study, it was found that the thermodynamic properties of parallel binary solutions show similar trends in most cases. For example, in the case of the $\text{MgAl}_2\text{O}_4\text{-MgCr}_2\text{O}_4$ and $\text{FeAl}_2\text{O}_4\text{-FeCr}_2\text{O}_4$ solutions, Al^{3+} and Cr^{3+} cations exist in both binary solutions. Therefore, due to the same (or similar) interaction between these

two cations regardless of the other divalent cations, the thermodynamic properties of these two parallel binary solutions may have a correlation with each other. This property is very important in modeling the general spinel solution. Although thermodynamic data are missing for many binary solutions, they can be well fixed by the properties of known parallel binary systems.

f) Miscibility gaps

Miscibility gaps are often found in binary spinel solutions below 1000°C. In certain cases, the miscibility gap can be well predicted by the models without excess interaction parameters. At other times the calculated critical temperature of the miscibility gap is somewhat lower than the observed value. In this case, small excess interaction parameters may be added. In this study, a slightly positive $L_{i;A,E}$ parameter was used for the MFe_2O_4 - MAI_2O_4 solutions ($M = Mg, Fe^{2+}, Ni$ and Co^{2+}) and similarly $L_{i;A,G}$ is used for the MCr_2O_4 - MFe_2O_4 system.

e) Cr^{2+} solubilities

The solubilities of Cr^{2+} in the spinel, that is the solubilities of Cr_3O_4 in $MgCr_2O_4$ and $FeCr_2O_4$ spinels, are also considered in this spinel model. Cr^{2+} can enter only on tetrahedral sites. To model the solubilities of Cr^{2+} in spinel solutions, the parameters in equations (3.2.72)-(3.2.76) are chosen. The first parameter, G_{CG}° , is the Gibbs energy of pure Cr_3O_4 spinel. All the other parameters in equations (3.2.72)-(3.2.76) are defined based on certain reciprocal reactions (cation exchange reactions) between tetrahedral and octahedral sites in the spinel solution. By setting these parameters equal to zero, the solubilities of Cr_3O_4 (Cr^{2+}) can be well predicted without any additional parameters. As can be seen in Figure 3.15, the predictive ability of the model is well demonstrated in the Fe-Cr-O system which is the only system in which Cr^{2+} solubilities have been well measured at several temperatures and oxygen partial pressures. For the Mg-Cr-O system, considerable Cr^{2+} solubilities are predicted in $MgCr_2O_4$ at low oxygen partial pressures. This prediction is supported by indirect experimental evidence. (See

Appendix VII.) This shows that the parameters for Cr^{2+} chosen in the present model are appropriate for a description of Cr^{2+} solubilities in the spinel solutions.

f) Different models in the same framework of the Compound Energy Formalism

Barry *et al.*(1992) demonstrated that different sets of model parameters can give equivalent descriptions of the properties of a simple spinel along the neutral compositional line. However, it should be noted that when the properties of a simple spinel are extrapolated to a multicomponent spinel solution, these different sets of model parameters may no longer necessarily give equivalent Gibbs-energy functions. Thus, it is important to note that different ways of defining model parameters, which are inter-related to the Gibbs energies of end-members of the model, eventually result in different models within the framework of the Compound Energy Formalism. (Appendix XI) It can be said that all previous models by Sundman (1991) and Hallstedt (1992) are essentially different from the present model because the present model uses a different way of defining the model parameters, although all models are formulated within the same Compound Energy Formalism. This is also true of the models for olivine and pyroxene developed in this study.

That is, the Compound Energy Formalism is not a model. It is a formalism which can be used as a framework for many models.

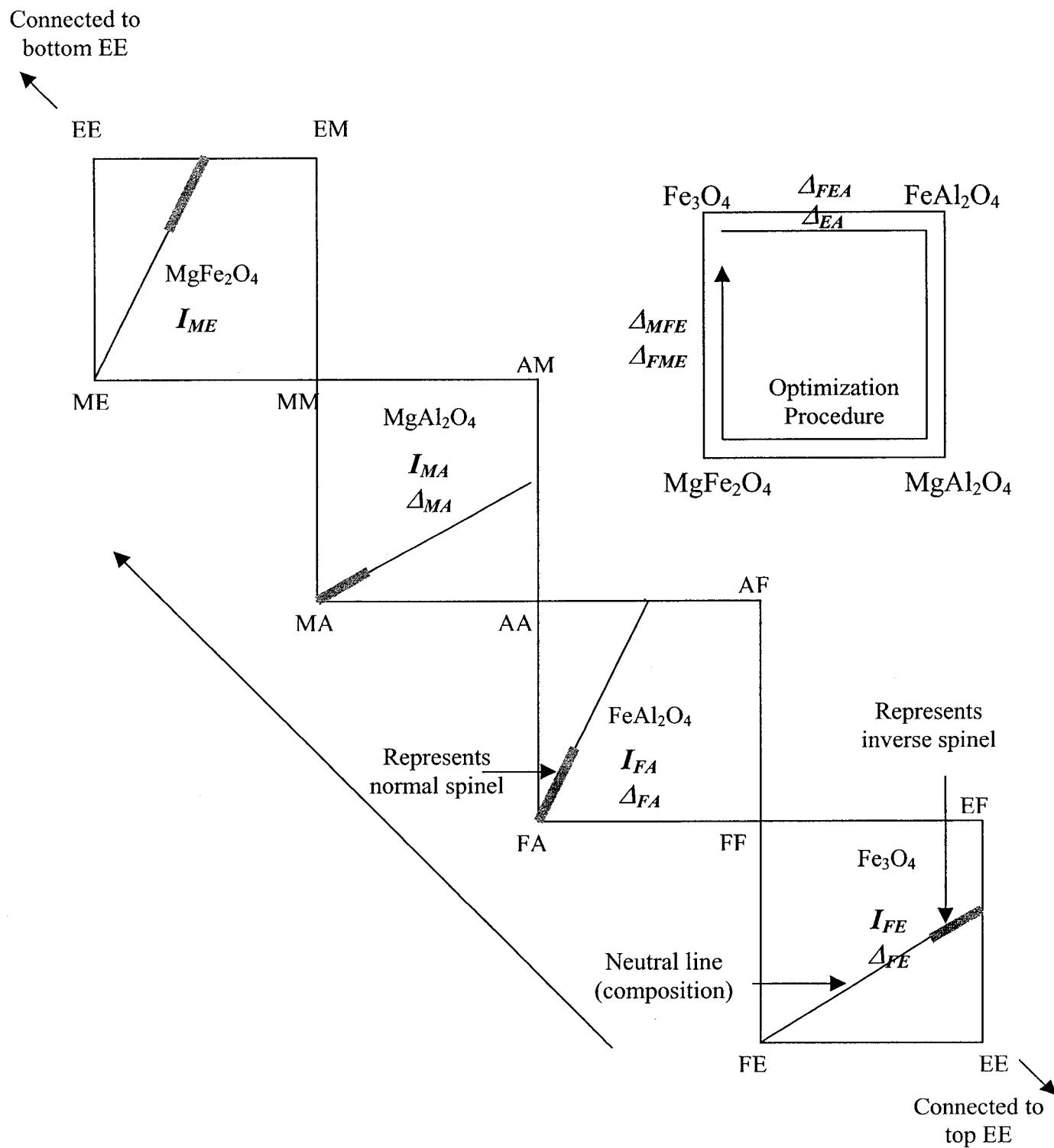


Figure 3.13 (a) : Schematic diagram for the end-members in the Fe-Al-Mg-O spinel solution in the present model (without vacancies).

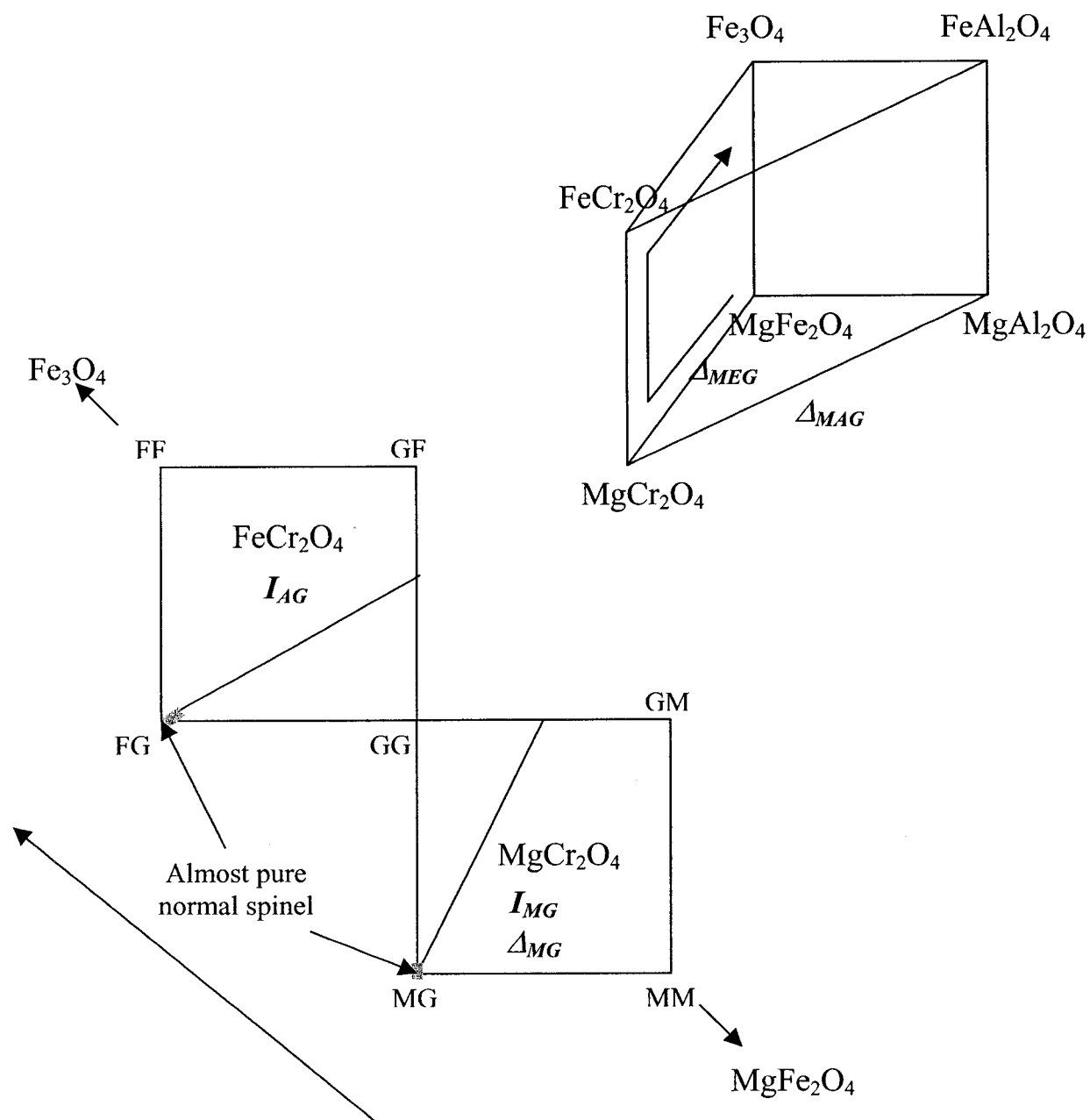
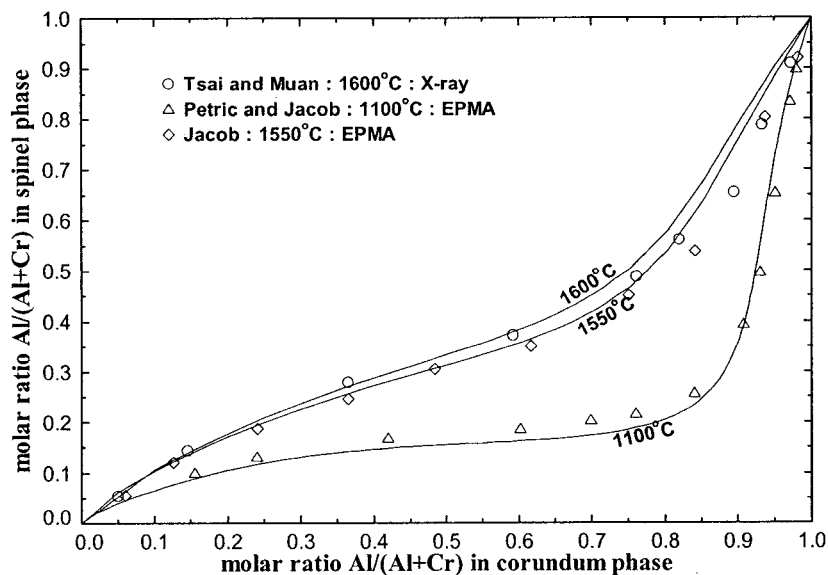
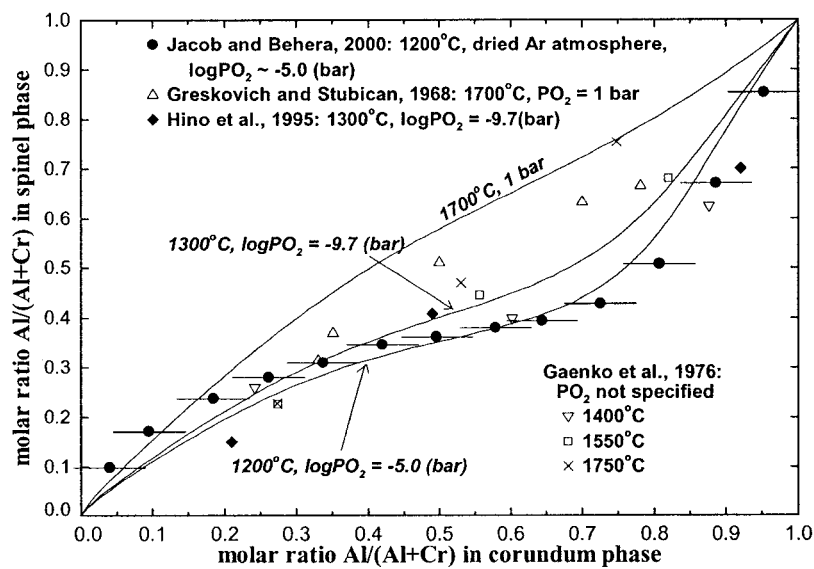


Figure 3.13 (b) : Schematic diagram for the end-members in the Fe-Al-Mg-Cr-O spinel solution in the present model (without vacancies and Cr^{2+}).



(a)



(b)

Figure 3.14 : Calculated tie-lines between spinel and the Al_2O_3 - Cr_2O_3 corundum phase. (a) FeAl_2O_4 - FeCr_2O_4 and (b) MgAl_2O_4 - MgCr_2O_4 . (See Appendix VII)

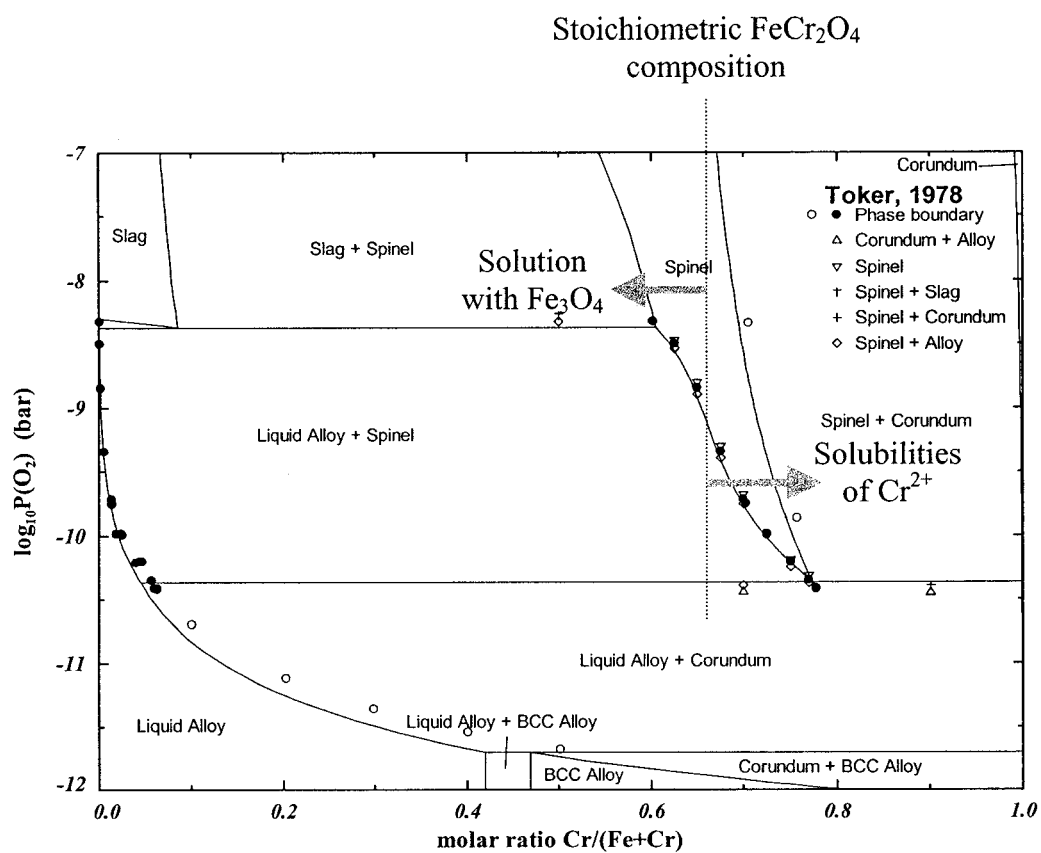


Figure 3.15 : Cr^{2+} solubilities in the Fe-Cr-O system at 1600°C predicted from the present spinel model. Two arrows in the figure show the directions of solubilities of $\text{Cr}^{2+}(\text{Cr}_3\text{O}_4)$ and Fe_3O_4 .

3.3. Olivine solution

3.3.1 Crystal structure

The structure of olivine is in the orthorhombic space group *Pbnm*. A general formula for olivine-type compounds is $(M_1)(M_2)TX_4$, where M_1 and M_2 represent octahedrally coordinated cations, T is a tetrahedrally coordinated cation and X represents the four-coordinated anions, which usually are oxygen but also may be fluorine, sulfur or selenium. M_1 and M_2 may be Li, Na, Mg, Al, Ca, Sc, Cr, Mn, Fe, Co, Ni, Zn, Ga, Y, Cd, Sm, Gd and Lu. T may be Be, B, Si, P, Ge, or Si_xGe_{1-x} . In the case of silicates, olivine is generally formulated as $(M_1)(M_2)SiO_4$. Al^{3+} , Fe^{3+} , Cr^{3+} , and Ti^{4+} are generally in low abundance in olivines. The assumption that all Fe is in the form of Fe^{2+} is generally accepted. There is no evidence of significant substitution of Al for Si in the tetrahedral site of the olivine structure.

Figures 3.16 and 3.17 show the crystal structure of olivine. The olivine structure consists of individual SiO_4 tetrahedral linked by divalent ions (Mg, Fe^{2+} , Ca, Mn, Co, Ni, *etc.*) each of which has six nearest oxygen neighbors. Divalent ions occupy one-half of the octahedral interstices and Si atoms occupy one-eighth of the tetrahedral interstices.

The M1 octahedron lies on a center of inversion and its six shared edges (four with other octahedra and two with tetrahedra) are significantly shorter (2.56-2.87 Å) than the six unshared edges (3.04-3.39 Å). The M2 octahedron is located on a mirror plane and its three shared edges (two with other octahedra and one with a silicate tetrahedron) (2.6-2.87 Å) are again shorter than the unshared edges. Thus, the M2 site is bigger than the M1 site and this difference results in the cation distributions observed in olivine solid solutions.

Since the replacement of divalent cations is accompanied by a linear increase in the cell parameters, the composition of olivine solutions is readily determined by X-ray powder diffraction. Lumpkin and Ribbe (1983a, 1983b) have quantified and analyzed the relationships among lattice parameters and effective ionic radii of M1, M2 and T sites using a linear regression technique following investigation of 52 natural and synthetic olivines.

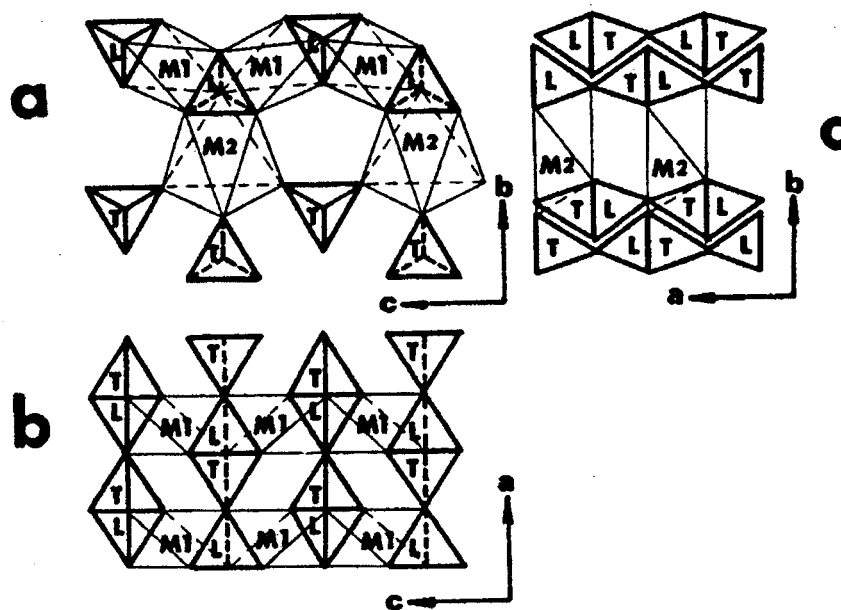


Figure 3.16 : Crystal structure of olivine. (after Lumpkin and Ribbe, 1983a) M1 and M2 are octahedral sites. T is a tetrahedral site and L is “leer” or an unoccupied tetrahedral site.

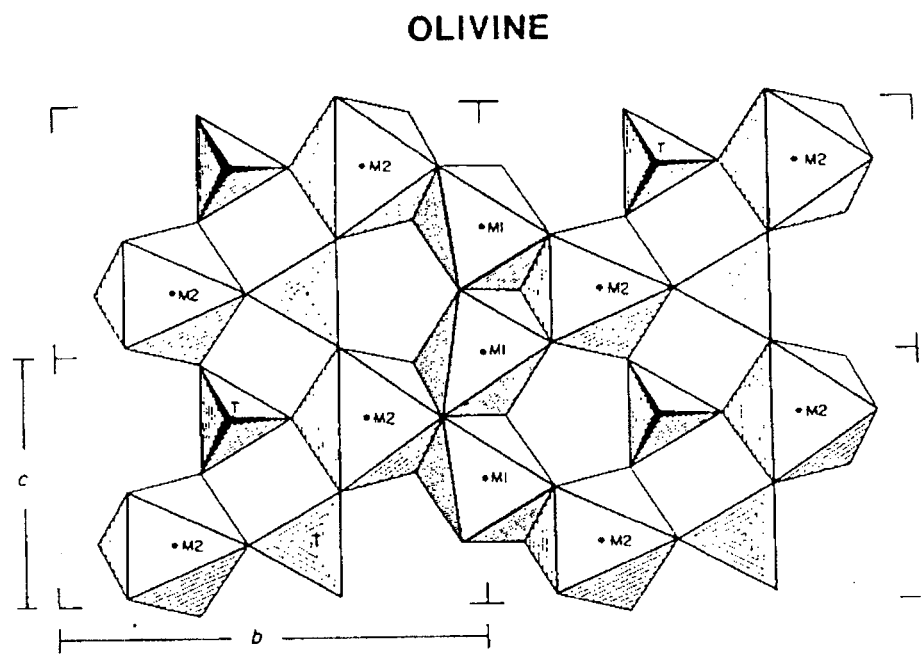


Figure 3.17 : Structure of olivine. (after Papike, 1987) M1 and M2 are octahedral sites.
T is a tetrahedral site.

3.3.2 Thermodynamic model

3.3.2.1 Previous model

Davison and Mukhopadhyay (1984) modeled the olivine quadrilateral (Mg_2SiO_4 - Fe_2SiO_4 - CaMgSiO_4 - CaFeSiO_4) for geological applications.



For quadrilateral olivines, the total free energy can be expressed by the non-convergent site-disorder model (Thompson, 1969), or equivalently by a reciprocal solution model. The total Gibbs energy can be expressed as:

$$G^m = \sum_i \sum_j Y_i^{\text{M2}} Y_j^{\text{M1}} G_{ij} - TS_C + G^E \quad (3.3.2)$$

where Y_i^{M2} and Y_j^{M1} are mole fraction of i and j on M2 and M1 sites, and G_{ij} is the Gibbs energy of an $[i][j]\text{SiO}_4$ end-member, S_C is the configurational entropy and G^E is excess Gibbs energy:

$$S_C = -R \left(\sum_i Y_i^{\text{M2}} \ln Y_i^{\text{M2}} + \sum_i Y_i^{\text{M1}} \ln Y_i^{\text{M1}} \right) \quad (3.3.3)$$

$$G^E = W_{\text{MgCa}} Y_{\text{Mg}}^{\text{M2}} Y_{\text{Ca}}^{\text{M2}} + W_{\text{FeCa}} Y_{\text{Fe}}^{\text{M2}} Y_{\text{Ca}}^{\text{M2}} \quad (3.3.4)$$

Davison and Mukhopadhyay assumed that Ca was restricted only to M2 sites. This is a poor assumption because $\gamma\text{-Ca}_2\text{SiO}_4$, $[\text{Ca}][\text{Ca}]\text{SiO}_4$, also has an olivine structure. That is, Ca can also enter M1 sites. Based on size considerations, (Fe-Mg) M1-M1 pairs may be considered to be ideal, so:

$$W_{\text{FeMg}}^{\text{M1}} = 2W_{\text{FeMg}}^{\text{M1M1}} - W_{\text{FeFe}}^{\text{M1M1}} - W_{\text{MgMg}}^{\text{M1M1}} = 0 \quad (3.3.5)$$

where $W_{\text{FeMg}}^{\text{M1M1}}$, for example, is the interaction energy of Fe and Mg on M1 sites. (Fe-Mg) M2-M2 pairs are also considered to be ideal, while (Fe-Ca) and (Mg-Ca) M2-M2 pairs are non-ideal. So that,

$$W_{\text{FeCa}} = W_{\text{FeCa}}^{\text{M2}} = 2W_{\text{FeCa}}^{\text{M2M2}} - W_{\text{FeFe}}^{\text{M2M2}} - W_{\text{CaCa}}^{\text{M2M2}} > 0 \quad (3.3.6)$$

$$W_{\text{MgCa}} = W_{\text{MgCa}}^{\text{M2}} = 2W_{\text{MgCa}}^{\text{M2M2}} - W_{\text{MgMg}}^{\text{M2M2}} - W_{\text{CaCa}}^{\text{M2M2}} > 0 \quad (3.3.7)$$

The W parameters in (3.3.6) and (3.3.7) are responsible for the miscibility gap in the Ca-Fe and Ca-Mg olivines respectively. Substituting the order parameter $t = Y_{\text{Fe}}^{\text{M2}} - Y_{\text{Fe}}^{\text{M1}}$ and

$$X = X_{\text{FeFe}}^{\text{M1M2}} = X_{\text{Fe2SiO4}} \quad (3.3.8)$$

$$Y = X_{\text{CaCa}}^{\text{M1M2}} = X_{\text{Ca2SiO4}} \quad (3.3.9)$$

$$\Delta G_{\text{E}}^{\circ} = G_{\text{MgFe}} - G_{\text{FeMg}} \quad (3.3.10)$$

$$\Delta G_{\star}^{\circ} = G_{\text{FeMg}} + G_{\text{MgFe}} - G_{\text{FeFe}} - G_{\text{MgMg}} \quad (3.3.11)$$

$$F^{\circ} = 2(G_{\text{CaMg}} - G_{\text{CaFe}}) + G_{\text{FeFe}} - G_{\text{MgMg}} \quad (3.3.12)$$

At equilibrium, $dG^m / dt = 0$. Hence:

$$\begin{aligned} dG^m / dt = & -RT \ln(Y_{\text{Fe}}^{\text{M1}} Y_{\text{Mg}}^{\text{M2}} / Y_{\text{Fe}}^{\text{M2}} Y_{\text{Mg}}^{\text{M1}}) - 2Y(W_{\text{MgCa}} - W_{\text{FeCa}}) \\ & + \Delta G_{\star}^{\circ}(Y + t) + F^{\circ}Y - \Delta G_{\text{E}}^{\circ}(1 - Y) \end{aligned} \quad (3.3.13)$$

So, they used five model parameters to model $[\text{Ca}, \text{Mg}, \text{Fe}^{2+}]^{\text{M2}}[\text{Mg}, \text{Fe}^{2+}]^{\text{M1}}\text{SiO}_4$ olivine solution: $\Delta G_{\text{E}}^{\circ}$, ΔG_{\star}° and F° to determine the unknown Gibbs energies of the end-

members ([Mg][Fe]SiO₄, [Fe][Mg]SiO₄ and [Ca][Fe]SiO₄) and the W parameters as excess interaction energy parameters. The Gibbs energies of real end-members such as Mg₂SiO₄, Fe₂SiO₄ and CaMgSiO₄ are well known.

3.3.2.2 Present model

The [Ca, Mg, Fe²⁺, Mn²⁺, Co²⁺]^{M2}[Ca, Mg, Fe²⁺, Mn²⁺, Co²⁺]^{M1}SiO₄ olivine system is modeled in this study. Al³⁺ and Fe³⁺ are not considered because observations show their solubilities to be very small. (Deer *et al.*, 1966) The two-sublattice Compound Energy Formalism (Appendix XI) is used to describe the olivine solution based on its crystal structure.

The Gibbs energy of the olivine solid solution is expressed as follows;

$$G^m = \sum_i \sum_j Y_i^{M2} Y_j^{M1} G_{ij} - TS_c + G^E \quad (3.3.14)$$

where Y_i^{M2} and Y_j^{M1} represent the site fractions of constituents i and j on the octahedral M2 and M1 sublattices, G_{ij} is the Gibbs energy of an end member $[i]^{M2}[j]^{M1}$ SiO₄, S_c is the configurational entropy assuming random mixing on each sublattice:

$$S_c = -R \left(\sum_i Y_i^{M2} \ln Y_i^{M2} + \sum_j Y_j^{M1} \ln Y_j^{M1} \right) \quad (3.3.15)$$

and G^E is an excess Gibbs energy:

$$G^E = \sum_i \sum_j \sum_k Y_i^{M2} Y_j^{M2} Y_k^{M1} L_{ij;k} + \sum_i \sum_j \sum_k Y_k^{M2} Y_i^{M1} Y_j^{M1} L_{k,ij} \quad (3.3.16)$$

where $L_{ij;k}$ and $L_{k;ij}$ are the interaction energies between cations i and j on M2 and M1 sublattices, respectively, when the other sublattice is occupied solely by k cations. The interaction energies, $L_{ij;k}$ and $L_{k;ij}$ are inherently set in the model as follows:

$$L_{ij;k} = L_{ij;s} = \dots \quad (3.3.17)$$

$$L_{k;ij} = L_{s;ij} = \dots \quad (3.3.18)$$

That is, the interaction between cations i and j on a sublattice is assumed to be the same regardless of the cation on the other sublattice.

In order to describe the $[\text{Ca}, \text{Mg}, \text{Fe}^{2+}, \text{Mn}^{2+}, \text{Co}^{2+}]^{\text{M2}}[\text{Ca}, \text{Mg}, \text{Fe}^{2+}, \text{Mn}^{2+}, \text{Co}^{2+}]^{\text{M1}}\text{SiO}_4$ olivine system, the Gibbs energies of 25 neutral end-members must be determined. Compared with the spinel model, the olivine solution model is straightforward to model because there are no hypothetical charged end-members. Some end-members are real compounds and the others are fictive. The model parameters are designed to use the known Gibbs energies of stable end-members, and the Gibbs energies of other fictive end-members are determined by the I_{ij} and Δ_{ij} parameters in order to reproduce the cation distribution data of the olivine solutions as well as all thermodynamic properties of the solutions. The details of the model parameters are described below.

$$[\text{Ca}, \text{Mg}, \text{Fe}^{2+}, \text{Mn}^{2+}, \text{Co}^{2+}]^{\text{M2}}[\text{Ca}, \text{Mg}, \text{Fe}^{2+}, \text{Mn}^{2+}, \text{Co}^{2+}]^{\text{M1}}\text{SiO}_4 \quad (3.3.19)$$

Model parameters

End-member Gibbs energy determined

$$G_{\text{CaCa}} = G^\circ(\gamma\text{-Ca}_2\text{SiO}_4) \quad G_{\text{CaCa}} \quad (3.3.20)$$

$$G_{\text{MgMg}} = G^\circ(\text{Mg}_2\text{SiO}_4) \text{ (forsterite)} \quad G_{\text{MgMg}} \quad (3.3.21)$$

$$G_{\text{FeFe}} = G^\circ(\text{Fe}_2\text{SiO}_4) \text{ (fayalite)} \quad G_{\text{FeFe}} \quad (3.3.22)$$

$$G_{\text{MnMn}} = G^\circ(\text{Mn}_2\text{SiO}_4) \text{ (tephroite)} \quad G_{\text{MnMn}} \quad (3.3.23)$$

$$G_{\text{CoCo}} = G^\circ(\text{Co}_2\text{SiO}_4) \quad G_{\text{CoCo}} \quad (3.3.24)$$

$$G_{\text{CaMg}} = G^0(\text{CaMgSiO}_4) \text{ (monticellite)} \quad G_{\text{CaMg}} \quad (3.3.25)$$

$$\Delta_{\text{CaMg}} = G_{\text{CaMg}} + G_{\text{MgCa}} - G_{\text{CaCa}} - G_{\text{MgMg}} \quad G_{\text{MgCa}} \quad (3.3.26)$$

$$I_{\text{CaFe}} = G_{\text{CaFe}} - (G_{\text{CaCa}} + G_{\text{FeFe}})/2 \quad G_{\text{CaFe}} \quad (3.3.27)$$

$$\Delta_{\text{CaFe}} = G_{\text{CaFe}} + G_{\text{FeCa}} - G_{\text{CaCa}} - G_{\text{FeFe}} \quad G_{\text{FeCa}} \quad (3.3.28)$$

$$I_{\text{CaMn}} = G_{\text{CaMn}} - (G_{\text{CaCa}} + G_{\text{MnMn}})/2 \quad G_{\text{CaMn}} \quad (3.3.29)$$

$$\Delta_{\text{CaMn}} = G_{\text{CaMn}} + G_{\text{MnCa}} - G_{\text{CaCa}} - G_{\text{MnMn}} \quad G_{\text{MnCa}} \quad (3.3.30)$$

$$I_{\text{CaCo}} = G_{\text{CaCo}} - (G_{\text{CaCa}} + G_{\text{CoCo}})/2 \quad G_{\text{CaCo}} \quad (3.3.31)$$

$$\Delta_{\text{CaCo}} = G_{\text{CaCo}} + G_{\text{CoCa}} - G_{\text{CaCa}} - G_{\text{CoCo}} \quad G_{\text{CoCa}} \quad (3.3.32)$$

$$I_{\text{MgFe}} = G_{\text{MgFe}} - (G_{\text{MgMg}} + G_{\text{FeFe}})/2 \quad G_{\text{MgFe}} \quad (3.3.33)$$

$$\Delta_{\text{MgFe}} = G_{\text{MgFe}} + G_{\text{FeMg}} - G_{\text{MgMg}} - G_{\text{FeFe}} \quad G_{\text{FeMg}} \quad (3.3.34)$$

$$I_{\text{MgMn}} = G_{\text{MgMn}} - (G_{\text{MgMg}} + G_{\text{MnMn}})/2 \quad G_{\text{MgMn}} \quad (3.3.35)$$

$$\Delta_{\text{MgMn}} = G_{\text{MgMn}} + G_{\text{MnMg}} - G_{\text{MgMg}} - G_{\text{MnMn}} \quad G_{\text{MnMg}} \quad (3.3.36)$$

$$I_{\text{MgCo}} = G_{\text{MgCo}} - (G_{\text{MgMg}} + G_{\text{CoCo}})/2 \quad G_{\text{MgCo}} \quad (3.3.37)$$

$$\Delta_{\text{MgCo}} = G_{\text{MgCo}} + G_{\text{CoMg}} - G_{\text{MgMg}} - G_{\text{CoCo}} \quad G_{\text{CoMg}} \quad (3.3.38)$$

$$I_{\text{FeMn}} = G_{\text{FeMn}} - (G_{\text{FeFe}} + G_{\text{MnMn}})/2 \quad G_{\text{FeMn}} \quad (3.3.39)$$

$$\Delta_{\text{FeMn}} = G_{\text{FeMn}} + G_{\text{MnFe}} - G_{\text{FeFe}} - G_{\text{MnMn}} \quad G_{\text{MnFe}} \quad (3.3.40)$$

$$I_{\text{FeCo}} = G_{\text{FeCo}} - (G_{\text{FeFe}} + G_{\text{CoCo}})/2 \quad G_{\text{FeCo}} \quad (3.3.41)$$

$$\Delta_{\text{FeCo}} = G_{\text{FeCo}} + G_{\text{CoFe}} - G_{\text{FeFe}} - G_{\text{CoCo}} \quad G_{\text{CoFe}} \quad (3.3.42)$$

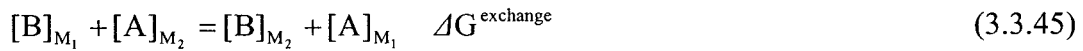
$$I_{\text{MnCo}} = G_{\text{MnCo}} - (G_{\text{MnMn}} + G_{\text{CoCo}})/2 \quad G_{\text{MnCo}} \quad (3.3.43)$$

$$\Delta_{\text{MnCo}} = G_{\text{MnCo}} + G_{\text{CoMn}} - G_{\text{MnMn}} - G_{\text{CoCo}} \quad G_{\text{CoMn}} \quad (3.3.44)$$

3.3.3 Discussion

The I_{ij} and Δ_{ij} model parameters were used to describe the olivine solution in each $i_2\text{SiO}_4$ - $j_2\text{SiO}_4$ binary system using the known Gibbs energies of the $i_2\text{SiO}_4$ and $j_2\text{SiO}_4$ end-members. These parameters can be optimized from the cation distribution data and thermodynamic property data. In the case of the Ca_2SiO_4 - Mg_2SiO_4 system, however, because the Gibbs energy of CaMgSiO_4 (monticellite), corresponding virtually to the Gibbs energy of $[\text{Ca}][\text{Mg}]\text{SiO}_4$, is well known, only the Δ_{CaMg} parameter was used (not I_{CaMg}) to determine the Gibbs energy of the hypothetical $[\text{Mg}][\text{Ca}]\text{SiO}_4$ end-member.

The cation distribution in olivine is important to modeling the thermodynamic properties of the olivine solutions. Since the M2 site is bigger than the M1 site, bigger atoms prefer M2 sites in order to reduce lattice energy. However, cation distribution data are rarely available for many systems. Thus, reasonable estimation of the cation distribution between M2 and M1 sublattices is necessary to model the olivine solution. If there are two different kinds of cations, A and B, where the ionic radius of A is larger than that of B, the cation distribution between sublattices can be expressed by the following exchange reaction:



and, an equilibrium constant for above reaction can be written as follows:

$$K_d = \frac{Y_{\text{B}}^{\text{M}_2} Y_{\text{A}}^{\text{M}_1}}{Y_{\text{A}}^{\text{M}_2} Y_{\text{B}}^{\text{M}_1}} \quad (3.3.46)$$

Because the cation distribution in the olivine solution results from the size differences of atoms, a relationship is expected between the cation distribution and the ionic size of cation.

Figure 3.18 shows the relationship between the equilibrium constant of cation distribution, K_d in equation (3.3.46), and the ratio of ionic radii of constituent cations of the olivine solution, r_B / r_A , where the radius of the A cation is bigger than that of B. The experimental data for known systems such as Ca-Mg, Mg-Fe, Fe-Mn, Fe-Co, Fe-Ni, Fe-Zn, *etc.* show that there is a linear relationship between the cation distribution constant and the ionic radius ratio. The ionic radii are taken from the recommended values of Shannon (1976) and the cation distribution data are obtained from Ericsson and Filippidis (1986), mainly at about 1000°C. From this relationship, the cation distributions in Ca-Fe, Ca-Mn, Ca-Co, Mg-Co, Mn-Co, *etc.* olivine solutions at 1000°C can be estimated. Thereafter, the model parameters I_{ij} and Δ_{ij} are optimized in order to reproduce these estimated cation distributions as well as the available thermodynamic data.

Generally, the cation distributions in olivine systems are known to be easily quenchable (Lumpkin and Ribbe, 1983a). However, in the case of the Mg-Fe olivine, the cation distributions measured using the quenching method and the *in situ* method are in disagreement. This suggests that the cation distribution is not quenchable above a certain temperature in this system as is the case for spinel solutions. (See Appendix III) Probably the cation distributions in other olivine systems exhibit similar behavior at high temperatures. Thus, new experimental studies of cation distribution in olivine solutions are required.

A miscibility gap appears on the M_2SiO_4 -rich side in Ca_2SiO_4 - M_2SiO_4 ($M = Mg, Fe, Mn$) olivine solutions. This seems to result from the large size difference between M^{2+} and Ca^{2+} cations. In order to reproduce this miscibility gap, excess Gibbs energy

parameters for the interaction between Ca^{2+} and M^{2+} ($L_{\text{Ca,M;N}}$ where N is a cation on M1 sites) were introduced. The calculated miscibility gaps in the $\text{Ca}_2\text{SiO}_4\text{-M}_2\text{SiO}_4$ (M = Mg, Fe, Mn) olivine are compared in Figure 3.19. The miscibility gap becomes larger in the order $\text{Fe} < \text{Mn} < \text{Mg}$. As can be seen in Figure 3.19, in the case of the $\text{Ca}_2\text{SiO}_4\text{-Mg}_2\text{SiO}_4$ solution, another metastable miscibility gap results from the model calculations in the Ca_2SiO_4 -rich region as a result of parameters introduced to reproduce phase equilibria in the CaO-MgO-SiO_2 system, although this miscibility gap cannot be observed (i.e., it is metastable) due to the presence of the $\text{Ca}_3\text{MgSi}_2\text{O}_8$ (merwinite) compound in the middle of the miscibility gap. (See Appendix I)

The predicted miscibility gap in the $[\text{Ca}, \text{Mg}, \text{Fe}^{2+}]^{\text{M2}}[\text{Ca}, \text{Mg}, \text{Fe}^{2+}]^{\text{M1}}\text{SiO}_4$ olivine quadrilateral ($\text{Mg}_2\text{SiO}_4\text{-Fe}_2\text{SiO}_4\text{-CaMgSiO}_4\text{-CaFeSiO}_4$) system are shown in Figure 3.20. The ternary miscibility gap is predicted solely from the binary model parameters with no additional ternary parameters. The agreement with experimental data is excellent. The olivine quadrilateral is very important to an understanding of the evolution of the mantle of the Earth and the rocks in the Moon and Mars.

The previous model by Davison and Mukhopadhyay (1984) considered Ca to exist only on M2 sites, while in reality it can enter both M2 and M1 sites as modeled in the present study ($\gamma\text{-Ca}_2\text{SiO}_4$ is stable: $[\text{Ca}][\text{Ca}]\text{SiO}_4$). Therefore, the present model should describe the thermodynamic properties better than the previous model.

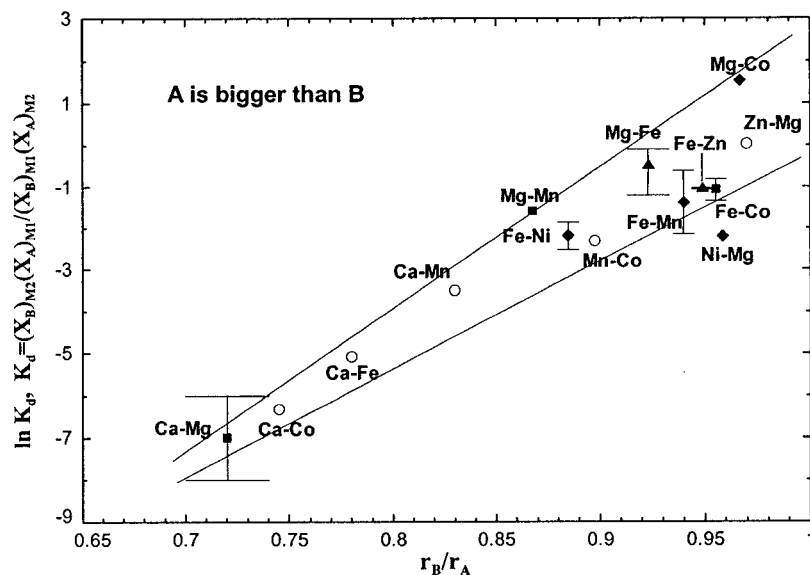


Figure 3.18 : The relationship between the cation distribution equilibrium constant, K_d , and the ratio of ionic radii of constituent cations of the olivine solution, r_B / r_A . The A cation is bigger than B. Open circles represents predicted cation distributions.

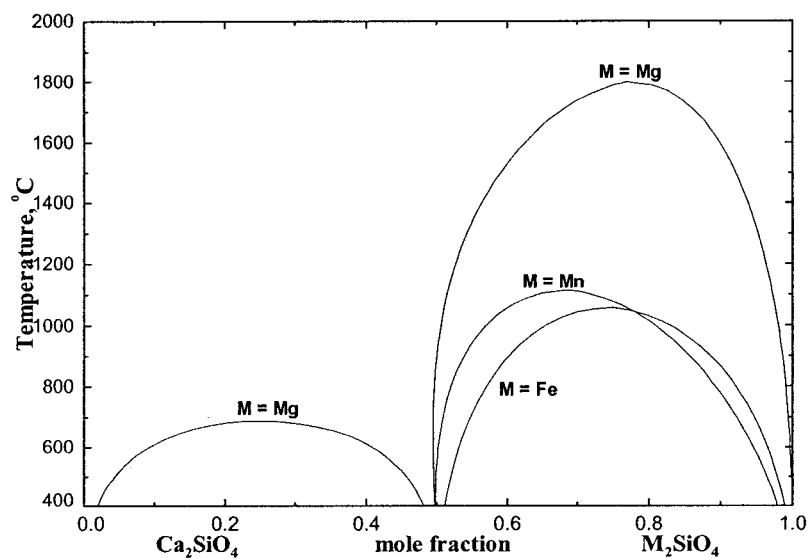


Figure 3.19 : Calculated miscibility gaps in the Ca_2SiO_4 - M_2SiO_4 olivine systems. (M = Mg, Mn and Fe)

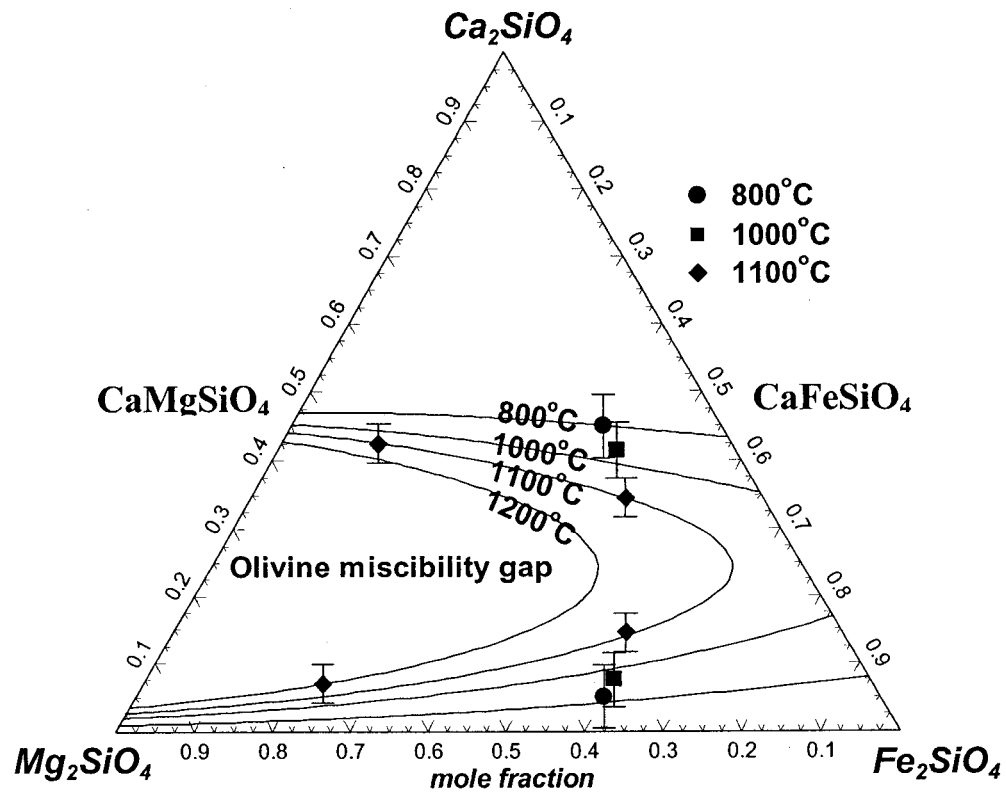


Figure 3.20 : Predicted miscibility gap in the $[\text{Ca}, \text{Mg}, \text{Fe}^{2+}]^{\text{M2}}[\text{Ca}, \text{Mg}, \text{Fe}^{2+}]^{\text{M1}}\text{SiO}_4$ olivine quadrilateral (Mg_2SiO_4 - Fe_2SiO_4 - CaMgSiO_4 - CaFeSiO_4). Experimental data from Davidson and Mukhopadhyay (1984).

3.4 Pyroxene solution

3.4.1 Crystal structure

The pyroxene solutions can be generally formulated as $(M2)(M1)(B)(A)O_6$ where $M2 = Ca^{2+}, Mg^{2+}, Fe^{2+}, Mn^{2+}, Na^+, Li^+$, $M1 = Mg^{2+}, Fe^{2+}, Mn^{2+}, Na^+, Li^+, Fe^{3+}, Al^{3+}, Cr^{3+}, Ti^{3+}$, $B = Si^{4+}, Fe^{3+}, Al^{3+}, Cr^{3+}, Ti^{3+}$ and $A = Si^{4+}$. M2 refers to cations in a generally distorted octahedral coordination, M1 to cations in a regular octahedral coordination and both B and A are tetrahedrally coordinated cations. It is noted that large cations like Ca^{2+} enter only on M2 sites.

Figure 3.21 shows the crystal structure of pyroxene. The structure of all pyroxenes can be described in terms of alternating tetrahedral and octahedral layers that lie parallel to the (100) plane. The tetrahedral layer is composed of infinite chains of corner-sharing tetrahedra running parallel to the c axis. Alternate chains along the b axis have tetrahedra pointing in the $+a$ or $-a$ directions. The base of each tetrahedron lies approximately parallel to the (100) plane, and the repeat unit along the c axis consists of two tetrahedra. The octahedral layer is composed of the six- to eight-coordinated M2 site and the octahedral M1 site. The M1 octahedra share edges to form infinite chains parallel to the c axis. The M2 polyhedra are either eight- or six-coordinated, depending on their occupancy by the cations: The site is eight-coordinated when it contains Ca^{2+} or Na^+ but is approximately six-coordinated when it contains the smaller $Mg^{2+}, Fe^{2+}, Mn^{2+}$ and Li^+ cations. Because the M2 site is bigger than the M1 site, cation distribution between M2 and M1 sites is observed, which depends on temperature.

Four different structural polymorphs of pyroxene are found under normal pressures: $C2/c$ (monoclinic: clino-pyroxene), $P21/c$ (monoclinic: low clino-pyroxene), $Pbca$ (orthorhombic: ortho-pyroxene) and $Pbcn$ (orthorhombic: proto-pyroxene). The four

different structures differ mainly in the manner in which the octahedral and tetrahedral layers are linked.

Trivalent cations such as Fe^{3+} , Al^{3+} , Cr^{3+} and Ti^{3+} are known to substitute for the divalent cations and for Si^{4+} (coupled substitution):

$$(\text{X}^{3+})_{\text{M1}} + (\text{X}^{3+})_{\text{B}} = (\text{M}^{2+})_{\text{M1}} + (\text{Si}^{4+})_{\text{B}} \quad (3.4.1)$$

More details about pyroxene solutions can be found in the literature (Morimoto, 1998; Deer *et al.*, 1966; Papke, 1987).

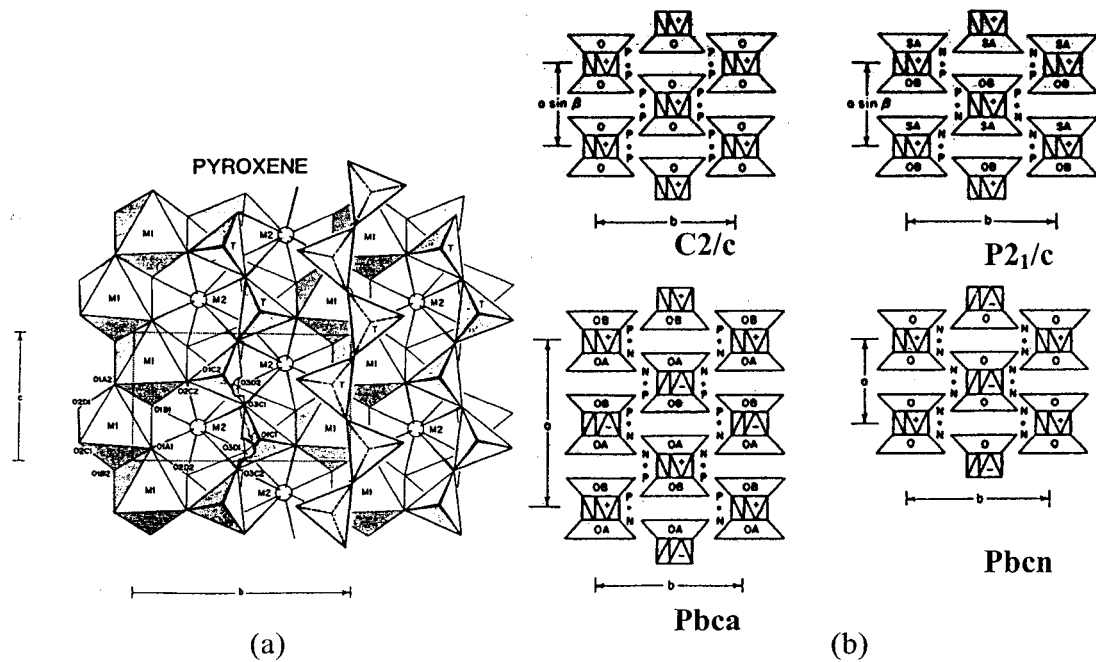


Figure 3.21 : Crystal structure of pyroxene. (after Papike, 1987) (a) Diopside projection on (110) plane. (b) I beam diagrams illustrating the four pyroxene structures.

3.4.2 Thermodynamic model

3.4.2.1 Previous model

Davidson and Lindsley (1985, 1989) modeled the pyroxene quadrilateral ($\text{Mg}_2\text{Si}_2\text{O}_6$ - $\text{Fe}_2\text{Si}_2\text{O}_6$ - $\text{CaMgSi}_2\text{O}_6$ - $\text{CaFeSi}_2\text{O}_6$) system using the non-convergent site-disorder model (Thompson, 1969): $[\text{Ca}, \text{Mg}, \text{Fe}^{2+}]^{\text{M2}}[\text{Mg}, \text{Fe}^{2+}]^{\text{M1}}\text{Si}_2\text{O}_6$. In this model the Gibbs energies of solutions are expressed as:

$$G^m = \sum_i \sum_j Y_i^{\text{M2}} Y_j^{\text{M1}} G_{ij} - TS_C + G^E \quad (3.4.2)$$

where Y_i^{M2} and Y_j^{M1} are mole fractions of i and j on M2 and M1 sites, G_{ij} is the Gibbs energy of the $[i][j]\text{Si}_2\text{O}_6$ end-member, S_C is the configurational entropy and G^E is the excess Gibbs energy given by:

$$S_C = -R \left(\sum_i Y_i^{\text{M2}} \ln Y_i^{\text{M2}} + \sum_i Y_i^{\text{M1}} \ln Y_i^{\text{M1}} \right) \quad (3.4.3)$$

$$G^E = G^{\text{E,M1}} + G^{\text{E,M2}} = RT \left(\sum_i Y_i^{\text{M1}} \ln \gamma_i^{\text{M1}} + \sum_i Y_i^{\text{M2}} \ln \gamma_i^{\text{M2}} \right) \quad (3.4.4)$$

Substituting the long-range order parameter $t = Y_{\text{Fe}}^{\text{M2}} - Y_{\text{Fe}}^{\text{M1}}$ and

$$X = X_{\text{MgMg}}^{\text{M1M2}} = X_{\text{Mg}_2\text{Si}_2\text{O}_6}, \quad Y = X_{\text{CaCa}}^{\text{M1M2}} = X_{\text{Ca}_2\text{Si}_2\text{O}_6}, \quad \Delta G_E^0 = G_{\text{MgFe}} - G_{\text{FeMg}} \quad (3.4.5)$$

$$\Delta G_\star^0 = G_{\text{MgFe}} + G_{\text{FeMg}} - G_{\text{FeFe}} - G_{\text{MgMg}} \quad (3.4.6)$$

$$F^0 = 2(G_{\text{CaMg}} - G_{\text{CaFe}}) + G_{\text{FeFe}} - G_{\text{MgMg}} \quad (3.4.7)$$

the Gibbs energy of the pyroxene solution can be expressed as:

$$\begin{aligned}
G^m = & \Delta G_*^\circ [X(I - X - Y) + Yt/2 + t^2/4] + F^\circ [Y(t/2 + X + Y)] \\
& + (I - X - 2Y)G_{\text{Fe}_2\text{Si}_2\text{O}_6}^\circ + 2YG_{\text{CaFeSi}_2\text{O}_6}^\circ + XG_{\text{Mg}_2\text{Si}_2\text{O}_6}^\circ - \Delta G_E^\circ [Y(I - X - Y - t/2) + t/2] \\
& + RT \left[\sum_{i=\text{Mg,Fe}} (Y_i^{\text{M1}} \ln Y_i^{\text{M1}} \gamma_i^{\text{M1}}) + \sum_{j=\text{Mg,Fe,Ca}} (Y_j^{\text{M2}} \ln Y_j^{\text{M2}} \gamma_j^{\text{M2}}) \right]
\end{aligned} \tag{3.4.8}$$

So the model parameters are: ΔG_E° , ΔG_*° , F° and G^E . Each term in G^E is a function of W parameters.

$$\begin{aligned}
RT \ln \gamma_{\text{Mg}}^\alpha = & W_{12}^\alpha [2X_{\text{Mg}} X_{\text{Fe}}^2 + X_{\text{Fe}} X_{\text{Ca}} / 2 + X_{\text{Mg}} X_{\text{Fe}} X_{\text{Ca}}] \\
& + W_{21}^\alpha [X_{\text{Fe}}^2 (1 - 2X_{\text{Mg}}) + X_{\text{Fe}} X_{\text{Ca}} / 2 - X_{\text{Mg}} X_{\text{Fe}} X_{\text{Ca}}] \\
& + W_{13}^\alpha [2X_{\text{Mg}} X_{\text{Ca}}^2 + X_{\text{Fe}} X_{\text{Ca}} / 2 + X_{\text{Mg}} X_{\text{Fe}} X_{\text{Ca}}] \\
& + W_{31}^\alpha [X_{\text{Ca}}^2 (1 - 2X_{\text{Mg}}) + X_{\text{Fe}} X_{\text{Ca}} / 2 - X_{\text{Mg}} X_{\text{Fe}} X_{\text{Ca}}] \\
& + W_{23}^\alpha [-X_{\text{Fe}} X_{\text{Ca}} / 2 - X_{\text{Fe}}^2 X_{\text{Ca}} + X_{\text{Fe}} X_{\text{Ca}}^2] \\
& + W_{32}^\alpha [-X_{\text{Fe}} X_{\text{Ca}} / 2 + X_{\text{Fe}}^2 X_{\text{Ca}} - X_{\text{Fe}} X_{\text{Ca}}^2]
\end{aligned} \tag{3.4.9}$$

$$\begin{aligned}
RT \ln \gamma_{\text{Fe}}^\alpha = & W_{12}^\alpha [X_{\text{Mg}}^2 (1 - 2X_{\text{Fe}}) + X_{\text{Mg}} X_{\text{Ca}} / 2 - X_{\text{Mg}} X_{\text{Fe}} X_{\text{Ca}}] \\
& + W_{21}^\alpha [2X_{\text{Mg}}^2 X_{\text{Fe}} + X_{\text{Mg}} X_{\text{Ca}} / 2 + X_{\text{Mg}} X_{\text{Fe}} X_{\text{Ca}}] \\
& + W_{13}^\alpha [X_{\text{Mg}} X_{\text{Ca}}^2 - X_{\text{Mg}} X_{\text{Ca}}^2 - X_{\text{Mg}} X_{\text{Ca}} / 2] \\
& + W_{31}^\alpha [X_{\text{Mg}}^2 X_{\text{Ca}} - X_{\text{Mg}} X_{\text{Ca}}^2 - X_{\text{Mg}} X_{\text{Ca}} / 2] \\
& + W_{23}^\alpha [2X_{\text{Fe}} X_{\text{Ca}}^2 + X_{\text{Mg}} X_{\text{Ca}} / 2 + X_{\text{Mg}} X_{\text{Fe}} X_{\text{Ca}}] \\
& + W_{32}^\alpha [X_{\text{Ca}}^2 (1 - 2X_{\text{Fe}}) + X_{\text{Mg}} X_{\text{Ca}} / 2 - X_{\text{Mg}} X_{\text{Fe}} X_{\text{Ca}}]
\end{aligned} \tag{3.4.10}$$

$$\begin{aligned}
RT \ln \gamma_{\text{Ca}}^\alpha = & W_{12}^\alpha [X_{\text{Mg}} X_{\text{Fe}}^2 - X_{\text{Mg}}^2 X_{\text{Fe}} - X_{\text{Fe}} X_{\text{Mg}} / 2] \\
& + W_{21}^\alpha [X_{\text{Mg}}^2 X_{\text{Fe}} - X_{\text{Mg}} X_{\text{Fe}}^2 - X_{\text{Mg}} X_{\text{Fe}} / 2] \\
& + W_{13}^\alpha [X_{\text{Mg}}^2 (1 - 2X_{\text{Ca}}) + X_{\text{Mg}} X_{\text{Fe}} / 2 - X_{\text{Mg}} X_{\text{Fe}} X_{\text{Ca}}] \\
& + W_{31}^\alpha [2X_{\text{Mg}}^2 X_{\text{Ca}} + X_{\text{Mg}} X_{\text{Fe}} / 2 + X_{\text{Mg}} X_{\text{Fe}} X_{\text{Ca}}] \\
& + W_{23}^\alpha [X_{\text{Fe}}^2 (1 - 2X_{\text{Ca}}) + X_{\text{Mg}} X_{\text{Fe}} / 2 - X_{\text{Mg}} X_{\text{Fe}} X_{\text{Ca}}] \\
& + W_{32}^\alpha [2X_{\text{Fe}}^2 X_{\text{Ca}} + X_{\text{Mg}} X_{\text{Fe}} / 2 + X_{\text{Mg}} X_{\text{Fe}} X_{\text{Ca}}]
\end{aligned} \tag{3.4.11}$$

where the superscripts α are omitted from the mole-fraction terms for simplicity; subscripts on W terms represent Mg(1), Fe(2) and Ca(3). Since Ca is only considered to exist in M2 sites, W_{13} , W_{31} , W_{23} and W_{32} pertain to the M2 site only and their superscripts are omitted. Also because the only mixing considered on both M1 and M2 sites is Fe-Mg and because no asymmetry in Fe-Mg mixing is required, $W_{12}^{M1}(=W_{21}^{M1})$ and $W_{12}^{M2}(=W_{21}^{M2})$ are abbreviated as W^{M1} and W^{M2} , respectively.

At equilibrium, $dG^m / dt = 0$. Hence:

$$\begin{aligned}
 dG^m / dt = & \Delta G_*^o(Y+t)/2 + F^o Y/2 - \Delta G_E^o(1-Y)/2 + W_{13}[Y(-1/2 + t/2 - X + 2Y)] \\
 & + W_{31}[Y(-1/2 - t/2 + X - 2Y)] + W_{23}[Y(3/2 + t/2 - X - 2Y)] \\
 & + W_{32}[Y(-1/2 - t/2 + X + 2Y)] + W^{M1}[(1/2 - t/2 - X - Y)/2] \\
 & + W^{M2}[(1/2 - t/2 + X)/2] - 1/2 RT \ln(Y_{Fe}^{M1} Y_{Mg}^{M2} / Y_{Fe}^{M2} Y_{Mg}^{M1})
 \end{aligned}
 \tag{3.4.12}$$

So, nine model parameters were used to model the $[Ca, Mg, Fe^{2+}]^{M2}[Mg, Fe^{2+}]^{M1}Si_2O_6$ pyroxene solution: ΔG_E^o , ΔG_*^o and F^o to determine the unknown Gibbs energies of the end-members ($[Mg][Fe]Si_2O_6$, $[Fe][Mg]Si_2O_6$ and $[Ca][Fe]Si_2O_6$), and the W parameters as excess interaction energy parameters. The Gibbs energies of real end-members such as Mg_2SiO_4 , Fe_2SiO_4 and $CaMgSiO_4$ are well known.

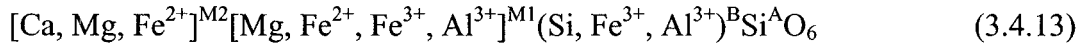
Sack and Ghiorso (1994) also modeled the pyroxene quadrilateral $[Ca, Mg, Fe^{2+}]^{M2}[Mg, Fe^{2+}]^{M1}Si_2O_6$ using a similar model.

However, both thermodynamic modelings (Davidson and Lindsley, 1985, 1989; Sack and Ghiorso, 1994) were limited to pyroxene solutions in the pyroxene quadrilateral ($Mg_2Si_2O_6$ - $Fe_2Si_2O_6$ - $CaMgSi_2O_6$ - $CaFeSi_2O_6$) system with no consideration of equilibria

with other phases such as olivine, spinel, wollastonite and slag. That is, in both thermodynamic modelings, the model parameters were optimized in order to reproduce the phase equilibria between pyroxenes.

3.4.2.2 Present model

Four pyroxene solid solutions; clino-, proto-, ortho- and low clino-pyroxene, are modeled in this study. Although the crystal structures are slightly different, the same model can be used for all pyroxene polymorphs. The structure of pyroxene in the present study may be formulated as follow based on its crystal structure:



In order to describe the Gibbs energy of solution, the Compound Energy Formalism (Appendix XI) is used.

$$G^m = \sum_i \sum_j \sum_k Y_i^{\text{M2}} Y_j^{\text{M1}} Y_k^{\text{B}} G_{ijk} - TS_C + G^E \quad (3.4.14)$$

where Y_i^{M2} , Y_j^{M1} and Y_k^{B} represent the site fractions of constituents i , j and k on the octahedral M2 and M1 sublattices and tetrahedral B sublattice, respectively. G_{ijk} is the Gibbs energy of an end-member $[i]^{\text{M2}}[j]^{\text{M1}}(k)^{\text{B}}\text{SiO}_6$, S_C is the configurational entropy assuming the random mixing of cations on each sublattice:

$$S_C = -R \left(\sum_i Y_i^{\text{M2}} \ln Y_i^{\text{M2}} + \sum_j Y_j^{\text{M1}} \ln Y_j^{\text{M1}} + \sum_k Y_k^{\text{B}} \ln Y_k^{\text{B}} \right) \quad (3.4.15)$$

and G^E is the excess Gibbs energy:

$$G^E = \sum_a \sum_b \sum_c \sum_d Y_a^l Y_b^l Y_c^m Y_d^n L_{ab;c;d}^{l;m;n} \quad (3.4.16)$$

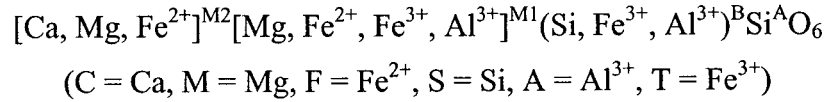
where $L_{ab;c;d}^{l;m;n}$ is the interaction energy between cations a and b on the l sublattice when the other sublattices, m and n , are occupied solely by cations c and d , respectively. The L parameters may be expanded as Redlich-Kister polynomials in the site fractions:

$$L_{ab;c;d}^{l;m;n} = \sum_k L_{ab;c;d}^{l;m;n} (Y_a^l - Y_b^l)^k \quad (3.4.17)$$

It is assumed that the interaction energy $L_{ab;c;d}^{l;m;n}$ between a and b on the l sublattice is the same regardless of the cations c and d on the m and n sublattices.

The pyroxene model in equation (3.4.14) contains 36 end-members. Many of them are fictive or hypothetical charged end-members. The Gibbs energies G_{ij} for only a small number of neutral end-members are known. Thus, as for the spinel model discussed above (See section 3.2.2), certain logical and rational methods to determine unknown Gibbs energy of fictive and hypothetical charged end-members are required due to the lack of sufficient thermodynamic data to fix the Gibbs energies of all end-members.

The following set of model parameters and associated optimization strategy are used to determine the model parameters for pyroxene solutions. The known Gibbs energies of stable end-members are directly used as model parameters in the present model. The Δ and Ψ parameters, related to certain reciprocal site exchange reactions, are used to determine the Gibbs energies of fictive and hypothetical end-members. The Gibbs energies of all site exchange reactions are expected to be small and so can often be set to zero. In this way, most of the model parameters are set to zero. Thus, the sequence of optimization is important in the present model, as is the case for spinel solutions.



$$G_{\text{CMS}} = G^0(\text{CaMgSi}_2\text{O}_6) \text{ (diopside)} \quad (3.4.18)$$

$$G_{\text{CFS}} = G^0(\text{CaFeSi}_2\text{O}_6) \text{ (hedenbergite)} \quad (3.4.19)$$

$$G_{\text{FFS}} = G^0(\text{Fe}_2\text{Si}_2\text{O}_6) \text{ (ferrosilicate)} \quad (3.4.20)$$

$$G_{\text{MMS}} = G^0(\text{Mg}_2\text{Si}_2\text{O}_6) \text{ (enstatite)} \quad (3.4.21)$$

$$G_{\text{CAA}} = G^0(\text{CaAl}_2\text{SiO}_6) \text{ (Ca-Tschermak)} \quad (3.4.22)$$

$$G_{\text{CTA}} = G^0(\text{CaFeAlSiO}_6) \text{ (esseneite)} \quad (3.4.23)$$

$$\Delta_{\text{MF}}^{\text{S}} = G_{\text{MMS}} + G_{\text{FFS}} - G_{\text{MFS}} - G_{\text{FMS}} \quad (3.4.24)$$

$$I_{\text{MF}}^{\text{S}} = G_{\text{MFS}} - G_{\text{FMS}} \quad (3.4.15)$$

$${}^{\text{C}}\Delta_{\text{AT}} = G_{\text{CTT}} + G_{\text{CAA}} - G_{\text{CAT}} - G_{\text{CTA}} \quad (3.4.26)$$

$${}^{\text{C}}I_{\text{AT}} = G_{\text{CAT}} - G_{\text{CTA}} \quad (3.4.27)$$

$$\Psi_{\text{FAA}} = G_{\text{FAA}} + G_{\text{CFS}} - G_{\text{FFS}} - G_{\text{CAA}} \quad (3.4.28)$$

$$\Psi_{\text{MAA}} = G_{\text{MAA}} + G_{\text{CMS}} - G_{\text{MMS}} - G_{\text{CAA}} \quad (3.4.29)$$

$$\Delta_{\text{CF,TA}}^{\text{T}} = G_{\text{CTA}} + G_{\text{FTT}} - G_{\text{CTT}} - G_{\text{FTA}} \quad (3.4.30)$$

$$\Delta_{\text{CF,TA}}^{\text{A}} = G_{\text{CAA}} + G_{\text{FTA}} - G_{\text{CTA}} - G_{\text{FAA}} \quad (3.4.31)$$

$${}^{\text{F}}\Delta_{\text{AT}} = G_{\text{FTT}} + G_{\text{FAA}} - G_{\text{FAT}} - G_{\text{FTA}} \quad (3.4.32)$$

$$\Delta_{\text{CM,TA}}^{\text{T}} = G_{\text{CTA}} + G_{\text{MTT}} - G_{\text{CTT}} - G_{\text{MTA}} \quad (3.4.33)$$

$$\Delta_{\text{CM,TA}}^{\text{A}} = G_{\text{CAA}} + G_{\text{MTA}} - G_{\text{CTA}} - G_{\text{MAA}} \quad (3.4.34)$$

$${}^{\text{M}}\Delta_{\text{AT}} = G_{\text{MTT}} + G_{\text{MAA}} - G_{\text{MAT}} - G_{\text{MTA}} \quad (3.4.35)$$

$$G_{\text{FTS}} = G_{\text{FFS}} \quad (3.4.36)$$

$${}^{\text{C}}\Delta_{\text{FTS}} = G_{\text{CTT}} + G_{\text{CFS}} - G_{\text{CFT}} - G_{\text{CTS}} \quad (3.4.37)$$

$${}^{\text{M}}\Delta_{\text{FTS}} = G_{\text{MTT}} + G_{\text{MFS}} - G_{\text{MFT}} - G_{\text{MTS}} \quad (3.4.38)$$

$${}^F\Delta_{\text{FTS}} = G_{\text{FTT}} + G_{\text{FFS}} - G_{\text{FFT}} - G_{\text{FTS}} \quad (3.4.39)$$

$${}^C\Delta_{\text{FT,SA}} = G_{\text{CFA}} + G_{\text{CTS}} - G_{\text{CFS}} - G_{\text{CTA}} \quad (3.4.40)$$

$${}^M\Delta_{\text{FT,SA}} = G_{\text{MFA}} + G_{\text{MTS}} - G_{\text{MFS}} - G_{\text{MTA}} \quad (3.4.41)$$

$${}^F\Delta_{\text{FT,SA}} = G_{\text{FFA}} + G_{\text{FTS}} - G_{\text{FFS}} - G_{\text{FTA}} \quad (3.4.42)$$

$${}^C\Delta_{\text{FA,SA}} = G_{\text{CFA}} + G_{\text{CAS}} - G_{\text{CFS}} - G_{\text{CAA}} \quad (3.4.43)$$

$${}^M\Delta_{\text{FA,SA}} = G_{\text{MFA}} + G_{\text{MAS}} - G_{\text{MFS}} - G_{\text{MAA}} \quad (3.4.44)$$

$${}^F\Delta_{\text{FA,SA}} = G_{\text{FFA}} + G_{\text{FAS}} - G_{\text{FFS}} - G_{\text{FAA}} \quad (3.4.45)$$

$$\Delta_{\text{MFT}}^{\text{S}} = G_{\text{FFS}} + G_{\text{MTS}} - G_{\text{MFS}} - G_{\text{FTS}} \quad (3.4.46)$$

$${}^C\Delta_{\text{MTS}} = G_{\text{CTT}} + G_{\text{CMS}} - G_{\text{CMT}} - G_{\text{CTS}} \quad (3.4.46)$$

$${}^M\Delta_{\text{MTS}} = G_{\text{MTT}} + G_{\text{MMS}} - G_{\text{MMT}} - G_{\text{MTS}} \quad (3.4.47)$$

$${}^F\Delta_{\text{MTS}} = G_{\text{FTT}} + G_{\text{FMS}} - G_{\text{FMT}} - G_{\text{FTS}} \quad (3.4.48)$$

$${}^C\Delta_{\text{MAS}} = G_{\text{CAA}} + G_{\text{CMS}} - G_{\text{CMA}} - G_{\text{CAS}} \quad (3.4.49)$$

$${}^M\Delta_{\text{MAS}} = G_{\text{MAA}} + G_{\text{MMS}} - G_{\text{MMA}} - G_{\text{MAS}} \quad (3.4.50)$$

$${}^F\Delta_{\text{MAS}} = G_{\text{FAA}} + G_{\text{FMS}} - G_{\text{FMA}} - G_{\text{FAS}} \quad (3.4.51)$$

$$\Delta_{\text{CFT}}^{\text{S}} = G_{\text{FFS}} + G_{\text{CTS}} - G_{\text{CFS}} - G_{\text{FTS}} \quad (3.4.52)$$

The first six parameters are the Gibbs energies of neutral pyroxene components. The Δ and Ψ parameters are related to the reciprocal reactions and were initially set to zero. The I parameters are related to the cation distributions between sublattices. For example, the cation distribution of Mg and Fe^{2+} between M2 and M1 sites is determined mainly by the parameter I_{MF}^{S} and that of Fe^{3+} and Al^{3+} by ${}^C I_{\text{AT}}$. $G_{\text{FTS}} = G_{\text{FFS}}$ in equation (3.4.36) is set, without loss of generality, as the reference state for hypothetical charged end-members. Using the above model parameters, the Gibbs energies of all 36 end-members can be determined in a logical sequence.

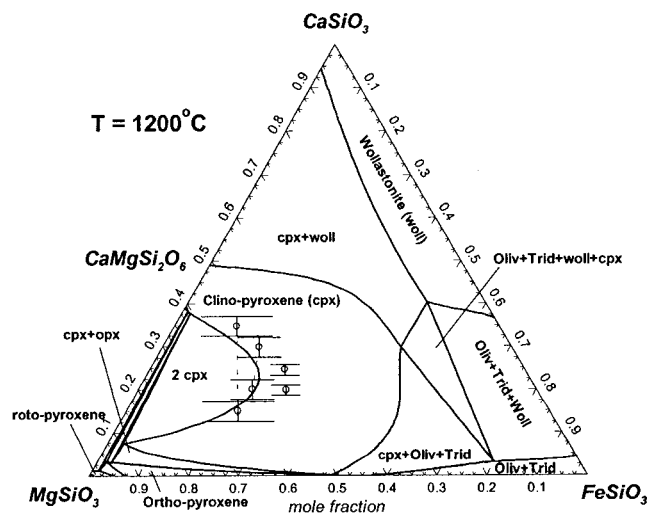
3.4.3 Discussion

The $[\text{Ca}, \text{Mg}, \text{Fe}^{2+}]^{\text{M2}}[\text{Mg}, \text{Fe}^{2+}]^{\text{M1}}\text{Si}_2\text{O}_6$ system was first optimized because most of the required experimental data are available in this pyroxene quadrilateral system. Next, the solubilities of Al^{3+} and Fe^{3+} in pyroxenes were modeled with expansion to the B sublattice. Figure 3.22 shows the calculated pyroxene quadrilateral ($\text{Mg}_2\text{Si}_2\text{O}_6$ - $\text{Fe}_2\text{Si}_2\text{O}_6$ - $\text{CaMgSi}_2\text{O}_6$ - $\text{CaFeSi}_2\text{O}_6$) system at 1200° and 900°C. This quadrilateral system is very important, along with the corresponding olivine quadrilateral, for geological applications.

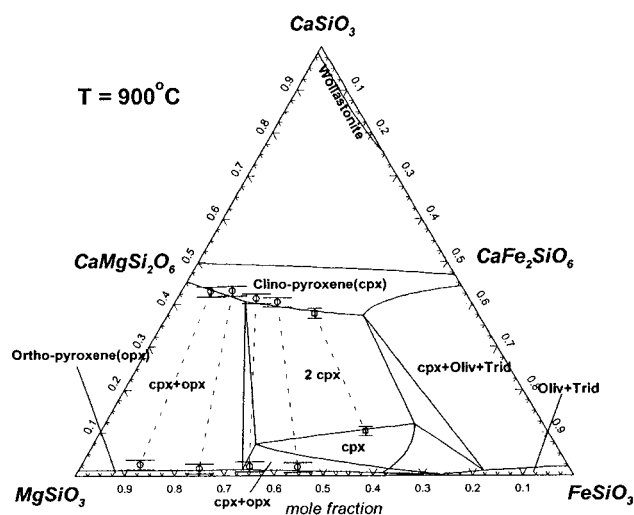
In the case of pyroxene, there are few data for the cation distribution except in the MgSiO_3 - FeSiO_3 binary system. Even in this case, the cation distribution is known only for the ortho-pyroxene solution. Figure 3.23 show the calculated optimized cation distribution of ortho MgSiO_3 - FeSiO_3 pyroxene along with the experimental data. (Details are in Appendix III.)

A positive enthalpy of mixing of the clino-pyroxene solution was measured in the $\text{CaMgSi}_2\text{O}_6$ - $\text{Mg}_2\text{Si}_2\text{O}_6$ system (see Appendix I). Moreover, as can be seen in Figure 3.24, the phase diagram in this binary section shows a very large miscibility gap in the pyroxene solution. The miscibility gap of pyroxenes in the $\text{CaMgSi}_2\text{O}_6$ - $\text{Mg}_2\text{Si}_2\text{O}_6$ system seems to result from the large size difference between Ca^{2+} and Mg^{2+} cations ($r_{\text{Ca}^{2+}} = 1.00 \text{ \AA}$ and $r_{\text{Mg}^{2+}} = 0.68 \text{ \AA}$) on octahedral sites M2 and M1. For a similar reason, a miscibility gap may exist in the $\text{CaFeSi}_2\text{O}_6$ - $\text{Fe}_2\text{Si}_2\text{O}_6$ solution. These two binary miscibility gaps extend to a very large ternary miscibility gap in the pyroxene quadrilateral system as seen in Figure 3.22

The dissolution of trivalent cations such as Al^{3+} and Fe^{3+} in pyroxene were modeled by the coupled substitution of divalent cations and Si^{4+} as in equation (3.4.1). Solubilities of Al^{3+} in pyroxenes have been reported for the sections, $\text{CaMgSi}_2\text{O}_6$ - $\text{CaAl}_2\text{SiO}_6$ (Ca-Tschermak), $\text{CaMgSi}_2\text{O}_6$ - $\text{MgAl}_2\text{SiO}_6$ (Mg-Tschermak) and $\text{Mg}_2\text{Si}_2\text{O}_6$ - $\text{MgAl}_2\text{SiO}_6$ (Mg-Tschermak) (Hytonen and Schairer, 1961). The solubilities of Al^{3+} in the first two sections (maximum about 25 wt% Ca-Ts and 20 wt% Mg-Ts, respectively) are quite extensive while the last one is smaller (maximum about 7 wt% Mg-Ts). The enthalpy of mixing of pyroxene in the $\text{CaMgSi}_2\text{O}_6$ - $\text{CaAl}_2\text{SiO}_6$ section shows a positive deviation from ideal behavior (Newton *et al.* 1977) which results in a miscibility gap in this section at low temperatures. The immiscibility seems to result from the size difference between Mg^{2+} and Al^{3+} cations on octahedral M1 sites. This is modeled by an excess Gibbs energy parameter for the interaction of Mg^{2+} and Al^{3+} on M1 sites.

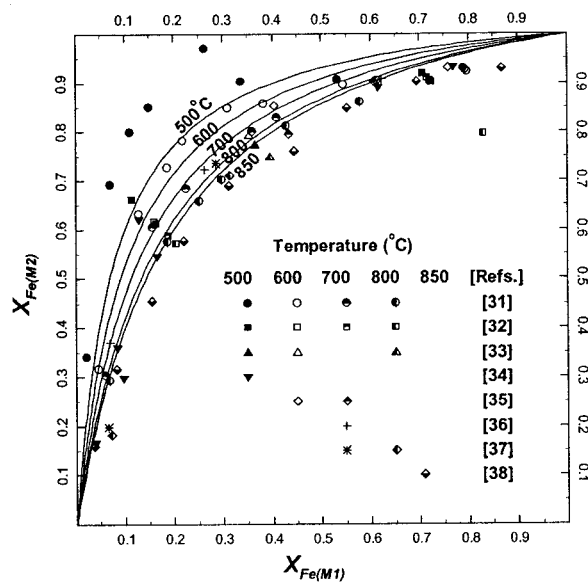


(a)

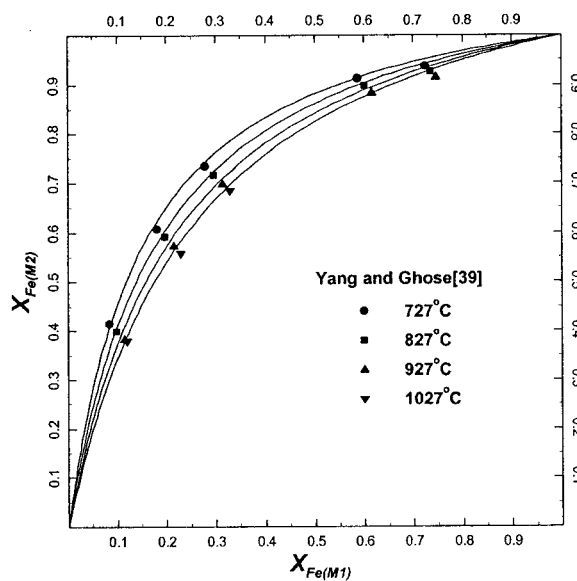


(b)

Figure 3.22 : Predicted pyroxene quadrilateral ($\text{Mg}_2\text{Si}_2\text{O}_6$ - $\text{Fe}_2\text{Si}_2\text{O}_6$ - $\text{CaMgSi}_2\text{O}_6$ - $\text{CaFeSi}_2\text{O}_6$) at 1200° and 900°C in this study. Noted that olivine (Oliv), tridymite (Trid) and wollastonite (Woll) appear in the quadrilateral because FeSiO_3 is not stable at normal pressures and $\text{CaFeSi}_2\text{O}_6$ is stable below about 950°C . Experimental points from Davidson and Lindsley (1985).



(a)



(b)

Figure 3.23 : Calculated cation distribution of $[\text{Mg}][\text{Mg}]\text{Si}_2\text{O}_6$ - $[\text{Fe}][\text{Fe}]\text{Si}_2\text{O}_6$ orthopyroxene compared with experimental data at different temperatures. Axes are mole fraction of Fe in octahedral sites M1 and M2. (See Appendix III)

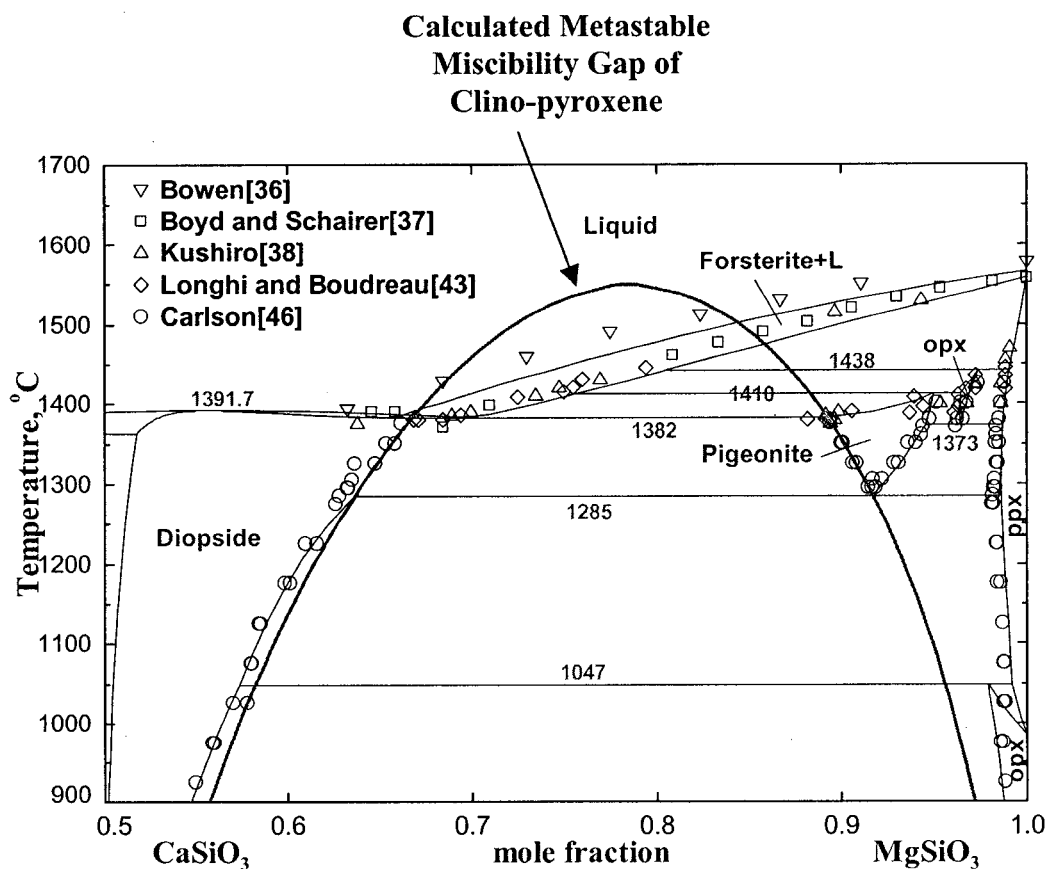


Figure 3.24 : Calculated optimized phase diagram of the $\text{CaMgSi}_2\text{O}_6$ - Mg_2SiO_6 pyroxene section. The thick line shows the calculated metastable miscibility gap in the $\text{CaMgSi}_2\text{O}_6$ - Mg_2SiO_6 clino-pyroxene solution. opx (ortho-pyroxene) and ppx (proto-pyroxene) also have similar miscibility gaps. (See Appendix I.)

3.5 Monoxide solution

3.5.1 Crystal structure

The monoxide solid solution (space group: $Fm3m$) is the solid solution based on MO oxides where M^{2+} is a divalent cation such as Mg, Ca, Fe^{2+} , Mn^{2+} , Co^{2+} , Ni^{2+} , *etc.* Almost complete solid solubility occurs across the monoxide solution except in the CaO-MgO system, which exhibits limited mutual solubilities. The monoxide solution can also dissolve limited amounts of N_2O_3 type solid oxides where N is a trivalent cation such as Al^{3+} , Cr^{3+} and Fe^{3+} . The monoxide solution is often called the “halite (rock salt)” solution because it has a structure similar to that of NaCl (halite). When two MO oxides mix in the monoxide solution, it is easily understood that the mixing occurs only on the cation sites for divalent metals. However, the defect model of the monoxide solution with the dissolution of N_2O_3 type oxides has not yet been clearly elucidated.

In the case of the Fe-Mg-O (magnesio-wustite) solution, several investigations on the defects accompanying the dissolution of Fe_2O_3 have been conducted. To characterize the properties based on the point defect structure of the $(Mg_{1-x}Fe_x)_{1-\delta}O$ solution, various techniques were applied during the last decades. Recently, *in situ* techniques such as Mossbauer spectroscopy, X-ray absorption spectroscopy (XAS), X-ray absorption near edge structure (XANES), extended X-ray absorption fine structure (EXAFS), thermopower and conductivity measurements have gained in importance for studying the structure of the $(Mg_{1-x}Fe_x)_{1-\delta}O$ phase. The necessity of performing *in situ* measurements results from the fact that quenching does not ensure that the equilibrium state established at high temperatures is frozen in.

In general, the *in situ* spectroscopic measurements on the $(Mg_{1-x}Fe_x)_{1-\delta}O$ solution (Hillbrandt and Martin, 1998; Waychunas, 1983) reveal that: (1) Divalent cations (Fe^{2+}) are randomly distributed on the cation sublattice. (2) Trivalent cations (Fe^{3+}) form

various defect associates involving Fe^{3+} cations and cation vacancies. Associates are mainly of the form of two Fe^{3+} cations and a cation vacancy ($\text{Fe}^{3+}\text{-Va-Fe}^{3+}$).

Based on this structural information, the $(\text{Mg}_{1-x}\text{Fe}_x)_{1-\delta}\text{O}$ solution may be represented as follows:

$$(\text{Mg}^{2+}, \text{Fe}^{2+}, \text{'Fe}^{3+}\text{-Va-Fe}^{3+}\text{'})_{1-\delta}\text{O} \quad (3.5.1)$$

where Va means vacancy. It is noted that the vacancies are always associated with Fe^{3+} . That is, Fe^{3+} and Va are not distributed randomly in the cation sublattice but the associates of Fe^{3+} and the vacancy mix randomly with Mg^{2+} and Fe^{2+} .

Although widely studied, especially under *in situ* conditions, there is still a lack of direct information on the dopant's charge and on details of the local environment. Hence, the point defect structure of $(\text{Mg}_{1-x}\text{Fe}_x)_{1-\delta}\text{O}$ is still under debate. Also, the defect structure of the $(\text{Mg}_{1-x}\text{Fe}_x)_{1-\delta}\text{O}$ solutions was studied mostly when x is small, so that structural information at larger values of x is still lacking.

3.5.2 Thermodynamic model

3.5.2.1 Previous model

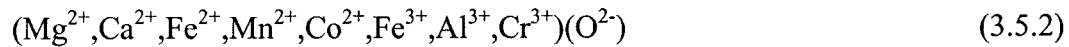
Fabrichnaya (1998) modeled the magnesio-wustite solution as $(\text{Mg}^{2+}, \text{Fe}^{2+}, \text{Fe}^{3+}, \text{Va})(\text{O}^{2-})$. The model assumed the random distribution of Fe^{3+} and Va on the cationic sublattice. The Gibbs energies of hypothetical end-members such as FeO^{1+} and VaO^{2-} were determined arbitrarily in order to reproduce the measured phase equilibria under various oxygen partial pressures. Hallstedt (1992) modeled the $\text{MgO-Al}_2\text{O}_3$ monoxide solution with a small solubility of Al_2O_3 using a similar model: $(\text{Al}^{3+}, \text{Ca}^{2+}, \text{Mg}^{2+},$

Va)(O²⁻). The Gibbs energies of both solution models were based on the binary model parameters using a symmetric “Muggianu-like” approximation (Pelton, 2001).

Inherently, the previous models assume the random distribution of Fe³⁺ and Va on the cationic sublattice.

3.5.2.2 Present model

The monoxide solution in the MgO-FeO-MnO-CaO-CoO-FeO_{1.5}-AlO_{1.5}-CrO_{1.5} system is optimized in this study. In the present model, all divalent and trivalent cations are assumed to mix randomly on the cationic sublattice:



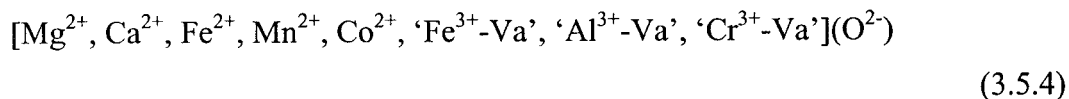
The Gibbs energy of the solution is described by a polynomial expansion of the excess Gibbs energy function:

$$G^m = \sum_i X_i G_i^o + RT \sum_i X_i \ln X_i + \sum_i \sum_j X_i X_j \left(\frac{X_i}{X_i + X_j} \right)^m \left(\frac{X_j}{X_i + X_j} \right)^n q_{ij}^{mn} \quad (3.5.3)$$

where X_i and G_i^o are the mole fraction and the Gibbs energy of component i and q_{ij}^{mn} is a binary interaction parameter which can be temperature dependent, and powers m and n are ≥ 0 . No ternary excess parameters were used in this study.

From a structural standpoint, the present model assumes inherently that vacancies, which are introduced by the dissolution of trivalent cations, are all associated with the trivalent cations and hence do not contribute to the configurational entropy.

Alternatively, the structure of the monoxide solid solution by this model may be schematically written as follows:



That is, the dissolved trivalent ions (A^{3+}) are assumed to be always associated with vacancies (Va) in the form of ' $\text{A}^{3+}\text{-Va}$ ' pairs.

The Gibbs energy of the binary monoxide solution is expressed by a polynomial expansion of the excess Gibbs energy. The Gibbs energies of ternary and multicomponent monoxide solutions are calculated from the binary q_{ij}^{mn} parameters using a symmetric "Kohler-like" extension (Appendix XII) (Pelton, 2001) except for the MgO-FeO-FeO_{1.5} system. Thermodynamic and structural properties of the MgO-FeO-FeO_{1.5} monoxide solution are very well studied. Figure 3.25 shows the calculated optimized MgO-FeO-Fe₂O₃ phase diagram at 1160°C. The monoxide solution MgO-FeO-FeO_{1.5} (magnesio-wustite) exhibits complete solid solution between MgO and FeO, and it can dissolve up to 10 mole percent FeO_{1.5}. The nonstoichiometry of magnesiowustite with variation of oxygen partial pressure is calculated in Figure 3.26. In order to describe this monoxide solid solution, it was found that an asymmetric "Toop-like" interpolation technique with FeO_{1.5} as the "asymmetric" component (Appendix XII) (Pelton, 2001) was more efficient than the symmetric "Kohler-like" technique. (See Appendix II). All experimental data involving the magnesiowustite phase can be described satisfactorily in the present study using seven binary parameters with no ternary parameters, while Fabrichnaya (1998) could not reproduce all data satisfactorily even when using ten parameters.

The assumption of the present model (Fe^{3+} and vacancies are associated) is closer to the observations than the previous models (Fe^{3+} and vacancies are randomly distribution in the cation sublattice).

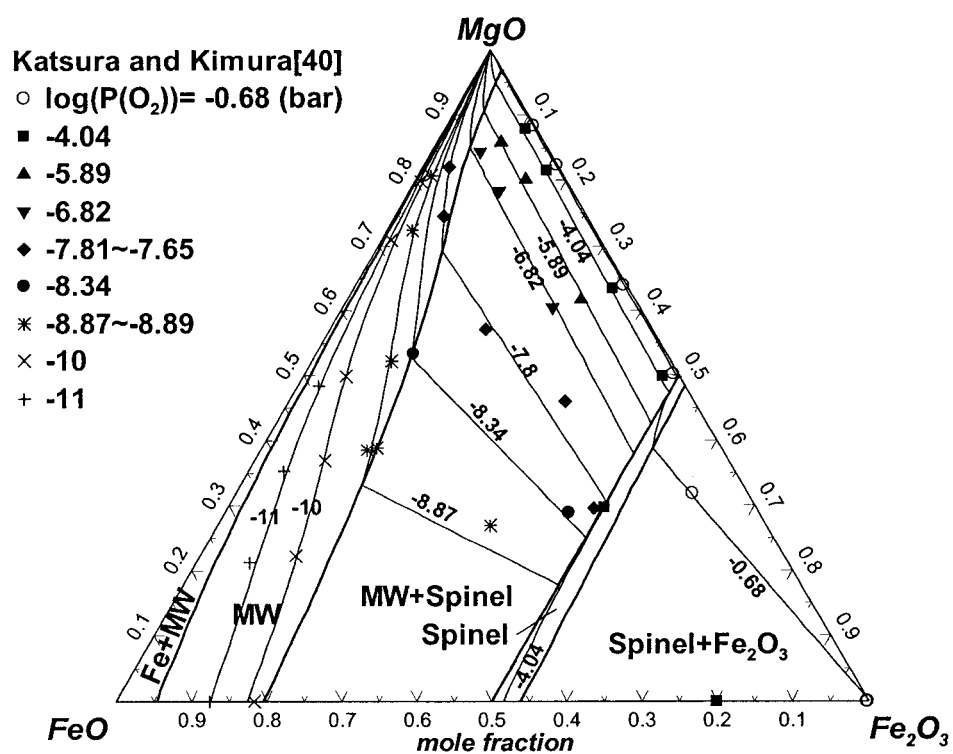
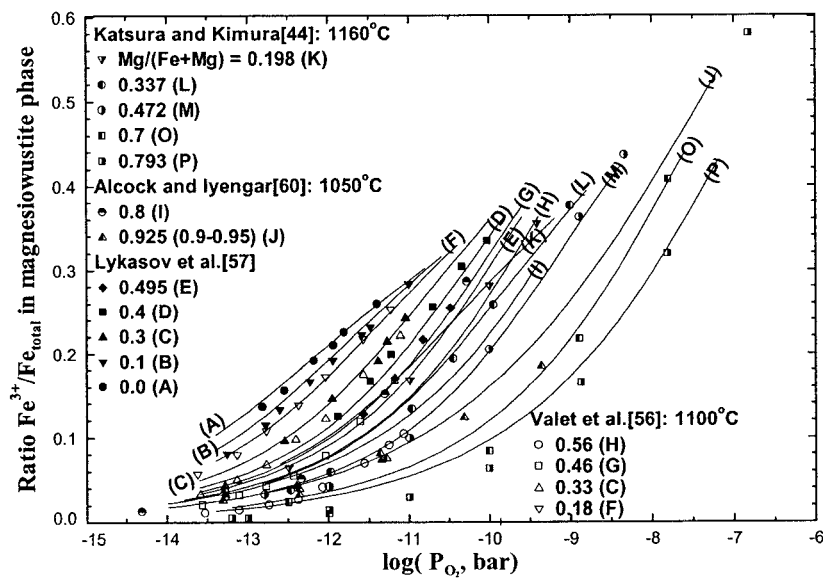
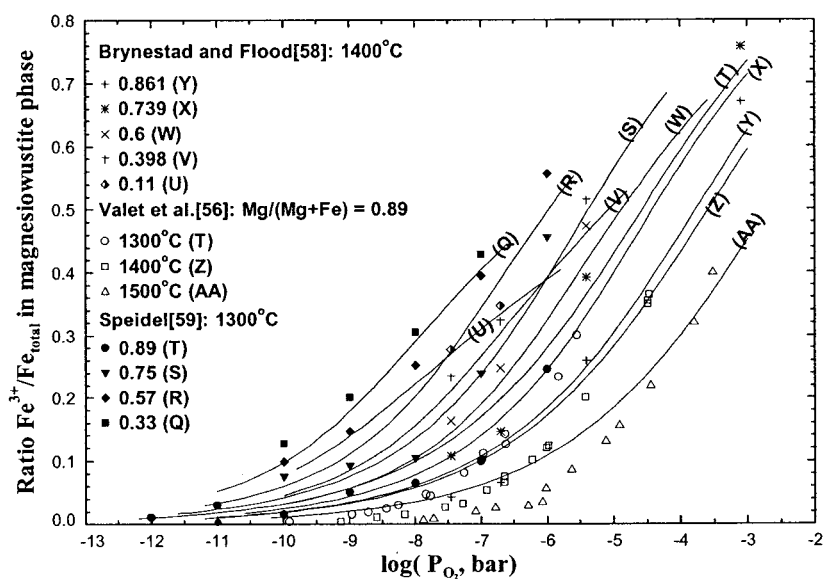


Figure 3.25 : Optimized MgO-FeO-Fe₂O₃ phase diagram with $\log P_{\text{O}_2}$ (bar) isobars at 1160°C. Thick lines are calculated phase boundaries and thin lines are calculated oxygen isobars. (See Appendix II)



(a)



(b)

Figure 3.26 : Calculated nonstoichiometries of magnesiowustite phases with the variation of oxygen partial pressure at various temperatures and molar $\text{Mg}/(\text{Mg}+\text{Fe})$ ratios. (See Appendix II)

3.6 Wollastonite solution

3.6.1 Crystal structure

Wollastonite is a chain silicate solid solution (pyroxenoid) based on CaSiO_3 in the triclinic space group: $P\bar{1}$. The wollastonites are not structurally related to the pyroxene group but have a different type of infinite chain structure, with three tetrahedra per unit cell arranged parallel to the b -axis, this repeat unit consisting of a pair of tetrahedra joined apex to apex as in the $[\text{Si}_2\text{O}_7]$ group, alternating with a single tetrahedron with one edge parallel to the chain direction.

The crystal structure of wollastonite is illustrated in Figure 3.27. In wollastonite with a chain repeat of three, octahedral bands are composed of infinite chains running parallel to the c axis that are three octahedra wide. The central chain in each band is composed of edge-sharing M3 octahedra. The M sites in wollastonite are occupied principally by Ca, Mg, Fe and Mn. The three 'M polyhedra' in wollastonite have similar occupancy, size, and distortion.

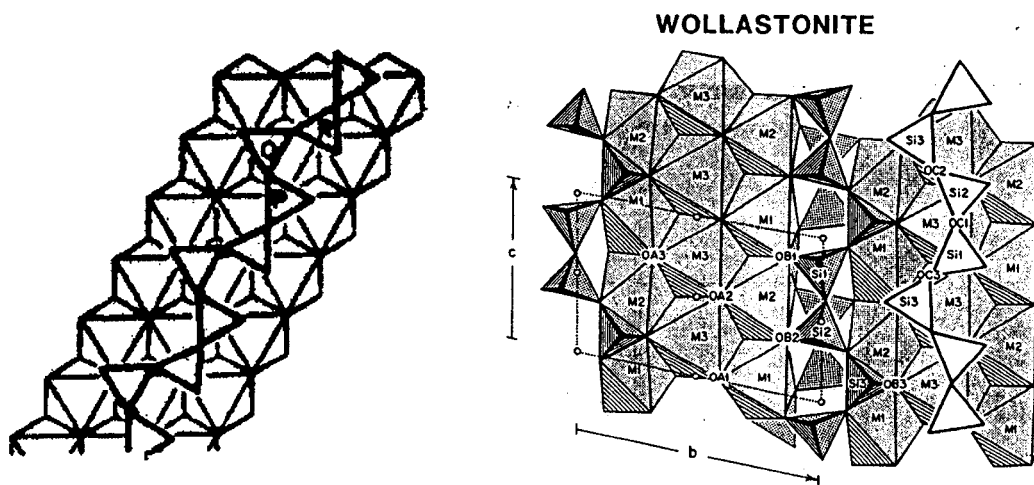


Figure 3.27 : Crystal structure of wollastonite. (After Papike, 1987)

3.6.2 Thermodynamic model

As mentioned above, wollastonite is a CaSiO_3 -based solid solution. The divalent cations such as Mg^{2+} , Fe^{2+} and Mn^{2+} can be dissolved in three indistinguishable ‘M’ sites. Thus, the wollastonite solution can be formulated as follows:



The excess Gibbs energy of wollastonite is described by a polynomial expansion with a symmetric “Kohler-like” extension (Pelton, 2001) of binary terms into multicomponent systems:

$$G^m = \sum_i X_i G_i^\circ + RT \sum_i X_i \ln X_i + \sum_i \sum_j X_i X_j \left(\frac{X_i}{X_i + X_j} \right)^m \left(\frac{X_j}{X_i + X_j} \right)^n q_{ij}^{mn} \quad (3.6.2)$$

where X_i and G_i° are the mole fraction and the Gibbs energy of component i , q_{ij}^{mn} is a binary interaction parameter which can be temperature dependent, and powers m and n are ≥ 0 . No ternary excess parameters were used in the present study.

3.7 α -Ca₂SiO₄ and α' -Ca₂SiO₄ solutions

3.7.1 Crystal structure

Pure α -Ca₂SiO₄ and α' -Ca₂SiO₄ have the orthorhombic and hexagonal structure respectively. The crystal structures of their solid solutions are not well known because Ca₂SiO₄ can easily transform to different polymorphic forms depending on the thermal history. γ -Ca₂SiO₄ is a component of the olivine solution discussed previously.

3.7.2 Thermodynamic model

α -Ca₂SiO₄ and α' -Ca₂SiO₄ are Ca₂SiO₄-based solid solutions. In this study, Ca₂SiO₄ with limited solubilities of divalent cations such as Mg²⁺, Fe²⁺ and Mn²⁺ is modeled as follows:



The excess Gibbs energy of the solution is described by a polynomial expansion with a symmetric “Kohler-like” extension (Appendix XII) (Pelton, 2001) of binary and ternary terms into multicomponent systems:

$$G^m = \sum_i X_i G_i^\circ + 2RT \sum_i X_i \ln X_i + \sum_i \sum_j X_i X_j \left(\frac{X_i}{X_i + X_j} \right)^m \left(\frac{X_j}{X_i + X_j} \right)^n q_{ij}^{mn} \quad (3.7.2)$$

where X_i and G_i° are the mole fraction and the Gibbs energy of component i , q_{ij}^{mn} is a binary interaction parameter which can be temperature dependent, and powers m and n

are ≥ 0 . The mixing of cation occurs on 2 moles of cation sublattice sites. No ternary excess parameters were used in the present study.

3.8 Liquid Fe solution

3.8.1 Thermodynamic model

3.8.1.1 Previous model: Classical Wagner Interaction Parameter Formalism

Thermodynamic properties of steel have usually been described by the well-known Classical Wagner Interaction Parameter Formalism (CWIPF). This model implicitly assumes that all atoms dissolved in liquid Fe are distributed randomly and separately, although the fact that this assumption is made is often overlooked. According to this model, the Gibbs energy of an Fe-M-O liquid solution can be described as:

$$G^m = (X_{Fe}g_{Fe} + X_Mg_M + X_Og_O) + RT(X_{Fe}\ln X_{Fe} + X_M\ln X_M + X_O\ln X_O) + RT(X_{Fe}\ln \gamma_{Fe} + X_M\ln \gamma_M + X_O\ln \gamma_O) \quad (3.8.1)$$

where the g_i are the standard Gibbs energies of the elements, X_M and X_O are the mole fractions of dissolved M and oxygen, and γ_M and γ_O are activity coefficients of M and oxygen. The g_i can be converted to g_i° , the standard Gibbs energies of the elements in the infinite dilution (Henrian) standard state, as follows:

$$g_i^\circ = g_i + RT \ln \gamma_i^\circ \quad (3.8.2)$$

where γ_i° is the Henrian activity coefficient at infinite dilution. Accordingly, equation (3.8.1) can be written as:

$$G^m = (X_{Fe}g_{Fe}^o + X_Mg_M^o + X_Og_O^o) + RT(X_{Fe}\ln X_{Fe} + X_M\ln X_M + X_O\ln X_O) \\ + RT(X_{Fe}\ln f_{Fe} + X_M\ln f_M + X_O\ln f_O) \quad (3.8.3)$$

where f_M and f_O are activity coefficients relative to the infinite dilution standard state given by:

$$\ln f_M = \varepsilon_M^M X_M + \rho_M^M X_M^2 + \varepsilon_M^O X_O + \rho_M^O X_O^2 + \rho_M^{M,O} X_M X_O + \dots \quad (3.8.4)$$

$$\ln f_O = \varepsilon_O^O X_O + \rho_O^O X_O^2 + \varepsilon_O^M X_M + \rho_O^M X_M^2 + \rho_O^{O,M} X_O X_M + \dots \quad (3.8.5)$$

where the ε and ρ coefficients are called first- and second-order interaction parameters. Note that $\varepsilon_M^O = \varepsilon_O^M$. Other interaction parameters may be included in the expansion to account for interactions with other alloying elements.

It is usually necessary for the cross-interaction parameters ε_M^O , ρ_M^O , ρ_O^M , $\rho_M^{M,O}$ and $\rho_O^{O,M}$ to be very negative in order to account for the very strong attractive interactions between dissolved M and O atoms. Furthermore, in order to reproduce the measured data over a range of temperature, the interaction parameters must generally have a strong empirical temperature dependence, usually expressed as:

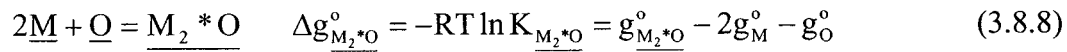
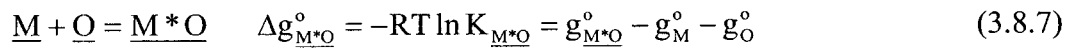
$$\varepsilon = a + b/T \quad (3.8.6)$$

(and $\rho = c + d/T$). By using many empirical parameters, it is often possible to reproduce the measured equilibria over a limited range of temperature and composition. However, the resultant equations extrapolate very poorly outside this range. In the case of very

strong deoxidants such as Ca and Mg, the interaction parameter formalism has been found to be incapable of providing a satisfactory description of the deoxidation equilibria even over the temperature and composition ranges of the measured data.

3.8.1.2 Present model: Associate Model

A new model (Associate Model) has been developed in the present study to explain the deoxidation process in liquid Fe more accurately. Schematic diagrams of the old and new models are compared in Figure 3.28. Consider a ternary liquid solution Fe-M-O, where Fe is the solvent and M is a metal solute. The solution is assumed to contain dissolved unassociated M and O atoms as well as molecules (associates) M*O and, in some systems at the highest concentrations of M, a small amount of M₂*O associates. The equilibria among the dissolved associates and the dissolved unassociated M and O atoms are represented by:



where the g_i° are standard Gibbs energies in the infinite dilution (Henrian) standard state.

Dissolved species are underlined (M and O) to distinguish them from the total amount of M and O in solution. Hence, $n_{\underline{M}}$ and $n_{\underline{O}}$ are the numbers of moles of unassociated M and O atoms, while n_M and n_O are the total numbers of moles of M and O in solution. From mass balance considerations:

$$n_M = n_{\underline{M}} + n_{\underline{M*O}} + 2n_{\underline{M_2*O}} \quad (3.8.9)$$

$$n_O = n_{\underline{O}} + n_{\underline{M^*O}} + n_{\underline{M_2^*O}} \quad (3.8.10)$$

Let $n_{Fe} = n_{\underline{Fe}}$ be the number of moles of solvent. Species mole fractions X_i may be defined as:

$$X_i = n_i / (n_{\underline{M}} + n_{\underline{O}} + n_{\underline{M^*O}} + n_{\underline{M_2^*O}} + n_{\underline{Fe}}) \quad (3.8.11)$$

($i = \underline{M}, \underline{O}, \underline{M^*O}, \underline{M_2^*O}, \underline{Fe}$), while overall component mole fractions X_i are defined as:

$$X_i = n_i / (n_M + n_O + n_{Fe}) \quad (3.8.12)$$

($i = M, O, Fe$). Note that although $n_{Fe} = n_{\underline{Fe}}$, $X_{Fe} \neq X_{\underline{Fe}}$.

The total Gibbs energy of the solution is then given by assuming random mixing of all species:

$$\begin{aligned} G = & (n_{\underline{Fe}} g_{\underline{Fe}}^o + n_{\underline{M}} g_M^o + n_{\underline{O}} g_O^o + n_{\underline{M^*O}} g_{\underline{M^*O}}^o + n_{\underline{M_2^*O}} g_{\underline{M_2^*O}}^o) \\ & + RT(n_{\underline{Fe}} \ln X_{\underline{Fe}} + n_{\underline{M}} \ln X_{\underline{M}} + n_{\underline{O}} \ln X_{\underline{O}} + n_{\underline{M^*O}} \ln X_{\underline{M^*O}} + n_{\underline{M_2^*O}} \ln X_{\underline{M_2^*O}}) \quad (3.8.13) \\ & + RT(n_{\underline{Fe}} \ln f_{\underline{Fe}} + n_{\underline{M}} \ln f_{\underline{M}} + n_{\underline{O}} \ln f_{\underline{O}} + n_{\underline{M^*O}} \ln f_{\underline{M^*O}} + n_{\underline{M_2^*O}} \ln f_{\underline{M_2^*O}}) \end{aligned}$$

Substitution of equations (3.8.7-10) into (3.8.13) yields:

$$\begin{aligned} G^m = & (n_{Fe} g_{Fe}^o + n_M g_M^o + n_O g_O^o + n_{\underline{M^*O}} \Delta g_{\underline{M^*O}}^o + n_{\underline{M_2^*O}} \Delta g_{\underline{M_2^*O}}^o) \\ & + RT \sum n_i \ln X_i + RT \sum n_i \ln f_i \quad (3.8.14) \end{aligned}$$

Equation (3.8.14) applies in the general case. However, for all systems in the present study, excellent results were obtained by assuming:

$$f_{\underline{O}} = f_{\underline{M^*O}} = f_{\underline{M_2^*O}} = 1 \quad (3.8.15)$$

That is, interaction parameters such as $\varepsilon_M^{M^*O}$, $\varepsilon_{M^*O}^{M^*O}$, *etc.* for interactions among the various species were found to be unnecessary, as was also the case for ε_O^O . The only excess Gibbs energy terms required were:

$$\ln f_{\underline{M}} = \varepsilon_M^M X_{\underline{M}} - \frac{1}{2} \varepsilon_M^M X_{\underline{M}}^2 \quad (3.8.16)$$

$$\ln f_{\underline{Fe}} = \frac{1}{2} \varepsilon_M^M X_{\underline{M}}^2 \quad (3.8.17)$$

As discussed by Pelton and Bale (Pelton and Bale, 1986; Bale and Pelton, 1990; Pelton, 1997), equations (3.8.16) and (3.8.17) are modified forms of the Wagner formalism for the Fe-M binary solution in which the final term in equation (3.8.16) has been included in order to make equations (3.8.16) and (3.8.17) consistent with the Gibbs-Duhem equation and other thermodynamic relationships. Such consistency is not found in the Classical Wagner formalism except at infinite dilution. Note that this modification does not increase the number of model parameters.

For every system Fe-M-O, the only interaction parameter used in the present study was the binary first-order parameter ε_M^M . The binary parameters ε_M^M and g_M^O are obtained by evaluation/optimization of available data for the oxygen-free Fe-M binary systems. The parameters $\Delta g_{\underline{M^*O}}^O$ and $\Delta g_{\underline{M_2^*O}}^O$ are then obtained by evaluation/optimization of available data for the Fe-M-O systems. For all systems studied, temperature-independent (i.e. constant) values of $\Delta g_{\underline{M^*O}}^O$ and $\Delta g_{\underline{M_2^*O}}^O$ were found to be sufficient.

For quaternary and higher-order systems Fe-M₁-M₂-....-O, the extension of the model equations is straightforward and will not be given explicitly here. Additional first-order cross-interaction parameters $\varepsilon_{M_1}^{M_2}$ may be required. These may be obtained by evaluation/optimization of data for the oxygen-free Fe-M₁-M₂ systems.

Finally, the activities of M and O can easily be shown to be equal to the activities of M and O (in all cases relative to the infinite dilution Henrian standard states). Hence:

$$a_M = X_{\underline{M}} f_{\underline{M}} \quad (3.8.18)$$

$$a_O = X_{\underline{O}} f_{\underline{O}} \quad (3.8.19)$$

3.8.2 Discussion

The differences between the old and new models are depicted schematically in Figure 3.28. The major difference is whether M and O are distributed separately or form some associates when M and O have a strong affinity for each other.

The failure of the CWIPF for very strong deoxidation systems results essentially from a wrong assumption of the behavior of solute atoms in liquid Fe. When Wagner applied his formalism to the deoxidation in liquid Fe, the expressions for the interaction parameters shown in equations (3.8.4) and (3.8.5) were originally taken from the Taylor expansion for more than one independent variable. For example, the interaction parameter $\ln f_M$ can be expressed by the Taylor expansion:

$$\begin{aligned}
\ln f_M = \ln f_M^o + \frac{\partial \ln f_M}{\partial X_M} X_M + \frac{\partial \ln f_M}{\partial X_O} X_O + \frac{1}{2!} \left[\frac{\partial^2 \ln f_M}{\partial X_M^2} X_M^2 + 2 \frac{\partial^2 \ln f_M}{\partial X_M \partial X_O} X_M X_O \right. \\
\left. + \frac{\partial^2 \ln f_M}{\partial X_O^2} X_O^2 \right] + \dots
\end{aligned}
\tag{3.8.20}$$

In this expression the partial derivatives are the limiting values at $X_M \rightarrow 0$ and $X_O \rightarrow 0$. From the above equation, therefore, the interaction parameters are defined as:

$$\begin{aligned}
\varepsilon_M^M = \frac{\partial \ln f_M}{\partial X_M}, \quad \varepsilon_M^O = \frac{\partial \ln f_M}{\partial X_O} \\
\rho_M^M = \frac{1}{2} \frac{\partial^2 \ln f_M}{\partial X_M^2}, \quad \rho_M^{M,O} = \frac{\partial^2 \ln f_M}{\partial X_M \partial X_O}, \quad \rho_M^O = \frac{\partial^2 \ln f_M}{\partial X_O^2} X_O^2
\end{aligned}
\tag{3.8.21}$$

The most important assumption of the Taylor expansion is that the variables X_M and X_O are independent of each other. That is, \underline{M} and \underline{O} in liquid Fe should behave independently of each other. However, when the cross-interaction parameters are very negative, then this already contradicts the assumption of the classical Wagner interaction parameter formalism itself. This is why the classical Wagner interaction parameter formalism cannot properly describe the strong deoxidation phenomena caused by Ca, Mg and Ba. Less strong deoxidation phenomena (by Al, Cr, Ti, Mn, *etc.*) may be described using the model, although several temperature-dependent cross-interaction parameters are usually necessary, and extrapolations to other compositions and temperatures are poor.

Several authors have attempted to model the Ca and Mg deoxidation curves using the classical Wagner formalism without considering the formation of associates. Figure 3.29 shows several assessed Ca deoxidation curves from previous studies. Usually authors only considered their own experimental data in their assessments. In some

cases, the shapes of the assessed curves are very strange. The model parameters used in the previous studies are summarized in Table I. As can be seen, very large negative temperature-dependent first- and second-order interaction parameters ε_M^O , ρ_M^O , $\rho_M^{M,O}$ were required. Furthermore, most authors also had to arbitrarily adjust the equilibrium constant K_{MO} for the formation of solid MO ($M = \text{Ca, Mg and Ba}$) by two or three orders of magnitude from its literature value in order to fit the data.

Thus, the difficulty in describing strong deoxidation by the classical Wagner interaction parameter formalism essentially originates from its assumption that all dissolved solutes such as M and oxygen are distributed randomly and behave separately. This assumption leads to the wrong configurational entropy, especially when M has a strong affinity for oxygen.

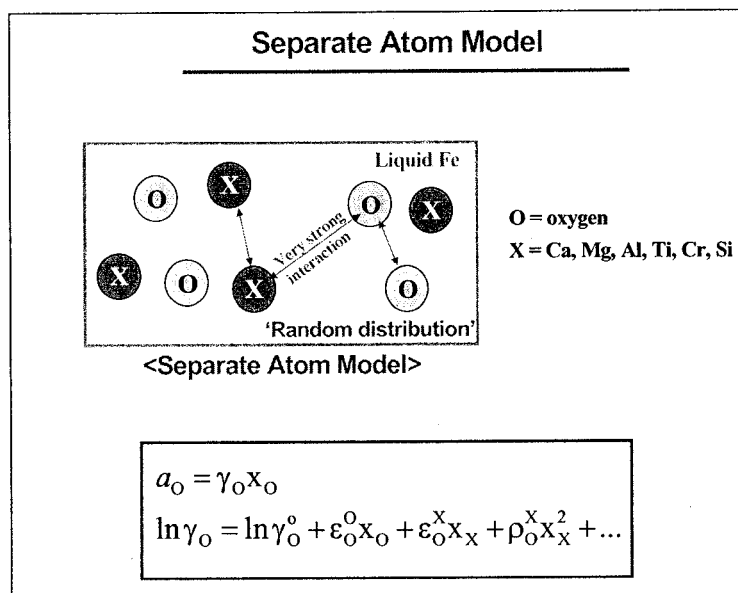
On the other hand, the Associate Model assumes the possible formation of associates in order to describe the configurational entropy of dilute solutions when M has a strong affinity to O. Although the Unified Interaction Parameter Formalism (UIPF) (Pelton and Bale, 1986; Bale and Pelton, 1990; Pelton, 1997) is used to describe the Gibbs energies of solution in a more thermodynamically correct manner, it is not the key of the model. The key of the new model is an associate reaction in solution. Thus, the model parameters of the Associate Model are the Gibbs energies of the associate formation, while the CWIPF uses the cross-interaction parameters. Moreover, the Gibbs energies for the association reactions, $\Delta g_{M^*O}^O$ and $\Delta g_{M_2^*O}^O$, in equations (3.8.7) and (3.8.8) were found to be temperature-independent and to reproduce the experimental data for all Fe-M-O systems studied in this study. This indicates strongly that the configurational entropy of the systems is well described by the model.

Figures 3.30 to 3.32 show the calculated optimized deoxidation curves in the Fe-Ca-O, Fe-Mg-O and Fe-Ba-O systems using the Associate Model. The curves in the figures

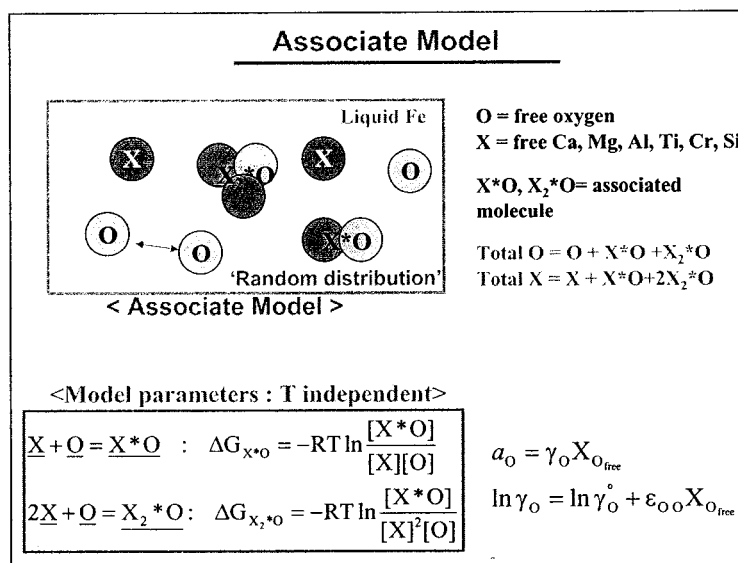
are calculated from the Associate Model with the assumed dissolved associate M^*O ($M = Ca, Mg \text{ and } Ba$), with one temperature-independent parameter, Δg_{M^*O} for the association reaction $\underline{M} + \underline{O} = \underline{M^*O}$. Using the Associate Model, no cross-interaction parameter are necessary. Moreover, the accepted literature values, as recommended by Turkdogan (1991), for the equilibrium constants for the reaction: $\underline{M} + \underline{O} = MO(s)$ were used.

The calculated solubility (deoxidation) curves by other authors all have strange shapes, some with minima and maxima, and even one in the form of a circle. The model of JSPS (1988) is the most widely used; the “deoxidation curve” calculated from this model, and reported in the literature, is shown in Figure 3.29 by the dashed line. Hence, it is believed that the present calculations elucidate the deoxidation behavior of Ca, Mg and Ba for the first time.

It is shown that the Associate Model can be applied to all general deoxidation systems Fe-M-O ($M = Ca, Mg, Ba, Al, Ti, Cr, V, Mn, Si, B, Ce, Nb, Zr, \dots$) The details of the model and results of the optimization of these Fe-M-O systems are shown in Appendix IX.



(a)



(b)

Figure 3.28 : Comparison of the models for deoxidation equilibria of liquid Fe. (a) previous model (Classical Wagner Interaction Parameter Formalism: separate atom model) and (b) new model (Associate Model).

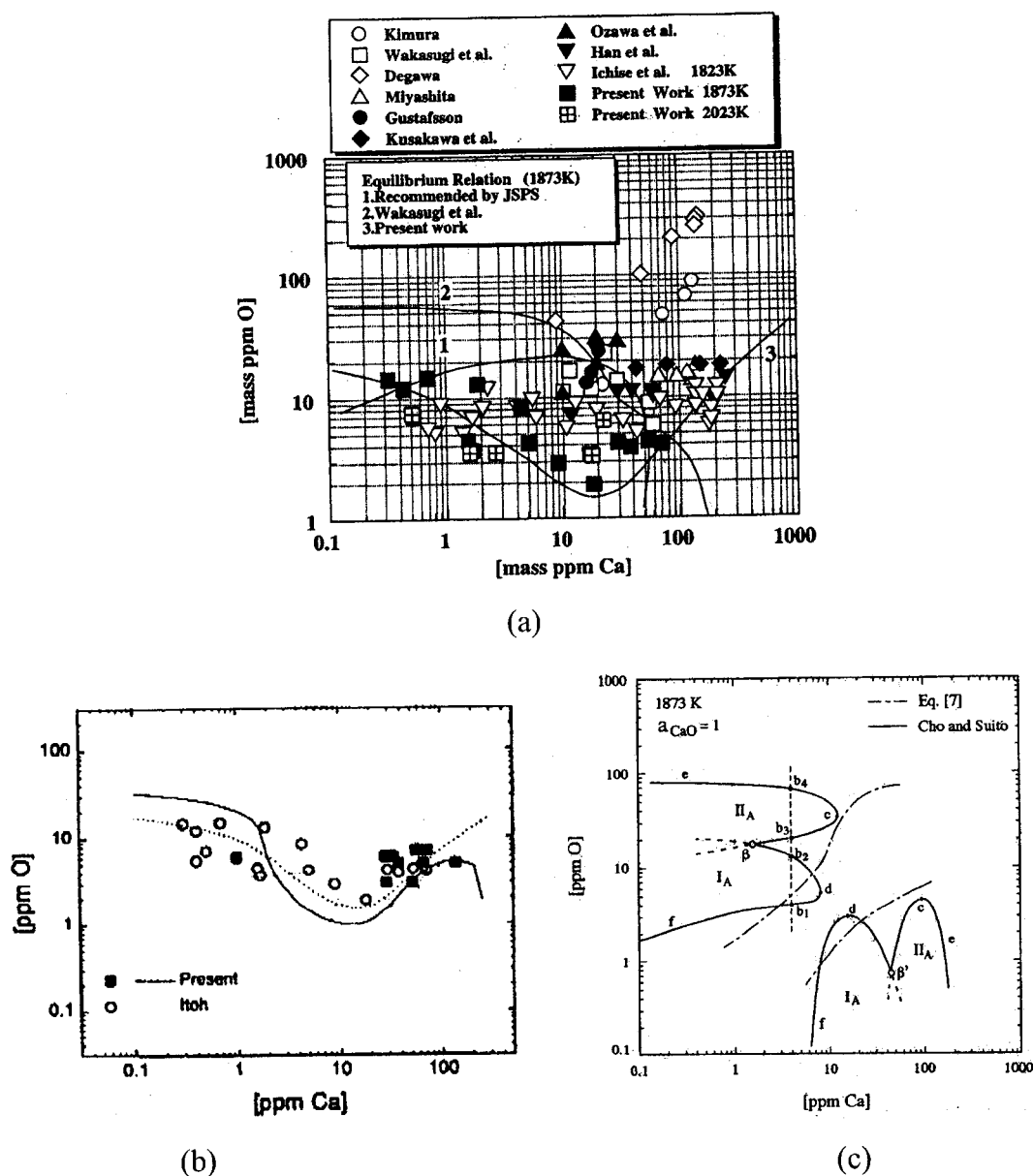


Figure 3.29 : Assessed deoxidation equilibria in previous studies using the Classical Wagner Interaction Parameter Formalism. (a) Itoh *et al.* (1997): '3' and JSPS (1988): '1' (b) Seo and Kim (2001) and (c) Cho and Suito (1994) and Ohta and Suito (1997): 'Eq.[7]'. Neither model can explain the entire region by one equation (need different set of model parameters depending on composition range).

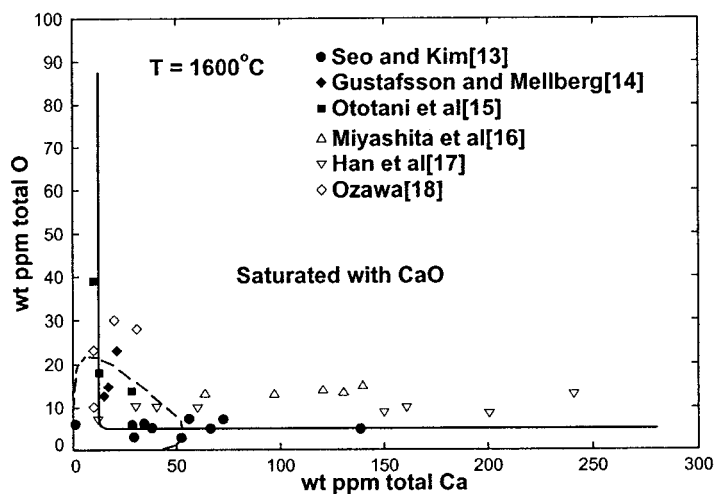


Figure 3.30 : Total dissolved oxygen and total dissolved Ca contents of liquid Fe in equilibrium with solid CaO. Lines calculated from database with the Associate Model. Dashed line calculated from the Classical Wagner Formalism with parameters of JSPS (1988). See Appendix IX.

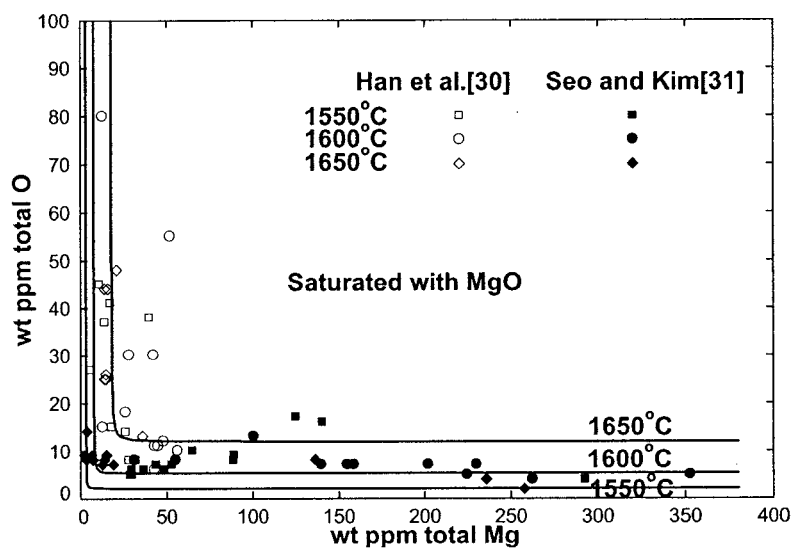


Figure 3.31 : Total dissolved oxygen and total dissolved Mg contents of liquid Fe in equilibrium with solid MgO. Lines calculated from the Associate Model. See Appendix IX.

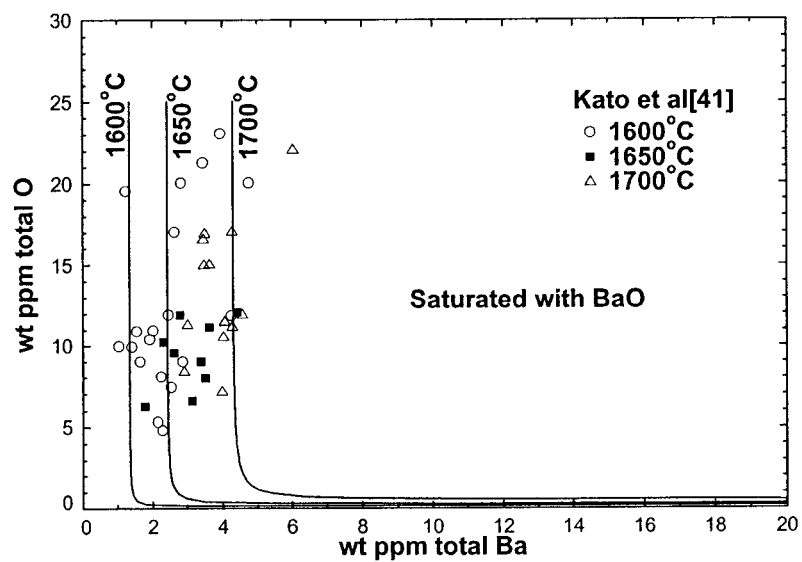


Figure 3.32 : Total dissolved oxygen and total dissolved Ba contents of liquid Fe in equilibrium with solid BaO. Lines calculated from the Associate Model. See Appendix IX.

Table 3.1 : Comparison of the model parameters for the Fe-Mg-O and Fe-Ca-O systems obtained in previous studies using the Classical Wagner Interaction Parameter Formalism with the present study using the Associate Model.

System	MO(s) = $\underline{M}(x, l) + \underline{O}(x, l)$ at 1873 K	Interaction parameter, ϵ_M^O at 1873 K	Ref.
Fe-Mg-O	$\log K_{\text{MgO}} = -9.89$	$\epsilon_{\text{Mg}}^O = -28094$ and 2 nd order	[2]
	$\log K_{\text{MgO}} = -9.02$	$\epsilon_{\text{Mg}}^O = -8018$	[3]
	$\log K_{\text{MgO}} = -10.31$	$\epsilon_{\text{Mg}}^O = -37084$ and 2 nd order	[4]
	$\log K_{\text{MgO}} = -10.96$	$\epsilon_{\text{Mg}}^O = -30364$ and 2 nd order	[9]
	$\log K_{\text{MgO}} = -10.84$	-	[1]
	$\log K_{\text{MgO}} = -10.86$	Formation of Mg*O $\Delta G_{\text{Mg}^*\text{O}} = -222.46\text{kJ/mol}$	This study
Fe-Ca-O	$\log K_{\text{CaO}} = -10.46$	$\epsilon_{\text{Ca}}^O = -54224$ and 2 nd order	[2]
	$\log K_{\text{CaO}} = -11.57$	$\epsilon_{\text{Ca}}^O = -78489$	[5]
	$\log K_{\text{CaO}} = -10.76$	$\epsilon_{\text{Ca}}^O = -65270$ and 2 nd order	[4]
	$\log K_{\text{CaO}} = -9.11$	$\epsilon_{\text{Ca}}^O = -10245$	[6]
	$\log K_{\text{CaO}} = -13.14$	$\epsilon_{\text{Ca}}^O = -88403$	[7]
	$\log K_{\text{CaO}} = -13.53$	Similar to ref. [9] (4 separate regions)	[8]*
	$\log K_{\text{CaO}} = -13.53$	$\epsilon_{\text{Ca}}^O = -594086$ or -165023 and 2 nd order (2 separate regions)	[9]*
	$\log K_{\text{CaO}} = -13.65$	-	[1]
	$\log K_{\text{CaO}} = -13.32$	Formation of Ca*O $\Delta G_{\text{Ca}^*\text{O}} = -305.83\text{kJ/mol}$	This study

[1] Turkdogan (1991), [2] Itoh et al. (1997), [3] Han et al. (1997), [4] Seo and Kim (1999), [5] Han et al. (1998), [6] Gustafsson and Mellberg (1980), [7] Kobayashi et al. (1970), [8] Cho and Suito (1994) and [9] Ohta and Suito (1997).

* These models cannot explain the entire region by one equation (need different set of model parameters depending on composition range).

4. Application of the Thermodynamic Database to VOD Process Simulation in Stainless Steelmaking

4.1. Introduction

The Vacuum Oxygen Decarburization (VOD) process is a secondary refining process in the production of stainless steel. The main goal of the process is the reduction of carbon in stainless steel by oxygen blowing as well as the refinement of other impurities such as sulfur, phosphorus and nitrogen under reducing atmosphere. However, the process is quite difficult to investigate and understand due to the complex thermodynamic equilibria among ‘liquid steel-slag-refractories-solid oxides-gases’ involving vacuum and oxygen blowing. The main components in the VOD process are:

Refractories: Spinel solution of MgCr_2O_4 - MgAl_2O_4 - MgFe_2O_4 - Fe_3O_4 - FeCr_2O_4
 + Periclase (MgO-rich) with minor Cr_2O_3 , Al_2O_3 , FeO and Fe_2O_3
 Slags: CaO - MgO - Al_2O_3 - SiO_2 - CrO - Cr_2O_3 with minor FeO, Fe_2O_3 and MnO
 Liquid stainless steel: Fe-18wt%Cr-8wt%Ni-Al-Si-Mn-C-O *etc.*
 Gases: oxygen blowing with Ar bubbling

One of the current issues in the VOD process is the extension of the lifetime of refractories under harsh process conditions. Possible dissolution mechanisms of the refractories have been investigated by analysis of real plant refractories after long term use in operation.[Jones, 2001; Jones *et al.*, 2000] Although the thermodynamic equilibria between slags and refractories under reduced oxygen partial pressure should be investigated in order to understand the mechanisms more clearly, this has not been well investigated thermodynamically because of experimental difficulties: VOD is a closed operating system under vacuum.

Therefore, in order to investigate the refractory dissolution mechanism in more detail, two groups, the CRCT at Ecole Polytechnique in Montreal and MTM at K.U. Leuven, Belgium (led by Prof. P. Wollants) started a cooperative project on the VOD process.

As a first step in the project, all available thermodynamic data related to the VOD system were gathered and the thermodynamic optimizations of the system were performed. The main oxide system in the VOD process is $\text{CaO-MgO-Al}_2\text{O}_3\text{-SiO}_2\text{-CrO-Cr}_2\text{O}_3\text{-FeO-Fe}_2\text{O}_3$. The major part of this oxide system has now been optimized. The spinel and monoxide databases for the Fe-Mg-Al-Cr-Ni-O system were developed in the present study partially as part of this cooperation. New experiments on phase equilibria and kinetics related to the VOD processes are being conducted by MTM.

The goal of this chapter is to apply the thermodynamic database to the simulation of the VOD processes in order to better understand the corrosion mechanism of refractories.

4.2 VOD process simulation

4.2.1 Overview of VOD process

The VOD process consists of three stages. While the actual process conditions are a function of the initial metal conditions and the steel grade, the general features are as follows:

Oxygen blowing: The purpose of this stage is the decarburization of liquid stainless steel by oxygen blowing. Alloys and fluxes can be added in advance. The oxygen flow rate is between 30 and 60 Nm^3/min and the blowing times range from 30 to 60 minutes. The process is performed at pressures between 100 and 200 mbar. To enhance the kinetics of the decarburization, bottom argon bubbling is performed.

Degassing: The degassing stage can reduce the carbon content in the steel further by reducing the total pressure to between 1 mbar and 5 mbar usually for 10 minutes. During this stage, only bottom argon bubbling is performed.

Reduction: During the reduction stage, a reducing agent such as Al or Si is added to recover the chromium that has been oxidized during the blowing stage. Also fluxes such as dolomite, lime and fluorspar are added to control the slag composition and fluidity. Some alloying elements are also added to produce the desired steel grade. The reduction stage lasts more than 20 minutes and the total pressure is about 1 to 5 mbar. Bottom argon bubbling is performed during the reduction stage.

Due to the bottom argon bubbling during all stages, the kinetics are fast in the VOD process. Hence, the process is close to the equilibrium state and thus it can be well simulated based on thermodynamic calculations.

4.2.2 VOD simulation (No consideration of refractories)

The equilibria between (gas/slag/liquid stainless steel/solid oxide) phases were calculated using the FactSage (2002) software. FactSage has a special feature termed an “open calculation.” This feature makes it possible to simulate gas blowing in an open system. In a gas blowing process, gas is continuously injected into the reactor vessel. The gas reacts, rapidly achieving equilibrium, and the equilibrium gases are continuously removed from the system. The FactSage “open calculation” simulates this process. During the VOD process, oxygen and Ar are continuously blown into the vessel. It is assumed that equilibrium is attained rapidly.

In this study, the specific conditions (Jones, 2001) of the VOD process were chosen on the basis of real plant process data at ALZ (Stainless steel company in Genko, Belgium). In order to understand how the slag composition changes during the process, initially the

refractory is not taken into account in the calculations. Actually, the refractory mainly reacts with molten slag in the reduction stage. To investigate the dissolution mechanism of refractory materials, the reaction between the final slag and refractories after the reduction stage will be calculated later.

The specific conditions of the calculations are:

- Temperature: 1650°C (For convenience of the calculations. T is fixed. The actual temperature range during VOD is between 1550°C and 1750°C)
- Amount of liquid steel per charge in VOD: 120 tonnes
- Initial steel composition in VOD process: Fe-18Cr-8Ni-0.4C-0.4Si-0.4Mn (in wt%)

- Oxygen blowing stage

Flow rate of oxygen: 35 Nm³/min (0.05 tonnes of O₂/min)

Oxygen blowing efficiency: 80% (0.04 tonnes of O₂/min)

Flow rate of Ar: 0.35 Nm³/min

Duration: 50 minutes

Total pressure: 0.1 bar

Addition of fluxes: 0.45 tonnes CaO

- Degassing stage:

Flow rate of Ar: 0.35 Nm³/min

Duration: 10 minutes

Total pressure: 0.001 bar

- Reduction stage:

Duration: 40minutes

Flow rate of Ar: 0.5 Nm³/min

Total pressure: 0.001 bar

Addition of fluxes: 1.8CaO, 0.2MgO, 1.0Si, 0.15Al, 0.27Cr, 1.0Mn
(in tonnes)

The results of the VOD simulation are shown in Figures 4.1 to 4.3. Refractories are not taken into account in these calculations. A second calculation will be performed below to investigate the reaction between the slag (final slag in the reduction stage) and the refractories.

Oxygen blowing stage:

As can be seen in Figure 4.1, the amount of solid and liquid (slag) oxide phases vary during the process. CaO fluxed at the beginning of the oxygen blowing stage is first transformed to Ca_2SiO_4 because the blown oxygen reacts with Si in the reaction: $2\text{CaO(s)} + \text{Si} + 1/2\text{O}_2(\text{g}) = \text{Ca}_2\text{SiO}_4(\text{s})$. Next, slag saturated with Ca_2SiO_4 is formed as oxygen reacts with more Si. Once the slag is formed, oxygen begins to react with Cr to increase the Cr oxide content (mainly as CrO) in the slag. (See Figure 4.2) As oxygen blowing continues, more Cr reacts and eventually Cr_2O_3 (s) begins to precipitate from the slag. At the end of the oxygen blowing stage, the amount of Cr_2O_3 and slag are calculated to be 2.6 and 1.8 tonnes respectively.

During the oxygen blowing stage, C is decreased by reaction with oxygen. (See Figure 4.3) But it should be noted that no decarburization occurs in the initial few minutes because the blown oxygen reacts only with Si. Also, C is not reduced significantly after the formation of $\text{Cr}_2\text{O}_3(\text{s})$ begins (after about 35 minutes) because the blown oxygen is thereafter mainly consumed to oxidize Cr in the stainless steel to form chromium oxide rather than being consumed in the decarburization reaction. Therefore, according to the calculations, blowing oxygen for more than 35 minutes results in excess Cr_2O_3 being formed and so more time will be needed to reduce Cr_2O_3 in the reduction stage. This is

uneconomical. These results show that shortening the oxygen blowing time may increase the efficiency of the VOD process.

Degassing stage:

In the degassing stage, the carbon is reduced thermodynamically to 20 wt ppm under 0.001 bar pressure. Simultaneously, most of the $\text{Cr}_2\text{O}_3(\text{s})$ formed during the oxygen blowing stage is reduced to Cr in the liquid stainless steel. Small amounts of Mn may be volatilized.

Reduction stage:

Lime, dolomite, ferro-Al and ferro-Si alloys are added in the beginning of the reduction stage in order to reduce the chromium oxide content in the slag and to recover Cr in the liquid stainless steel. Ferro-Cr and ferro-Mn may be added to adjust the final steel composition. The amount of slag increases up to about 4 tonnes. The chromium oxide content of the slag decreases from 40 wt% to less than 1 wt%. As can be seen in Figure 4.1, the final slag is saturated with neither the periclase nor spinel phase of the VOD refractories. Therefore, significant corrosion reactions can be expected to occur between slag and refractories.

4.2.3 Slag and refractories reaction

In the oxygen blowing stage, because the liquid slag mixes with a great amount of solid Cr_2O_3 , the corrosion of refractories may not be so severe. However, during the reduction stage, because only liquid slag exists and the slag is less viscous (high CaO), more reaction between slag and refractories can be expected. Hence, it is assumed that the corrosion of refractories only occurs in the reduction stage. Therefore, the corrosion

of refractories was simulated in a separate calculation using the final slag obtained after the reduction stage.

The initial composition of the refractories (Jones, 2001) is: $58\text{MgO} + 6.5\text{Al}_2\text{O}_3 + 21\text{Cr}_2\text{O}_3 + 13.5\text{FeO}$ (in wt%). For this composition, periclase and spinel are calculated to coexist at 1650°C under reducing condition: 73wt% Periclase (composition: $72.8\text{MgO} + 0.6\text{Al}_2\text{O}_3 + 9.1\text{Cr}_2\text{O}_3 + 17.5\text{FeO}$ in wt%) and 27 wt% spinel (composition: $21.5\text{MgO} + 22.5\text{Al}_2\text{O}_3 + 53.4\text{Cr}_2\text{O}_3 + 2.6\text{FeO}$ in wt%). That is, this is the calculated equilibrium phase assemblage in the refractories.

Thermodynamic calculations were performed for reaction between the final slag obtained in the reduction stage and the refractories. The change of slag composition and the equilibrium phases were calculated with increasing dissolution of the refractories into the slag. In the calculations, small amounts of refractory were “added” to the slag incrementally, and the equilibrium was re-calculated after each incremental addition. Figure 4.4 shows the amount of the equilibrium phases with the dissolution of refractories. As can be seen in the figure, up to 0.5 tonnes of refractories can dissolve before the slag becomes saturated in spinel. Thereafter, an additional 0.3 tonnes can dissolve until saturation with periclase occurs. Thereafter, the corrosion rate should decrease markedly.

The change of slag composition during the dissolution of refractories is calculated in Figure 4.5. With the dissolution of refractories, the content of MgO increases while the contents of CaO and SiO_2 decrease accordingly. The composition of slag analyzed at ALZ after VOD process is (Jones 2001; Szabo, 2003): $\text{CaO}(45 \pm 3)\text{-SiO}_2(35 \pm 3)\text{-MgO}(9 \pm 2)\text{-Al}_2\text{O}_3(7 \pm 2)$, etc. in wt%. According to the calculations, the analyzed slag composition can be located about between 0.5 to 0.7 tonnes, as marked in Figure 4.5. (Although the calculated concentrations of CaO and SiO_2 are different from the

analyzed values by about 2 wt%, these concentrations could be highly dependent on the fluxes added in the VOD processes.)

Therefore, from the present calculations it may be said that the slag dissolves the refractories up to about 0.5 to 0.8 tonnes and that the periclase phase in the refractories is corroded more severely than the spinel phase as can be seen in Figure 4.4. This was also found from the analysis of worn refractories in the plant. (Jones, 2001) In order to protect the refractories in the VOD vessel, therefore, more MgO flux should be added to ensure that the slag phase is saturated with both periclase and spinel phase. Moreover, additions of different types of flux can be easily simulated using the current thermodynamic databases in order to determine the best refractories and fluxes for the VOD process.

4.3 Summary

The thermodynamic databases developed in the present study were applied to the simulation of the VOD process in stainless steelmaking. The complex ‘gas/slag/solid oxides/refractories/liquid stainless steel’ equilibria under reducing atmospheres were calculated using the “open calculation” option of the FactSage (2002) software. From the simulated results, the dissolution mechanism of the refractories could be understood more clearly and suggestions have been made to prolong the lifetime of refractories and to make the blowing process more efficient.

Currently, on the basis of the present results, equilibrium and kinetic experiments for better understanding the VOD process are being conducted by the MTM group in Belgium. Process simulation software such as SimuSage (2002) will be used to better model the process kinetics using the current thermodynamic databases. In the near future, therefore, better modeling of the VOD process will be achieved in cooperation

with the MTM group, with a view to improving the VOD process for stainless steelmaking.

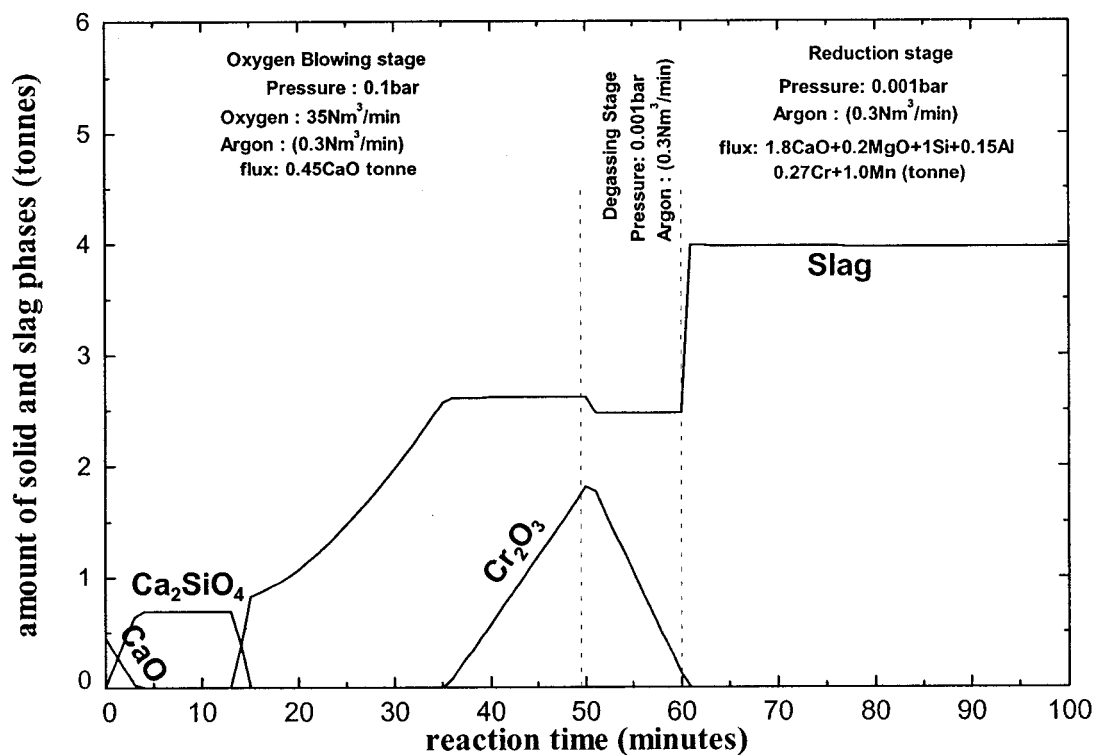


Figure 4.1 : The calculated amount of solid and slag phases formed during the VOD process at 1650°C for 120 tonnes stainless steel. The specific process conditions are from real plant data at ALZ in Belgium.

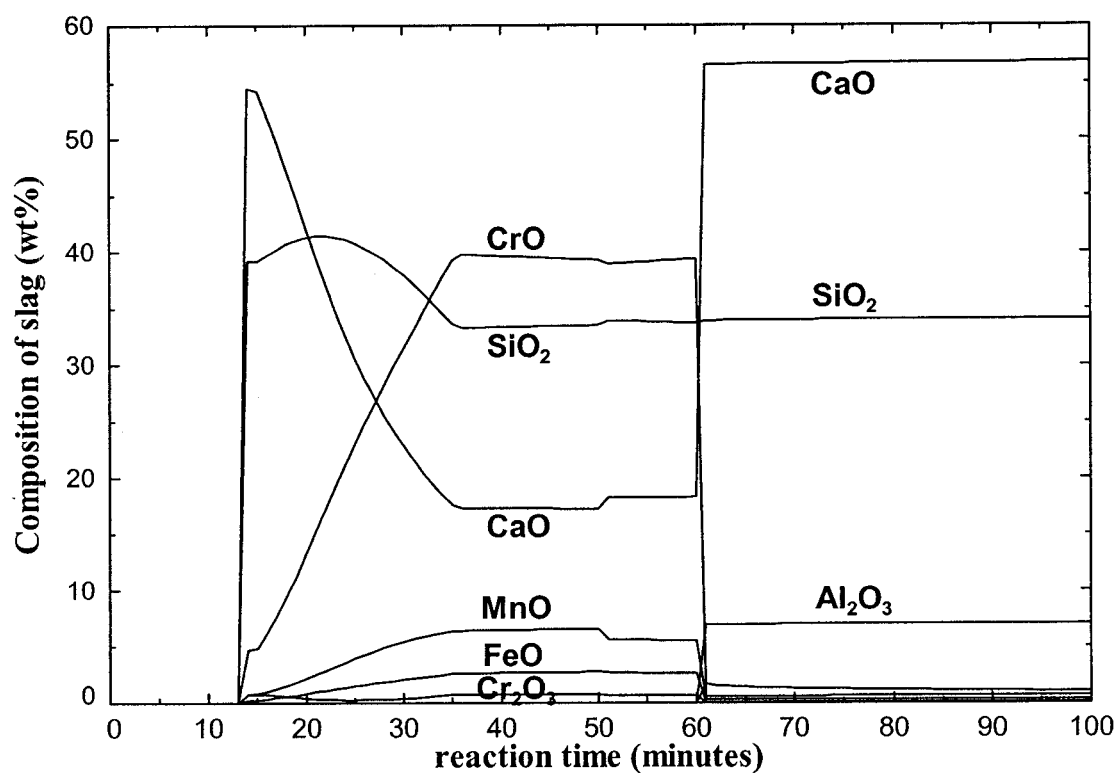


Figure 4.2 : The calculated slag composition during the VOD process at 1650°C for 120 tonnes stainless steel.

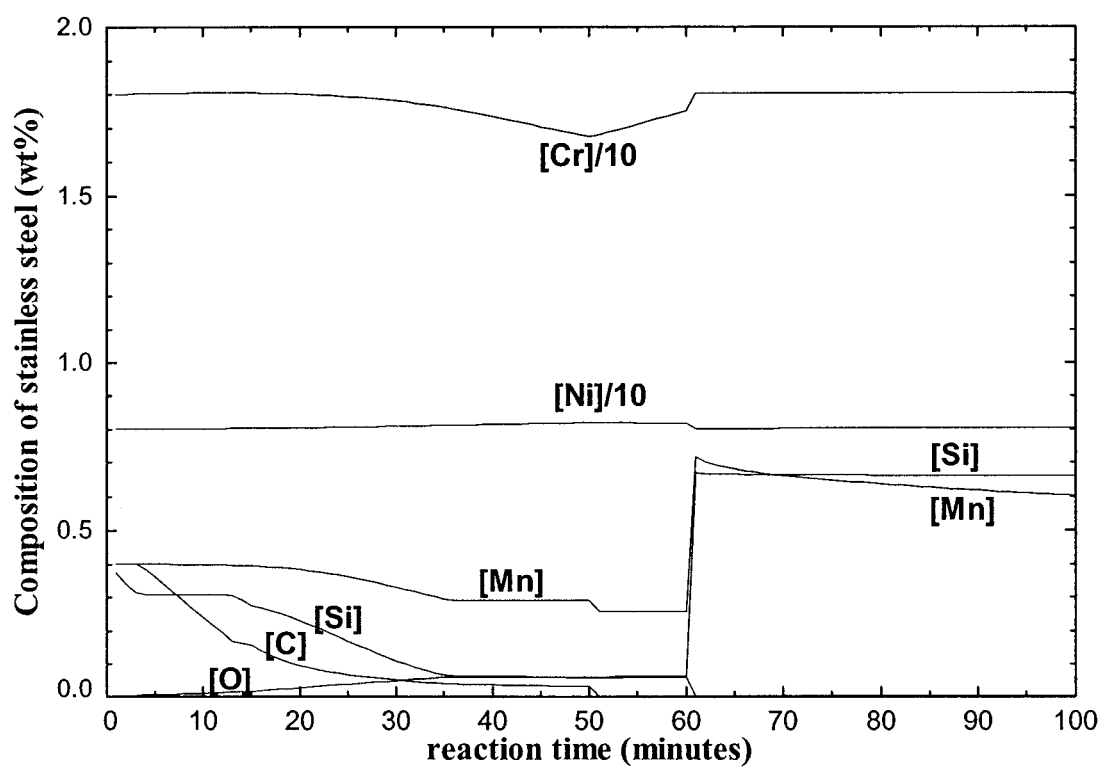


Figure 4.3 : The calculated composition of liquid stainless steel during the VOD process at 1650°C for 120 tonnes stainless steel.

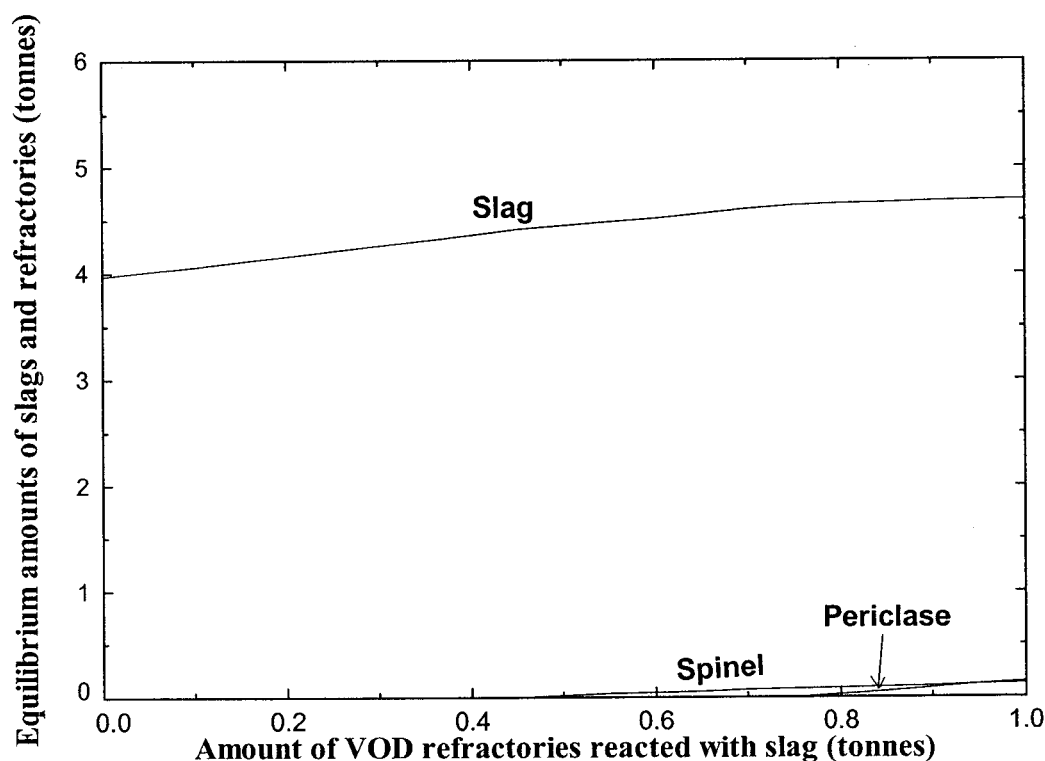


Figure 4.4 : The change of the phases at equilibrium during the dissolution of refractories at 1650°C. In the simulation, the slag is taken from the final reduction slag in Figures 4.1 and 4.2 and additions of small amounts of refractory are made incrementally, with equilibrium being recalculated after each addition. The overall refractories composition is 58MgO + 6.5Al₂O₃ + 21Cr₂O₃ + 13.5FeO (in wt%), composed of spinel and periclase phases. The formation of periclase and spinel phases in the figure means that the slag has become saturated in these phases and so the rate of corrosion should decrease markedly.

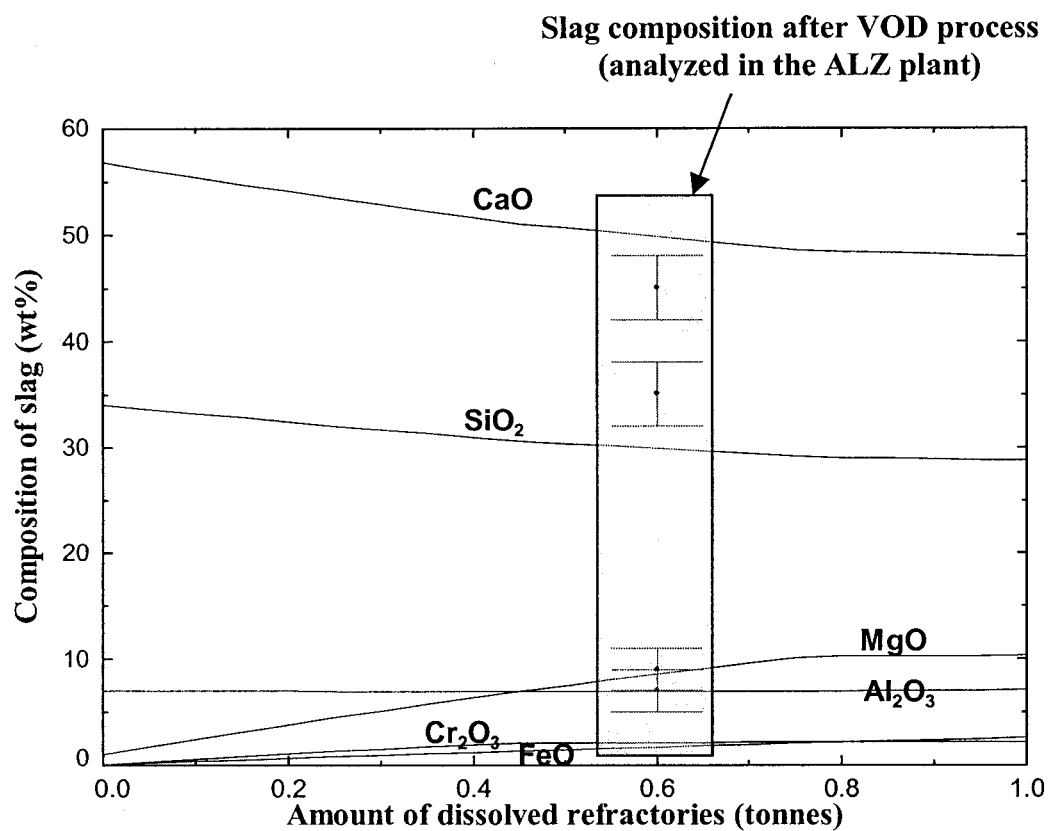


Figure 4.5 : The calculated change of slag composition during the dissolution of refractories at 1650°C. The shaded square means the position of average slag composition analyzed in ALZ after the VOD process. (See text for details)

5. Discussions and Conclusions

5 binary, 9 ternary and 5 multicomponent systems (including all solid and liquid phases) in the $\text{CaO-MgO-Al}_2\text{O}_3\text{-SiO}_2\text{-FeO-Fe}_2\text{O}_3\text{-MnO-CrO-Cr}_2\text{O}_3\text{-CoO}$ were critically evaluated and optimized in the course of the present study. All oxide systems were optimized to be thermodynamically consistent with existing alloy and salt databases.

In Chapter 3, all thermodynamic models used in this study were described in detail. All thermodynamic models are based on the structures of the solutions. The advantages of the present models were discussed in comparison with previous models. All present thermodynamic models show very high predictive ability. The complex spinel solid solution in the Fe-Mg-Al-Cr-Co-O system was completely optimized with consideration of non-stoichiometry. The liquid oxide and monoxide solutions were optimized. Extensive silicate solid solutions such as olivine, pyroxene, wollastonite, *etc.* were also well optimized.

A new Associate Model for molten steel was developed in order to explain the deoxidation equilibria in liquid Fe. This model can accurately describe the deoxidation phenomena of strong deoxidants such as Ca, Mg and Ba using only one temperature-independent model parameter. This is not possible with the Classical Wagner Interaction Parameter Formalism. This is, the first time the deoxidation equilibria of these strong deoxidants has been elucidated. The model can be applied to the deoxidation equilibria of all common deoxidant elements in liquid Fe and can explain the deoxidation equilibria with fewer model parameters than the classical interaction parameter model.

The thermodynamic databases developed in this study were applied, by way of example, to industrial processes: inclusion engineering in the steelmaking industry and vacuum

oxygen decarburization (VOD) simulation in the stainless steelmaking process. The usefulness of the present optimized databases can be confirmed from the results.

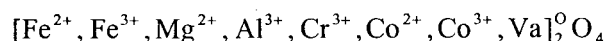
The newly optimized databases and thermodynamic models for the oxide phases and liquid Fe have been incorporated into the FACT databases. Consequently, the accuracy and range of applicability of the FACT thermodynamic database to industrial and natural processes has been expanded significantly.

The phases and systems evaluated and optimized in the present study are summarized below:

Phases:

Liquid oxides (slag): $\text{SiO}_2\text{-CaO-MgO-AlO}_{1.5}\text{-FeO-FeO}_{1.5}\text{-MnO-CrO-CrO}_{1.5}\text{-CoO}$

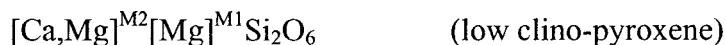
Spinel: $(\text{Fe}^{2+}, \text{Fe}^{3+}, \text{Mg}^{2+}, \text{Al}^{3+}, \text{Cr}^{2+}, \text{Cr}^{3+}, \text{Co}^{2+}, \text{Co}^{3+})^T$



Olivine: $[\text{Ca}, \text{Mg}, \text{Fe}^{2+}, \text{Mn}^{2+}, \text{Co}^{2+}]^{\text{M2}}[\text{Ca}, \text{Mg}, \text{Fe}^{2+}, \text{Mn}^{2+}, \text{Co}^{2+}]^{\text{M1}}\text{SiO}_4$

Pyroxene: $[\text{Ca}, \text{Mg}, \text{Fe}^{2+}]^{\text{M2}}[\text{Mg}, \text{Fe}^{2+}, \text{Fe}^{3+}, \text{Al}^{3+}]^{\text{M1}}(\text{Si}, \text{Fe}^{3+}, \text{Al}^{3+})^{\text{B}}\text{Si}^{\text{A}}\text{O}_6$

(clino-, ortho-, proto-pyroxene)



Monoxide: $(\text{Mg}^{2+}, \text{Ca}^{2+}, \text{Fe}^{2+}, \text{Mn}^{2+}, \text{Co}^{2+}, \text{Fe}^{3+}, \text{Al}^{3+}, \text{Cr}^{3+})(\text{O}^{2-})$

Wollastonite: $(\text{Ca}, \text{Mg}, \text{Fe}, \text{Mn})\text{SiO}_3$

$\alpha\text{-Ca}_2\text{SiO}_4$ and $\alpha'\text{-Ca}_2\text{SiO}_4$: $[\text{Ca}, \text{Mg}, \text{Fe}, \text{Mn}]_2\text{SiO}_4$

Numerous stoichiometric unary, binary and ternary oxide compounds: CoO(solid and liquid), solid $\text{Ca}_3\text{MgSi}_2\text{O}_8$ (merwinite), $\text{Ca}_2\text{MgSi}_2\text{O}_7$ (akermanite), $\text{CaMg}_2\text{Al}_{16}\text{O}_{27}$, $\text{Ca}_2\text{Mg}_2\text{Al}_{28}\text{O}_{46}$, $\text{Ca}_3\text{MgAl}_4\text{O}_{10}$, MnAl_2O_4 (galaxite), $\text{Mn}_2\text{Al}_4\text{Si}_5\text{O}_{18}$ (Mn-cordierite), $\text{Mn}_3\text{Al}_2\text{Si}_2\text{O}_{12}$ (spessartite), $\text{Mg}_4\text{Al}_{10}\text{Si}_2\text{Si}_{23}$ (sapphirine), $\text{Mg}_2\text{Al}_4\text{Si}_5\text{O}_{18}$ (cordierite), as well as all end-members in solid solutions.

Liquid Fe: Deoxidation equilibria of liquid Fe containing Al, B, Ba, C, Ca, Ce, Cr, Hf, La, Mg, Mn, Nb, Nd, Ta, Ti, Th, Si, V and Zr.

Systems:

(1) CaO-MgO-SiO₂ system (Appendix I)

A complete critical evaluation and thermodynamic modeling of phase diagrams and thermodynamic properties of the CaO-MgO-SiO₂ system at 1 bar pressure are presented. The molten oxide phase is described by the Modified Quasichemical Model, and the Gibbs energies of the olivine and pyroxene solid solutions are modeled using the Compound Energy Formalism. A set of optimized model parameters of all phases is obtained which reproduces all available and reliable thermodynamic and phase equilibrium data within experimental error limits from 25°C to above the liquidus temperatures over the entire composition range. The database of the model parameters can be used along with software for Gibbs energy minimization in order to calculate any phase diagram section or phase equilibrium of interest.

(2) Mg-Fe-O system (Appendix II)

Complete critical evaluation/optimization of experimental data at 1 bar total pressure for the FeO-Fe₂O₃-MgO system is performed in this study. The optimized model parameters can reproduce all reliable thermodynamic and structural data as well as the phase diagrams

of the FeO-Fe₂O₃-MgO system within experimental error limits. No ternary model parameters were required. For the spinel phase, no model parameters for interaction energies between cations on the same sublattice were needed. Using a proper thermodynamic model for each phase minimizes the number of model parameters required in the optimization and improves the extrapolation of binary and ternary parameters into multicomponent systems. The optimized parameters can be readily used with general thermodynamic software and databases, such as FactSage, to calculate phase equilibria at any given set of conditions and to model various industrial and natural processes.

(3) MgO-FeO-Fe₂O₃-SiO₂ system (Appendix III)

The liquid and solid phases in the FeO-Fe₂O₃-MgO-SiO₂ system are of importance in ceramics, metallurgy and petrology. A complete critical evaluation and thermodynamic modeling of the phase diagrams and thermodynamic properties of oxide phases in this system at 1 bar total pressure are presented. Optimized equations for the thermodynamic properties of all phases are obtained which reproduce all available thermodynamic and phase equilibrium data within experimental error limits from 25 °C to above the liquidus temperatures at all compositions and oxygen partial pressures. The database of the model parameters can be used along with software for Gibbs energy minimization in order to calculate any type of phase diagram section.

(4) MgO-Al₂O₃, CaO-MgO-Al₂O₃ and MgO-Al₂O₃-SiO₂ systems (Appendix IV)

A complete critical evaluation of all available phase diagram and thermodynamic data for the MgO-Al₂O₃, CaO-MgO-Al₂O₃ and MgO-Al₂O₃-SiO₂ systems has been carried out, and a database of optimized model parameters has been developed. A wide variety of available data is reproduced within experimental error limits by a very few model parameters. With the present optimized database, it is possible to calculate any phase diagram section for all compositions.

(5) MnO-Al₂O₃ and MnO-Al₂O₃-SiO₂ systems (Appendix V)

A complete critical evaluation and optimization of all available phase diagram and thermodynamic data for the $\text{MnO-Al}_2\text{O}_3\text{-SiO}_2$ system has been made, and a database of model parameters has been prepared. All data are reproduced within experimental error limits. Together with the model and database for molten steel and the FactSage software for Gibbs energy minimization, thermodynamic calculations have been performed to demonstrate the application to inclusion control of Mn/Si deoxidized steel. The calculated results are in good agreement with experimental data, showing that the thermodynamic databases can be a useful tool in predicting equilibria of interest in inclusion engineering. Future developments include integrating this database with the present $\text{SiO}_2\text{-CaO-MgO-Al}_2\text{O}_3\text{-FeO-Fe}_2\text{O}_3\text{-TiO-TiO}_2\text{-CrO-Cr}_2\text{O}_3\text{-S}$ database, thereby increasing the range of applicability.

(6) $\text{CaO-MnO-Al}_2\text{O}_3\text{-SiO}_2$ system (Appendix VI)

The thermodynamic properties of the $\text{CaO-MnO-Al}_2\text{O}_3\text{-SiO}_2$ system were optimized, using all available thermodynamic and phase diagram data. Solid solutions were modeled with a polynomial expansion for the excess Gibbs energies and the Compound Energy Formalism. The Modified Quasichemical Model was used for the liquid slag phase. The optimized phase diagrams are presented. Equilibria between inclusions and Mn/Si-killed steel were calculated with the FactSage software (1), using this newly optimized oxide database and the previously optimized database for liquid Fe solutions; the accuracy and capability of the databases were verified by comparing the calculations with experimental data. The databases were used to calculate suitable ranges of Mn/Si ratio in liquid steel in order to obtain deformable inclusions during the wire-making process for Mn/Si-killed tire-cord steel, and the rolling process for Fe-36%Ni Invar steel. Finally, the effect of CaO-based top slags on inclusions was discussed.

(7) Mg-Cr-Al-O system (Appendix VII)

The $\text{MgO-Al}_2\text{O}_3\text{-CrO-Cr}_2\text{O}_3$ system at a total pressure of 1 bar was critically evaluated and optimized based on all available and reliable thermodynamic and phase diagram

data. As a result of the optimization, one set of model parameters has been obtained which reproduces all the data within experimental error limits in the temperature range from 25°C to above the liquidus and for oxygen partial pressures up to 1 bar. The variation of the melting temperature of MgCr_2O_4 with oxygen partial pressure and of the $\text{MgO-Cr}_2\text{O}_3$ phase diagram with oxygen partial pressure are elucidated for the first time. Phase equilibria can be calculated for temperatures, compositions and oxygen partial pressures where data are unavailable.

(8) Fe-Co-O system (Appendix VIII)

The $\text{CoO-Co}_3\text{O}_4$ and Fe-Co-O systems are critically evaluated and optimized over the entire range of composition and temperature up to oxygen pressures of 100 bars. Cobaltwustite and spinel solid solutions are modeled with a polynomial expansion for the excess Gibbs energies and the Compound Energy Formalism respectively. The Modified Quasichemical Model is used for the liquid slag phase. The evaluation/optimization results show that the previous phase diagram of the Fe-Co-O system proposed by Muan may be erroneous, and is not consistent with other experimental data. New optimized phase diagrams for the $\text{CoO-Co}_3\text{O}_4$ and Fe-Co-O systems are presented in this study.

(9) Liquid Fe system (Appendix IX)

A new deoxidation model (Associate Model) is developed for liquid Fe. This model is applied to the general deoxidation equilibria in liquid Fe containing Al, B, Ba, C, Ca, Ce, Cr, Hf, La, Mg, Mn, Nb, Nd, Ta, Ti, Th, Si, V, Zr. The deoxidation curves for Ca, Mg and Ba are elucidated for the first time.

Applications of the databases to calculations involving “Inclusion Engineering” are illustrated in Appendix X. Several case studies are presented illustrating applications to complex steelmaking processes such as: Ca injection processes (Fe-Ca-Al-O inclusion diagram), corrosion of refractories, Mn/Si deoxidation, Ti/Al deoxidation (Fe-Al-Ti-O

inclusion diagram), spinel formation (Fe-Mg-Al-O inclusion diagram), (Ti,N)(N,C) inclusion formation, oxide metallurgy.

References

- Bale, C.W. and Pelton, A.D., 1990. "The unified interaction parameter formalism: thermodynamic consistency and applications". *Metall. Trans. A*. 21A. 1997-2002.
- Bale, C. W., Chartrand, P., Degterov, S. A., Eriksson, G., Hack, K., Ben Mahfoud, R., Melancon, J., Pelton, A. D., Petersen, S., 2002. "FactSage thermochemical software and databases". *Calphad*. 26. 189-228.
- Barry, T.I., Dindale, A.T., Gisby, J.A., Hallstedt, B.H., Hillert, M., Jonsson, B., Jonsson, S., Sundman, B., Taylor, J.R. 1992. "The Compound Energy Model for Ionic Solutions with Applications to Solid Oxides". *J. Phase Equil.* 13. 459-475.
- Bockris, J.O'M., Mackenzie, J.D. and Kitchener, J.A., 1954. *Trans. Faraday Soc.*, 51. 1794.
- Chartrand, P. and Pelton, A.D., 2000. "On the Choice of Geometric Thermodynamic Models". *J. Phase Equil.* 21. 141-149.
- Cho, S. W. and Suito, H., 1994. "Assessment of calcium-oxygen equilibrium in liquid iron". *ISIJ Inter.* 34. 265-269.
- Davidson, P. M. and Lindsley, D.H., 1985. "Thermodynamic analysis of quadrilateral pyroxene. Part II: Model calibration from experiments and applications to geothermometry". *Contrib. Mineral. Petrol.* 91. 390-404.
- Davidson, P.M. and Lindsley, D.H., 1989. "Thermodynamic analysis of pyroxene-olivine-quartz equilibria in the system CaO-MgO-FeO-SiO₂". *Am. Mineral.* 74. 18-30.

Davidson, P. and Mukhopadhyay, D.K., 1984. "Ca-Fe-Mg olivines: phase relations and a solution model". *Contrib. Mineral. Petrol.* 86. 256-263.

Davidson, P. M. and Lindsley, D.H., 1985. "Thermodynamic analysis of quadrilateral pyroxene. Part II: Model calibration from experiments and applications to geothermometry". *Contrib. Mineral. Petrol.* 91. 390-404.

Decterov, S. A., Jak, E., Hayes, P. C., and Pelton, A. D., 2001. "Experimental Study of Phase Equilibria and Thermodynamic Optimization of the Fe-Zn-O System". *Metall. Mater. Trans. B.* 32B. 643-657.

Deer, W.A., Howie, R.A. and Zussman, J., 1966. *An Introduction to the Rock-Forming Minerals*, Longman House, Hong Kong.

DeVries, R. C. and Osborn, E. F., 1957. "Phase equilibria in high-alumina part of the system CaO-MgO-Al₂O₃-SiO₂". *J. Am. Ceram. Soc.* 40. 6-15.

Eriksson, G. and Hack, K., 1990. "ChemSage - a computer program for the calculation of complex chemical equilibria" *Metall. Trans. B.* 21B. 1013-23.

Ericsson, T. and Filippidis, A., 1986. "Cation ordering in the limited solid solution Fe₂SiO₄-Zn₂SiO₄". *Am. Mineral.* 71. 1502-1509.

Fabrichnaya, O., 1998. "The assessment of thermodynamic parameters for solid phases in the Fe-Mg-O and Fe-Mg-Si-O systems". *Calphad.* 22. 85-125.

FactSage, 2002. www.factsage.com, Montreal.

Gaye, H. and Welfringer, J., 1984. "Proceedings of the Second International Symposium on Metallurgical Slags and Fluxes". TMS-AIME, Warrendale, PA, 357.

- Gustafsson, S. and Mellberg, P.O., 1980. "On the free energy interaction between some strong deoxidizers, especially Calcium and Oxygen in liquid Iron". *Scand. J. Metallurgy*. 9. 111-116.
- Hallstedt, B. 1990. "Assessment of the CaO-Al₂O₃ System". *J. Am. Ceram. Soc.* 73. 15-23.
- Hallstedt, B. 1992. "Thermodynamic Assessment of the system MgO-Al₂O₃". *J. Am. Ceram. Soc.* 75. 1497-1507.
- Hallstedt, B. 1995. "Thermodynamic Assessment of the CaO-MgO-Al₂O₃". *J. Am. Ceram. Soc.* 78. 193-198.
- Han, Q., Zhou, D. and Xiang, C., 1997. "Determination of dissolved sulfur and Mg-S, Mg-O equilibria in molten iron". *Steel Res.* 68. 9-14.
- Han, Q., Zhang, X., Chen, D. and Wang, P. 1998. "The calcium-phosphorus and the simultaneous calcium-oxygen and calcium-sulfur equilibria in liquid iron". *Metall. Mater. Trans. B.* 19B. 617-622.
- Hilbrandt, N. and Martin, M., 1998. "High Temperature Point Defect Equilibria in Iron-Doped MgO: An *in situ* Fe-K XAFS Study on the Valence and Site Distribution of Iron in (Mg_{1-x}Fe_x)O". *Ber. Bunsenges. Phys. Chem.* 102. 1747-1759.
- Hillert, M. and Jarl, M., 1978. "A model for alloying effects in ferromagnetic metals". *Calphad*. 2. 227-238.
- Hillert, M., Jansson, B., and Sundman, B., 1988. "Application of the Compound-Energy Model to Oxide Systems". *Z. Metallkd.* 79. 81-87.

Huang, W., Hillert, M. and Wang, X., 1995. "Thermodynamic Assessment of the CaO-MgO-SiO₂ System". *Metall. Mater. Trans. A*. 26A. 2293-2310.

Hytonen, K. and Scharier, J. F., 1961. "The plane enstatite-anorthite-diopside and its relation to basalts". *Carnegie Inst. Washington Yearbook*. YB60. 125-141.

Inden, G., 1975. "Determination of chemical and magnetic interchange energies in bcc. alloys. I. General treatment". *Z. Metallkd.* 66. 577-582.

Itoh, H., Hino, M. and Banya, S., 1997. "Thermodynamics on the formation of spinel nonmetallic inclusion in liquid steel". *Metall. Mater. Trans. B*. 28B. 953-956.

Jamieson, H. E. and Roeder, P. L., 1984. "The Distribution of Mg and Fe²⁺ between Olivine and Spinel at 1300°C". *Am. Mineral.* 69. 283-291.

JISI, 1988. *Steelmaking Data Sourcebook*, Japan Society for the Promotion of Science, 19th Comm. On Steelmaking, Gordon & Breach Science, New York, NY.

Jones, P.T., Blanpain, B., Wollants, P., Ding, R., and Halleman, B. 2000. "Degradation mechanism of magnesia-chromite refractories in vacuum-oxygen decarburization ladles during production of stainless steel". *Ironmaking and Steelmaking*. 27:3. 228-237.

Jones, P.T., 2001. "Degradation Mechanisms of Basic Refractory Materials during the Secondary Refining of Stainless Steel in VOD Ladles". Ph.D dissertation, K.U. Leuven, Leuven, Belgium.

Kapoor, M.L. and Froberg, G.M., 1973. *Chemical Metallurgy of Iron and Steel*, Iron and Steel Institute, London, p.17.

Kobayashi, S., Omori, Y. and Sanbongi, K., 1970. "Ca deoxidation equilibria". *Testu-to-Hagane*. 56. 998-1013.

Lehmann, J. and Roux, J., 1986. "Experimental and theoretical study of $(\text{Fe}^{2+}, \text{Mg}) (\text{Al}, \text{Fe}^{3+})_2\text{O}_4$ spinels: Activity-composition relationships, miscibility gaps, vacancy contents". *Geochim. Cosmochim. Acta*. 50. 1765-1783.

Lumpkin, G.; Ribbe, P. H., 1983a. "Composition, order-disorder and lattice parameters of olivines: relationships in silicate, germanate, beryllate, phosphate and borate olivines". *Am. Mineral*. 68. 164-176.

Lumpkin, G. R.; Ribbe, P. H.; Lumpkin, N. E., 1983b. "Composition, order-disorder and lattice parameters of olivines: determinative methods for Mg-Mn and Mg-Ca silicate olivines" *Am. Mineral*. 68. 1174-1182.

Morimoto, N., 1988. "Nomenclature of pyroxenes". *Mineral. Mag.* 52. 535-550.

MTDATA, 2002. www.npl.co.uk, Teddington, UK.

Navrotsky, A. and Kleppa, O. J., 1967. "The thermodynamics of cation distributions in simple spinels". *J. Inorg. Nucl. Chem.* 29. 2701-2714.

Navrotsky, A., 1986. "Cation distribution energies and heats of mixing in MgFe_2O_4 - MgAl_2O_4 - ZnFe_2O_4 - ZnAl_2O_4 , and NiAl_2O_4 - ZnAl_2O_4 spinels: study by high-temperature calorimetry". *Am. Mineral*. 71. 1160-1169.

Navrotsky, A., 1994. *Physics and Chemistry of Earth materials*, Cambridge University Press, New York, NY.

Newton, R.C., Charlu, T.V. and Kleppa, O.J., 1977. "Thermochemistry of high pressure garnets and clinopyroxenes in the system $\text{CaO-MgO-Al}_2\text{O}_3\text{-SiO}_2$ ". *Geochim. Cosmochim. Acta*. 41. 369-377.

NIST, 2002. www.nist.gov, Gaithersburg.

Ohta, H and Suito, H., 1997. "Deoxidation equilibria of calcium and magnesium in liquid iron". *Metall. Mater. Trans. B*. 28B. 1131-1139.

O'Neill, H. S. C. and Navrotsky, A., 1983. "Simple spinels: crystallographic parameters, cation radii, lattice energies, and cation distribution". *Am. Mineral*. 68. 181-194.

O'Neill, H. S. C. and Navrotsky, A., 1984. "Cation distributions and thermodynamic properties of binary spinel solid solutions". *Am. Mineral*. 69. 733-753.

Park, J.-H. and Rhee, C.-H., 2001. "Ionic properties of oxygen in slag". *J. Non-Crystalline Solids*. 282. 7-14.

Papike, J.J., 1987. "Chemistry of the Rock-Forming Silicates: Ortho, Ring, and Single-Chain Structures". *Rev. Geophysics*. 25. 1483-1526.

Pelton, A.D., Schmalzried, H. and Sticher, J., 1979. "Computer -assisted analysis and claculation of phase diagrams of the Fe-Cr-O, Fe-Ni-O and Cr-Ni-O systems". *J. Phys. Chem. Solids*. 40. 1103-1122.

Pelton, A.D. and Blander, M., 1984. "Computer-assisted analysis of the thermodynamic properties and phase diagrams of slags" Proceedings of the Second International Symposium on Metallurgical Slags and Fluxes, TMS-AIME, Warrendale, PA, 281-294.

Pelton, A.D. and Blander, M., 1986. "Thermodynamic Analysis of Ordered Liquid Solutions by a Modified Quasi-Chemical Approach. Application to Silicate Slags". *Metall. Trans. B.* 17B. 805-815.

Pelton, A.D. and Bale, C.W., 1986. "A modified interaction parameter formalism for non-dilute solutions". *Metall. Trans. A.* 17A. 1211-1215.

Pelton, A.D. 1997. "The polynomial representation of thermodynamic properties in dilute solutions". *Metall. Mater. Trans. B.* 28B. 869-76.

Pelton, A.D. and Chartrand, P., 2001. "The modified quasichemical model. II - Multicomponent solutions". *Metall. Mater. Trans. A.* 32A. 1355-1360.

Pelton, A.D., Decterov, S.A., Eriksson, G., Robelin, C., and Dessureault Y., 2000. "The modified quasichemical model. I - Binary solutions". *Metall. Mater. Trans. B.* 31B. 651-659.

Pelton, A.D., 2001. "A General "Geometric" Thermodynamic Model for Multicomponent Solutions". *Calphad.* 25. 319-328.

Sack, R. O. and Ghiorso, M. S., 1994. "Thermodynamics of multicomponent pyroxenes: II. Phase relations in the quadrilateral". *Contrib. Mineral. Petrol.* 116. 287-300.

Seo, J.D. and Kim, S.H., 1999. "Thermodynamic assessment of Al, Mg, and Ca deoxidation reaction for the control of Alumina inclusions in liquid steel". *Bul. Kor. Inst. Met. & Mater.* 12. 402-410.

SGTE, 2002. www.sgte.org

Shannon, R. D., 1976. "Revised Effective Ionic Radii in Halides and Chalcogenides". *Acta Crystallogr.* A32. 751-767.

SimuSage, 2002. www.gtt-technologies.de, Aachen.

Subramanian, R., Dieckmann, R., Eriksson, G. and Pelton, A.D., 1994. "Model calculations of phase stabilities of oxide solid solutions in the Co-Fe-Mn-O system at 1200°C". *J. Phys. Chem. Solids.* 55. 391-404.

Sundman, B., 1991. "An Assessment of the Fe-O System". *J. Phase Equil.* 12. 127-140.

Szabo, O., 2003. *Personal communication*.

Taylor, J. R. and Dinsdale, A. T., 1990. "A thermodynamic assessment of the Ni-O, Cr-O and Cr-Ni-O systems using the Ionic Liquid and Compound Energy models". *Z. Metallkd.* 81. 354-366.

Taylor, J. R. and Dinsdale, A. T., 1993. "A Thermodynamic Assessment of the Cr-Fe-O System". *Z. Metallkd.* 84. 335-345.

Thermo-Calc, 2002. www.thermocalc.com, Stockholm.

THERMODATA, 2002. www.thermodata.online.fr, Grenoble.

Thermotech, 2002. www.thermotch.co.uk, Surrey, UK.

Thompson, J.B. Jr., 1969. "Chemical reactions in crystals". *Am. Mineral.* 54. 341-375.

Toker, N. Y., 1978. "Equilibrium phase relations and thermodynamics for the systems chromium-oxygen and iron-chromium-oxygen in the temperature range from 1500°C to 1825°C". *Ph.D dissertation*, Pennsylvania State Univ, USA.

Turkdogan, E.T., 1991. "Possible failure of emf oxygen sensor in liquid iron containing dissolved calcium or magnesium". *Steel Res.* 62. 379-382.

Wagner, C., 1962. *Thermodynamics of Alloys*, Addison-Wesley, Reading, MA, p. 51.

Warren, B.E. and Biscoe, J.J., 1938. *J. Am. Ceram. Soc.* 21. 259.

Waychunas, G.A., 1983. "Mossbauer, EXAFS, and X-ray diffraction study of Fe^{3+} clusters in MgO: Fe and magnesiowustite $(\text{Mg,Fe})_{1-x}\text{O}$ – evidence for specific cluster geometries". *J. Mater. Sci.* 18. 195-207.

Welch, J. H., 1956. "The system $\text{CaO-MgO-Al}_2\text{O}_3\text{-SiO}_2$. Phase-equilibrium relations along the join anorthite-spinel". *J. Iron Steel Inst.* 183. 275-283.

Appendix I

Article :

Thermodynamic Modeling of the CaO-MgO-SiO₂ System

In-Ho Jung, Sergei A. Decterov and Arthur D. Pelton

Submitted to *Metallurgical and Materials Transactions*, 2003

Thermodynamic Modeling of the CaO-MgO-SiO₂ System

IN-HO JUNG, SERGEI A. DECTEROV, and ARTHUR D. PELTON

A complete critical evaluation and thermodynamic modeling of phase diagrams and thermodynamic properties of the CaO-MgO-SiO₂ system at 1 bar pressure are presented. The molten oxide phase is described by the Modified Quasichemical Model, and the Gibbs energies of the olivine and pyroxene solid solutions are modeled using the Compound Energy Formalism. A set of optimized model parameters of all phases is obtained which reproduces all available and reliable thermodynamic and phase equilibrium data within experimental error limits from 25 °C to above the liquidus temperatures over the entire composition range. The database of the model parameters can be used along with software for Gibbs energy minimization in order to calculate any phase diagram section or phase equilibrium of interest.

I. INTRODUCTION

The CaO-MgO-SiO₂ system is of great importance in metallurgy and geochemistry. The phase equilibria, thermodynamic properties of solid and liquid phases and structural properties of solid solutions have been widely investigated at 1 bar and also at high pressure. The purpose of this study is to critically evaluate and optimize all available experimental data at 1 bar pressure.

In a thermodynamic "optimization" of a system, all available thermodynamic and phase-equilibrium data are evaluated simultaneously in order to obtain one set of model equations for the Gibbs energies of all phases as functions of temperature and composition. From these equations, all of the thermodynamic properties and the phase diagrams can be back-calculated. In this way, all the data are rendered self-consistent and consistent with thermodynamic principles. Thermodynamic property data, such as activity data, can aid in the evaluation of the phase diagram, and phase diagram measurements can be used to deduce thermodynamic properties. Discrepancies in the available data can often be resolved, and interpolations and extrapolations can be made in a thermodynamically correct manner. A small set of model parameters is obtained. This is ideal for computer storage and calculation of properties and phase diagrams.

Thermodynamic optimizations for this system have already been reported by Pelton and Eriksson^[1] using simple solid solution models and the Modified Quasichemical Model^[2-5] for the liquid oxide, and by Huang *et al.*^[6] who used the two-sublattice Compound Energy Formalism^[7] for the solid solutions and the ionic liquid model^[8] for the liquid oxide. However, several

important experimental studies of thermodynamic properties and phase equilibria have been performed subsequently. A wider range of experimental data, including structural information on solid solutions such as olivine, has been collected, evaluated and optimized in the course of the present study, and a better overall description of all the experimental data was obtained compared to the previous optimizations.

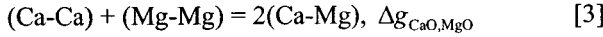
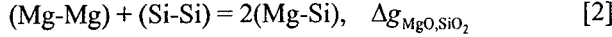
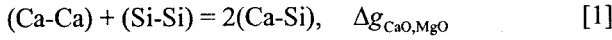
The binary sub-systems, CaO-MgO,^[9] CaO-SiO₂^[10] and MgO-SiO₂^[11] have already been optimized and the optimized binary model parameters are used without change in the present study. Phase diagrams calculated from the optimized parameters are shown in Figures 1 to 3. In the evaluations/optimizations, all available phase diagram data from several sources, metastable phase equilibrium data, data on the Gibbs energies of all compounds, and measured activities of SiO₂ in the CaO-SiO₂ and MgO-SiO₂ slags were simultaneously taken into account. The optimized binary model parameters for the Modified Quasichemical Model for the liquid phase as well as optimized expressions for the Gibbs energies of all compounds and for the CaO-MgO solid solution are given in References [9-11]. Based on these binary assessments, the CaO-MgO-SiO₂ system is optimized in the present study.

II. THERMODYNAMIC MODELS

All compounds and solutions are summarized in Table I to clarify the names of the minerals and solutions used in this study. All optimized model parameters are listed in Table II.

A. Molten Oxide (Slag)

For the molten oxide (slag) phase, the Modified Quasichemical Model^[2,3] has been used. This model has been recently further developed and summarized.^[4,5] Short-range-ordering is taken into account by considering second-nearest-neighbor pair exchange reactions. For example, for the CaO-MgO-SiO₂ slags these reactions are:

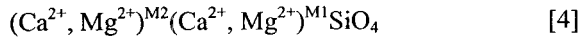


where (A-B) represents a second-nearest-neighbor A-B pair. The parameters of the model are the Gibbs energies $\Delta g_{A,B}$ of these reactions, which may be expanded as empirical functions of composition.

The optimized binary model parameters as well as the optimized expressions for the Gibbs energies of all stoichiometric compounds are given in References [9-11] along with the second-nearest neighbor “coordination numbers” of Ca, Mg and Si used in the Modified Quasichemical Model. The asymmetric “Toop-like”^[12] extension of binary model parameters is used in order to calculate the Gibbs energy of the ternary liquid, with SiO₂ as the “asymmetric component”. In order to reproduce the ternary phase diagram of the CaO-MgO-SiO₂ system, three small optimized ternary model parameters were added in the present study. These are listed in Table II.

B. Olivine Solid Solution

The olivine solid solution has two distinct octahedral sublattices, called M2 and M1:^[13-15]



where cations shown within a set of brackets occupy the same sublattice.

Because the M2 sites are bigger than M1 sites, Ca²⁺ preferentially enters the M2 sites. Monticellite, CaMgSiO₄, is part of the olivine solution. For the olivine solution, the model is developed within the framework of the Compound Energy Formalism (CEF).^[7] The Gibbs energy expression in the CEF per formula unit of a solution is as follows:

$$G = \sum_i \sum_j Y_i^{M2} Y_j^{M1} G_{ij} - TS_C + G^E \quad [5]$$

where Y_i^{M2} and Y_j^{M1} represent the site fractions of constituents i and j on the M2 and M1 sublattices, G_{ij} is the Gibbs energy of an “end-member” $(i)^{M2}(j)^{M1}SiO_4$, in which the M2 and M1 sublattices are occupied only by i and j cations respectively, S_C is the configurational entropy assuming random mixing on each sublattice given by:

$$S_C = -R \left(\sum_i Y_i^{M2} \ln Y_i^{M2} + \sum_j Y_j^{M1} \ln Y_j^{M1} \right) \quad [6]$$

and G^E is the excess Gibbs energy given by:

$$G^E = \sum_i \sum_j \sum_k Y_i^{M2} Y_j^{M2} Y_k^{M1} L_{ij,k} + \sum_i \sum_j \sum_k Y_k^{M2} Y_i^{M1} Y_j^{M1} L_{k,ij} \quad [7]$$

where $L_{ij,k}$ and $L_{k,ij}$ are interaction energies between cations i and j on one sublattice when the other sublattice is occupied by k . The dependence of the interaction energies on composition can be expressed by Redlich-Kister power series:

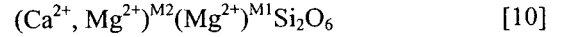
$$L_{ij,k} = \sum_m L_{ij,k}^m (Y_j^{M2} - Y_i^{M2})^m \quad [8]$$

$$L_{ij,k} = \sum_m L_{k,ij}^m (Y_j^{M1} - Y_i^{M1})^m \quad [9]$$

Optimized model parameters are listed in Table II.

C. Pyroxene Solid Solution

There are four pyroxene solutions with different crystal structures: ortho-, proto-, clino-, and low clino-. Like olivine, the pyroxenes have two distinct octahedral sublattices, M2 and M1.^[15-17] However, unlike olivine, the amount of Ca on the M1 sites is negligibly small, so that the formula unit of pyroxenes can be written as



In the CaO-MgO-SiO₂ system, the end members of the pyroxene solutions are Mg₂Si₂O₆ and CaMgSi₂O₆, and the mixing of cations occurs only on the M2 sites. The Gibbs energy of a pyroxene solution is expressed using Eq. [5] of the Compound Energy Formalism. Optimized model parameters are listed in Table II.

C. Wollastonite, α -Ca₂SiO₄ and α' -Ca₂SiO₄ Solid Solutions

Magnesium can substitute for calcium in wollastonite, CaSiO₃, which has a silicate chain structure and in α - and α' -Ca₂SiO₄. A simple random mixing model with a polynomial expansion of the excess Gibbs energy is used for these solutions:

$$G = (G_A^0 X_A + G_B^0) + nRT(X_A \ln X_A + X_B \ln X_B) + G^E \quad [11]$$

$$G^E = \sum q_{AB}^{ij} (X_A)^i (X_B)^j \quad [12]$$

where G is the Gibbs energy per formula unit of a solution (see Table I), G_A^0 and G_B^0 are the Gibbs energies of the pure end-members, G^E is the excess Gibbs energy, X_A and X_B are mole fractions of end-members, q_{AB}^{ij} are the model parameters, and $n=1$ for wollastonite and $n=2$ for the α -

and α' - Ca_2SiO_4 solutions. Optimized model parameters are listed in Table II.

D. Monoxide Solid Solution

The monoxide solid solution exists in the CaO-MgO binary system. (See Figure 1.) MgO and CaO have limited solubilities in each other forming a solid miscibility gap. The model parameters were taken from the previous study by Wu *et al.*^[9]

E. Stoichiometric Compounds

Pseudowollastonite (CaSiO_3), hatrurite (Ca_3SiO_5), rankinite ($\text{Ca}_3\text{Si}_2\text{O}_7$), SiO_2 , akermanite ($\text{Ca}_2\text{MgSi}_2\text{O}_7$) and merwinite ($\text{Ca}_3\text{MgSi}_2\text{O}_8$) are considered to be stoichiometric compounds in this study.

III. EVALUATION/OPTIMIZATION OF EXPERIMENTAL DATA

The liquidus surface calculated from the optimized parameters is shown in Figure 4. Along the orthosilicate and metasilicate sections, extensive solid solutions such as olivine and pyroxenes exist. The other solid solutions such as wollastonite, α - and α' - Ca_2SiO_4 exhibit limited solubility. All calculated invariant points involving the liquid oxide are given in Table III. The details of various phase diagram sections will be discussed below. The Gibbs energies of the akermanite, diopside, merwinite and monticellite ternary compounds were taken from the assessment by Berman,^[18] with small corrections being made to the enthalpies of formation, $H_{298.15}^\circ$ as shown in Table II in order to reproduce the phase diagram data.

A. Orthosilicate Section

Figure 5 shows the calculated phase diagram of the Ca_2SiO_4 - Mg_2SiO_4 section. γ - Ca_2SiO_4 , monticellite and forsterite all belong to the olivine solution. Between monticellite and forsterite, the olivine solution is known to exhibit a miscibility gap. MgO dissolving a small amount of CaO appears as a primary crystalline phase in the middle of the phase diagram.

Gutt^[19] measured the phase diagram over the composition region between Ca_2SiO_4 and merwinite from 25 °C to liquidus temperatures. His results are shown on Figure 6. Liquidus temperatures between 1800° and 2130 °C were measured by high-temperature microscopy. The subsolidus regions were studied systematically by high-temperature X-ray analysis up to 1575 °C, and quenching in combination with X-ray analysis was used between 1575° to 1590 °C. Gutt found very limited solubility of Mg^{2+} in α' - and γ - Ca_2SiO_4 , and no solubility in α - Ca_2SiO_4 . Phase transitions from α to α' and from α' to γ - Ca_2SiO_4 were reported at 1360 °C and 990 °C, respectively. The so called "T" phase, $\text{Ca}_{1.7}\text{Mg}_{0.3}\text{SiO}_4$, was found to be stable up to

1460 °C and to decompose to α - Ca_2SiO_4 and merwinite. However, the topology of the phase diagram constructed by Gutt^[19] is incorrect.

Schlaudt and Roy^[20] studied the Ca_2SiO_4 -monticellite join at temperatures up to 1600 °C using a standard quenching technique followed by microscopic and X-ray analysis. (See Figure 6.) For temperatures higher than 1600 °C, a platinum or iridium strip furnace was used and temperatures were determined by an optical pyrometer. High-temperature DTA and high-temperature X-ray diffraction were used to study the α' to α transition in Ca_2SiO_4 , which was found to occur at 1400° C. X-ray diffraction was shown to be unsuitable for determination of the solubility of Mg^{2+} in Ca_2SiO_4 because the shifts in the diffraction peaks with additions of magnesium were less than the experimental uncertainty. (This might explain the underestimated magnesium solubility in Ca_2SiO_4 reported by Gutt^[19]). Therefore, the phase boundaries of the Ca_2SiO_4 solid solutions were determined by the first appearance of phases other than Ca_2SiO_4 . Merwinite was found to melt incongruently at 1575 °C to form Ca_2SiO_4 , MgO and liquid. The "T" phase was observed in the temperature range from 979° to 1381 °C when gel starting materials were used. However, when crystalline oxide starting materials were used, this phase was not found. Schludt and Roy^[20] reported very limited solubility of monticellite in merwinite. Sharp *et al.*^[21] also observed a small solubility from electron microprobe analysis of merwinite samples equilibrated at about 5 to 10 kbar by Yoder.^[22] The molar $\text{Mg}/(\text{Ca}+\text{Mg})$ ratio in merwinite varied from 0.25 to 0.26 (0.25 corresponds to stoichiometric merwinite), but the $(\text{Ca}+\text{Mg})/\text{Si}$ ratio was equal to 2.00 indicating that the merwinite solution exists only along the Ca_2SiO_4 - Mg_2SiO_4 orthosilicate join. In the present study the limited homogeneity range of merwinite is ignored; i. e. merwinite is considered to be a stoichiometric compound.

Osborn^[23] investigated phase relations in the merwinite-monticellite region using a quenching technique followed by microscopic phase determination. (See Figure 6.) Merwinite was found to melt incongruently to MgO, Ca_2SiO_4 and liquid at 1575 °C. The liquidus of MgO was measured above 1700 °C.

Ricker and Osborn^[24] investigated the monticellite-forsterite part of the orthosilicate section from 1100° to 1750 °C using a quenching technique followed by optical and X-ray phase analysis. (See Figure 7.) Maximum solubilities of 30 wt % monticellite in forsterite and of 30 wt % forsterite in monticellite were observed at 1500 °C.

The olivine miscibility gap was investigated more thoroughly in several studies.^[25-29] Biggar and O'Hara^[26] studied subsolidus phase equilibria between monticellite and forsterite from 1200° to 1490 °C by the quenching technique using both gel and crystalline precursors in combination with optical and X-ray analysis. Yang^[25] used EPMA of quenched samples to obtain the compositions of coexisting forsterite and monticellite solid solutions over the temperature range between 1440° and 1496°C. Hatfield *et al.*^[28] used the quenching method and microscopic analysis to measure the compatibility triangles among MgO

solid solution, olivine and liquid oxide at 1550 °C and 1700 °C. The phase boundary of the forsterite solid solution obtained from these triangles substantiates the data of Biggar and O'Hara^[26] and Yang.^[25] The high pressure experiments by Warner and Luth^[29] and by Adams and Bishop^[27] also confirmed that the miscibility gap reported by Ricker and Osborn^[24] is too narrow.

Monticellite (CaMgSiO_4) is often considered to be a stoichiometric mineral. Ricker and Osborn^[24] reported that the olivine solid solution extends from the CaMgSiO_4 composition towards Mg_2SiO_4 , but not towards merwinite. Strictly speaking, monticellite of the exact stoichiometric CaMgSiO_4 composition is not stable. Biggar and O'Hara^[26] equilibrated this composition for 21 days at about 1500 °C and observed a mixture of 90 % monticellite (olivine solid solution) and 10 % merwinite identified by optical microscopy and X-ray diffraction. The instability of stoichiometric monticellite was also reported in other studies.^[29-33]

The calculated Ca_2SiO_4 - CaMgSiO_4 phase diagram section is compared with experimental data in Figure 6. Because the existence of the "T" phase as a stable compound is still questionable, this phase is not shown. As seen on Figure 6, Schlautdt and Roy^[20] observed two or three phases in regions where the calculations indicate the existence of one or two phases respectively. The phases were not identified by Schlautdt and Roy.^[20] The most likely explanation is that the overall compositions of their samples did not lie exactly on the orthosilicate section.

Kosa *et al.*^[34] reported the enthalpy of incongruent decomposition of merwinite into liquid, Ca_2SiO_4 and MgO at 1575 °C to be 125 ± 15 kJ per mole of merwinite. The calculated value is 120.0 kJ/mol at 1576 °C.

Figure 7 compares the calculated CaMgSiO_4 - Mg_2SiO_4 phase diagram section with experimental data. The solubility of monticellite in forsterite and vice versa (that is, the miscibility gap in the olivine solution) and the nonstoichiometry of monticellite are well reproduced. Figure 8 shows an enlargement of the peritectic melting of monticellite (olivine solid solution). In the previous assessment by Huang *et al.*,^[6] the range of stoichiometry of monticellite (olivine) was shown extending from the CaMgSiO_4 composition not only towards the Mg_2SiO_4 side, but also towards the Ca_2SiO_4 side in contradiction to several studies mentioned above.^[26,29-33] The liquidus of MgO at the monticellite composition measured by Ricker and Osborn^[24] is substantially lower than the calculated liquidus which is consistent with the results of Osborn^[23] and Ricker and Osborn at other compositions. This could result from a small deviation of their experimental samples from the orthosilicate section combined with the very steep MgO liquidus in that region. (See Figure 4.) Overall, the calculated Ca_2SiO_4 - Mg_2SiO_4 phase diagram section and the experimental data agree within experimental error limits.

Lumpkin and Ribbe^[13] and Lumpkin *et al.*^[14] studied the distribution of Ca^{2+} and Mg^{2+} cations between the M1 and M2 sites of the olivine solid solution by measuring lattice parameters. Ca^{2+} , with an ionic radius of 1.00\AA ^[35], strongly prefers the larger M2 sites, whereas Mg^{2+} (ionic

radius of 0.72\AA ^[35]) is distributed between the M1 and M2 sites. The degree of disordering was determined from the *a* and *b* lattice parameters of olivine, which are affected sufficiently by the distribution of Ca and Mg cations. Adams and Bishop^[27] used the same technique as Lumpkin *et al.* to study the cation distribution in olivine solutions from 1200° to 1400 °C. They found the amount of Ca on the M1 sites to be from 11 to 15 % and 2 to 5 % of the total Ca on the forsterite-rich side and monticellite-rich side of the miscibility gap, respectively. The calculated cation distribution in olivine is compared with experimental data in Figure 9. The more ordered structure is calculated in monticellite at lower temperatures. This is consistent with the experimental data.

The olivine solution is modeled by the two-sublattice Compound Energy Formalism. The Gibbs energies of three out of four end-members are known:^[18,35] $(\text{Mg})^{\text{M2}}(\text{Mg})^{\text{M1}}\text{SiO}_4$ (forsterite), $(\text{Ca})^{\text{M2}}(\text{Ca})^{\text{M1}}\text{SiO}_4$ (γ - Ca_2SiO_4) and $(\text{Ca})^{\text{M2}}(\text{Mg})^{\text{M1}}\text{SiO}_4$ (monticellite). The Gibbs energy of $(\text{Mg})^{\text{M2}}(\text{Ca})^{\text{M1}}\text{SiO}_4$ was optimized as shown in Table II to reproduce the measured cation distribution. In order to reproduce the measured phase equilibrium diagrams, two miscibility gaps are necessary, on the Mg_2SiO_4 - CaMgSiO_4 side and on the Ca_2SiO_4 - CaMgSiO_4 side. The miscibility gap between monticellite and forsterite was modeled using an asymmetric $L_{\text{Ca,Mg;Mg}}$ ($=L_{\text{Ca,Mg;Ca}}$) parameter. The second miscibility gap between γ - Ca_2SiO_4 and monticellite was modeled using the parameter $L_{\text{Ca;Ca,Mg}}$ ($=L_{\text{Mg;Ca,Mg}}$). Without this gap, merwinite becomes thermodynamically unstable. The model parameters are listed in Table II.

B. Metasilicate Section

Figure 10 shows the calculated phase diagram of the CaSiO_3 - MgSiO_3 metasilicate section. The phase equilibria between the pyroxene solutions are very complicated in the $\text{CaMgSi}_2\text{O}_6$ (diopside) - $\text{Mg}_2\text{Si}_2\text{O}_6$ (enstatite) region. Wollastonite dissolves up to about 10 mol % of MgSiO_3 , while pseudo-wollastonite is a stoichiometric compound.

The phase equilibria in the diopside-enstatite section, which are of particular importance in geochemistry, have been studied extensively. Bowen^[36] investigated the phase equilibria in the forsterite-diopside- SiO_2 section using the quenching technique followed by optical microscopic phase determination. In the experiments, primary crystallization of SiO_2 , pyroxene and forsterite was detected. Moreover, the phase diagrams of the diopside-enstatite, diopside- SiO_2 and diopside-forsterite pseudo-binary joins were measured. Boyd and Schairer^[37] studied the diopside-enstatite section using the quenching technique followed by optical microscopic and X-ray phase determination. The liquidus was measured for forsterite and pyroxene solutions. The phase equilibria between diopside and enstatite (proto- and ortho-pyroxene) solid solutions were studied in the temperature range between 800° and 1380 °C. The compositions of the solid solutions were determined by X-ray measurements of lattice parameters. Kushiro^[38] studied the forsterite-diopside-silica system using electron probe

analysis of quenched samples. The phase equilibria between enstatite and diopside were measured and a small deviation of the diopside solid solution from the metasilicate section towards lower silica was reported. Schairer and Yoder^[39] studied phase equilibria in the forsterite-diopside-silica system below 1410 °C using the quenching technique. Kushiro and Schairer^[40] obtained the diopside-enstatite phase diagram using the quenching technique and reported a maximum on the diopside liquidus at about 90 percent $\text{CaMgSi}_2\text{O}_6$. Yang^[41] and Longhi^[42] studied the metastable phase equilibria of ortho-pyroxene in the metasilicate section.

The phase diagram of the diopside-enstatite section was constructed by Longhi and Boudreau^[43] based on measurements of the ortho-enstatite liquidus in the forsterite-diopside- SiO_2 system using the quenching technique followed by EPMA (EDS) and X-ray phase analysis. Jenner and Green^[44] determined the phase equilibria in the Mg-rich part of the pyroxene quadrilateral $\text{Mg}_2\text{Si}_2\text{O}_6$ - $\text{CaMgSi}_2\text{O}_6$ - $\text{CaFeSi}_2\text{O}_6$ - $\text{Fe}_2\text{Si}_2\text{O}_6$. Biggar^[45] reviewed the compositions of proto-pyroxene, ortho-pyroxene and pigeonite (clino-pyroxene), coexisting with liquid in the CaO - MgO - SiO_2 system using previously published data and his new data obtained by X-ray diffraction on quenched samples. Recently, a more accurate phase diagram was proposed by Carlson^[46] based on his own experiments as well as on previous studies. Carlson measured the phase equilibria between pyroxene solid solutions in the enstatite-diopside section over the temperature range from 925° to 1425 °C. Each point on a phase boundary was bracketed by two measured compositions. V_2O_5 and PbO solvents were used to facilitate equilibration and to promote crystal growth to sizes permitting unambiguous phase identification by X-ray diffraction and accurate chemical analysis by the electron microprobe, thereby resolving substantial discrepancies among previous studies of pyroxene phase equilibria.

Figure 11 compares the calculated phase diagram of the $\text{CaMgSi}_2\text{O}_6$ - $\text{Mg}_2\text{Si}_2\text{O}_6$ section with experimental data. Diopside and forsterite (olivine containing less than 1 mol % of Ca_2SiO_4) appear as primary crystalline phases. Pigeonite and diopside have the same clino-pyroxene structure. Ortho-pyroxene reappears in the narrow temperature range between 1373° and 1441 °C. The calculated liquidus of forsterite is systemically lower than the experimental data of Bowen^[36] by about 30 °C. This could be the result of a small deviation of the experimental samples from the metasilicate stoichiometry combined with the steep slope of the forsterite liquidus. (A section calculated at $X_{\text{SiO}_2} = 0.49$ is in good agreement with the experimental liquidus). An enlargement of the small pigeonite and ortho-pyroxene fields is shown in Figure 12.

Figure 13 shows the calculated enthalpy of the $\text{CaMgSi}_2\text{O}_6$ - $\text{Mg}_2\text{Si}_2\text{O}_6$ clino-pyroxene solution at 970 K. Newton *et al.*^[47] measured the enthalpy of dissolution of synthetic clino-pyroxenes in $2\text{PbO}\cdot\text{B}_2\text{O}_3$ melts at 970 K. The measured enthalpy showed positive deviations from ideality. This is well reproduced by the calculated curve in

Figure 13. This positive deviation implies the existence of a miscibility gap in the clino-pyroxene solution.

Before modeling the pyroxene solutions, the Gibbs energies of the MgSiO_3 enstatite phases had to be determined because the phase transformations of enstatite were not well treated in the previous optimization of the MgO - SiO_2 binary system.^[11] The Gibbs energies of different crystal modifications of enstatite, MgSiO_3 , were taken from the assessment of Huang *et al.*^[6] and then slightly modified to reproduce the metastable phase transitions of enstatite. Perrotta and Stephenson^[48] and Smith^[49] reported the metastable transformation from low clino-enstatite to clino-enstatite at about 995 °C. The transition temperature calculated in the present study is 978 °C. Newton *et al.*^[47] estimated the enthalpy of transition from clino-enstatite to ortho-enstatite to be about -4.6 ± 0.45 kJ/mol at 970 K from extrapolation of the measured enthalpy of dissolution of the clino-pyroxene solution to the pure MgSiO_3 composition and from the dissolution enthalpy of ortho-enstatite. If the enthalpy of dissolution of ortho-enstatite obtained by Shearer and Kleppa^[50] is used instead of the value of Newton *et al.*, the corresponding enthalpy of transition is -3.6 ± 0.6 kJ/mol. In the present study, the enthalpy of transition from clino-enstatite to ortho-enstatite is calculated to be -3.55 kJ/mol. The slightly modified Gibbs energies of Huang *et al.*^[6] are now stored in the F*A*C*T database.^[35] It should be noted that the Gibbs energies of ortho- and proto- enstatite used in the present study are very close to Berman's recommended values.^[18]

The pyroxene solutions were modeled based on the calorimetric data (Figure 13) and the phase diagram (Figure 11). Clino-pyroxene was modeled first, taking advantage of the available thermodynamic data. Pigeonite and diopside have the same clino-pyroxene structure and are modeled as one solution with a miscibility gap. A slightly asymmetric interaction energy involving ${}^0L_{\text{Ca,Mg:Mg}}$ and ${}^1L_{\text{Ca,Mg:Mg}}$ parameters was found necessary to reproduce the measured miscibility gap between diopside and pigeonite. Low clino-pyroxene and proto-pyroxene were modeled using similar excess parameters and optimized Gibbs energies of the $\text{CaMgSi}_2\text{O}_6$ end-members as shown in Table II. The excess parameters for all pyroxene phases can be seen in Table II to have very similar numerical values except in the case of ortho-pyroxene. An interaction energy $L_{\text{Ca,Mg:Mg}}$ with negative temperature dependence was necessary to reproduce the reappearance of ortho-pyroxene at high temperatures.

The calculated phase diagram of the CaSiO_3 - $\text{CaMgSi}_2\text{O}_6$ section is compared with experimental data in Figure 14. Allen *et al.*^[51] were the first to study the phase relations in this section. They used heating curves and microscopic phase examination. They reported the presence of up to 17 wt % of diopside in wollastonite, about 3 to 4 wt % of diopside in pseudo-wollastonite and less than 3 wt % of CaSiO_3 in diopside. Ferguson and Merwin^[31] investigated the CaO - MgO - SiO_2 system below 1600 °C using a quenching technique followed by microscopic phase determination. The solid solution of

diopside in wollastonite was observed. Later, Schairer and Bowen^[52] used the same method for a thorough study of phase equilibria between CaSiO_3 and diopside. They concluded that a maximum of 22 wt % diopside dissolves in wollastonite and there is almost no solubility of wollastonite in diopside. Osborn^[53] measured the primary crystallization region of the wollastonite solution in the CaO-MgO-SiO_2 system using quenching in combination with optical microscopic phase determination. The calculated diagram is in good agreement with the experimental data of Schairer and Bowen. No excess Gibbs energy parameter was necessary to model wollastonite. However the Gibbs energy of the fictive MgSiO_3 end-member was optimized as shown in Table II.

Tarina *et al.*^[54] used transposed-temperature drop calorimetry to measure the enthalpy change for the heating and melting of (pseudo-wollastonite+diopside) mixtures. (See Figure 15.) The results showed a very small negative enthalpy of mixing. DeYoreo *et al.*^[55] measured the heat content of the mixture of wollastonite and diopside (83 mol % diopside) using a scanning calorimetric technique in the temperature range from 1375 to 1750 K. Navrotsky *et al.*^[56] and Ziegler and Navrotsky^[57] obtained the heat content of diopside using drop calorimetry. The incongruent melting behavior of diopside above 1634 K was observed. Lange *et al.*^[58] measured the heat content of diopside between 1403 and 1763 K using scanning calorimetry. They found that incongruent melting begins approximately at 1606 K. Stebbins *et al.*^[59] and Richet and Bottinga^[60] also reported the heat content of the liquid at the diopside composition. Their data are in agreement with the measurements of Lange *et al.*^[58]

The enthalpy of the liquid phase between the CaSiO_3 and diopside compositions, and the enthalpy of melting of diopside are calculated in Figures 15 and 16. The calculated curves are in excellent agreement with experimental data. In particular, in the case of the enthalpy change during the melting of stoichiometric diopside, the incongruent melting behavior pointed out by Ziegler and Navrotsky^[57] is well reproduced. This can be understood by reference to Figure 16. Diopside begins to melt at 1636 K and melting is complete at 1665 K. The calculated enthalpy of fusion is 129.6 kJ/mol, which is slightly lower than the experimental data.^[57,58] The measurements of DeYoreo *et al.*^[55] are also well reproduced by the calculations.

C. Other Phase Diagram Sections

The calculated phase diagram of the diopside-forsterite section is compared with the experimental data in Figure 17. Bowen^[36] measured the liquidus of forsterite in this section using a quenching technique and optical microscopic phase determination, and suggested that this system is a quasi-binary system with a eutectic at 12 wt % forsterite and 1387 °C. Later, the phase equilibria in the diopside-forsterite section were studied by Kushiro and Schairer^[40] using a quenching technique followed by X-ray diffraction. The diopside and forsterite solutions were

found to be in equilibrium with compositions off this join. Therefore, the diopside-forsterite section is not a true quasi-binary system. It was reported that forsterite can contain up to about 8 mol % of monticellite in equilibrium with the diopside solution at 1350 °C. The value calculated in the present study from the optimized model parameters is 11 mol %. As can be seen from Figure 17, the calculated liquidus and the phase boundary of diopside are in good agreement with the experimental data. The eutectic point mentioned by Bowen is actually a saddle point. (See also Figure 4).

The calculated phase diagram of the diopside- SiO_2 section is shown in Figure 18. This section was also first studied by Bowen.^[36] Schairer and Kushiro^[62] found a three-phase region (diopside+ SiO_2 +liquid) and reported that X-ray patterns of diopside coexisting with liquid or with liquid and tridymite were different from those of pure diopside. They concluded that the diopside- SiO_2 section is not a true quasi-binary system. Diopside was reported to dissolve up to 7.5 mol % of enstatite based on X-ray diffraction analysis. The calculated maximum solubility is about 8.5 mol % $\text{Mg}_2\text{Si}_2\text{O}_6$. The calculated phase diagram is in excellent agreement with the experimental data.

The phase diagrams of the diopside-akermanite and CaSiO_3 -akermanite sections are given in Figures 19 and 20. Kushiro and Schairer^[63] obtained the phase diagram of the diopside-akermanite section using a quenching technique followed by X-ray analysis. They reported up to about 5 mol % solubility of akermanite in diopside at 1355 °C based on X-ray measurements of the diopside lattice parameters. A very small solubility of akermanite in diopside was also deduced by Valley and Essene^[64] from the similar X-ray experiments on the quenched samples from the earlier study^[22] which contained both diopside and akermanite. A substantial solubility of akermanite in diopside seems unlikely and was neglected in the present study. More direct evidence such as EPMA measurements, is needed to prove the extension of the diopside solid solution towards akermanite. The minimum on the liquidus in the $\text{Ca}_2\text{MgSi}_2\text{O}_7$ - $\text{CaMgSi}_2\text{O}_6$ section was measured at 1367 °C in the quenching experiments of Ferguson and Merwin.^[31]

Schairer and Bowen^[65] studied the phase equilibria in the CaSiO_3 -akermanite section using a quenching technique and microscopic phase determination. They found no solid solutions in this section contrary to the earlier study of Ferguson and Merwin^[31] who reported that the wollastonite solid solution extended towards akermanite.

Yoder^[66,67] suggested that akermanite may form a solid solution with other phases in the CaO-MgO-SiO_2 system at about 10 kbar. The EPMA study of Yoder's samples^[66] at about 5-10 kbar by Sharp *et al.*^[21] revealed the possibility of up to 2% substitution of Mg for Ca in $\text{Ca}_2\text{MgSi}_2\text{O}_7$. On the other hand, a constant (Ca+Mg)/Si ratio of 3/2 was obtained, indicating no detectable solid solution towards olivine. In the present study, akermanite is assumed to be a stoichiometric compound at ambient pressure.

Proks *et al.*^[68] measured the heat content of akermanite from 1469 to 1865 K using drop calorimetry. The enthalpy

of fusion of akermanite at its melting temperature of 1725 K was found to be 123.9 ± 3.2 kJ/mol. The calculated enthalpy of fusion is 118.7 kJ/mol at 1727 K. Adamkovicova *et al.*^[69,70] measured the enthalpy of melts in the CaSiO_3 -akermanite section over the temperature range from 1760 to 1930 K using high-temperature drop calorimetry and solution calorimetry. The enthalpy of mixing was found to be almost zero at any composition. The calculated enthalpy of mixing of the akermanite- CaSiO_3 liquid shows a minimum of -1.4 kJ/mol at a mole fraction of CaSiO_3 equal to 0.62 which is in agreement with the calorimetric data within experimental error limits.

The calculated phase diagrams of the Ca_2SiO_4 -akermanite, merwinite-akermanite and monticellite-akermanite sections are presented in Figures 21 to 23. Osborn^[23] investigated the first two sections by quenching experiments and microscopic phase determination. The Ca_2SiO_4 and merwinite phases were not distinguishable by microscopic analysis. Osborn^[23] reported problems with quenching for most of the studied compositions. Instead of the glass phase, a product of devitrification was commonly observed in quenched samples. The calculated liquidus is somewhat lower than the experimental data.^[23] This is most likely due to the unquenchability of the liquid.

Osborn^[23] tried to establish the primary phase region of rankinite, $\text{Ca}_3\text{Si}_2\text{O}_7$. The exaggerated rankinite primary region in his tentative phase diagram is not supported by solid experimental evidence. The rankinite primary phase region calculated in the present study is very small as can be seen from Figure 4. Similarly, the primary crystallization field of Ca_3SiO_5 was exaggerated in the tentative phase diagram of Ricker and Osborn.^[24] Since quenching of liquid is problematic in this area, a substantial primary phase region of Ca_3SiO_5 is not supported by direct experimental evidence. Even in the binary CaO - SiO_2 system, several experimental studies reported contradictory results on the upper temperature of stability of Ca_3SiO_5 . In the latest optimization of the CaO - SiO_2 system (see Figure 2), preference was given to the experimental data indicating decomposition of Ca_3SiO_5 below the liquidus. Therefore, there is no primary field of this compound on the calculated liquidus projection shown in Figure 4.

Spencer *et al.*^[71] measured several tie-lines between liquid and forsterite or periclase at 1800 °C using an air quenching technique followed by X-ray diffraction and EPMA analysis. Sakai and Suito^[72] measured the liquidus of forsterite, periclase and Ca_2SiO_4 at 1600 °C using equilibration in MgO or Pt crucibles followed by quenching and EPMA or inductively couple plasma analysis. These phase equilibrium data are also well reproduced by the calculations based on the optimized model parameters. (See the corresponding isotherms in Figure 4.)

Greig^[73] studied the (2 liquids+crystobalite) univariant line by a quenching technique and microscopic analysis. He found this line to be slightly convex, whereas a slightly concave univariant line is calculated in the present study. (See Figure 4.) It should be noted that the latter shape is due to the contribution of the configurational entropy to the Gibbs energy of liquid and this shape is found in many

similar ternary systems. The liquid miscibility gap was also studied by Kirschen and DeCapitani^[74] at temperatures up to 1940 °C using the levitation technique. A few tie-lines were obtained by EPMA analysis of quenched samples.

D. Sub-Solidus Equilibria

Harker and Tuttle^[75] and Yoder^[22] determined the low-temperature stability limit of akermanite. The temperature versus pressure univariant line was obtained for the equilibrium reaction (wollastonite + monticellite = akermanite) from 6 kbar to 0.8 kbar total pressure. Extrapolation of these data to ambient pressure suggests that akermanite dissociates into wollastonite and monticellite below about 700 °C. The dissociation temperature calculated in the present study is 701 °C.

Walter^[76] and Yoder^[22] obtained the pressure versus temperature univariant line for the equilibrium (diopside + monticellite = forsterite + akermanite) from 5 kbar to 1 bar. They found that the equilibrium low temperature phase assemblage (diopside + monticellite) gave way to the (forsterite + akermanite) assemblage above about 870 °C at ambient pressure. The calculated transition temperature is 838 °C.

E. Activities of Components in Molten Oxide

Rein and Chipman^[77] obtained the activities of silica in the CaO - MgO - SiO_2 liquid at 1600 °C from the composition of the slag and Fe-Si-C alloys equilibrated in carbon or silicon carbide crucibles in atmospheres of CO . Morita *et al.*^[78] also reported the activities of SiO_2 in the slag at 1600 °C based on equilibration of the slag and Si alloys in graphite crucibles. The measured compositions of the slag and alloy in combination with known Henrian activity coefficients of Ca and Mg in Si alloys allowed the authors to calculate the activities of all slag components using the Gibbs-Duhem relationship. The results of Morita *et al.*^[78] and Rein and Chipman^[77] are compared with the activities of SiO_2 calculated in the present study in Figure 24.

Henderson and Taylor^[79] determined the activity of silica in CaO - MgO - SiO_2 liquid slags saturated with both graphite and SiC at 1500° and 1550 °C by measuring the slag composition and the equilibrium pressure of CO . Figure 25 shows these experimental data and the calculated activities of SiO_2 in slags of constant MgO content. The activities of CaO in the CaO - MgO - SiO_2 slag were reported in two studies.^[80,81] The first set of data was obtained by a complex emf technique at 1600 °C. In the second study, the CaO activities in the slag at 1500 °C were calculated from the equilibrium constant of the reaction ($\text{CaO} + 1/2\text{S}_2 = \text{CaS} + 1/2\text{O}_2$). The composition of the slag was measured, including the CaS content. The activity coefficient of CaS in the slag was assumed to be equal to 1.0, and the partial pressures of O_2 and S_2 were calculated from the equilibrium gas composition. The reliability of the reported^[80,81] CaO activities is believed to be relatively low due to experimental difficulties, the assumptions made in

calculating the activities, and the sensitivity of small activity values to experimental errors.

IV. CONCLUSIONS

A complete critical evaluation of all available phase diagram, thermodynamic and structural data for the CaO-MgO-SiO₂ system at a total pressure of 1 bar has been made, and parameters of thermodynamic models have been optimized to reproduce all experimental data within experimental error limits. The evaluation /optimization of the CaO-MgO-SiO₂ system reported in this study is part of a wider research program aimed at complete characterization of phase equilibria and thermodynamic properties of the entire six-component system CaO-MgO-Al₂O₃-FeO-Fe₂O₃-SiO₂, which has numerous applications in the ceramic, cement and glass industries, metallurgy, geochemistry, etc. The model parameters obtained in this study are included in the general F*A*C*T^[35] database of optimized model parameters for the CaO-MgO-Al₂O₃-FeO-Fe₂O₃-SiO₂ system. This database can be readily used with software for Gibbs energy minimization in order to calculate any phase equilibrium or phase diagram of interest.

ACKNOWLEDGMENTS

This project was supported by a CRD grant from the Natural Sciences and Engineering Research Council of Canada in collaboration with INCO, Noranda, Rio Tinto, Teck Cominco, Alcoa, Dupont, Shell, Corning, Pechiney, Norsk Hydro, Sintef, Schott Glas, St.-Gobain Recherche, Mintek and IIS Materials.

REFERENCES

1. A. D. Pelton and G. Eriksson: *Advances in the Fusion of Glasses*, Am. Ceramic Soc., Westerville, OH, 1988, pp. 27.1-27.11.
2. A. D. Pelton and M. Blander: *Proceedings of the Second International Symposium on Metallurgical Slags and Fluxes, TMS-AIME, Warrendale, PA*, 1984, pp. 281-94.
3. A. D. Pelton and M. Blander: *Metall. Trans. B*, 1986, vol. 17B, pp. 805-815.
4. A. D. Pelton, S. A. Decterov, G. Eriksson, C. Robelin, and Y. Dessureault: *Metall. Mater. Trans. B*, 2000, vol. 31B, pp. 651-659.
5. A. D. Pelton and P. Chartrand: *Metall. Mater. Trans. A*, 2001, vol. 32A, pp. 1355-1360.
6. W. Huang, M. Hillert, and X. Wang: *Metall. Mater. Trans. A*, 1995, vol. 26A, pp. 2293-2310.
7. M. Hillert, B. Jansson, and B. Sundman: *Z. Metallkd.*, 1988, vol. 79, pp. 81-87.
8. M. Hillert, B. Jansson, and B. Sundman: *Metall. Trans. A*, 1985, vol. 16A, pp. 261-266.
9. P. Wu, G. Eriksson, and A. D. Pelton: *J. Am. Ceram. Soc.*, 1993, vol. 76, pp. 2065-75.
10. G. Eriksson, P. Wu, M. Blander, and A. D. Pelton: *Can. Metall. Q.*, 1994, vol. 33, pp. 13-21.
11. P. Wu, G. Eriksson, A. D. Pelton, and M. Blander: *ISIJ Inter.*, 1993, vol. 33, pp. 26-35.
12. A. D. Pelton: *Calphad*, 2001, vol. 25, pp. 319-328.
13. G. Lumpkin and P. H. Ribbe: *Am. Mineral.*, 1983, vol. 68, pp. 164-176.
14. G. R. Lumpkin, P. H. Ribbe, and N. E. Lumpkin: *Am. Mineral.*, 1983, vol. 68, pp. 1174-1182.
15. W. A. Deer, R. A. Howie, J. Zussman: *An Introduction to the Rock Forming Minerals*, Longman House, Hong Kong, 1966.
16. P. Shi, S. K. Saxena, Z. Zang, and B. Sundman: *Calphad*, 1994, vol. 18, pp. 47-69.
17. N. Morimoto: *Mineral. Mag.*, 1988, vol. 52, pp. 535-50.
18. R. G. Berman: *J. Petrol.*, 1988, vol. 29, pp. 445-522.
19. W. Gutt: *Nature*, 1965, vol. 207, pp. 184-185.
20. C. M. Schlautdt and D. M. Roy: *J. Am. Ceram. Soc.*, 1966, vol. 49, pp. 430-432.
21. Z. D. Sharp, E. J. Essene, L. M. Anovitz, G. W. Metz, Jr E. F. Westrum, B. S. Hemingway, and J. W. Valley: *Geochim. Cosmochim. Acta.*, 1986, vol. 50, pp. 1475-1484.
22. H. S. Jr. Yoder: *Carnegie Inst. Washington, Yearbook*, 1968, Yb.67, pp. 471-483.
23. E. F. Osborn: *J. Am. Ceram. Soc.*, 1943, vol. 26, pp. 321-332.
24. R. W. Ricker and E. F. Osborn: *J. Am. Ceram. Soc.*, 1954, vol. 37, pp. 133-39.
25. H. Y. Yang: *Am. Mineral.*, 1973, vol. 58, pp. 343-345.
26. G. M. Biggar and M. J. O'Hara: *J. Am. Ceram. Soc.*, 1969, vol. 52, pp. 249-252.
27. G. E. Adams and C. F. Bishop: *Am. Mineral.*, 1985, vol. 70, pp. 714-722.
28. T. Hatfield, C. Richmond, W. F. Ford, and J. White: *Trans. Br. Ceram. Soc.*, 1970, vol. 69, pp. 53-58.
29. R. D. Warner and W. C. Luth: *Am. Mineral.*, 1973, vol. 58, pp. 998-1008.
30. C. Brousse, R. C. Newton, and O. J. Kleppa: *Geochim. Cosmochim. Acta*, 1984, vol. 48, pp. 1081-1088.
31. J. B. Ferguson and H. E. Merwin: *Am. J. Sci.*, 4th Ser., 1919, vol. 284, pp. 81-123.
32. Biggar G.M. and M. J. O'hara: *J. Am. Ceram. Soc.*, 1970, vol. 53, pp. 538-540.
33. Della M. Roy: *Mineral. Mag. J. Mineral Sci.*, 1956, vol. 31, pp. 187-194.
34. L. Kosa, K. Adamkovicova, and I. Proks: *Silikaty Prague*, 1985, vol. 25, pp. 199-206.
35. *www.factsage.com*, Montreal, 2002.
36. N. L. Bowen: *Am. J. Sci.*, 1914, vol. 38, pp. 207-264.
37. F. R. Boyd and J. F. Schairer: *J. Petrol.*, 1964, vol. 5, pp. 275-309.
38. I. Kushiro: *Am. Mineral.*, 1972, vol. 57, pp. 1260-70.
39. J. F. Schairer and Jr. H. S. Yoder: *Carnegie Inst. Washington, Yearbook*, 1962, Yb. 61, pp. 75-82.
40. I. Kushiro and J. F. Schairer: *Carnegie Inst. Washington, Yearbook*, 1963, Yb. 62, pp. 95-103.
41. H. Y. Yang: *Am. J. Sci.*, 1973, vol. 273, pp. 488-497.
42. J. Longhi: *Proc. Lunar Planet. Sci. Conf. 9th*, 1978, pp. 285-306.
43. J. Longhi and A. E. Boudreau: *Am. Mineral.*, 1980, vol. 65, pp. 563-73.
44. G. A. Jenner and D. H. Green: *Mineral. Mag.*, 1983, vol. 47, pp. 153-160.
45. G. M. Biggar: *Mineral. Mag.*, 1985, vol. 49, pp. 49-58.
46. W. D. Carlson: *Am. Mineral.*, 1988, vol. 73, pp. 232-241.
47. R. C. Newton, T. V. Charlu, P. A. M. Andreson, and O. J.

- Kleppa: *Geochim. Cosmochim. Acta*, 1979, vol. 41, pp. 55-60.
48. A. J. Perrotta and D. A. Stephenson: *Science*, 1965, vol. 148, pp. 1090-1091.
 49. J. V. Smith: *Nature*, 1969, vol. 222, pp. 256-257.
 50. J. A. Shearer and O. J. Kleppa: *J. Inorg. Nucl. Chem.*, 1973, vol. 35, pp. 1073-1078.
 51. T. Allen, F. P. White, F. E. Wright, and E. S. Larsen: *Am. J. Sci.*, 1909, vol. 27, pp. 1-47.
 52. J. F. Schairer and N. L. Bowen: *Am. J. Sci.*, 1942, vol. 240, pp. 725-742.
 53. E. F. Osborn: *Am. J. Sci.*, 1942, vol. 240, pp. 751-788.
 54. I. Tarina, A. Navrotsky, and H. Gan: *Geochim. Cosmochim. Acta*, 1994, vol. 58, pp. 3665-73.
 55. J. J. De Yoreo, R. A. Lange, and A. Navrotsky: *Geochim. Cosmochim. Acta*, 1995, vol. 59, pp. 2701-2707.
 56. A. Navrotsky, D. Ziegler, R. Oestrike, and P. Maniar: *Contrib. Mineral. Petrol.*, 1989, vol. 101, pp. 122-130.
 57. D. Ziegler and A. Navrotsky: *Geochim. Cosmochim. Acta*, 1986, vol. 50, pp. 2461-2466.
 58. R. A. Lange, J. J. D. Yoreo, and A. Navrotsky: *Am. Mineral.*, 1991, vol. 76, pp. 904-912.
 59. J. F. Stebbins, I. S. E. Carmichael, and D. E. Weill: *Am. Mineral.*, 1983, vol. 68, pp. 717-30.
 60. P. Richet and Y. Bottinga: *Earth Planet. Sci. Lett.*, 1984, vol. 67, pp. 415-32.
 61. A. Navrotsky, D. Ziegler, R. Oestrike, and P. Maniar: *Contrib. Mineral. Petrol.*, 1989, vol. 101, pp. 122-30.
 62. J. F. Schairer and I. Kushiro: *Carnegie Inst. Washington, Yearbook*, 1964, Yb. 63, pp. 130-132.
 63. I. Kushiro and J. F. Schairer: *Carnegie Inst. of Washington*, 1964, Yb. 63, pp. 132-133.
 64. J. W. Valley and E. J. Essene: *Contrib. Mineral. Petrol.*, 1980, vol. 74, pp. 143-152.
 65. J. F. Schairer and N. L. Bowen: *Am. J. Sci.*, 1942, vol. 240, pp. 725-42.
 66. H. S. Jr. Yoder: *Fortschr. Mineral.*, 1973, vol. 50, pp. 140-173.
 67. H. S. Jr. Yoder: *Phys. Chem. Earth*, 1975, vol. 9, pp. 883-894.
 68. I. Proks, M. Eliasova, and L. Kosa: *Silikaty*, 1977, vol. 1, pp. 3-9.
 69. K. Adamkovicova, I. Nerad, L. Kosa, M. Liska, J. Strecko, and I. Proks: *Chem. Geol.*, 1996, vol. 128, pp. 107-112.
 70. I. Nerad, K. Adamkovicova, and L. Strecko: *J. Proks I. Kosa: Thermochimica acta*, 1996, vol. 276, pp. 49-55.
 71. D. R. Spencer, T. W. Beamond, and D. S. Coleman: *Trans. Brit. Ceram. Soc.*, 1970, vol. 70, pp. 31-33.
 72. H. Sakai and H. Suito: *ISIJ Inter.*, 1996, vol. 34, pp. 138-142.
 73. J. W. Greig: *Am. J. Sci., 5th Ser.*, 1927, vol. 13, pp. 1-44.
 74. M. Kirschen and C. DeCapitani: *J. Phase Equilib.*, 1999, vol. 20, pp. 593-611.
 75. R. J. Harker and O. F. Tuttle: *Am. J. Sci.*, 1956, vol. 254, pp. 468-478.
 76. L. S. Walter: *Am. J. Sci.*, 1963, vol. 261, pp. 488-500.
 77. R. H. Rein and J. Chipman: *TMS-AIME*, 1965, vol. 233, pp. 415-25.
 78. K. Morita, K. Kume, and N. Sano: *ISIJ Inter.*, 2000, vol. 40, pp. 554-560.
 79. D. Henderson and Taylor J.: *J. Iron Steel Inst.*, 1966, pp. 39-43.
 80. M. R. Kalyanram, T. G. MacFarlane, and H. Bell: *J. Iron Steel Inst.*, 1960, vol. 58-64, pp. 195.
 81. K. Sawamura: *Tetsu-to-Hagane Overseas*, 1962, vol. 2, pp. 219-225.

Table I. Names of all solid and liquid phases in the CaO-MgO-SiO₂ system at 1 bar pressure.

Phase Name	Formula	Other names
Olivine	(Ca ²⁺ ,Mg ²⁺)(Ca ²⁺ ,Mg ²⁺)SiO ₄	Forsterite (Fors): Mg ₂ SiO ₄ rich olivine Monticellite (Mont): CaMgSiO ₄ rich olivine γ -Ca ₂ SiO ₄ (γ): Ca ₂ SiO ₄ rich olivine
Clino-pyroxene (cpx) (monoclinic, C2/c)	(Ca ²⁺ ,Mg ²⁺)(Mg ²⁺)Si ₂ O ₆	Diopside (Diop): CaMgSi ₂ O ₆ rich clino-pyroxene Pigeonite (Pig): MgSiO ₃ rich clino-pyroxene
Ortho-pyroxene (opx) (orthorhombic, Pbcn)	(Ca ²⁺ ,Mg ²⁺)(Mg ²⁺)Si ₂ O ₆	Ortho-enstatite (MgSiO ₃ rich ortho-pyroxene)
Proto-pyroxene (ppx) (orthorhombic, Pbcn)	(Ca ²⁺ ,Mg ²⁺)(Mg ²⁺)Si ₂ O ₆	Proto-enstatite (MgSiO ₃ rich proto-pyroxene)
Low clino-pyroxene (monoclinic, P21/c)	(Ca ²⁺ ,Mg ²⁺)(Mg ²⁺)Si ₂ O ₆	Low clino-enstatite (MgSiO ₃ rich low clino-pyroxene)
Monoxide	(Ca ²⁺ ,Mg ²⁺)O	Lime (CaO): CaO rich monoxide Periclase (MgO): MgO rich monoxide
Wollastonite (Woll)	(Ca ²⁺ ,Mg ²⁺)SiO ₃	
α' -Ca ₂ SiO ₄ (α')	(Ca ²⁺ ,Mg ²⁺) ₂ SiO ₄	
α -Ca ₂ SiO ₄ (α)	(Ca ²⁺ ,Mg ²⁺) ₂ SiO ₄	
Molten oxide (L)	CaO-MgO-SiO ₂	Slag
Akermanite (Aker)	Ca ₂ MgSi ₂ O ₇	
Merwinite (Merw)	Ca ₃ MgSi ₂ O ₈	
Pseudo-wollastonite (P-Woll)	CaSiO ₃	
Silica	SiO ₂	Quartz, Tridymite (Trid), Cristobalite (Crist)
Hatrurite (Hatr)	Ca ₃ SiO ₅	
Rankinite (Rank)	Ca ₃ Si ₂ O ₇	

Table II. Optimized model parameters of solutions and compounds in the CaO-MgO-SiO₂ system (J/mol).

Olivine: (Ca²⁺, Mg²⁺)^{M2}(Ca²⁺, Mg²⁺)^{M1}SiO₄	
$G_{\text{MgMg}} = G^{\circ}(\text{Mg}_2\text{SiO}_4)^{[35]}$	
$G_{\text{CaCa}} = G^{\circ}(\text{Ca}_2\text{SiO}_4)^{[35]}$	
$G_{\text{CaMg}} = G^{\circ}(\text{CaMgSiO}_4 \text{ from Reference [18]}) - 3345$	
$G_{\text{MgCa}} = G_{\text{CaMg}} + 146440$	
${}^0L_{\text{CaMg:Ca}} = {}^0L_{\text{CaMg:Mg}} = 32235.53$	
${}^1L_{\text{CaMg:Ca}} = {}^1L_{\text{CaMg:Mg}} = 4279.92$	
${}^0L_{\text{Ca:CaMg}} = {}^0L_{\text{Mg:CaMg}} = 28032.8 - 12.55T$	
Pyroxene: (Ca²⁺, Mg²⁺)^{M2}(Mg²⁺)^{M1}Si₂O₆	
$G^{\circ}(\text{MgSiO}_3, \text{ low clino-}), G^{\circ}(\text{MgSiO}_3, \text{ proto-}), G^{\circ}(\text{MgSiO}_3, \text{ ortho-}) \text{ from F*A*C*T.}^{[35]}$	
$G^{\circ}(\text{MgSiO}_3, \text{ clino-}) = G^{\circ}(\text{MgSiO}_3, \text{ low clino-}) + 4694.5 - 3.70 T$	
$G^{\circ}(\text{CaMgSi}_2\text{O}_6, \text{ clino-}) = G^{\circ}(\text{clino-CaMgSi}_2\text{O}_6 \text{ from Reference [18]}) + 837$	
$G^{\circ}(\text{CaMgSi}_2\text{O}_6, \text{ low clino-}) = G^{\circ}(\text{CaMgSi}_2\text{O}_6, \text{ clino-}) + 28368$	
$G^{\circ}(\text{CaMgSi}_2\text{O}_6, \text{ ortho-}) = G^{\circ}(\text{CaMgSi}_2\text{O}_6, \text{ clino-}) + 19740 + 0.02 T$	
$G^{\circ}(\text{CaMgSi}_2\text{O}_6, \text{ proto-}) = G^{\circ}(\text{CaMgSi}_2\text{O}_6, \text{ clino-}) + 17071.2$	
Low clino-pyroxene: ${}^0L_{\text{CaMg:Mg}} = 25304.0 + 2.358T$	
Ortho-pyroxene: ${}^0L_{\text{CaMg:Mg}} = 27247.8 - 8.622T$	
Proto-pyroxene: ${}^0L_{\text{CaMg:Mg}} = 25304.0 + 2.358T$	
Clino-pyroxene: ${}^0L_{\text{CaMg:Mg}} = 25304.0 + 2.358T, {}^1L_{\text{CaMg:Mg}} = -3018.6$	
Wollastonite: (Ca²⁺, Mg²⁺)SiO₃	
$G^{\circ}(\text{MgSiO}_3) = G^{\circ}(\text{MgSiO}_3, \text{ ortho-pyroxene}) + 48987.6 - 17.145T$	
α-Ca₂SiO₄: (Ca²⁺, Mg²⁺)₂SiO₄	
$G^{\circ}(\alpha\text{-Mg}_2\text{SiO}_4) = G^{\circ}(\text{Mg}_2\text{SiO}_4, \text{ olivine}) + 83680.0$	
$q_{\text{MgCa}}^{03} = -35564$	
α'-Ca₂SiO₄: (Ca²⁺, Mg²⁺)₂SiO₄	
$G^{\circ}(\alpha'\text{-Mg}_2\text{SiO}_4) = G^{\circ}(\text{Mg}_2\text{SiO}_4, \text{ olivine}) + 85772$	
$q_{\text{MgCa}}^{03} = -35564$	
Liquid Oxide: CaO-MgO-SiO₂	
$q_{\text{MgO, SiO}_2(\text{CaO})}^{001} = 4184$	
$q_{\text{CaO, SiO}_2(\text{MgO})}^{001} = 8368$	
$q_{\text{CaO, SiO}_2(\text{MgO})}^{021} = -29288$	
The quasichemical parameters are defined in References [4,5]. The other binary model parameters for the liquid oxide can be found in the previous studies. ^[9-11]	

Thermodynamic properties ($S_{298.15}$, $H_{298.15}$, C_p) of CaMgSiO₄, clino-CaMgSi₂O₆, Ca₂MgSi₂O₇ and Ca₃MgSi₂O₈ were taken from Berman^[18] with the enthalpies of formation at 298.15 K changed by -3345, 837, -5850 and -18280 J/mol, respectively.

The Gibbs energies of the other end-members of the solid and liquid solutions and of the other stoichiometric compounds in the CaO-MgO-SiO₂ system are taken from the F*A*C*T database^[35] and previous studies.^[9-11] The binary model parameters for the monoxide and liquid oxide solutions are given in the previous studies.^[9-11]

Table III. Comparison of the calculated and experimental ternary invariant points involving liquid oxide in the CaO-MgO-SiO₂ system.

(*)Invariant point	T (°C)		Liquid Composition (mole %)						Reference
			CaO		MgO		SiO ₂		
	Calc.	Exp.	Calc.	Exp.	Calc.	Exp.	Calc.	Exp.	
L→CaO+MgO+α	1923		63.0		8.4		28.6		
L+ MgO+α→Merw	1576	1575	41.5	41.1	24.6	24.3	33.9	34.6	21
L+MgO+Merw→Mont	1507		34.1		31.6		34.3		
L+MgO+Fors→Mont	1516	1502	29.8	29.8	35.9	34.2	34.3	36.0	22
L+Merw+Mont→Aker	1438	1436	35.5	37.4	26.6	24.4	37.9	38.2	28
L+Mont+Fors→Aker	1429	1430	31.4	31.5	29.7	29.3	38.9	39.2	28
L+Merw+Aker→P-woll	1392		49.7		8.8		41.5		
L→α+Merw+P-woll	1391		51.2		7.6		41.2		
L+Rank→α+P-woll	1461		56.5		1.5		42.0		
L→Aker+Diop+Fors	1366	1357	27.0	26.9	28.2	28.5	44.8	44.6	28
L→Aker+Diop+Woll	1361	1350	33.7	35.1	18.0	17.5	48.3	47.4	53
L+Aker+P-woll→Woll	1366	1360	34.4	36.4	17.3	16.2	48.3	47.4	53
L+Tridy+P-woll→Woll	1336	1336	31.0	32.0	12.0	9.5	57.0	58.5	53
L→Woll+Tridy+Diop	1331	1320	30.3	30.8	12.6	11.2	57.1	58.0	53
L+Fors+ppx→opx	1438	1445	10.1	11.7	38.6	35.8	51.3	52.5	43
L+Fors+opx→Pige	1410	1410	12.4	14.8	36.3	32.7	51.3	52.5	43
L+Fors→Diop+Pige	1382	1385	15.1	17.0	33.9	31.0	51.0	52.0	43
L+ppx+Tridy→opx	1409	1419	11.7	12.7	33.4	31.0	54.9	56.3	43
L+opx+Tridy→Pige	1395	1387	12.8	15.0	32.4	28.4	54.8	56.6	43
L→Pige+Diop+Tridy	1369	1373	15.1	16.4	30.1	27.5	54.8	56.1	43

* The ambiguous invariant points involving hatrurite (Ca₃SiO₅) and rankinite (Ca₃Si₂O₇) estimated by Ricker and Osborn^[24] and Osborn^[23] are not included in the table (see text for details).

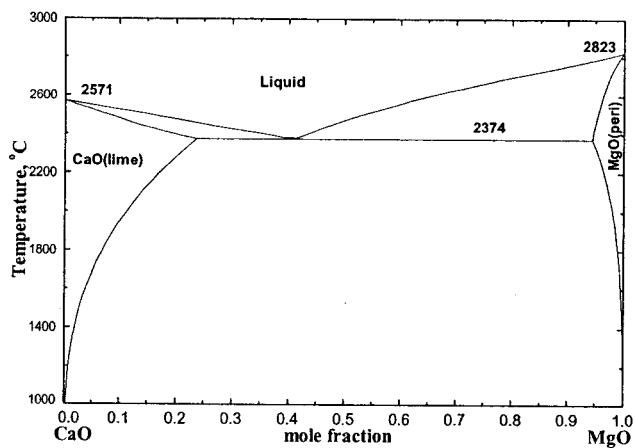


Fig. 1 – Calculated CaO-MgO phase diagram.^[9]

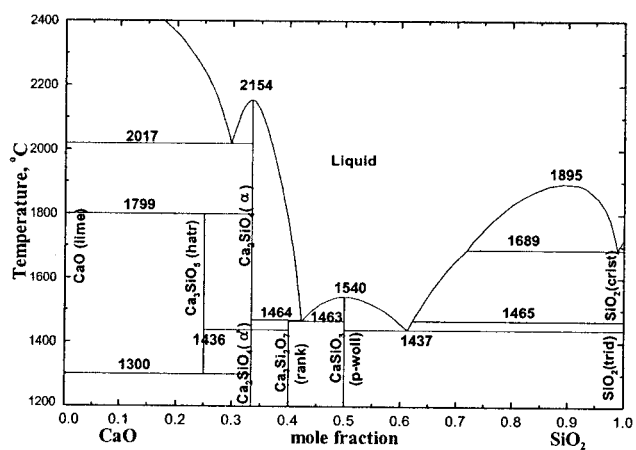


Fig. 2 – Calculated CaO-SiO₂ phase diagram.^[10]

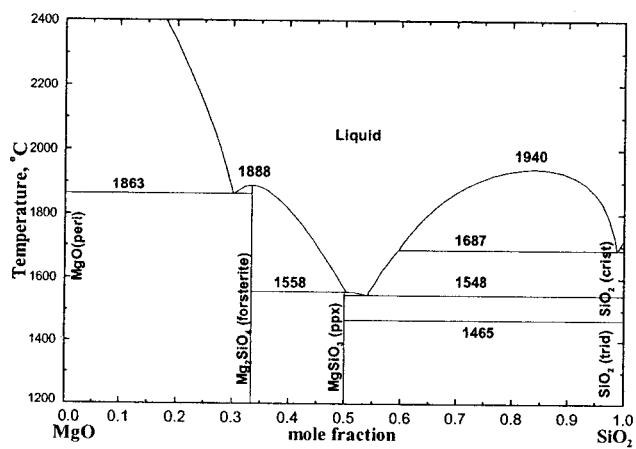


Fig. 3 – Calculated MgO-SiO₂ phase diagram.^[11]

Fig. 4 – Calculated (optimized) liquidus surface of the CaO-MgO-SiO₂ system at 1 bar pressure. Temperatures in °C. See Table I for abbreviations of phase names.

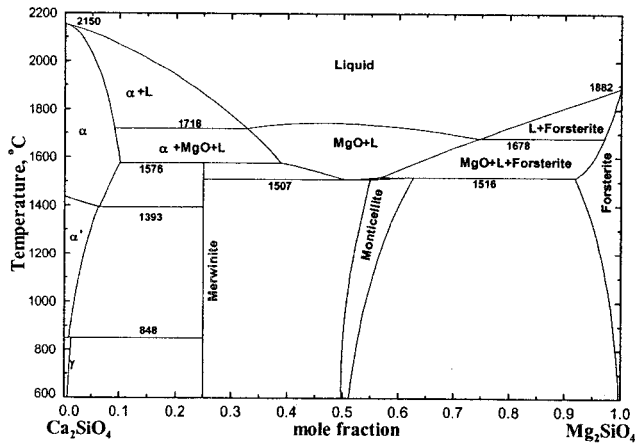


Fig. 5 – Calculated phase diagram of the Ca_2SiO_4 - Mg_2SiO_4 orthosilicate section.

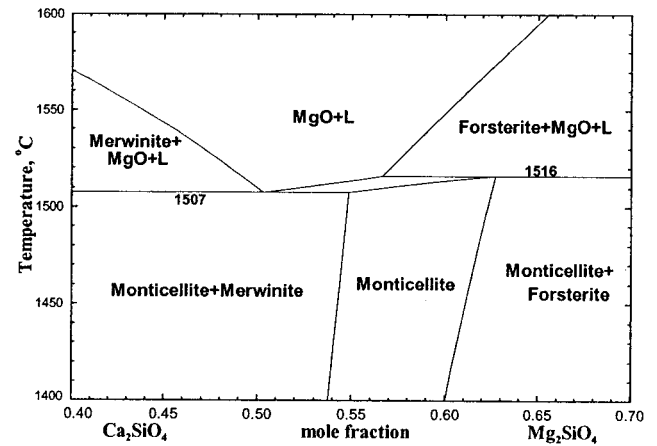


Fig. 8 – Melting behavior of monticellite (olivine solid solution). Phase diagram is calculated from the optimization.

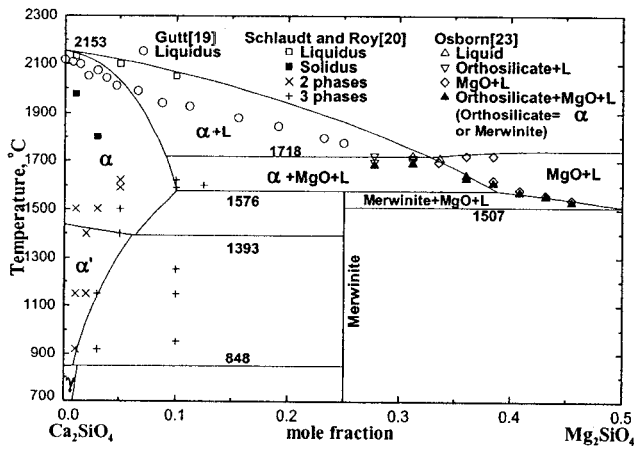


Fig. 6 – Calculated phase diagram of the Ca_2SiO_4 - CaMgSiO_4 section.

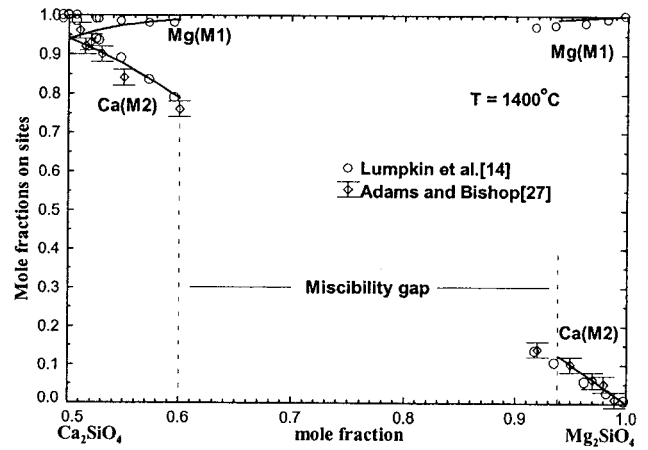


Fig. 9 – Calculated cation distribution of Ca and Mg between M2 and M1 sites in olivine solid solutions at 1400 °C. Mole fractions of Ca and Mg on M2 and M1 sites.

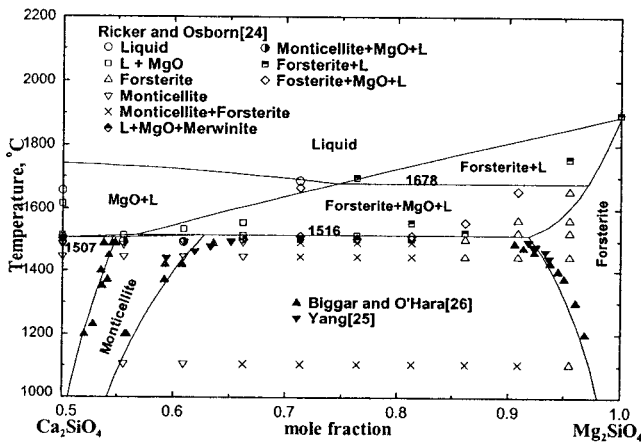


Fig. 7 – Calculated phase diagram of the CaMgSiO_4 - Mg_2SiO_4 section.

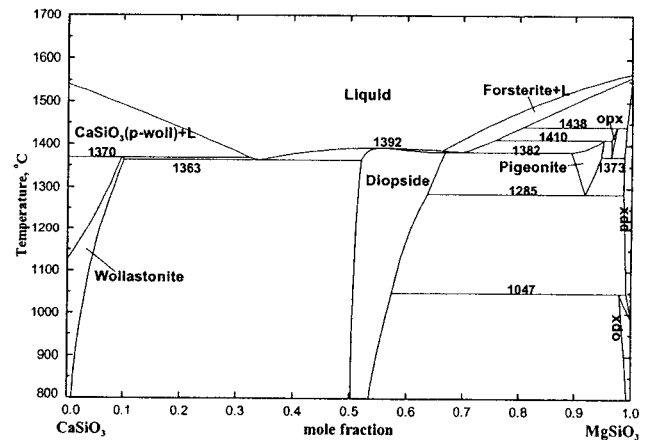


Fig. 10 – Calculated phase diagram of the CaSiO_3 - MgSiO_3 metasilicate section.

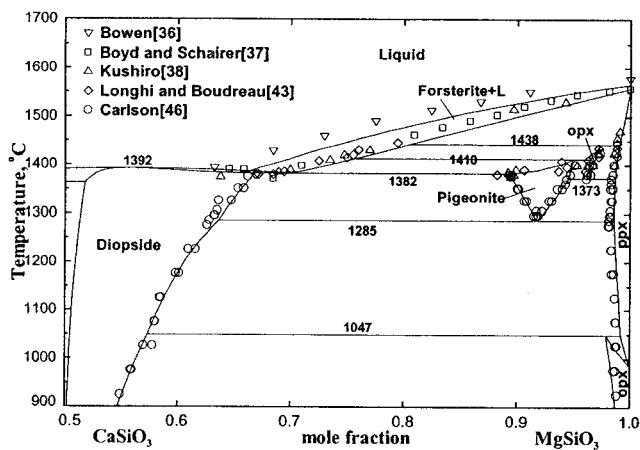


Fig. 11 – Calculated phase diagram of the $\text{CaMgSi}_2\text{O}_6$ - MgSiO_3 section.

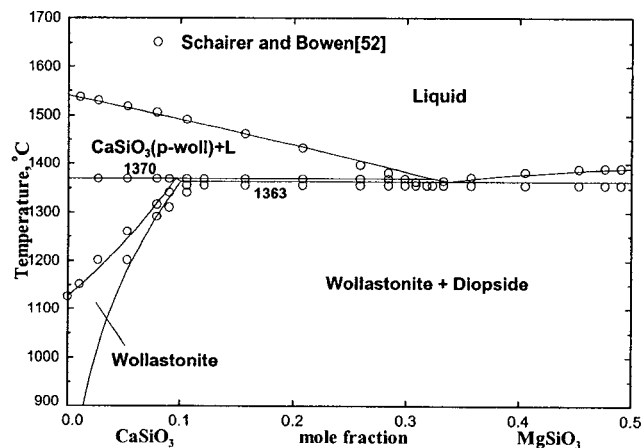


Fig. 14 – Calculated phase diagram of the CaSiO_3 - $\text{CaMgSi}_2\text{O}_6$ section.

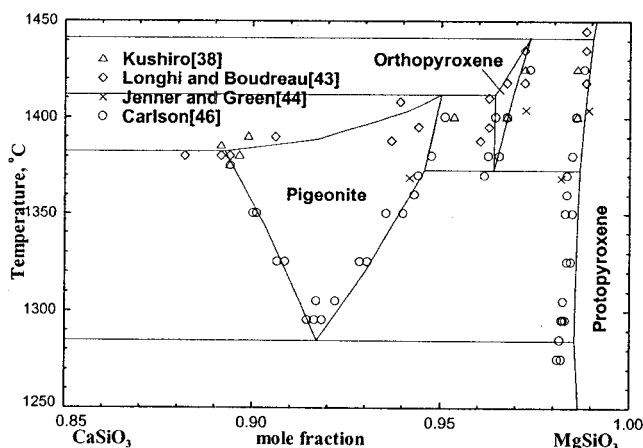


Fig. 12 – Enlargement of the calculated phase diagram around the pigeonite (clino-pyroxene) region in the metasilicate section.

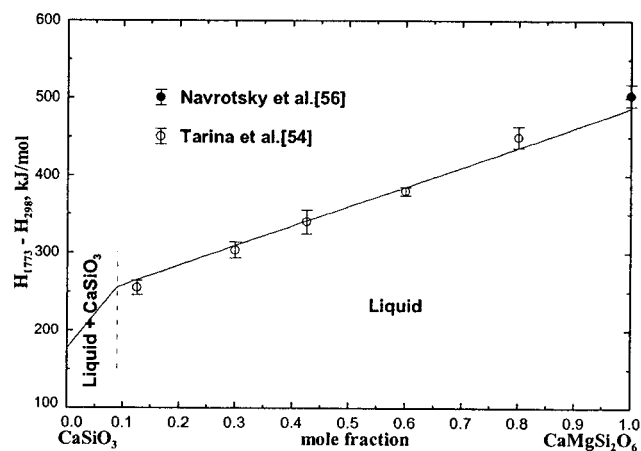


Fig. 15 – The calculated and experimental enthalpy change for the heating and melting of (pseudowollastonite + diopside) mixtures.

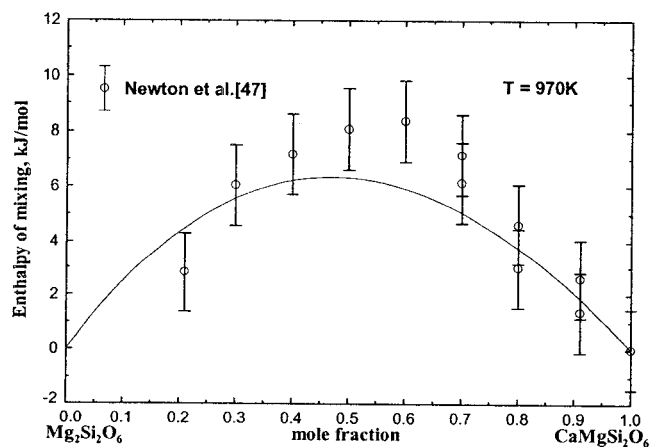


Fig. 13 – Calculated enthalpy of mixing of the clino-pyroxene solution at 970 K.

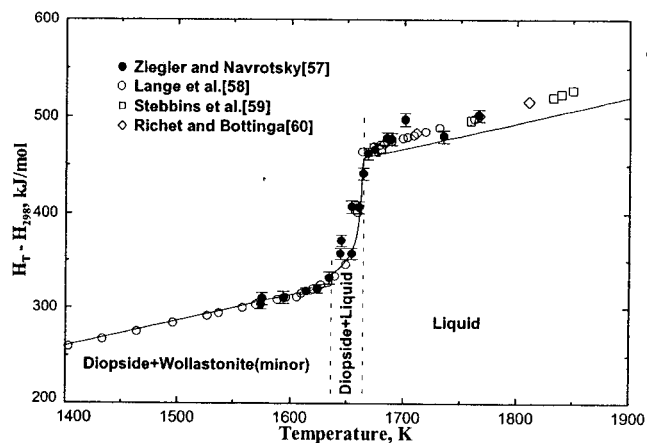


Fig. 16 – Comparison of calculated and experimental enthalpy at the stoichiometric $\text{CaMgSi}_2\text{O}_6$ composition.

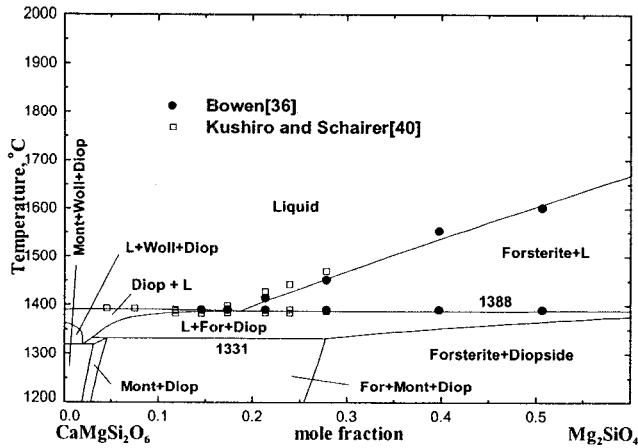


Fig. 17 – Calculated phase diagram of the $\text{CaMgSi}_2\text{O}_6$ - Mg_2SiO_4 section.

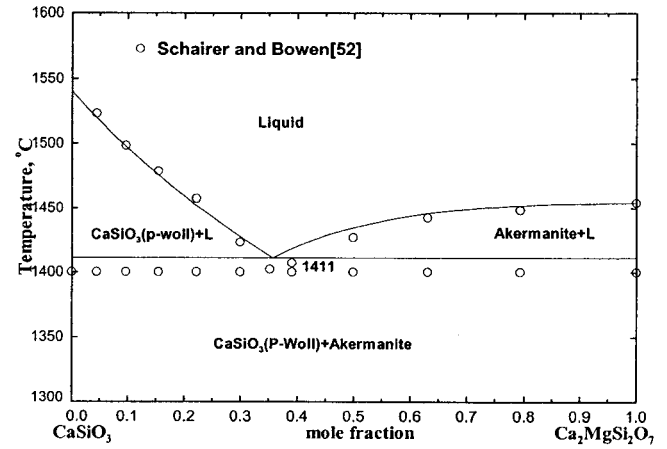


Fig. 20 – Calculated phase diagram of the CaSiO_3 - $\text{Ca}_2\text{MgSi}_2\text{O}_7$ section.

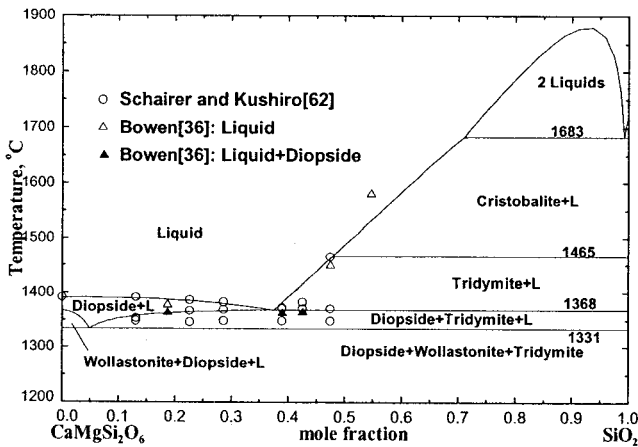


Fig. 18 – Calculated phase diagram of the $\text{CaMgSi}_2\text{O}_6$ - SiO_2 section.

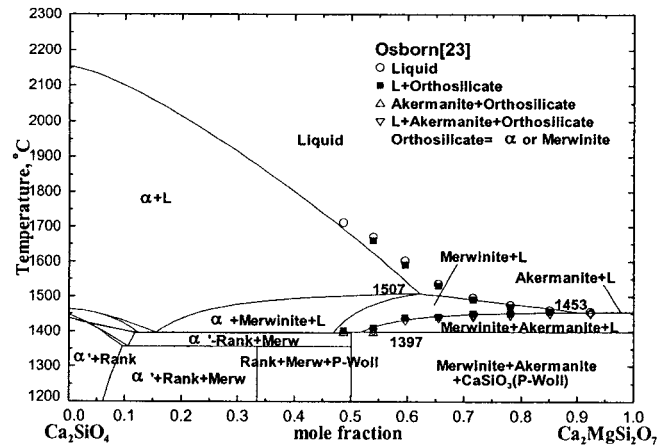


Fig. 21 – Calculated phase diagram of the Ca_2SiO_4 - $\text{Ca}_2\text{MgSi}_2\text{O}_7$ section.

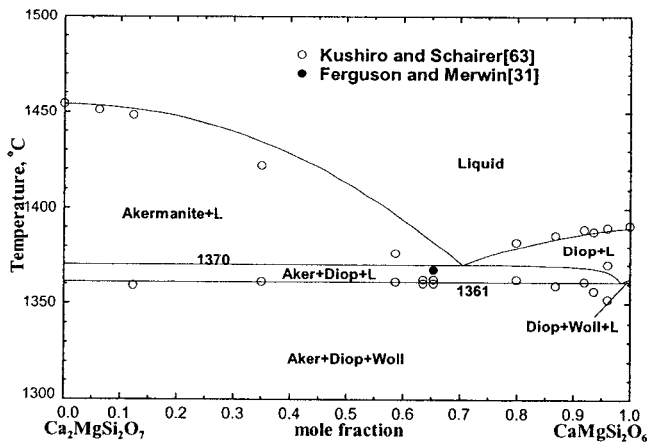


Fig. 19 – Calculated phase diagram of the $\text{Ca}_2\text{MgSi}_2\text{O}_7$ - $\text{CaMgSi}_2\text{O}_6$ section.

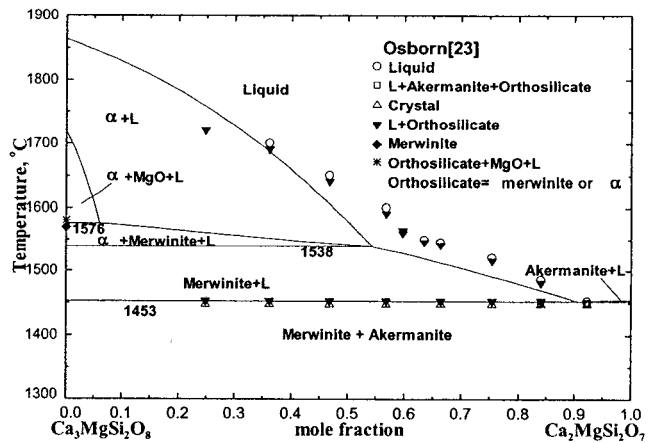


Fig. 22 – Calculated phase diagram of the $\text{Ca}_3\text{MgSi}_2\text{O}_8$ - $\text{Ca}_2\text{MgSi}_2\text{O}_7$ section.

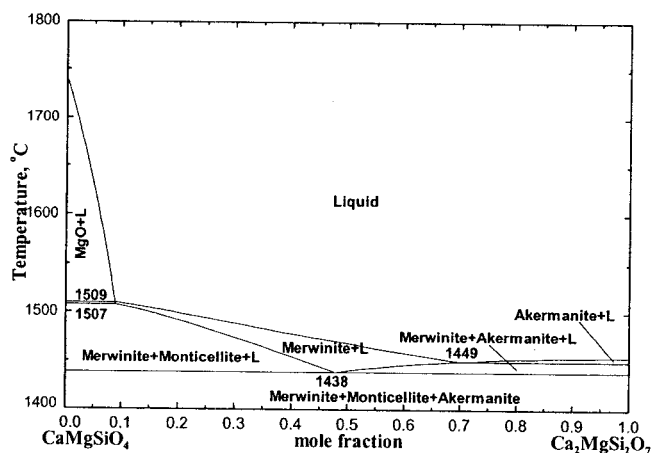


Fig. 23 – Calculated phase diagram of the CaMgSiO_4 - $\text{Ca}_2\text{MgSi}_2\text{O}_7$ section.

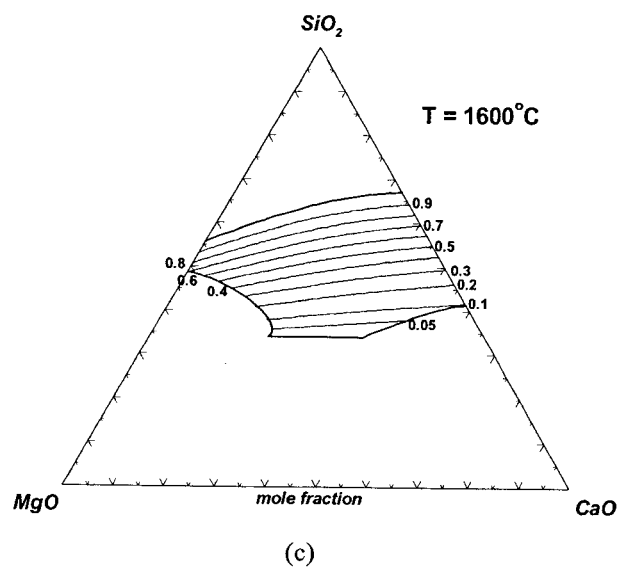
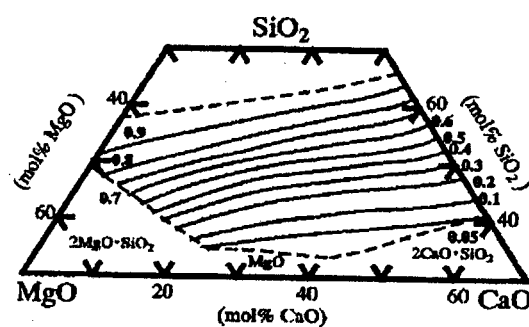
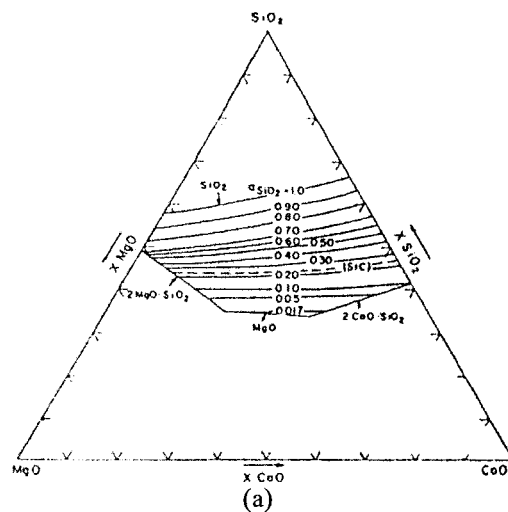


Fig. 24 – Activities of SiO_2 (relative to solid cristobalite) in the CaO - MgO - SiO_2 liquid slag at 1600°C . (a) Rein and Chipman,^[77] (b) Morita *et al.*,^[78] (c) calculated in the present study.

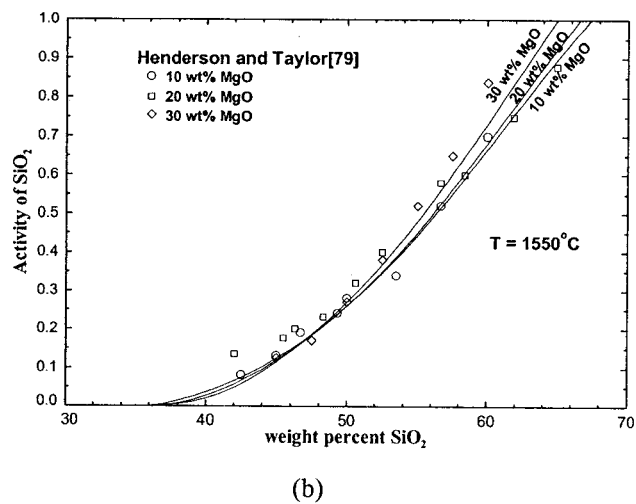
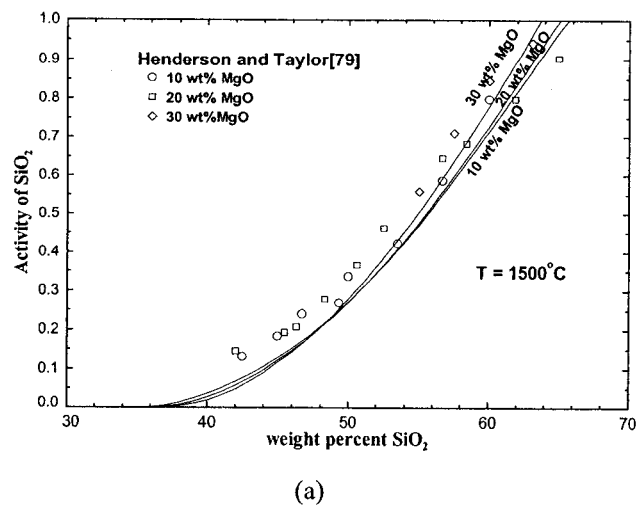


Fig. 25 – Comparison of the calculated activities of SiO_2 (relative to solid cristobalite standard state) in the CaO-MgO-SiO_2 slag with experimental data by Henderson and Taylor.^[79] (a) 1500 °C and (b) 1550 °C.

Appendix II

Article :

Thermodynamic Modeling of the Fe-Mg-O System

In-Ho Jung, Sergei A. Decterov and Arthur D. Pelton

Submitted to *Metallurgical and Materials Transactions*, 2003

Thermodynamic Modeling of the Fe-Mg-O System

IN-HO JUNG, SERGEI A. DECTEROV, and ARTHUR D. PELTON

A complete critical evaluation and thermodynamic modeling of the phase diagrams and thermodynamic properties at 1 bar total pressure of oxide phases in the Fe-Mg-O system are presented. Optimized equations for the thermodynamic properties of all phases are obtained which reproduce all available thermodynamic and phase equilibrium data within experimental error limits from 25 °C to above the liquidus temperatures at all compositions and oxygen partial pressures. The database of the model parameters can be used along with software for Gibbs energy minimization in order to calculate any type of phase diagram section.

I. INTRODUCTION

THE Fe-Mg-O system is important in industrial and natural processes. Magnesium ferrite spinel has interesting magnetic properties. The magnesiowustite phase is very important to an understanding of the Earth's mantle. This system is also important in the corrosion of magnesite refractories by iron oxide in steelmaking processes. Experimental study of this system is difficult because the phase equilibria strongly depend on oxygen partial pressure. Therefore, critical assessment of experimental data and thermodynamic optimization is necessary to model this system more accurately. Fabrichnaya^[1] reported an optimization of the Fe-Mg-O system which was mainly concerned with the phase equilibria at high pressure. Complete optimization of this system has not yet been performed satisfactorily.

The optimization of the Fe-O binary sub-system was reported earlier.^[2] The main goal of the present study is to perform a critical assessment and optimization of thermodynamic properties of oxide phases in the Fe-Mg-O (FeO-Fe₂O₃-MgO) system at 1 bar pressure. In the thermodynamic "optimization" of a chemical system, all available thermodynamic and phase equilibrium data are evaluated simultaneously in order to obtain one set of model equations for the Gibbs energies of all phases as functions of temperature and composition. From these equations, all of the thermodynamic properties and the phase diagrams can be back-calculated. In this way, all the data are rendered self-consistent and consistent with thermodynamic principles. Thermodynamic property data, such as activity data, can aid in the evaluation of the phase diagram, and phase diagram measurements can be used to deduce thermodynamic properties. Discrepancies in the available data can often be resolved, and interpolations and extrapolations can be made in a thermodynamically correct manner.

The evaluation/optimization of the FeO-Fe₂O₃-MgO system reported in this study is part of a wider research project aimed at complete optimization of the Al₂O₃-CaO-FeO-Fe₂O₃-MgO-SiO₂ system which is of primary importance in the metallurgical, ceramics, glass and cement industries, geochemistry, etc. The present optimization covers the range of oxygen partial pressures from equilibrium with pure oxygen to metal saturation and temperatures from 25 °C to above the liquidus. A wide variety of different data types was used in the optimization. It will be shown how these data are reproduced by the model equations.

II. THERMODYNAMIC MODELS

Figure 1 shows the calculated phase diagram of the Fe-Mg-O system at 1200 °C and 1 bar pressure. The following solution phases are found in this system.

Slag (molten oxide phase): MgO-FeO-FeO_{1.5},
Magnesiowustite (MW): MgO-FeO-FeO_{1.5},
Spinel (encompassing magnetite Fe₃O₄ and magnesioferrite MgFe₂O₄): (Fe²⁺, Fe³⁺, Mg²⁺)^T [Fe²⁺, Fe³⁺, Mg²⁺, Va]^{O₂O₄}

Alloy phases: Liquid, bcc and fcc.

In the spinel phase, the Fe²⁺, Fe³⁺, and Mg²⁺ cations are present on both tetrahedral and octahedral sites which are denoted above by round and square brackets, respectively. The oxygen nonstoichiometry is modeled by introducing vacancies on the octahedral sites as is suggested by the experimental evidence as discussed previously.^[2]

For the spinel solution, a two sublattice spinel model^[2] has been developed within the framework of the Compound Energy Formalism (CEF).^[3] The Gibbs energy expression in the CEF per formula unit is

$$G = \sum_i \sum_j Y_i' Y_j'' G_{ij} - TS_C + G^E \quad [1]$$

where Y_i' and Y_j'' represent the site fractions of cations i and j on the first and second sublattices, G_{ij} is the Gibbs energy of an "end-member" ij of the solution, in which the first sublattice is occupied only by cations i and the second

sublattice is occupied only by cations j . G^E is the excess Gibbs energy and S_c is the configurational entropy assuming random mixing on each sublattice:

$$S_c = -R \left(n_1 \sum_i Y_i' \ln Y_i' + n_2 \sum_j Y_j' \ln Y_j' \right) \quad [2]$$

where n_1 and n_2 are the numbers of sites on the first and second sublattice per formula unit of a solution. For the spinel phase in the present study, G^E is set equal to zero and certain linear combinations of Gibbs energies of end-members, which have physical sense, are used as model parameters. The magnetism of the spinel solution is also taken into account. The empirical relationship suggested by Hillert and Jarl^[4] is used for the magnetic contribution to thermodynamic properties.

Of the 12 parameters G_{ij} , six were fixed during the earlier optimization^[2] of magnetite ($\text{Fe}^{2+}, \text{Fe}^{3+}$)^T [$\text{Fe}^{2+}, \text{Fe}^{3+}, \text{Va}$]₂O₄, and two more (G_{MM} and G_{MV}) were fixed in the optimization^[5] of the Al-Mg-O spinel solution. (M, V, H and F stand for Mg^{2+} , Va, Fe^{3+} and Fe^{2+} respectively.) Optimized values of the four remaining parameters (G_{FM} , G_{HM} , G_{MF} and G_{MH}) were obtained in the present study as described in the following sections. These are listed in Table I. The physical significance of the linear combinations I_{MH} , $\Delta_{\text{MH:MV}}$ and $\Delta_{\text{FM:FH}}$ is discussed in Reference [2]. These linear combinations are related to the energies of classical site exchange reactions.

The Modified Quasichemical Model^[6-9], which accounts for short-range-ordering of second-nearest-neighbor cations in ionic melts, was used for the molten slag solution. Optimized parameters for the binary FeO-FeO_{1.5} slag solution were obtained previously.^[2] The second-nearest-neighbor "coordination numbers" of Fe^{2+} , Fe^{3+} and Mg^{2+} used in the present study are the same as in previous studies.^[2,10] Optimized binary parameters for the FeO-MgO and FeO_{1.5}-MgO slag solutions were obtained in the present study as described in the following sections. These are listed in Table I. The properties of the ternary FeO-FeO_{1.5}-MgO slag solution were calculated from the binary parameters with the symmetric "Kohler-like" approximation.^[11] No ternary parameters were required.

The FeO-FeO_{1.5}-MgO magnesiowustite phase was modeled as a simple random mixture of Fe^{2+} , Fe^{3+} and Mg^{2+} ions on cation sites with simple polynomial excess Gibbs energy terms.^[11] It is assumed that cation vacancies remain associated with Fe^{3+} ions and so do not contribute to the configurational entropy. Binary excess Gibbs energies were modeled by simple polynomial expansions in the mole fractions.^[11] Optimized parameters for wustite (FeO-FeO_{1.5}) were obtained previously.^[2] Optimized binary parameters for the FeO-MgO and FeO_{1.5}-MgO solutions were obtained in the present study as described in the following sections. These are listed in Table I. The properties of the ternary monoxide FeO-FeO_{1.5}-MgO solution were calculated from the binary parameters with the asymmetric "Toop-like" approximation^[11] with FeO_{1.5} as the "asymmetric component." No ternary parameters were required.

The thermodynamic properties of solid solutions based on bcc and fcc iron from the SGTE (Scientific Group Thermodata Europe)^[12] database were used for calculations of phase equilibria in the Fe-Mg-O system at metal saturation. For liquid iron, the F*A*C*T database^[13] was used. This database implements a recently developed model^[14] to accurately describe the solubility of oxygen and many other elements in molten iron. For liquid iron containing dissolved Mg and O, this model assumes the presence of dissolved Mg*O associates.

Hematite, Fe_2O_3 , is treated as a stoichiometric compound since its nonstoichiometry is believed to be negligibly small.

III. CRITICAL EVALUATION OF EXPERIMENTAL DATA AND OPTIMIZATION

A great many experimental measurements have been performed for the FeO-Fe₂O₃-MgO system. Most of the phase diagram data in this system are presented in two ways: one type of diagram plots the oxygen partial pressure versus composition (such as metallic ratio, Mg/Fe+Mg) and the other type is a ternary diagram of the FeO-Fe₂O₃-MgO system with superimposed oxygen partial pressure isobars. As pointed out by Pelton,^[15,16] these two types of phase diagram can be converted into each other. Therefore, most of the experimental measurements in this system can be presented by either type of phase diagram and can be compared with each other.

The experimental data below the liquidus temperature are mainly classified into three groups: non-stoichiometry in the magnesiowustite phase, thermodynamic and structural data for the spinel phase, and the phase equilibria iron-magnesiowustite, magnesiowustite-spinel and spinel-Fe₂O₃. Therefore, in the optimization, the magnesiowustite phase and the spinel phase were first optimized separately in order to describe the experimental data in their single-phase fields; then the overall optimization including the slag was carried out with further slight adjustment of the model parameters of the solid phases in order to reproduce all the data within experimental error limits. The results of the optimization of the single-phase spinel and magnesiowustite phases are presented first, followed by the discussion of phase equilibria in the entire Fe-Mg-O system.

A. Structural Data

MgFe₂O₄ is an inverse spinel at low temperatures^[17-24] as can be seen from Figure 2. In the optimization, after careful examination of both sample preparation and experimental conditions of all experiments, more weight was given to the results of O'Neill *et al.*,^[24] who took special precautions to obtain stoichiometric samples. The cation distribution does not reach equilibrium below about 500 °C on the laboratory time scale. On the other hand, it is not quenchable from temperatures higher than about 1100 °C. The data of O'Neill *et al.*,^[24] were fitted with the parameter I_{MH} which strongly affects the cation distributions.

Figure 3 shows the calculated cation distribution in the $\text{MgFe}_2\text{O}_4\text{-Fe}_3\text{O}_4$ spinel at 1000 °C. Trestman-Matts *et al.*^[25] and Nell *et al.*^[26] measured the cation distribution using a thermopower technique. The calculated cation distributions are in agreement with the experimental data within experimental error limits. It should be noted that the amounts of Mg on the sublattices reported by Nell *et al.*^[26] would extrapolate to values for pure MgFe_2O_4 which tend to deviate from the selected data of O'Neill *et al.*^[24] On the other hand, the amounts of Fe^{3+} reported by Trestman-Matts *et al.*^[25] show clear maxima and minima in the $\text{Fe}_3\text{O}_4\text{-MgFe}_2\text{O}_4$ solution, which are unlikely to be real.

B. Thermodynamic and Magnetic Properties of MgFe_2O_4

The heat capacity and entropy at 25 °C of the MgFe_2O_4 spinel were derived from the low-temperature heat capacity measurements of King^[27] and the heat content measurements from 25 °C to 1577 °C of Bonnickson.^[28] The effect of the probable change in cation distribution during the latter experiments was taken into account. Since it would take a much longer time than normally used in drop calorimetry experiments to re-equilibrate the cation distribution of a sample at low temperature before a drop, the cation distribution was assumed frozen for drops from temperatures below 450 °C. From this temperature up to about 1100 °C, the cation distribution was assumed to reach an equilibrium value before the drop which quenches during the drop. Above 1100 °C, the cation distribution is not quenchable. Therefore, after reaching an equilibrium value before a drop, the cation distribution was assumed to quench during the drop at an equilibrium value corresponding to 1100 °C. The heat capacity measured by Reznitskii *et al.*^[29] at ambient temperature is substantially higher than the one reported by King.^[27] Therefore, a systematic error was assumed to be present in the former measurements and they were corrected by subtracting 12.8 J/mol·K. It should be noted that the corrected values at high temperatures are still higher than the values derived from the heat content measurements of Bonnickson.^[28] The optimized heat capacity and heat content of MgFe_2O_4 are shown in Figures 4 and 5 along with the experimental data. The magnetic phase transition from the ferrimagnetic to the paramagnetic state can be seen on the heat capacity curve at 689.5 K.

The standard enthalpy of formation of the $(\text{Mg})[\text{Fe}]_2\text{O}_4$ end-member of the spinel solution was optimized to reproduce the phase equilibrium data and the calorimetric measurements of the enthalpy of formation of MgFe_2O_4 from MgO and Fe_2O_3 near 970 K.^[30-32] In the present study, the most recent measurements (Navrotsky^[31]) of the enthalpy of dissolution of MgFe_2O_4 in $2\text{PbO}\cdot\text{B}_2\text{O}_3$ melts were used along with the enthalpies of dissolution of Fe_2O_3 and MgO reported by Shearer and Kleppa^[30] which appear to be of good accuracy. Koehler *et al.*^[33] determined the enthalpy of formation of MgFe_2O_4 using HF acid calorimetry. However, their value, adjusted to 970 K using the heat content data of Bonnickson,^[28] is about 9 kJ/mol higher than the heat of formation reported by

Navrotsky.^[30,31] For magnesioferrite, dissolution calorimetry in lead borate melts is believed to be more reliable than in HF. Therefore, the measurements of Koehler *et al.*^[33] were not used in the present optimization.

Tretyakov and Schmalzried^[34] reported measurements of the Gibbs energy of MgFe_2O_4 using an emf technique. However, their measurements were not taken into account in this study because they used an electrode consisting of $(\text{MgFe}_2\text{O}_4 + \text{MgO} + \text{Fe})$ which cannot coexist at equilibrium.

The optimized entropy of MgFe_2O_4 at 25 °C is 115.6 J/mol/K which is close to the value 118.4 ± 1 J/mol/K reported by King.^[27] The optimized enthalpy of formation of MgFe_2O_4 from MgO and Fe_2O_3 at 25 °C is -13.7 kJ/mol, which is believed to be within the error limits of the recent measurement by Navrotsky,^[30,31] -9.76 kJ/mol. The experimental information mentioned above was used to obtain the parameter G_{MH} of the spinel model given in Table I.

Paladino^[35] reported considerable dissolution of Fe_2O_3 in MgFe_2O_4 spinel at 1300 °C from the results of thermogravimetric measurements. Later, by careful quenching experiments and X-ray phase identification,^[36] it was shown that his reported solubility was actually a metastable phase boundary. The solubility of MgO in the spinel phase has been measured in several studies.^[35-39] Since the solubility of MgO is small, it was neglected in the present study.

Many investigations^[20,21,24,29,40,41] reported the Curie temperature of MgFe_2O_4 at about 690 K. The magnetic moment (β_{MH}) was determined from the heat capacity data as shown in Figure 4. The magnetic parameters are listed in Table I.

C. Magnesioferrite in Equilibrium with Iron

The experimental results for the phase boundary between magnesioferrite and alloy (virtually pure Fe) are shown in Figures 6 and 7. Several investigators^[42-45] measured the Fe^{3+} content in magnesioferrite in saturation with metallic Fe using equilibration followed by quenching and chemical analysis. These data reveal almost no temperature dependence as can be seen from Figure 6. Figure 7 shows the variation of oxygen partial pressure along the magnesioferrite/iron phase boundary. Many experiments^[42,46-52] have been performed in the temperature range between 800 °C and 1300 °C. Oxygen partial pressures were controlled by gas mixtures (such as $\text{H}_2\text{O}/\text{H}_2$, CO_2/CO or CO_2/H_2) or were measured by an emf technique. Srecec *et al.*^[42] had difficulties in obtaining stable results by the emf technique with calcia-stabilized zirconia electrolytes. The gas equilibration and emf data are in poor agreement especially at low MgO contents. The emf measurements by Srecec *et al.*^[42] were not taken into account in the optimization. All other experimental data are well reproduced.

In the Fe-O system, wustite dissociates into $(\text{Fe}+\text{Fe}_3\text{O}_4)$ below about 564 °C. This dissociation also takes place in the Fe-Mg-O system. Figure 8 shows the temperature of dissociation of magnesioferrite into Fe and

spinel. Several authors^[51,53-55] measured this temperature but the results are widely scattered. The calculated line agrees with the experimental data within the experimental scatter.

D. Non-stoichiometry of Magnesio-wustite

The non-stoichiometry of the magnesio-wustite phase is shown in Figure 9. Valet *et al.*^[56] equilibrated magnesio-wustite of known Mg/(Mg+Fe) ratio with gas mixtures of known oxygen partial pressure. The samples were then quenched and the amount of Fe³⁺ in the magnesio-wustite phase was measured using chemical analysis (titration technique). Similar experiments were performed by other investigators.^[44,57-60] Hilbrandt and Martin^[61] calculated the amount of Fe³⁺ in magnesio-wustite based on structural information retrieved from *in situ* EXAFS studies. The experimental data for the non-stoichiometry of magnesio-wustite are rather scattered. Specifically, the Fe³⁺ contents reported in some experiments by Valet *et al.*^[56] (e. g. at Mg/(Mg+Fe) = 0.89 from 1300 °C to 1500 °C) are even lower than the Fe³⁺ content at saturation with iron (see Figure 6). This might be due to a systematic analytical error. The data by Hilbrandt and Martin,^[61] based on EXAFS measurements, were not used in the optimization since they reported much lower Fe³⁺ contents than were reported in the other studies which used quenching and chemical analysis. The curves calculated from the optimized parameters reproduce the experimental data within the experimental error limits, as can be seen from Figure 9.

The FeO-FeO_{1.5}-MgO magnesio-wustite phase was first modeled with a symmetric “Kohler-like”^[11] and with asymmetric “Muggianu-like” extension of the binary terms into the ternary system. Using these interpolation techniques, ten parameters including ternary parameters, were needed to reproduce the experimental data in the FeO-FeO_{1.5}-MgO magnesio-wustite phase. By changing the interpolation technique to the asymmetric “Toop-like”^[11] technique (with FeO_{1.5} as the “asymmetric component”), the experimental data were reproduced better, and furthermore, only seven binary, and no ternary, terms were required. Three of the binary parameters were reported previously in the optimization of the FeO-FeO_{1.5} wustite phase,^[2] and the other four are shown in Table I. In the previous optimization by Fabrichnaya^[1], although ten model parameters were used for the magnesio-wustite phase with a “Muggianu-like” interpolation technique. The results were less satisfactory than in the present study.

E. Phase Diagrams

Different types of phase diagrams for the Fe-Mg-O system, calculated from the optimized model parameters, are shown in Figures 10, 11, and 13 to 16. As discussed above, all these phase diagrams are interrelated.

1. Isothermal sections with oxygen isobars

Calculated isothermal sections of the FeO-Fe₂O₃-MgO phase diagram are shown in Figure 10 over the temperature range from 1160 °C to 1400 °C. Katsura and Kimura^[44]

reported measurements at 1160 °C using a thermogravimetric technique. A sample consisting initially of MgO and Fe₂O₃ was reduced by a gas mixture of known oxygen partial pressure. During the reduction, the weight change of the sample was recorded, and was used to calculate the FeO-Fe₂O₃-MgO composition. Some of the samples were quenched and the equilibrium phases were identified by X-ray diffraction. Similar measurements^[35,36,41,51,58,59,62,63] were performed at various temperatures, but the equilibrium phases were rarely examined. The experimental data of Katsura and Kimura are in excellent agreement with the present calculations. The oxygen isobars in the magnesio-wustite single-phase region correspond to the data points shown in Figure 9. The oxygen isobars in the two-phase region (magnesio-wustite+spinel) are also well reproduced. However, the slopes of two isobars in the (magnesio-wustite+spinel) two-phase region measured by Speidel^[59] at 1300 °C are quite different from the slope obtained by Katsura and Kimura at 1160 °C. Such a large difference over such a small temperature interval is unlikely to be real. As can be seen from Figure 10, however, a small error in oxygen partial pressure (even less than 0.5 on a log scale) can significantly change the composition of the equilibrium phases at oxygen partial pressure as low as 10⁻⁶ or 10⁻⁷ bar.

Therefore, the slope of the tie-lines reported by Speidel^[59] is probably erroneous, and can be explained by a lack of equilibration with the gas phase at low oxygen potential, particularly in the two-phase region.

2. Phase diagrams in air

White and colleagues^[39,64,65] and Reijnen^[36] investigated the phase diagram in air from 800 °C to 1750 °C. The calculated isobars in air are in good agreement with the experimental data as can be seen in Figure 11. In particular, it should be noted that the phase compositions for the invariant equilibria among magnesio-wustite, spinel, slag and air are well reproduced at 1711 °C.

Figure 12 shows the dissociation (reduction) curves for MgO-Fe₂O₃ mixtures in air with increasing temperature. As can be seen in Figure 10, when the MgO content is higher than 50 mol %, initial MgO-Fe₂O₃ mixtures are reduced to (spinel+magnesio-wustite) with increasing temperature. On the other hand, mixtures containing less than 50 mol % MgO are reduced to (spinel+Fe₂O₃). The experimental data at exactly 50 mol % MgO are not well reproduced. This can be explained either by a small excess of MgO in the spinel, which is neglected in the spinel model, or by a small excess of Fe₂O₃ in the experimental mixture (see the calculated curve at 48 mol % MgO). The model parameters optimized in the present study can accurately simulate the reduction process as can be seen in Figure 12.

The phase diagram of the MgO-Fe₂O₃-O₂ system in air is shown in Figure 13. This diagram corresponds to Figure 11. For example, the invariant line (magnesio-wustite+spinel+slag) corresponds to the three-phase triangle in Figure 11. Roberts and Merwin^[66] and

Phillips *et al.*^[67] determined the phase diagram in air using quenching experiments followed by phase identification using optical or X-ray techniques. These data and the points from References [39,65] are compared with the calculated lines in Figure 13. The calculated phase diagram is in good agreement with the experimental data. However, the experimental point by Schurmann and Kolm^[68] is inconsistent with the other data. This will be discussed in more detail below in relation to Figure 17.

3. Phase diagram at iron saturation

Figure 14 shows the phase diagram of the "MgO-FeO" system in saturation with the alloy phase, which is almost pure iron. This diagram gives the phase equilibria under the most reducing conditions. Schenck and Pfaff^[54] measured solidus temperatures by detecting when the liquid phase appeared from initial solid oxide mixtures as the temperature was increased to 2400 °C. Several authors^[69-74] measured the liquidus using a quenching technique but the results are considerably scattered, possibly due to the difficulty in quenching very fluid slags. It is very difficult to distinguish which experimental results are more reliable just from an evaluation of the experimental techniques. The liquidus data of Scheel *et al.*^[73] and Shim and Ban-Ya^[74] are difficult to extrapolate to the melting temperature of pure MgO. Experimental data^[71,75-77] on the quaternary phase diagrams MgO-FeO-Fe₂O₃-SiO₂ and CaO-MgO-FeO-Fe₂O₃ seem to be in better agreement with the data by Fetters and Chipman,^[71] Taylor and Chipman^[70] and Fisher and Ende.^[72] Therefore, these data were used in the optimization. In experimental measurements and, hence, in the calculated lines of Figure 14, all iron is assumed to be divalent. In reality, there is a small amount of Fe³⁺ in both the liquid and solid phases. This amount increases from the MgO side to the FeO side of the diagram, reaching a maximum of 3 mol % and 5 mol % in the slag and magnesiowustite respectively.

4. Oxygen potential versus metal ratio diagrams

Another type of phase diagram, showing oxygen partial pressure versus metal ratio, is presented in Figure 15. Equilibrium oxygen pressures were measured from 800 °C to 1600 °C in various two-phase regions by many authors.^[35-37,41,42,44,46-52,58,59,61-68,78-80] The oxygen partial pressures along phase boundaries were usually determined by gas equilibration or emf techniques, except in the study by Kang *et al.*^[78] who determined phase boundaries from measurements of electrical conductivity and thermoelectric power as a function of oxygen partial pressure. Some of the experimental data points already shown in Figures 7, 10 and 11 are also plotted in Figure 15. All experimental data are reproduced within experimental error limits.

5. Isothermal sections obtained by quenching experiments

Figure 16 shows several isothermal sections of the FeO-Fe₂O₃-MgO phase diagram. Phillips and Muan^[81] determined the equilibrium phases in the temperature range from 1400 °C to 1800 °C by equilibration in a sealed tube

followed by quenching. The composition of a sample was determined from the initial MgO, FeO and Fe₂O₃ contents. Equilibrium phases in the quenched sample were determined using optical microscopy and X-ray diffraction. Because the reaction tube was sealed, the oxygen partial pressure was not known and is defined by the overall composition and temperature. Equilibrium phase assemblages obtained experimentally are in good agreement with the calculated phase boundaries at all temperatures.

Schurmann and Kolm^[68] equilibrated molten MgO-FeO-Fe₂O₃ slags and gas mixtures of known oxygen potential in MgO crucibles at 1600 °C for about 2 hr. Subsequently, samples of the slag were taken by a suction technique using an SiO₂ tube and were analyzed by chemical analysis. The liquid compositions and oxygen partial pressures are plotted in Figure 17. Although experimental points mostly fall on the calculated oxygen partial pressure isobars, the measured compositions of the liquid are richer in MgO than the calculated. This could be the result of incomplete equilibration in the MgO crucibles: the layer of magnesiowustite or spinel that formed on the surface of the crucible may not have reached the equilibrium concentration of iron, which is relatively high, but remained too rich in MgO. Therefore, activities of MgO under experimental conditions would have been higher than the equilibrium values, resulting in an apparent solubility of MgO in the slag which was too high. It should be noted that the liquidus composition in air was reported to fall within the calculated spinel field, in disagreement with the other experimental data as can be seen from Figures 11 and 13.

To reproduce all the phase diagram data discussed above, one small model parameter for the liquid slag was optimized for each binary system, MgO-FeO and MgO-FeO_{1.5} as shown in Table I.

IV. CONCLUSIONS

Complete critical evaluation/optimization of experimental data at 1 bar total pressure for the FeO-Fe₂O₃-MgO system is performed in this study. The optimized model parameters can reproduce all reliable thermodynamic and structural data as well as the phase diagrams of the FeO-Fe₂O₃-MgO system within experimental error limits. No ternary model parameters were required. For the spinel phase, no model parameters for interaction energies between cations on the same sublattice were needed. Using a proper thermodynamic model for each phase minimizes the number of model parameters required in the optimization and improves the extrapolation of binary and ternary parameters into multicomponent systems. The optimized parameters can be readily used with general thermodynamic software and databases, such as FactSage,^[13] to calculate phase equilibria under any given set of conditions and to model various industrial and natural processes.

ACKNOWLEDGEMENTS

This project was supported by a CRD grant from the Natural Sciences and Engineering Research Council of Canada in collaboration with the following: Alcoa, Corning, Dupont, IIS Materials, INCO, Mintek, Noranda, Norsk Hydro, Pechiney, Rio Tinto, Schott Glass, Shell, Sintef, St.-Gobain Recherche and Teck Cominco.

REFERENCES

- O. Fabrichnaya: *Calphad*, 1998, vol. 22, pp. 85-125.
- S. A. Decterov, E. Jak, P. C. Hayes, and A. D. Pelton: *Metall. Mater. Trans. B.*, 2001, vol. 32 B, pp. 643-657.
- M. Hillert, B. Jansson, and B. Sundman: *Z. Metallkd.*, 1988, vol. 79, pp. 81-87.
- M. Hillert and M. Jarl: *Calphad*, 1978, vol. 2, pp. 227-238.
- I.-H. Jung, S. A. Decterov, and A. D. Pelton: *Metall. Mater. Trans.* "Critical Thermodynamic Evaluation and Optimization of the MgO-Al₂O₃, CaO-MgO-Al₂O₃ and MgO-Al₂O₃-SiO₂ Systems", submitted.
- A. D. Pelton and M. Blander: *Proceedings of the Second International Symposium on Metallurgical Slags and Fluxes, TMS-AIME, Warrendale, PA*, 1984, pp. 281-94.
- A. D. Pelton and M. Blander: *Metall. Trans. B*, 1986, vol. 17B, pp. 805-815.
- A. D. Pelton, S. A. Decterov, G. Eriksson, C. Robelin, and Y. Dessureault: *Metall. Mater. Trans. B*, 2000, vol. 31B, pp. 651-659.
- A. D. Pelton and P. Chartrand: *Metall. Mater. Trans. A*, 2001, vol. 32A, pp. 1355-1360.
- P. Wu, G. Eriksson, and A. D. Pelton: *J. Am. Ceram. Soc.*, 1993, vol. 76, pp. 2065-75.
- A. D. Pelton: *Calphad*, 2001, vol. 25, pp. 319-328.
- <http://www.sgte.org/>, Scientific Group Thermodata Europe, 2002.
- www.factsage.com, Montreal, 2002.
- I.-H. Jung, S. A. Decterov, and A. D. Pelton: *Metall. Mater. Trans.*, accepted, 2002.
- A. D. Pelton and H. Schmalzried: *Metall. Trans.*, 1973, vol. 4, pp. 1395-1404.
- A. D. Pelton: *Phase Transformations in Materials*, in: Gernot Kostorz, Wiley-VCH, 2001.
- C. J. Kriessman and S. E. Harrison: *Phys. Rev.*, 1956, vol. 134, pp. 857-860.
- K. Seshan, A. S. Bommanavar, and D. K. Chakrabarty: *J. Solid State Chem.*, 1983, vol. 47, pp. 107-112.
- J. G. Faller and C. E. Birchenall: *J. Appl. Crystallogr.*, 1970, vol. 3, pp. 496-503.
- J. C. Tellier: *Rev. Chim. Miner.*, 1967, vol. 4, pp. 325-365.
- D. J. Epstein and B. Frackiewicz: *J. Appl. Phys.*, 1958, vol. 29, pp. 376-377.
- L. Bochirol and R. Pauthenet: *J. Phys. Radium*, 1951, vol. 12, pp. 249-251.
- R. L. Mozzi and A. E. Paladino: *J. Chem. Phys.*, 1963, vol. 39, pp. 435-439.
- H. St. C. O'Neill, H. Annersten, and D. Virgo: *Am. Mineral.*, 1992, vol. 77, pp. 725-740.
- A. Trestman-Matts, S. E. Dorris, and T. O. Mason: *J. Am. Ceram. Soc.*, 1984, vol. 67, pp. 69-74.
- J. Nell, Bernard J. Wood, and Thomas O. Mason: *Am. Mineral.*, 1989, vol. 74, pp. 339-351.
- E. G. King: *J. Am. Ceram. Soc.*, 1954, vol. 76, pp. 5849-5850.
- K. R. Bonnickson: *J. Am. Chem. Soc.*, 1954, vol. 76, pp. 1480-1482.
- L. A. Reznitskii, K. G. Khomyakov, N. G. Korzhukov, and S. E. Orel: *Zh. Fiz. Khim.*, 1969, vol. 43, pp. 2165-2169.
- J. A. Shearer and O. J. Kleppa: *J. Inorg. Nucl. Chem.*, 1973, vol. 35, pp. 1073-1078.
- A. Navrotsky: *Amer. Mineral.*, 1986, vol. 71, pp. 1160-1169.
- A. Navrotsky and O. J. Kleppa: *J. Inorg. Nucl. Chem.*, 1968, vol. 30, pp. 479-498.
- M. F. Koehler, R. Barany, and K. K. Kelley: Report of Investigation RI 5711, *Heats and Free Energies of Formation of Ferrites and Aluminates of Calcium, Magnesium, Sodium, and Lithium*, U. S. Dept. of the Interior, Bureau of Mines, Washington, 1961.
- J. D. Tretyakov and H. Schmalzried: *Ber. Bunsenges. Phys. Chem.*, 1965, vol. 69, pp. 396-402.
- A. E. Paladino: *J. Am. Ceram. Soc.*, 1960, vol. 43, pp. 183-91.
- P. Reijnen: *Philips Res. Rep.*, 1968, vol. 23, pp. 151-188.
- H. Schmalzried and J. D. Tretyakov: *Ber. Bunsenges. Phys. Chem.*, 1966, vol. 70, pp. 180-188.
- S.-H. Kang and H.-I. Yoo: *J. Solid State Chem.*, 1998, vol. 139, pp. 128-134.
- D. Woodhouse and J. White: *Trans. Br. Ceram. Soc.*, 1955, vol. 54, pp. 333-66.
- W. C. Allen: *J. Am. Ceram. Soc.*, 1966, vol. 49, pp. 257-260.
- M. C. Trinel-Dufour and P. Perrot: *Ann. Chim. (Paris)*, 1977, vol. 2, pp. 309-18.
- I. Srecec, A. Ender, E. Woermann, W. Gans, E. Jacobsson, G. Eriksson, and E. Rosen: *Phys. Chem. Miner.*, 1987, vol. 14, pp. 492-498.
- R. A. Giddings and R. S. Gordon: *J. Am. Ceram. Soc.*, 1973, vol. 56, pp. 111-116.
- T. Katsura and S. Kimura: *Bull. Chem. Soc. Jpn.*, 1965, vol. 38, pp. 1664-70.
- B. Simons: *Carnegie Inst. Wash., Yearb.*, pp. 376-380.
- W. C. Hahn and A. Muan: *Trans. Met. Soc. AIME.*, 1962, vol. 224, pp. 416-420.
- N. M. Wiser and B. J. Wood: *Contrib. Mineral. Petrol.*, 1991, vol. 108, pp. 146-153.
- A. V. Shashkina and Ya. I. Gerasimov: *Zh. Fiz. Khim.*, 1953, vol. 27, pp. 399.
- N. Wallet and F. Marion: *C. R. Hebd. Seances Acad. Sci.*, 1963, vol. 256, pp. 1790-1796.
- P. Saha and G. M. Biggar: *Indian J. Earth Sci.*, 1974, vol. 1, pp. 131-40.
- N. G. Schmahl, B. Frisch, and G. Stock: *Arch. Eisenhuettenwes.*, 1961, vol. 32, pp. 297-302.
- M. Maja and F. Abbattista: *Metall. Ital.*, 1973, vol. 10, pp. 565-570.
- S. Yu. Gurevich: *Research of electron exchange between iron cations in solid solutions of magnesium oxide in wustite*, UPI, 1970.
- H. Schenck and W. Pfaff: *Arch. Eisenhuettenwes.*, 1961, vol. 32, pp. 741-51.
- O. Evrard: University Nancy, France, 1970.
- P. M. Valet, W. Pluschkell, and H. J. Engell: *Arch. Eisenhuettenwes.*, 1975, vol. 46, pp. 383-388.
- A. A. Lykasov and V. A. Kozheurov: *Izv. Vyssh. Ucheb. Zaved., Chern. Met.*, 1970, vol. 13, pp. 5-8.
- J. Brynestad and H. Flood: *Z. Elektrochem.*, 1958, vol. 62, pp. 953-958.
- D. H. Speidel: *J. Am. Ceram. Soc.*, 1967, vol. 50, pp. 243-8.

60. C. B. Alcock and G. N. K. Iyengar: *Proc. Br. Ceram. Soc.*, 1967, vol. 8, pp. 219-29.
61. N. Hilbrandt and M. Martin: *Ber. Bunsen-Ges. Phys. Chem.*, 1998, vol. 102, pp. 1747-1759.
62. V. I. Shishkov, A. A. Lykasov, and A. F. Ilina: *Zh. Fiz. Khim.*, 1980, vol. 54, pp. 440-441.
63. N. N. Oleinikov, Y. G. Saksonov, and Y. D. Tret'yakov: *Izv. Akad. Nauk. SSSR, Neorg. Mater.*, 1965, vol. 1, pp. 246-53.
64. R. G. Richards and J. White: *Trans. J. Br. Ceram. Soc.*, 1954, vol. 53, pp. 422-459.
65. J. C. Willshee and J. White: *Trans. Br. Ceram. Soc.*, 1967, vol. 66, pp. 541-55.
66. H. S. Roberts and H. E. Merwin: *Am. J. Sci.*, 1931, vol. 21, pp. 145-157.
67. B. Phillips, S. Somiya, and A. Muan: *J. Am. Ceram. Soc.*, 1961, vol. 44, pp. 167-169.
68. E. Schurmann and I. Kolm: *Steel Res.*, 1988, vol. 59, pp. 185-191.
69. N. A. Gokcen: *J. Metals*, 1956, pp. 1558-1567.
70. C. R. Taylor and J. Chipman: *Trans. AIME*, 1943, vol. 154, pp. 228-247.
71. K. L. Fettes and J. Chipman: *Trans. AIME*, 1941, vol. 145, pp. 95-112.
72. W. A. Fischer and H. Vom Ende: *Arch. Eisenhüttenwes.*, 1952, vol. 23, pp. 21-33.
73. R. Scheel: *Sprechsaal Keram., Glas. Bautoffe*, 1975, vol. 108, pp. 685-6.
74. J. D. Shim and S. Ban-Ya: *Tetsu To Hagane*, 1981, vol. 67, pp. 1735-44.
75. G. Tromel, K. H. Obst, E. Gori, and J. Stradtman: *Tonind.-Ztg., Keram. Rundsch.*, 1966, vol. 90, pp. 193-209.
76. W. A. Fischer and H. Spitzer: *Arch. Eisenhüttenwes.*, 1958, vol. 29, pp. 611-617.
77. I.-H. Jung, S. A. Decterov, and A. D. Pelton: *Metall. Mater. Trans.* "Thermodynamic Modeling of the FeO-Fe₂O₃-MgO-SiO₂ System", submitted.
78. S.-H. Kang, S.-H. Chang, and H.-I. Yoo: *J. Solid State Chem.*, 2000, vol. 149, pp. 33-40.
79. Y. D. Tret'yakov: *Thermodynamics of Ferrites, Khimiya, Leningrad*, 1967, vol. 59, pp. 1299.
80. M. Wallace, S. Sun, and S. Jahanshahi: *6th AusIMM Extractive Metallurgy Conference*, Brisbane, 1994, pp. 37-40.
81. B. Phillips and A. Muan: *J. Am. Ceram. Soc.*, 1962, vol. 45, pp. 588-591.

Table I. Optimized model parameters of solutions in the FeO-Fe₂O₃-MgO system (J/mol).

<p>(*)Spinel: (Fe²⁺, Fe³⁺, Mg) [Fe²⁺, Fe³⁺, Mg, Va]₂O₄</p> $G_{MH} = 7 (-207977 + 566.737 T + 0.0106868 T^2 - 4112.06 T^{0.5} - 8.04145E-7 T^3 + 3790.43 \ln(T) - 72.6736 T \ln(T))$ $I_{MH} = G_{HH} + G_{HM} - 2G_{MH} = -112130 + 56.580 T$ $\Delta_{MF:MH} = G_{MM} + G_{FH} - G_{MH} - G_{FM} = -41840$ $\Delta_{FM:FH} = G_{FF} + G_{MH} - G_{FH} - G_{MF} = 0$ <p>Magnetic properties:</p> $\beta_{MH} = \beta_{MH}^i = 2.186 \text{ (magnetic moment)}^{(**)}$ $T_{MH} = T_{MH}^i = 689.5 \text{ K (Curie temperature)}^{(**)}$ $P = 0.28 \text{ (P factor)}$
<p>(**)Magnesiowustite: MgO-FeO-FeO_{1.5}</p> $q_{FeO, MgO}^{00} = 8368$ $q_{FeO_{1.5}, MgO}^{10} = -27196 - 20.92 T$ $q_{FeO_{1.5}, MgO}^{02} = 4184$
<p>(***)Liquid Oxide: MgO-FeO-FeO_{1.5}</p> $\Delta g_{FeO, MgO}^o = 6276$ $\Delta g_{MgO, FeO_{1.5}}^o = -20920$

(*) Notations M, F and H are used for Mg, Fe²⁺ and Fe³⁺, respectively.

(**) β_{MH} and β_{MH}^i are the magnetic moments of the hypothetical completely normal and completely inverse spinel MgFe₂O₄, respectively. T_{MH} and T_{MH}^i are the Curie temperatures of the hypothetical completely normal and completely inverse spinel MgFe₂O₄, respectively (see Reference [2]).

(**) The polynomial “q” parameters are defined in Reference [11].

(***) The quasichemical parameters are defined in References [8] to [9].

The other model parameters for spinel, magnesiowustite and slag can be found in the previous study.^[2]

Gibbs energies of the pure components of the magnesiowustite and liquid oxide solutions, and the Gibbs energies of Fe₂O₃ (hematite) and O₂ gas are taken from the F*A*C*T database.^[13]

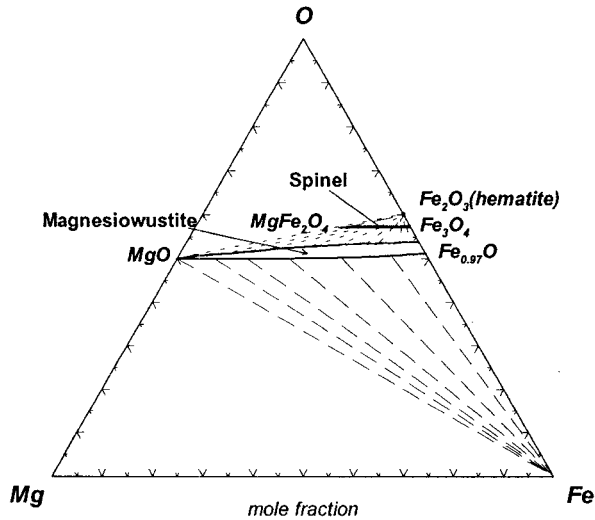


Fig. 1 – Calculated isothermal section of the Fe-Mg-O phase diagram at 1200 °C and $P_{\text{Total}} = 1$ bar.

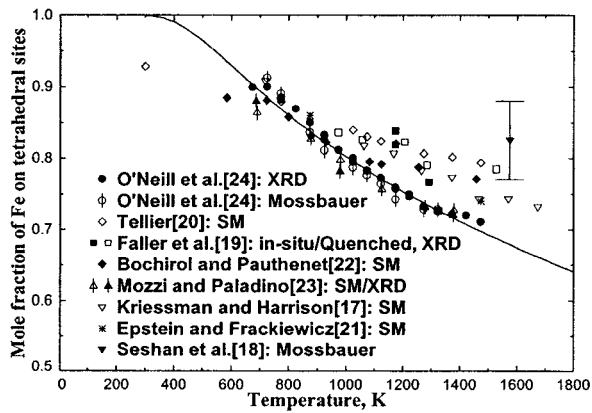


Fig. 2 – Calculated cation distribution in the MgFe_2O_4 spinel. Experimental points were obtained from Mossbauer, X-ray diffraction (XRD) and saturation magnetization (SM) measurements.

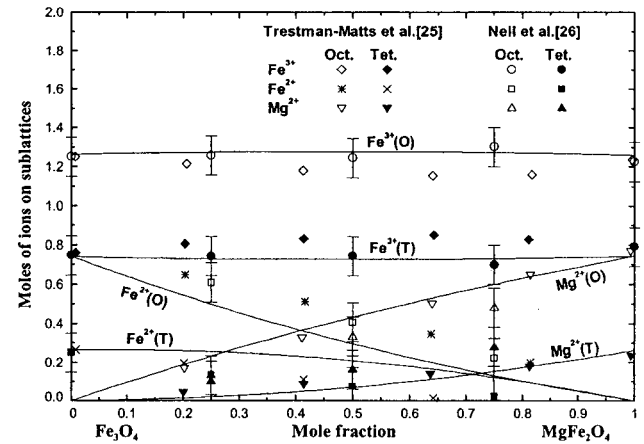


Fig. 3 – Calculated cation distribution in the Fe_3O_4 - MgFe_2O_4 spinel solid solution at 1000 °C. Moles of ions on octahedral and tetrahedral sublattices per mole of spinel solution.

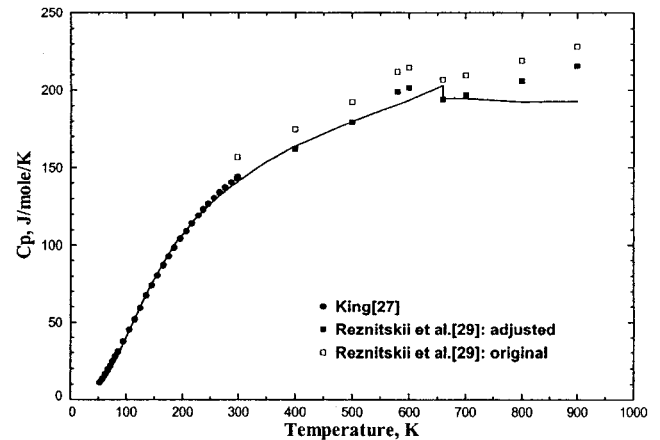


Fig. 4 – Optimized heat capacity of MgFe_2O_4 spinel.

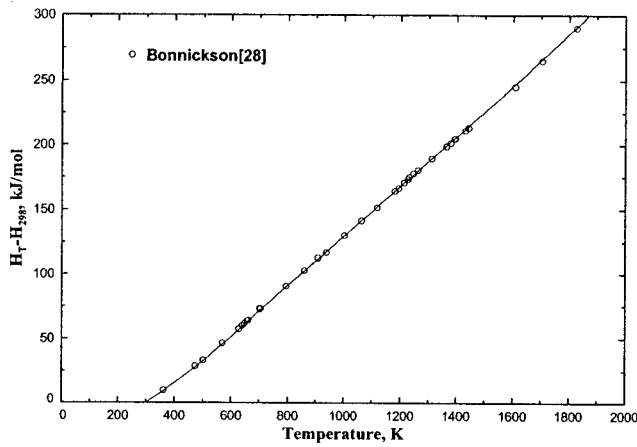


Fig. 5 – Optimized heat content of MgFe_2O_4 spinel. In the calculation, the heat of cation redistribution is taken into account (see text).

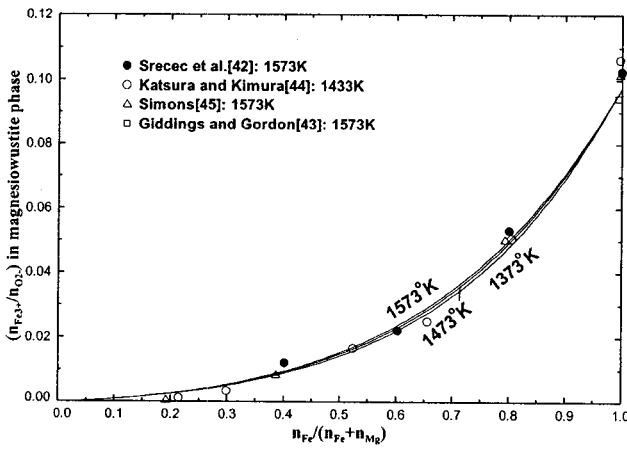


Fig. 6 - Calculated molar ratio $n_{\text{Fe}^{3+}}/n_{\text{O}^{2-}}$ in the magnesiowustite phase in equilibrium with metallic iron.

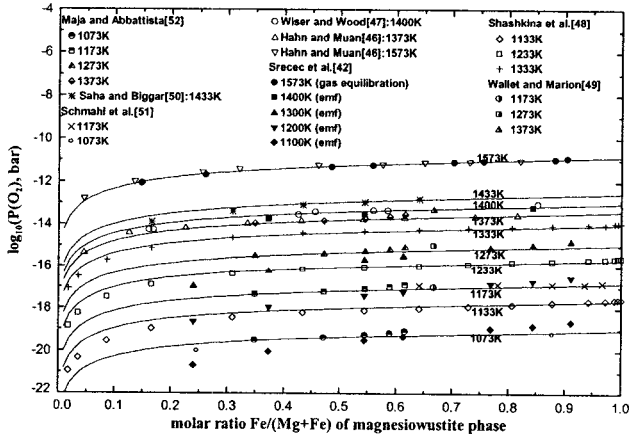


Fig. 7 – Calculated oxygen partial pressures for the equilibrium between magnesiowustite and metallic iron.

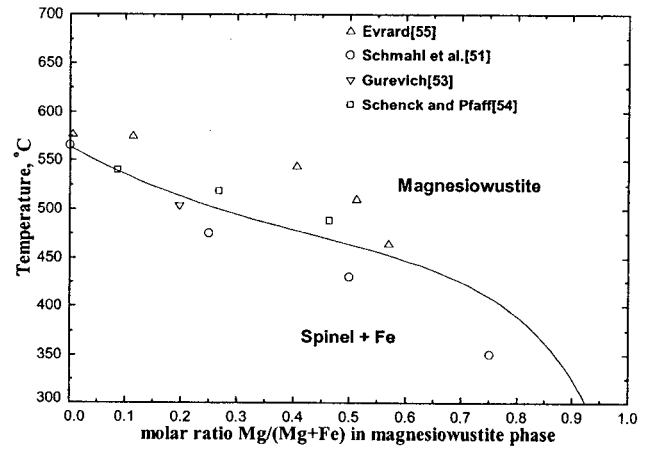
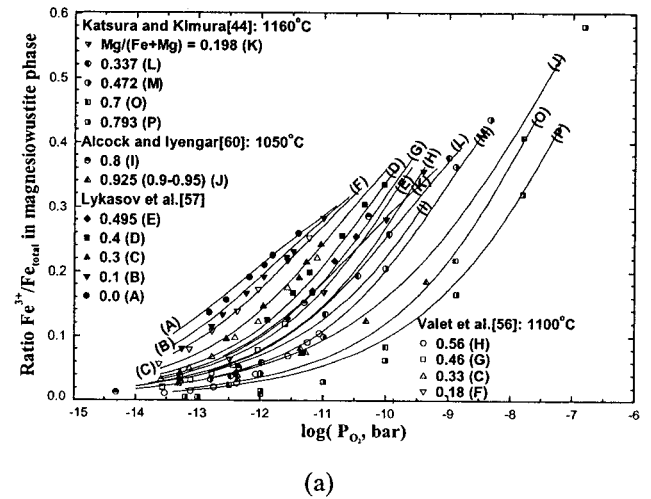
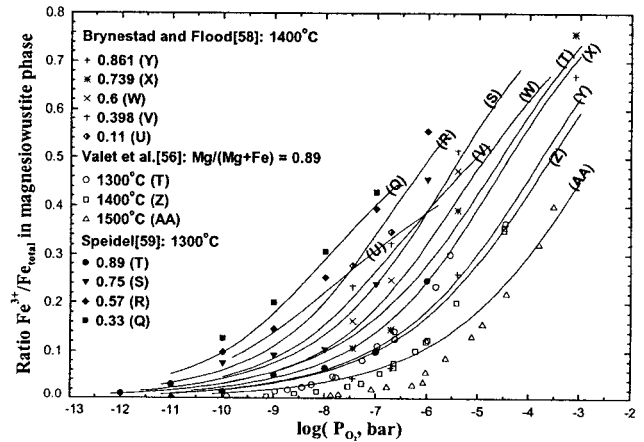


Fig. 8 – Calculated temperature of dissociation of magnesiowustite phase into spinel and Fe.



(a)



(b)

Fig. 9 – Calculated nonstoichiometry of magnesiowustite as a function of oxygen partial pressure at various temperatures and $\text{Mg}/(\text{Mg}+\text{Fe})$ ratios.

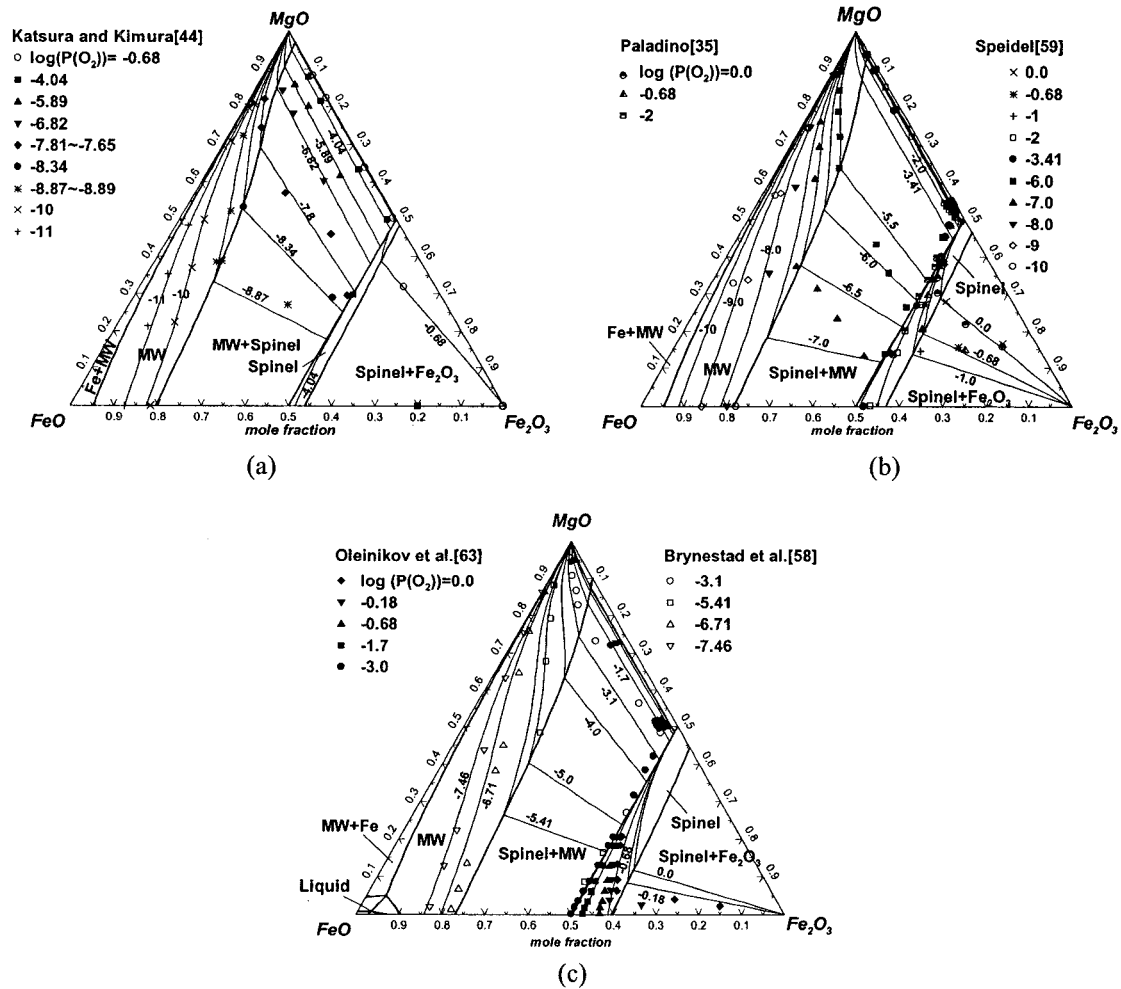


Fig. 10 – Calculated FeO-Fe₂O₃-MgO phase diagram at 1 bar total pressure with log P_{O₂}(bar) isobars: (a) 1160 °C, (b) 1300 °C, (c) 1400 °C. Thick lines are calculated phase boundaries and thin lines are calculated oxygen isobars (MW=magnesiowustite).

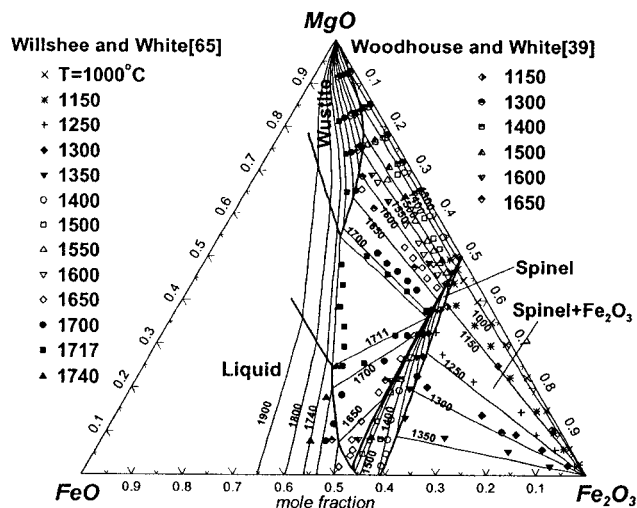


Fig. 11 – Calculated MgO-FeO-Fe₂O₃ phase diagram in air.

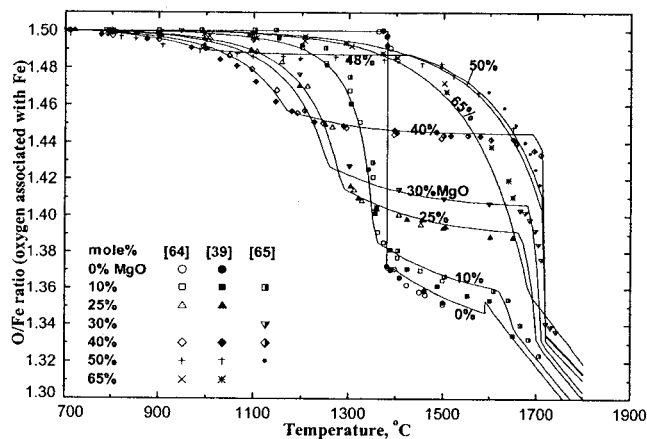


Fig. 12 – Calculated dissociation (reduction) curves of MgO-Fe₂O₃ initial mixtures in air with increasing temperature. The vertical axis gives the oxygen associated with Fe (excluding oxygen associated with Mg) which can vary from 1.5 in Fe₂O₃ to 1.0 in FeO during the reduction process.

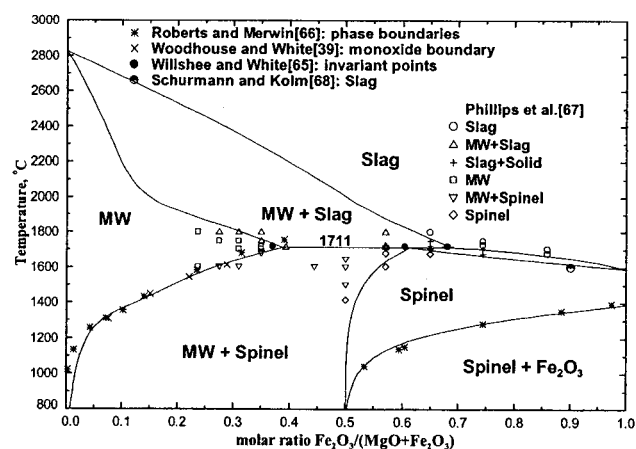


Fig. 13 – Calculated phase diagram of the MgO-Fe₂O₃-O₂ system in air (MW=magnesiowustite).

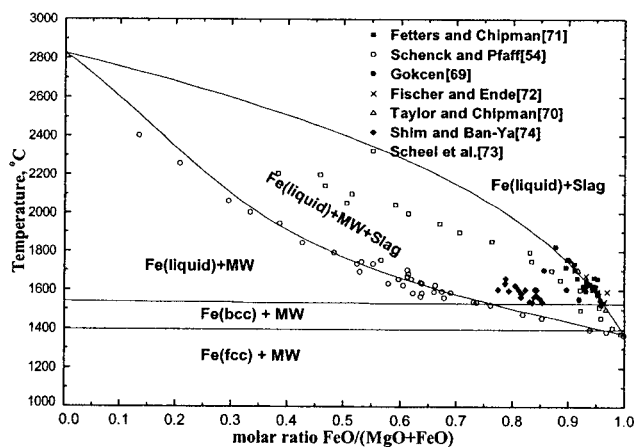


Fig. 14 – Calculated phase diagram of the "MgO-FeO" system in equilibrium with metallic Fe. All Fe³⁺ has been recalculated as Fe²⁺ (MW=magnesiowustite).

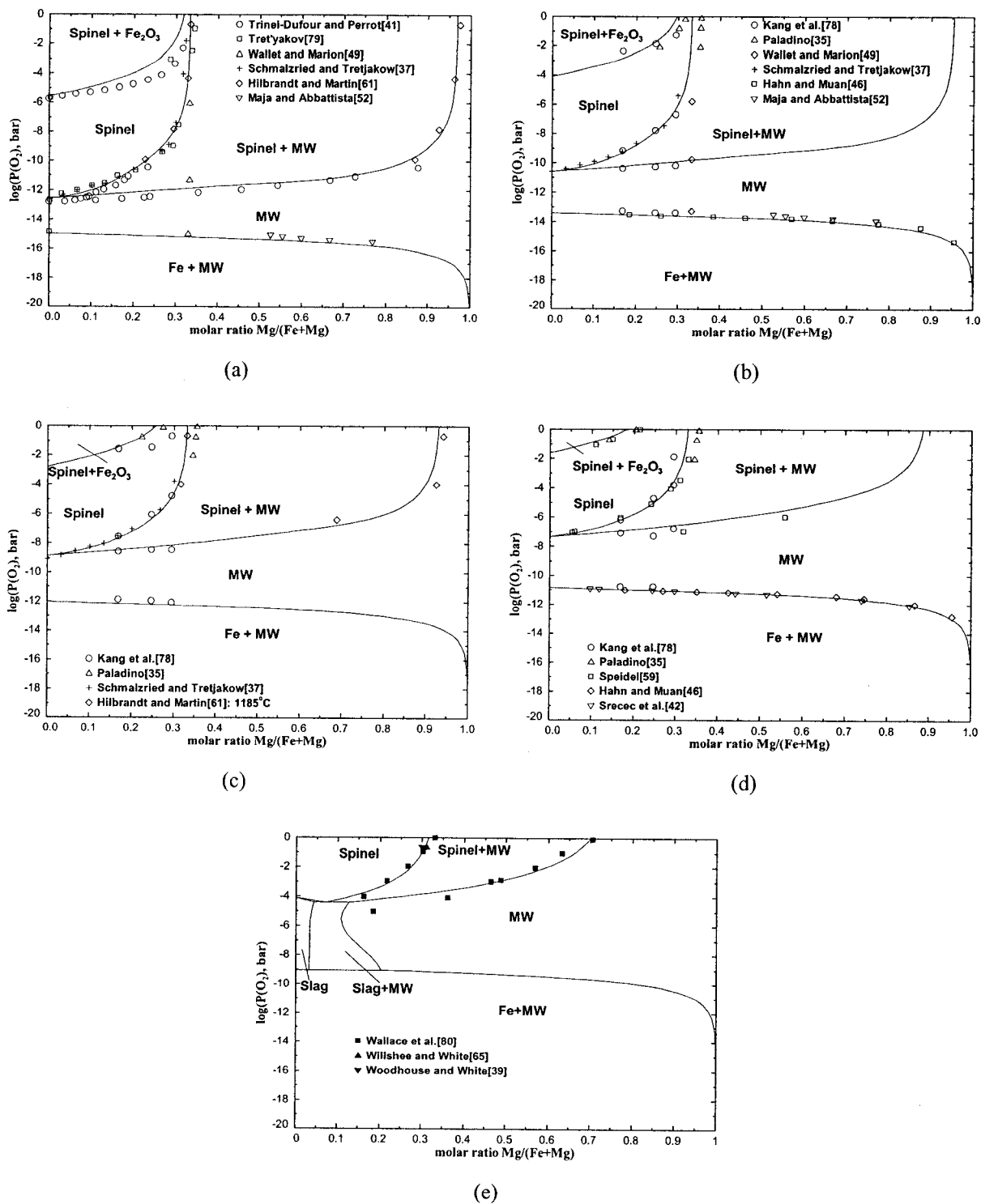


Fig. 15 – Calculated phase diagrams of the Fe-Mg-O system at various temperatures: (a) 1000 °C, (b) 1100 °C, (c) 1200 °C, (d) 1300 °C and (e) 1500 °C (MW=magnesiowustite).

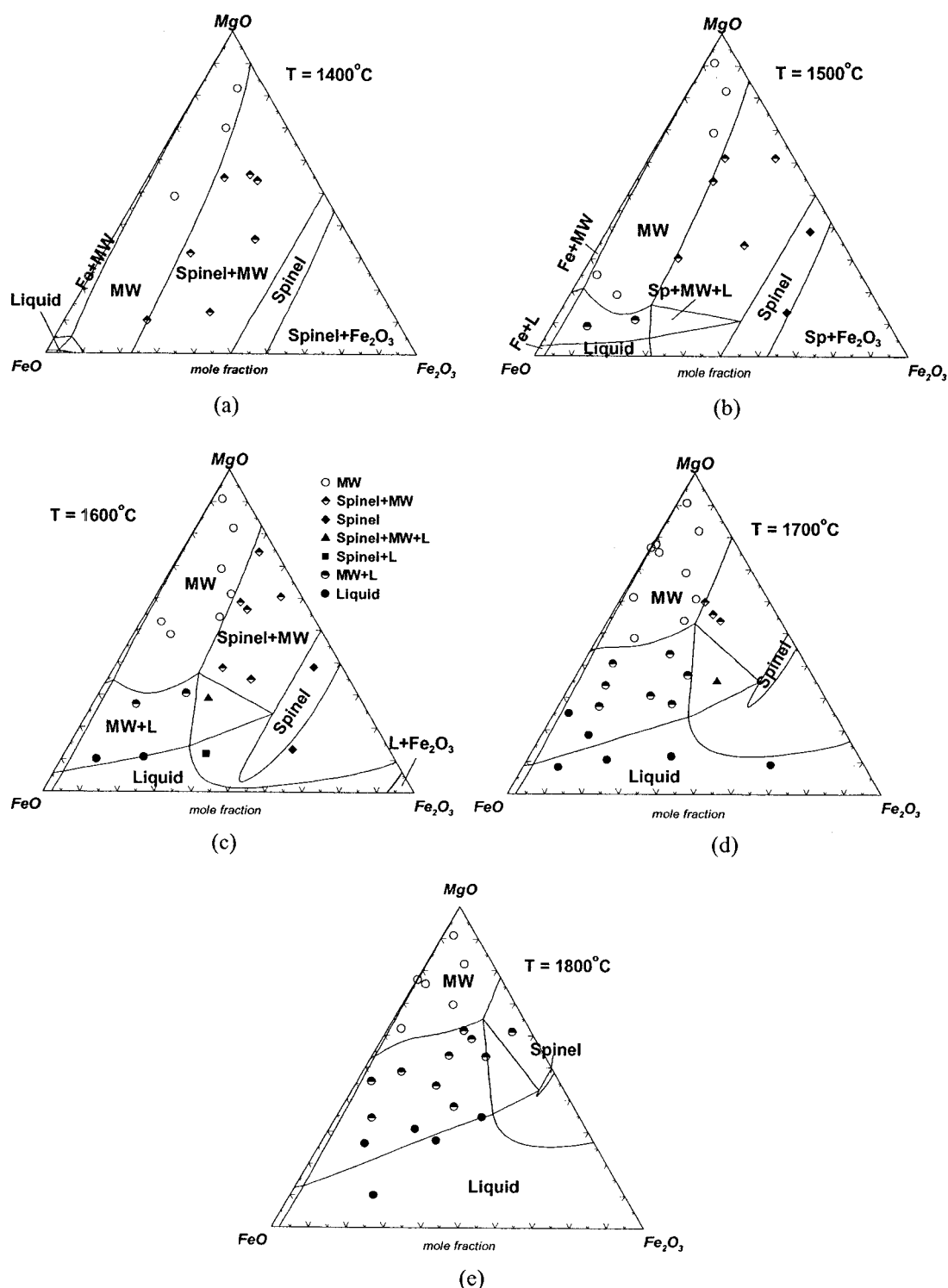


Fig. 16 – Calculated isothermal sections of the MgO-FeO-Fe₂O₃ system at (a) 1400°C, (b) 1500°C, (c) 1600°C, (d) 1700°C and (e) 1800°C. Experimental data from Phillips and Muan^[81] (MW=magnesiowustite, total pressure=1 bar).

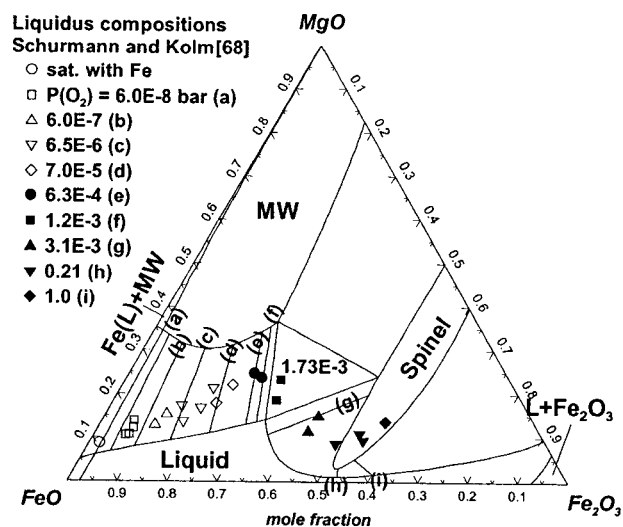


Fig. 17 - Calculated phase diagram section of the MgO-FeO-Fe₂O₃ system at 1600 °C and 1 bar total pressure. See text for detailed discussion of experimental data from Schurmann and Kolm^[68] on liquidus compositions at different oxygen partial pressures (MW=magnesiowustite).

Appendix III

Article :

Thermodynamic Modeling of the FeO-Fe₂O₃-MgO-SiO₂ System

In-Ho Jung, Sergei A. Decterov and Arthur D. Pelton

Submitted to *Metallurgical and Materials Transactions*, 2003

Thermodynamic Modeling of the FeO-Fe₂O₃-MgO-SiO₂ System

IN-HO JUNG, SERGEI A. DECTEROV, and ARTHUR D. PELTON

A complete critical evaluation and thermodynamic modeling of the phase diagrams and thermodynamic properties of oxide phases in the FeO-Fe₂O₃-MgO-SiO₂ system at 1 bar total pressure are presented. Optimized equations for the thermodynamic properties of all phases are obtained which reproduce all available thermodynamic and phase equilibrium data within experimental error limits from 25 °C to above the liquidus temperatures at all compositions and oxygen partial pressures. The database of the model parameters can be used along with software for Gibbs energy minimization in order to calculate any type of phase diagram section.

I. INTRODUCTION

THE FeO-Fe₂O₃-MgO-SiO₂ system is important for many industries and processes. This system is a key system in the corrosion of magnesite refractories by iron oxide in steelmaking processes and is also a fundamental system in pyrometallurgical processes. Magnesium ferrite spinel has interesting magnetic properties, and solid solution phases such as magnesiowustite, olivine and pyroxenes are of primary importance in understanding the Earth's mantle. Experimental study of this system is complicated by the strong dependence of phase equilibria on oxygen partial pressure. Therefore, critical assessment of experimental data and thermodynamic optimization is required in order to understand and model this system more accurately. Fabrichnaya^[1] roughly modeled the solidus and liquidus data in this system. Wu *et al.*^[2] optimized the FeO-MgO-SiO₂ system at metallic iron saturation. However, complete optimization of this quaternary system has not yet been performed.

Optimizations of the binary and ternary subsystems Fe-O, MgO-SiO₂, FeO-Fe₂O₃-MgO and FeO-Fe₂O₃-SiO₂ were reported earlier.^[2-4] The calculated phase diagrams of the MgO-SiO₂ and FeO-Fe₂O₃-SiO₂ systems at iron saturation and in air are given in Figures 1 to 3.

The main goal of the present study is to perform a critical assessment and optimization of thermodynamic properties at 1 bar total pressure of oxide phases in the FeO-Fe₂O₃-MgO-SiO₂ (Fe-Mg-Si-O) system. In the thermodynamic "optimization" of a chemical system, all available thermodynamic and phase equilibrium data are evaluated simultaneously in order to obtain one set of model equations for the Gibbs energies of all phases as functions of temperature and composition. From these equations, all of the

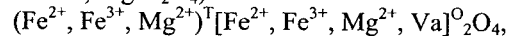
thermodynamic properties and the phase diagrams can be back-calculated. In this way, all the data are rendered self-consistent and consistent with thermodynamic principles. Thermodynamic property data, such as activity data, can aid in the evaluation of the phase diagram, and phase diagram measurements can be used to deduce thermodynamic properties. Discrepancies in the available data can often be resolved, and interpolations and extrapolations can be made in a thermodynamically correct manner.

The evaluation/optimization of the FeO-Fe₂O₃-MgO-SiO₂ system reported in this study is part of a wider research program aimed at complete characterization of phase equilibria and thermodynamic properties of the entire six-component system CaO-MgO-Al₂O₃-FeO-Fe₂O₃-SiO₂, which has numerous applications in the ceramic, cement and glass industries, metallurgy, geochemistry, *etc.* The present optimization covers the range of oxygen partial pressures from equilibrium with pure oxygen to metal saturation, and temperatures from 25 °C to above the liquidus.

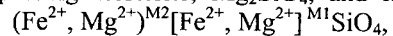
II. PHASES AND THERMODYNAMIC MODELS

The following solution phases are found in the FeO-Fe₂O₃-MgO-SiO₂ system (see Figure 4):

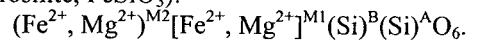
Slag (molten oxide phase): FeO-FeO_{1.5}-MgO-SiO₂,
Monoxide (magnesiowustite): FeO-FeO_{1.5}-MgO,
Spinel (encompassing magnetite, Fe₃O₄, and magnesioferrite, MgFe₂O₄):



Olivine (encompassing forsterite, Mg₂SiO₄, and fayalite, Fe₂SiO₄):



Pyroxenes (proto-, ortho-, clino-) (encompassing enstatite, MgSiO₃, and ferrosilite, FeSiO₃):



Cations shown within a set of brackets for spinel, olivine and pyroxene occupy the same sublattice.

The Modified Quasichemical Model,^[5-8] which takes into account short-range ordering of second-nearest-neighbor cations in the ionic melt, is used for modeling the slag. The binary and ternary sub-systems MgO-SiO₂, FeO-FeO_{1.5}, FeO-FeO_{1.5}-SiO₂ and MgO-FeO-FeO_{1.5}^[4] have already been critically evaluated and optimized, and these optimized model parameters are used as the basis of the present study. All second-nearest-neighbor “coordination numbers” used in the model for the slag are the same as in previous studies.^[2-4,9] The properties of the quaternary slag solution were calculated from the binary and ternary parameters using an asymmetric “Toop-like”^[10] approximation with SiO₂ as the “asymmetric component”. Two additional optimized ternary parameters for the FeO-MgO-SiO₂ and FeO_{1.5}-MgO-SiO₂ solutions were added in the present study. These are listed in Table I.

The olivine, pyroxene and spinel solution models were developed within the framework of the Compound Energy Formalism (CEF).^[11,12] The Gibbs energy expression in the CEF per formula unit is:

$$G = \sum_i \sum_j Y_i' Y_j'' G_{ij} - TS_c + G^E \quad [1]$$

where Y_i' and Y_j'' represent the site fractions of cations i and j on the first and second sublattices, G_{ij} is the Gibbs energy of an “end-member” ij of the solution, in which the first sublattice is occupied only by cations i and the second sublattice is occupied only by cations j , G^E is the excess Gibbs energy and S_c is the configurational entropy assuming random mixing on each sublattice:

$$S_c = -R \left(n_1 \sum_i Y_i' \ln Y_i' + n_2 \sum_j Y_j'' \ln Y_j'' \right) \quad [2]$$

where n_1 and n_2 are the numbers of sites on the first and second sublattice per formula unit of a solution.

The models for the olivine and pyroxene solutions in the FeO-Fe₂O₃-MgO-SiO₂ system are straightforward since all cations on the distinct octahedral M2 and M1 sites have the same charge and therefore all end-members are neutral.

For each of the olivine and pyroxene solutions, there are four parameters G_{FM} , G_{MF} , G_{MM} and G_{FF} (where M and F denote Mg²⁺ and Fe²⁺ respectively). In the case of the pyroxene solutions the parameter G_{MM} equals $2 G_{MgSiO_3}^0$ where $G_{MgSiO_3}^0$ is the Gibbs energy of stoichiometric MgSiO₃. For the olivine solution, $G_{MM} = G_{Mg_2SiO_4}^0$ which is the Gibbs energy of stoichiometric Mg₂SiO₄, and $G_{FF} = G_{Fe_2SiO_4}^0$ which is the Gibbs energy of stoichiometric Fe₂SiO₄. These parameters were optimized previously.^[2] For the pyroxene solutions, $G_{FF} = 2 G_{FeSiO_3}^0$, the Gibbs energy of ferrosilite. For ortho-ferrosilite, $G_{FF} = 2 G_{FeSiO_3}^0$ as given in Table I was taken from Berman^[13]

with an adjustment of -996 J/mol to $H_{298.15}^0$ as introduced by Saxena *et al.*^[14] to reproduce high pressure phase equilibria. The values of G_{FF} of clino- and ortho-pyroxene were optimized in the present study in order to best reproduce the experimental phase equilibrium data. The parameters G_{MF} and G_{FM} were also optimized in the present study and are listed in Table I. The linear combination I_{MF} has the physical significance of being equal to the energy change of the reaction when Fe²⁺ and Mg²⁺, occupying M2 and M1 sites respectively, change places. The linear combination $\Delta_{MF:MF}$ similarly has physical significance as the energy charge of the reciprocal exchange reaction among end-members.

The spinel solution was modeled previously^[3,4] using the CEF. The magnesiowustite solution was also modeled previously.^[3,4] Since SiO₂ is insoluble in both these phases, no further optimization of the models for these solutions was required.

The thermodynamic properties of solid solutions based on bcc and fcc iron from the SGTE (Scientific Group Thermodata Europe)^[15] database were used for the calculations of phase equilibria in the FeO-Fe₂O₃-MgO-SiO₂ system at metal saturation. For liquid iron, the F*A*C*T database^[9] was used. This database implements a recently developed model^[16] to accurately describe the solubility of oxygen and many other elements in molten iron. For liquid iron containing dissolved Mg and O, this model assumes the presence of dissolved Mg*O associates.

Hematite, Fe₂O₃, and silica, SiO₂, are treated as stoichiometric compounds since their nonstoichiometry is believed to be negligibly small.

III. EVALUATION/OPTIMIZATION OF EXPERIMENTAL DATA

Calculated liquidus projections of the FeO-Fe₂O₃-MgO-SiO₂ system at two opposite extremes of oxygen potential (metallic iron saturation and in air) are shown in Figures 5 and 6. As can be seen from the figures, the olivine solution extends from forsterite, Mg₂SiO₄, to fayalite, Fe₂SiO₄. Pyroxenes, on the other hand, do not extend all the way to the FeO-SiO₂ binary system because ferrosilite, FeSiO₃, is not stable in the Fe-Si-O system at a total pressure of 1 bar, although orthopyroxene FeSiO₃ is stable at high pressure. The magnesiowustite solution extends from wustite in the Fe-O system to pure MgO. A spinel solution, MgFe₂O₄-Fe₃O₄, appears under oxidizing condition.

In the first step of the optimization, the model parameters of the olivine and pyroxene solutions were optimized to reproduce the thermodynamic and structural data in the single- phase fields and the sub-solidus phase equilibria magnesiowustite/olivine and olivine/pyroxene. Subsequently, all other phase equilibria, including those involving liquid slag, were predicted and compared with experimental data. Although the predicted results were already good, two small ternary parameters for the liquid slag were added to give the best reproduction of the data. At this stage, the optimized model parameters for the olivine and pyroxene solutions were

also slightly modified. The final optimized model parameters are listed in Table I. The details of the optimization are given below.

A. Structural Data

Olivine and pyroxenes have two distinct octahedral sites called M2 and M1, which are occupied by the Fe^{2+} and Mg^{2+} cations. M2 sites are bigger than M1 sites. The calculated distribution of cations between the M2 and M1 sites in olivine and orthopyroxene are shown in Figures 7 and 8 along with experimental data. The cation distribution in olivine was measured by several authors.^[17-22] The most recent *in situ* neutron diffraction measurements performed by Redfern *et al.*^[20] on a synthesized MgFeSiO_4 sample seem to be the most reliable. These authors found that the cation distribution does not reach an equilibrium state below about 800 K; therefore only the high-temperature data were used to optimize the parameter I_{MF} of the olivine model. As can be seen in Figure 7, the optimized cation distribution curve is in good agreement with the results of Redfern *et al.*^[20] above 800 K.

Since the cation distribution in orthopyroxene is used as a geo-barometer, it has been well studied^[23-31] using different techniques such as Mössbauer spectroscopy and X-ray diffraction. As can be seen from Figure 8a, the data are widely scattered. The scatter is caused in part by the kinetics of cation ordering in the pyroxenes which is extremely slow at low temperatures as pointed out by Anovitz *et al.*^[26] The recent measurements by Yang and Ghose^[23] are believed to be the most reliable. The authors used an *in situ* single-crystal X-ray diffraction method and synthetic orthopyroxene samples. These data were used to optimize the parameter I_{MF} of the orthopyroxene model. The same value was used for the parameters I_{MF} for the other pyroxene solutions since no reliable cation distribution data are available for clino- and proto-pyroxene. The cation distributions calculated at different temperatures from 500° to 1027 °C are compared with experimental data in Figure 8. As can be seen from Figure 8b, the data by Yang and Ghose^[23] are well reproduced.

B. Subsolidus Phase Equilibria

1. Tie-lines between solid solutions

Figures 9 to 11 show the calculated tie-lines between solid solutions at sub-solidus temperatures. Williams^[32] and Nafziger and Muan^[33] equilibrated solid solutions at metallic iron saturation and determined the compositions of the solutions from X-ray measurements of lattice parameters. Similar techniques were used in other studies.^[34-36] Wiser and Wood^[37] and Jacobsson^[38] obtained the compositions of equilibrated phases using the EPMA (WDS) technique. It is not clear what experimental technique was used by Goresy and Woermann.^[39] Phase equilibria between spinel and olivine solid solutions were measured by Jamieson and Roeder.^[40] They equilibrated the mixtures of olivine and spinel under different oxygen partial pressures. At low oxygen potential, the three-phase

equilibrium (spinel+olivine+pyroxene) was achieved, while the two-phase equilibrium (spinel+olivine) was obtained at high oxygen pressure. After equilibration, the composition of each phase was determined by EPMA (EDS) under the assumption that there were no vacancies (i. e. no oxygen nonstoichiometry) in the spinel. Actually, there should be not one, but several calculated lines in Figure 11 corresponding to different oxygen pressures. However, these lines are almost coincident. As can be seen from Figures 9 to 11, all sub-solidus experimental data are in good agreement with the calculated lines.

2. Equilibrium oxygen partial pressures in three-phase regions

The equilibrium oxygen partial pressures for sub-solidus phase equilibria are calculated in Figures 12 to 14. Several authors^[32-34,37,41,42] determined the oxygen partial pressure by emf measurements or by gas equilibration experiments. As can be seen from Figure 12, the oxygen partial pressure over the (olivine+magnesiowustite+Fe) phase assemblage is well reproduced. However, experimental data in Figures 13 and 14 appear to be systematically higher than the calculated lines, especially at low temperatures. It should be noted that the experimental data in Figure 13 are in disagreement with more recent data^[43,44] on the oxygen partial pressure over the (olivine+tridymite+Fe) field in the Fe-Si-O system (at a mole fraction of Fe_2SiO_4 equal to 1.0 in Figure 13). Therefore, between the two sets of data, the results of Jacob^[43] and Darken^[44] were selected and it was concluded that the experimental data in Figure 13 probably contain a systematic error. This also explains a systematic deviation between the results from the same studies^[32-34] and the calculated lines in Figure 14. Note also the large scatter of the experimental points by Williams.^[32] Furthermore, these experimental studies^[32-34,41,42] do not report the crystal structure of the pyroxene solutions. The presence of metastable pyroxene modifications is another possible source of error. In Figure 14, the oxygen partial pressure of the metastable equilibrium with proto-pyroxene instead of ortho-pyroxene is plotted to demonstrate this effect.

3. Enthalpies of mixing

The calculated enthalpies of mixing of the olivine and orthopyroxene solid solutions are shown in Figures 15 and 16 along with the experimental data.^[45-47] Thierry *et al.*^[46] and Wood and Kleppa^[47] measured the enthalpy of olivine using solution calorimetry at 1180 K and 970 K, respectively. Although the measured and calculated values are not in good accord, the agreement is essentially within the experimental error limits. Such large scatter is typical of such measurements in oxide systems. The calculated curves in Figures 15 and 16 are consistent with the measured phase equilibria and cation distribution data.

One adjustable parameter, $\Delta_{\text{MF:MF}}$, was optimized for the olivine solution, mainly to reproduce the phase equilibria. For the pyroxene solutions, $\Delta_{\text{MF:MF}}$ was set to zero and slight adjustments were made to G_{FF} to reproduce the phase equilibria data.

C. Liquidus and Solidus Data

For the liquid slag, two small ternary parameters listed in Table I were optimized to reproduce the phase diagram data discussed below. It should be noted that even without these two parameters, most of the phase equilibrium data are very well predicted by the Quasichemical Model.^[5-8]

1. Phase diagrams at different oxygen potentials

Calculated phase diagram sections of the Fe_2O_3 -MgO- SiO_2 -O₂ system in air are shown in Figure 17 at different SiO_2 contents. Figure 18 shows calculated liquidus projections from the oxygen corner of the Fe_3O_4 -MgO- SiO_2 -O₂ tetrahedron onto the Fe_3O_4 -MgO- SiO_2 basal plane for different oxygen partial pressures. The calculated phase diagrams are compared with experimental data.^[48-50] Correia and White^[48] determined the phase relationships of this system in air at temperatures between 1300° and 1700 °C using a quenching technique followed by X-ray diffraction for phase identification and EPMA (EDS) for phase composition determination. Muan and Osborn^[49] determined the phase equilibria under various oxygen partial pressures, including air, using a quenching technique and optical and X-ray phase identification. Ambruz *et al.*^[50] determined the phase relationships in the Mg_2SiO_4 - MgFe_2O_4 section at temperatures from 1550° to 1770 °C in air.

Strictly speaking, the results of the studies [49] and [50] do not lie exactly on the sections shown in Figure 17, which were studied by Correia and White.^[48] However, when the data from References [49,50] are close to these sections, they are also shown in Figure 17 for comparison. As can be seen from Figures 17 and 18, the experimental data are often contradictory. For example, Muan and Osborn^[49] reported the eutectic reaction (liquid \rightarrow olivine + spinel + monoxide) at about 1700 °C in air. This was later reported by Correia and White^[48] and Ambruz *et al.*^[50] to be a peritectic reaction (monoxide + liquid \rightarrow olivine + spinel) at about 1655 °C. Actually, Muan and Osborn discussed the difficulty of quenching in their experiments, which may explain the contradictory conclusions. As can be seen in Figures 17 and 18, the peritectic reaction is well reproduced in this study. Furthermore, it should be noted that the phase boundaries obtained by Muan and Osborn^[49] (and also by Speidel and Osborn^[51]) are systematically lower in SiO_2 by about 5 to 10 weight % as compared to the more recent results by Correia and White.^[48] The calculated phase diagrams in Figures 17 and 18 are more consistent with the latter data. On the other hand, Correia and White^[48] reported that their data obtained by EPMA (EDS) are not always consistent with those obtained by ceramography and XRD. For example, the calculated phase boundaries at low temperature in the iron-rich part of Figure 17 and the (Oliv+Sp)/(Oliv+Sp+L) phase boundary are closer to the EPMA (EDS) data (not shown in Figure 17).

Speidel and Osborn^[51] used microscopy and XRD to identify crystalline phases, as well as EPMA (EDS) to

establish phase compositions in equilibrium phase assemblages among spinel, olivine, pyroxene, liquid and tridymite which were equilibrated at appropriate temperatures and oxygen partial pressures and quenched. The calculated and experimental invariant points are compared in Tables II and III.

Schurmann and Kolm^[52] studied the effect of SiO_2 content on the liquidus in the FeO - Fe_2O_3 -MgO- SiO_2 system at 1600 °C. The iron-rich slag was equilibrated in magnesia crucibles under various oxygen partial pressures and the slag compositions were measured by wet chemical analysis. The reported results are compared with calculated curves in Figure 19, where the liquidus is projected onto the FeO - Fe_2O_3 -MgO plane through the SiO_2 corner. The saturation phases are also marked in the figure. The calculated curves agree well with the experiments for slags containing less than 50 weight % Fe_2O_3 . However, the experimental MgO contents of the slag are much higher than the calculated values in the spinel saturation region. Most likely, this results from a lack of equilibration due to the fact that the experiments were performed in MgO crucibles. Similar problems with data from the same authors were encountered in evaluating the FeO - Fe_2O_3 -MgO system as discussed earlier.^[4]

2. Phase diagrams in equilibrium with iron

The calculated phase diagrams of the FeO - Fe_2O_3 -MgO- SiO_2 system at saturation with metallic iron are shown in Figures 20 to 22 along with experimental data. Bowen and Schairer^[53] investigated this system using a classical quenching technique and optical microscopic phase determination. They determined the phase diagram of the orthosilicate olivine section (Mg_2SiO_4 - Fe_2SiO_4) and the metasilicate section (MgSiO_3 - FeSiO_3), and also measured the liquidus projection at saturation with metallic iron. Nafziger and Muan^[33] measured the solidus in the FeO - Fe_2O_3 -MgO- SiO_2 system at various SiO_2 contents using quenching experiments. Kojima *et al.*^[54] and Shim and Ban-Ya^[55] measured the liquidus composition of the magnesio-wustite and olivine phases from 1550° to 1650 °C by equilibration of slag and metallic iron in MgO crucibles. As can be seen from Figure 20, their data are not fully consistent with the experimental results of Bowen and Schairer^[53] which seem to be more reliable. When an experiment is performed in an oxide crucible, the analyzed slag composition is often shifted towards the crucible composition, either because particles of the crucible are entrapped in the analyzed slag or because of rapid dissolution of the crucible by the slag. Greig^[56] studied the miscibility gap in the FeO - Fe_2O_3 -MgO- SiO_2 system. However, the experiments were performed for only two compositions at unspecified temperatures. The calculated liquidus projection in Figure 20 is in good agreement with the results of Bowen and Schairer. The solidus of olivine is also well reproduced in Figure 21.

Phase relationships in the metasilicate section have not been well studied. As mentioned by Bowen and Schairer,^[53] this is due to the slow kinetics of phase transformations of pyroxenes and the difficulty in distinguishing among the

different crystal structures of pyroxenes using optical microscopy or X-ray diffraction. Thus, the reported experimental data are not sufficient to construct the phase equilibria between pyroxenes. The metasilicate section is calculated in the present study based on the following data: (a) pure MgSiO_3 transforms from ortho- to proto-pyroxene at about 984 °C; (b) the shape of the phase boundaries of proto-pyroxene is similar to that in the MgSiO_3 - MnSiO_3 system;^[57] (c) the pyroxene phase in equilibrium with liquid is clino-pyroxene as reported by Bowen and Schairer;^[53] (d) the shape of the phase boundaries between clino-pyroxene and ortho-pyroxene corresponds to the MgSiO_3 - FeSiO_3 phase diagram estimated by Huebner and Turnock^[58] from their study of the CaSiO_3 - MgSiO_3 - FeSiO_3 system. The pyroxene solid solution dissociates into olivine and tridymite. However, as can be seen from Figure 22, the data on the maximum solubility of FeSiO_3 in MgSiO_3 are contradictory. The calculated phase diagram of the MgSiO_3 - FeSiO_3 metasilicate section is shown in Figure 22. In order to extend the stoichiometry range of pyroxene further to the FeSiO_3 side, the pyroxene solution must be stabilized by making the Gibbs energy of mixing of pyroxene and/or the Gibbs energy of the FeSiO_3 end-member more negative. However, these thermodynamic properties are constrained by the phase equilibria shown in Figures 8, 10 and 14 as well as by the high-pressure equilibrium^[14] $2\text{FeSiO}_3 = \text{Fe}_2\text{SiO}_4 + \text{SiO}_2$ (the latter fixes the Gibbs energy of FeSiO_3). Therefore, the calculated MgSiO_3 - FeSiO_3 section is believed to represent the best overall fit of various types of available experimental data.

Yang and Ghose^[23] found that ortho-pyroxene of the $(\text{Mg}_{0.25}\text{Fe}_{0.75})\text{SiO}_3$ composition transformed to clino-pyroxene above 1200 K during their cation distribution measurements. The temperature of this metastable phase transition is calculated to be 1138 K. The calculated SiO_2 liquidus in the metasilicate section is slightly lower than the experimental data of Bowen and Schairer.^[53] However, as can be seen from the dotted line in Figure 22, when just 2 weight % of excess SiO_2 is present in the system, the liquidus temperature in the FeSiO_3 rich region is significantly increased. Hence, the higher measured liquidus temperatures may be explained by small deviations of the experimental samples from the metasilicate stoichiometry.

3. Activities of FeO

Figure 23 shows the calculated activities of FeO with respect to the liquid standard state in liquid FeO - MgO - SiO_2 slags saturated with metallic iron at 1600 °C and 1900 °C. Shim and Ban-Ya^[55] reported the oxygen content of liquid iron equilibrated with slags in magnesia crucibles. The activity of FeO was calculated from these data in the present study using the present optimized activity coefficient of oxygen in liquid iron.^[16] These activities are very scattered probably due to a lack of equilibration in the MgO crucibles. The oxygen solubilities in liquid iron as measured by Kojima *et al.*^[54] and by Sakawa *et al.*^[59] are not reported in their articles. Only the activities of FeO calculated by the authors from the solubility data are given.

Overall, the iso-activity curves calculated in the present study agree with the results of Kojima *et al.* and Sakawa *et al.* within the experimental error limits as can be seen in Figure 23.

IV. CONCLUSIONS

A complete critical evaluation of all available phase diagram and thermodynamic data at 1 bar total pressure for the FeO - Fe_2O_3 - MgO - SiO_2 system has been carried out, and a database of optimized model parameters has been developed. A wide variety of available data is reproduced within experimental error limits by a very few model parameters. With the present optimized database, it is possible to calculate any phase diagram section for all compositions and oxygen partial pressures. The optimized parameters form part of the F*A*C*T* database, which can be used together with the FactSage software^[9] for thermodynamic modeling of various industrial and natural processes.

ACKNOWLEDGMENTS

This project was supported by a CRD grant from the Natural Sciences and Engineering Research Council of Canada in collaboration with INCO, Noranda, Rio Tinto, Teck Cominco, Alcoa, Dupont, Shell, Corning, Pechiney, Norsk Hydro, Sintef, Schott Glas, St.-Gobain Recherche, Mintek and IIS Materials.

REFERENCES

1. O. B. Fabrichnaya: *Calphad*, 2000, vol. 24, pp. 113-131.
2. P. Wu, G. Eriksson, A. D. Pelton, and M. Blander: *ISIJ Inter.*, 1993, vol. 33, pp. 26-35.
3. S. A. Decterov, E. Jak, P. C. Hayes, and A. D. Pelton: *Metall. Mater. Trans. B*, 2001, vol. 32 B, pp. 643-657.
4. I.-H. Jung, S. A. Decterov, and A. D. Pelton: *Metall. Mater. Trans. B*, "Thermodynamic Modeling of the Fe-Mg-O System", submitted.
5. A. D. Pelton and M. Blander: *Proceedings of the Second International Symposium on Metallurgical Slags and Fluxes, TMS-AIME, Warrendale, PA*, 1984, pp. 281-94.
6. A. D. Pelton and M. Blander: *Metall. Trans. B*, 1986, vol. 17B, pp. 805-815.
7. A. D. Pelton, S. A. Decterov, G. Eriksson, C. Robelin, and Y. Dessureault: *Metall. Mater. Trans. B*, 2000, vol. 31B, pp. 651-659.
8. A. D. Pelton and P. Chartrand: *Metall. Mater. Trans. A*, 2001, vol. 32A, pp. 1355-1360.
9. *www.factsage.com*, Montreal, 2002.
10. A. D. Pelton: *Calphad*, 2001, vol. 25, pp. 319-328.
11. M. Hillert, B. Jansson, and B. Sundman: *Z. Metallkd.*, 1988, vol. 79, pp. 81-87.
12. M. Hillert and L.-I. Staffansson: *Acta Chem. Scand.*, 1970, vol. 24, pp. 3618-3626.
13. R. G. Berman: *J. Petrol.*, 1988, vol. 29, pp. 445-522.
14. S. K. Saxena, N. Chatterjee, Y. Fei, and G. Shen: *publ. Springer-Verlag Berlin Heidelberg Germany*, 1993, pp.

- 428 p.
15. <http://www.sgte.org/>, Scientific Group Thermodata Europe, 2002.
 16. I.-H. Jung, S. A. Decterov, and A. D. Pelton: *Metall. Mater. Trans.*, submitted, 2002.
 17. F. Princivalle: *Mineral. Petrol.*, 1990, vol. 43, pp. 121-129.
 18. G. Artioli, R. Rinaldi, C. C. Wilson, and P. F. Zanazzi: *Am. Mineral.*, 1995, vol. 80, pp. 197-200.
 19. G. Artioli, M. Bellotto, and B. Palosz: *Powder Diffr.*, 1994, vol. 9, pp. 63-67.
 20. S. A. T. Redfern, G. Artioli, R. Rinaldi, C. M. B. Henderson, K. S. Knight, and B. J. Wood: *Phys. Chem. Miner.*, 2000, vol. 27, pp. 630-637.
 21. R. Rinaldi, G. Artioli, C. C. Wilson, and G. McIntyre: *Phys. Chem. Miner.*, 2000, vol. 27, pp. 623-629.
 22. R. Basso, A. Dal Negro, G. Della, and G. Rossi: *N. Jb. Miner. Mh.*, 1979, pp. 197-202.
 23. H. Yang and S. Ghose: *Am. Mineral.*, 1994, vol. 79, pp. 633-643.
 24. S. K. Saxena and S. Ghose: *Am. Mineral.*, 1971, vol. 56, pp. 532-559.
 25. J. R. Besancon: *Am. Mineral.*, 1981, vol. 66, pp. 965-973.
 26. L. M. Anovitz, E. Essene, and W. R. Dunham: *Am. Mineral.*, 1988, vol. 73, pp. 1060-1073.
 27. M. C. Domeneghetti, G. M. Molin, and V. Tazzoli: *Am. Mineral.*, 1985, vol. 70, pp. 987-995.
 28. S. Grammenopoulou: Christian-Albrechts University, 1981.
 29. J. R. Besancon, Sposato, and Grover: *Personal comm. in the article by Anovitz, L.M.; Essene, E.; Dunham, W.R. in Am. Mineral.*, 1988, vol. 73, pp. 1060-1073.
 30. J. Sykes and G. M. Molin: *Int. Miner. Assoc. Abstr. Program*, 1986, vol. 14, pp. 243.
 31. D. Virgo and S. S. Hafner: *Am. Mineral.*, 1970, vol. 55, pp. 210-223.
 32. R. J. Williams: *Am. J. Sci.*, 1971, vol. 270, pp. 334-360.
 33. R. H. Nafziger and A. Muan: *Am. Mineral.*, 1967, vol. 52, pp. 1364-1385.
 34. K. Kitayama and T. Katsura: *Bull. Chem. Soc. Jpn.*, 1968, vol. 41, pp. 1146-1151.
 35. J. W. Larimer: *Geochim. Cosmochim. Acta*, 1968, vol. 32, pp. 1187-1207.
 36. L. G. Medaris: *Am. J. Sci.*, 1969, vol. 267, pp. 945-968.
 37. N. M. Wiser and B. J. Wood: *Contrib. Mineral. Petrol.*, 1991, vol. 108, pp. 146-153.
 38. E. Jacobsson: *Phase equilibria in the MgO-Fe_{1-y}O-SiO₂-TiO₂-Fe assemblage and an emf study of the Fe-Fe₂O₃ system*, University Umeå, Sweden, 1985.
 39. A. El Goresy and E. Woermann: *NATO Adv. Study Inst. Ser., Ser. C*, 1977, vol. C30, pp. 249.
 40. H. E. Jamieson and P. L. Roeder: *Am. Mineral.*, 1984, vol. 69, pp. 283-291.
 41. K. C. Sharma, R. D. Agrawal, and M. L. Kappor: *Intl. Conf. on Progress in Metallurgical Research: Fundamental and Applied Aspects*, IIT Kanpur, India, 1985, pp. 381-385.
 42. K. C. Sharma, R. D. Arwaral, and M. L. Kapoor: *Earth Planet. Sci. Lett.*, 1987, vol. 85, pp. 302-310.
 43. K. T. Jacob, G. M. Kale, and G. N. K. Iyengar: *Metall. Trans. B*, 1989, vol. 20B, pp. 679-685.
 44. L. S. Darken and K. Schwerdtfeger: *Trans. Metall. Soc. of AIME*, 1966, vol. 236, pp. 201-211.
 45. C. Chatillon-Colinet, R. C. Newton, D. III Perkins, and O. J. Kleppa: *Geochim. Cosmochim. Acta*, 1983, vol. 47, pp. 1597-1603.
 46. P. Thierry, C. Chatillon Colinet, J. C. Mathieu, J. R. Regnard, and J. Amosse: *Phys. Chem. Miner.*, 1981, vol. 7, pp. 43-46.
 47. B. J. Wood and O. J. Kleppa: *Geochim. Cosmochim. Acta*, 1981, vol. 45, pp. 529-534.
 48. R. N. Correia and J. White: *Trans. Brit. Ceram. Soc.*, 1988, vol. 87, pp. 195-199.
 49. A. Muan and E. F. Osborn: *J. Am. Ceram. Soc.*, 1956, vol. 39, pp. 121-140.
 50. V. Ambruz, E. Havlica, and E. Kanclir: *Chem. Zvesti*, 1981, vol. 35, pp. 51-55.
 51. D. H. Speidel and E. F. Osborn: *Am. Mineral.* 1967, vol. 52, pp. 1139-52.
 52. E. Schurmann and I. Kolm: *Steel Res.*, 1988, vol. 59, pp. 185-191.
 53. N. L. Bowen and J. F. Schairer: *Am. J. Sci.*, 1935, vol. 29, pp. 151-217.
 54. Y. Kojima, M. Inoue, and K. Sano: *Arch. Eisenhüttenwes.*, 1969, vol. 40, pp. 37-40.
 55. J. D. Shim and S. Ban-Ya: *Tetsu To Hagane*, 1981, vol. 67, pp. 1735-44.
 56. J. W. Greig: *Am. J. Sci.*, 5th Ser., 1927, vol. 13, pp. 1-44.
 57. F. P. Glasser and E. F. Osborn: *J. Am. Ceram. Soc.*, 1969, vol. 43, pp. 132-140.
 58. J. S. Huebner and A. C. Turnock: *Am. Mineral.*, 1980, vol. 65, pp. 225-71.
 59. M. Sakawa, S. G. Whiteway, and C. R. Masson: *Trans. Iron Steel Inst. Jpn.*, 1978, vol. 18, pp. 173-176.

Table I. Optimized model parameters of solutions in the FeO-Fe₂O₃-MgO-SiO₂ system (J/mol and J/mol.K).

Olivine: (Fe²⁺, Mg²⁺)^{M2}(Fe²⁺, Mg²⁺)^{M1}SiO₄	
$\Delta_{MF:MF} = G_{MM} + G_{FF} - G_{MF} - G_{FM}$	-4602.4
$I_{MF} = G_{MF} - G_{FM}$	-8884.3 + 10.878 <i>T</i>
Ortho-pyroxene: (Fe²⁺, Mg²⁺)^{M2}(Fe²⁺, Mg²⁺)^{M1}(Si)^B(Si)^AO₆	
G_{FeSiO_3} (*)	$H_{298.15}^o$ (298.15K) = -1195369.76, $S_{298.15}^o = 95.88317$
	$C_p = 169.06 - 2097318T^{-2} - 1192.97 T^{-0.5} + 292532958 T^{-3}$
$\Delta_{MF:MF} = G_{MM} + G_{FF} - G_{MF} - G_{FM}$	0.0
$I_{MF} = G_{MF} - G_{FM}$	16736
Clino-pyroxene: (Fe²⁺, Mg²⁺)^{M2}(Fe²⁺, Mg²⁺)^{M1}(Si)^B(Si)^AO₆	
$G_{FF}(\text{clino}) - G_{FF}(\text{ortho})$	-519
$\Delta_{MF:MF} = G_{MM} + G_{FF} - G_{MF} - G_{FM}$	0.0
$I_{MF} = G_{MF} - G_{FM}$	16736
Proto-pyroxene: (Fe²⁺, Mg²⁺)^{M2}(Fe²⁺, Mg²⁺)^{M1}(Si)^B(Si)^AO₆	
$G_{FF}(\text{clino}) - G_{FF}(\text{ortho})$	10360
$\Delta_{MF:MF} = G_{MM} + G_{FF} - G_{MF} - G_{FM}$	0.0
$I_{MF} = G_{MF} - G_{FM}$	16736
Liquid Oxide: FeO-FeO_{1.5}-MgO-SiO₂	
$q_{MgO, SiO_2(FeO)}^{101}$ (**)	20920
$q_{MgO, SiO_2(FeO)}^{201}$	46024
All other model parameters for binary and ternary subsystems were reported earlier. ^[2-4,9]	

Notations M and F are used for Mg²⁺ and Fe²⁺, respectively.

(*) The Gibbs energy is taken from Berman^[13] and $H_{298.15}^o$ is slightly modified by - 996 J/mol in order to reproduce high pressure phase equilibria.^[14]

(**) The quasichemical parameters are defined in References [7,8].

Gibbs energies of the pure components of the olivine solution, liquid oxide solution, proto-, ortho-, and clino-MgSiO₃ and ortho-FeSiO₃ are taken from the F*A*C*T database.^[9]

Table II. Calculated and experimental invariant points in air of the FeO-Fe₂O₃-MgO-SiO₂ system.

T (°C)		Phases	Composition (in weight percent)						
Exp.	Calc.		MgO		SiO ₂		Fe ₂ O ₃ equivalent**		Reference
			Exp.	Calc.	Exp.	Calc.	Exp.	Calc.	
1650	1656	MW*	35.2	35.1	1.0	0.0	63.8	64.9	[43]
		Spinel	16.6	15.5	0.4	0.0	83.0	84.5	[43]
		Olivine	54.3	54.3	41.2	41.9	4.5	3.8	[43]
		Liquid	29.5	32.7	19.5	21.3	51	46.0	[43]
			40		13		47		[44]
1390 1375	1375	Spinel	11.4	9.7	0.5	0.0	88.1	90.3	[43]
			13.5		0.0		86.5		[46]
	Olivine	51.2	51.3	40.5	41.1	8.3	7.6	[43]	
		50		41		9		[46]	
	Pyroxene	36.5	37.8	57.7	58.8	5.8	3.4	[43]	
		37		58		5		[46]	
	Liquid	22.0	19.6	47.0	46.7	31.0	33.7	[43]	
		18		40		42		[46]	
1365 1339	1365	Spinel	10	8.8	0.5	0.0	89.5	91.2	[43]
			12.5		0.0		87.5		[46]
	Pyroxene	35.7	37.6	57.8	58.8	6.5	3.6	[43]	
		37		57.5		5.5		[46]	
	Tridymite	0.1	0.0	97.9	100	2	0.0	[43]	
		0.0		100		0.0		[46]	
	Liquid	19.3	16.0	47.7	49.1	33	34.9	[43]	
		16		44		40		[46]	

* MW represents the Magnesiowustite phase.

** All iron assumed to be trivalent.

Table III. Calculated and experimental invariant points of the FeO-Fe₂O₃-MgO-SiO₂ system at different oxygen pressures and in equilibrium with iron.

log (P _{O₂} , bar)	T (°C)		Phases	MgO		SiO ₂		FeO equivalent***		Reference
	Exp.	Calc.		Exp.	Calc.	Exp.	Calc.	Exp.	Calc.	
-5.6	1285	1268	Olivine		27.0		35.7	35	37.3	[46]
			Pyroxene	12.5	22.7	67.5	53.7	20	23.6	
			Spinel		1.8		0.0	98	98.2	
			Liquid		7.8		39.2	52	53.0	
-5.8	1277	1255	Pyroxene		21.3		53.2	22	25.5	[46]
			Spinel		1.5		0.0	97.5	98.5	
			Liquid	10	7.2	39.5	38.8	50.5	54.0	
			Tridymite	0.0	0.0	100	100	0.0	0.0	
-7.1*	1255	1211	Olivine		14.6		32.9	40	52.5	[46]
			Spinel		0.7		0.0	98.5	99.3	
			Liquid	6.5	3.6	37.0	36.0	56.5	60.4	
			Tridymite	0.0	0.0	100	100	0.0	0.0	
			Pyroxene		—		—	27.5	—	
-8.8**	1160		Olivine					48		[46]
			Spinel					99		
			Liquid	1.5		34		64.5		
			Tridymite			100				
Metallic iron	1305	1295	Olivine		21.3		34.4		44.3	[47]
			Pyroxene	16.1	19.0	51.3	52.3	32.7	28.7	
			Liquid		7.6		43.7		48.7	
			Tridymite	0.0	0.0	100	100	0.0	0.0	

* Only 4 condensed phases can coexist in equilibrium at a fixed oxygen potential.

** Calculations show that this phase assemblage is metastable.

*** All iron assumed to be divalent.

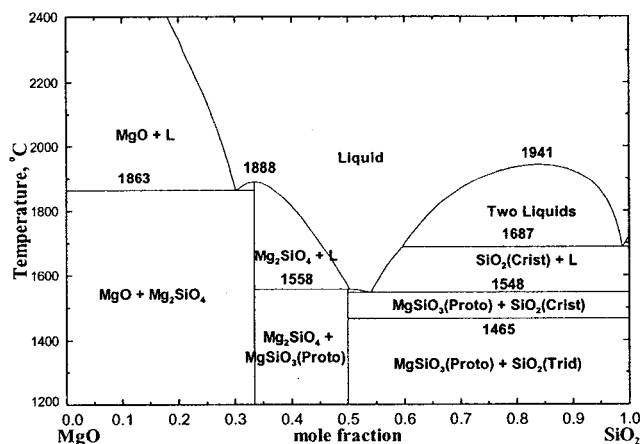


Fig. 1 – Calculated optimized MgO-SiO₂ phase diagram.^[2]

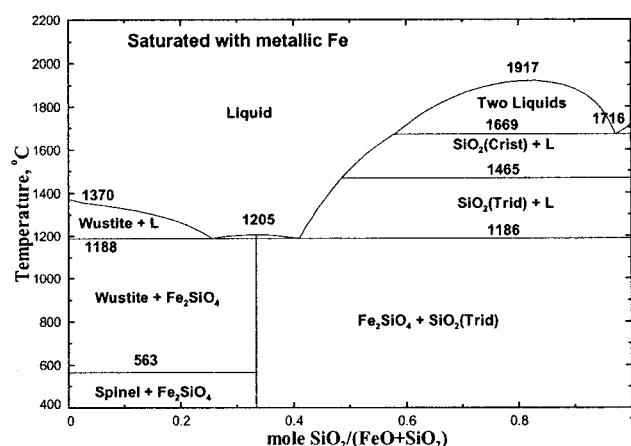


Fig. 2 – Calculated optimized FeO-Fe₂O₃-SiO₂ phase diagram in equilibrium with iron.^[2]

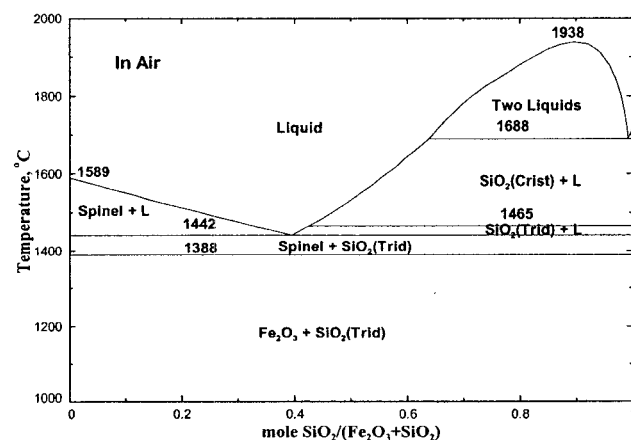


Fig. 3 – Calculated optimized FeO-Fe₂O₃-SiO₂ phase diagram in air.

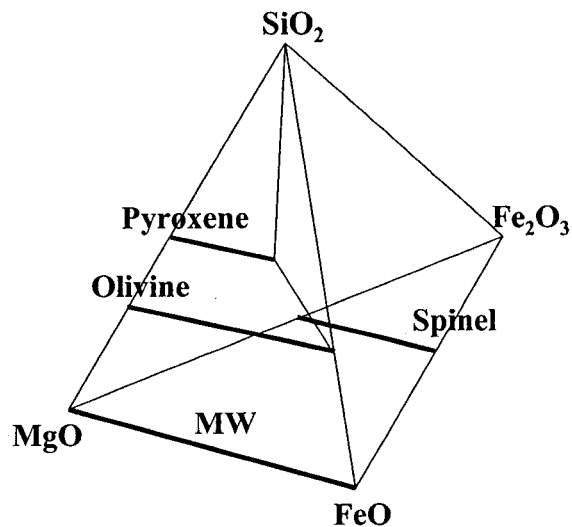


Fig. 4 – Schematic representation of phases in the FeO-Fe₂O₃-MgO-SiO₂ system (MW=magnesiowustite).

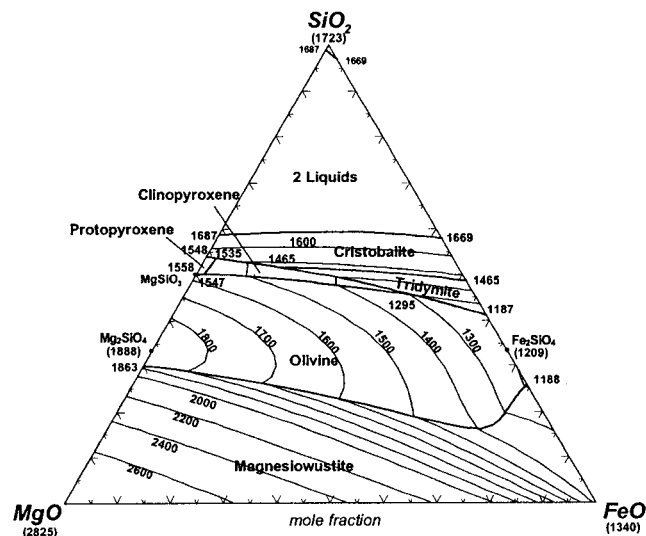


Fig. 5 – Calculated liquidus projection of the FeO-Fe₂O₃-MgO-SiO₂ system at 1 bar total pressure in equilibrium with metallic iron. The thin solid lines are calculated isotherms; temperatures are in °C. The univariant lines are bold. (Projection from the Fe- corner of the Fe-FeO-MgO-SiO₂ tetrahedron onto the basal plane).

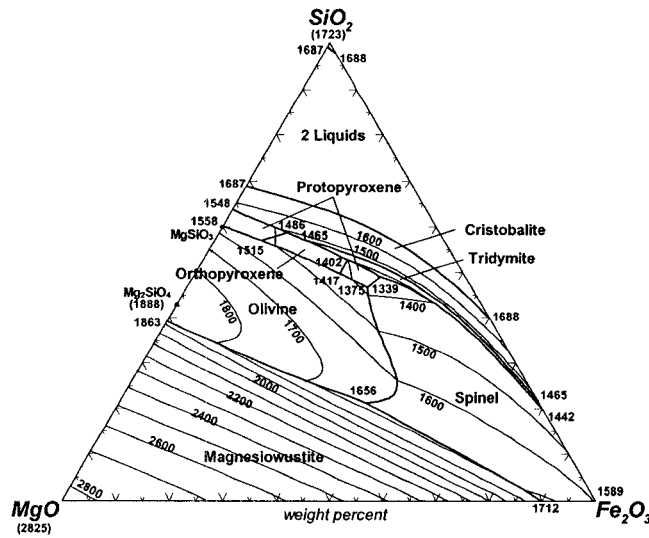


Fig. 6 – Calculated liquidus projection of the FeO-Fe₂O₃-MgO-SiO₂ system in air (presented in wt %). The thin solid lines are calculated isotherms; temperatures are in °C. The univariant lines are bold. Total pressure = 1 bar. (Projection from the O₂- corner of the Fe₂O₃-MgO-SiO₂-O₂ tetrahedron onto the basal plane).

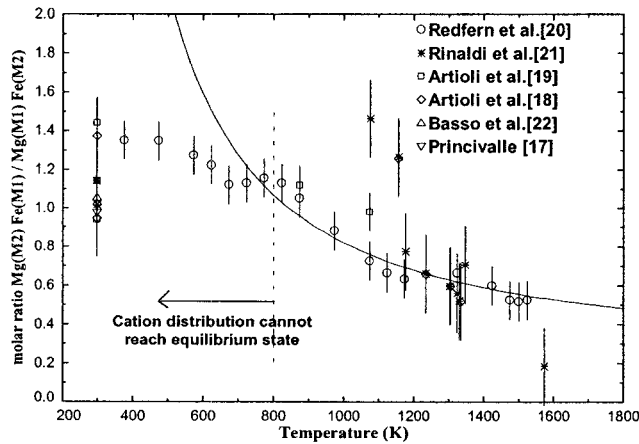


Fig. 7 – Calculated cation distribution in MgFeSiO₄ olivine as a function of temperature.

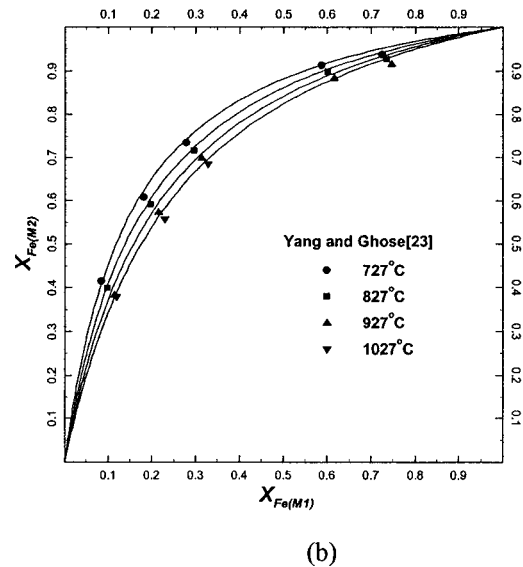
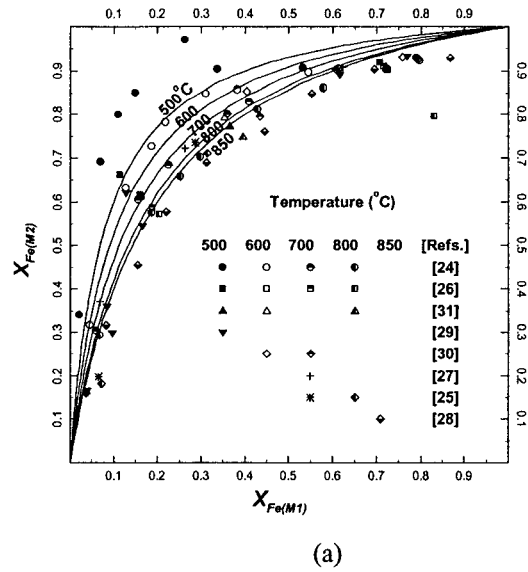


Fig. 8 – Calculated cation distribution in ortho-pyroxene at different temperatures. Axes are the mole fractions of Fe on the M1 and M2 sites.

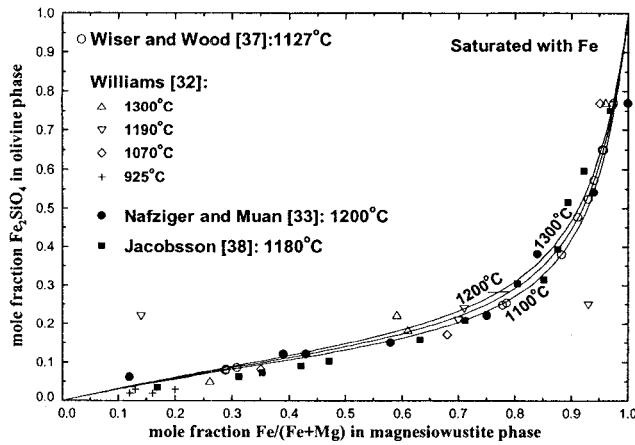


Fig. 9 – Calculated tie-lines between magnesiowustite and olivine in equilibrium with Fe at 1100 to 1300 °C.

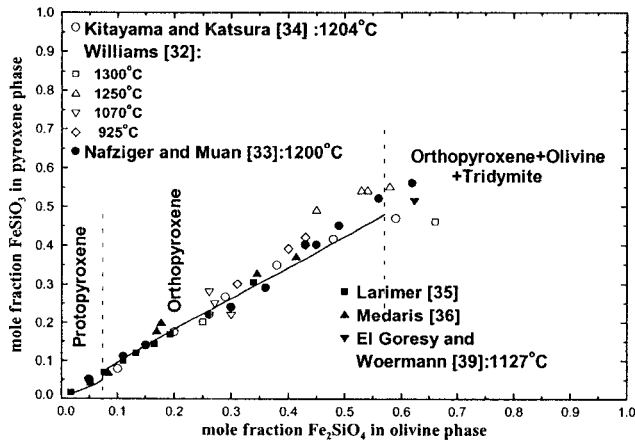


Fig. 10 – Calculated tie-lines between olivine and pyroxenes in equilibrium with Fe at 1200 °C.

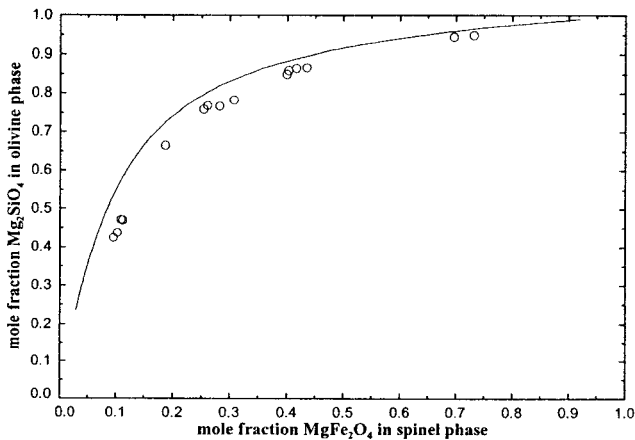


Fig. 11 – Calculated tie-lines between spinel and olivine phases at 1300 °C. Experimental data are from Jamieson and Roeder.^[40] Calculated curve is virtually independent of O_2 pressure over the range $10^{-8} < P_{O_2} < 1$ bar.

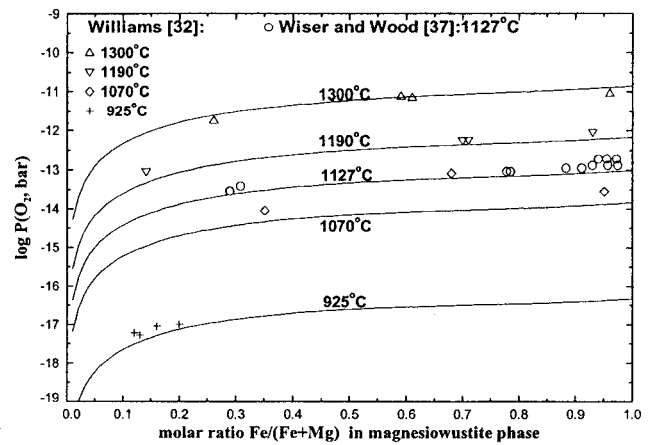


Fig. 12 – Calculated oxygen partial pressure over the (magnesiowustite + olivine + Fe) three-phase region.

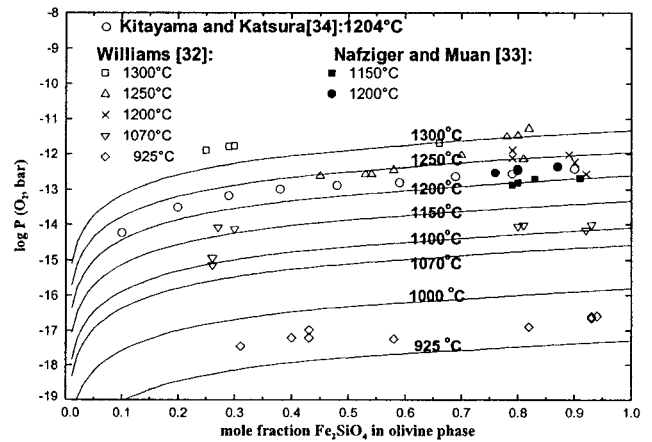


Fig. 13 – Calculated oxygen partial pressure over the (olivine + pyroxene + Fe) and (olivine + SiO_2 (tridymite) + Fe) three-phase regions.

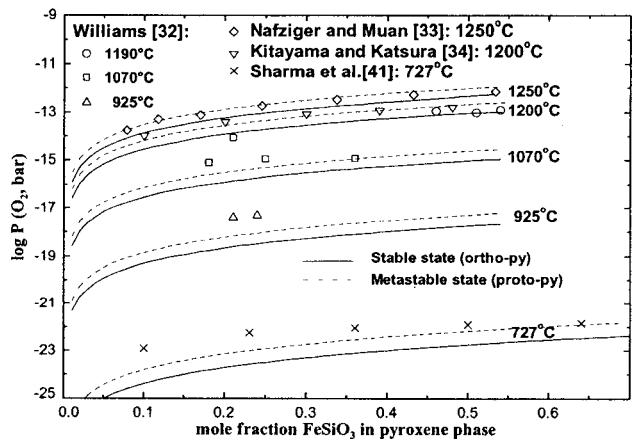


Fig. 14 – Calculated oxygen partial pressure over the (pyroxene + SiO_2 (tridymite) + Fe) three-phase region.

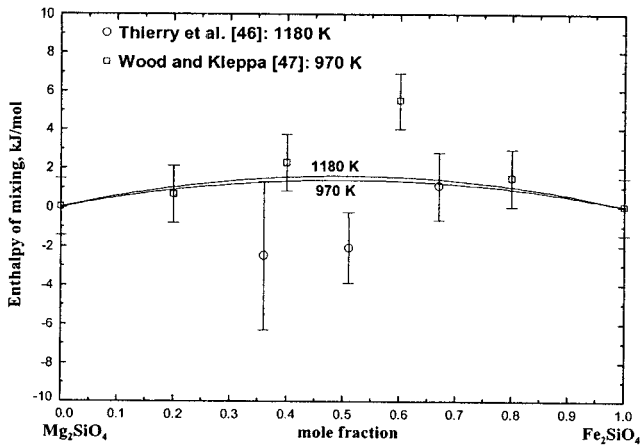


Fig. 15 – Calculated enthalpy of mixing of the Mg_2SiO_4 - Fe_2SiO_4 olivine solution (error bars represent one standard deviation).

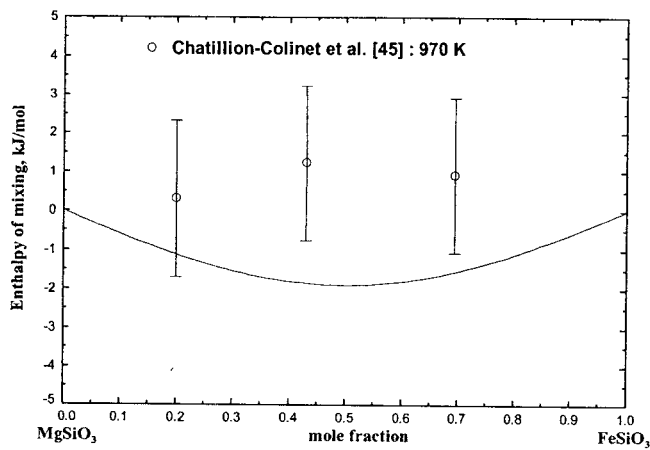
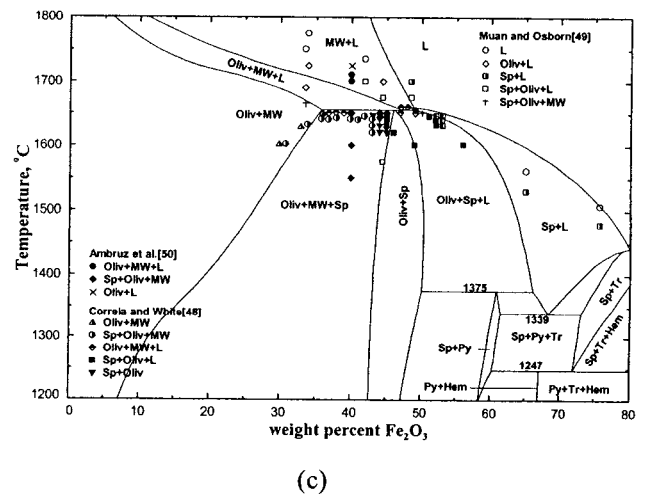
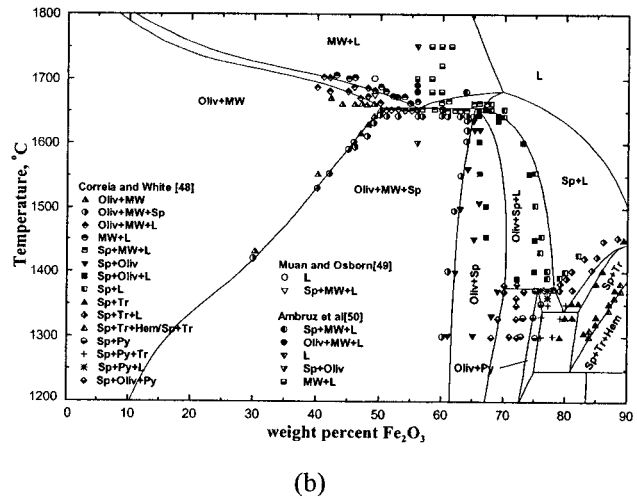
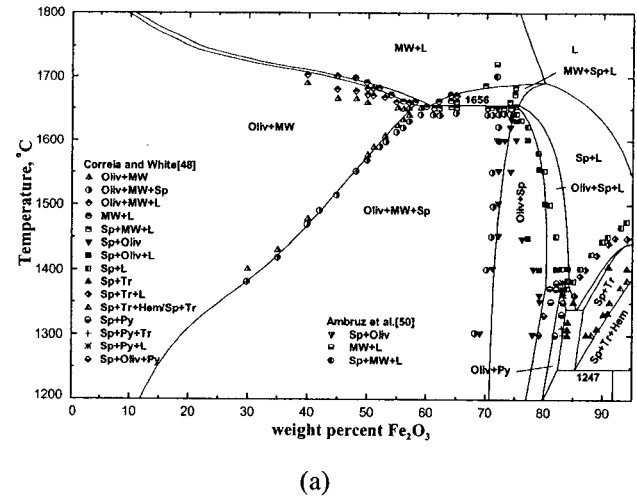
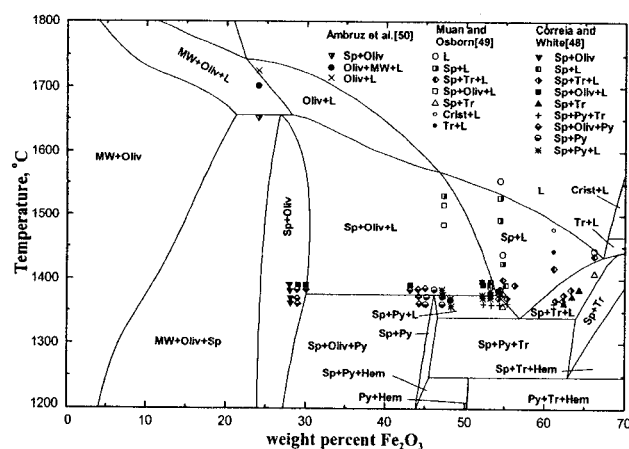
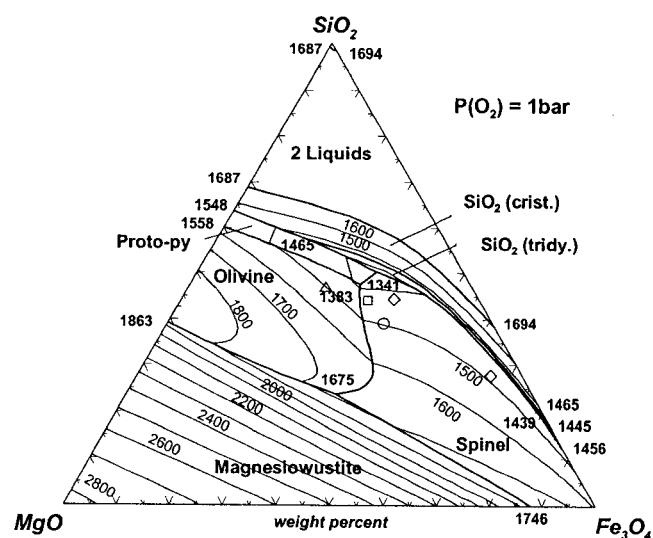


Fig. 16 – Calculated enthalpy of mixing of the MgSiO_3 - FeSiO_3 ortho-pyroxene solution at 970 K (error bars represent one standard deviation).

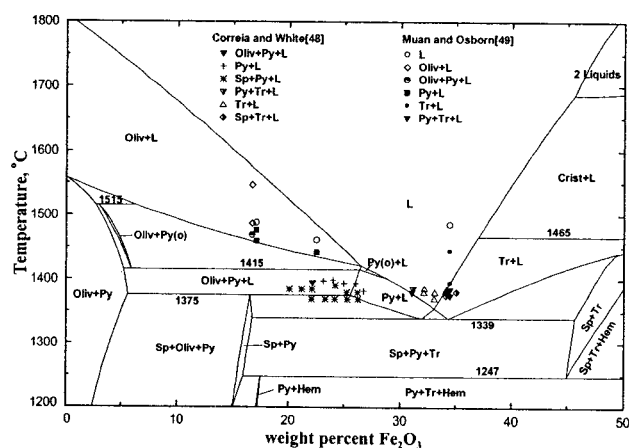




(d)

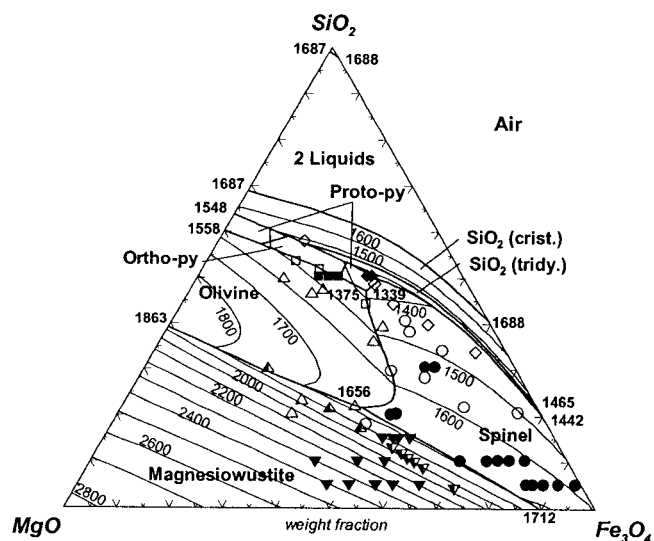


(a)



(e)

Fig. 17 – Calculated sections of the $\text{Fe}_2\text{O}_3\text{-MgO-SiO}_2\text{-O}_2$ phase diagram in air at different ratios of $\text{SiO}_2/(\text{MgO}+\text{Fe}_2\text{O}_3+\text{SiO}_2)$. (a) $\text{SiO}_2 = 5$ wt %, (b) 10 wt %, (c) 20 wt %, (d) 30 wt %, (e) 50 wt %.



(b)

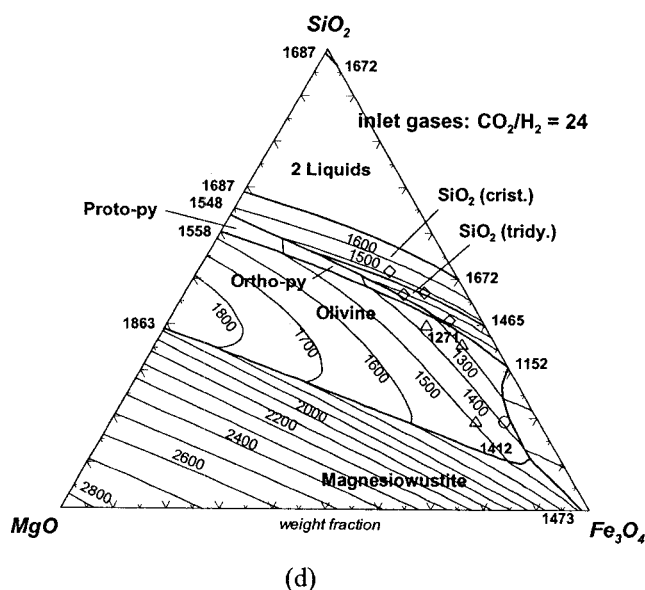
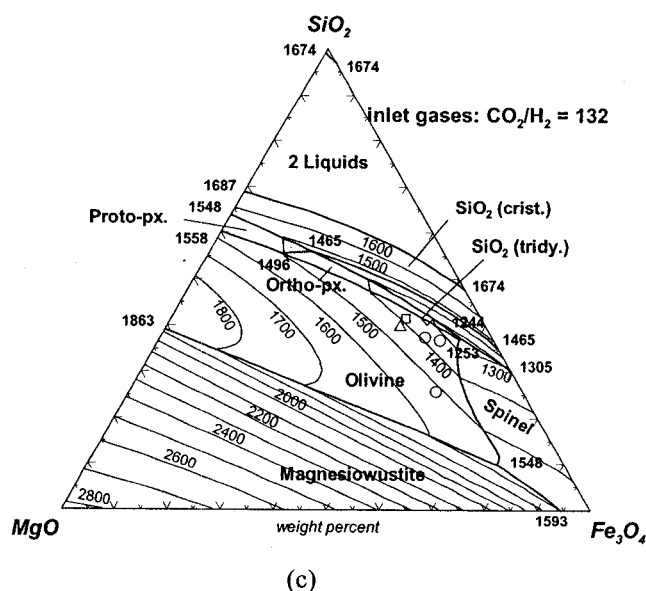


Fig. 18 – Calculated liquidus projections through the O_2 corner of the Fe_3O_4 - MgO - SiO_2 - O_2 tetrahedron onto the basal plane under different oxygen partial pressures. (a) $P_{O_2} = 1$ bar, (b) air, (c) $CO_2/H_2 = 132$, (d) $CO_2/H_2 = 24$. Symbols: Circle-Spinel, Triangle-Olivine, Diamond-Silica, Inverted Triangle- Magnesiowustite, Rectangle-Pyroxene primary phase. (Filled: Reference [48], Open: Reference [49] and Half-filled: Reference [50]).

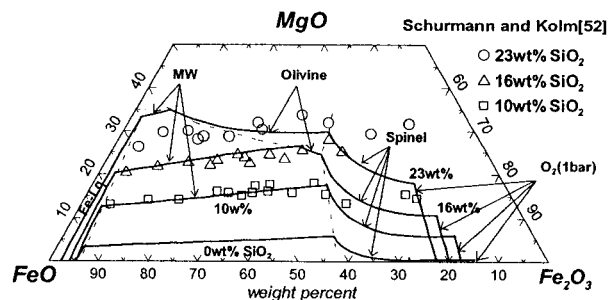


Fig. 19 – Calculated liquidus projection from the SiO_2 corner of the FeO - Fe_2O_3 - MgO - SiO_2 tetrahedron onto the basal plane at 1600 °C. Dotted lines show the boundaries between different primary fields.

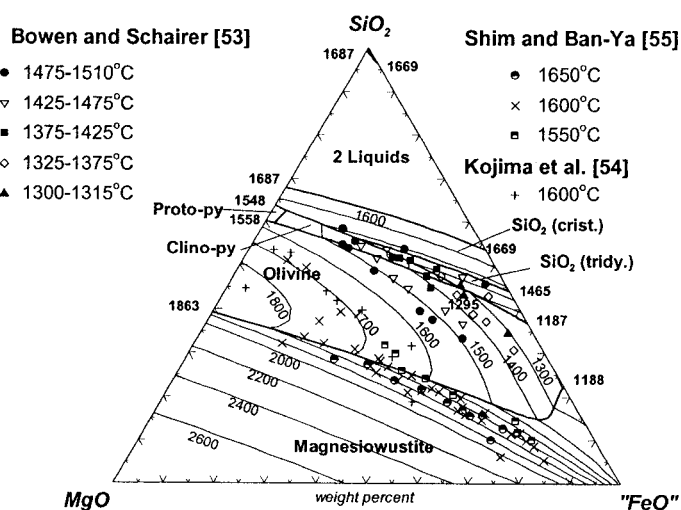


Fig. 20 – Calculated liquidus projection in the “ FeO ”- MgO - SiO_2 system in equilibrium with metallic iron in comparison with experimental data (all iron is assumed to be divalent). (Temperature in °C).

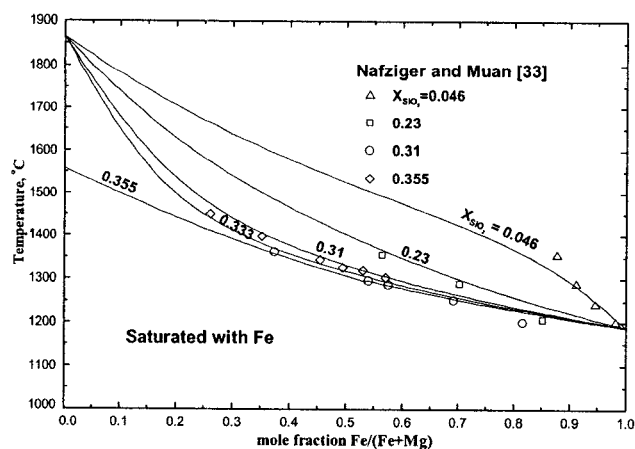


Fig. 21 – Calculated solidus temperature of the Mg_2SiO_4 - Fe_2SiO_4 olivine solid solution at various SiO_2 contents in equilibrium with metallic iron.

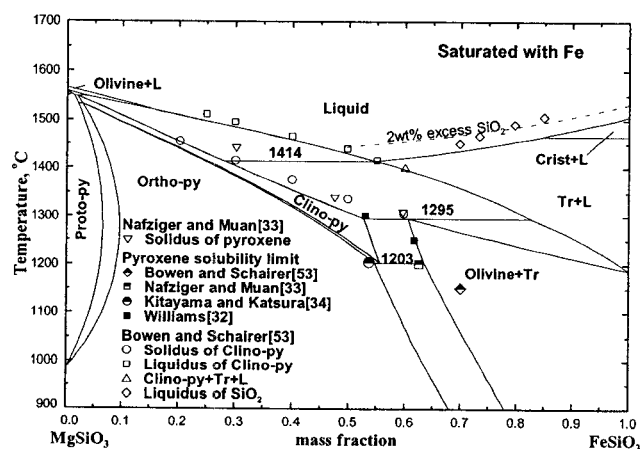


Fig. 22 – Calculated phase diagram of the MgSiO_3 - FeSiO_3 metasilicate section in equilibrium with metallic iron. See details in the text.

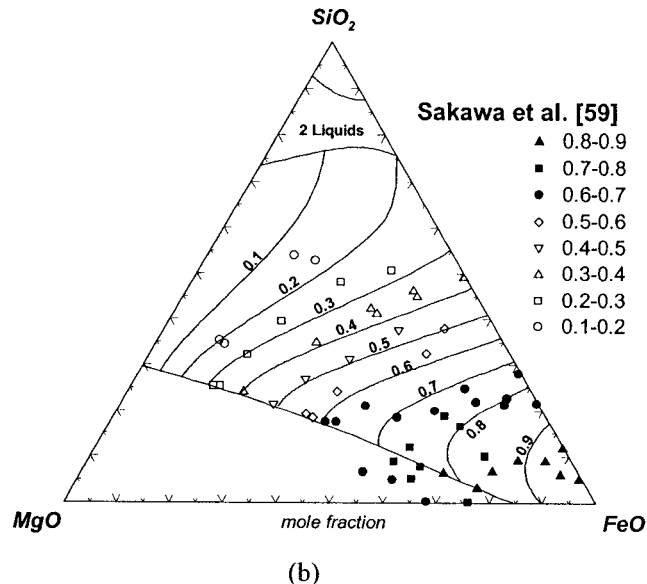
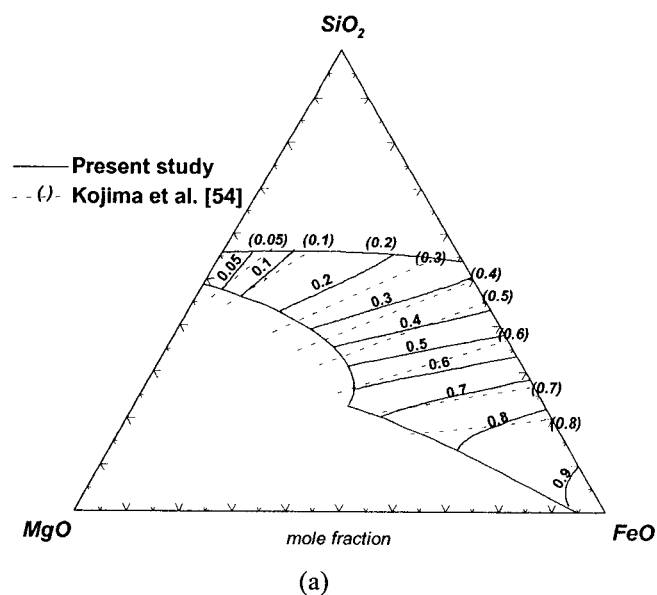


Fig. 23 – Calculated activities of FeO with respect to the liquid standard state in FeO - MgO - SiO_2 liquid slag in equilibrium with metallic iron: (a) 1600 °C, and (b) 1900 °C.

Appendix IV

Article :

Critical Thermodynamic Evaluation and Optimization of the MgO-Al₂O₃, CaO-MgO-Al₂O₃ and MgO-Al₂O₃-SiO₂ Systems

In-Ho Jung, Sergei A. Decterov and Arthur D. Pelton

Submitted to *Metallurgical and Materials Transactions*, 2003

Critical Thermodynamic Evaluation and Optimization of the MgO-Al₂O₃, CaO-MgO-Al₂O₃ and MgO-Al₂O₃-SiO₂ Systems

IN-HO JUNG, SERGEI A. DECTEROV, and ARTHUR D. PELTON

A complete critical evaluation and thermodynamic modeling of the phase diagrams and thermodynamic properties of oxide phases in the MgO-Al₂O₃, CaO-MgO-Al₂O₃ and MgO-Al₂O₃-SiO₂ systems at 1 bar total pressure are presented. Optimized equations for the thermodynamic properties of all phases are obtained which reproduce all available thermodynamic and phase equilibrium data within experimental error limits from 25°C to above the liquidus temperatures at all compositions. The database of the model parameters can be used along with software for Gibbs energy minimization in order to calculate any type of phase diagram section.

I. INTRODUCTION

The MgO-Al₂O₃, CaO-MgO-Al₂O₃ and MgO-Al₂O₃-SiO₂ systems are fundamental to the understanding of metallurgical slags, refractories, ceramic materials and geological phenomena. Eriksson *et al.*^[1] reported a thermodynamic evaluation/optimization of the MgO-Al₂O₃ system using a simplified model for the spinel solution. Hallstedt^[2] described the spinel solution using a two-sublattice Compound Energy Formalism in his optimization of the MgO-Al₂O₃ system. He modeled the liquid slag using a two-sublattice ionic model. Hallstedt also reported an optimization of the ternary CaO-MgO-Al₂O₃ system.^[3]

Recently, a new formulation of the spinel model^[4] has been developed. Furthermore, many new structural and thermodynamic data for the spinel phase have been reported, and two new ternary phases in the CaO-MgO-Al₂O₃ system have been reported. A new and more accurate thermodynamic optimization/evaluation of the MgO-Al₂O₃ and CaO-MgO-Al₂O₃ systems, using the most recent models and data, is warranted. A thermodynamic evaluation/optimization of the MgO-Al₂O₃-SiO₂ system has not previously been reported.

The main goal of the present study is to perform a critical assessment and optimization of thermodynamic properties at 1 bar total pressure of oxide phases in the MgO-Al₂O₃, CaO-MgO-Al₂O₃ and MgO-Al₂O₃-SiO₂ systems. In the thermodynamic "optimization" of a chemical system, all available thermodynamic and phase equilibrium data are evaluated simultaneously in order to obtain one set of model equations for the Gibbs energies of

all phase as functions of temperature and composition. From these equations, all of the thermodynamic properties and the phase diagrams can be back-calculated. In this way, all the data are rendered self-consistent and consistent with thermodynamic principles. Thermodynamic property data, such as activity data, can aid in the evaluation of the phase diagram, and phase diagram measurements can be used to deduce thermodynamic properties. Discrepancies in the available data can often be resolved, and interpolations and extrapolations can be made in a thermodynamically correct manner.

The thermodynamic evaluation/optimization of the MgO-Al₂O₃, CaO-MgO-Al₂O₃ and MgO-Al₂O₃-SiO₂ systems reported in the present study is part of a wider research program aimed at complete characterization of phase equilibria and thermodynamic properties of the entire six-component system CaO-MgO-Al₂O₃-FeO-Fe₂O₃-SiO₂, which has numerous applications in the ceramic, cement and glass industries, metallurgy, geochemistry, etc. The present optimization covers the range of temperatures from 25°C to above the liquidus.

II. PHASES AND THERMODYNAMIC MODELS

The following solution phases are found in the CaO-MgO-Al₂O₃ and MgO-Al₂O₃-SiO₂ systems:

Slag (molten oxide phase): CaO-MgO-SiO₂-AlO_{1.5}

Spinel: $(\text{Mg}^{2+}, \text{Al}^{3+})^T [\text{Mg}^{2+}, \text{Al}^{3+}, \text{Va}]_2^O \text{O}_4$

Pyroxene:

$(\text{Mg})^{\text{M}2} (\text{Mg}^{2+}, \text{Al}^{3+})^{\text{M}1} (\text{Al}^{3+}, \text{Si}^{4+})^{\text{B}} (\text{Si})^{\text{A}} \text{O}_6$

Monoxide: MgO-CaO-AlO_{1.5}

Cations shown within a set of brackets for spinel and pyroxene occupy the same sublattice.

A. Slag (molten oxide)

The Modified Quasichemical Model^[5-8] which takes into account short-range-ordering of second-nearest-neighbor cation in the ionic melt, is used for modeling the slag. The sub-systems CaO-MgO,^[9] CaO-Al₂O₃,^[10] MgO-SiO₂^[11] and Al₂O₃-SiO₂^[10] have already been critically evaluated and optimized, and the optimized model parameters are used as the basis of the present study. All second-nearest-neighbor "coordination numbers" used in the model are the same as in the previous studies.^[9-11] Additional binary and ternary model parameters for the MgO-Al₂O₃ and MgO-Al₂O₃-SiO₂ ternary slag solutions were optimized in the present study. These are listed in Table I. The properties of the CaO-MgO-Al₂O₃ ternary solution were calculated from the binary parameters using an asymmetric "Toop-like" approximation^[12] with AlO_{1.5} as the "asymmetric" component, and the properties of the MgO-Al₂O₃-SiO₂ ternary solution were also calculated from the binary and ternary parameters using an asymmetric "Toop-like" approximation^[12] with SiO₂ as the "asymmetric" component.

B. Compound Energy Formalism (CEF)

The spinel and pyroxene solution models were developed within the framework of the two-sublattice Compound Energy Formalism (CEF).^[13] The Gibbs energy expression in the CEF per formula unit is:

$$G = \sum_i \sum_j Y_i' Y_j'' G_{ij} - TS_C + G^E \quad [1]$$

where Y_i' and Y_j'' represent the site fractions of constituents i and j on the first and second sublattices, G_{ij} is the Gibbs energy of an "end-member" ij of the solution in which the first sublattice is occupied only by cation i and the second sublattice is occupied only by cation j , G^E is the excess Gibbs energy and S_C is the configurational entropy assuming random mixing on each sublattice:

$$S_C = -R(n_1 \sum_i Y_i' \ln Y_i' + n_2 \sum_j Y_j'' \ln Y_j'') \quad [2]$$

where n_1 and n_2 are the numbers of sites on the first and second sublattices per formula unit of a solution. G^E is expanded as:

$$G^E = \sum_i \sum_j \sum_k Y_i' Y_j' Y_k'' L_{ij:k} + \sum_i \sum_j \sum_k Y_i' Y_i'' Y_j' L_{k:ij} \quad [3]$$

where the parameters $L_{ij:k}$ are related to interactions between cations i and j on the first sublattice when the second sublattice is occupied only by k cations, and the parameters $L_{k:ij}$ are related to interactions between i and j

cations on the second sublattice when the first sublattice is occupied only by k cations.

1. Spinel Solution

The spinel solution is modeled as $(Mg^{2+}, Al^{3+})^T [Mg^{2+}, Al^{3+}, Va]_2^O O_4$ with $n_1 = 1$ and $n_2 = 2$ sites on the tetrahedral and octahedral sublattices respectively. Non-stoichiometry can occur through the introduction of vacancies, Va , on octahedral sites.

G^E was set to zero in the present study, so that the six end-member Gibbs energies G_{ij} are used to describe the system. Certain linear combinations of these end-member Gibbs energies, which have physical significance, are used as the optimized parameters as discussed in Reference [4]. The optimized parameters are listed in Table I. Details of the optimization are given in the following sections.

The parameter G_{MA} is equal to $G^o(MgAl_2O_4)$ the Gibbs energy of normal $MgAl_2O_4$ spinel. (The notations M, A, V denote Mg^{2+} , Al^{3+} and Va .) The parameters I_{MA} , $\Delta_{MA:MA}$ and $\Delta_{MA:MV}$ are the Gibbs energy changes of the spinel inversion reaction and of reciprocal site exchange reactions, respectively.

The spinel solid solution can be considered as a solution of $MgAl_2O_4$ and γ -Al₂O₃: $(Al^{3+})(Al_{5/6}^{3+}Va_{1/6})_2O_4$. Assuming a random mixture of Al^{3+} and vacancies on the octahedral sites, the Gibbs energy of γ -Al₂O₃ is given by:

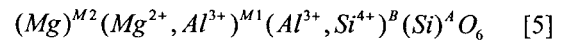
$$8G^o(\gamma - Al_2O_3) = G_{AV} + 5G_{AA} + 2RT(5 \ln 5 + 6 \ln 6) \quad [4]$$

The Gibbs energy of γ -Al₂O₃ was optimized as equal to $G^o(\alpha$ -Al₂O₃) plus an increment as shown in Table I.

Following O'Neill and Navrotsky^[14] the parameter $\Delta_{MA:MA}$ was set to 40 kJ/mol. Since the present study is part of a larger study^[15] of the entire Fe-Mg-Al-Cr-Co-Ni-Zn-O system, model parameters must be consistent with those obtained in optimization of other subsystems. The parameter G_{AA} was already optimized in evaluating the Fe-Al-O spinel solution. Similarly, $G^o(\gamma$ -Al₂O₃) must be optimized to simultaneously reproduce the solubilities of Al₂O₃ in all spinel solutions.

2. Pyroxene Solutions

In the absence of Ca, there are three polymorphs of pyroxene: ortho-pyroxene (*Pbca*, orthorhombic), proto-pyroxene (*Pbcn*, orthorhombic), and low clino-pyroxene (*P21/c*, monoclinic). All three are considered in the present study. Pyroxenes have two distinct octahedral sublattices (M1 and M2) and two distinct tetrahedral sublattices (A and B). Because the amount of Al on A sites is small,^[16] the following simplified^[17] pyroxene structure is used in the present model:



That is, mixing occurs only on the M1 and B sites, and so there are four end-member G_{ij} parameters in the model for each of the three polymorphs: G_{MA} , G_{MS} , G_{AA} and G_{AS}

(where the notation M, A and S indicates Mg^{2+} , Al^{3+} and Si^{4+} respectively)

The parameters G_{MS} are equal to $G^\circ(\text{Mg}_2\text{Si}_2\text{O}_6)$, the Gibbs energies of stable $\text{Mg}_2\text{Si}_2\text{O}_6$ enstatite (ortho-, proto- and low clino-). These were evaluated previously.^[18] For all polymorphs it was assumed that the Gibbs energy of the site exchange reaction is zero: $(G_{\text{MS}} + G_{\text{AA}}) - (G_{\text{AS}} + G_{\text{MA}}) = 0$. Furthermore, with no loss of generality, one can set $G_{\text{AS}} = G_{\text{MA}}$.

The parameter G_{AA} is equal to the Gibbs energy $G^\circ(\text{MgAl}_2\text{SiO}_6)$ of Mg-Tschermak which is not stable at 1.0 bar pressure, and for which no thermodynamic data exist. This was evaluated, for each polymorph, through the Gibbs energy $\Delta_{\text{Mg-Ts}}$ of the exchange reaction:

$$\Delta_{\text{Mg-Ts}} = (G_{\text{CaMgSi}_2\text{O}_6}^\circ + G_{\text{MgAl}_2\text{SiO}_6}^\circ) - (G_{\text{Mg}_2\text{Si}_2\text{O}_6}^\circ + G_{\text{CaAl}_2\text{SiO}_6}^\circ) \quad [6]$$

where the Gibbs energies of $\text{CaMgSi}_2\text{O}_6$, $\text{Mg}_2\text{Si}_2\text{O}_6$ and $\text{CaAl}_2\text{SiO}_6$, for all polymorphs are taken from previous optimizations.^[18,19]

Finally G^E parameter $L_{\text{M,A:A}} = L_{\text{M,A:S}}$ related to interaction between Mg^{2+} and Al^{3+} on the M1 sites when the B sites are occupied by either Al^{3+} or Si^{4+} was used. However, this parameter was not optimized in the present study, its value having already been fixed in an earlier study^[15,20] to reproduce phase equilibrium and enthalpy of mixing data for $\text{CaMgSi}_2\text{O}_6$ - $\text{CaAl}_2\text{SiO}_6$ (diopside - Ca-Tschermak) solutions.

D. Monoxide Solution

The MgO-CaO- $\text{AlO}_{1.5}$ monoxide solution was modeled as a simple random mixture of Mg^{2+} , Ca^{2+} and Al^{3+} ions on cation sites with simple polynomial excess Gibbs energy terms.^[12] It is assumed that cation vacancies remain associated with Al^{3+} ions and so do not contribute to the configurational entropy. Binary excess Gibbs energies were modeled by simple polynomial expansions in the mole fractions. Optimized parameters for the MgO-CaO binary system were obtained previously.^[9] These model parameters reproduce the solid-solid miscibility gap in the MgO-CaO system. Additional parameters were optimized in the present study as described in the following sections. These are listed in Table I. The properties of the ternary MgO-CaO- $\text{AlO}_{1.5}$ solution were calculated from the symmetric "Kohler-like" approximation.^[12]

III. THERMODYNAMIC EVALUATIONS AND OPTIMIZATIONS

A. MgO- Al_2O_3 System

1. Summary of Available Experimental Data

The phase diagram of the MgO- Al_2O_3 system is shown in Figure 1. In a preliminary study, Rankin and Merwin^[21] determined the congruent melting temperature of MgAl_2O_4 .

Alper *et al.*^[22] determined the phase diagram of the MgO- MgAl_2O_3 system using a quenching technique followed by XRD or optical phase identification. Viechnicki *et al.*^[23] investigated the solidus and liquidus under Ar atmospheres using the collapsing cone technique. They reported a eutectic reaction between spinel and Al_2O_3 at 1975 °C which is higher than the temperature of 1925 °C reported by Rankin and Merwin.^[21]

Many investigations have been performed to measure the solubility of Al_2O_3 in MgO (periclase)^[22,24-28] and in the spinel solution^[21,29-34] in the temperature range between 1230° and 1975°C. Usually the solubilities were determined from the change of lattice parameters of quenched samples as determined by XRD. While the measured solubilities of Al_2O_3 in periclase show good agreement among authors, there is more scatter in the reported solubilities of Al_2O_3 in the spinel phase. Shirasuka and Yamaguchi^[29] measured the solubility at temperatures between 1327° and 1927°C. Viertel and Seifert^[30] measured the solubility, seemingly with good accuracy, at 1 kbar total pressure in the temperature range between 1125° and 1625°C using an equilibrium exsolution and homogenization technique.

According to Lejus and Collongues^[35] and Lejus,^[33] MgO is nearly insoluble in MgAl_2O_4 . On the other hand, Alper *et al.*,^[22] Chiang and Kingery^[36] and Fujii *et al.*^[37] reported a small solubility (less than 3 mole %) of MgO in MgAl_2O_4 . In general, solubility of MO in MAI_2O_4 spinels is rarely observed. The solubility of MgO in MgAl_2O_4 spinel was assumed to be negligible in the present study. Roy and Coble^[38] reported a solubility of MgO in Al_2O_3 of about 0.1 mol % at 1830°C and Ando and Momoda^[39] reported a solubility of 0.012 mol %. The solubility of MgO in Al_2O_3 was assumed to be negligible in the present study.

The thermodynamic and structural properties of MgAl_2O_4 have been measured with good accuracy. The low temperature heat capacity of MgAl_2O_4 was measured by King^[40] using adiabatic calorimetry and its entropy at 298.15 K was determined. Heat contents of MgAl_2O_4 were measured by Bonnickson,^[41] Landa and Naumova,^[42] and Richet and Fiquet^[43] at temperatures from 400 to 2200 K. The measured values are in good agreement with each other. The enthalpy of formation of MgAl_2O_4 from MgO and Al_2O_3 was measured at temperatures from 970 to 1173 K using calorimetric techniques.^[44-46]

Gibbs energies of formation of MgAl_2O_4 from MgO and Al_2O_3 were measured by several authors^[37,47-50] using different techniques. Taylor and Schmalzried,^[46] and more recently Jacob and Jayadevan,^[48] used a MgF_2 electrolyte to measure the Gibbs energy of MgAl_2O_4 . Chamberlin *et al.*^[49] equilibrated spinel and liquid Pd, and measured the Mg and Al contents in the Pd. The oxygen partial pressure (controlled by H_2/CO_2 mixtures) was measured using a solid electrolyte. From the known activity coefficients of Mg and Al in the Pd alloy, the Gibbs energy of MgAl_2O_4 could thereby be calculated. Fujii *et al.*^[37] performed similar measurements using liquid Cu. Rosen and Muan^[50] equilibrated CoO-MgO and CoAl_2O_4 - MgAl_2O_4 solid

solutions under controlled P_{O_2} . From the known activities of CoO and MgO in the CoO-MgO solution (a nearly ideal solution) and the known Gibbs energy of $CoAl_2O_4$, the Gibbs energy of $MgAl_2O_4$ could be estimated using a Gibbs-Duhem integration technique.

Grjorthem *et al.*^[51] measured the equilibrium partial pressure of Mg vapor over the three-phase mixture [MgO + $MgAl_2O_4$ + liquid Al] between 1143 and 1414 K. Altman^[52] and Sasamoto *et al.*^[53] measured the partial pressure of Mg over MgO and over $MgO \cdot xAl_2O_3$ spinel solutions ($x = 1.0, 2.0$ and 2.8) for the congruent vaporization of MgO (to $Mg + 1/2 O_2$ in *vacuo*) using a mass spectrometric/Knudsen-cell technique at temperatures between 1850 and 2300 K.

Navrotsky *et al.*^[34] measured the enthalpy of formation of spinel solutions containing excess γ -alumina at 975 K using $2PbO \cdot B_2O_3$ solution calorimetry. McHale *et al.*^[54] reinvestigated the enthalpy of transformation from α - Al_2O_3 (corundum) to γ - Al_2O_3 by calorimetric measurements on nano-sized γ - Al_2O_3 with a correction being made for surface energy.

The cation distribution in spinel was measured for *in situ* or quenched samples by several authors^[55-61] using several different techniques: XRD, neutron powder diffraction, NMR, ESR, *etc.* Redfern *et al.*^[55] measured the cation distribution using an *in situ* neutron spectroscopic technique. They also examined the effect of non-stoichiometry of the spinel on the cation distribution. Navrotsky *et al.*^[62] measured the enthalpy change for cation redistribution from 1200 to 973 K.

2. Evaluation and Optimization

Figure 1 shows the calculated optimized phase diagram of the MgO - Al_2O_3 binary system. All phase diagram data are reproduced within experimental error limits. The Al_2O_3 solubilities in spinel were optimized based mainly on the studies of Shirasuka and Yamaguchi^[29] and Viertel and Seifert.^[30]

At 25°C, $MgAl_2O_4$ is a fully normal spinel. At higher temperatures, however, a significant degree of inversion occurs as can be seen in Figure 2. The calculated optimized cation distribution is based mainly on the data of Redfern *et al.*^[55] who appears to have taken care with sample preparation and experimental technique. The calculated cation distribution depends mainly on the optimized parameter I_{MA} .

In the experiments, the cation distribution becomes frozen in as the samples are cooled below $T_{frozen} \sim 973$ K, this temperature being estimated from the results of Redfern *et al.*^[55] as seen in Figure 2. Furthermore, above a temperature of $T_{unquen} \sim 1200$ K, the high temperature cation distribution cannot be retained by quenching, this temperature being estimated very roughly from the results of Wood *et al.*^[59] which appear to level off above this temperature. Hence, above ~ 1200 K the cation distribution can only be determined by *in situ* measurements.

Redfern *et al.*^[55] also investigated the influence of the non-stoichiometry of spinel on the cation distribution and found that the degree of inversion increases with increasing Al_2O_3 dissolution. This possibly explains the scatter in the results of Peterson *et al.*^[58] whose samples had lower lattice parameters than the samples in other studies. Andreozzi *et al.*^[60] recently measured the cation distribution using XRD. However, this technique is not sensitive because there is very little scattering contrast between Mg and Al.^[55] In agreement with the results of Redfern *et al.*, the degree of inversion was calculated to increase with increasing dissolution of Al_2O_3 .

Calculated optimized thermodynamic properties of $MgAl_2O_4$ are shown in Figures 3 to 8. As can be seen in Figure 3, the calculated heat capacity is in good agreement with experimental data. The optimized entropy at 298.15 K is 80.14 J/mol·K which agrees well with the experimental value of 80.58 ± 0.5 J/mol·K of King.^[40] $S_{298.15}^0$ of pure normal spinel in Table I is 80.00 J/mol·K. The difference is due to the slight degree of inversion at 298.15 K. The heat content measurements in Figure 4 were obtained experimentally by quenching samples from a temperature T to 298.15 K. As discussed above, it is assumed that the cation distribution becomes frozen at its value at $T_{frozen} \sim 973$ K when a sample is quenched below this temperature, and that the cation distribution cannot be retained when quenched from temperatures above $T_{unquen} \sim 1200$ K. Therefore, the actual measured enthalpy difference in the quenching experiments, ΔH_{meas} , is assumed to be equal to:

$$T < 973: \Delta H_{meas} = H_T (\text{c.d. at } 973) - H_{298.15} (\text{c.d. at } 973) \quad [7]$$

$$973 < T < 1200: \Delta H_{meas} = H_T (\text{c.d. at } T) - H_{298.15} (\text{c.d. at } T) \quad [8]$$

$$T > 1200: \Delta H_{meas} = H_T (\text{c.d. at } T) - H_{298.15} (\text{c.d. at } 1200) \quad [9]$$

where H_T (c.d. at T') is the enthalpy at T' of a sample having the equilibrium cation distribution of a sample at T'' . This correction to the reported heat contents is of the order of a few kJ/mol. With this correction, the measured and calculated heat contents are in excellent agreement as can be seen in Figure 4.

Navrotsky^[62] measured the annealing enthalpy for cation redistribution from 1200 to 973 K with the assumption that the heat capacity is independent of cation distribution. The calculated value of 1.9 kJ/mol agrees reasonably with the value of 1.1 ± 0.7 kJ/mol reported by Navrotsky.

The enthalpy of formation of $MgAl_2O_4$ from MgO and Al_2O_3 was calculated as -22.7 kJ/mole at 970 K and -21.8 kJ/mole at 1173 K, in good agreement with the experimental data^[44-46] (-24.7 or -22.5 ± 2.5 kJ/mol at 970 K, and -22.3 ± 2.8 kJ/mol at 1173 K). The value initially reported by Navrotsky and Kleppa^[46] was revised by Scheerer and Kleppa^[45] using a more recent value of the enthalpy of dissolution of MgO in $PbO \cdot B_2O_3$. This revised value was used in the optimization in the present study.

The calculated Gibbs energy of formation of MgAl_2O_4 from solid MgO and Al_2O_3 is calculated and compared with experimental data in Figure 5. The data of Taylor and Schmalzried^[47] are not in agreement with the data of other authors. Also it was difficult to reproduce the measurements of Jacob and Jayadevan^[48] who used emf cells with MgF_2 electrolytes as did Taylor and Schmalzried.

The calculated partial pressure of $\text{Mg}(\text{gas})$ at equilibrium with $(\text{MgO} + \text{liquid alloy} + \text{MgAl}_2\text{O}_4)$ compares well with the measurements^[51] as shown in Figure 6. The $\text{F}^*\text{A}^*\text{C}^*\text{T}^*$ ^[19] database was used for the properties of $\text{Mg}(\text{gas})$ and for the activity of Mg in molten Al-Mg alloys. The calculated equilibrium solubility of Mg in the molten Al also agrees well with the reported^[51] solubilities.

Figure 7 compares the calculated and experimental^[52,53] equilibrium pressure of $\text{Mg}(\text{gas})$ for the congruent vaporization of MgO (to $\text{Mg}(\text{g}) + 1/2 \text{O}_2$ in *vacuo*) from MgO and from $\text{MgO} \cdot x\text{Al}_2\text{O}_3$ spinel solutions ($x = 1.0, 2.0$ and 2.8) at various temperatures. The data are reproduced within the experimental error limits.

The enthalpy of formation of the spinel solution ($\text{MgAl}_2\text{O}_4 - \gamma\text{-Al}_{8/3}\text{O}_4$) from MgO and $\alpha\text{-Al}_{8/3}\text{O}_4$ is plotted in Figure 8. At an alumina mole fraction of 1.0, this enthalpy corresponds to the enthalpy of transformation of $4/3$ moles of $\alpha\text{-Al}_2\text{O}_3$ to $4/3$ moles of $\gamma\text{-Al}_2\text{O}_3$. The point of McHale *et al.*^[54] was obtained for nano-sized materials with a correction being made for surface energy. The optimized value of 40 kJ per mole of $\text{Al}_{8/3}\text{O}_4$ is larger than the reported value because the optimized value was chosen to reproduce solubility data of Al_2O_3 not just in MgAl_2O_4 but in several other spinel phases^[15] in the $\text{Fe-Mg-Al-Cr-Co-Ni-Zn-O}$ system (CoAl_2O_4 , NiAl_2O_4 , FeAl_2O_4 and ZnAl_2O_4) simultaneously. If the spinel/(spinel+ Al_2O_3) phase boundary in Figure 1 is extrapolated to a mole fraction of Al_2O_3 of 1.0, the resultant temperature is the equilibrium temperature for the transformation of $\alpha\text{-Al}_2\text{O}_3$ to metastable pure $\gamma\text{-Al}_2\text{O}_3$. Since this temperature must be the same for all spinel systems, similar extrapolations were made for Fe- , Co- , Ni- and Zn-spinels and an average temperature of 2400 K was determined. Taking the above value of 30 kJ per mole of Al_2O_3 for the transformation enthalpy, the entropy of transformation is then calculated as $30000/2400 = 12.500 \text{ J/mol}\cdot\text{K}$. These values are shown in Table I.

B. $\text{CaO-MgO-Al}_2\text{O}_3$ System

1. Summary of Available Experimental Data

The liquidus surface of the $\text{CaO-MgO-Al}_2\text{O}_3$ system is shown in Figure 9. Rankin and Merwin^[21] measured the phase diagram using a classical quenching technique followed by microscopic primary phase determination. The $\text{Ca}_3\text{MgAl}_4\text{O}_8$ compound was first reported by Welch,^[63] who also reported a metastable $\text{Ca}_7\text{MgAl}_{10}\text{O}_{23}$ ternary compound. Majumdar^[64] investigated the primary crystallization region of the ternary $\text{Ca}_3\text{MgAl}_4\text{O}_8$ compound using XRD phase determination on quenched samples. Rao^[65] determined phase diagrams of the CaAl_2O_4 -

MgAl_2O_4 and $\text{CaAl}_4\text{O}_7\text{-MgAl}_2\text{O}_4$ sections using hot stage microscopy. Melnik *et al.*^[66] measured fusion temperatures in the $\text{CaO-Al}_2\text{O}_3\text{-MgAl}_2\text{O}_4\text{-MgO}$ section but details of the experimental technique were not given and the measured data are ambiguous. Recently, De Aza *et al.*^[67,68] investigated the phase diagram of the $\text{CaO-MgO-Al}_2\text{O}_3$ section extensively using a quenching technique (air quenched at $T < 1725^\circ\text{C}$; quenched inside the furnace by switching off the power at $T > 1725^\circ\text{C}$) in the temperature range from 1350° to 2000°C . The phases in the quenched samples were determined by XRD, and several compositions of the spinel solution were also measured by EPMA (WDS). This study reconfirmed the existence of the $\text{CaMg}_2\text{Al}_{16}\text{O}_{27}$ and $\text{Ca}_2\text{Mg}_2\text{Al}_{28}\text{O}_{46}$ phases originally reported by Gobbels *et al.*^[69] and Iyi *et al.*^[70] and showed that these phases actually exist as solid solutions over very limited ranges of composition.^[68-70] In the present study, these compounds were treated as stoichiometric. The liquidus isotherms at 1550° , 1600° and 1650°C were also measured by Ohta and Suito^[71] and Hino *et al.*^[72] from analysis of slags at saturation in CaO , MgO , or Al_2O_3 crucibles.

Allibert *et al.*^[73] measured the activities of CaO and MgO in molten slags at 1687°C by a mass spectrometric/effusion cell technique. Activities of Al_2O_3 were then calculated from the Gibbs-Duhem equation. Hino *et al.*^[72] equilibrated slags and liquid Cu at 1600°C in carbon crucibles under a CO atmosphere and measured the Al , Ca and Mg contents in the liquid Cu . From the known activity coefficients of Al , Ca and Mg in liquid Cu , the activities of Al_2O_3 , CaO and MgO in the liquid slags were computed. Ohta and Suito^[71] employed a similar technique using liquid Fe at 1550° and 1600°C and calculated activities in the molten slags saturated with CaO , MgO or spinel.

2. Evaluation and Optimization

For the molten slag phase, no additional ternary model parameters were used; the properties of the ternary liquid were calculated entirely from the model parameters for the three binary subsystems using an asymmetric "Toop-like" approximation^[12] with $\text{AlO}_{1.5}$ taken as the "asymmetric" component. The entropies and heat capacities of the ternary compounds $\text{Ca}_3\text{MgAl}_4\text{O}_8$, $\text{CaMg}_2\text{Al}_{16}\text{O}_{27}$ and $\text{Ca}_2\text{Mg}_2\text{Al}_{28}\text{O}_{46}$ were estimated as the weighted averages of the entropies and heat capacities of solid MgO , CaO and Al_2O_3 . The enthalpies of formation at 298.15 K were optimized in the present study to reproduce the phase equilibrium measurements. These are the only additional model parameters which were added in the optimization of the ternary system. The calculated liquidus projection is shown in Figure 9.

The calculated primary crystallization fields in the $\text{CaO-MgO-Al}_2\text{O}_3$ system are plotted in Figure 10 along with the experimental data of Rankin and Merwin,^[21] Majumdar,^[63] Rao^[64] and De Aza *et al.*^[67,68] De Aza *et al.*^[67,68] measured liquid compositions along the phase boundaries by EPMA (WDS) analysis of quenched samples. A $\text{Ca}_{12}\text{Al}_{14}\text{O}_{33}$ phase was observed by Rankin and

Merwin and Majumdar. However it was concluded by Nurse *et al.*^[74] that this compound is not stable in the anhydrous CaO-Al₂O₃ system but is only stabilized by the presence of moisture. Unstable Ca₅Al₆O₁₄, Ca₃Al₁₀O₁₈ and β -Al₂O₃ compounds were also observed by Rankin and Merwin. These compounds were not considered in the present study. The primary crystallization fields of CaMg₂Al₁₆O₂₇ and Ca₂Mg₂Al₂₈O₄₆ have not been investigated. Agreement between calculations and measurements is satisfactory as can be seen in Figure 10.

Measured^[21] and calculated liquidus temperatures are compared in Table II. For the first listing in the table, the composition lies in the steepest part of the CaO liquidus (see Figure 9). On the second line in Table II it is shown that a composition change of only 0.7% decreases the calculated liquidus temperature by 87°. The composition (eleventh line in Table II), for which a temperature of 1710°C is calculated, also lies in this region and very close to the boundary of the MgO crystallization field. In general, agreement in Table II is within experimental error limits. Calculated ternary invariant points are listed in Table III along with reported values. The values reported by De Aza *et al.*^[68] are not shown because they were only estimated from widely spread experimental points.

Figure 11 shows the calculated CaO-MgO-Al₂O₃ phase diagram section. Phase relations in this section were comprehensively measured by De Aza *et al.*^[67,68] Since the samples were air quenched at $T < 1725^\circ\text{C}$ and were quenched inside the furnace by switching off the power at $T > 1725^\circ\text{C}$, the quenching, especially from high temperatures, may have been too slow to assure that the equilibrium phase assemblages were retained. Solid phases could have precipitated during quenching. For example, CaAl₁₂O₁₉ is shown as stable up to 1875°C, although the melting temperature of CaAl₁₂O₁₉ has been reported^[11] to be about 1830°C. Because liquidus temperatures are well predicted over a wide range of compositions in the ternary system (see Table II), the inconsistency between De Aza *et al.*'s measurements and the calculations in Figure 11 could be due to experimental errors caused by the quenching process. The enthalpies of the two ternary compounds, CaMg₂Al₁₆O₂₇ and Ca₂Mg₂Al₂₈O₄₆ were optimized assuming that reported temperatures in Figure 11 are 30° to 50° too high. With this provision, the complex phase relations in the CaO-MgO-Al₂O₃ section are satisfactorily reproduced.

Calculated liquidus isotherms of the CaO-MgO-Al₂O₃ system at 1550°, 1600° and 1650°C are compared with experimental data^[71,72] in Figure 12. Agreement is within experimental error limits.

The CaAl₄O₇-MgAl₂O₄ phase diagram section reported by Rao^[65] is compared with calculations in Figure 13. Agreement is not good. Hallstedt^[3] observed similar disagreement with his calculations. However, the calculations are consistent with liquidus measurements of other authors in the same composition range. Also, as can be seen in Figure 13, extrapolation of Rao's points to zero wt% MgAl₂O₄ gives a liquidus temperature which is much higher than that obtained in the earlier^[11] evaluation of the

CaO-Al₂O₃ binary system in which all available binary data were considered. Similarly, the phase diagram measurements of Rao^[65] in the CaAl₂O₄-MgAl₂O₄ section (up to 20 wt% MgAl₂O₄) are not well reproduced unless it is assumed that excess Al₂O₃ was present in the experiments. This observation was also made by Hallstedt.^[3]

Calculated iso-activity curves in CaO-MgO-Al₂O₃ liquid slags are shown in Figures 14 and 15. The calculations are not in good agreement with the data of Ohta and Suito,^[71] Hino *et al.*^[72] and Allibert *et al.*^[73] However, the disagreement among the different authors is as great as their disagreement with the calculations. The activities of CaO reported by Ohta and Suito were calculated by Ohta and Suito from the measured equilibrium concentration of Ca in molten Fe in equilibrium with the slags, using their own assessed value of the activity coefficient of Ca in Fe. However, this activity coefficient is not well-known and could be in serious error.

C. MgO-Al₂O₃-SiO₂ System

1. Summary of Available Experimental Data

The liquidus projection of the MgO-Al₂O₃-SiO₂ system is shown in Figure 16. Greig^[75] studied the liquid miscibility gap using a quenching technique. Rankin and Merwin^[76] investigated the phase diagram mainly below 1550°C using a classical quenching technique. They determined the primary phase regions of pyroxene, forsterite, spinel, Al₂O₃, SiO₂ and the ternary cordierite (Mg₂Al₄Si₅O₁₈) phase. The unstable sillimanite (Al₂SiO₅) phase was observed instead of mullite at certain compositions. Later, Schreyer and Schairer^[77] comprehensively investigated the phase equilibria related to the ternary cordierite phase. Keith and Schairer^[78] investigated the tiny stability field of sapphirine using a quenching technique. Aramaki and Roy^[79] studied the phase boundary between mullite and corundum using a quenching technique with optical and XRD phase identification. Schlaut and Roy^[80] investigated the periclase (MgO) solid solution. Both Al₂O₃ and SiO₂ were reported to be soluble. However, in an earlier evaluation of the MgO-SiO₂ system^[12] it was concluded that the solubility of SiO₂ in solid MgO is negligible. Onuma and Arima^[81] investigated the solubilities of Al³⁺ in the MgSiO₃ pyroxene phase using a technique of quenching with optical and XRD phase analysis. They found that proto-enstatite (MgSiO₃) dissolves Mg-Tschermak MgAl₂SiO₆ up to about 6 wt% at a pressure of 1 bar. Anastasiou and Seifert^[82] measured the solubility of Al₂O₃ in ortho-enstatite at pressures of 1 to 5 kbar using a quenching technique, finding a nearly pressure-independent solubility of about 5 wt% near 1000°C.

Cordierite has two polymorphic forms. Low temperature cordierite has a completely ordered orthorhombic structure (*Cccm*). It transforms to the high temperature form with a hexagonal structure (*P6/mmc*) with long range ordering of Al and Si at about 1450°C, before

melting at 1460°C. Cordierite exhibits a range of solid solution, dissolving up to approximately 20 wt% of the theoretical compound Mg-beryl ($\text{Mg}_3\text{Al}_2\text{SiO}_{23}$).^[76,77,83] Smart and Glasser^[83] reported very complex phase equilibria involving the cordierite solid solution within a very narrow range of composition and temperature. The ternary sapphirine phase exhibits a very limited range of solid solution over the composition range $\text{Mg}_7\text{Al}_{22-x}\text{Si}_{0.75x}\text{O}_{40}$ ($1.5 < x < 5.6$).^[83] These complexities of cordierite and sapphirine were not considered in the present study. For the sake of simplicity, only orthorhombic cordierite was considered, and it and sapphirine were taken to be stoichiometric ternary compounds. The formula of sapphirine was assumed to be $\text{Mg}_4\text{Al}_{10}\text{Si}_2\text{O}_{23}$ following Osborn and Muan^[84] and Foster.^[85]

Sub-solidus phase equilibria were investigated by several authors^[83,85-87] using a sintering technique and X-ray phase determination. Smart and Glasser^[86] and Foster^[85] reported that the (sapphirine + corundum + mullite) phase assemblage transformed to (spinel + mullite + corundum) above about 1460°C. Smart and Glasser^[86] reported that the (sapphirine + cordierite + corundum) phase assemblage transformed to (sapphirine + cordierite + mullite) above about 1386°C. Sakai and Kawasaki^[87] found that the (MgSiO_3 + cordierite + spinel) phase assemblage transformed to (Mg_2SiO_4 + cordierite + spinel) at a temperature between 1000° and 1050°C.

The thermodynamic properties of cordierite and sapphirine have been measured. Weller and Kelley^[88] measured the heat capacity of stoichiometric ordered orthorhombic cordierite at low temperatures using adiabatic calorimetry. Geiger and Voigtlander^[89] measured the heat capacity of cordierite from 330K to 950K using differential scanning calorimetry (DSC). The heat content of stoichiometric cordierite was measured by Pankratz and Kelly^[90] and Muller *et al.*^[91] using calorimetry. No heat capacity measurements for sapphirine ($\text{Mg}_4\text{Al}_{10}\text{Si}_2\text{O}_{23}$) have been reported. Charlu *et al.*^[92] measured enthalpies of formation of $4\text{MgO} \cdot 5\text{Al}_2\text{O}_3 \cdot 2\text{SiO}_2$ sapphirine and aluminous ortho-enstatite, $(\text{MgSiO}_3)_{0.9}(\text{Al}_2\text{O}_3)_{0.1}$, from the oxides at 970K using $2\text{PbO} \cdot \text{B}_2\text{O}_3$ solution calorimetry. Roy and Navrotsky^[93] measured the enthalpy of $\text{MgO} \cdot \text{Al}_2\text{O}_3 \cdot \text{SiO}_2$ glasses by $2\text{PbO} \cdot \text{B}_2\text{O}_3$ solution calorimetry at 970K. Courtial and Richet^[94] also measured the heat content of $\text{MgO} \cdot \text{Al}_2\text{O}_3 \cdot \text{SiO}_2$ glasses. However, since both of these experiments investigated the enthalpy of glasses rather than of the molten slag, these data were not used in the present optimizations.

Rein and Chipman^[95] investigated the activity of SiO_2 in ternary liquid slags using the equilibria between slags and Fe-Si-C alloys in graphite or SiC crucibles at 1600°C under pure CO gas atmospheres. Henderson and Taylor^[96] determined the activity of SiO_2 in liquid slags at 1500°C and 1550°C by measuring the equilibrium CO pressure for the equilibrium: $\text{SiO}_2 + \text{C} = \text{SiC} + 2\text{CO}$.

2. Evaluation and Optimization

In the present optimization, three additional ternary model parameters for the liquid slag (Table I) and one

additional model parameter $\Delta_{\text{Mg-Ts}}$ (Table I) for the pyroxene solutions were required to reproduce the available data for the $\text{MgO} \cdot \text{Al}_2\text{O}_3 \cdot \text{SiO}_2$ system.

The entropy and heat capacity of $\text{Mg}_2\text{Al}_4\text{Si}_5\text{O}_{18}$ cordierite (Table I) were taken from Berman.^[97] Its enthalpy of formation was altered by -9 kJ/mol from the value recommended by Berman in order to best reproduce the phase equilibrium data. The enthalpy of formation of $\text{Mg}_4\text{Al}_{10}\text{Si}_2\text{O}_{23}$ sapphirine shown in Table I was optimized in order to reproduce its reported primary crystallization field. Its entropy and heat capacity were estimated as the weighted averages of those of solid MgO , Al_2O_3 and SiO_2 . The optimized enthalpy of formation of sapphirine from the oxides is -188.2 kJ/mol at 970K which may be compared to the reported -161.5 ± 5 kJ/mol.^[92]

The calculated liquidus projection is shown in Figure 16. The primary crystallization fields are plotted again in Figure 17 along with data taken from several studies.^[76-79,81,87]

In general, the calculated cordierite phase field is displaced to the left (towards the $\text{MgO} \cdot \text{SiO}_2$ side) relative to the measurements. This discrepancy can also be seen in Table IV where the calculated invariant points are compared with reported values from several studies.^[76-78,85-87] The calculated and reported invariant temperatures are generally in good agreement, but the calculated invariant liquid compositions are generally shifted by a few wt% to higher MgO and lower Al_2O_3 contents relative to the measured compositions.

In Figure 17, it is seen that Rankin and Merwin^[76] observed spinel as the primary phase at two compositions where the calculations predict MgO . However, small amounts of MgO and MgAl_2O_4 embedded in a glassy phase are difficult to distinguish by optical microscopy.^[98] The calculated liquid miscibility gap extends to 11.5 wt% Al_2O_3 at 1615°C. Greig^[75] reported that the liquid miscibility gap extends to 5 wt% Al_2O_3 at 1600°C. Such a rapid disappearance of the miscibility gap with small additions of Al_2O_3 is surprising and is very difficult to reproduce with the slag model. On the other hand, the measurements in viscous high- SiO_2 slags are very difficult.

Calculated and measured liquidus temperatures are compared in Table V. Agreement with the data of Rankin and Merwin^[76] (from 1918) is reasonable.

The calculated phase diagrams for the cordierite- SiO_2 , cordierite- MgAl_2O_4 , and MgSiO_3 - $\text{MgAl}_2\text{SiO}_6$ sections are presented in Figures 18, 19 and 20. The calculated diagrams agree with the experimental data^[77,81] within the experimental error limits. The enthalpy of formation of aluminous ortho-enstatite, $(\text{MgSiO}_3)_{0.9}(\text{Al}_2\text{O}_3)_{0.1}$, from solid MgO , SiO_2 and Al_2O_3 is calculated as -22.5 kJ/mole at 970K which may be compared with the value of -29.3 ± 0.6 kJ/mol measured by Charlu *et al.*^[92]

It was difficult to reproduce the sub-solidus phase equilibria in this study. The phase assemblage of (sapphirine + corundum + mullite) is calculated to transform to (spinel + mullite + corundum) at 1366°C, which is almost 100°C lower than the reported temperature^[83,85]. The reported three-phase fields of (sapphirine + cordierite + corundum)^[86] and (MgSiO_3 +

cordierite + spinel)^[87] are never calculated to be stable. This discrepancy may be partially due to the fact that solid solubility in cordierite and sapphirine was ignored in the present study.

Figure 21 shows calculated activities of SiO₂ (solid cristobalite standard state) in MgO-Al₂O₃-SiO₂ liquid slags at 1500°, 1550° and 1600°C along with reported values. The discrepancy between the two experimental studies is evident. The calculated activities are closer to the results of Henderson and Taylor.^[96]

In general, the difficulties encountered during optimization of the MgO-Al₂O₃-SiO₂ system were greater than with most other oxide systems which we have evaluated/optimized. Some of the remaining discrepancies may be due to our ignoring solid solubility in cordierite and sapphirine. On the other hand, there have been no extensive phase diagram studies since 1918.^[76]

IV. CONCLUSIONS

A complete critical evaluation of all available phase diagram and thermodynamic data for the MgO-Al₂O₃, CaO-MgO-Al₂O₃ and MgO-Al₂O₃-SiO₂ systems has been carried out, and a database of optimized model parameters has been developed. A wide variety of available data is reproduced within experimental error limits by a very few model parameters. With the present optimized database, it is possible to calculate any phase diagram section for all compositions. The optimized parameters form part of the F*A*C*T* database, which can be used together with the FactSage^[19] software for thermodynamic modeling of various industrial and natural processes.

ACKNOWLEDGEMENT

This project was supported by a CRD grant from the Natural Sciences and Engineering Research Council of Canada in collaboration with INCO, Noranda, Rio Tinto, Teck Cominco, Alcoa, Dupont, Shell, Corning, Pechiney, Norsk Hydro, Sintef, Schott Glas, St.-Gobain Recherche, Mintek and IIS Materials.

REFERENCES

- G. Eriksson, P. Wu and A.D. Pelton: *Calphad*, 1993, vol. 17, pp.189-206.
- B. Hallstedt: *J. Am. Ceram. Soc.*, 1992, vol. 75(6), pp. 1497-1507.
- B. Hallstedt: *J. Am. Ceram. Soc.*, 1995, vol. 78(1), pp. 193-198.
- S.A. Decterov, E. Jak, P.C. Hayes and A.D. Pelton: *Metall. Mater. Trans. B.*, 2001, vol. 32B, pp. 643-657.
- A.D. Pelton and M. Blander: *Proc. 2nd Int. Symp. Metall. Slags and Fluxes*, TMS-AIME, Warrendale, PA. 1994, pp. 281-91.
- A.D. Pelton and M. Blander: *Metall. Trans. B.*, 1986, vol. 17B, pp. 805-815.
- A.D. Pelton and P. Chartrand: *Metall. Mater. Trans. A*, 2001, vol. 32A, pp. 1355-1360.
- A.D. Pelton, S.A. Decterov, G. Eriksson, C. Robelin and Y. Dessureault: *Metall. Mater. Trans. B.*, 2000, vol. 31B, pp. 651-660.
- P. Wu, G. Eriksson and A.D. Pelton: *J. Am. Ceram. Soc.*, 1993, vol. 76, pp. 2065-2075.
- G. Eriksson and A.D. Pelton: *Metall. Trans. B.*, 1993, vol.24B, pp. 807-816.
- P. Wu, G. Eriksson, A.D. Pelton and M. Blander: *ISIJ Inter.*, 1993, vol. 33, pp. 26-35.
- A. D. Pelton: *Calphad*, 2001, vol. 25, pp. 319-328.
- M. Hillert, B. Jansson and B. Sundman: *Z. Metallkd.*, 1988, vol. 79, pp. 81-87.
- H.St.C. O'Neill and A. Navrotsky: *Am. Mineral.*, 1984, vol. 69, pp. 733-753.
- S.A. Decterov, I.-H. Jung, Y.-B. Kang, V. Swamy, E. Jak, D. Kevorkov and A.D. Pelton: "Report for Oxide Database Development," 2002, CRCT, Ecole Polytechnique, Montreal.
- N. Morimoto: *Mineral. Mag.*, 1988, vol. 52, pp. 535-550.
- P. Shi, S.K. Saxena, Z. Zang and B. Sundman: *Calphad*, 1994, vol. 18, pp. 47-69.
- I.-H. Jung, S.A. Decterov and A.D. Pelton: *Metall. Mater. Trans.* "Thermodynamic Modeling of the CaO-MgO-SiO₂ System," (submitted)
- www.factsage.com, Montreal, 2002.
- I.-H. Jung, S.A. Decterov and A.D. Pelton: "Thermodynamic Modeling of the CaO-MgO-Al₂O₃-SiO₂ System," (in preparation)
- G.A. Rankin and H.E. Merwin: *J. Am. Chem. Soc.*, 1916, vol. 38, pp. 568-588.
- A. M. Alper, R.N. McNally, P.H. Ribbe and R.C. Doman: *J. Am. Ceram. Soc.*, 1962, vol. 45, pp. 263-268.
- D. Viechnicki, F. Schmid, and J.W. McCauley: *J. Am. Ceram. Soc.*, 1974, vol. 57, pp. 47-48.
- T. Mori: *Yogyo Kyokaishi*, 1982, vol. 90, pp. 551-552.
- V.S. Stubican and R. Roy: *J. Phys. Chem. Solids*, 1965, vol. 26, pp. 1293-1297.
- A.S. Frenkel, K.M. Shmukler, D.Ya. Sukharevskij and N.V. Gul'ko: *Dokl. Akad. Nauk SSSR*, 1960, vol. 130, pp. 1095-1098.
- A.F. Henriksen and W.D. Kingery: *Ceram. Int.*, 1979, vol. 5, pp. 11-17.
- W.P. Whitney and V.S. Stubican: *J. Am. Ceram. Soc.*, 1971, vol. 54(7), pp. 349-352.
- K. Shirasuka and G. Yamaguchi: *Yogyo Kyokaishi*, 1974, vol. 82(12), pp. 34-37.
- H.U. Viertel and F. Seifert: *Neues Jahrb. Mineral., Abh.*, 1980, vol. 140, pp. 89-101.
- D. M. Roy, R. Roy and E.F. Osborn: *Am. J. Sci.*, 1953, vol. 251, pp. 337-361.
- H. Saalfeld and H. Jagodzinski: *Z. Krist.*, 1957, vol. 109, pp. 87-109.
- A.M. Lejus: *Rev. Int. Hautes Temp. Refract.*, 1964, vol. 1, pp. 53-95.
- A. Navrotsky, B.A. Wechsler, K. Geisinger and F. Seifert: *J. Am. Ceram. Soc.*, 1986, vol. 69, pp. 418-422.
- A.M. Lejus and R. Collongues: *Compt. Rend.*, 1962, vol. 254, pp. 2780-2781.
- Y.-M. Chiang and W.D. Kingery: *J. Am. Ceram. Soc.*, 1989, vol. 72, pp. 271-277.
- K. Fujii, T. Nagasaka and M. Hino: *ISIJ Inter.*, 2000, vol. 40, pp. 1059-1066.
- S.K. Roy and R.L. Coble: *J. Am. Ceram. Soc.*, 1968, vol. 51, pp. 1-6.

39. K. Ando and M. Momoda: *J. Ceram. Soc. Jpn. Int. Ed.*, 1987, vol. 95, pp. 343-347.
40. E.G. King: *J. Phys. Chem.*, 1955, vol. 59(3), pp. 218-219.
41. K.R. Bonnickson: *J. Phys. Chem.* 1955, vol. 59(3), pp. 220-221.
42. Ya. A. Landa and I.A. Naumova: *Ozneupory*, 1979, (6), pp. 9-12.
43. P. Richet and G. Fiquet: *J. Geophys. Res., B*, 1991, vol. 96(B1), pp. 445-456.
44. T.V. Charlú, R.C. Newton and O.J. Kleppa: *Geochim. Cosmochim. Acta*, 1975, vol. 39, pp. 1487-1497.
45. J. A. Shearer and O.J. Kleppa: *J. Inorg. Nucl. Chem.*, 1973, vol. 35, pp. 1073-1078.
46. A. Navrotsky and O.J. Kleppa: *J. Inorg. Nucl. Chem.*, 1968, vol. 30, pp. 479-498.
47. R.W. Taylor and H. Schmalzried: *J. Phys. Chem.*, 1964, vol. 68(9), pp. 2444-2449.
48. K.T. Jacob, K.P. Jayadevan and Y. Waseda: *J. Am. Ceram. Soc.*, 1998, vol. 81, pp. 209-212.
49. L. Chamberlin, J.R. Beckett and E. Stolper: *Am. Mineral.*, 1995, vol. 80, pp. 285-296.
50. E. Rosen and A. Muan: *J. Am. Ceram. Soc.*, 1966, vol. 49(2), pp. 107-108.
51. K. Grjotheim, O. Herstad and J.M. Toguri: *Can. J. Chem.*, 1961, vol. 39, pp. 443-450.; K. Grjotheim, O. Herstad and J.M. Toguri: *Can. Min. Metall. Bull.*, 1962, vol. 55(6), pp. 396-399.
52. R.L. Altman: *J. Phys. Chem.*, 1963, vol. 67, pp. 366-369.
53. T. Sasamoto, H. Hara and T. Sata: *Bull. Chem. Soc. Jpn.*, 1981, vol. 54, pp. 3327-33.
54. J.M. McHale, A. Auroux, A.J. Perrotta and A. Navrotsky: *Science*, 1997, vol. 277, pp. 788-791.
55. S.A.T. Redfern, R.J. Harrison, H.St.C. O'Neill and D.R.R. Wood: *Am. Mineral.*, 1999, vol. 84, pp. 299-310.
56. H. Maekawa, S. Kato, K. Kawamura and T. Yokokawa: *Am. Mineral.*, 1997, vol. 82, pp. 1125-1132.
57. R.L. Millard, R.C. Peterson and B.K. Hunter: *Am. Mineral.*, 1992, vol. 77, pp. 44-52.
58. R.C. Peterson, G.A. Lager and R.L. Hitterman: *Am. Mineral.*, 1991, vol. 76, pp. 1455-1458.
59. B.J. Wood, R.J. Kirkpatrick and B. Montez: *Am. Mineral.*, 1986, vol. 71, pp. 999-1006.
60. G.B. Andreozzi, F. Princivalle, H. Skogby and A.D. Giusta: *Am. Mineral.*, 2000, vol. 85, pp. 1164-1171.
61. T. Yamanaka and Y. Takeuchi: *Z. Kristallogr.*, 1983, vol. 165, pp. 65-78.
62. A. Navrotsky: *Am. Mineral.*, 1986, vol. 71, pp. 1160-69.
63. J. H. Welch: *Nature*, 1961, vol. 191, pp.559-560.
64. A.J. Majumdar: *Trans. Br. Ceram. Soc.*, 1964, vol. 63, pp.347-364.
65. M.R. Rao: *J. Am. Ceram. Soc.*, 1968, vol. 51, pp.50-54.
66. M.T. Melnik, A.A. Kachura and N.V. Mokritskaya: *Ogneupory*, 1989, vol. 222(4), pp. 27-28.
67. A.H. De Aza, P. Pena and S. De Aza: *J. Am. Ceram. Soc.*, 1999, vol. 82, pp. 2193-203.
68. A.H. De Aza, J.E. Iglesias, P. Pena and S. De Aza: *J. Am. Ceram. Soc.*, 2000, vol. 83, pp. 919-927.
69. M. Gobbels, E. Woermann and J. Jung: *J. Solid State Chem.*, 1995, vol. 120, pp. 358-63.
70. N. Iyi, M. Gobbels and Y. Matsui: *J. Solid State Chem.*, 1995, vol. 120, pp. 364-371.
71. H. Ohta and H. Suito: *ISIJ Inter.*, 1996, vol. 36, pp.983-990.
72. M. Hino, S. Kinoshita, Y. Ehara, H. Itoh and S. Ban-Ya: *Proc. 5nd Int. Conf. Molten Slags, Fluxes and Salts*, Sydney, 1997, pp. 53-57.
73. M. Allibert, C. Chatillon and R. Lourtau: *Rev. Int. Hautes Temp. Refract.*, 1979, vol. 16, pp. 33-37.
74. R. W. Nurse, J.H. Welch and A.J. Majumdar: *Trans. Br. Ceram. Soc.*, 1965, vol. 64, pp. 409-418.
75. J.W. Greig: *Amer. J. Sci.*, 1927, vol. 13, pp.1-44.
76. G.A. Rankin and H.E. Merwin: *Amer. J. Sci.*, 1918, 4th ser., vol. 45, pp. 301-325.
77. W. Schreyer and J.F. Schairer: *J. Petrol.*, 1961, vol. 2, pp. 324-406.; W. Schreyer and J.F. Schairer : *Carnegie Inst. Washington Year Book*, 1961, YB.60., pp. 144-147.
78. M.L. Keith and J.F. Schairer: *J. Geol.*, 1952, vol. 60(2), pp. 181-186
79. S. Aramaki and R. Roy: *J. Am. Ceram. Soc.*, 1959, vol. 42(12), pp. 644-645.
80. C.M. Schlautd and D.M. Roy: *J. Am. Ceram. Soc.*, 1965, vol. 48, pp. 248-51.
81. K. Onuma and M. Arima: *J. Japan Assoc. Min. Petr. Econ. Geol.*, 1975, vol. 70, pp. 53-60.
82. P. Anastasiou and F. Sefert: *Contrib. Mineral. Petrol.*, 1972, vol. 34, pp. 272-87.
83. R.M. Smart and F.P. Glasser: *Ceram. Int.*, 1981, vol. 7(3), pp. 90-97.
84. E.F. Osborn and A. Muan: "Phase Equilibrium Diagram of Oxide System", Amer. Ceram. Soc., Columbus, Ohio, 1960.
85. W.R. Foster: *J. Am. Ceram. Soc.*, 1950, vol. 33(3), pp. 73-84.
86. R.M. Smart and F.P. Glasser: *J. Mater. Sci.*, 1976, vol. 11, pp. 1459-64.
87. S. Sakai and T. Kawasaki: *Ganko*, 1998, vol. 93(1), pp. 18-26.
88. W.W. Weller and K.K. Kelley: *U.S. Bur. Mines Rep. Invest.*, 6343, 1963, 7p.
89. C.A. Geiger and H. Voigtlander: *Contrib. Mineral. Petrol.*, 2000, vol. 138, pp. 46-50.
90. L.B. Pankratz and K.K. Kelley: *U.S. Bur. Mines Rep. Invest.*, 6555, 1964, 7p.
91. R. Muller, R. Naumann and S. Reinsch: *Thermochimica Acta*, 1996, vol. 280/281, pp. 191-204.
92. T.V. Charlú, R.C. Newton and O.J. Kleppa: *Geoch. Cosmochim. Acta*, 1975, vol. 39, pp. 1487-97.
93. B.N. Roy and A. Navrotsky: *J. Am. Ceram. Soc.*, 1984, vol. 67, pp. 606-610.
94. P. Courtial and P. Richet: *Geochim. Cosmochim. Acta*, 1993, vol. 57, pp. 1267-1275.
95. R.H. Rein and J. Chipman: *Trans. Metall. Soc. AIME*, 1965, vol. 233, pp. 415-425.
96. D. Henderson and J. Taylor: *JISI*, 1966, vol. 204, pp. 39-43.
97. R.G. Berman: *J. Petrology*, 1988, vol. 29, pp. 445-522.
98. A.T. Prince: *J. Am. Ceram. Soc.*, 1954, vol. 37, pp. 402-408.

Table I. Optimized Model Parameters of the CaO-MgO-Al₂O₃ and MgO-Al₂O₃-SiO₂ Systems (J/mol).

Ternary Compounds		
	$H_{298.15}^{\circ}$ (J/mol)	$S_{298.15}^{\circ}$ and C_P (J/mol·K)
Ca ₃ MgAl ₄ O ₁₀	-5971170.0	$S_{298.15}^{\circ} = 3 S_{298.15}^{\circ}(\text{CaO}) + S_{298.15}^{\circ}(\text{MgO}) + 2 S_{298.15}^{\circ}(\text{Al}_2\text{O}_3)$ $C_P = 3 C_P(\text{CaO}) + C_P(\text{MgO}) + 2 C_P(\text{Al}_2\text{O}_3)$
CaMg ₂ Al ₁₆ O ₂₇	-15438690.0	$S_{298.15}^{\circ} = S_{298.15}^{\circ}(\text{CaO}) + 2 S_{298.15}^{\circ}(\text{MgO}) + 8 S_{298.15}^{\circ}(\text{Al}_2\text{O}_3)$ $C_P = C_P(\text{CaO}) + 2 C_P(\text{MgO}) + 8 C_P(\text{Al}_2\text{O}_3)$
Ca ₂ Mg ₂ Al ₂₈ O ₄₆	-26217079.9	$S_{298.15}^{\circ} = 2 S_{298.15}^{\circ}(\text{CaO}) + 2 S_{298.15}^{\circ}(\text{MgO}) + 14 S_{298.15}^{\circ}(\text{Al}_2\text{O}_3)$ $C_P = 2 C_P(\text{CaO}) + 2 C_P(\text{MgO}) + 14 C_P(\text{Al}_2\text{O}_3)$
Mg ₂ Al ₄ Si ₅ O ₁₈	-9167727.0	$^{[97]} S_{298.15}^{\circ} = 417.9700$ $^{[97]} C_P = 954.39 - 370210000T^{-3} - 2317300T^{-2} - 7962.3T^{-0.5}$
Mg ₄ Al ₁₀ Si ₂ O ₂₃	-12790590.2	$S_{298.15}^{\circ} = 4 S_{298.15}^{\circ}(\text{MgO}) + 5 S_{298.15}^{\circ}(\text{Al}_2\text{O}_3) + 2 S_{298.15}^{\circ}(\text{SiO}_2, \text{tridymite})$ $C_P = 4 C_P(\text{MgO}) + 5 C_P(\text{Al}_2\text{O}_3) + 2 C_P(\text{SiO}_2, \text{tridymite})$

Data for all other compounds were taken from Wu *et al.*^[9] and Eriksson *et al.*^[10]

Liquid Oxide: CaO-MgO-AlO_{1.5} and MgO-AlO_{1.5}-SiO₂

$$\Delta g_{\text{MgO}, \text{AlO}_{1.5}}^{\circ} = -31518.04$$

$$q_{\text{MgO}, \text{AlO}_{1.5}}^{03} = -225764.46 + 66.72T$$

$$q_{\text{MgO}, \text{AlO}_{1.5}}^{06} = 80688.02$$

$$q_{\text{MgO}, \text{AlO}_{1.5}}^{07} = -48435.77$$

$$q_{\text{MgO}, \text{AlO}_{1.5}(\text{SiO}_2)}^{001} = 104600.0$$

$$q_{\text{MgO}, \text{SiO}_2(\text{AlO}_{1.5})}^{002} = 62395.99 - 52.30T$$

$$q_{\text{AlO}_{1.5}, \text{SiO}_2(\text{MgO})}^{001} = 250705.0 - 167.36T$$

All other model parameters for binary systems were reported earlier.^[9-11]

The quasichemical parameters are defined in Reference [8].

Monoxide: MgO-CaO-AlO_{1.5}

$$G_{\text{AlO}_{1.5}}^{\circ} = 1/2 G^{\circ}(\alpha - \text{Al}_2\text{O}_3) + 38702.0$$

$$q_{\text{MgO}, \text{AlO}_{1.5}}^{00} = 1548080 - 1347.68T + 0.286478T^2$$

Parameters for the MgO-CaO subsystem were obtained previously.^[9]

The polynomial q parameters are defined in Reference [12].

Spinel: $(\text{Mg}^{2+}, \text{Al}^{3+})^{\text{T}}[\text{Mg}^{2+}, \text{Al}^{3+}, \text{Va}]_2^{\text{O}}\text{O}_4$

$$G_{\text{MA}} = G^{\circ}(\text{MgAl}_2\text{O}_4):$$

$$H_{298.15}^{\circ} = -2304994.88$$

$$S_{298.15}^{\circ} = 80.00$$

$$C_P = 795.470 - 0.33724T + 9.92769(10^{-5})T^2 + 79789.79T^{-1} - 761956.61T^{-2} - 14619.66T^{-0.5} \quad (15 \text{ K} < T < 3000 \text{ K})$$

G_{AA} is from Reference [15]

$$\Delta_{\text{MA:MA}} = G_{\text{AA}} + G_{\text{MM}} - G_{\text{MA}} - G_{\text{AM}} = 40000.0$$

$$I_{\text{MA}} = G_{\text{AA}} + G_{\text{AM}} - 2G_{\text{MA}} = 21756.8 + 19.6648T$$

$$\Delta_{\text{MA:MV}} = G_{\text{MM}} + G_{\text{AV}} - G_{\text{MV}} - G_{\text{AM}} = -83680.00$$

$$G_{\text{AV}} = 8G^{\circ}(\gamma\text{-Al}_2\text{O}_3) - 2RT(5\ln 5 - 6\ln 6) - 5G_{\text{AA}}, \text{ where}$$

$$G^{\circ}(\gamma\text{-Al}_2\text{O}_3) = G^{\circ}(\alpha\text{-Al}_2\text{O}_3) + 30000.0 - 12.500T$$

Notations M, A, and V are used for Mg^{2+} , Al^{3+} and vacancy, respectively.

Pyroxene: $(\text{Mg})^{\text{M}2}(\text{Mg}^{2+}, \text{Al}^{3+})^{\text{M}1}(\text{Al}^{3+}, \text{Si}^{4+})^{\text{B}}(\text{Si})^{\text{A}}\text{O}_6$

G_{MS} are from Reference [18] for ortho-, proto-, and low clino-pyroxenes.

$$G_{\text{MS}} + G_{\text{AA}} - G_{\text{AS}} - G_{\text{MA}} = 0.0$$

$$G_{\text{AS}} = G_{\text{MA}}$$

$$\Delta_{\text{Mg-Ts}} = (G_{\text{CaMgSi}_2\text{O}_6}^{\circ} + G_{\text{AA}}) - (G_{\text{Mg}_2\text{Si}_2\text{O}_6}^{\circ} + G_{\text{CaAl}_2\text{SiO}_6}^{\circ}) = 15899.2$$

$L_{\text{MA:A}} = L_{\text{MA:S}}$ are from Reference [20]

Notations M, A, and S are used for Mg^{2+} , Al^{3+} and Si^{4+} , respectively.

$G_{\text{CaMgSi}_2\text{O}_6}^{\circ}$ and $G_{\text{Mg}_2\text{Si}_2\text{O}_6}^{\circ}$ are from previous study by Jung *et al.*^[18]

$G_{\text{CaAl}_2\text{SiO}_6}^{\circ}$ is from F*A*C*T^[19] database.

Gibbs energies of the pure components of the solutions and of all binary stoichiometric compounds are taken from the F*A*C*T^[19] database.

Table II. Comparison of calculated liquidus temperature and primary solid phase with experimentally determined values^[21] in the CaO-MgO-Al₂O₃ system.

Composition (wt%)			Measured (°C)	Calculated (°C)
CaO	MgO	Al ₂ O ₃		
55	3	42	1525-1500, C	1617, C
(54.3)	(3)	(42.7)	-	(1530)
54	3	43	1490-1480, C3A	1487, C
48	4	48	1385-1378, C3A	1327, C3MA2
51	6	43	1450-1435, C3A	1506, M
35.2	2.8	62	1560-1550, CA	1543, CA
45	3	52	1395-1390, CA	1383, CA
42	5	53	1390-1360, CA	1381, CA
37	10	53	1525-1500, Sp	1490, Sp
34	12	54	1610-1575, Sp	1554, Sp
51.5	8	40.5	1540-1500, M	1710, C
45	8	47	1500-1450, M	1501, M
43	8	49	1500-1450, M	1459, M
40	10	50	1535-1510, M	1518, M

Sp: Spinel, $CiMjAk = iCaO \cdot jMgO \cdot kAl_2O_3$

Table III. Comparison of calculated ternary invariant points with experimental results in the CaO-MgO-Al₂O₃ system.

Equilibrium solid phases	Composition (mole %)			Temperature (°C)
	MgO	CaO	Al ₂ O ₃	
CaO + MgO + C3A: Per	8.2	62.9	28.9	1422 calc.
	10.3	61.8	27.9	1450 ± 5 ^[21]
MgO + C3A + C3MA2: Per	8.3	59.7	32.0	1333 calc.
MgO + Sp + C3MA2: Per	11.1	53.6	35.3	1349 calc.
MgO + CA + C3MA2: Per	11.0	53.6	35.4	1350 ^[64]
C3A + CA + C3MA2: Eu	4.9	60.6	34.5	1309 calc.
CA + Sp + C3MA2: Per	9.9	53.7	36.4	1344 calc.
CA + CA2 + Sp: Per	7.4	42.8	49.8	1522 calc.
CA2 + Sp + CM2A8: Per	9.2	28.4	62.4	1690 calc.
CA2 + CM2A8 + C2M2A14: Per	6.6	27.2	66.2	1708 calc.
CA2 + CA6 + C2M2A14: Per	5.5	27.0	67.5	1714 calc.
Sp + CM2A8 + C2M2A14: Per	9.0	21.5	69.5	1758 calc.
CA6 + Sp + C2M2A14: Per	8.4	20.8	70.8	1766 calc.
CA6 + Sp + Al ₂ O ₃ : Per	8.2	20.0	71.8	1778 calc.

Sp: Spinel, $CiMjAk = iCaO \cdot jMgO \cdot kAl_2O_3$

Eu: Eutectic, Per: Peritectic reaction.

calc.: calculated value from optimized phase diagram.

Table IV. Comparison of calculated ternary invariant points with experimental results in the MgO-Al₂O₃-SiO₂ system.

Equilibrium solid phases	Liquid Composition (wt%)			Temperature (°C)
	MgO	Al ₂ O ₃	SiO ₂	
Py + Tr + Cord: Eu	24.0	14.5	61.5	1361 calc.
	20.3	18.3	61.4	1345 ± 5 ^[76]
	20.5	17.5	62	1356 ^[77]
				1345 ± 2 ^[86]
For + Py + Cord: Eu	28.5	16.7	54.8	1371 calc.
	25.0	21.0	54.0	1360 ± 5 ^[76]
	24.87	20.22	54.91	1364 ± 2 ^[77]
				1360 ± 2 ^[86]
For + Sp + Cord: Per	29.3	19.6	51.1	1381 calc.
	25.7	22.8	51.5	1370 ± 5 ^[76]
	24.9	23.0	52.1	1380 ^[87]
				1373 ± 2 ^[86]
Mull + Tr + Cord: Per (<i>Sil instead of Mull</i>)	10.3	23.6	66.1	1445 calc.
	10.0	23.5	66.5	1425 ± 5 ^[76]
				1443 ± 5 ^[78]
				1444 ± 2 ^[86]
Sp + Sa + Cord: Per	22.4	27.9	49.6	1435 calc.
	17.4	33.5	49.1	1453 ± 5 ^[78]
				1448 ± 2 ^[86]
Sp + Mull + Sa: Per	19.0	33.7	47.3	1465 calc.
	16.9	36.8	46.3	1482 ± 3 ^[78]
				1475 ^[85]
Mull + Sa + Cord: Per				1469 ± 2 ^[86]
	18.9	32.6	48.5	1454 calc.
	16.3	34.4	49.3	1460 ± 5 ^[78]
				1454 ± 2 ^[86]
Cor + Sp + Mull: Per	16.1	46.4	37.5	1575 calc.
				1560 ± 15 ^[86]
For + Per + Sp: Per	46.4	15.1	38.5	1645 calc.
	56.0	16.0	28.0	1700 ± 25 ^[78]
Tr + Cris + Py: Per	30.3	6.3	63.4	1465 calc.
Tr + Cris + Mull: Per	9.3	23.2	67.5	1465 calc.
Sil + Sp + Cord: Per	16.1	34.8	49.1	1460 ± 5 ^[76]
Cor + Sp + Sil: Per	15.2	42.0	42.8	1575 ± 5 ^[76]

Tr: Tridymite (SiO₂), Crist: Cristobalite (SiO₂), Mu: Mullite (Al₆Si₂O₁₃), Cor: Corundum (Al₂O₃), Sp: Spinel solution, Py: Pyroxene solution, For: Forsterite (Mg₂SiO₄), Cord: Cordierite (Mg₂Al₄Si₅O₁₈), Sa: Sapphirine (Mg₄Al₁₀Si₂O₂₃), Sil: Sillimanite (Al₂SiO₅). (Sillimanite is unstable)

Eu: Eutectic, Per: Peritectic reaction.

calc.: calculated value from optimized phase diagram.

Table V. Comparison of calculated liquidus temperature and primary solid phase with experimentally determined values^[76] in the MgO-Al₂O₃-SiO₂ system.

Composition (wt%)			Measured (°C)	Calculated (°C)
MgO	Al ₂ O ₃	SiO ₂		
17.5	42.5	40	1583-1570, Sp	1553, Sp
29	23	48	1450-1430, Sp	1448, Sp
20	30	50	1450-1435, Sp	1449, Cord
25	25	50	1410-1390, Sp	1423, Sp
26	23	51	1380-1376, Sp	1407, Cord
35	20	45	1555-1550, For	1497, Sp
35	15	50	1560-1530, For	1485, For
26	21	53	1375-1365, For	1402, Cord
27	18	55	1415-1390, For	1385, Cord
25	20	55	1375-1365, Py	1402, Cord
24	17	59	1383-1370, Py	1385, Cord
35	5	60	1515-1510, Py	1489, Py
21	18	61	1370-1360, Py	1398, Cord
25	12	63	1440-1420, Py	1413, SiO ₂
30	6	64	1500-1498, Py	1488, SiO ₂
25	11	64	1450-1425, Py	1446, SiO ₂
20	15	65	1455-1450, SiO ₂	1449, SiO ₂
11	22	67	1455-1435, SiO ₂	1461, SiO ₂
20	18	62	1355-1352, SiO ₂	1399, Cord
15	15	70	1530-1500, SiO ₂	1538, SiO ₂
16	34	50	1460-1457, Cord	1503, Mull
20	23	57	1400-1375, Cord	1434, Cord
18	30	52	1450-1425, Cord	1458, Cord
25	23	52	1370-1365, Cord	1413, Cord
20	25	55	1415-1400, Cord	1441, Cord
15	30	55	1460-1450, Cord	1470, Mull
23	20	57	1375-1350, Cord	1409, Cord
15	27	58	1450-1425, Cord	1458, Cord
20	20	60	1365-1340, Cord	1416, Cord
15	23	62	1425-1400, Cord	1443, Cord
11	23	66	1450-1440, Cord	1445, SiO ₂

Sp: Spinel, For: Forsterite(Mg₂SiO₄), Py: Pyroxene (MgSiO₃ solution), Cord: Cordierite (Mg₂Al₄Si₅O₁₈), Mull: Mullite.

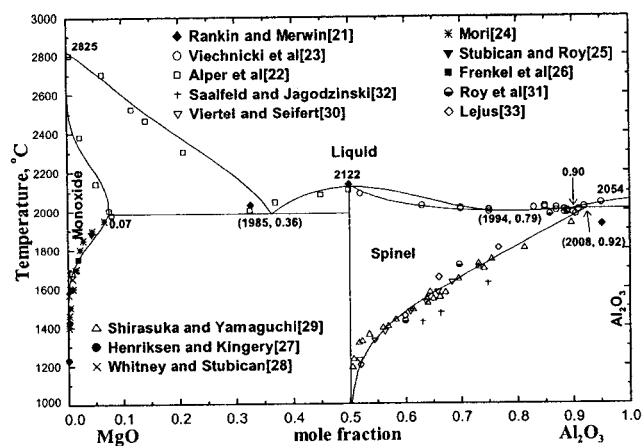


Fig. 1 – Calculated phase diagram of the MgO-Al₂O₃ binary system.

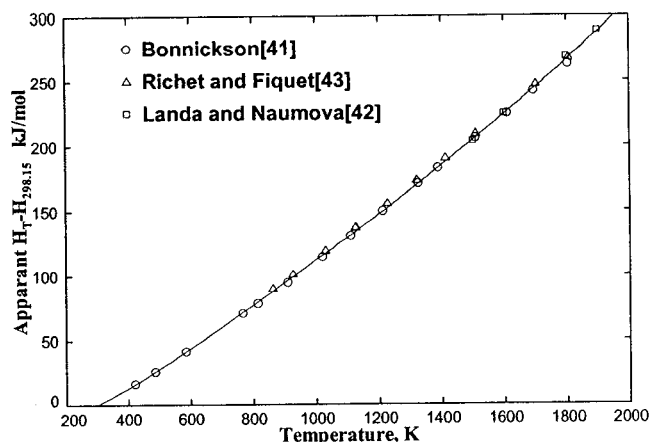


Fig. 4 – Apparent heat content ($H_T-H_{298.15}$) of MgAl₂O₄ as reported in three studies. Line is calculated from the optimized model parameters with correction made for non-equilibrium cation distribution during the experiments. (See text for details.)

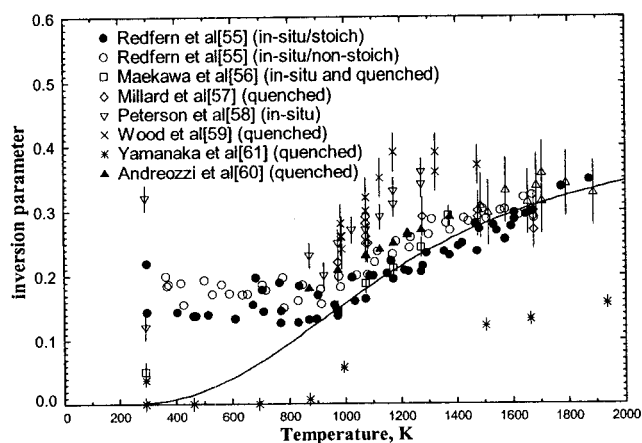


Fig. 2 – Calculated variation of cation distribution in MgAl₂O₄. The inverse parameter is defined as the mole fraction of Al³⁺ on tetrahedral sites.

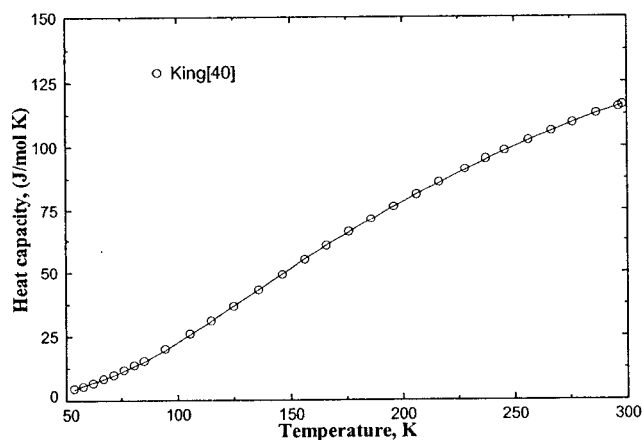


Fig. 3 – Calculated heat capacity of MgAl₂O₄.

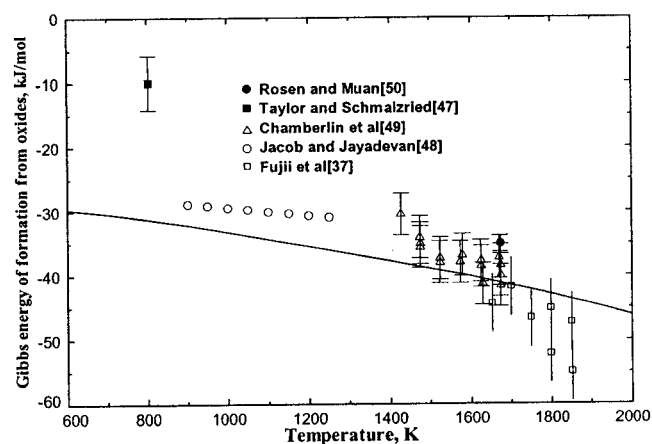


Fig. 5 – Calculated Gibbs energy of formation for MgAl₂O₄ from solid MgO and Al₂O₃.

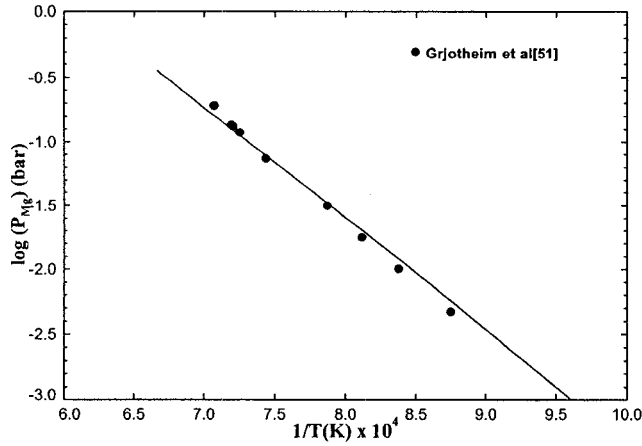


Fig. 6 – Calculated partial pressure of Mg (gas) at equilibrium with (MgO + liquid Al alloy + MgAl_2O_4)

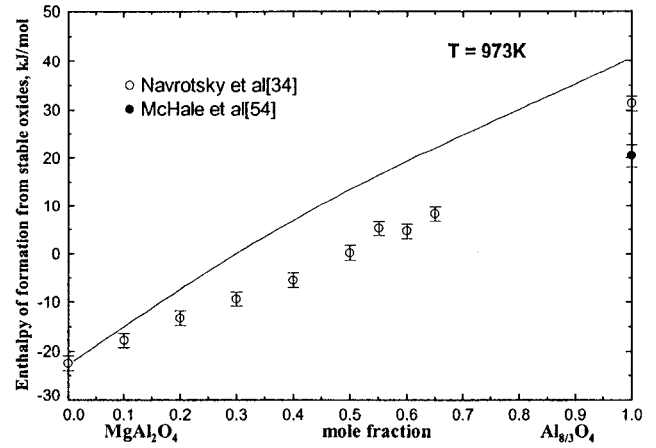


Fig. 8 – Calculated enthalpy of formation of the spinel solution from MgO and $\alpha\text{-Al}_2\text{O}_3$ at 973K.

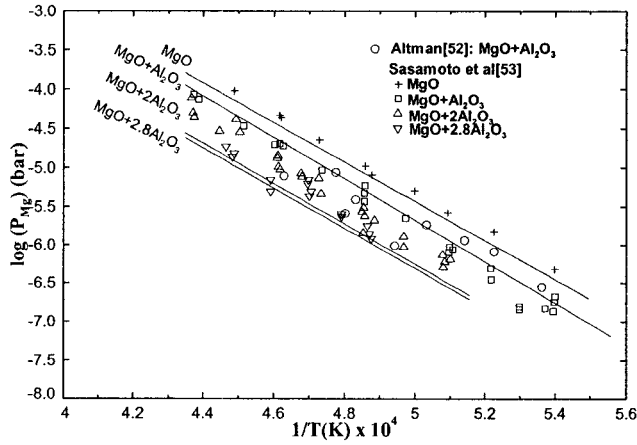


Fig. 7 – Calculated partial pressure of Mg (gas) over MgO and over the spinel solid solution ($\text{MgO} + x\text{Al}_2\text{O}_3$) for congruent vaporization of MgO (to $\text{Mg(g)} + 1/2\text{O}_2$ in vacuo)

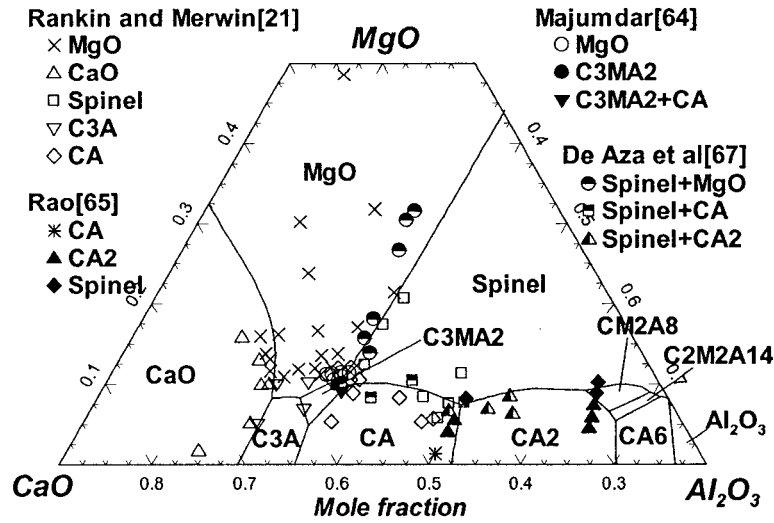


Fig. 10 – Calculated primary crystallization fields of in the CaO-MgO-Al₂O₃ system. (C = CaO, A = Al₂O₃ and M = MgO)

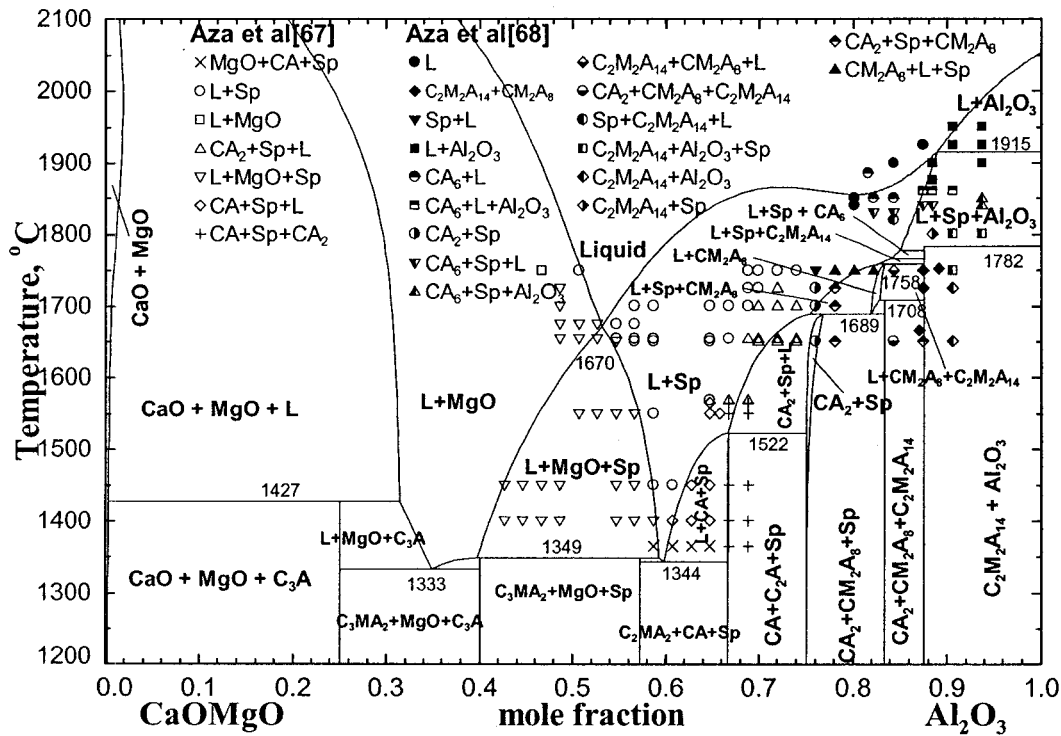


Fig. 11 – Calculated phase diagram for the CaMgO₂-Al₂O₃ section. (Sp = spinel, L = liquid, C = CaO, A = Al₂O₃ and M = MgO)

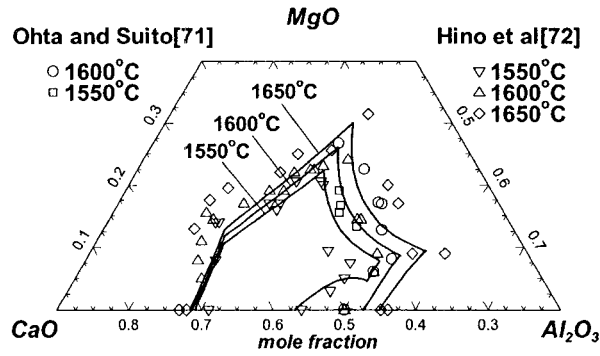


Fig. 12 – Calculated liquidus of the CaO-MgO- Al_2O_3 system at 1550°, 1600° and 1650°C.

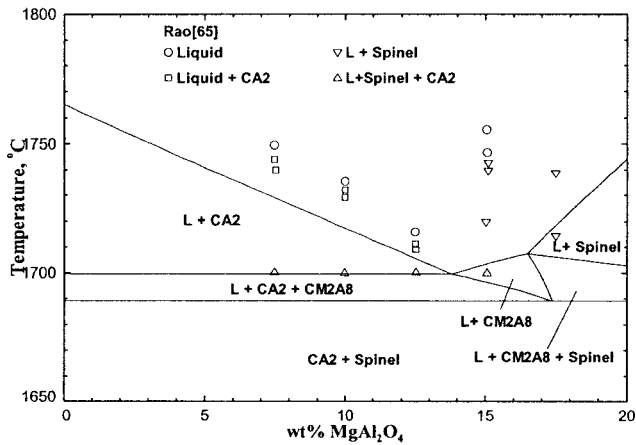
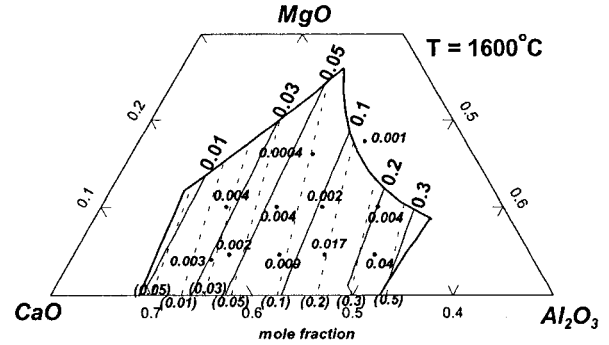
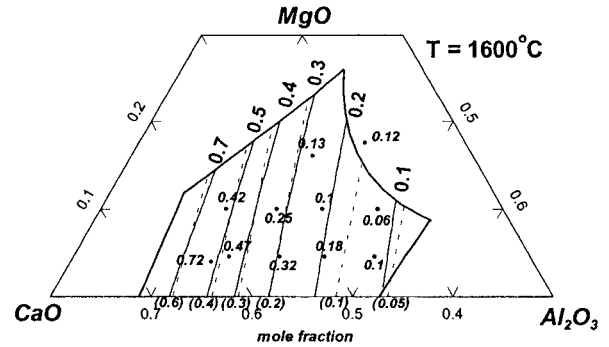


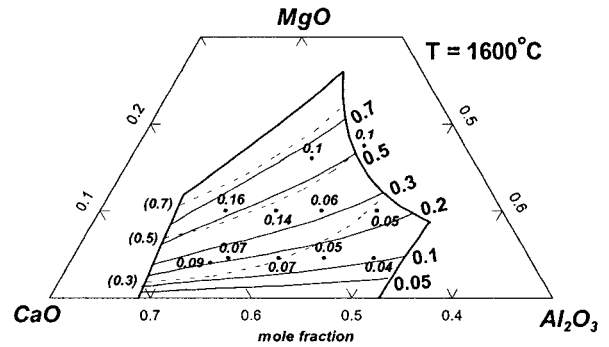
Fig. 13— Calculated phase diagram of the CaAl_4O_7 - MgAl_2O_4 section. (L = liquid, C = CaO, A = Al_2O_3 and M = MgO)



(a)

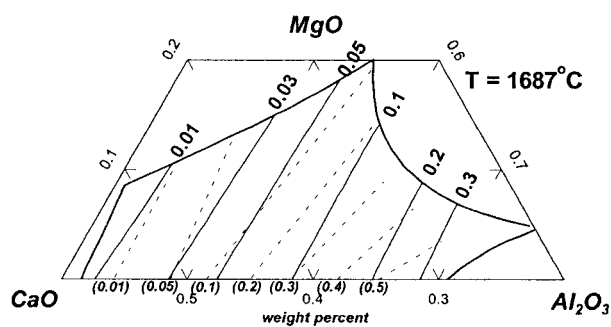


(b)

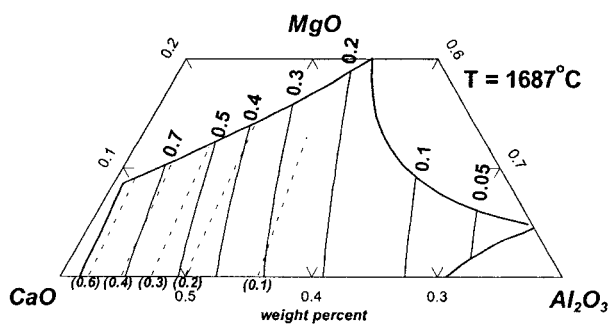


(c)

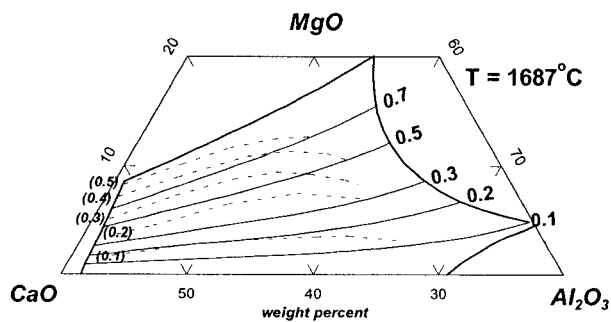
Fig. 14— Calculated activities in CaO-MgO- Al_2O_3 liquid slags at 1600°C. (a) Al_2O_3 (solid standard state) (b) CaO (solid standard state) (c) MgO (solid standard state). Experimental points from Hino *et al.*^[72], and dotted lines from Ohta and Suito.^[71]



(a)



(b)



(c)

Fig. 15— Calculated activities in CaO-MgO- Al_2O_3 liquid slags at 1687°C. (a) Al_2O_3 (solid standard state) (b) CaO (solid standard state) (c) MgO (solid standard state). Dotted lines from Allibert *et al.*^[73]

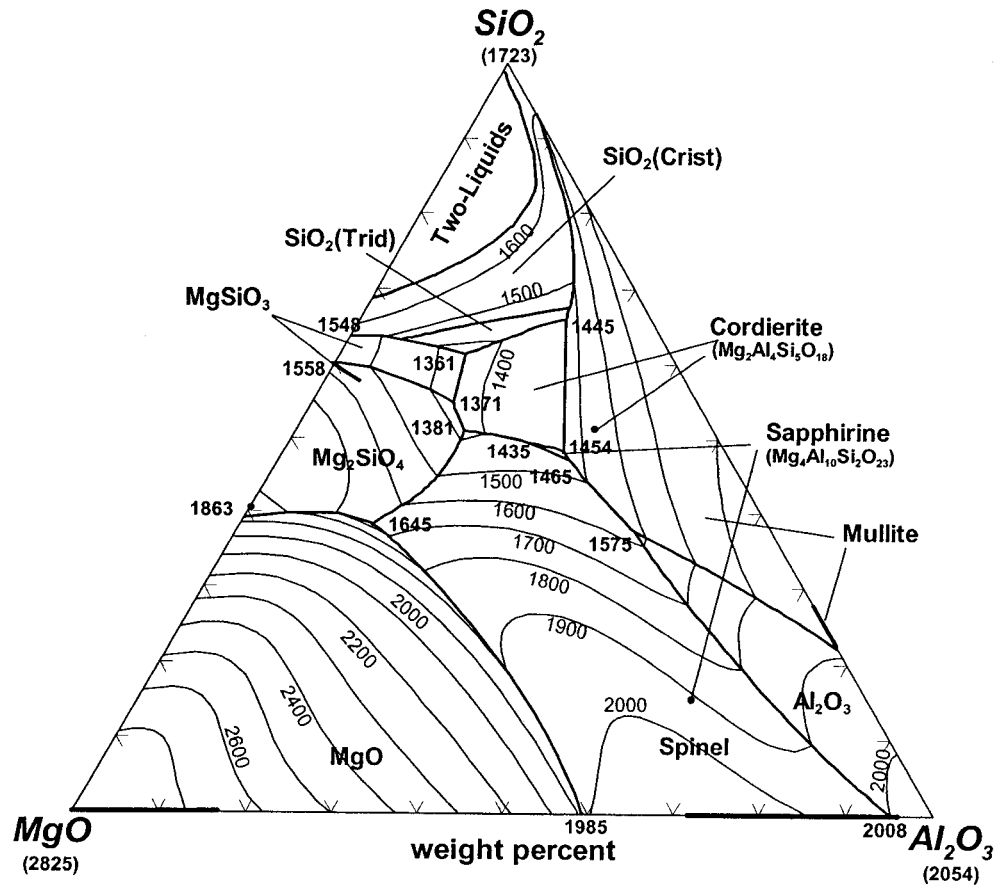


Fig. 16 – Calculated liquidus surface of the $\text{MgO}-\text{Al}_2\text{O}_3-\text{SiO}_2$ system. Temperatures in °C.

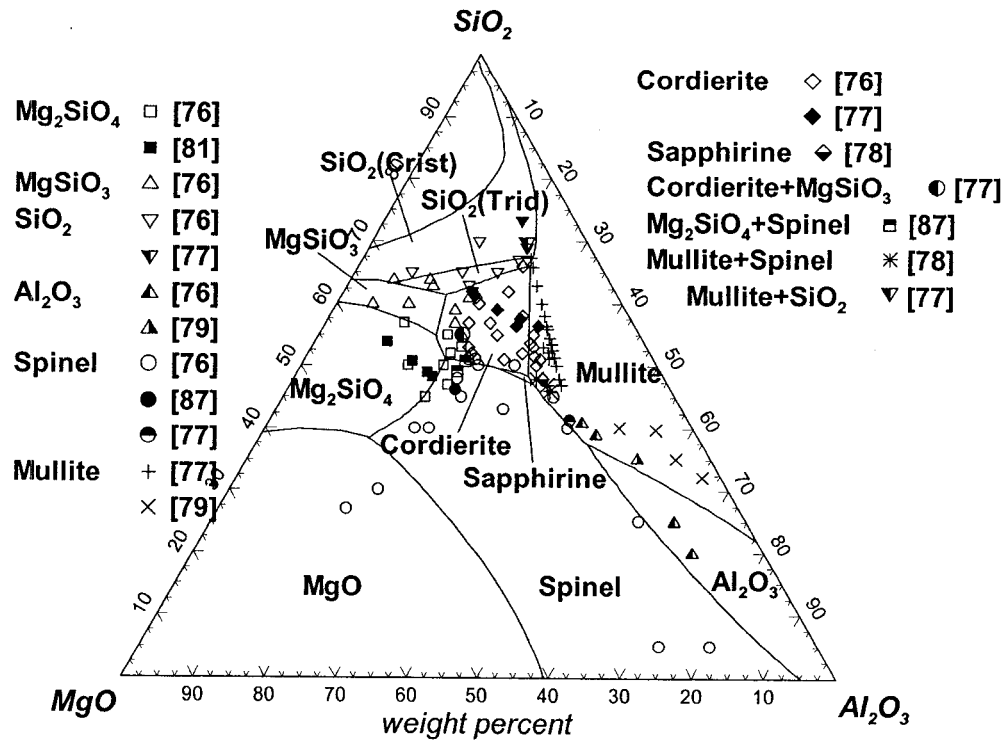


Fig. 17 – Calculated liquidus surface of the MgO-Al₂O₃-SiO₂ system showing primary crystallization fields.

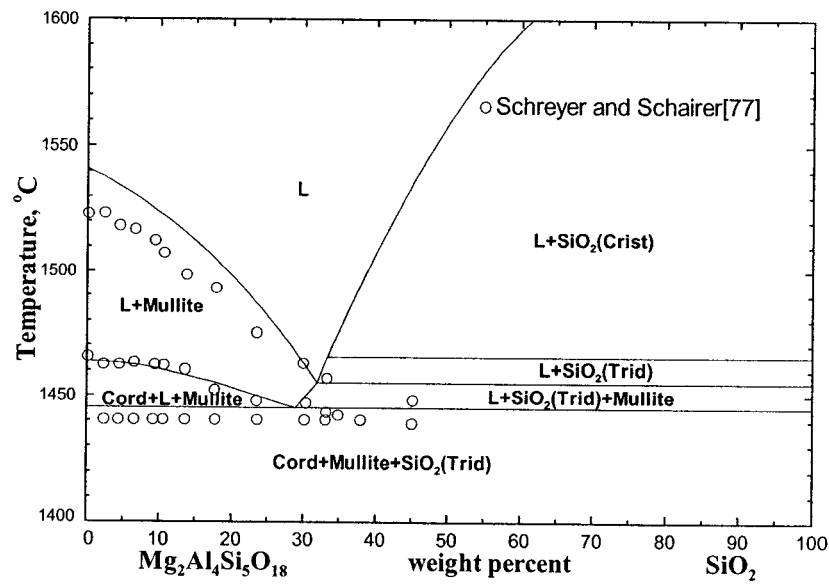


Fig. 18 – Calculated phase diagram for the Mg₂Al₄Si₅O₁₈ (cordierite) - SiO₂ section.

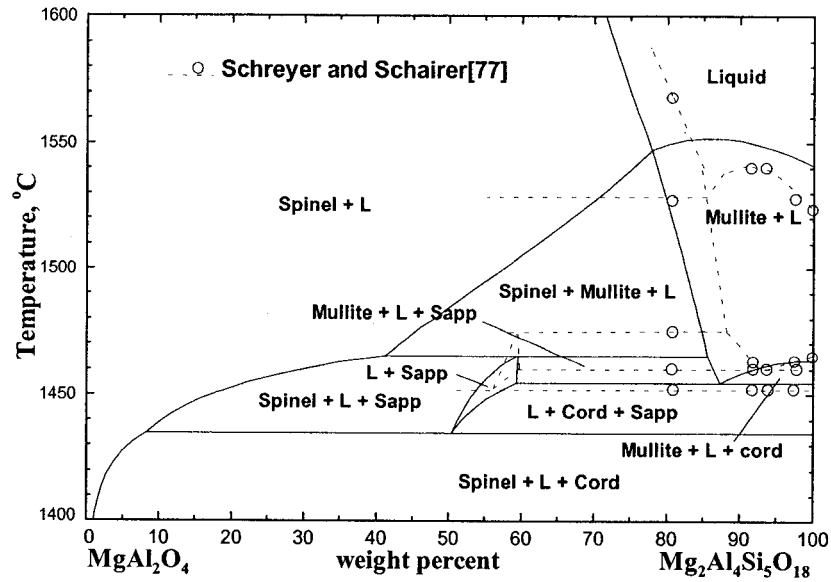


Fig. 19 – Calculated phase diagram for the MgAl_2O_4 - $\text{Mg}_2\text{Al}_4\text{Si}_5\text{O}_{18}$ (cordierite) section. Dotted lines indicate diagram proposed by Schreyer and Schairer.^[77]

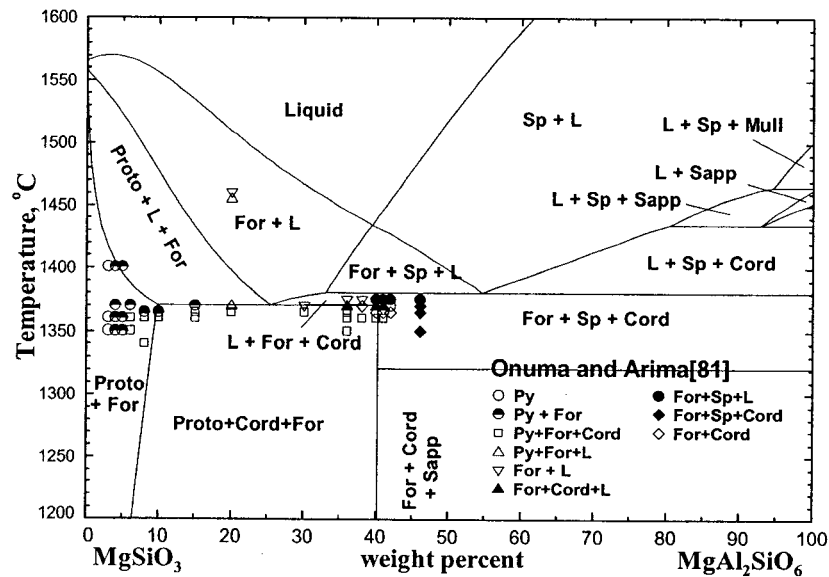


Fig. 20 – Calculated phase diagram for the MgSiO_3 - $\text{MgAl}_2\text{SiO}_6$ section. (For: forsterite, Sp: Spinel, Proto: proto-pyroxene, Cord: cordierite, Sapp: sapphirine, L: liquid and Mull: mullite)

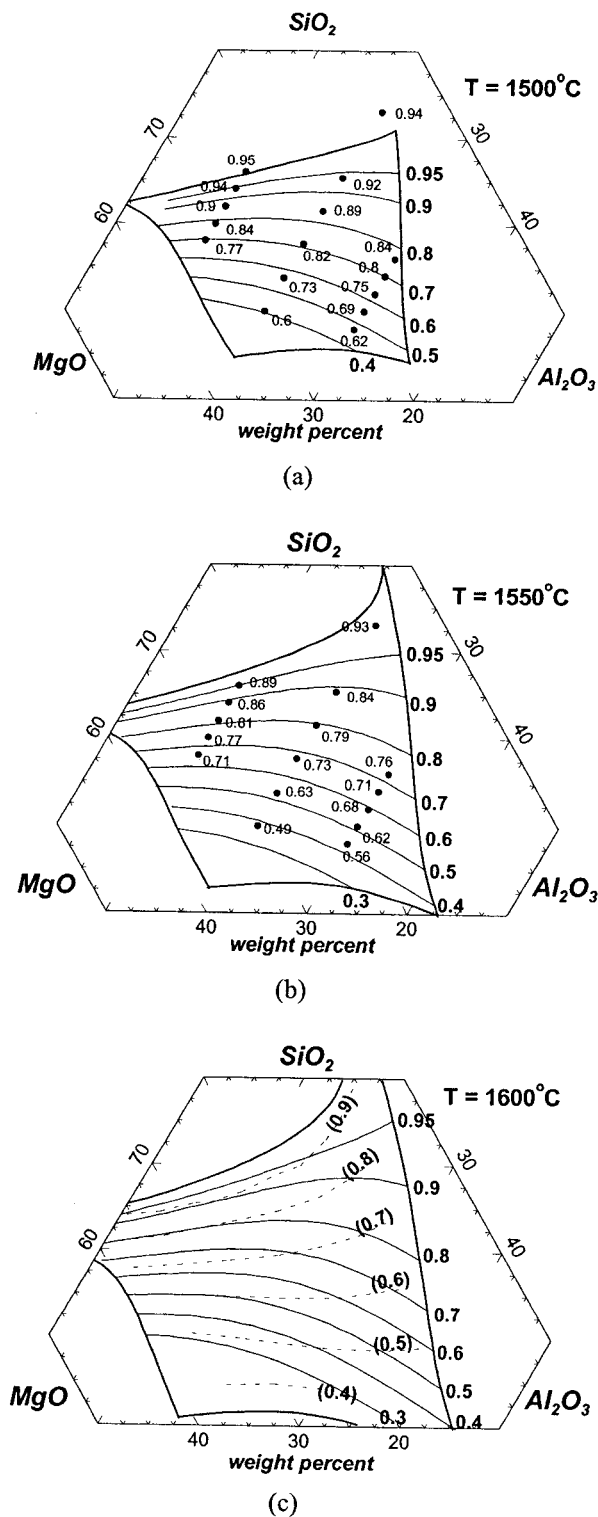


Fig. 21 – Calculated activities of SiO_2 (solid cristobalite standard state) in $\text{MgO-Al}_2\text{O}_3\text{-SiO}_2$ liquid slags. (a) 1500°C (b) 1550°C (c) 1600°C . Experimental points (a,b) from Henderson and Taylor^[96], and dotted lines (c) from Rein and Chipman.^[95]

Appendix V

Article :

Thermodynamic Evaluation and Optimization of the MnO-Al₂O₃ and MnO-Al₂O₃-SiO₂ Systems and Applications to Inclusion Engineering

In-Ho Jung, Youn-Bae Kang, Sergei A. Decterov and Arthur D. Pelton

Submitted to *Metallurgical and Materials Transactions*, 2003

Thermodynamic Evaluation and Optimization of the MnO-Al₂O₃ and MnO-Al₂O₃-SiO₂ Systems and Applications to Inclusion Engineering

IN-HO JUNG, YOUN-BAE KANG, SERGEI A. DECTEROV,
and ARTHUR D. PELTON

All available thermodynamic and phase diagram data are critically evaluated and optimized for the liquid slag phase and for all solid phases at 1 bar pressure from 298K to above the liquidus temperatures for the systems MnO-Al₂O₃ and MnO-Al₂O₃-SiO₂, and a database of model parameters is prepared. The Modified Quasichemical Model is used for the molten slag phase. Calculations using the database are performed with applications to inclusion engineering for Mn/Si killed steel.

I. INTRODUCTION

THE MnO-Al₂O₃-SiO₂ ternary system is of interest for inclusion control in Mn/Si-killed steel. Mn/Si complex deoxidation is indispensable for the production of high value steel such as tire-cord steel and high-Ni steel (Fe-36%Ni Invar steel) in order to avoid the harmful effects of solid Al₂O₃ inclusions formed during Al deoxidation. Al₂O₃ inclusions usually cause wire breakage during tire-cord production where inclusions should be deformable during the wire-making process. Therefore Mn/Si deoxidation, which results in MnO-SiO₂-(Al₂O₃) inclusions of low melting temperature, is usually preferred. In order to control inclusions precisely, inclusion engineering, based on the thermodynamic relations between inclusions and liquid steel, should be carried out during the secondary refining stage in the ladle and tundish.

In the present study, a thermodynamic database of model parameters for the MnO-Al₂O₃-SiO₂ system has been developed by evaluation/optimization of all available thermodynamic and phase diagram data. This database, together with the previously developed database for molten steels can be used to perform calculations of importance to inclusion engineering.

II. THERMODYNAMIC OPTIMIZATION

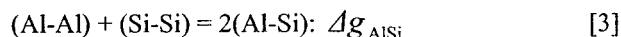
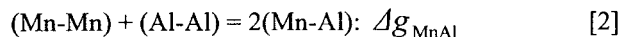
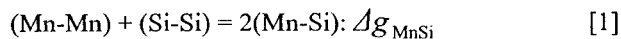
In a thermodynamic "optimization" of a system, all available thermodynamic and phase-equilibrium data are evaluated simultaneously in order to obtain one set of model equations for the Gibbs energies of all phases as functions of temperature and composition. From these equations, all of the thermodynamic properties and the phase diagrams can be back-calculated. In this way, all the data are rendered self-consistent and consistent with thermodynamic principles. Thermodynamic property data, such as activity data, can aid in the evaluation of the phase diagram, and phase diagram measurements can be used to deduce thermodynamic properties. Discrepancies in the available data can often be resolved, and interpolations and extrapolations can be made in a thermodynamically correct manner. A small set of model parameters is obtained. This is ideal for computer storage and calculation of properties and phase diagrams.

The first step is to optimize the binary subsystems. In the second step, the models are used to predict the thermodynamic properties of ternary solutions from the optimized binary model parameters. The predictions are compared with measured ternary properties and phase diagrams, and small optimized ternary model parameters are added if necessary. Finally, from the optimized binary and ternary parameters, thermodynamic properties and phase diagrams of multicomponent systems can be predicted.

Several hundred oxide, salt, alloy, and other systems have been systematically optimized in this way in order to develop the present large database of the FACT^[1] computer system. A few examples of optimizations of oxide systems are given in references [2-11].

For the molten oxide (slag) phase, the Modified Quasichemical Model^[12,13] has been used. This model has been recently summarized.^[14,15] Short-range-ordering is taken into account by considering second-nearest-neighbor

pair exchange reactions. For example, for MnO-Al₂O₃-SiO₂ slags these reactions are:



where (A-A) represents a second-nearest-neighbor pair. The parameters of the model are the Gibbs energies Δg_{AB} of these reactions, which may be expanded as empirical functions of composition.

A. MnO-SiO₂ and Al₂O₃-SiO₂ Systems

These systems were optimized previously.^[7,10] Phase diagrams calculated from the optimized parameters are shown in Figures 1 and 2. In the evaluations/optimizations, all available phase diagram data from several sources, metastable phase equilibrium data, data on the Gibbs energies of all compounds, and measured activities of MnO in the MnO-SiO₂ slags were simultaneously taken into account. The optimized binary model parameters as well as optimized expressions for the Gibbs energies of all compounds are given in references [7,10] along with the "coordination numbers" of Mn, Si and Al used in the Modified Quasichemical Model for the slags, and the optimized model parameters for the non-stoichiometric mullite solid solution.

The quasichemical parameter Δg_{MnSi} for the MnO-SiO₂ slag phase is very negative, indicating a strong tendency to short-range-ordering in this solution.

B. MnO-Al₂O₃ System

The calculated phase diagram (back-calculated from the optimized parameters) is shown in Figure 3 along with selected experimental points of Jacob^[16] and Olsen and Heynert.^[17] The earliest reported phase diagram of Hay *et al.*^[18] is not in agreement with subsequent measurements, probably because the O₂ pressure was not sufficiently low.

Olsen and Heynert^[17] obtained their liquidus measurements by equilibrating metal-saturated oxide melts with Al₂O₃ crucibles followed by quenching and analysis. They state that their melts may have contained up to 20 % FeO. They report eutectic and peritectic temperatures of 1520°C and 1720°C measured by a calorimetric technique; however no experimental details are given.

Jacob^[16] measured the liquidus temperatures shown on Figure 3 at 1600°C and 1650°C by equilibration under controlled oxygen pressures of 10⁻⁵ to 10⁻⁶ bar, followed by quenching and electron microprobe analysis. These same experiments showed approximately 1 % solubility of Al₂O₃ in solid MnO and no solubility of MnO in MnAl₂O₄. In similar experiments, Jacob heated Mn and MnO in sealed

Al₂O₃ crucibles at 1600°C and 1650°C, followed by quenching and electron microprobe analysis. A solubility of MnO in Al₂O₃ of approximately 1 % and a solubility of Al₂O₃ in MnAl₂O₄ of approximately 3 % were observed.

The invariant temperatures and the melting points of pure MnO, Al₂O₃ and MnAl₂O₄ were measured by Jacob^[16] by examination, either visual or under an optical microscope, of pellets quenched from high temperature under purified Ar. He reported that MnAl₂O₄ melts congruently at 1850°C and hence that the invariant shown at 1769°C in Figure 3 is actually a eutectic. Furthermore, he claims to have determined the eutectic composition by electron microprobe analysis of the liquid phase in samples heat treated about 10°C above this temperature. However, he does not report this measured composition.

In an earlier study, Novokhatskii *et al.*^[19] performed similar measurements of the melting points of the pure compounds and of the invariant temperatures by observing the softening of pyrometric cones. Like Jacob, they report MnAl₂O₄ to melt congruently at 1850°C, with eutectic temperatures at 1520°C and 1770°C. Eutectic compositions were also reported from observations of the relative amounts of the phases present in samples held for 6 to 10 minutes above the eutectic temperatures and then quenched.

Finally, from the constancy of their X-ray diffraction patterns, Novokhatskii *et al.*^[19] confirmed that Al₂O₃ and MnAl₂O₄ exhibit virtually no mutual solid solubility.

Although the results of both Jacob and Novokhatskii *et al.* point to the congruent melting of MnAl₂O₄, it was impossible to reconcile this melting behavior with the available thermodynamic data for this system as will be discussed below.

As shown in Figure 4, many independent measurements have been made of the Gibbs energy of formation of MnAl₂O₄. Jacob^[16] equilibrated mixtures of MnAl₂O₄ and Al₂O₃ with Pt foil under fixed oxygen partial pressures and then measured the Mn content of the Pt. From the known activity coefficients of Mn in Pt-Mn solid solutions, the Gibbs energy of MnAl₂O₄ could thereby be calculated. Zhao *et al.*^[20] performed similar measurements using molten Ag-Mn solutions rather than Pt-Mn solutions. Lenev and Novokhatskii^[21] measured $P_{\text{H}_2\text{O}}/P_{\text{H}_2}$ ratios in equilibrium with MnAl₂O₄/Al₂O₃/Mn(liq) mixtures. Dimitrov *et al.*^[22] equilibrated liquid Fe with a crucible made of Al₂O₃ and MnAl₂O₄, measuring P_{O_2} with a solid electrolyte probe. From the measured Mn content of the Fe and the known activity coefficient of Mn in Fe, the Gibbs energy of MnAl₂O₄ could thereby be determined. Kim and McLean^[23] equilibrated liquid Fe and Al₂O₃ with an MnAl₂O₄-FeAl₂O₄ solid solution and measured the Mn and O contents of the liquid Fe. The Gibbs energy of MnAl₂O₄ was then calculated under the assumption that the MnAl₂O₄-FeAl₂O₄ spinel is an ideal solution. Finally, Timucin and Muan^[24] equilibrated MnO-NiO and NiAl₂O₄-MnAl₂O₄ solid solutions with Ni under controlled P_{O_2} , thereby fixing the NiO activity. By making measurements

over a range of compositions and using a ternary Gibbs-Duhem integration technique, they determined the Gibbs energy of MnAl_2O_4 . As can be seen from Figure 4, the various measurements are all in reasonable agreement. The curve given in the compilation of Barin^[25] (which was taken from an earlier estimate^[26]) is also shown in Figure 4.

Jacob^[16] also measured the activity of MnO across the entire composition range at 1600°C and 1650°C by equilibrating the mixtures with Pt-Mn foils under controlled P_{O_2} . Results are shown in Figure 5 along with earlier measurements of Sharma and Richardson^[27] who used an identical technique.

All these data (phase diagrams, Gibbs energies of MnAl_2O_4 , activities of MnO) were treated in a simultaneous least-squares optimization. The optimized expression for the Gibbs energy of MnAl_2O_4 is given in Table I. Its heat capacity was assumed to be the weighted sum of the heat capacities of MnO and Al_2O_3 . The quasichemical model was used for the liquid phase with the same "coordination numbers" Z_{MnMn} and Z_{AlAl} as were used previously^[7,10] for the MnO-SiO₂ and Al_2O_3 -SiO₂ systems. The optimized expression for the parameter Δg_{MnAl} is given in Table I. In this expression, $Y_{\text{AlO}_{1.5}}$ is the "coordination equivalent mole fraction" of $\text{AlO}_{1.5}$ as defined in reference [15]. Note that no temperature-dependent terms were required. Solid MnO, Al_2O_3 and MnAl_2O_4 were assumed to be stoichiometric compounds. The phase diagram, Gibbs energy of MnAl_2O_4 and activity of MnO, back-calculated from the optimized parameters, are shown in Figures 3 to 5.

It was impossible to obtain a calculated congruent melting of MnAl_2O_4 with any reasonable set of parameters for the liquid phase. Essentially, from the reported Gibbs energy of formation of MnAl_2O_4 and the activities of MnO in the liquid, an incongruent melting of MnAl_2O_4 near 1769°C is predicted, and this is also consistent with the liquidus measurements. This result is independent of any assumptions of the model or of the assumed Gibbs energy of fusion of Al_2O_3 . It is noteworthy that the predicted peritectic temperature is very close to the "eutectic" temperatures reported by Jacob^[16] and Novokhatskii *et al.*,^[19] and that the "congruent melting point" of 1850°C reported by these authors lies very close to the predicted Al_2O_3 -liquidus as can be seen in Figure 3.

In order to obtain a calculated congruent melting of MnAl_2O_4 near 1850°C, it would be necessary to decrease its Gibbs energy of formation by ~ 40 kJ. As can be seen from Figure 4, such a large change is far outside the experimental error limits of the many independent measurements of this quantity. (In an earlier^[28] optimization of this system, in which a congruent melting of MnAl_2O_4 was calculated, the Gibbs energy curve of Barin^[25] was used. As can be seen from Figure 4, this curve lies, coincidentally, ~ 40 kJ below the present optimized curve.) Finally, the optimization of the MnO-SiO₂- Al_2O_3 ternary system (Section II. C) is consistent with the present binary optimization.

We thus conclude that Jacob and Novokhatskii *et al.* probably erred in assigning congruent melting behavior to MnAl_2O_4 . Nevertheless, this part of the phase diagram is shown by dashed lines in Figure 3 in order to indicate that this region should be re-investigated.

C. $\text{MnO-Al}_2\text{O}_3\text{-SiO}_2$ System

The calculated ternary liquidus surface (back-calculated from the optimized parameters) is shown in Figure 6.

Snow^[29] observed two ternary compounds in this system, spessartite ($\text{Mn}_3\text{Al}_2\text{Si}_3\text{O}_{12}$) and Mn-cordierite ($\text{Mn}_2\text{Al}_4\text{Si}_5\text{O}_{18}$), which are isostructural with pyrope ($\text{Mg}_3\text{Al}_2\text{Si}_3\text{O}_{12}$) and cordierite ($\text{Mg}_2\text{Al}_4\text{Si}_5\text{O}_{18}$) respectively.^[29] Roghani *et al.*^[30], from EPMA compositional analysis, reported spessartite and, rather than Mn-cordierite, a compound $\text{MnAl}_2\text{Si}_2\text{O}_8$. The composition of this compound is very close to that of Mn-cordierite and, to our knowledge, no compound similar to $\text{MnAl}_2\text{Si}_2\text{O}_8$ has been reported in other systems. Therefore in the present study we show spessartite and Mn-cordierite as the two ternary compounds in the MnO- Al_2O_3 -SiO₂ system. It is known^[31] that the heat capacities and standard entropies S_{298}° of pyrope and cordierite are very nearly equal to the

weighted sums of C_p and S_{298}° of MgO, SiO₂ and Al_2O_3 . Hence, this approximation was used to estimate C_p and S_{298}° of spessartite and Mn-cordierite as shown in Table I.

The values of H_{298}° shown in Table I were then obtained by optimization to reproduce the ternary experimental data as discussed below. In the absence of any evidence to the contrary, all compounds were assumed to be stoichiometric except for the small non-stoichiometry of mullite as shown on Figures 2 and 6.

The Gibbs energy surface of the ternary liquid solution was calculated with the quasichemical model using the "asymmetric approximation" (see reference [14]) with SiO₂ taken as "acidic" and MnO and Al_2O_3 taken as "basic", using the optimized parameters of the three binary subsystems and the two small ternary parameters shown in Table I. The values of these ternary parameters were optimized using the available ternary data as discussed below. It may be noted that these two parameters are very close to the ternary parameters which were found^[10] to give the best optimization of the CaO- Al_2O_3 -SiO₂ liquid phase.

An extensive study of the central region of the ternary phase diagram was carried out by Snow^[29] using a technique of equilibration under purified N₂, quenching and optical examination and very recently by Roghani *et al.*^[30] using an equilibration technique with Mn-Si alloy saturation followed by quenching and optical and EPMA analysis. Chemical analysis by Snow showed the Mn³⁺ content to be negligible. Two major differences can be found between the studies of Snow and Roghani *et al.* Firstly, Snow reported spessartite to melt congruently at $1200 \pm 5^\circ\text{C}$ with a relatively wide primary crystallization

region, while Roghani *et al.* reported peritectic melting of spessartite with a very small primary crystallization region; Roghani *et al.* reported liquidus temperatures below 1100°C, with rhodonite as the primary phase in the central composition region where Snow reported spessartite to be the primary phase. The lowest liquidus temperature reported by Snow was 1140°C. Secondly, Roghani *et al.* reported a much wider primary phase field of corundum (Al_2O_3) at lower temperatures than did Snow. Figure 7 shows all compositions at which Snow^[29] unambiguously identified the primary solid phase, along with similar determinations of Roghani *et al.*, superimposed on the calculated phase diagram. It can be seen that Snow identified spessartite as the primary solid at several compositions where Roghani *et al.* reported rhodonite, and that Snow identified mullite at several compositions where Roghani *et al.* reported corundum.

In the present study we calculate that spessartite melts at 1200°C, the melting behavior being just at the border between congruent and incongruent. The calculated primary phase field of spessartite is slightly smaller than that reported by Snow. Similarly, the calculated primary phase field of corundum is closer in shape to that reported by Snow; the calculations are in agreement with Snow except for four points at which he reported a primary corundum phase while the calculations show mullite (although two of these points are in conflict with another point at which Snow reported mullite in agreement with the calculations.)

The calculations were performed using only the binary model parameters with two small ternary parameters. Many more and much larger ternary terms would be required to reproduce the wide corundum primary phase field reported by Roghani *et al.* Furthermore, the simple model calculations give the ternary invariant points which are listed in Table II along with the values reported by Snow, and these are in agreement within experimental uncertainty in all cases. (The calculations also show four saddle points at 1138°, 1144°, 1157° and 1200°C as shown on Figure 6). In Snow's studies, the samples were first heated well into the single-phase liquid region before being equilibrated at the experimental temperatures, whereas Roghani *et al.* first heated their samples to 50° above the final equilibration temperatures. Possibly some unmelted nuclei of rhodonite or corundum remained in the samples of Roghani *et al.*, and nucleation of spessartite or mullite did not occur.

Although we have favored the primary phase field identifications of Snow, in the optimization we accorded more weight to the actual liquidus temperatures reported by Roghani *et al.* since their technique of using EPMA to measure the compositions of equilibrated phases is expected to be more accurate than the classical quenching technique employed by Snow. Liquidus temperatures reported by the two authors often differ by over 80°C, particularly in the galaxite and mullite phase fields where the liquidus temperatures reported by Roghani *et al.* are higher. Liquidus points reported by Roghani *et al.* between 1200° and 1500°C are shown on Figure 8. Liquidus points

at 1550°, 1580° and 1600°C, measured by Fujisawa and Sakao,^[32] Sakao,^[33] Ohta and Suito^[34] and Kang and Lee^[35] from analysis of melts equilibrated with Fe in Al_2O_3 crucibles are also shown on Figure 8; the melts contained less than 3 % FeO which was included (on a molar basis) with MnO when the experimental points were plotted on Figure 8; the saturated solid phases were not identified in the experiments.

The dashed line on Figure 8 is the calculated metastable extension of the 1300°C isotherm for corundum saturation. It can be seen that this curve passes almost exactly through the experimental liquidus points at 1300°C which were reported by Roghani *et al.* to be in the corundum primary phase region. Similarly, the calculated metastable extensions of the 1400° and 1500°C isotherms for Al_2O_3 -saturation pass also almost exactly through the experimental points of these authors. This observation supports the contention that Roghani *et al.* may actually have measured the metastable corundum liquidus in this composition region.

As can be seen from Figure 8, the agreement between the calculations and reliable liquidus measurements is within the limits of experimental uncertainty.

Sharma and Richardson^[27] and Woo and Lee^[36] measured MnO activities in the slags at 1650°C and 1550°C respectively by equilibration with Pt-Mn foils under controlled oxygen partial pressures. Their results are compared with the calculated activities in Figures 9 to 11. Agreement is well within the experimental error limits.

Fujisawa and Sakao^[32] and Ohta and Suito^[34] measured MnO and SiO_2 activities at mullite- and Al_2O_3 -saturation by equilibrating the melts with liquid Fe in Al_2O_3 crucibles, followed by quenching and analysis of the Fe for dissolved Mn, Si and O. From the known activity coefficients of these elements in molten Fe, the activities of MnO and SiO_2 could then be calculated. The melts contained from 1 to 5 % FeO. Only those points where the reported FeO content was less than 3 % are plotted on Figures 11 and 12. In the calculations, the FeO was included (on a molar basis) with the MnO. Agreement with the calculations is within experimental uncertainty in view of the large error limits inherent in this experimental technique.

Calculated iso-activity curves of SiO_2 and Al_2O_3 in the melts at 1600°C are shown in Figures 13 and 14.

III. APPLICATIONS TO INCLUSION ENGINEERING

Control of inclusions is important in the production of high quality steels such as tire-cord steel. In order to control the inclusion compositions accurately, thermodynamic information for both inclusions and liquid steel is needed. Calculations based on accurate thermodynamic databases can give very useful information such as the variation of inclusion composition with Mn/Si ratio in Mn/Si killed liquid steel and the evolution of the inclusions with decreasing temperature.

Recently^[37] we developed a thermodynamic model and database for molten steel in which the interactions of strong deoxidants M (such as M = Al, Ca, Mg,...) with dissolved oxygen are modeled by explicitly considering the formation of M^*O associates or "molecules" in solution. This model has been shown^[37] to have excellent predictive capability over wide ranges of temperature and composition. By using this molten steel database with the present database for the oxides, many calculations of importance to inclusion engineering can be made.

Ohta and Suito^[34] and Kang and Lee^[35] equilibrated molten steel containing Mn and Si with molten oxide and, simultaneously, with either solid Al_2O_3 or mullite at 1550° and 1600°C. Equilibrium slag and metal compositions were measured. Results are shown in Figures 15 and 16. The small (< 3 %) measured FeO contents of the slag were included (on a molar basis) with MnO when the experimental points were plotted on the figure.

In Figure 15 the reported slag compositions at 1600°C are shown along with the calculated liquidus. Also shown on Figure 15 are the measured Mn/Si ratios in the steel at each experimental point as well as iso-Mn/Si lines calculated from the models. It can be seen that the points all lie very close to the calculated phase boundaries and that the calculated Mn/Si ratios agree with the measured ratios within the experimental error limits.

In Figure 16 the measured oxygen contents of the steel are plotted as functions of the Mn/Si ratio in the steel and are compared to the curves calculated from the models. Fujisawa and Sakao^[32,38] performed similar measurements at 1550° and 1535°C; these are also plotted on Figure 16. The experimental results exhibit a large amount of scatter. Agreement between the measurements and the calculations is within the experimental error limits.

The calculated 1200°C liquidus is superimposed upon the diagrams in Figure 15. In order that the inclusions remain liquid at the rolling temperature of 1200°C, it is necessary that the compositions of the inclusions lie inside the 1200°C isotherm. As can be seen from Figs. 15a to 15c, the positions of the iso-Mn/Si lines are nearly independent of the total (Mn + Si) content. Furthermore, the calculated positions of these lines at 1550°C (which is near the solidification temperature of the steel) are nearly the same as at 1600°C. Thus it can be seen from Figure 15 that the Mn/Si weight ratio of the steel should be controlled to within the approximate limits: $1 < Mn/Si < 10$.

IV. CONCLUSIONS

A complete critical evaluation and optimization of all available phase diagram and thermodynamic data for the $MnO-Al_2O_3-SiO_2$ system has been made, and a database of model parameters has been prepared. All data are reproduced within experimental error limits. Together with the model and database for molten steel^[37] and the FactSage software^[1] for Gibbs energy minimization, thermodynamic calculations have been performed to demonstrate the application to inclusion control of Mn/Si

deoxidized steel. The calculated results are in good agreement with experimental data, showing that the thermodynamic databases can be a useful tool in predicting equilibria of interest in inclusion engineering. Future developments include integrating this database with the present^[1] $SiO_2-CaO-MgO-Al_2O_3-FeO-Fe_2O_3-TiO-TiO_2-CrO-Cr_2O_3-S$ database, thereby increasing the range of applicability.

ACKNOWLEDGMENTS

This project was supported by a CRD grant from the Natural Sciences and Engineering Research Council of Canada in collaboration with INCO, Noranda, Rio Tinto, Teck Cominco, Alcoa, Dupont, Shell, Corning, Pechiney, Norsk Hydro, Sintef, Schott Glas, St.-Gobain Recherche, Mintek and IIS Materials.

REFERENCES

1. www.factsage.com, Montreal, 2002.
2. E. Jak, S. Degterov, P. Hayes and A.D. Pelton: *Canad. Metall. Quart.*, 1998, vol. 37, pp. 41-47.
3. E. Jak, S. Degterov, P. Wu, P. Hayes and A.D. Pelton: *Metall. Mater. Trans. B*, 1997, vol. 28B, pp. 1011-18.
4. S. Degterov and A.D. Pelton: *Metall. Mater. Trans. B*, 1997, vol. 28B, pp. 235-42.
5. S. Degterov and A.D. Pelton: *J. Phase Equilibria*, 1996, vol. 17, pp. 476-87.
6. S. Degterov and A.D. Pelton: *J. Phase Equilibria*, 1996, vol. 17, pp. 488-94.
7. G. Eriksson, P. Wu, M. Blander and A.D. Pelton: *Canad. Metall. Quart.*, 1994, vol. 33, pp. 13-22.
8. P. Wu, G. Eriksson and A.D. Pelton: *J. Am. Ceram. Soc.*, 1993, vol. 76, pp. 2065-75.
9. P. Wu, G. Eriksson and A.D. Pelton: *J. Am. Ceram. Soc.*, 1993, pp. 2059-63.
10. G. Eriksson and A.D. Pelton: *Metall. Trans. B*, 1993, vol. 24B, pp. 807-816.
11. G. Eriksson and A.D. Pelton: *Metall. Trans. B*, 1993, vol. 24B, pp. 795-805.
12. A.D. Pelton and M. Blander: *Proc. 2nd Int. Symp. Metall. Slags and Fluxes*, TMS-AIME, Warrendale, PA. 1984, pp. 281-91.
13. A.D. Pelton and M. Blander: *Metall. Trans. B*, 1986, vol. 17B, pp. 805-15.
14. A.D. Pelton and P. Chartrand: *Metall. Mater. Trans. A*, 2001, vol. 32A, pp. 1355-60.
15. A.D. Pelton, S.A. Degterov, G. Eriksson, C. Robelin and Y. Dessureault: *Metall. Mater. Trans. B*, 2000, vol. 31B, pp. 651-60.
16. K.T. Jacob: *Canad. Metall. Quart.*, 1981, vol. 20, pp. 89-92.
17. W. Oelsen and G. Heynert: *Arch. Eisenhüttenw.*, 1955, vol. 26, pp. 567-575.
18. R. Hay, J. White and A.B. McIntosh: *J. West. Scot. Iron Steel Inst.*, 1934/1935, vol. 42, pp. 99-104.
19. I.A. Novokhatskii, L.M. Lenev, A.A. Savinskaya and A.V. Gorokh: *Zh. Neorg. Khim.*, 1966, vol. 11, pp. 427-428.
20. Y. Zhao, K. Morita and N. Sano: *Metall. Mater. Trans. B*, 1995, vol. 26B, pp. 1013-1017.

21. L.M. Lenev and I.A. Novokhatskii: *Izv. Akad. Nauk. SSSR. Metall.*, 1966, vol. 3, pp. 73-78.
22. S. Dimitrov, A. Weyl and D. Janke: *Steel Res.*, 1995, vol. 66, pp. 87-92.
23. C.K. Kim and A. McLean: *Metall. Trans. B*, 1979, vol. 10B, pp. 575-584.
24. M. Timucin and A. Muan: *J. Amer. Ceram. Soc.*, 1992, vol. 75, pp. 1399-1406.
25. I. Barin: "Thermochemical Data of Pure Substances", 1989, VCH, Weinheim, Germany.
26. V.A. Medvedev, G.A. Bergman, L.V. Gurvich, V.S. Yungman, A.F. Vorobiev, V.P. Kolesov *et al.*: "Thermicheskie Konstanty, Veshchestv (Thermal Constants of Substances)," Edited by V.P. Glushko, vol 1(1965), 2(1966), 3(1968), 4(1970), 5(1971), 6/1(1972), 6/2(1973), 7(1974), 8(1978), 9(1979), 10(1981), Akad. Nauk USSR, Viniti, Moscow.
27. R.A. Sharma and F.D. Richardson: *Trans. Metall. Soc. AIME*, 1965, vol. 233, pp. 1586-1592.
28. G. Eriksson, P. Wu and A.D. Pelton: *Calphad Journal*, 1993, vol. 17, pp. 189-206.
29. R.B. Snow: *J. Amer. Ceram. Soc.*, 1943, vol. 26, pp. 11-20.
30. G. Roghani, E. Jak and P. Hayes: *Metall. Mater. Trans. B*, 2002, vol. 33B, pp. 827-38.
31. R.G. Berman: *J. Petrology*, 1988, vol. 29, pp. 445-522.
32. T. Fujisawa and H. Sakao: *Tetsu-to-Hagané*, 1977, vol. 63, pp. 1504-1511.
33. Sakao: *Tetsu-to-Hagané*, 1970, vol. 56, S621-624.
34. H. Ohta and H. Suito: *Metall. Mater. Trans. B*, 1996, vol. 27B, pp. 263-270.
35. Y.-B. Kang and H.-G. Lee: *unpublished work*.
36. D.-H. Woo, Y.-B. Kang and H.-G. Lee: *Metall. Mater. Trans. B*, 2002, vol. 33B, pp. 915-20.
37. I.-H. Jung, S.A. Decterov and A.D. Pelton: *Metall. Mater. Trans. (accepted)*.
38. T. Fujisawa and H. Sakao: *Tetsu-to-Hagané*, 1977, vol. 63, pp. 1494-1503.

Table I. Optimized Thermodynamic Properties of Compounds Relative to Elements at 298.15 K and Optimized Model Parameters for Liquid Slag.

Phase	Temperature range (K)	$H_{298.15K}^{\circ}$ J/mol	$S_{298.15}^{\circ}$ J/mol-K	C_P J/mol-K
$MnAl_2O_4$ (s)	298-2042	-2084283.0	113.363	$C_P(MnO(s)) + C_P(Al_2O_3(s))$
$Mn_3Al_2Si_3O_{12}$ (s)	298-1475	-5659394.5	$S_{298.15}^{\circ} = 3 S_{298.15}^{\circ}(MnO(s)) + S_{298.15}^{\circ}(Al_2O_3(s)) + 3 S_{298.15}^{\circ}(SiO_2(tr))$ $C_P = 3 C_P(MnO(s)) + C_P(Al_2O_3(s)) + 3 C_P(SiO_2(tr))$	
$Mn_2Al_4Si_5O_{18}$ (s)	298-1453	-8743256.0	$S_{298.15}^{\circ} = 2 S_{298.15}^{\circ}(MnO(s)) + 2 S_{298.15}^{\circ}(Al_2O_3(s)) + 5 S_{298.15}^{\circ}(SiO_2(tr))$ $C_P = 2 C_P(MnO(s)) + 2 C_P(Al_2O_3(s)) + 5 C_P(SiO_2(tr))$	

Data for all other compounds were taken from Eriksson *et al.*^[7] and Eriksson and Pelton.^[10]

MnO- Al_2O_3 binary system

$$\Delta G_{MnAl} = -6426.79 - 35761.1 Y_{AlO_{1.5}} + 62222.3 Y_{AlO_{1.5}}^6 \quad (J/mol)$$

MnO- Al_2O_3 - SiO_2 ternary system

$$q_{MnSi(Al)}^{002} = -41840, \quad q_{AlSi(Mn)}^{001} = -37656 \quad (J/mol)$$

Binary parameters for MnO- SiO_2 and Al_2O_3 - SiO_2 were taken from Eriksson *et al.*^[7] and Eriksson and Pelton^[10] respectively.

Table II. Comparison of calculated ternary invariant points (not in parentheses) with reported values of Snow^[29] (in parentheses).

Equilibrium solid phases	Composition (wt%)			Temperature (°C)
	MnO	Al ₂ O ₃	SiO ₂	
Sp + Tr + Mn-Cord: Eutectic	33.3 (30)	17.3 (19)	49.4 (51)	1143 (1140 ± 10)
Tr + Mu + Mn-Cord: Peritectic	29.7 (24)	19.4 (23)	50.9 (53)	1180 (1200 ± 10)
(Sp + Cor + Ga: Peritectic)	(40)	(24)	(36)	(1190 ± 5)
Ga + Mu + Sp: Peritectic	39.5	22.0	38.5	1194
Rh + Tr + Sp: Eutectic	41.4 (38)	11.4 (13)	47.2 (49)	1119 (1140 ± 10)
Rh + Sp + Te: Eutectic	51.2 (50)	9.6 (11)	39.2 (39)	1135 (1160 ± 10)
Te + Sp + Ga: Eutectic	53.5	13.8	32.7	1156
Te + MnO + Ga: Peritectic	64.7	11.1	24.2	1239
Sp + Mu + Mn-Cord: Peritectic	34.6	19.7	45.7	1166
(Sp + Cor + Mn-Cord: Peritectic)	(33)	(24)	(43)	(1162 ± 5)
(Mu + Cor + Mn-Cord: Peritectic)	(32)	(25)	(43)	(1168 ± 5)
Cor + Ga + Mu: Peritectic	39.2	22.4	38.4	1249

Tr: Tridymite (SiO₂)

Mu: Mullite (Al₆Si₂O₁₃)

Cor: Corundum (Al₂O₃)

Sp: Spessartite (Mn₃Al₂Si₃O₁₂)

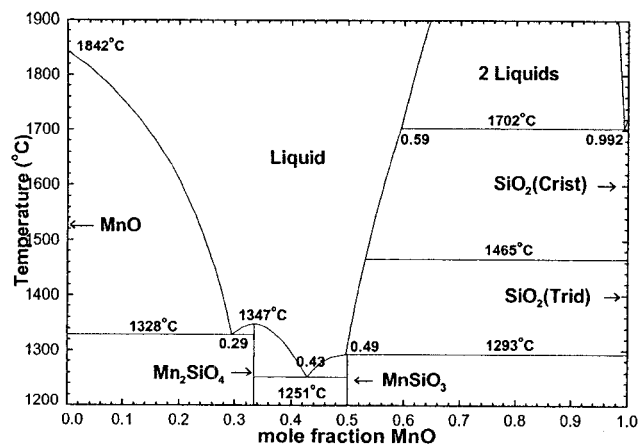
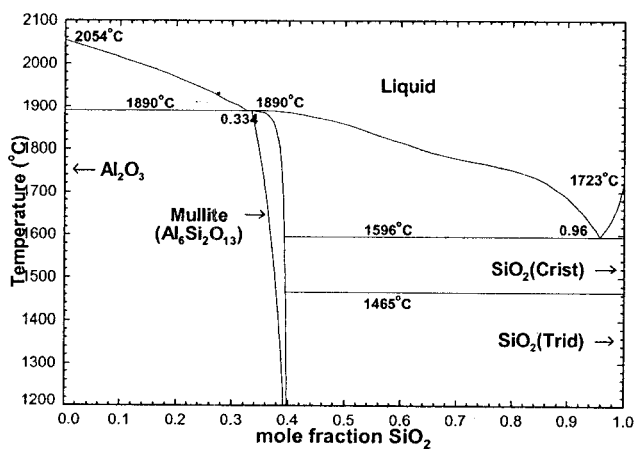
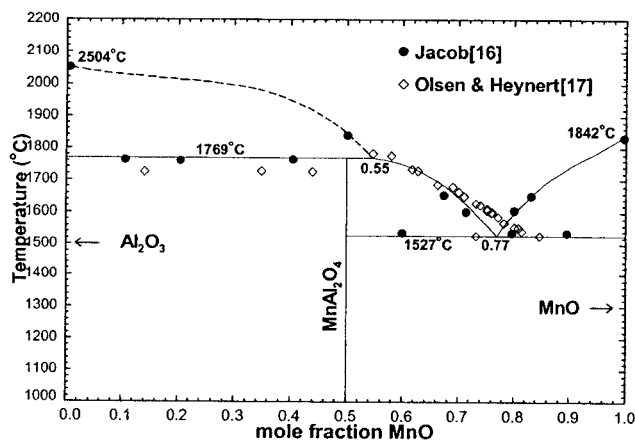
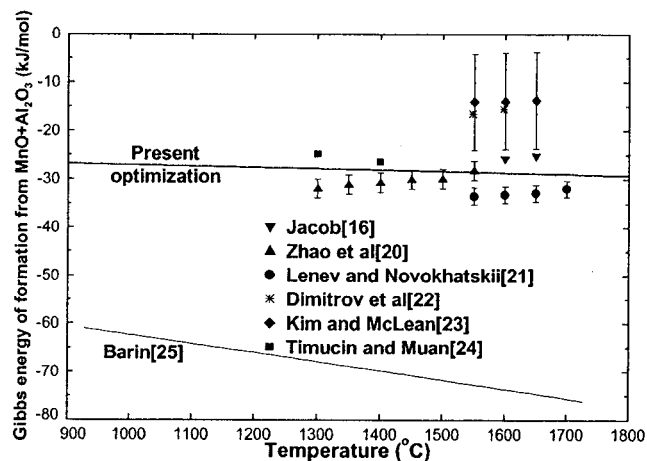
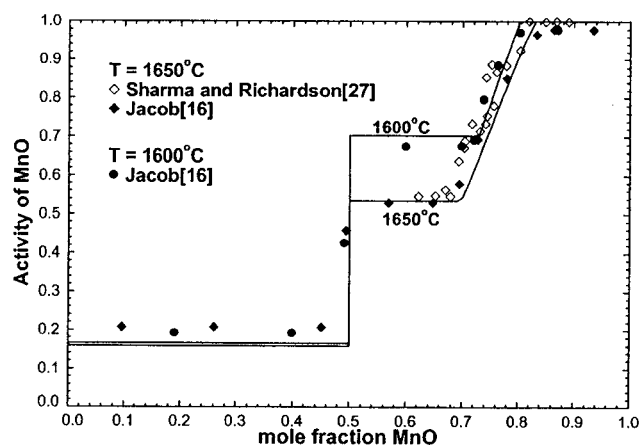
Mn-Cord: Mn-Cordierite (Mn₂Al₄Si₅O₁₈)

Rh: Rhodonite (MnSiO₃)

Ga: Galaxite (MnAl₂O₄)

Te: Tephroite (Mn₂SiO₄)

MnO: MnO

Fig. 1 – Optimized MnO-SiO₂ phase diagram.^[7]Fig. 2 – Optimized Al₂O₃-SiO₂ phase diagram.^[10]Fig. 3 – Calculated (optimized) MnO-Al₂O₃ phase diagram.Fig. 4 – Optimized Gibbs energy of formation of MnAl₂O₄ from solid MnO and Al₂O₃ (at the same temperature).Fig. 5 – Calculated (optimized) activity of MnO (with respect to solid standard state) in the MnO-Al₂O₃ system at 1600°C and 1650°C.

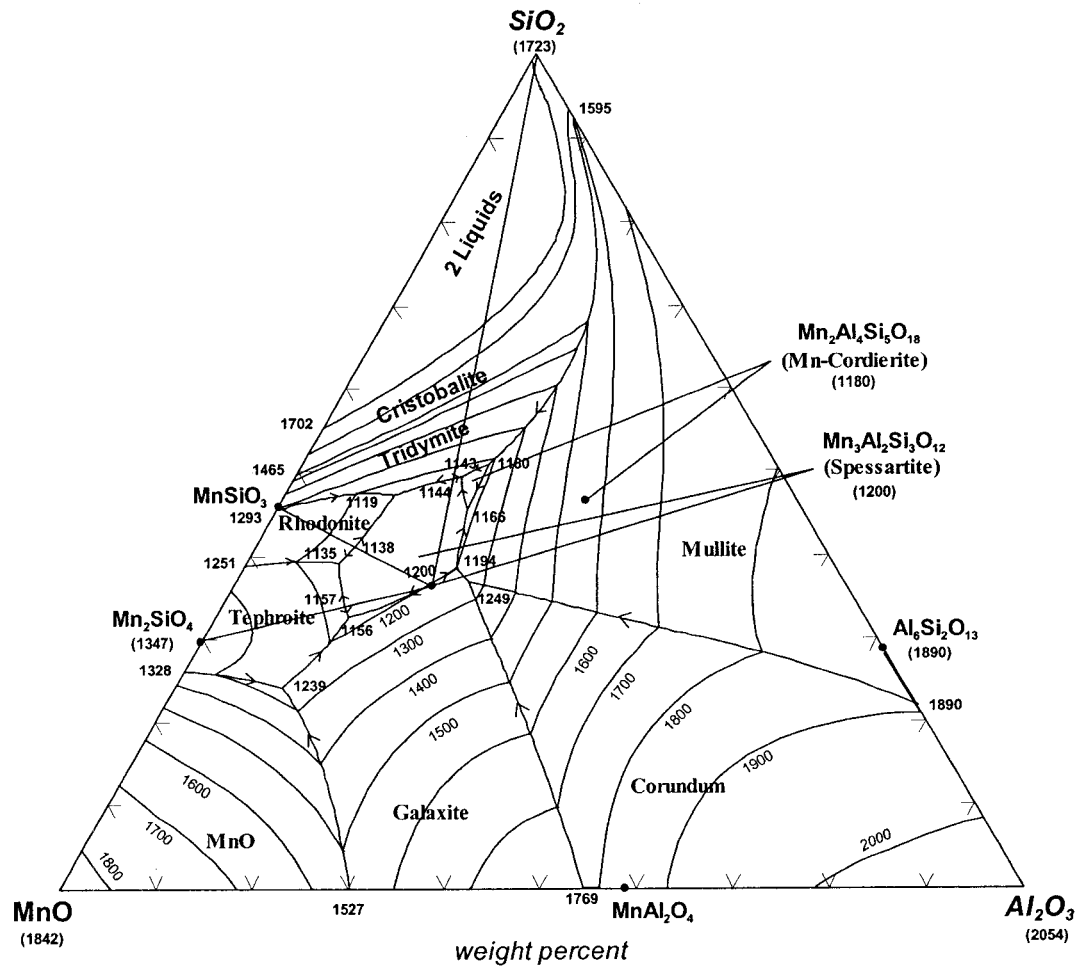


Fig. 6 – Calculated (optimized) liquidus surface of the MnO-Al₂O₃-SiO₂ system. Temperature in °C.

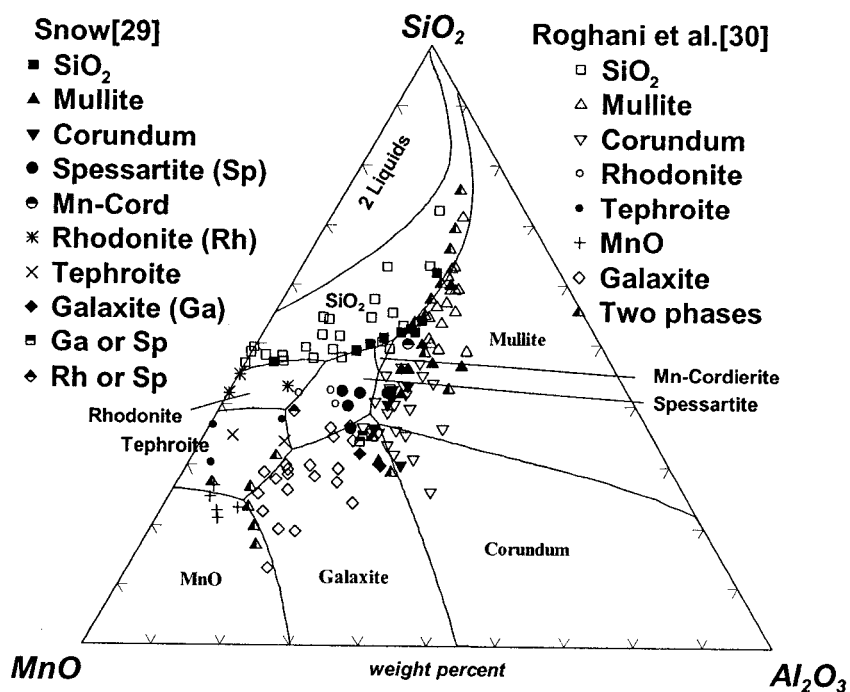


Fig. 7 – Calculated (optimized) primary phase regions of the MnO-Al₂O₃-SiO₂ system with primary phases reported by Snow^[29] and Roghani *et al.*^[30] at various compositions.

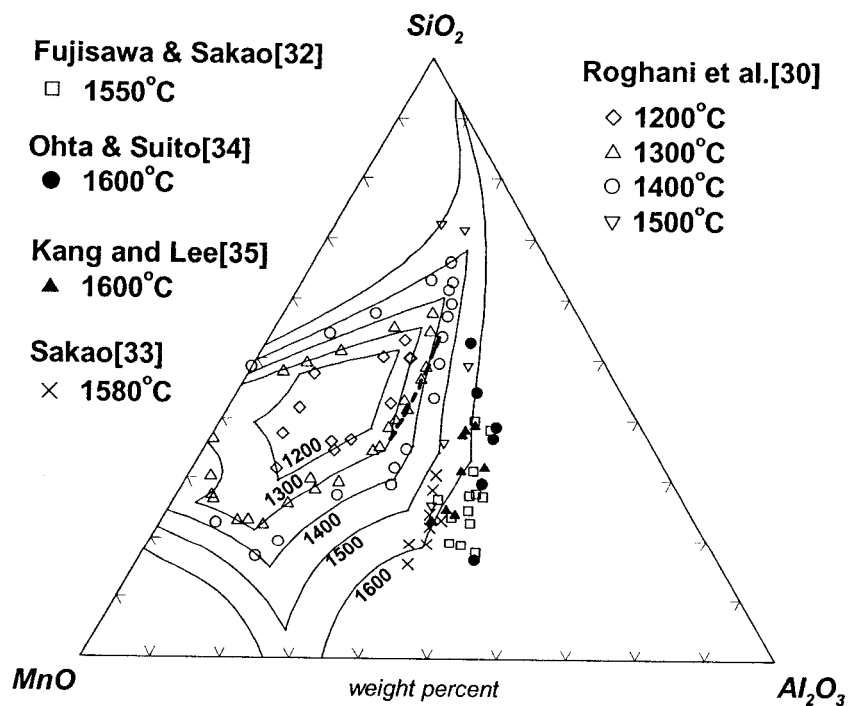


Fig. 8 – Calculated liquidus of the MnO-Al₂O₃-SiO₂ system at temperatures between 1200°C and 1600°C compared with experimental data. Dashed line is calculated metastable liquidus of Al₂O₃ (corundum) at 1300°C.

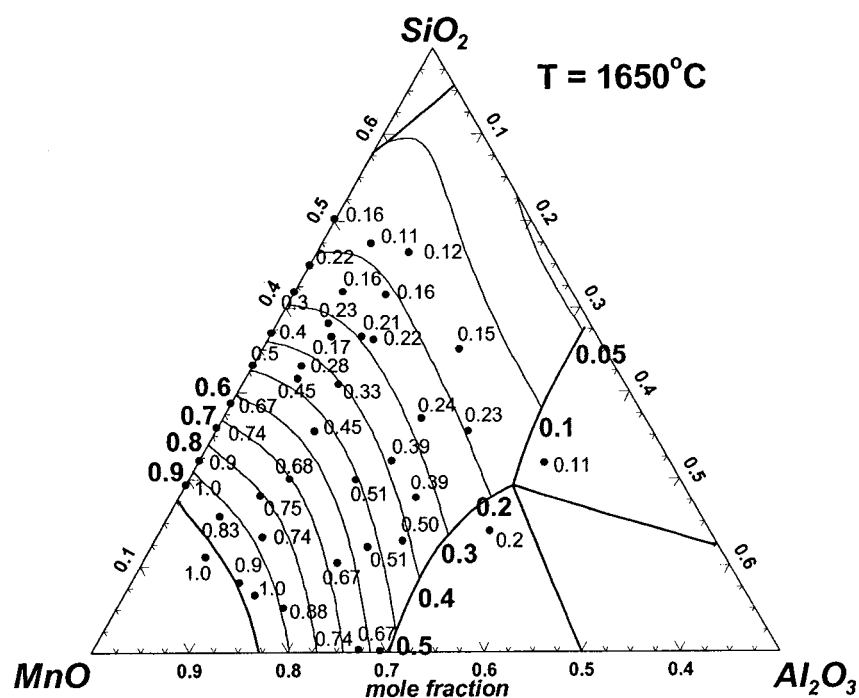


Fig. 9 – Calculated activities of MnO (solid standard state) in MnO- Al_2O_3 - SiO_2 liquid slags at 1650°C and experimental data points from Sharma and Richardson.^[27]

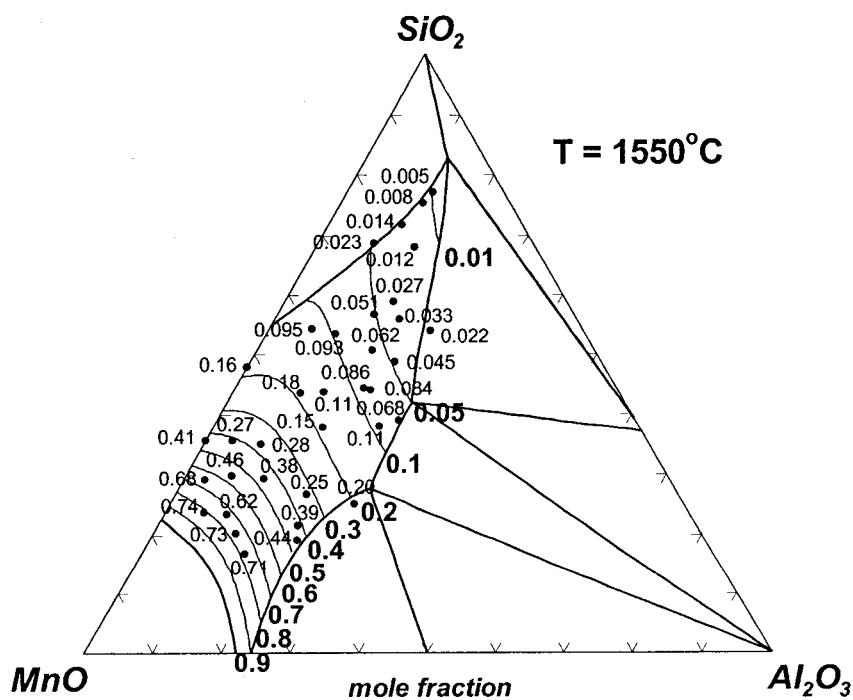


Fig. 10 – Calculated activities of MnO (solid standard state) in MnO- Al_2O_3 - SiO_2 liquid slags at 1550°C and experimental data points from Woo *et al.*^[36]

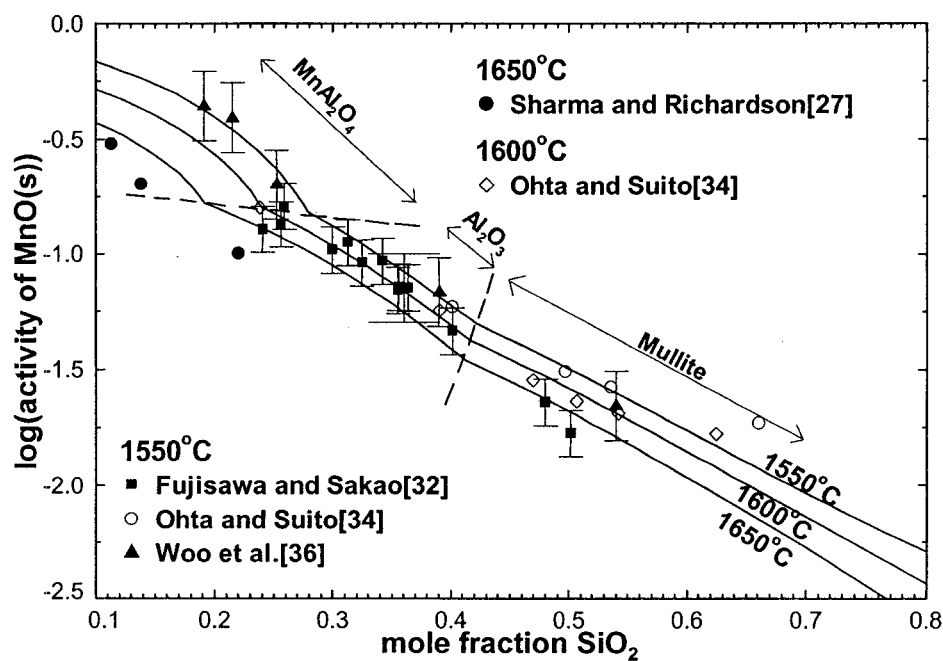


Fig. 11 – Calculated activities of MnO (solid standard state) in MnO- Al_2O_3 - SiO_2 liquid slags at 1550°, 1600° and 1650°C at saturation with solid MnAl_2O_4 , Al_2O_3 or mullite.

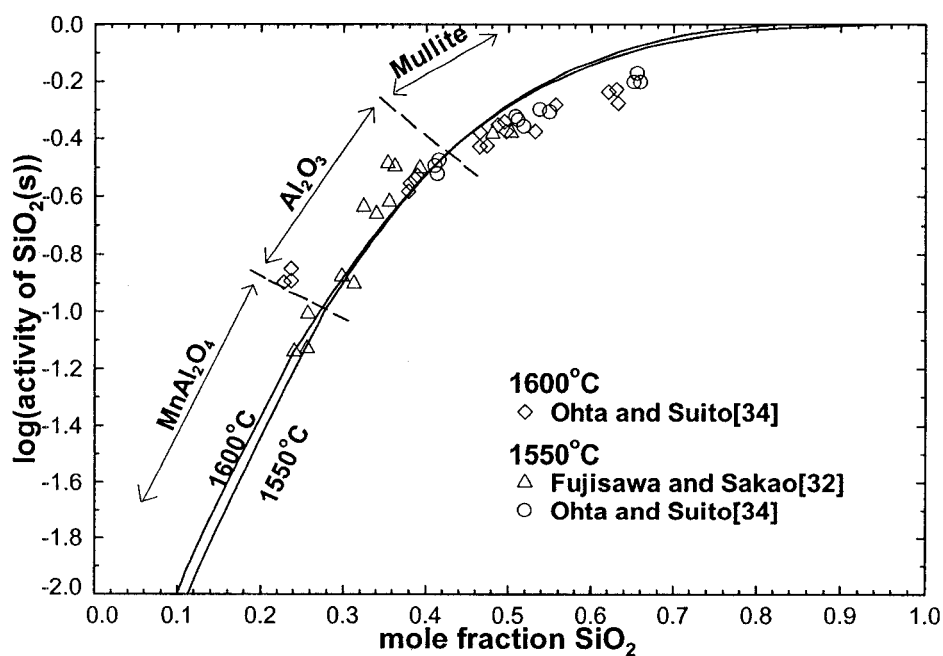


Fig. 12 – Calculated activities of SiO_2 (solid cristobalite standard state) in MnO- Al_2O_3 - SiO_2 liquid slags at 1550° and 1600°C at saturation with solid MnAl_2O_4 , Al_2O_3 or mullite.

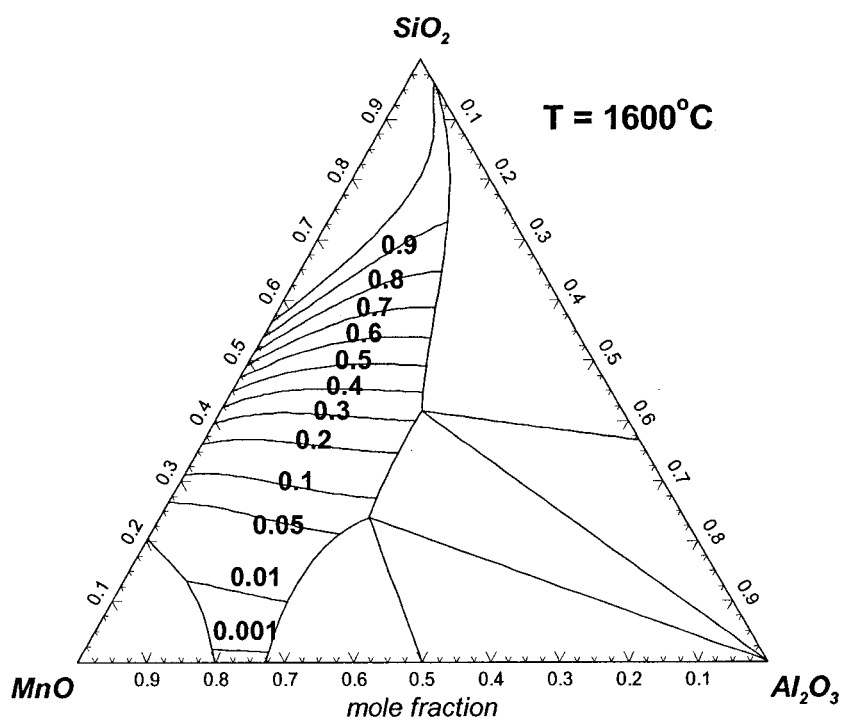


Fig. 13 – Calculated iso-activity curves of SiO_2 (solid cristobalite standard state) in $\text{MnO-Al}_2\text{O}_3\text{-SiO}_2$ liquid slags at 1600°C .

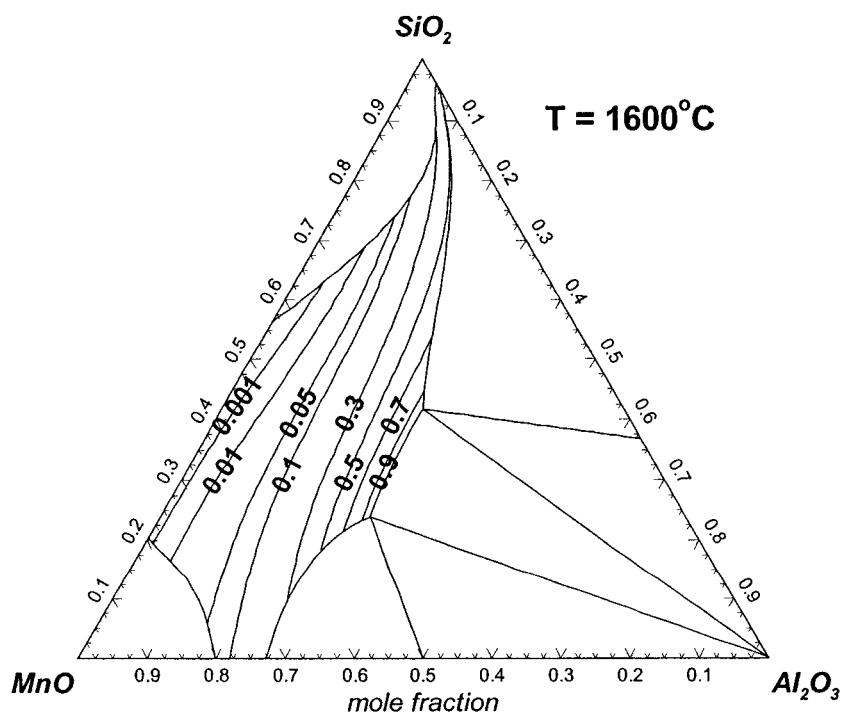


Fig. 14 – Calculated iso-activity curves of Al_2O_3 (solid corundum standard state) in $\text{MnO-Al}_2\text{O}_3\text{-SiO}_2$ liquid slags at 1600°C .

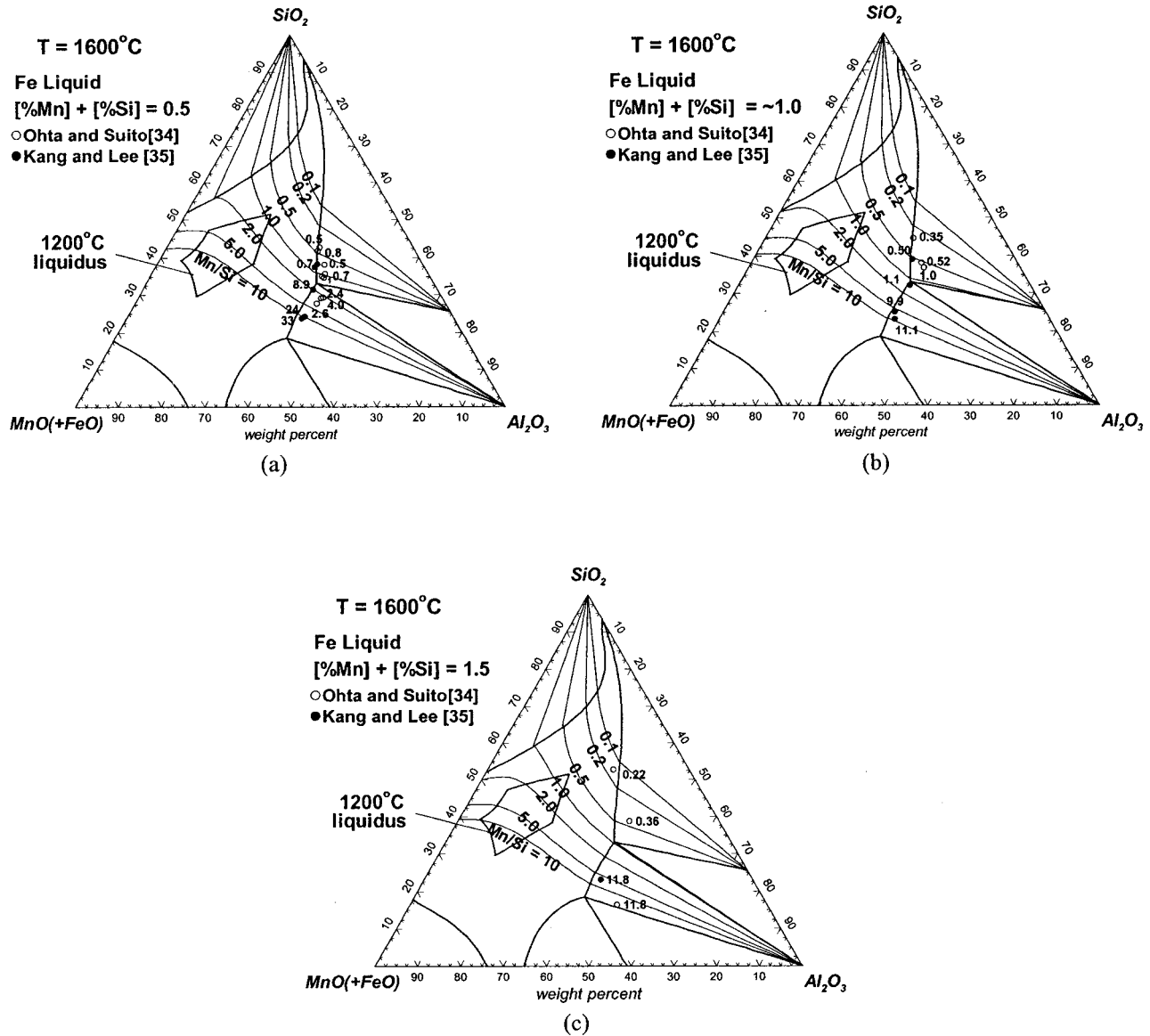


Fig. 15 – Calculated compositional trajectories of $\text{MnO-Al}_2\text{O}_3\text{-SiO}_2$ inclusions in equilibrium with liquid Fe containing various Mn/Si weight ratios and total dissolved ($\text{Mn} + \text{Si}$) contents of 0.5 (Fig. 15 a), 1.0 (Fig. 15 b) and 1.5 (Fig. 15 c) at 1600°C . Experimental Mn/Si ratios at alumina or mullite saturation are shown beside each experimental point. The calculated liquidus curves at 1600°C and 1200°C are also shown.

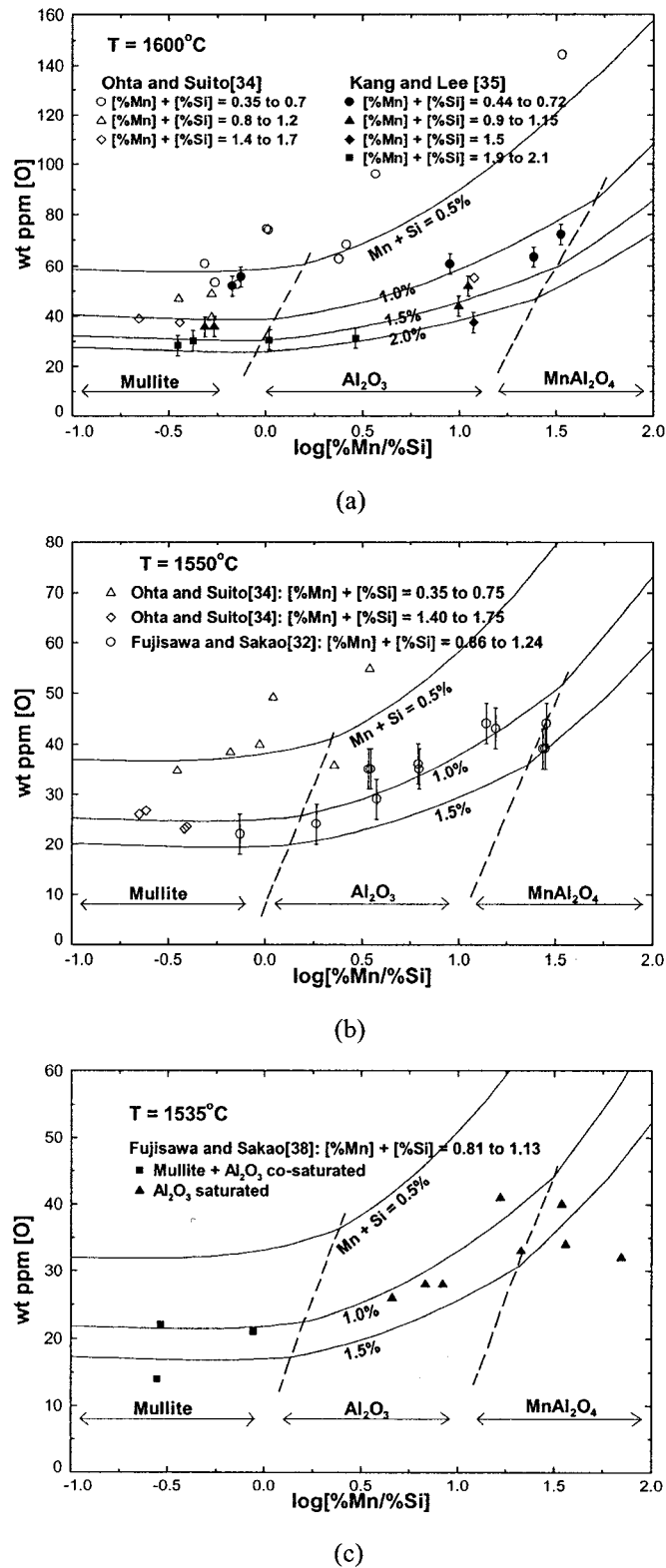


Fig. 16 – Calculated oxygen content versus dissolved Mn/Si weight ratio at various total dissolved (Mn + Si) contents in liquid Fe in equilibrium with liquid MnO-Al₂O₃-SiO₂ inclusions saturated with MnAl₂O₄, Al₂O₃, or mullite at 1600°C (Fig. 16 a), 1550°C (Fig. 16 b) and 1535°C (Fig. 16 c).

Appendix VI

Article :

Critical Thermodynamic Evaluation and Optimization of the CaO-MnO-Al₂O₃-SiO₂ System and Application to Inclusion Control

In-Ho Jung, Sergei Decterov, Arthur D. Pelton,
Youn-Bae Kang and Hae-Geon Lee

Published in COM2002 Conference

“Ladle and Tundish Metallurgy,” pp. 131-147, 2002.

INTRODUCTION

Mn/Si complex deoxidation is indispensable for the production of high value steel such as tire-cord steel and high-Ni steel (Fe-36%Ni Invar steel) in order to avoid the harmful effect of solid Al_2O_3 inclusions formed during Al deoxidation. Al_2O_3 inclusions usually cause wire breakage during tire-cord production. High-Ni steel is rolled to a thin sheet (150 μm thickness) for electronic materials such as IC lead frame and shadow mask; Al_2O_3 inclusions are particularly detrimental to the quality of the thin sheet. Inclusions in these steels should be deformable during the wire-making or rolling process. Therefore Mn/Si deoxidation, which results in inclusions of low melting temperature, is usually preferred. In order to control inclusions precisely, inclusion engineering, based on the thermodynamic relations between inclusions and liquid steel, should be carried out during the secondary refining stage in the ladle and tundish.

The MnO- Al_2O_3 - SiO_2 ternary system is of great interest for inclusion control in Mn/Si-killed steel. Moreover, inclusions can react with CaO-containing top slag in the ladle, resulting in quaternary CaO-MnO- Al_2O_3 - SiO_2 inclusions. To control inclusion composition accurately, the equilibria between inclusions and liquid steel should be investigated comprehensively. Therefore, our two research groups have begun a collaborative project aimed at improving the cleanliness of Mn/Si-killed steel. The project involves both experimentation and thermodynamic database development.

Some of the results from this project will be presented in this article. The thermodynamic properties of the CaO-MnO- Al_2O_3 - SiO_2 quaternary system were critically evaluated and optimized over the entire composition range at temperatures from 298 K to 3000 K. The results of the optimization are presented and compared with experimental data. The optimized oxide database was stored in the FactSage computing system (1) and thermodynamic equilibria between liquid steel and inclusions were calculated. Useful information for inclusion control in Mn/Si-killed tire-cord steel and Fe-36%Ni Invar steel was derived from these calculations.

THERMODYNAMIC OPTIMIZATION

Based on a proper thermodynamic model for every phase of a given system, all available thermodynamic and phase equilibrium data for the system are evaluated simultaneously in order to obtain one set of model equations for the Gibbs energies of all phases as functions of temperature and composition. In this way, all data are rendered self-consistent, any discrepancies in the data can often be resolved, and the data can be properly interpolated and extrapolated. The resulting database of model parameters can be used for calculating phase equilibria and thermodynamic properties using Gibbs energy minimization software.

In this study, the liquid slag is modeled by the modified quasichemical model (2), and solid solutions are described by a polynomial expansion for the excess Gibbs energies using a one- or two-sublattice Compound Energy Formalism (3) depending upon the crystal structure of the solid solution. Thermodynamic data for pure compounds were taken from the FactSage thermodynamic database (1) except for some newly evaluated compounds discussed later. Full details of the optimizations and the optimized model parameters will be published elsewhere (4-5).

MnO-Al₂O₃ binary system

The previous optimization of this system (6) was based upon the recommended data of Barin (7) for MnAl₂O₄ and does not satisfactorily reproduce recent measurements of the properties of MnAl₂O₄ nor of MnO activities. During the present re-optimization, the thermodynamic properties of the MnAl₂O₄ (galaxite) spinel phase were re-evaluated. Although MnAl₂O₄ spinel exists over a narrow range of composition, it was approximated in the present study as a stoichiometric compound.

Several investigations (8-12) have been performed to determine the Gibbs energy of MnAl₂O₄ as shown in Figure 1(a). As can be seen, the recommended values from the compilation by Barin (7) differ from the measurements by more than 40 kJ. Activities of MnO(solid) measured by Sharma and Richardson (13) and Jacob (14) using gas/slag/Pt equilibration techniques are shown in Figure 1(b).

There is still disagreement about the melting behavior of MnAl₂O₄. Hay et al. (15) reported that MnAl₂O₄ melts incongruently at 1560°C. However, Novokhatskii et al. (16) and Jacob (14) observed a congruent melting point of MnAl₂O₄ at about 1850°C by indirect methods. Oelsen and Heynert (17) reported incongruent peritectic melting of MnAl₂O₄ at 1720°C which is close to the eutectic temperature reported at high Al₂O₃ concentrations by Jacob(1760±15°C) and Novokhatskii et al.(1770±20°C)

By simultaneous optimization of all data, we found that peritectic melting of MnAl₂O₄ is thermodynamically more consistent with the phase diagram, the MnO activities and the Gibbs energy of MnAl₂O₄. As can be seen in Figures 1(a)-(c), all experimental data for MnO activities, the phase diagram and the Gibbs energy of MnAl₂O₄ are well reproduced within experimental error limits. Only three temperature-independent model parameters (of the quasichemical model) were required for the liquid slag.

MnO-Al₂O₃-SiO₂ ternary system

The MnO-SiO₂ (18) and Al₂O₃-SiO₂ (19) systems were optimized previously. The quasichemical model was used to estimate the properties of the ternary MnO-Al₂O₃-SiO₂ liquid slag from the optimized parameters of the three binary sub-systems. One small optimized ternary parameter was then included in order to reproduce the reported phase

diagram and thermodynamic data in the ternary system. Since no thermodynamic properties of $\text{Mn}_3\text{Al}_2\text{Si}_3\text{O}_{12}$ (spessartite) or $\text{Mn}_2\text{Al}_4\text{Si}_5\text{O}_{18}$ (Mn-cordierite) have been reported, the enthalpy and entropy of formations of these ternary compounds were also obtained from the ternary optimization, their heat capacities being estimated as the weighted average of those of MnO , SiO_2 and Al_2O_3 .

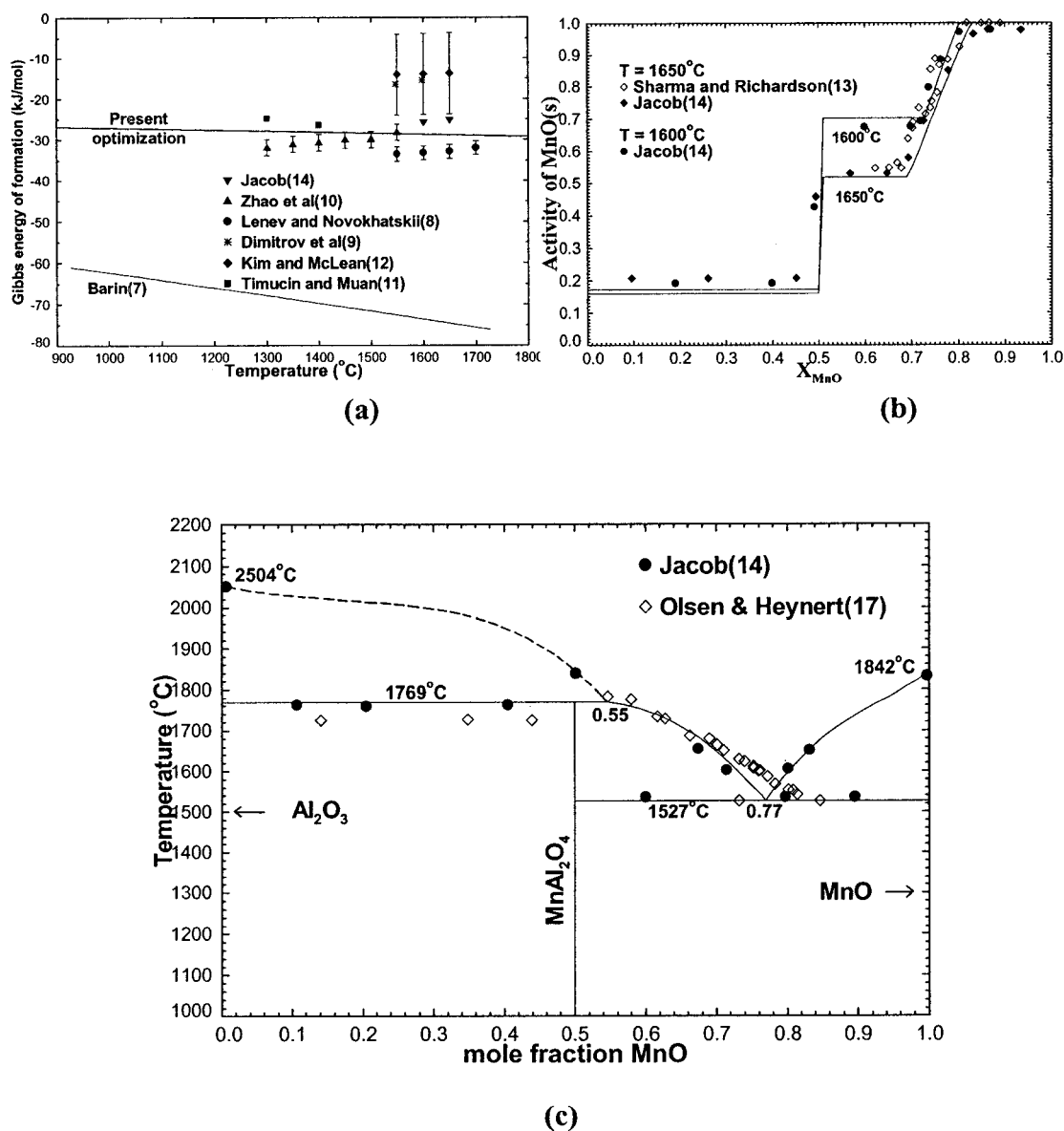


Figure 1. MnO-Al₂O₃ binary system. All curves are calculated from the optimizations. (a) Gibbs energy of formation of MnAl_2O_4 from solid MnO and Al_2O_3 . (b) Activity of MnO(solid) at 1600°C and 1650°C. (c) Optimized phase diagram.

Snow (20) investigated the primary crystallization regions in this ternary system below 1300°C using a quenching technique followed by X-ray and optical analysis. The calculated optimized ternary phase diagram is shown in Figure 2 along with the phase diagram proposed by Muan and Osborn (21) based on the experiments of Snow (20) and Hay et al (15). Since we optimized the MnO-Al₂O₃ system (Figure 1(c)) based upon the results of Oelsen and Heynert (17) who reported a higher incongruent melting point than did Hay et al. (15), the MnAl₂O₄ (galaxite) primary crystallization region in the optimized ternary diagram is much wider than in the diagram of Muan and Osborn (21). Otherwise, Figures 2(a) and 2(b) are in good agreement. Liquidus measurement near 1600°C by Sakao (22), Fujisawa and Sakao (23) and Ohta and Suito (24) were also taken into account in the optimization.

Sharma and Richardson (13) measured activities of MnO in MnO-Al₂O₃-SiO₂ liquid slags at 1650°C using a gas/slag/Pt equilibration technique. Similar measurements were made at 1550°C using the same technique as part of the current project (25). The calculated optimized iso-activity lines of MnO are in good agreement with the measured points as shown in Figure 3.

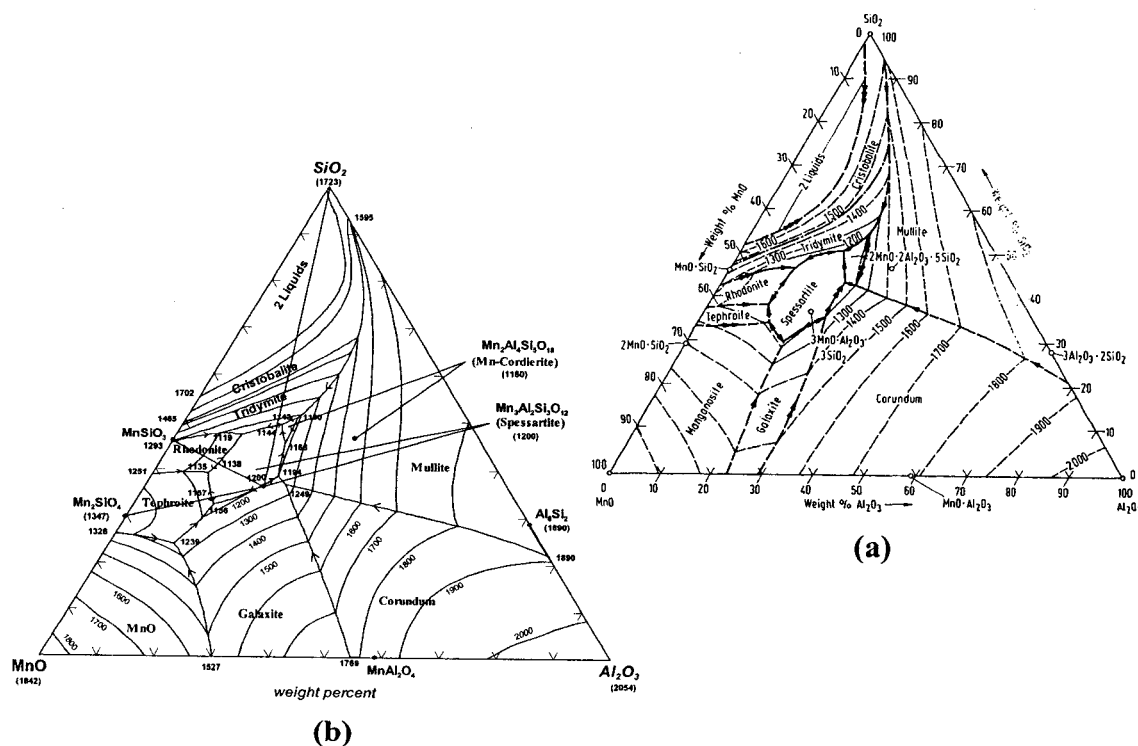


Figure 2. Phase diagram of the MnO-Al₂O₃-SiO₂ system (a) from Muan and Osborn (21) (b) Optimized (calculated) phase diagram (T = °C)

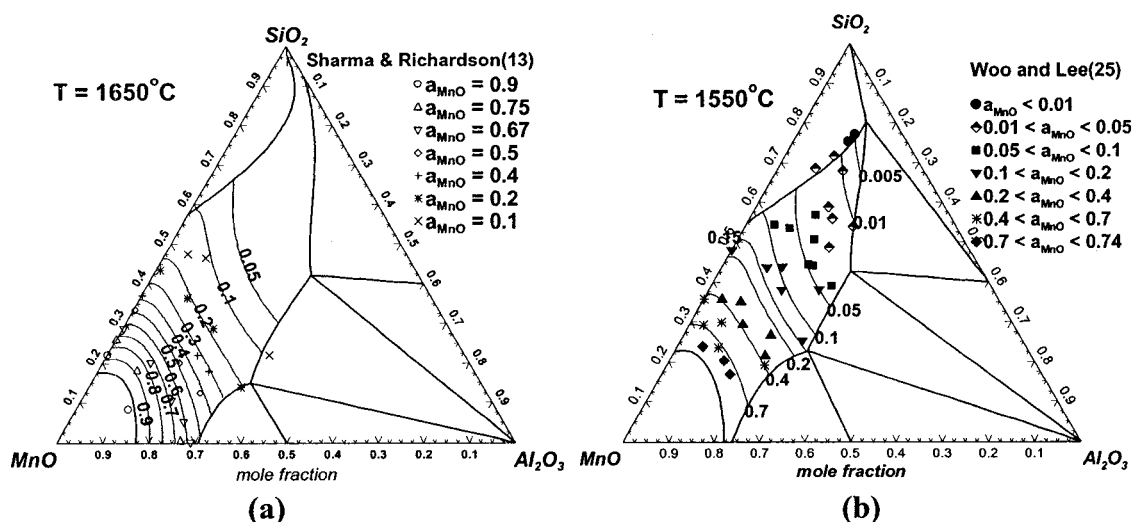


Figure 3. Activities of MnO(solid) in MnO-Al₂O₃-SiO₂ liquid slags. (a) T = 1650°C, (b) T = 1550°C (Curves are calculated from the optimization)

CaO-MnO-SiO₂ ternary system

The CaO-MnO-SiO₂ system exhibits two pseudo-binary joins: the Ca₂SiO₄-Mn₂SiO₄ orthosilicate section, and the CaSiO₃-MnSiO₃ metasilicate section. In the orthosilicate section, three solid solutions, α -Ca₂SiO₄, α' -Ca₂SiO₄ and olivine, exist at sub-solidus temperatures. The α -Ca₂SiO₄ and α' -Ca₂SiO₄ solutions dissolve Mn₂SiO₄. These were modeled simply as solutions between α (or α')-Ca₂SiO₄ and metastable Mn₂SiO₄, with polynomial expansions for the excess Gibbs energies. Since olivine has two distinct cation sublattices, it was modeled by a two-sublattice Compound Energy Formalism (3) taking into account the distribution of Ca²⁺ and Mn²⁺ cations between sublattices. In the metasilicate section are found the wollastonite and rhodonite solid solution phases, both of which have a linear chain silicate structure. They were described with simple polynomial expansions for the excess Gibbs energies. The thermodynamic properties of the ternary liquid slag were estimated by the quasichemical model from the previously optimized parameters (18, 26) of the binary sub-systems. One small additional ternary parameter was included in order to reproduce the reported phase diagram and activities of MnO in the ternary system more accurately.

The calculated optimized phase diagram is shown in Figure 4(b). It is very similar to the diagram experimentally determined by Glasser (27) (Figure 4(a)), but is thermodynamically more consistent. As shown in Figures 5(a) and (b), the calculated activities of MnO agree well with experimental data obtained by Mehta and Richardson (28) and by Abraham et al. (29) using gas/slag/Pt equilibration techniques.

CaO-MnO-Al₂O₃ ternary system

No phase diagram of the CaO-MnO-Al₂O₃ ternary system has been reported. The only thermodynamic data available are for the activities of MnO which were measured by Mehta and Richardson (28) using a gas/slag/Pt equilibration technique and by Morita et al. (30) using a gas/slag/Cu equilibration technique. There is considerable disagreement between the activities reported in the two investigations. No ternary compounds or solid solutions were assumed. The calculated (predicted) phase diagram is shown in Figure 6(a) and the calculated activities of MnO are plotted in Figure 6(b) where they are compared with the measurements (28, 30).

CaO-MnO-Al₂O₃-SiO₂ quaternary system

By combining the present optimized results with the previous optimization of the CaO-Al₂O₃-SiO₂ system (19), the database for the quaternary CaO-MnO-Al₂O₃-SiO₂ system was constructed. No additional model parameters were introduced. All experimental data related to the quaternary system are well predicted. Figure 7(a) shows the predicted (calculated) liquidus curves in the quaternary system compared with experimental results by Rait and Olsen (31) at the composition ratio (wt%Al₂O₃ / wt%SiO₂) = 0.5 at temperatures between 1450° and 1550°C. Agreement is within experimental error limits. The activities of MnO are also well predicted as shown in Figure 7(b).

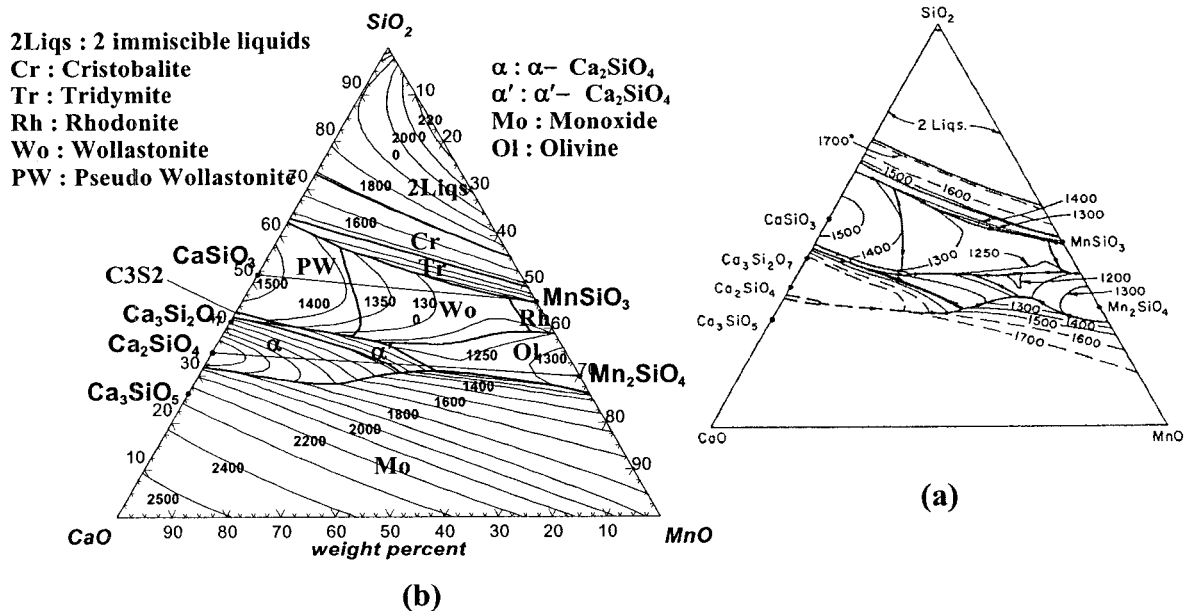


Figure 4. Phase diagram of the CaO-MnO-SiO₂ ternary system (a) from Glasser (27), (b) Optimized (calculated) (T=°C)

• Mehta and Richardson(28)

○ Abraham et al(italic) (29)

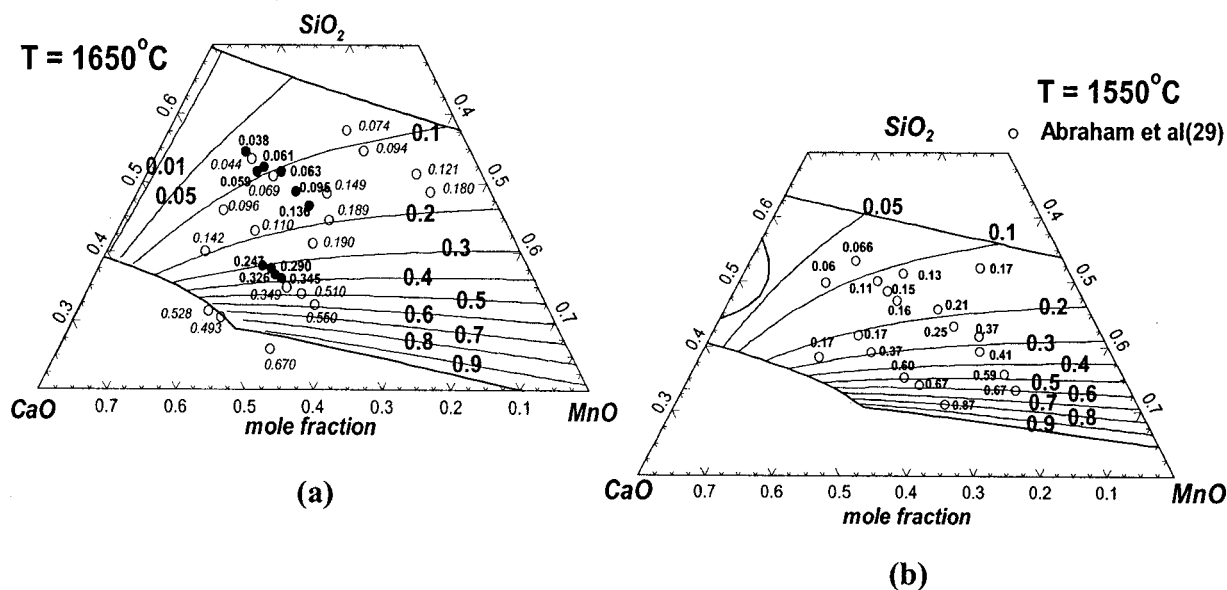


Figure 5. Activity of MnO(solid) in CaO-MnO-SiO₂ liquid slags. (a) T = 1650°C, (b) T = 1550°C (Curves are calculated from the optimization)

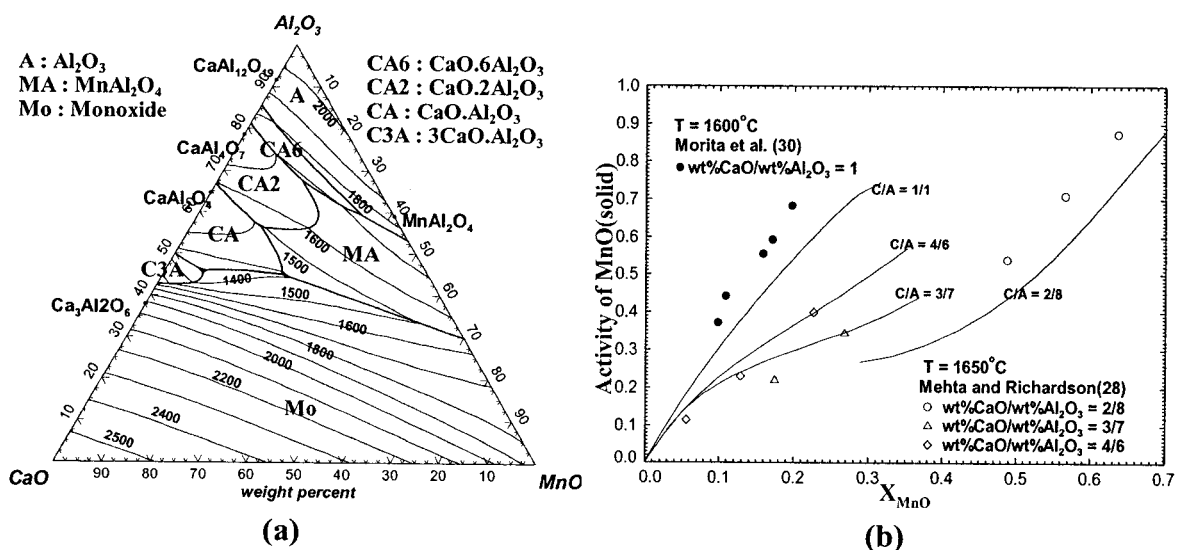


Figure 6. CaO-MnO-Al₂O₃ system. (a) Predicted phase diagram assuming no ternary compounds or solid solutions. (b) Activities of MnO (Lines are calculated from the optimization).

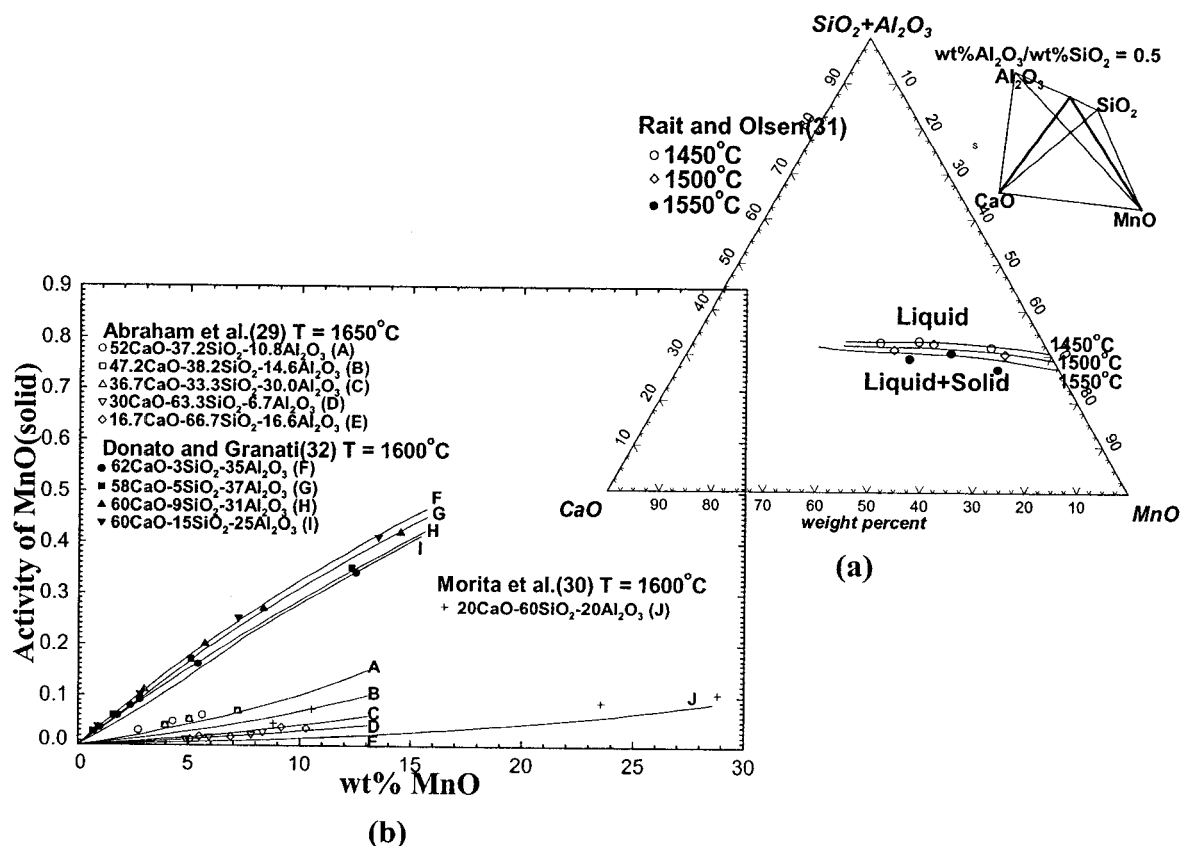


Figure 7. CaO-MnO-Al₂O₃-SiO₂ system. (a) Liquidus at weight ratio Al₂O₃/SiO₂ = 0.5 in the temperature range 1450° to 1550°C, (b) Activities of MnO(solid) (lines are calculated from the optimization).

APPLICATION TO INCLUSION CONTROL

The thermodynamic calculations involving equilibria between inclusions and liquid steel were performed using the FactSage computing system (1). The new optimized CaO-MnO-Al₂O₃-SiO₂ database was used for the oxide inclusions, and our previously optimized (33) database was used for the liquid steel phase. Some experiments (34) were also conducted to validate the results of the thermodynamic calculations.

In actual plant processes, Mn/Si deoxidation usually results in MnO-Al₂O₃-SiO₂ inclusions as deoxidation products. During the refining stage, these MnO-Al₂O₃-SiO₂ inclusions can react with CaO-containing top slags to become CaO-MnO-Al₂O₃-SiO₂ inclusions. In this study, the relationship between the Mn/Si ratio in the liquid steel (tire-

cord steel and Fe-36%Ni Invar steel) and the composition of MnO-Al₂O₃-SiO₂ and CaO-MnO-Al₂O₃-SiO₂ inclusions was investigated with a view to forming inclusions with low melting temperatures in order to minimize their harmful effects.

Figure 8 shows the variation of oxygen content with Mn/Si ratio in liquid Fe in equilibrium with liquid MnO-Al₂O₃-SiO₂ inclusions saturated with Al₂O₃, mullite or MnAl₂O₄ at 1535° and 1550°C. Lines are calculated using the optimized databases. The oxygen content of the liquid steel decreases with increasing total ([Mn]+[Si]) as well as with increasing Mn/Si ratio in the steel. The calculated curves agree well with experimental results (23-24, 35) as can be seen in Figure 8.

Figure 9 shows the compositional trajectory of MnO-Al₂O₃-SiO₂ inclusions with the Mn/Si deoxidant ratio in liquid steels. Figures 9(a) and 9(b) correspond to the tire-cord steel ([C] = 0.7wt%) at 1550°C and to Fe-36%Ni Invar steel at 1500°C respectively. The total amount of ([Mn]+[Si]) is 1.0 wt%. The calculated phase diagrams at 1550° or 1500°C are superimposed on the figures. A small amount of Fe₂O (less than 1 wt%) always exists in such inclusions. In Figure 9 this is included with MnO as shown.

Measurements of Lee and Lee (34), preformed as part of the present project are shown on Figure 9. To overcome the limitation of classical equilibrium experiments using a crucible (where the liquid inclusions are necessarily always saturated with solid phases such as Al₂O₃ or mullite), a cold crucible technique was used, in which the liquid steel droplets, covered with inclusions, are levitated. The thermodynamic calculations predict the compositional trajectories of inclusions within experimental error limits for both steels.

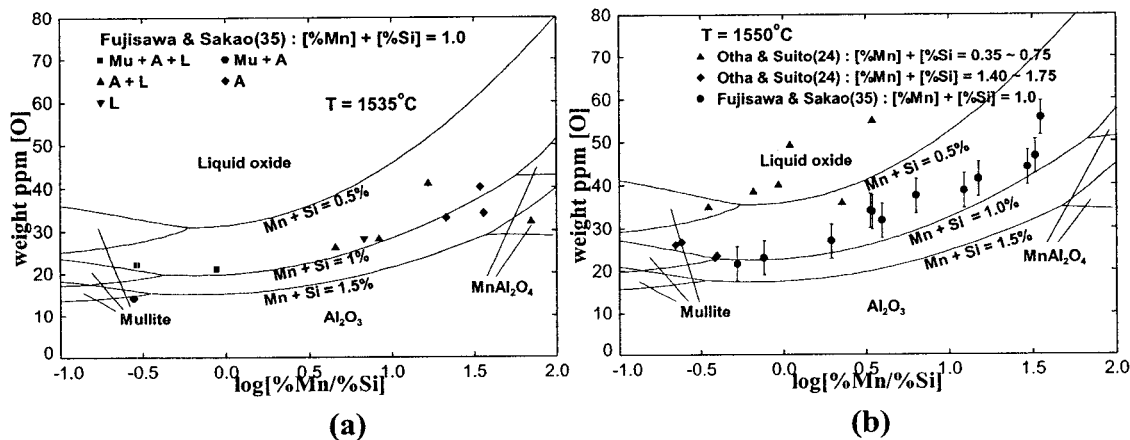


Figure 8. The variation of oxygen content with Mn/Si ratio in liquid Fe in equilibrium with liquid MnO-Al₂O₃-SiO₂ inclusions saturated with Al₂O₃, mullite, or MnAl₂O₄. (a) T = 1535°C, (b) T = 1550°C. (Lines are calculated using the optimized databases)

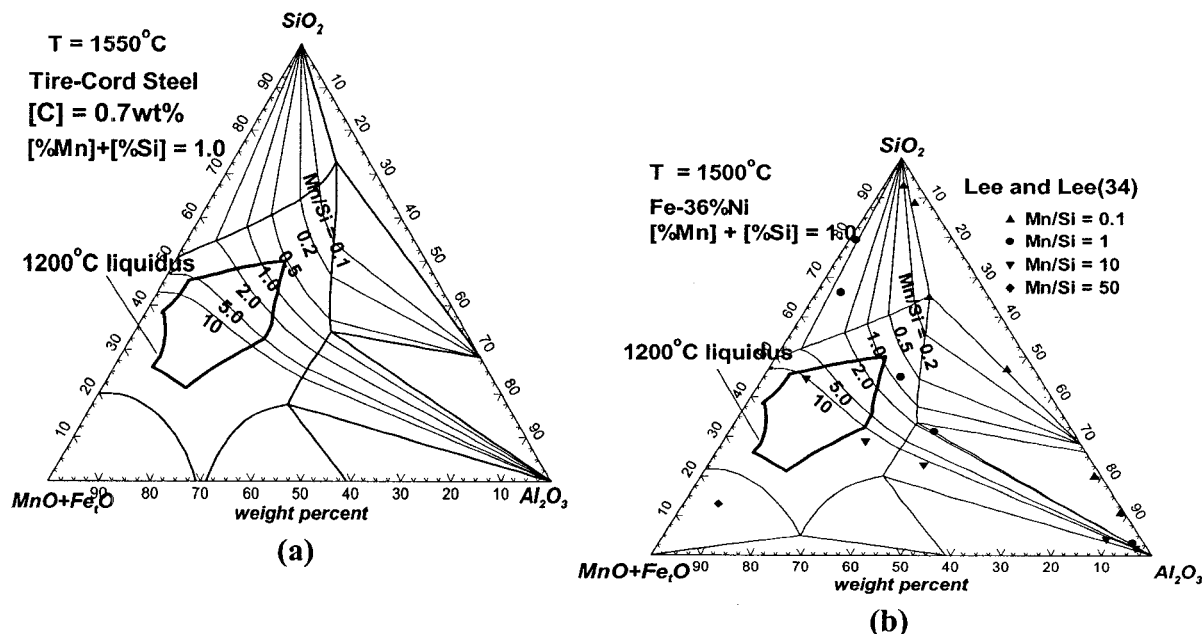


Figure 9. Calculated compositional trajectory of MnO-Al₂O₃-SiO₂ inclusions with the variation of Mn/Si ratio in liquid steels, and targeting the inclusion composition of MnO-Al₂O₃-SiO₂ inclusions for hot working at 1200°C. (a) Tire-cord steel ([C] = 0.7wt%) with ([%Mn] + [%Si]) = 1 at 1550°C, (b) Fe-36%Ni Invar steel with ([%Mn] + [%Si]) = 1 at 1500°C.

The main interest of this study is to maintain the inclusions in the liquid state at the temperature of the wire production process in the case of tire-cord steel and of the rolling process in the case of high-Ni steel. Therefore, the liquidus curve of the MnO-Al₂O₃-SiO₂ system at 1200°C is superimposed on the diagrams in Figure 9. This permits us to target the appropriate ranges of Mn/Si ratios to maintain the inclusions in the liquid state at 1200°C. Since ferromanganese is more expensive than ferrosilicon, lower ratios of Mn/Si are preferable. Therefore, the proper ranges of the Mn/Si alloying ratio in liquid steels with ([Mn] + [Si]) = 1wt% in the secondary refining process may be suggested as follows:

$$\begin{aligned}
 &1 < \text{Mn/Si} < 2 : \text{For tire-cord steel ([C] = 0.7wt\%)} \\
 &2 < \text{Mn/Si} < 5 : \text{For Fe-36\%Ni Invar steel} \\
 &\text{when ([Mn] + [Si]) = 1wt\% in both steels}
 \end{aligned}$$

Inclusions formed by Mn/Si deoxidation can react with top slags during the refining process. Figure 10 shows the effect of top slags on the melting temperature of MnO-Al₂O₃-SiO₂ inclusions. The composition of the top slags was assumed to be 55wt%CaO-15wt%Al₂O₃-30wt%SiO₂. The target inclusion composition for the suggested Mn/Si ratio of 2.0 is MnO-SiO₂-15wt%Al₂O₃ (i.e. MnO/SiO₂ ~ 1). Therefore, the inclusion composition can change during the reaction with the top slag as shown in

the figure. Calculated liquidus isotherms are also plotted on Figure 10. It is noted that as CaO dissolves in the inclusions to between 5 and 15wt%, the melting temperature of the inclusions is reduced by 50° to 100°C. Thus, if the reaction between inclusions and top slags can be accurately controlled, the inclusions in Mn/Si killed steel can be modified to more favourable compositions with lower melting temperatures.

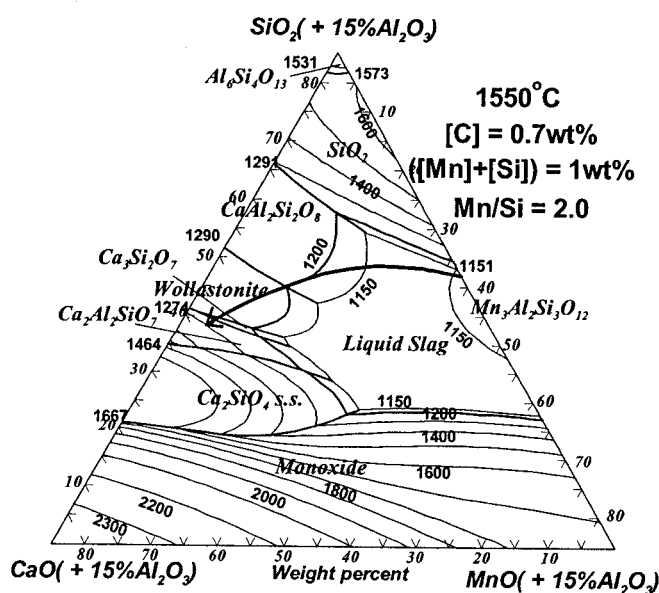


Figure 10. Calculated change of composition of inclusions formed during Mn/Si deoxidation (as shown by arrows) when the Mn/Si ratio equals 2.0 for tire-cord steel ([C]=0.7wt%) by reaction with CaO-containing top slag at 1550°C (Assumed top slag composition: 55wt% CaO - 15wt% Al₂O₃ - 30wt% SiO₂). Predicted liquidus isotherms (T=°C) are also plotted.

CONCLUSIONS

The thermodynamic properties and phase equilibria of the MnO-Al₂O₃, MnO-Al₂O₃-SiO₂, CaO-MnO-Al₂O₃ and CaO-MnO-Al₂O₃-SiO₂ systems were critically evaluated and optimized, using all available thermodynamic and phase diagram data. The resultant thermodynamic database for the quaternary CaO-MnO-Al₂O₃-SiO₂ system was combined with the previously optimized database for liquid steel and used with the FactSage software (1) to calculate optimal conditions for inclusion control in Mn/Si-killed steel. It has been shown that the newly optimized database is accurate and gives good predictions for calculations of equilibrium between inclusions and liquid steel.

Thermodynamic calculations were performed for the prediction of inclusion

behaviour in tire-cord steel and in Fe-36%Ni Invar steel. The compositional trajectories of MnO-Al₂O₃-SiO₂ inclusions with the variation of the Mn/Si ratio in liquid steel were calculated, and the calculated results agree well with experimental data. Suitable ranges of Mn/Si ratios in liquid steels were recommended in order to maintain the MnO-Al₂O₃-SiO₂ inclusions in the liquid state, and hence deformable, at the hot working temperature of 1200°C.

The effect of reaction with CaO-containing top slags on MnO-Al₂O₃-SiO₂ inclusions was also calculated. It is found that the dissolution of CaO up to between 5 to 15% will decrease the melting temperature of the inclusions and will thus increase the deformability at low temperature.

ACKNOWLEDGEMENTS

This project is supported by a CRD grant from the Natural Sciences and Engineering Research Council of Canada in collaboration with the following: INCO, Noranda, Rio Tinto, COMINCO, Alcoa, Dupont, Shell, Corning, Pechiney, Norsk Hydro, Sintef, Schott Glas, St.-Gobain Recherche, Mintek, IIS technologies. The authors also wish to thank POSCO Steel, Korea, for supporting the experimental part of the project.

REFERENCES

1. FactSage <www.factsage.com>.
2. A.D. Pelton and M. Blander : Proc. 2nd Int. Symp. Metall. Slags and Fluxes, TMS-AIME, Warrendale, PA, 1984, 281-291;
A.D. Pelton and M. Blander : "Thermodynamic Analysis of Ordered Liquid Solutions by a Modified Quasichemical Approach-Application to Silicate Slags", Metall. Trans. B, Vol. 17B, No. 4, 1986, 805-815.
3. M. Hillert, B. Jansson and B. Sundman : "Application of the Compound Energy Model to Oxide Systems", Z. Metallkunde, Vol. 79, No. 2, 1988, 81-87.
4. I.-H. Jung, Y.-B. Kang, S. Degterov, A.D. Pelton and H.-G. Lee : to be published.
5. Y.-B. Kang, I.-H. Jung, S. Degterov, A.D. Pelton and H.-G. Lee : to be published.
6. G. Eriksson, P. Wu and A.D. Pelton : "Critical Evaluation and Optimization of the Thermodynamic Properties and Phase Diagrams of the MgO-Al₂O₃, MnO-Al₂O₃, FeO-Al₂O₃, Na₂O-Al₂O₃ and K₂O-Al₂O₃ Systems", Calphad Journal, Vol. 17, No. 2, 1993, 189-206.
7. I. Barin, Thermochemical Data of Pure Substances, VCH, Weinheim, Germany, 1989.
8. L.M. Lenev and I.A. Novokhatskii : Izv. Akad. Nauk. SSSR. Metall., Vol. 3, 1966, 73-78.
9. S. Dimitrov, A. Weyl and D. Janke : "Control of the Manganese-Oxygen Reaction

- in Pure Iron Melts”, Steel Research, Vol. 66, No. 3, 1995, 87-92.
10. Y. Zhao, K. Morita and N. Sano : “Thermodynamic Properties of the MgAl_2O_4 - MnAl_2O_4 Spinel Solid Solution”, Metall. Mater. Trans. B, Vol. 26B, 1995, vol. 26B, pp. 1013-1017.
 11. M. Timucin and A. Muan : “Activity-Composition Relations in NiAl_2O_4 - MnAl_2O_4 Solid Solutions and Stabilities of NiAl_2O_4 and MnAl_2O_4 at 1300° and 1400°C”, J. Amer. Ceram. Soc., Vol. 75, No. 6, 1992, 1399-1406.
 12. C.K. Kim and A. McLean : “Thermodynamics of Iron-Manganese Aluminate Spinel Inclusions in Steel”, Metall. Trans., Vol. 10B, 1979, 575-584.
 13. R.A. Sharma and F.D. Richardson, “Activities of Manganese Oxide, Sulfide Capacities, and Activity Coefficients in Aluminate and Silicate Melts”, Trans. Metall. Soc. AIME, Vol. 233, 1965, 1586-1592.
 14. K. T. Jacob : “Revision of Thermodynamic Data on $\text{MnO-Al}_2\text{O}_3$ Melts”, Canad. Metall. Quart., Vol. 20, No.1, 1981, 89-92.
 15. R. Hay, J. White and A.B. McIntosh : “Slag Systems”, J. W. Scotl. Iron Steel Inst., Vol. 42, 1934/1935, 99-104.
 16. I.A. Novokhatskii, L.M. Lenev, A.A. Savinskaya and A.V. Gorokh : “Equilibrium Diagram of the Al_2O_3 - MnO System”, Zh. Neorg. Khim., Vol. 11, 1966, 427-428.
 17. W. Oelsen and G. Heynert : Arch. Eisenhüttenw., Vol. 26, 1955, 567-575.
 18. G. Eriksson, P. Wu, M. Blander and A.D. Pelton : “Critical Evaluation and Optimization of the Thermodynamic Properties and Phase Diagrams of the MnO-SiO_2 and CaO-SiO_2 Systems”, Canad. Metall. Quart., Vol. 33, No. 1, 1994, 13-21.
 19. G. Eriksson and A.D. Pelton, “Critical Evaluation and Optimization of the Thermodynamic Properties and Phase Diagrams of the $\text{CaO-Al}_2\text{O}_3$, Al_2O_3 - SiO_2 , $\text{CaO-Al}_2\text{O}_3$ - SiO_2 Systems”, Metall. Mater. Trans. B, Vol. 24B, No. 5, 1993, 807-815.
 20. R.B. Snow : “Equilibrium Relationships on the Liquidus Surface in Part of the $\text{MnO-Al}_2\text{O}_3$ - SiO_2 System”, J. Amer. Ceram. Soc., Vol. 26, No. 1, 1943, 11-20.
 21. A. Muan and E. F. Osborn, Phase Equilibria among Oxides in Steelmaking, Addison-Wesley Publishing Co., Reading, MA, 1965.
 22. H. Sakao : “Thermodynamics of the Complex Deoxidation of Liquid Iron : Si-Mn-Al Deoxidation ”, Tetsu-to-Hagane, Vol. 56, 1970, S621-624.
 23. T. Fujisawa and H. Sakao : “Equilibrium Between MnO-SiO_2 - Al_2O_3 - FeO Slags and Liquid Steel”, Tetsu-to-Hagane, Vol. 63, No. 9, 1977, 1504-1511.
 24. H. Ohta and H. Suito : “Activities in MnO-SiO_2 - Al_2O_3 Slags and Deoxidation Equilibria of Mn and Si”, Metall. Mater. Trans. B, Vol. 27B, 1996, 263-270.
 25. D.-H. Woo and H.-G. Lee : “Thermodynamic Study on the Activities of Manganese Oxide in MnO-SiO_2 - Al_2O_3 Slags”, J. Kor. Inst. Met. & Mater. (submitted)
 26. P. Wu, G. Eriksson and A.D. Pelton : “Critical Evaluation and Optimization of the Thermodynamic Properties and Phase Diagrams of the CaO-FeO , CaO-MgO , CaO-MnO , FeO-MgO , FeO-MnO , and MgO-MnO Oxide Systems” , J. Am. Ceram. Soc., Vol. 76, No. 8, 1993, 2065-2075.
 27. F.P. Glasser : “The Ternary System CaO-MnO-SiO_2 ”, J. Am. Ceram. Soc., Vol. 45, No. 5, 1962, 242-249.

28. S.R. Mehta and F.D. Richardson : "Activity of MnO in Silicate and Aluminate Melts", J. Iron and Steel Inst., Vol. 203, No. 27, 1965, 524-528.
29. K.P. Abraham, M.W. Davies and F.D. Richardson : "Activities of Manganese Oxide in Silicate Melts", J. Iron and Steel Inst., Vol. 196, 1960, 82-88.
30. K. Morita, M. Miwa and M. Ohta : "Thermodynamic Properties of Manganese Oxide in Steelmaking Slags and Inclusions", 2nd International Congress, Science and Technology of Steelmaking, Univ. of Wales, Swansea, UK, 2001.
31. R. Rait and S.E. Olsen : "Liquidus Relations of Ferromanganese Slags", Scand J. of Metall., Vol.28, No. 2, 1999, pp.53-58.
32. A.D. Donato and P. Granati : "Experimental Determination of Activity of FeO, MnO and Cr₂O₃ in slag", Proceedings of the Sixth International Conference on Molten Slags, Fluxes and Salts, S. Seetharaman and D. Sichen Eds., Stockholm, Sweden - Helsinki, Finland, 2000.
33. I.-H. Jung and A.D. Pelton : to be published.
34. S.-B. Lee and H.-G. Lee : to be published.
35. T. Fujisawa and H. Sakao : "Equilibrium Relations between Liquid Iron Alloys and the Deoxidation Products Resulting from Mn-Si-Al Complex Deoxidation", Tetsu-to-Hagane, Vol. 63, No. 9, 1977, 1494-1503.

Appendix VII

Article :

Thermodynamic Modeling of the MgO-Al₂O₃-CrO-Cr₂O₃ System

In-Ho Jung, Sergei A. Decterov and Arthur D. Pelton

Submitted to *J. Am. Ceram. Soc.*, 2003

Thermodynamic Modeling of the MgO-Al₂O₃-CrO-Cr₂O₃ System

In-Ho Jung, Sergei Decterov and Arthur D. Pelton

Centre de Recherche en Calcul Thermochimique (CRCT), École Polytechnique de Montréal,
Montréal, Québec, H3C 3A7, Canada

A complete critical evaluation and thermodynamic modeling of the phase diagrams and thermodynamic properties of the MgO-Al₂O₃-CrO-Cr₂O₃ system at 1 bar total pressure are presented. Optimized equations for the thermodynamic properties of all phases are obtained which reproduce all available thermodynamic and phase equilibrium data within experimental error limits from 25°C to above the liquidus temperatures at all compositions and oxygen partial pressures. The optimized thermodynamic properties and phase diagrams are believed to be the best estimates presently available. The database of the model parameters can be used along with software for Gibbs energy minimization in order to calculate any type of phase diagram section.

I. Introduction

THE Mg-Cr-Al-O system is important in the ceramics and metallurgical industries, particularly for its role in many refractories. Despite its importance, the phase equilibria in this system have not been well studied. Experimental study of the system is complicated by the strong dependence of the equilibria on oxygen pressure and by the high melting temperature of the spinel phase. Therefore, critical assessment and optimization of the data is required in order to understand and model this system more accurately.

Optimizations of the MgO-Al₂O₃, CrO-Cr₂O₃ and CrO-Cr₂O₃-Al₂O₃ systems have been reported previously.^{1,2} The main goal of the present study is to perform a critical assessment and optimization of the thermodynamic properties and phase equilibria at 1 bar total pressure of oxide phases of the MgO-Al₂O₃-CrO-Cr₂O₃ (Mg-Al-Cr-O) system. In the thermodynamic "optimization" of a chemical system, all available thermodynamic and phase equilibrium data are evaluated simultaneously in order to obtain one set of model equations for the Gibbs energies of all phases as

functions of temperature and composition. From these equations, all of the thermodynamic properties and the phase diagrams can be back-calculated. In this way, all the data are rendered self-consistent and consistent with thermodynamic principles. Thermodynamic property data, such as activity data, can aid in the evaluation of the phase diagram, and phase diagram measurements can be used to deduce thermodynamic properties. Discrepancies in the available data can often be resolved, and interpolations and extrapolations can be made in a thermodynamically correct manner.

The present optimization covers the range of oxygen partial pressures from equilibration with pure oxygen to metal saturation, and temperatures from 25°C to above the liquidus. All calculations in this study were performed with the FactSage³ software.

II. Phases and Thermodynamic Models

The following solution phases are found in the MgO-Al₂O₃-CrO-Cr₂O₃ system: (i) slag (molten oxide phase): MgO-CrO-CrO_{1.5}-AlO_{1.5}, (ii) monoxide (periclase): MgO-CrO_{1.5}-AlO_{1.5}, (iii) spinel (encompassing MgCr₂O₄, MgAl₂O₄ and Cr₃O₄): (Mg²⁺, Al³⁺, Cr²⁺, Cr³⁺)^T [Mg²⁺, Al³⁺, Cr³⁺, Va]₂O₄, (iv) corundum: Al₂O₃-Cr₂O₃, (v) liquid, bcc and fcc alloys: Mg-Cr-Al. Cations shown within a set of brackets for spinel occupy the same sublattice.

(I) Molten Oxide (slag)

The Modified Quasichemical Model^{4,5,6,7} which takes into account short-range ordering of second-nearest-neighbor cations in the ionic melt, is used for modeling the slag.

The components of the slag are taken as MgO-CrO-CrO_{1.5}-AlO_{1.5}. Although Cr can have higher oxidation states, only the Cr²⁺ and Cr³⁺ oxidation states which predominate at oxygen partial pressures less than 1.0 bar, are considered in the present study.

The binary and ternary sub-systems MgO-AlO_{1.5}, CrO-CrO_{1.5} and AlO_{1.5}-CrO-CrO_{1.5} have already been critically evaluated and optimized,^{1,2} and these optimized model parameters are used as the basis of the present study. All second-nearest-neighbor "coordination numbers" used in the present model for the slag are the same as in previous studies.^{1,2} The properties of the quaternary slag solution were calculated from the binary and ternary parameters using a symmetric "Kohler-like"⁸ approximation.

One additional optimized binary parameter related to Mg²⁺-Cr³⁺ interactions was added in the present study. This is listed in Table I.

This study is based in part on the thesis submitted by I.-H. Jung for the Ph.D degree in Materials and Metallurgical Engineering, École Polytechnique de Montréal, Montréal, Québec, H3C 3A7, Canada.

Supported by a CRD grant from the Natural Sciences and Engineering Research Council of Canada in collaboration with the following: Alcoa, Corning, Dupont, INCO, Mintek, Noranda, Norsk Hydro, Pechiney, Rio Tinto, Schott Glass, Shell, Sintef, St.-Gobain Recherche, Teck Cominco and IIS Materials.

The authors wish to thank Profs. P. Wollants and B. Blanpain and Ms. O. Szabo of K.U. Leuven, Belgium, and Mr. Y.-B. Kang of POSTECH, Korea for many fruitful discussions and advice.

(2) Spinel Solution

The model for the spinel solution was developed within the framework of the Compound Energy Formalism (CEF).⁹ The Gibbs energy expression in the CEF per formula unit is:

$$G = \sum_i \sum_j Y_i^T Y_j^O G_{ij} - TS_C + G^E$$

where Y_i^T and Y_j^O represent the site fractions of constituents i and j on the tetrahedral and octahedral sublattices, G_{ij} is the Gibbs energy of an "end-member" $(i)^T[j]_2^O\text{O}_4$ of the solution, in which the first sublattice is occupied only by cation i and the second only by cation j , G^E is the excess Gibbs energy, and S_C is the configurational entropy assuming random mixing on each sublattice:

$$S_C = -R \left(\sum_i Y_i^T \ln Y_i^T + 2 \sum_j Y_j^O \ln Y_j^O \right)$$

The excess Gibbs energy is expanded as:

$$G^E = \sum_i \sum_j \sum_k Y_i^T Y_j^T Y_k^O L_{ij:k} + \sum_i \sum_j \sum_k Y_k^T Y_i^O Y_j^O L_{k:ij}$$

where the parameters $L_{ij:k}$ are related to interactions between cations i and j on tetrahedral sites when all octahedral sites are occupied by k cations, and the parameters $L_{k:ij}$ are related to interactions between i and j cations on octahedral sites when the tetrahedral sites are all occupied by k cations. In the present study, only one small $L_{k:ij}$ parameter, and no $L_{ij:k}$ parameters, were used.

The main model parameters are the end-member Gibbs energies, G_{ij} . These are listed in Table I. Details of the optimization are given in the following sections. As seen in Table I, certain linear combinations of the G_{ij} parameters, which have physical sense, are used as the optimized model parameters. The physical significance of these linear combinations (I_{MG} , $\Delta_{MG:MG}$, etc.) is discussed in reference [10]. These linear combinations are related to the energies of classical site exchange reactions.

Parameters not shown in Table I (such as G_{AA} , G_{MA} , ...) were obtained in the previous¹ optimization of the Mg-Al-O system. The parameter G_{CG} , which is equal to the Gibbs energy of Cr_3O_4 , $G_{\text{Cr}_3\text{O}_4}^0$, was evaluated previously.²

Since the present spinel model reduces to the model of O'Neill and Navrotsky¹¹ as a limiting case, the values of the parameters I_{MG} and $\Delta_{MG:MG}$ were determined from values and site preference energies recommended by these authors. The parameters $\Delta_{AG:AG}$, $\Delta_{MC:GV}$, $\Delta_{MC:MG}$ and $\Delta_{MA:GA}$ are the energies of reciprocal reactions among the end members and are expected to be small. Three of these were set to zero, and the fourth, $\Delta_{MA:GA}$, was optimized to reproduce the available data as discussed below. The reciprocal parameter $\Delta_{CF:AG}$ is equal to $(G_{CA} + G_{FG} - G_{FA} - G_{CG})$, where G_{FG} and G_{FA} are the Gibbs energies of the end-members $(\text{Fe}^{2+})[\text{Cr}^{3+}]_2\text{O}_4$ and $(\text{Fe}^{2+})[\text{Al}^{3+}]_2\text{O}_4$ evaluated in

previous studies.^{12,13} This parameter is also expected to be small, and was set to zero.

As discussed below, non-stoichiometry of MgCr_2O_4 towards excess chromium is due principally to the dissolution of Cr^{2+} as Cr_3O_4 . On the other hand, non-stoichiometry of MgAl_2O_4 spinel towards excess aluminum is due to the formation of vacancies on octahedral sites. In the previous optimization of the Mg-Al-O system¹ this was modeled as a solution of MgAl_2O_4 and $\gamma\text{-Al}_2\text{O}_3$, $(\text{Al}^{3+})[\text{Al}_{5/6}^{3+}\text{Va}_{1/6}]_2\text{O}_4$, and the end-member parameter G_{AV} was related to the Gibbs energy of $\gamma\text{-Al}_2\text{O}_3$. In the present case, in order to be able to model the mixed spinel phase, the parameter G_{GV} is related to the Gibbs energy of " $\gamma\text{-Cr}_2\text{O}_3$," $G_{\gamma\text{-Cr}_2\text{O}_3}^0$, using a similar equation as shown in Table I. In order to assure that the concentration of vacancies in the absence of Al is very low, $G_{\gamma\text{-Cr}_2\text{O}_3}^0$ was assigned a large positive value equal to $(G_{\text{Cr}_2\text{O}_3}^0 + 200 \text{ kJ/mol})$ as shown in Table I.

No excess parameters $L_{ij:k}$ or $L_{k:ij}$ of the spinel phase were required in the previous optimization of the Mg-Al-O system.¹ In the present study, one small parameter $L_{k:GA}$ related to the interaction of Cr^{3+} and Al^{3+} ions on octahedral sites was required. It was assumed that this parameter is independent of the ions occupying the tetrahedral sites. That is, $L_{C:GA} = L_{G:GA} = L_{M:GA} = L_{A:GA}$. In summary, the only additional parameters for the spinel phase which were optimized in the present study are $\Delta_{MA:GA}$ and $L_{k:GA}$. Also, $H_{298.15}^0$ of MgCr_2O_4 was slightly adjusted as discussed below.

The compound Cr_3O_4 is stable in a narrow temperature range between 1650° and 1700°C. It has a distorted tetragonal spinel structure. The lattice parameters of $\text{MgCr}_2\text{O}_4\text{-Cr}_3\text{O}_4$ spinel solutions have been measured over the entire composition range.¹⁴⁻¹⁷ The lattice parameters are observed to vary smoothly and continuously with composition, exhibiting no discontinuities. The cubic to tetragonal transition, which is due to the Jahn-Teller distortion,^{14,15} is thus not modeled as a first-order transition, and only one thermodynamic model for the spinel phase, valid at all compositions, is required. Similar behavior is observed for the spinel phase in the Fe-Cr-O system.^{13,18,19}

(3) Periclase Solution

The periclase solution was modeled as a simple random mixture of Mg^{2+} , Cr^{3+} and Al^{3+} ions on cation sites with simple polynomial excess Gibbs energy terms.⁸ It is assumed that cation vacancies remain associated with Cr^{3+} or Al^{3+} ions and so do not contribute to the configurational entropy.

Binary excess Gibbs energies were modeled by simple polynomial expansions in the mole fraction.⁸ Optimized parameters for $\text{MgO-AlO}_{1.5}$ solutions were obtained previously.¹ Optimized parameters for the $\text{MgO-CrO}_{1.5}$ solution were obtained in the present study as

described in the following sections. These are listed in Table I. The properties of the ternary periclase solution were calculated from the binary parameters with the symmetric "Kohler-like" approximation.⁸

(4) Other Solutions

Thermodynamic properties of the corundum solution $\text{Al}_2\text{O}_3\text{-Cr}_2\text{O}_3$ were optimized previously.² The thermodynamic properties of liquid, bcc and fcc metallic solutions from the SGTE (Scientific Group Thermodata Europe)²⁰ database were used for calculations of phase equilibria at metallic saturation.

III. Results of Evaluation/Optimization

(1) MgCr_2O_4 Spinel

The thermodynamic properties of stoichiometric MgCr_2O_4 spinel have been well studied. The heat capacity of MgCr_2O_4 was measured from 54 K to 296 K by Shomate²¹ and the enthalpy from 298 K to 1773 K was measured by Naylor.²² Plumier²³ and Shaked *et al.*²⁴ reported two distinct antiferromagnetically ordered states at 16 K and 13.5 K from neutron diffraction studies at low temperature, whereas Blasse and Fast²⁵ reported a paramagnetic to antiferromagnetic transition at 15 K. From Mossbauer spectroscopy and X-ray techniques, Hartmann-Boutron *et al.*²⁶ reported that the transition reflects a change in crystallographic symmetry through the Jahn-Teller effect. Recently, Klemme *et al.*²⁷ measured the heat capacity from 1.5 K to 340 K. In their measurements, a substantial magnetic contribution to the entropy was revealed by a very high sharp peak in the heat capacity at 12.55 K, associated with the transition to antiferromagnetic long-range order. Klemme *et al.*²⁷ calculated the entropy at 298.15 K taking into account this magnetic contribution.

O'Neill and Dollase²⁸ recently analyzed the fine structure of XRD measurements to investigate the cation distribution of MgCr_2O_4 synthesized at various temperatures and oxygen partial pressures. They found that all samples had the fully normal spinel structure within the accuracy of the analysis. Hence, the parameter G_{MG} is equal to $G_{\text{MgCr}_2\text{O}_4}^\circ$, the Gibbs energy of stoichiometric MgCr_2O_4 . The values of $H_{298.15}^\circ$, $S_{298.15}^\circ$ and the heat capacity function shown in Table I were taken from the values recommended by Klemme *et al.*²⁷ based on their assessment of all available thermodynamic data. The value of $H_{298.15}^\circ$ was further adjusted slightly by -1.13 kJ/mol in the present optimization. The value of $S_{298.15}^\circ$ takes account of the magnetic transition at 12.55 K. The heat capacity expression is valid from 15 K up to the melting temperature.

Fig. 1 shows the variation in oxygen partial pressure of MgCr_2O_4 in equilibrium with Cr and MgO. Tretjakow and Schmalzried²⁹ and Jacob³⁰ measured the oxygen partial pressure between 750° and 1250°C by an emf technique

using $\text{ZrO}_2\text{-CaO}$ and $\text{Y}_2\text{O}_3\text{-ThO}_2$ electrolytes respectively. The calculated curve is slightly lower than the experimental points because of the slight adjustment to $H_{298.15}^\circ$ of MgCr_2O_4 mentioned above. However, this adjustment was required in order to better fit the data in Fig. 6 as discussed below. In any case, the agreement in Fig. 1 is within the experimental error limits. Muller and Kleppa³¹ measured the enthalpy of formation of MgCr_2O_4 from MgO and Cr_2O_3 oxides at 900°C using $2\text{PbO}\cdot\text{B}_2\text{O}_3$ solution calorimetry. The measured value of -46.3 kJ/mol is very close to the present calculated optimized value, -46.9 kJ/mol. Sata and Lee^{32,33} studied the evaporation of MgCr_2O_4 using Knudsen cell and Langmuir techniques. The results were quite different for the different experimental techniques, and were not considered in the present optimization.

The melting temperature of MgCr_2O_4 depends strongly on the partial pressure of oxygen, mainly because the $\text{Cr}^{2+}/\text{Cr}^{3+}$ ratio in the liquid phase depends upon P_{O_2} . For this reason, the melting temperature has been the subject of controversy for some time. The melting temperature, calculated from the present model, is shown in Fig. 2 as a function of P_{O_2} . Melting points reported by several authors³⁴⁻³⁸ are also shown in Fig. 2. In none of these experiments was P_{O_2} controlled. However, each author also measured the melting point of Cr_2O_3 in the same apparatus under similar conditions. Since the melting point of Cr_2O_3 as a function of P_{O_2} is known,² the oxygen partial pressures in the various studies can thereby be estimated. Agreement between the measurements and the calculations are good. Under normal conditions, MgCr_2O_4 melts congruently. However, the calculations show that when $\log P_{\text{O}_2} < -8.6$ it melts incongruently to form liquid and periclase. The variation of the melting temperature of MgCr_2O_4 with oxygen partial pressure is elucidated for the first time in the present study.

(2) $\text{MgO-CrO-Cr}_2\text{O}_3$ System

Optimized " $\text{MgO-Cr}_2\text{O}_3$ " phase diagrams at various constant oxygen partial pressures are shown in Fig. 3. Since Cr^{2+} is also present in some phases, the horizontal axis of these diagrams is more correctly the molar metal ratio $\frac{\text{Cr}}{2} / (\frac{\text{Cr}}{2} + \text{Mg})$.

It is assumed in the present model that Cr dissolves in periclase only as Cr^{3+} , since no investigation has shown evidence of Cr^{2+} . Therefore, the phase boundary between the periclase and (periclase+spinel) region in Fig. 3 should be independent of P_{O_2} as shown. This boundary was first measured by Frenkel *et al.*,³⁹ by Alper *et al.*³⁶ using a quenching technique, and by Hering,¹⁹ Henriksen and Kingery⁴⁰ and Greskovich and Stubican^{14,41} from inter-diffusion studies. The various experimental studies are in good agreement with each other and with the calculations

using the optimized parameters for periclase given in Table I.

Alper *et al.*³⁶ measured solidus and liquidus temperatures under N_2 atmospheres by a technique of quenching followed by optical and X-ray analysis. Using their reported melting point of Cr_2O_3 as an indicator as discussed above, the oxygen partial pressure in their apparatus is estimated as $\log P_{O_2} \sim -1.5$. Wilde and Rees³⁷ reported solidus and eutectic temperatures measured in a carbon tube furnace. Again using their reported melting point of Cr_2O_3 as an indicator, we estimated that $\log P_{O_2} \sim -5.5$ in their apparatus. As can be seen in Fig. 3, there is good agreement between the measurements and the calculations.

The solubility of MgO in Cr_2O_3 has been shown^{14,37,41} from lattice parameter measurements by XRD to be negligible. Gee³⁴ reported the existence of a compound $4MgO \cdot Cr_2O_3$, but more recent studies^{36,37} do not confirm its existence.

As discussed above, the spinel phase in the absence of Al is considered to be a solid solution of $MgCr_2O_4$ and Cr_3O_4 . No additional model parameters were added in the present study. As can be seen in Fig. 3, the calculated solubility of Cr_3O_4 increases significantly as the oxygen partial pressure decreases. The solidus point of Wilde and Rees³⁷ at $\log P_{O_2} \sim -5.5$ in Fig. 3 (c) is well reproduced by the calculations. Greskovich and Stubican,^{14,15} from lattice parameter measurements, observed single-phase spinel up to a molar ratio $Cr/(Mg+Cr)$ of 0.8 at $1950^\circ C$ under reducing conditions (exact P_{O_2} unspecified), while negligible solubility at $1700^\circ C$ in an oxygen atmosphere was reported. Hashimoto *et al.*¹⁷ observed single-phase spinel up to a molar ratio $Cr/(Mg+Cr)$ of 0.773 at $1700^\circ C$ under unknown reducing conditions (exact P_{O_2} unspecified; samples were embedded in graphite powder), while Li *et al.*¹⁶ observed solubilities up to $Cr/(Mg+Cr) = 0.9$ at metallic Cr saturation at temperatures between $1200^\circ C$ and $1500^\circ C$ at total pressures of 4.8 to 28.8 kbar. Wilde and Rees³⁷ estimated negligible solubility of Cr_3O_4 from the observation of only very small changes in lattice parameter with increased Cr_3O_4 content under reducing conditions. However, their conclusion that the solubility is negligible is incorrect because the lattice parameter changes only slightly^{14,16} with increased Cr_3O_4 until relatively large concentrations are reached.

Finally, it may be mentioned that similar assumptions and model parameters reproduce solubility data for Cr_3O_4 as a function of temperature and P_{O_2} in the $FeCr_2O_4$ - Cr_3O_4 spinel solution^{12,13} where experimental data are more abundant.

Fig. 4 shows the phase diagram (oxygen partial pressure versus molar metallic ratio $Cr/(Mg+Cr)$) predicted at various temperatures. The SGTE database²⁰ was used for the properties of the metallic phases. The single-phase spinel solution is calculated to extend to about $Cr/(Mg+Cr)$

$= 0.9$ at $1500^\circ C$ in good agreement with the measured data by Li *et al.*¹⁶ as discussed above. The other experimental data^{14,15,17} discussed above for the solubility of Cr_3O_4 in $MgCr_2O_4$ spinel are also qualitatively well reproduced by the calculated phase diagram in Fig. 4. Between 1650° and $1700^\circ C$, the spinel solution is calculated to extend to pure Cr_3O_4 spinel. No molten oxide phase appears at temperatures below $1650^\circ C$. In this study, the Cr_3O_4 -rich spinel with distorted tetrahedral structure is modeled as being continuous with the cubic $MgCr_2O_4$ -rich spinel as discussed earlier.

The calculated liquidus projection of the MgO - CrO - Cr_2O_3 ternary system is shown in Fig. 5. The primary crystallization fields of metallic chromium, periclase, spinel and Cr_2O_3 are noted in the figure. Caution should be exercised in interpreting this diagram since P_{O_2} varies greatly across it.

(3) MgO - CrO - Cr_2O_3 - Al_2O_3 System

$MgCr_2O_4$ and $MgAl_2O_4$ are completely miscible at high temperatures. Tie-lines between the $MgCr_2O_4$ - $MgAl_2O_4$ spinel solution and the Cr_2O_3 - Al_2O_3 corundum solution were measured recently by Jacob and Behera⁴² under dried argon atmospheres ($\log P_{O_2} \sim -5.0$) using EPMA analysis for the spinel composition and lattice parameter measurements (from XRD) for the corundum phase. These results are considered the most reliable and were used in the present optimization to obtain the model parameters Δ_{MAG} and L_{kGA} shown in Table I. Experimental and calculated tie-lines are compared in Fig. 6. It should be noted that the same parameter $L_{kGA} = 33472$ J was used to reproduce the measured spinel-corundum tie-lines and the measured miscibility gap in $FeCr_2O_4$ - $FeAl_2O_4$ spinel solutions in our optimization of the Fe - Cr - Al - O system.¹²

Results of other authors are also plotted in Fig. 6. Hino *et al.*⁴³ used a similar technique to that of Jacob and Behera,⁴² while Greskovich and Stubican⁴¹ obtained the composition of the corundum phase from lattice parameter measurements and then calculated the spinel composition by the difference between this and the overall sample composition. Gaenko⁴⁴ investigated the phase equilibria by XRD of quenched samples; however P_{O_2} was unspecified.

The calculated cation distribution in the $MgCr_2O_4$ - $MgAl_2O_4$ spinel solution at $1200^\circ C$ is shown in Fig. 7. The variations in the moles of ions on the various sites are nearly linear with composition. The calculated concentration of Cr^{3+} ions on tetrahedral sites is less than 0.1 mole percent in agreement with the results of O'Neill and Dollase.²⁸ A nearly symmetrical miscibility gap is predicted at lower temperatures, with a consolute temperature of $713^\circ C$.

A calculated isothermal section at $1700^\circ C$ at $P_{O_2} = 1$ bar is shown in Fig. 8 along with experimental points reported by Greskovich and Stubican.⁴¹ The calculated and reported phase boundaries between the spinel and (spinel+corundum) regions are not in good agreement.

However, the extrapolation of the experimental phase boundary to the MgO-Al₂O₃ system results in a substantially lower solubility of Al₂O₃ than indicated by numerous studies taken into account in our earlier optimization¹ of the MgO-Al₂O₃ system.

Solidus measurement at $\log P_{O_2} \sim -5.5$ (see above) were performed by Wilde and Rees.³⁷ The calculations reproduce the measurements within the very wide scatter exhibited by the latter.

The solubility of spinel in the ternary periclase solution was measured by Dewendra *et al.*⁴⁵ by a quenching technique. The calculations, with no additional ternary parameters, reproduce the measurements within experimental uncertainty.

Fig. 9 shows the calculated (predicted) liquidus projection at various oxygen partial pressures. The liquidus temperature is independent of P_{O_2} in the MgO-Al₂O₃ system, but is highly dependent on P_{O_2} in the MgO-Cr₂O₃ system. This results in several interesting features of the calculated phase diagram. Under oxidizing conditions, the melting temperature of MgCr₂O₄ is higher than that of MgAl₂O₄. However, this situation reverses under reducing conditions. Similar behavior is observed for the Cr₂O₃-Al₂O₃ corundum solution. The primary phase field of periclase expands significantly as P_{O_2} is decreased.

The effect of the addition of Al on the phase equilibria in the Mg-Cr-O system is illustrated in Fig. 10, which may be compared to Fig. 4. The addition of Al stabilizes the spinel field. In particular it stabilizes the two-phase region (spinel+bcc) where the spinel is mainly composed of MgAl₂O₄.

V. Conclusions

The MgO-Al₂O₃-CrO-Cr₂O₃ system at a total pressure of 1 bar was critically evaluated and optimized based on all available and reliable thermodynamic and phase diagram data. As a result of the optimization, one set of model parameters has been obtained which reproduces all the data within experimental error limits in the temperature range from 25°C to above the liquidus and for oxygen partial pressures up to 1 bar. The variation of the melting temperature of MgCr₂O₄ with oxygen partial pressure and of the MgO-Cr₂O₃ phase diagram with oxygen partial pressure are elucidated for the first time. Phase equilibria can be calculated for temperatures, compositions and oxygen partial pressures where data are unavailable.

The optimized model parameters can be readily used with general thermodynamic software and databases, such as FactSage,³ to calculate phase equilibria at any given set of conditions and to model various industrial and natural processes. An article on applications to magnesia-chromite refractories is being prepared in collaboration with K.U. Leuven, Belgium.

References

1. I.-H. Jung, S. A. Decterov, and A. D. Pelton, "Thermodynamic Modeling of the MgO-Al₂O₃, CaO-MgO-Al₂O₃ and MgO-Al₂O₃-SiO₂ Systems," *Metall. Mater. Trans.*, (submitted).
2. S. Decterov and A. D. Pelton, "Critical Evaluation and Optimization of the Thermodynamic Properties and Phase Diagrams of the CrO-Cr₂O₃, CrO-Cr₂O₃-Al₂O₃ and CrO-Cr₂O₃-CaO Systems," *J. Phase Equilib.*, **17**, 476-487 (1996).
3. www.factsage.com. Montreal, 2002.
4. A.D. Pelton, and M. Blander, "Computer-assisted analysis of the thermodynamic properties and phase diagrams of slags"; pp. 281-94 in *Proceedings of the Second International Symposium on Metallurgical Slags and Fluxes*, TMS-AIME, Warrendale, PA, 1984.
5. A. D. Pelton and M. Blander, "Thermodynamic Analysis of Ordered Liquid Solutions by a Modified Quasi-Chemical Approach. Application to Silicate Slags," *Metall. Trans. B*, **17B**, 805-815 (1986).
6. A. D. Pelton, S. A. Decterov, G. Eriksson, C. Robelin, and Y. Dessureault, "The modified quasichemical model. I - Binary solutions," *Metall. Mater. Trans. B*, **31B**, 651-659 (2000).
7. A. D. Pelton and P. Chartrand, "The Modified Quasichemical Model. II - Multicomponent Solutions," *Metall. Mater. Trans. A*, **32A**, 1355-1360 (2001).
8. A. D. Pelton, "A General "Geometric" Thermodynamic Model for Multicomponent Solutions," *Calphad*, **25**, 319-328 (2001).
9. M. Hillert, B. Jansson, and B. Sundman, "Application of the Compound-Energy Model to Oxide Systems," *Z. Metallkd.*, **79**, 81-87 (1988).
10. S. A. Decterov, E. Jak, P. C. Hayes, and A. D. Pelton, "Experimental Study of Phase Equilibria and Thermodynamic Optimization of the Fe-Zn-O System," *Metall. Mater. Trans. B*, **32B**, 643-657 (2001).
11. H. S. C. O'Neill and A. Navrotsky, "Cation distributions and thermodynamic properties of binary spinel solid solutions," *Amer. Mineral.*, **69**, 733-53 (1984).
12. S. Decterov, I.-H. Jung, Y.-B. Kang, E. Jak, V. Swamy, D. Kevorkov and A.D. Pelton, "Report for Oxide Database Development," CRCT, Ecole Polytechnique, Montreal. (2002)
13. Y.-B. Kang, I.-H. Jung S. A. Decterov A. D. Pelton and H. G. Lee, "Thermodynamic Modeling of the Fe-Cr-O system," (in preparation)
14. C. Greskovich and V. S. Stubican, "Divalent chromium in magnesium-chromium spinels," *J. Phys. Chem. Solids*, **27**, 1379-1384 (1966).
15. V. S. Stubican and C. Greskovich, "Trivalent and Divalent Chromium Ions in Spinels," *Geochim. Cosmochim. Acta*, **39**, 875-881 (1975).
16. J.-P. Li, H. S. C. O'Neil, and F. Seifert, "Subsolidus Phase Relations in the System MgO-SiO₂-Cr-O in Equilibrium with Metallic Cr, and their Significance for the Petrochemistry of Chromium," *J. Petrol.*, **36**, 107-132 (1995).
17. S. Hashimoto, S. Toda, and A. Yamaguchi, "Sintering Characteristics in the System MgO-Cr₂O₃ and Formation of (Mg_{3-x}Cr_x)Cr₁₆O₃₂ (0 ≤ x ≤ 2.88)," *J. Ceram. Soc. Jpn.*, **104**, 1121-1124 (1996).
18. J. R. Taylor and A. T. Dinsdale, "A Thermodynamic Assessment of the Cr-Fe-O System," *Z. Metallkd.*, **84**, 335-345 (1993).
19. H. Hering, "Diffusion in the ternary system magnesium oxide - iron(III) oxide - chromium(VI) oxide," *Ber. Deut. Keram. Ges.*, **48**, 67-73 (1971).
20. Scientific Group Thermodata Europe (SGTE), <http://www.sgte.org>, 2002.
21. C. H. Shomate, "Ferrous and Magnesium Chromites.

Specific Heats at Low Temperatures," *Ind. Eng. Chem.*, **36**, 910-911 (1944).

22. B. F. Naylor, "High-Temperature Heat Contents of Ferrous and Magnesium Chromites," *Ind. Eng. Chem.*, **36**, 933-934 (1944).

23. R. Plumier, "Neutron Diffraction Study on the Normal MgCr_2O_4 Spinel Composition," *Comptes Rendus de L'Academie des Sciences*, **267B**, 98-101 (1968).

24. H. Shaked, J. M. Hastings, and L. M. Corliss, "Magnetic structure of Magnesium Chromite," *Physical Review B*, **1**, 3316-3324 (1970).

25. G. Blasse and J. F. Fast, "Neel temperatures of some antiferromagnetic oxides with spinel structure," *Philips Research Reports*, **18**, 393-399 (1963).

26. F. Hartmann-Boutron, A. Gerard, P. Imbert, R. Kleinberger, and F. Varret, "First-order antiferro-paramagnetic transition in zinc and magnesium chromites," *C. R. Acad. Sci., Paris, Ser. A B*, **268B**, 906-908 (1969).

27. S. Klemme, H. St. C. O'Neill, W. Schnelle, and E. Gmelin, "The heat capacity of MgCr_2O_4 , FeCr_2O_4 , and Cr_2O_3 at low temperatures and derived thermodynamic properties," *Am. Mineral.*, **85**, 1686-1693 (2000).

28. H. St. C. O'Neill and W. A. Dollase, "Crystal structures and cation distributions in simple spinels from powder XRD structural refinements: MgCr_2O_4 , ZnCr_2O_4 , Fe_3O_4 and the temperature dependence of the cation distribution in ZnAl_2O_4 ," *Phys. Chem. Miner.*, **20**, 541-55 (1994).

29. J. D. Tretyakov and H. Schmalzried, "Thermodynamics of spinel phase (Chromite, Ferrite, Aluminate)," *Ber. Bunsenges. Phys. Chem.*, **69**, 396-402 (1965).

30. K. T. Jacob, "Potentiometric Determination of the Gibbs Free Energy of Formation of Cadmium and Magnesium Chromites," *J. Electrochem. Soc.*, **124**, 1827-1831 (1977).

31. F. Muller and O. J. Kleppa, "Thermodynamics of formation of chromite spinels," *J. Inorg. Nucl. Chem.*, **35**, 2673-2678 (1973).

32. T. Sata and H. L. Lee, "Vacuum Vaporization in the System $\text{MgO-Cr}_2\text{O}_3$," **61**, 326-329 (1978).

33. T. Sata, T. Sasamoto, H. L. Lee, and E. Maeda, "Vaporization processes from magnesia materials," *Rev. Int.*

Hautes Temp. Refract., **15**, 237-248 (1979).

34. K. W. Gee, "The System $\text{MgO-SiO}_2\text{-Cr}_2\text{O}_3$," Ph.D dissertation, The University of Scheffield, Sheffield, England, 1940

35. M. L. Keith, "Phase Equilibria in the System $\text{MgO-Cr}_2\text{O}_3\text{-SiO}_2$," *J. Am. Ceram. Soc.*, **37**, 490-496 (1954).

36. A. M. Alper, R. N. McNally, R. C. Doman, and F. G. Keihn, "Phase Equilibria in the System $\text{MgO-MgCr}_2\text{O}_4$," *J. Am. Ceram. Soc.*, **47**, 30-33 (1964).

37. W. T. Wilde and W. J. Rees, "The Ternary System $\text{MgO-Al}_2\text{O}_3\text{-Cr}_2\text{O}_3$," *Trans. Brit. Ceramic Soc.*, **42**, 123 (1943).

38. Z. Panek and E. Kanclir, "Determination of the melting point of picrochromite," *Silikaty*, **13**, 255-260 (1969).

39. A. S. Frenkel, K. M. Shmukler, B. Ya. Sukharevskii, and N. V. Gul'ko, "Mechanism of the formation and decomposition of solid solutions of spinels in periclase," *Dokl. Akad. Nauk SSSR*, **130**, 33-36 (1960).

40. A. F. Henriksen and W. D. Kingery, "The Solid Solubility of Sc_2O_3 , Al_2O_3 , Cr_2O_3 , SiO_2 and ZrO_2 in MgO ," *Ceramurgia Int.*, **5**, 11-17 (1979).

41. C. Greskovich and V. S. Stubican, "Coherent Precipitation in the System $\text{MgO-Al}_2\text{O}_3\text{-Cr}_2\text{O}_3$," *J. Am. Ceram. Soc.*, **51**, 42-46 (1968).

42. K.T. Jacob and C.K. Behera, "Spinel-corundum equilibria and activities in the system $\text{MgO-Al}_2\text{O}_3\text{-Cr}_2\text{O}_3$ at 1473 K," *Metall. Mater. Trans. B*, **31B**, 1323-1332 (2000).

43. M. Hino, K. Higuchi, T. Nagasaka, and S. Ban-ya, "Phase Equilibria and Thermodynamics of $\text{FeOCr}_2\text{O}_3\text{-MgOCr}_2\text{O}_3\text{-MgOAl}_2\text{O}_3$ Spinel Structure Solid Solution Saturated with $(\text{Cr, Al})_2\text{O}_3$," *ISIJ Inter.*, **35**, 851-858 (1995).

44. N. S. Gaenko, S. N. Razumovskii, and S. P. Shmitt-Fogeleovich, "Phase transformations and properties of refractories based on the magnesium oxide-aluminum oxide-chromium(III) oxide system," *Ogneupory*, 48-53 (1976).

45. J. D. Dewendra, C. M. Wilson, and N. H. Brett, "A quantitative investigation of phase compositions in magnesia- R_2O_3 -silicate systems. I. Solid solubility of binary mixtures of Al_2O_3 , Cr_2O_3 , Fe_2O_3 in the periclase phase," *Trans. J. Br. Ceram. Soc.*, **81**, 185-189 (1982).

Table I. Optimized model parameters of solutions in the MgO-CrO-Cr₂O₃-Al₂O₃ system (J/mol and J/mol·K).

Spinel: (Mg²⁺, Cr²⁺, Cr³⁺, Al³⁺)[Mg²⁺, Cr³⁺, Al³⁺, Va]₂O₄	
$G_{\text{MG}} = G^{\circ}(\text{MgCr}_2\text{O}_4)^*$	
$H_{298.15}^{\circ} = -1769907.76$	
$S_{298.15}^{\circ} = 118.300$	
$C_P = 221.24 - 0.001020T - 1.757(10^6)T^{-2} - 1247.9T^{-0.5}$ (15 K < T < 3000 K)	
$G_{\text{CG}} = G^{\circ}(\text{Cr}_3\text{O}_4)^{**}$	
$I_{\text{MG}} = G_{\text{GG}} + G_{\text{GM}} - 2G_{\text{MG}}^{***} = 320000.0 - 18.24T$	
$\Delta_{\text{MG:MG}} = G_{\text{MM}} + G_{\text{GG}} - G_{\text{MG}} - G_{\text{GM}}^{***} = 40000.0$	
$\Delta_{\text{AG:AG}} = G_{\text{AA}} + G_{\text{GG}} - G_{\text{AG}} - G_{\text{GA}} = 0.0$	
$\Delta_{\text{MA:GA}} = G_{\text{MG}} + G_{\text{AA}} - G_{\text{MA}} - G_{\text{AG}} = -16736.0$	
$\Delta_{\text{MC:GV}} = G_{\text{MG}} + G_{\text{CV}} - G_{\text{MV}} - G_{\text{CG}} = 0.0$	
$\Delta_{\text{MC:MG}} = G_{\text{MM}} + G_{\text{CG}} - G_{\text{MG}} - G_{\text{CM}} = 0.0$	
$\Delta_{\text{CF:AG}} = G_{\text{CA}} + G_{\text{FG}} - G_{\text{CG}} - G_{\text{FA}}^{****} = 0.0$	
$G_{\text{GV}} = 8G^{\circ}(\gamma\text{-Cr}_2\text{O}_3) - 2RT(5\ln 5 - 6\ln 6) - 5G_{\text{GG}}$, where $G^{\circ}(\gamma\text{-Cr}_2\text{O}_3) = G^{\circ}(\text{Cr}_2\text{O}_3)^{**} + 200000.0$	
$L_{\text{C:GA}} = L_{\text{G:GA}} = L_{\text{M:GA}} = L_{\text{A:GA}} = 33472.0$	
Notations M, C, G, A, F and V are used for Mg, Cr ²⁺ , Cr ³⁺ , Al ³⁺ , Fe ²⁺ and vacancy, respectively.	
* $H_{298.15}^{\circ}$ decreased by -1.13 kJ/mol from the value recommended by Klemme <i>et al.</i> ²⁷ $S_{298.15}^{\circ}$ and C_P taken from Klemme <i>et al.</i> ²⁷	
** Gibbs energies of Cr ₃ O ₄ and Cr ₂ O ₃ taken from Decterov and Pelton ²	
*** These parameters were determined from values recommended by O'Neill and Navrotsky. ¹¹	
**** G_{FG} and G_{FA} are the Gibbs energies of (Fe ²⁺)[Cr ³⁺] ₂ O ₄ and (Fe ²⁺)[Al ³⁺] ₂ O ₄ taken from previous studies ^{12,13}	
The other model parameters for spinel can be found in the study by Jung <i>et al.</i> ¹	

Periclase: MgO-CrO_{1.5}-AlO_{1.5}	
$G^{\circ}(\text{CrO}_{1.5}) = \frac{1}{2} G^{\circ}(\text{Cr}_2\text{O}_3)^* + 38702.0$	
$q_{\text{MgO,CrO}_{1.5}}^{00} = 39692.35 - 31.66T$	
* Gibbs energy of Cr ₂ O ₃ taken from Decterov and Pelton ²	
The polynomial “ q ” parameters are defined in Reference 8	
The other model parameters for periclase can be found in the study by Jung <i>et al.</i> ¹	

Liquid Oxide: MgO-CrO-CrO_{1.5}-AlO_{1.5}	
$\Delta g_{\text{MgO,CrO}_{1.5}}^{\circ} = -16736.0$	
The other model parameters for spinel can be found in the study by Jung <i>et al.</i> ¹	
The quasichemical parameters are defined in References 6 and 7.	

Gibbs energies of the pure components of the solutions and of O₂ gas are taken from the F*A*C*T database.³

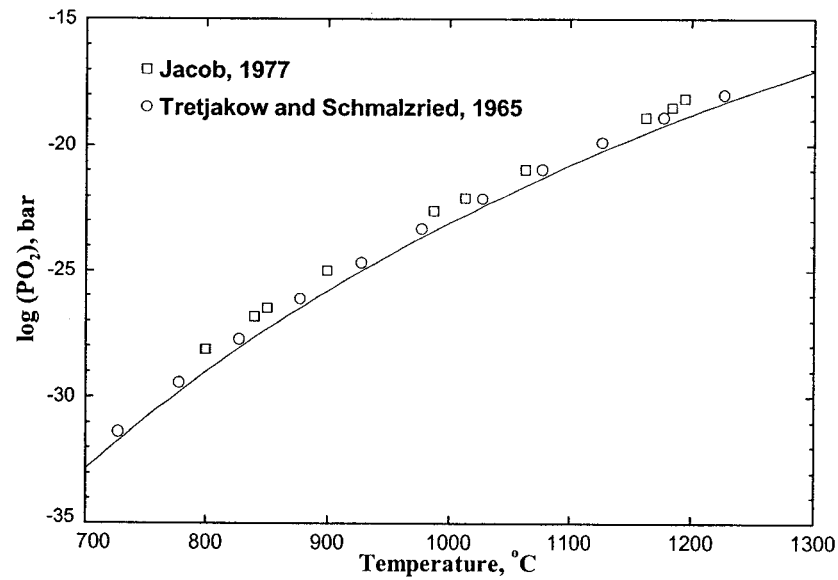


Fig. 1. Calculated oxygen partial pressure of $(\text{MgCr}_2\text{O}_4 + \text{MgO} + \text{Cr})$ three-phase assemblage.

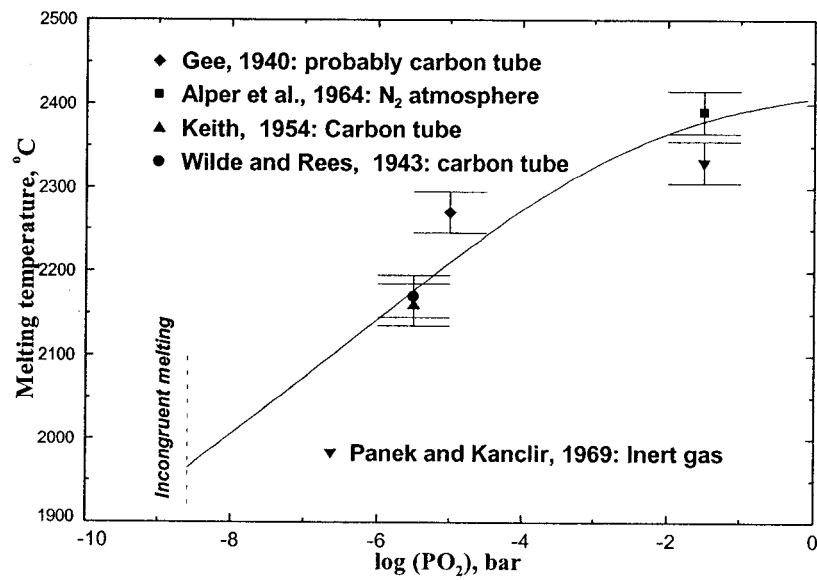


Fig. 2. Calculated melting temperature of MgCr_2O_4 as function of oxygen partial pressure.

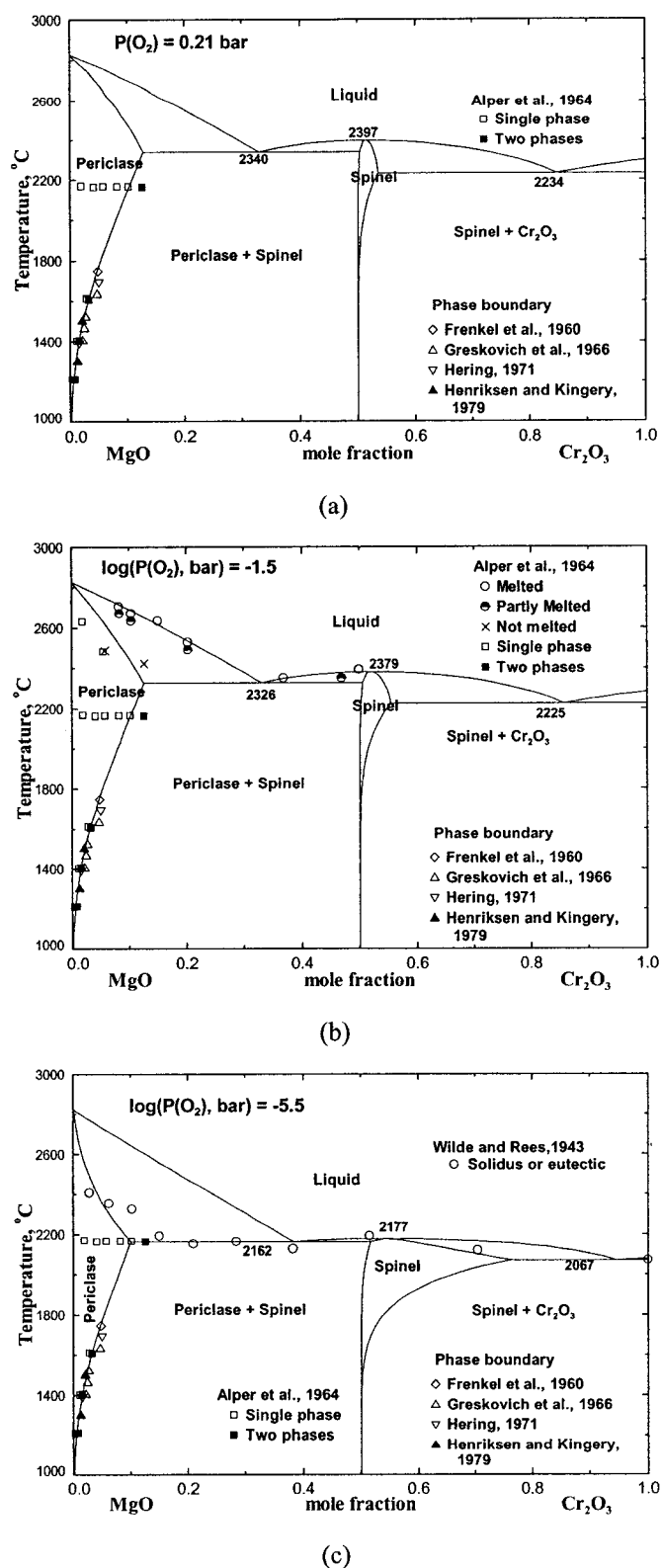


Fig. 3. Calculated phase diagram of the “MgO-Cr₂O₃” system at various oxygen partial pressures. Abscissa is more correctly the molar ratio $\frac{1}{2}\text{Cr}/(\frac{1}{2}\text{Cr} + \text{Mg})$.

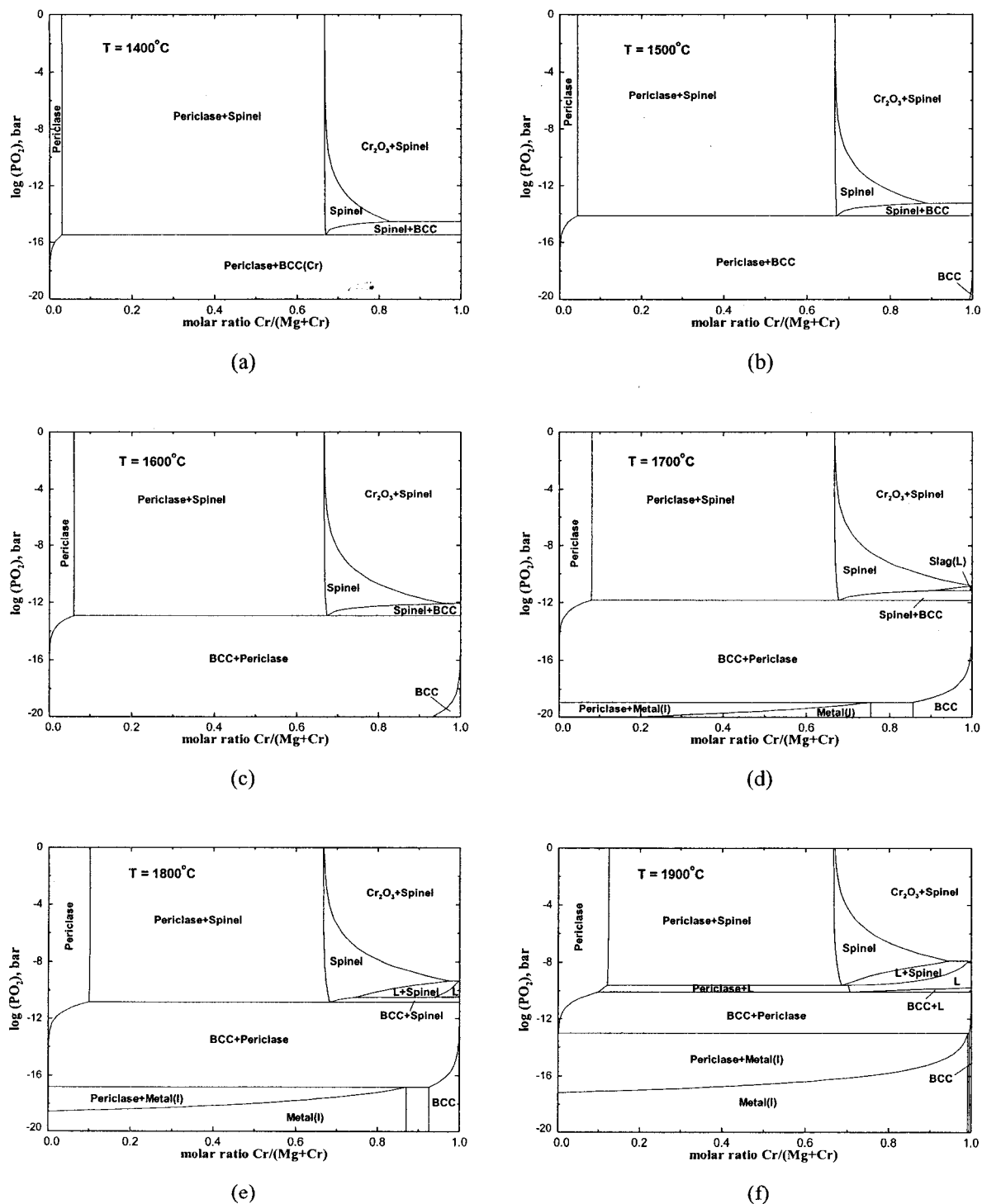


Fig. 4. Calculated (predicted) Mg-Cr-O phase diagram at various temperatures. Molar metal ratio versus equilibrium oxygen partial pressure.

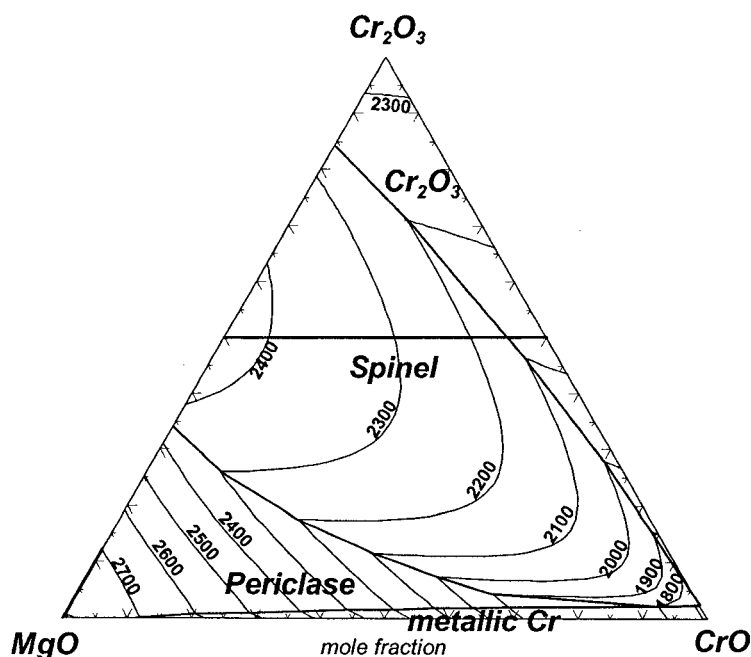


Fig. 5. Calculated (predicted) liquidus projection of the MgO-CrO-Cr₂O₃ system indicating primary phase fields. (Temperatures in °C).

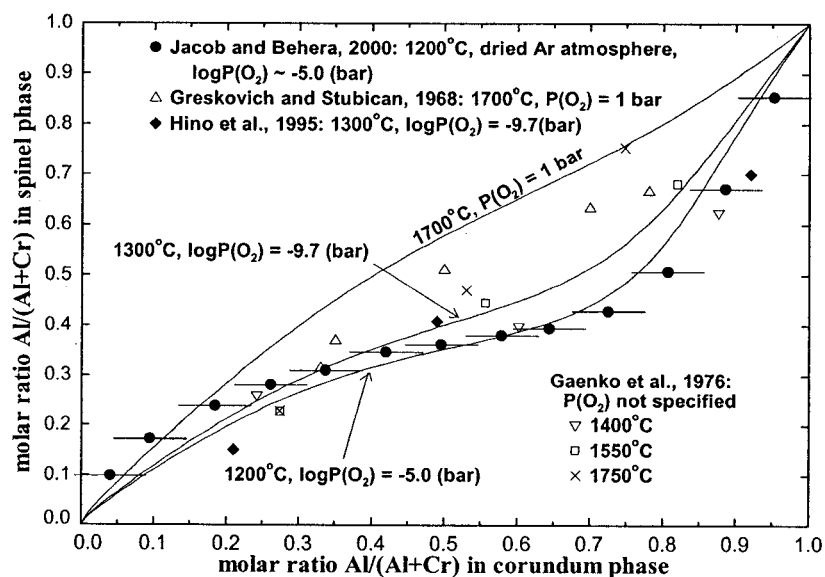


Fig. 6. Calculated tie-lines between spinel and corundum phases at various oxygen partial pressures.

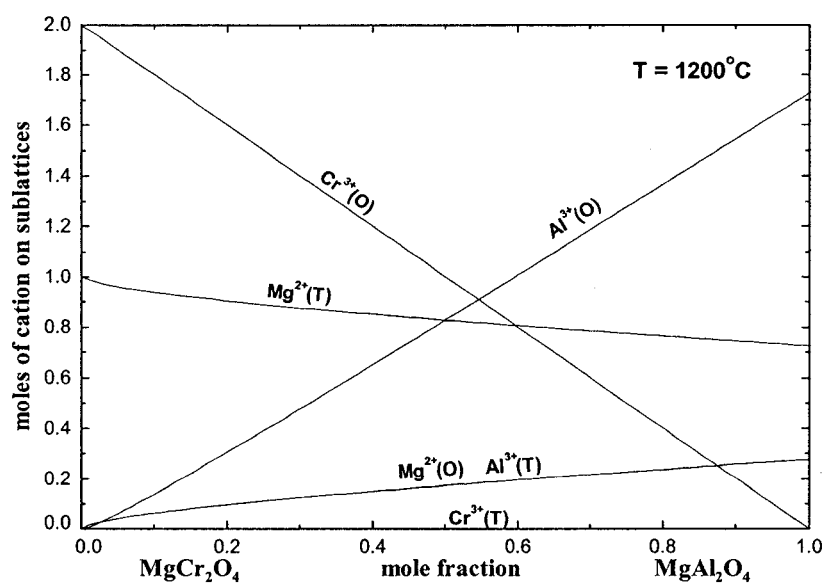


Fig. 7. Calculated cation distribution in MgCr_2O_4 - MgAl_2O_4 spinel solutions at 1200°C . O and T represent octahedral and tetrahedral sites respectively. Moles of cations on octahedral and tetrahedral sublattices per mole of spinel solution. The amount of $\text{Cr}^{3+}(\text{T})$ is calculated to be virtually zero.

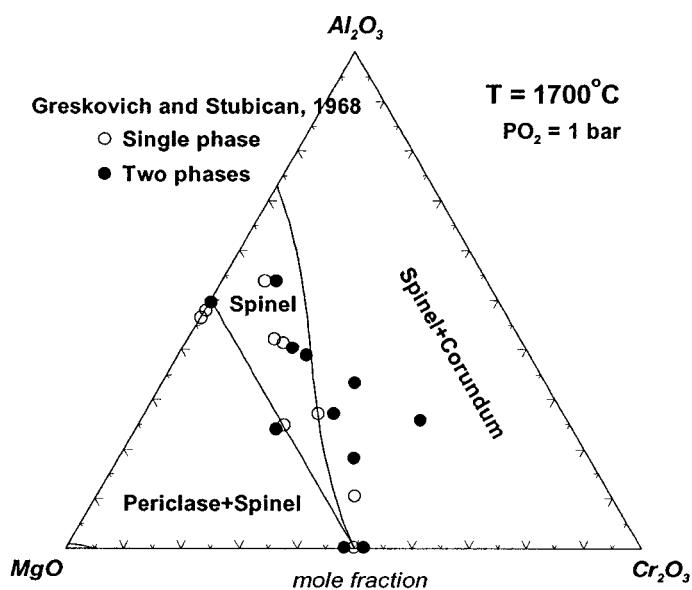


Fig. 8. Calculated iso-thermal section of the MgO - Al_2O_3 - Cr_2O_3 - CrO system at 1700°C and $\text{PO}_2 = 1.0$ bar.

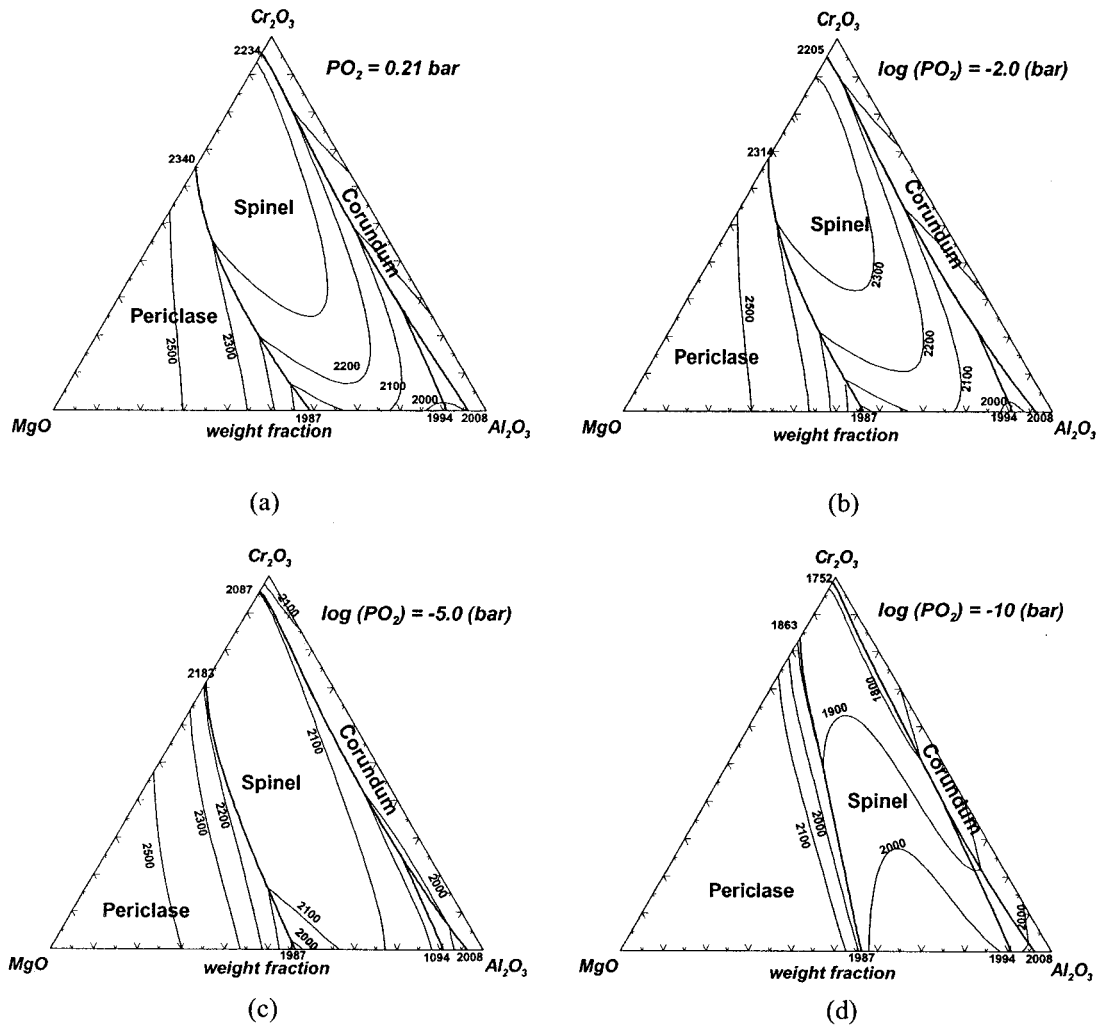


Fig. 9. Predicted liquidus projection of the MgO-Al₂O₃-Cr₂O₃-CrO system at various oxygen partial pressures. (Temperature in °C).

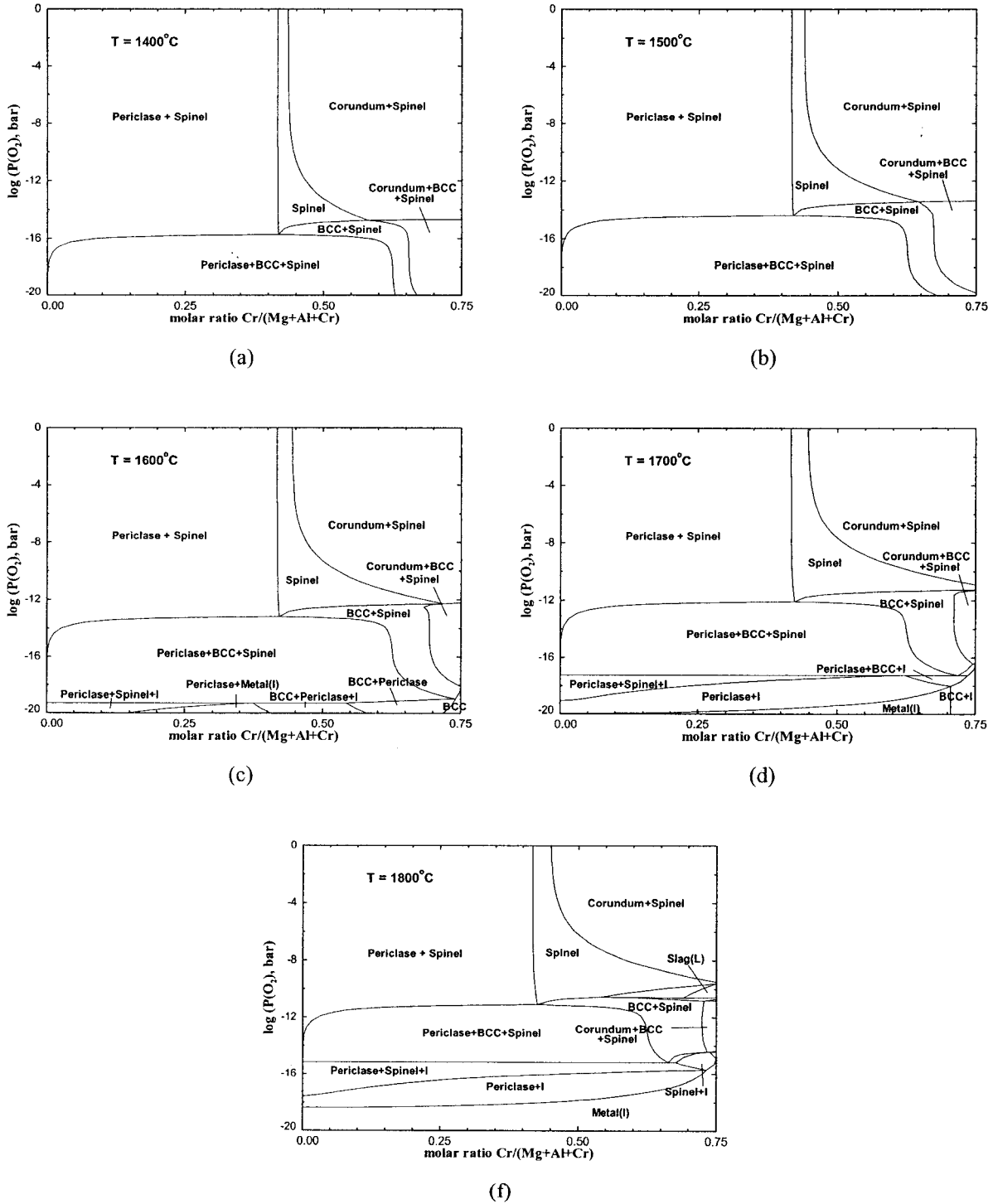


Fig. 10. Calculated (predicted) Mg-Cr-Al-O phase diagram at constant molar ratio $\text{Al}/(\text{Mg}+\text{Al}+\text{Cr}) = 0.25$ and various temperatures. Molar metal ratio versus equilibrium oxygen partial pressure.

Appendix VIII

Article :

Thermodynamic Evaluation and Modeling of the Fe-Co-O System

In-Ho Jung, Sergei A. Decterov, Arthur D. Pelton
Hyun-Min Kim and Youn-Bae Kang

Submitted to *J. Am. Ceram. Soc.*, 2003

neighbor cations in the ionic melt, is used for modeling the slag. The components of the slag are taken as CoO-FeO-FeO_{1.5}. Only divalent cobalt (Co²⁺) is considered for the molten oxide in the present study because no indications of higher oxidation states of Co have been reported.

The binary sub-system FeO-FeO_{1.5} has already been critically evaluated and optimized,³ and the optimized model parameters are used as the basis of the present study. The second-nearest-neighbor "coordination numbers" of Fe²⁺ and Fe³⁺ used in the present model for the slag are the same as in the previous study,³ and the "coordination number" of Co²⁺ is the same as that of Fe²⁺. The binary interaction parameters of the model are set to zero for the Co²⁺-Fe²⁺ and Co²⁺-Fe³⁺ interactions. The properties of the ternary slag are calculated from the binary parameters using the symmetric "Kohler-like"⁸ approximation. No ternary parameters are needed. That is, no additional adjustable model parameters for the slag solution were introduced in the present study. The thermodynamic properties of the slag, predicted by the Modified Quasichemical Model solely from the optimized model parameters of the FeO-FeO_{1.5} system, adequately reproduce available experimental data as is shown in the following sections.

(2) Spinel Solution

The model for the spinel solution was developed within the framework of the Compound Energy Formalism (CEF).⁹ The Gibbs energy expression in the CEF per formula unit is:

$$G = \sum_i \sum_j Y_i^T Y_j^O G_{ij} - TS_C + G^E$$

where Y_i^T and Y_j^O represent the site fractions of cations i and j on the tetrahedral and octahedral sublattices, G_{ij} is the Gibbs energy of an "end-member" $(i)^T[j]^O\text{O}_4$ of the solution, in which the first sublattice is occupied only by cation i and the second only by cation j , and S_C is the configurational entropy assuming random mixing on each sublattice:

$$S_C = -R(\sum_i Y_i^T \ln Y_i^T + 2 \sum_j Y_j^O \ln Y_j^O)$$

In the present study, no excess Gibbs energy terms were required; that is $G^E = 0$. The Gibbs energy of the spinel solution is thus fully defined if the Gibbs energies G_{ij} of the 20 end-members are known. Certain linear combinations of the G_{ij} , which have physical sense, are used as the optimized model parameters. These linear combinations are related to the energies of classical site exchange reactions and are listed in Table I. A more detailed description of these spinel model parameters is given in Reference 3.

Of the 20 parameters G_{ij} , six were optimized in the earlier³ optimization of magnetite $(\text{Fe}^{2+}, \text{Fe}^{3+})^T(\text{Fe}^{2+}, \text{Fe}^{3+}, \text{Va})_2\text{O}_4$. Two more, G_{CC} and G_{CV}

(where $C = \text{Co}^{2+}$ and $V = \text{vacancy}$), were defined in the optimization of the simple CoAl_2O_4 spinel phase and will be reported elsewhere. The remaining 12 were obtained in the present study as described in the following sections and are listed in Table I.

The contribution of magnetism to the Gibbs energy of the spinel phase is modeled by a semi-empirical equation¹⁰ and the model parameters optimized in the present study are listed in Table I.

(3) Cobaltowustite Solution

The cobaltowustite solution was modeled as a simple random mixture of Co²⁺, Fe²⁺ and Fe³⁺ ions on cation sites with simple polynomial excess Gibbs energy terms.⁸ It is assumed that cation vacancies remain associated with Fe³⁺ ions and so do not contribute to the configurational entropy.

Binary excess Gibbs energies were modeled by simple polynomial expansions in the mole fraction.⁸ Optimized parameters for the FeO-FeO_{1.5} (wustite) solution were obtained previously.³ The FeO-CoO solution is assumed to be ideal. One optimized excess parameter for CoO-FeO_{1.5} interactions was obtained in the present study as described in the following sections and is listed in Table I. The properties of the ternary cobaltowustite solution were calculated from the binary parameters by the symmetric "Kohler-like" approximation.⁸

(4) Metallic solutions

The thermodynamic properties of liquid, bcc, fcc and hcp alloys from the SGTE (Scientific Group Thermodata Europe)¹¹ database were used for calculations of phase equilibria at metallic saturation.

III. Evaluation/Optimization

(1) CoO-Co₃O₄ System

A small non-stoichiometry of solid CoO was measured by Fisher and Tannhauser¹² using an electric conductivity technique and by Aggarwal and Dieckmann¹³ using thermogravimetry. This solubility of less than 1 mol % Co₃O₄ in CoO was neglected in the present study, and CoO is considered to be a stoichiometric compound. The heat capacity of CoO was measured in the temperature range from 50 to 1000 K by King,¹⁴ Kleinclauss¹⁵ and Watanabe^{16,17} using adiabatic calorimetry. As can be seen from Fig. 2, the measured data are in good agreement with each other. The peak at 287 K corresponds to a phase transition from the anti-ferromagnetic to the paramagnetic state. The heat content of CoO above 300 K was measured by King and Christensen¹⁸ (see Fig. 3). Optimized thermodynamic parameters are given in Table I.

The melting temperature of CoO has been reported as 1810°C.¹⁹ Barin²⁰ reported the melting temperature to be 1830 °C and estimated the enthalpy of fusion. These values of Barin are consistent with the reported limiting slopes of the liquidus curves at 100% CoO (and assuming no solubility in solid CoO) in several binary systems such as CoO-SiO₂^{21,22} and CoO-AlO_{3/2},^{23,24} and were accepted in the present study. The heat capacity of liquid CoO has not

been reported. It was estimated as being equal to C_p of the solid at the melting temperature for temperatures above 1300 K. Below 1300 K it was set equal to C_p of the solid. The resultant thermodynamic properties of liquid CoO are given in Table I.

The heat capacity of Co_3O_4 below 300 K was measured by King¹⁴ (54 to 296 K) and Khriplovich *et al.*²⁵ (5 to 307 K) using adiabatic calorimetry. A phase transition from the antiferromagnetic to the paramagnetic state occurs near 30 K. King and Christensen¹⁸ measured the heat content of Co_3O_4 up to 1000 K and reported abnormal behavior of the heat content above this temperature. Mocala *et al.*²⁶ measured a strong anomaly in the heat capacity of Co_3O_4 between 1000 K and its decomposition temperature (about 1300 K in air and slightly higher in oxygen at 1 bar) using an HT 1500 Setaram calorimeter in step-scanning mode under both air and oxygen atmospheres. The measured heat capacity is almost independent of the oxygen partial pressure. This anomaly in the heat capacity of Co_3O_4 probably results from an electron spin unpairing transition of Co^{3+} ions²⁷: spins are paired at lower temperatures (low-spin state) and become unpaired at higher temperatures (high-spin state).

Pure Co_3O_4 is generally considered to be virtually a completely normal spinel at all temperatures: Co^{2+} and Co^{3+} occupy the tetrahedral and octahedral sites, respectively. However, when other ions are present, Co^{2+} and Co^{3+} can both be found on both the tetrahedral and octahedral sites. Since the spinel model used in the present study reduces to the simplified model of O'Neill and Navrotsky²⁸ as a limiting case, the values of the model parameters $C_{\text{CE:CE}}$ and I_{CE} were calculated from the site preference energies of Co^{2+} and low-spin Co^{3+} proposed by these authors. These parameters are given in Table I. The transition from low-spin to high-spin Co^{3+} was directly taken into account by fitting the heat capacity of Co_3O_4 to the experimental data as shown in Fig. 4. The amount of Co^{3+} on tetrahedral sites calculated from the model parameters is less than 1 mol % over the entire temperature range of existence of Co_3O_4 . Hence, the optimized Gibbs energy G_{CE} (for hypothetical purely normal $(\text{Co}^{2+})^{\text{T}}(\text{Co}^{3+})^{\text{O}}_2\text{O}_4$) is nearly identical to the Gibbs energy, $G_{\text{Co}_3\text{O}_4}^{\text{O}}$ of real Co_3O_4 .

The heat capacity and heat content of Co_3O_4 , calculated from the optimized parameters in Table I, are compared with the experimental data in Figs. 4 and 5. The absolute entropy of Co_3O_4 at 298.15 K obtained by Khriplovich *et al.*²⁵ (109.3 J/mol·K) is accepted in the present study. Since King¹⁴ measured the heat capacity only above the magnetic transition temperature, his entropy (102.5±0.8 J/mol·K), calculated from the Third law, is too low.

The oxygen partial pressures for the CoO/Co and CoO/ Co_3O_4 equilibria^{12,27,29-43} were measured by emf and gas equilibration techniques. The calculated phase diagram of the Co-O system (oxygen partial pressure versus $1/T$) is shown in Fig. 6. Only the major experimental studies are shown in the figure. The calculations are also in excellent agreement with the results of all other studies. The

parameters for $H_{298.15\text{K}}^{\text{O}}$, $S_{298.15\text{K}}^{\text{O}}$ and C_p for CoO(s) and Co_3O_4 (s) (G_{CE}) in Table I were optimized in order to reproduce the data in Figs. 2 to 6 simultaneously.

The non-stoichiometry of Fe_3O_4 spinel was modeled³ by the introduction of vacancies on octahedral sites. This can be viewed as a dissolution of $\gamma\text{-Fe}_2\text{O}_3$ in Fe_3O_4 where $\gamma\text{-Fe}_2\text{O}_3$ (similar to $\gamma\text{-Al}_2\text{O}_3$) is an unstable modification of Fe_2O_3 which has the spinel structure and can be written as $(\text{Fe}^{3+})[\text{Fe}_{5/6}^{3+}\text{Va}_{1/6}]\text{O}_4$. There is no experimental indication of any significant non-stoichiometry of Co_3O_4 . That is, in Co_3O_4 the concentration of vacancies is very low. This can be modeled by simply setting G_{EV} to a large arbitrary positive value. However, for internal consistency in the spinel model, this should be done in the same way as was done for Fe_3O_4 . That is, the non-stoichiometry is modeled as a dissolution of hypothetical $\gamma\text{-Co}_2\text{O}_3$ which is assigned a large arbitrary positive Gibbs energy equal to $(G_{\text{Co}_3\text{O}_4}^{\text{O}} - G_{\text{CoO}}^{\text{O}} + 200 \text{ kJ/mol})$, thereby assuring that the concentration of vacancies in the absence of Fe is very low. This results in the expression for G_{EV} given in Table I.

(2) Fe-Co-O System

(A) Spinel

CoFe_2O_4 is an inverse spinel at ambient temperature. The distribution of cations between octahedral and tetrahedral sites in CoFe_2O_4 as a function of temperature has been measured by several researchers.⁴⁴⁻⁵² As can be seen from Fig. 7, the experimental data are widely scattered and the temperature dependence of the cation distribution is not well established. Murray and Linnett⁴⁴ prepared their samples from oxides under undefined oxygen partial pressure and measured the cation distribution in quenched samples using Mössbauer spectrometry. Co^{2+} and Co^{3+} were not distinguished in their study. Yakel⁵⁰ prepared CoFe_2O_4 samples from CoO and Fe_2O_3 under flowing CO_2 at 1550°C and measured the cation distribution of quenched samples using Synchrotron X-rays. DeGuire *et al.*⁴⁸ used Mössbauer spectrometry to obtain the cation distribution in quenched CoFe_2O_4 samples prepared from oxides in air. They pointed out that the equilibrium cation distribution in spinel is very difficult to quench from high temperature. Waseda *et al.*⁴⁶ prepared CoFe_2O_4 samples from $\text{Fe}_2(\text{SO}_4)_3$ and CoSO_4 solutions. The samples were annealed at 800°C in air and quenched. The cation distribution was determined by anomalous X-ray scattering (AXS). Amer and Hemeda,⁴⁷ Van Noort *et al.*⁴⁹ and Popescu and Ghizdeanu⁵¹ measured the cation distribution of CoFe_2O_4 in slowly cooled samples. In other studies⁴⁵ the thermal history of the samples is not provided.⁵² The experimental data on cation distributions were fitted with the parameter I_{CH} of the spinel model (Table I).

The calculated cation distribution in $\text{Fe}_3\text{O}_4\text{-CoFe}_2\text{O}_4$ spinel solutions is shown in Fig. 8. Erikson and Mason,⁵³ using an *in situ* thermopower technique, measured the cation distribution in the spinel solution between Fe_3O_4 and CoFe_2O_4 , which was synthesized from oxide powders under CO_2/CO ratios between 100 and 1000. Murray and

Linnett⁴⁴ measured the cation distribution in this spinel solution using the same technique as for pure CoFe_2O_4 (see above). Mössbauer spectrometry was used by DeGuire *et al.*⁵⁴ to study the cation distribution of quenched Fe_3O_4 - CoFe_2O_4 samples prepared by a gas atomization technique with high pressure Ar gas. It should be noted that the amount of Co^{3+} cations in Fe_3O_4 - CoFe_2O_4 spinel solutions is very small because the reaction $\text{Fe}^{2+} + \text{Co}^{3+} \rightleftharpoons \text{Fe}^{3+} + \text{Co}^{2+}$ is strongly shifted to the right. However, when the spinel composition extends beyond CoFe_2O_4 towards Co_3O_4 , Co^{3+} ions enter octahedral sites in line with the fact that Co_3O_4 is a normal spinel.

The heat capacity of CoFe_2O_4 was measured at low temperatures by King⁵⁵ and at high temperatures by Landiya *et al.*,⁵⁶ Chachanidze⁵⁷ and Bochirol⁵⁸ using adiabatic calorimetry. CoFe_2O_4 is ferromagnetic below 784 K. The calculated heat capacity of CoFe_2O_4 is compared with the experimental data in Fig. 9. At these relatively low temperatures, there was probably insufficient time for the cation distribution to re-equilibrate during the adiabatic calorimetric measurements. Hence, the C_p curve in Fig. 9 was calculated under the assumption that there was no contribution to the measured C_p from the cation re-distribution.

King⁵⁵ synthesized a spinel sample of the FeCo_2O_4 composition from Fe_2O_3 and CoO in air and reported its entropy at 298.15 K from measurements of its heat capacity at low temperatures. It should be noted that spinel of this composition is actually not $\text{Fe}^{2+}\text{Co}_2^{3+}\text{O}_4$, but must be close to the formula $\text{Fe}^{3+}\text{Co}^{2+}\text{Co}^{3+}\text{O}_4$. The calculated entropy at 298.15 K for this spinel is 126.27 J/mol-K, in good agreement with the reported value of 125.5 ± 0.8 J/mol-K.

The enthalpy of formation of CoFe_2O_4 from solid CoO and Fe_2O_3 was measured by Navrotsky and Kleppa⁵⁹ at 973 K using $2\text{PbO} \cdot \text{B}_2\text{O}_3$ solution calorimetry. Their measured value, -24.6 ± 0.9 kJ/mol, is less negative than the optimized value in the present study, -30.86 kJ/mol, which is necessary to reproduce the measured phase diagrams as discussed below in Section III(2)(C).

The thermodynamic properties of CoFe_2O_4 spinel were reproduced by the optimized parameters of the Gibbs energy expression for the hypothetical completely normal end-member $(\text{Co}^{2+})[\text{Fe}^{3+}]_2\text{O}_4$ (see G_{CH} in Table I) and by the magnetic parameters β_{CH} , β'_{CH} , T_{CH} and T'_{CH} in Table I. There are no experimental data for the thermodynamic properties of the hypothetical $(\text{Fe}^{2+})[\text{Co}^{3+}]_2\text{O}_4$ end-member, since Fe^{2+} and Co^{3+} are not stable together, but react to form Fe^{3+} and Co^{2+} . Therefore, the Gibbs energy of this end-member has been estimated assuming that the Gibbs energy of the reciprocal reaction $\text{Fe}_3\text{O}_4 + \text{Co}_3\text{O}_4 = \text{FeCo}_2\text{O}_4 + \text{CoFe}_2\text{O}_4$ is equal to zero ($\dot{C}_{\text{FC:EH}} = 0$ in Table I). For the same reason, no experimental data are available on the cation distribution in the simple spinel containing mainly Fe^{2+} and Co^{3+} . Since the present spinel model reduces to the model of O'Neill and Navrotsky²⁸ as a limiting case, the parameter $\dot{C}_{\text{FE:FE}}$ was set equal to the

value of 40 kJ/mol recommended by these authors for all 2-3 spinels.

(B) Cobaltowustite

Aukrust and Muan⁶⁰ measured the non-stoichiometry of cobaltowustite as a function of oxygen partial pressure at 1200°C using thermogravimetry. The results were verified by measuring the amounts of Fe^{2+} and Fe^{3+} in quenched samples by chemical analysis. However, the equilibrium phases were not identified and some of the experimental points probably corresponded to the (cobaltowustite + spinel) or (cobaltowustite + alloy) two-phase regions. Raeder *et al.*,⁶¹ Subramanian *et al.*⁶² and Maksutov⁶³ also investigated the non-stoichiometry of cobaltowustite using the same technique. The experimental data are compared with the calculated lines in Fig. 10.

Benard⁶⁴ measured temperatures of dissociation of cobaltowustite solutions to spinel and alloy using quenching experiments and phase determination by X-ray diffraction. These results were later confirmed by Maksutov.⁶³ Touzelin⁶⁵ also mentioned the dissociation of cobaltowustite. Fig. 11 shows the calculated dissociation of cobaltowustite into Fe-Co alloy and spinel. The calculated curve is in excellent agreement with the experimental data.

The activity of CoO in the cobaltowustite phase saturated with Fe-Co alloy was measured by several researchers⁶⁶⁻⁷¹ (see Fig. 12). Aukrust and Muan⁶⁶ equilibrated cobaltowustite and Fe-Co alloy at 1200°C under controlled oxygen partial pressures. The compositions of the cobaltowustite were determined from X-ray measurements of lattice parameters. However, no details were given about the measurements of the alloy compositions. Seetharaman and Abraham⁶⁸ measured oxygen partial pressures over mixtures of cobaltowustite and metallic Co using an emf technique with ThO_2 - Y_2O_3 solid electrolytes at temperatures between 800° and 1000°C, and reported the activity of CoO in cobaltowustite. Although the compositions of the cobaltowustite and metallic phases must have changed during the experiments, no mention was made whether or not the phases were analyzed after the experiment. The reported activities deviate further from ideal solution behavior than those reported by other authors. Furthermore, the activities measured at 800°C may be in error due to possible decomposition of cobaltowustite into spinel and alloy (see Fig. 11). Several other studies^{63,67,70,71} reported activities of CoO which are in good agreement with those of Aukrust and Muan.⁶⁶ Ringsdorff⁷² obtained CoO activities at higher oxygen potentials, but these were not at saturation with the alloy phase. Viktorovich *et al.*⁶⁹ equilibrated cobaltowustite and alloy at 1000°C and measured the contents of Co in both phases by chemical analysis. However, these data were rejected in the present study because they show negative deviations of the CoO activities from ideality, contrary to all other studies shown in Fig. 12.

All thermodynamic and phase diagram data related to cobaltowustite were optimized simultaneously using just one model parameter $q_{\text{CoO,FeO}_{1.5}}^{00}$ which is given in Table I.

(C) Phase diagrams

Calculated phase diagrams of the Fe-Co-O system (oxygen partial pressure versus molar Co/(Fe+Co) metallic ratio at temperatures from 900° to 1300°C) are shown in Fig. 13 along with all available experimental data.

Thermogravimetry was used to measure phase boundaries in several studies.^{63,73-77} The weight change was recorded during the reduction of initial samples by inlet gas mixtures of controlled oxygen partial pressure, and phase boundaries were observed from the change of slope of recorded weight loss. No solubility of CoO in Fe₂O₃ was observed by X-ray lattice parameter determination.⁷⁴

Carter⁷⁸ and Schmalzried and Tretjakow⁷⁹ measured the oxygen partial pressure for the dissociation of spinel to cobaltowustite by an emf technique. The same phase boundary was obtained by Shchepetkin and Chufarov⁸⁰ using equilibration with CO/CO₂ gas mixtures. Lundberg and Rosen⁸¹ equilibrated spinel and cobaltowustite at fixed oxygen partial pressures at 1023°C and determined the compositions of both the spinel and cobaltowustite phases by EPMA (WDS). Roiter and Paladino³⁶ measured the cobaltowustite phase boundary in equilibrium with spinel at high oxygen partial pressure controlled by a mercury manometer. They also identified the equilibrium phases in quenched samples of various Co/(Co+Fe) ratios in air by XRD in order to determine the cobaltowustite phase boundary more accurately. Aukrust and Muan^{36,60} used both thermogravimetry and a quenching technique to determine the phase diagram at 1200°C. In the case of the quenching experiments, the compositions of spinel and cobaltowustite were determined from X-ray lattice parameter measurements. Similar quenching experiments were performed in air.⁸² The phase diagram in air below 1100°C was also studied by Robin and Benard⁸³ using a quenching technique followed by X-ray phase identification. A miscibility gap in the spinel phase was detected as can be seen in Fig. 14.

The calculated phase diagrams in Fig. 13 are in good agreement with the experimental data except for the experimental points of Aukrust and Muan⁶⁰ obtained from the X-ray measurements of the cobaltowustite compositions. The latter are subject to large experimental errors due to the small difference between the lattice parameters of Fe₂O and CoO in the rocksalt structure. The compositions were estimated from the measured d-spacings, d_{200} . The reported value of d_{200} of Fe₂O saturated with Fe was 2.153⁸⁴ and that of CoO was 2.137.⁶⁶ The difference between the two is comparable to the error in the d_{200} measurements as can be seen from similar data reported for the CoO-MnO and CoO-MgO solutions by the same authors.⁶⁶ On the other hand, the composition of the spinel phase can be accurately determined from X-ray lattice parameter measurements due to the strong dependence of the spinel lattice parameters on composition.

Fig. 14 shows the calculated phase diagram of the Fe-Co-O system in air. As mentioned above, the compositions of the cobaltowustite phase determined from the X-ray d-spacing measurements^{60,82} are not accurate. The phase boundary bracketed by Roiter and Paladino³⁶ using XRD phase identification is more reliable. The calculated miscibility gap in the spinel phase is only in fair agreement with the experimental one reported by Robin and Benard⁸³ based on quenching followed by XRD phase determination. It should be noted that no primary experimental results were given by the authors, and the flat shape of the proposed miscibility gap (dotted line in Fig. 14) seems unlikely. The calculated miscibility gap is affected most by the optimized parameter $\hat{C}_{\text{CF:CH}}$ of the spinel model (see Table I). One more Gibbs energy of a reciprocal reaction, the parameter $\hat{C}_{\text{HC:HE}}$, was optimized to reproduce the phase diagrams in Figs. 13 and 14, and two other parameters of the spinel model, $\hat{C}_{\text{FC:FH}}$ and $\hat{C}_{\text{EH:EH}}$, were set to zero. Also, as mentioned above, the enthalpy of formation of CoFe₂O₄ was also optimized (via the $H_{298.15}^{\circ}$ parameter of G_{CH} in Table I) in order to reproduce the phase diagram data.

The calculated phase equilibria between liquid Fe-Co alloy and slag at 1600° and 1660°C are shown in Fig. 15. The calculated curves are in good agreement with the experimental data of Jander and Krieger⁸⁵ who used a quenching technique followed by chemical analysis of each phase.

IV. Applications

To produce magnetic and electronic materials, CoFe₂O₄ is synthesized using different techniques such as vacuum evaporation, sputtering, the sol-gel method, molecular beam epitaxy, etc. However, after synthesis it is commonly annealed at temperatures from 500° to 800°C in order to homogenize the materials. As can be seen from Fig. 13, synthesized CoFe₂O₄ may partially transform to Fe₂O₃ or cobaltowustite during annealing.

Fig. 16 shows the calculated stability range of spinel of three compositions: pure CoFe₂O₄, (95 mol % CoFe₂O₄ + 5 mol % Co₃O₄), and (95 mol % CoFe₂O₄ + 5 mol % Fe₃O₄). As can be seen, the stability region of spinel varies significantly with temperature, oxygen partial pressure and composition. Therefore, during the annealing process the oxygen partial pressure of the system should be carefully controlled in order to stay within the single-phase spinel field.

Furthermore, samples synthesized at lower temperatures generally have non-equilibrium cation distributions, which are highly dependent on the synthesizing technique. However, during an annealing process at higher temperature, cations may redistribute between the tetrahedral and octahedral sites and approach the equilibrium site occupancies, which can be calculated using the results of the present study. For example, Fig. 17 shows the calculated equilibrium cation distribution in Fe₃O₄-Co₃O₄ spinel solutions at 700°C at saturation with cobaltowustite.

V. Conclusions

All available thermodynamic and phase equilibrium data for oxide phases in the Fe-Co-O system have been critically assessed. An appropriate thermodynamic model has been developed for each oxide phase, and a self-consistent set of model parameters has been optimized to reproduce all the data within experimental error limits in the temperature range from 25°C to above the liquidus and for oxygen partial pressures from metal saturation up to 100 bar. The database of model parameters can be used with general thermodynamic software, such as FactSage⁸⁶, in order to calculate the thermodynamic properties, the distribution of cations in the spinel solution, and phase equilibria for temperatures, compositions and oxygen partial pressures where experimental data are not available. In particular, this can be useful for a better understanding and optimization of the properties of magnetic materials.

References

1. A. D. Pelton, H. Schmalzried, and J. Sticher, "Thermodynamics of Mn_3O_4 - Co_3O_4 , Fe_3O_4 - Mn_3O_4 , and Fe_3O_4 - Co_3O_4 Spinel by Phase Diagram Analysis," *Ber. Bunsen-Ges. Phys. Chem.*, **83**, 241-252 (1979).
2. R. Subramanian, R. Dieckmann, G. Eriksson, and A. D. Pelton, "Model Calculations of Phase Stabilities of Oxide Solid Solutions in the Co-Fe-Mn-O System at 1200°C," *J. Phys. Chem. Solids*, **55**, 391-404 (1994).
3. S. A. Decterov, E. Jak, P. C. Hayes, and A. D. Pelton, "Experimental Study of Phase Equilibria and Thermodynamic Optimization of the Fe-Zn-O System," *Metall. Mater. Trans. B*, **32**, 643-657 (2001).
4. A. D. Pelton and M. Blander, "Computer-Assisted Analysis of the Thermodynamic Properties and Phase Diagrams of Slags"; pp. 281-294 in *Proceedings of the Second International Symposium on Metallurgical Slags and Fluxes*, TMS-AIME, Warrendale, PA, 1984.
5. A. D. Pelton and M. Blander, "Thermodynamic Analysis of Ordered Liquid Solutions by a Modified Quasi-Chemical Approach. Application to Silicate Slags," *Metall. Trans. B*, **17B**, 805-815 (1986).
6. A. D. Pelton, S. A. Decterov, G. Eriksson, C. Robelin, and Y. Dessureault, "The Modified Quasichemical Model. I - Binary Solutions," *Metall. Mater. Trans. B*, **31B**, 651-659 (2000).
7. A. D. Pelton and P. Chartrand, "The Modified Quasichemical Model. II - Multicomponent Solutions," *Metall. Mater. Trans. A*, **32A**, 1355-1360 (2001).
8. A. D. Pelton, "A General "Geometric" Thermodynamic Model for Multicomponent Solutions," *Calphad*, **25**, 319-328 (2001).
9. M. Hillert, B. Jansson, and B. Sundman, "Application of the Compound-Energy Model to Oxide Systems," *Z. Metallkd.*, **79**, 81-87 (1988).
10. M. Hillert and M. Jarl, "A Model for Alloying Effects in Ferromagnetic Metals," *Calphad*, **2**, 227-238 (1978).
11. Scientific Group Thermodata Europe, <http://www.sgte.org/>, 2002.
12. B. Fisher and D. S. Tannhauser, "The Phase Diagram of Cobalt Monoxide at High Temperatures," *J. Electrochem. Soc.*, **111**, 1194-1196 (1964).
13. S. Aggarwal and R. Dieckmann, *Ceram. Trans.*, **24**, 23 (1991).
14. E. G. King, "Heat Capacities at Low Temperatures and Entropies at 298.15 K of Nickelous Oxide, Cobaltous Oxide and Cobalt Spinel," *J. Am. Chem. Soc.*, **79**, 2399-2400 (1957).
15. J. Kleinclauss, R. Mainard, H. Fousse, N. Ciret, D. Bour, and A. J. Pointon, "Thermomagnetic Study of the Antiferromagnetic Solid Solutions of Manganese Oxide and Cobalt Oxide," *J. Phys. C*, **14**, 1163-1677 (1981).
16. H. Watanabe, "Thermal Constants for Nickel, Nickel Monoxide, Magnesia, Manganese Monoxide and Cobalt Monoxide at Low Temperatures," *Thermochim. Acta*, **218**, 365-372 (1993).
17. H. Watanabe, "Thermochemical Properties of Synthetic High-Pressure Compounds Relevant to the Earth's Mantle," *High-Pressure Res. Geophys.*, 441-464 (1982).
18. E. G. King, A. U. Christensen, Jr., "Heat Contents above 298.15 K of Oxides of Cobalt and Nickel," *J. Am. Chem. Soc.*, **80**, 1800-1801 (1958).
19. P. Asanti and E. J. Kohlmeyer, "Ober die thermischen Eigenschaften der Verbindungen von Kobalt mit Sauerstoff und Schwefel," *Z. Anorg. Allg. Chem.*, **265**, 90-98 (1951).
20. I. Barin, *Thermodynamic Data for Pure Substances*, VCH, Weinheim, Germany, **7**, 18 (1989).
21. D. P. Masse and A. Muan, "Phase Relations in the System CoO-SiO₂," *Trans. AIME*, **233**, 1448-1449 (1965).
22. I.-H. Jung, S. A. Decterov, A. D. Pelton, and H. M. Kim, "Thermodynamic Modeling of CoO-SiO₂ and CoO-FeO-Fe₂O₃-SiO₂ Systems," *will be submitted*.
23. T. Mori, "Phase Diagram of the System Cobalt (II) Oxide-Aluminum Oxide," *Yogyo Kyokaishi*, **90**, 100-101 (1982).
24. S. A. Decterov, I.-H. Jung, Y.-B. Kang, E. Jak, V. Swamy, D. Kevorkov, and A. D. Pelton, Consortium 2002 progress report, Ecole Polytechnique, Montreal, 2002.
25. L. M. Khriplovich, E. V. Kholopov, and I. E. Paukov, "Heat Capacity and Thermodynamic Properties of Cobalt Spinel from 5 to 307 K. Low-Temperature Transition," *J. Chem. Thermodyn.*, **14**, 207-217 (1982).
26. K. Mocala, A. Navrotsky, and D. M. Sherman, "High-Temperature Heat Capacity of Co₃O₄ Spinel: Thermally Induced Spin Unpairing Transition," *Phys. Chem. Miner.*, **19**, 88-95 (1992).
27. H. S. C. O'Neill, "Thermodynamics of Cobalt Oxide (Co₃O₄): a Possible Electron Spin Unpairing Transition in Cobalt (3+) Ion," *Phys. Chem. Miner.*, **12**, 149-154 (1985).
28. H. S. C. O'Neill and A. Navrotsky, "Cation Distributions and Thermodynamic Properties of Binary Spinel Solid Solutions," *Am. Mineral.*, **69**, 733-753 (1984).
29. V. F. Balakirev and G. I. Chufarov, "Equilibrium in Systems Co-O and Co-O-H," *Dokl. Akad. Nauk SSSR*, **138**, 112-114 (1961).
30. K. Kuikkola and C. Wagner, *J. Electrochem. Soc.*, **104**, 379-387 (1957).
31. G. M. Kale, S. S. Pandit, and K. T. Jacob, "Thermodynamics of Cobalt (II, III) Oxide (Co₃O₄): Evidence of Phase Transition," *Trans. Jpn. Inst. Met.*, **29**, 125-132 (1988).
32. O. M. Sreedharan and C. Mallika, "A Third Law Method for the Assessment of Standard Gibbs Energy Data on Cobalt Oxides from emf. Measurements," *Mater. Chem. Phys.*, **14**, 375-384 (1986).
33. H. Oppermann, G. Stoeber, L. M. Khriplovich, and I. E. Paukov, "Studies on the Thermodynamical Behavior of Cobalt Oxide (Co₃O₄)," *Z. Anorg. Allg. Chem.*, 173-176 (1980).
34. N. Kemori, I. Katayama, and Z. Kozuka, "Measurements of Standard Molar Gibbs Energies of Formation of Nickel (II) Oxide and Copper (I) Oxide, and Cobalt (II) Oxide from Solid and Liquid Metals and Oxygen Gas by an e.m.f. Method at High Temperatures," *J. Chem. Thermodyn.*, **11**, 215-228 (1979).
35. O. M. Sreedharan, M. S. Chandrasekharaiah, and M. D. Karkhanavala, "Thermodynamic Stabilities of Cobalt Oxides," *High Temp. Sci.*, **9**, 109-118 (1977).
36. B. D. Roiter and A. E. Paladino, "Phase Equilibria in the Ferrite Region of the System Fe-Co-O," *J. Am. Ceram. Soc.*, 128-132 (1962).
37. K. Naidu, "Thermodynamics of Spinel Solid Solutions. The Systems Co₃O₄-CoAl₂O₄ and CoO₄-CoCrO₄," Ph. D. Dissertation, University of Toronto, Department of Materials Science, 1978.
38. B. Björkman and E. Rosén, "Thermodynamic Studies of High Temperature Equilibria. Determination of the Stability of Co₃O₄ in the Temperature Range 970-1340 K by Solid State emf Measurements," *Chem. Scripta*, **13**, 139-142 (1978).
39. M. Watanabe, *Bull. Inst. Phys. Chem. (Tokyo)*, **12**, 16 (1933).
40. V. I. Smirnov and M. A. Abdeev, "Dissociation Pressure of Cobalt Oxides," *Izv. Akad. Nauk Kazakh. SSSR, Ser. Gorn. Dela, Metallurgii, Stroitel'stva, Stroimaterialov*, **1**, 97-101 (1957).
41. H. W. Foote and E. W. Smith, "On the Dissociation Pressures of Certain Oxides of Copper, Cobalt, Nickel and Antimony," *J. Am. Ceram. Soc.*, **30**, 1344-1350 (1908).
42. E. J. Grimsey and K. A. Reynolds, "Equilibrium Oxygen Pressure of Cobalt Oxide Mixture (Co₃O₄ + CoO) from 1173 to 1228 K," *J. Chem. Thermodyn.*, **18**, 473-476 (1986).
43. C. B. Alcock and G. P. Stavropoulos, "Ionic Transport Numbers

- of Group IIa Oxides under Low Oxygen Potentials," *J. Am. Ceram. Soc.*, **54**, 436-443 (1971).
44. P. J. Murray and J. W. Linnett, "Cation Distribution in the Spinels $\text{Co}_x\text{Fe}_{3-x}\text{O}_4$," *J. Phys. Chem. Solids*, **37**, 1041-1042 (1976).
45. G. A. Sawatzky, F. Van der Woude, and A. H. Morrish, "Moessbauer Study of Several Ferrimagnetic Spinels," *Phys. Rev.*, **187**, 747-757 (1969).
46. Y. Waseda, K. Shinoda, and K. Sugiyama, "Cation Distribution of ZnFe_2O_4 and CoFe_2O_4 Spinels from Anomalous X-ray Scattering," *Z. Naturforsch., A: Phys. Sci.*, **50**, 1199-1204 (1995).
47. M. A. Amer and O. M. Hemeda, " ^{57}Fe Moessbauer and Infrared Studies of the System $\text{Co}_{1-x}\text{Cd}_x\text{Fe}_2\text{O}_4$," *Hyperfine Interact.*, **96**, 99-109 (1995).
48. M. R. De Guire, R. C. O'Handley, and G. Kalonji, "The Cooling Rate Dependence of Cation Distributions in Cobalt Ferrite (CoFe_2O_4)," *J. Appl. Phys.*, **65**, 3167-3172 (1989).
49. H. M. Van Noort, J. W. D. Martens, and W. L. Peeters, "The Cation Distribution of Cobalt Iron Aluminum Oxide ($\text{CoFe}_{2-x}\text{Al}_x\text{O}_4$) as Determined by Conversion-Electron Moessbauer Spectroscopy," *Mater. Res. Bull.*, **20**, 41-47 (1985).
50. H. L. Yakel, "Determination of the Cation Site-Occupation Parameter in a Cobalt Ferrite from Synchrotron-Radiation Diffraction Data," *J. Phys. Chem. Solids*, **41**, 1097-1104 (1980).
51. M. Popescu and C. Ghizdeanu, "Cation Distribution in Cobalt Ferrite-Aluminates," *Phys. Status Solidi A*, **52**, K169-K172 (1979).
52. A. S. Vaingankar, S. A. Patil, and V. S. Sahasrabudhe, "Degree of Inversion in Cobalt Ferrite by EXAFS Study," *Trans. Indian Inst. Met.*, **34**, 387-389 (1981).
53. D. S. Erickson and T. O. Mason, "Nonstoichiometry, Cation Distribution, and Electrical Properties in Iron Oxide (Fe_3O_4)-Cobalt Iron Oxide (CoFe_2O_4) at High Temperature," *J. Solid State Chem.*, **59**, 42-53 (1985).
54. M. R. De Guire, G. Kalonji, and R. C. O'Handley, "Cation Distributions in Rapidly Solidified Cobalt Ferrite," *J. Am. Ceram. Soc.*, **73**, 3002-3006 (1990).
55. E. G. King, "Heat Capacities at Low Temperatures and Entropies of Five Spinel Minerals," *J. Phys. Chem.*, **60**, 410-412 (1956).
56. N. A. Landiya, G. D. Chachanidze, A. A. Chuprin, T. A. Pavlenishvili, N. G. Lezhava, and V. S. Varazashvili, "Determination of the High Temperature Enthalpies of Nickel and Cobalt Ferrites," *Izv. Akad. Nauk SSSR, Neorg. Mater.*, **2**, 2050-2057 (1966).
57. G. D. Chachanidze, "Thermodynamic Properties of Nickel and Cobalt Ferrites," *Izv. Akad. Nauk SSSR, Neorg. Mater.*, **26**, 376-379 (1990).
58. M. L. Bochirol, "Chaleur Specifique Vraie des Ferrites de Zinc, de Nickel et de Cobalt," *Compt. Rend.*, **232**, 1474-1477 (1951).
59. A. Navrotsky and O. J. Kleppa, "Thermodynamics of Formation of Simple Spinels," *J. Inorg. Nucl. Chem.*, **30**, 479-498 (1968).
60. E. Aukrust and A. Muan, "Thermodynamic Properties of Solid Solutions with Spinel-Type Structure. II. The System Co_3O_4 - Fe_3O_4 at 1200°C," *Trans. Met. Soc. AIME*, **230**, 1395-1399 (1964).
61. J. H. Raeder, J. L. Holm, and O. T. Sorensen, "Defects in Metal-Deficient Cobalt-Wustites, $(\text{Co}, \text{Fe})_{1-x}\text{O}$," *Solid State Ionics*, **12**, 155-159 (1984).
62. R. Subramanian, S. Tinkler, and R. Dieckmann, "Defects and Transport in the Solid Solution $(\text{Co}, \text{Fe})_{1-\delta}\text{O}$ at 1200°C - I. Nonstoichiometry," *J. Phys. Chem. Solids*, **55**, 69-75 (1994).
63. I. A. Maksutov, "Study of Thermodynamic Properties of Solid Wustite Solutions in System Fe-Co-O", 1974.
64. M. J. Benard, "Étude de la Stabilité des Solutions Solides entre les Protoxydes de Fer et de Cobalt," *Comptes Rendus*, **218**, 1356-1359 (1936).
65. B. Touzelin, "Study of the Iron-Cobalt-Oxygen System at 900°C by Thermogravimetry and High-Temperature X-ray Diffraction," *J. Less-Common Met.*, **77**, 11-27 (1981).
66. E. Aukrust and A. Muan, "Activities of Components in Oxide Solid Solutions: The Systems CoO - MgO , CoO - MnO , and CoO - FeO at 1200°C," *Trans. Met. Soc. AIME*, **227**, 1378-1380 (1963).
67. B. G. Brokhovetskii, V. F. Balakirev, G. P. Popov, and G. I. Chufarov, "Phase Equilibrium during the Reduction of a Solid Solution of Ferrite and Cobalt Aluminate," *Izv. Vyssh. Ucheb. Zaved., Tsvet. Met.*, **12**, 46-49 (1969).
68. S. Seetharaman and K. P. Abraham, "Activity Measurements in Cobalt Oxide-Iron (II) Oxide Solid Solutions," *Trans. Indian Inst. Metals*, **25**, 16-19 (1972).
69. G. S. Viktorovich, V. A. Gutin, and D. I. Lisovskii, "Wustite-Alloy Solid Phase Equilibria in an Iron-Nickel-Cobalt-Oxygen System," *Zh. Fiz. Khim.*, **43**, 3043-3046 (1969).
70. R. Yu. Dobrovinskii, V. F. Balakirev, A. N. Men', and G. I. Chufarov, "Thermodynamic Activity of Components of Solid Solution of Protoxides of Cobalt and Iron at 1000°C," *J. Phys. Chem.*, **42**, 1001-1003 (1968).
71. I. A. Maksutov and A. A. Lykasov, "Wustite Solutions in System Fe-Co-O," *Izv. Vuzov, Chernaya Metallurgiya*, **2**, 18-20 (1974).
72. M. Ringsdorff, *Ber. Bunsen-Ges. Phys. Chem.*, **72**, 754-764 (1968).
73. W. Muller and H. Schmalzried, "Fehlordnung in Kobaltferrit," *Ber. Bunsen-Ges. Phys. Chem.*, **68**, 270-276 (1964).
74. I. Katayama, T. Matsuda, and Z. Kozuka, "Thermodynamic Study of Spinel-Type Solid Solutions of Ferric Oxide-Cobalt Iron Oxide by EMF Method," *Nippon Kinzoku Gakkaishi*, **47**, 858-862 (1983).
75. J. Smiltens, "Investigation of the Ferrite Region of the Phase Diagram Fe-Co-O," *J. Am. Chem. Soc.*, **79**, 4881-4884 (1957).
76. S. Iida, "Phase Diagram of Iron-Cobalt-Oxygen System. (I) Experimental Study," *J. Phys. Soc. Jpn.*, **11**, 846-854 (1956).
77. R. Subramanian and R. Dieckmann, "Thermodynamics of the Oxide Solid Solution $(\text{Co}_x\text{Fe}_{1-x})_{1-\delta}\text{O}$ at 1200°C," *J. Phys. Chem. Solids*, **55**, 59-67 (1994).
78. R. E. Carter, "Dissociation Pressures of Solid Solutions from Fe_2O_3 to $0.4\text{Fe}_2\text{O}_3 \cdot 0.6\text{CoFe}_2\text{O}_4$," *J. Am. Ceram. Soc.*, **43**, 448-452 (1960).
79. H. Schmalzried and J. D. Tretjakow, "Fehlordnung in Ferriten," *Ber. Bunsen-Ges. Phys. Chem.*, **70**, 180-188 (1966).
80. A. A. Shchepetkin and G. I. Chufarov, "The Dissociation of Solid Solutions of Oxides in M-Fe-O Systems under Equilibrium Conditions," *Russ. J. Inorg. Chem.*, **17**, 792-794 (1972).
81. M. Lundberg and E. Rosén, "Equilibrium Studies of the System Iron Cobalt Oxide-Iron Cobalt Oxide ($(\text{Fe}, \text{Co})\text{O}$)- $(\text{Fe}, \text{Co})_3\text{O}_4$) by Solid-State emf Measurements in the Temperature Range 970 to 1370 K," *J. Am. Ceram. Soc.*, **75**, 1452-1457 (1992).
82. D. P. Masse and A. Muan, "Phase Equilibria at Liquidus Temperatures in the System Cobalt Oxide-Iron Oxide-Silica in Air," *J. Am. Ceram. Soc.*, **48**, 466-469 (1965).
83. M. M. J. Robin and J. Benard, "Recherches sur la Structure et la Stabilité des Phases dans le Système Fe_2O_3 - Co_3O_4 ," *Comptes Rendus*, **234**, 734-735, (1952).
84. W. C. Hahn and A. Muan, "Activity Measurements in Oxide Solid Solutions: The System FeO - MgO in the Temperature Interval 1100° to 1300°C," *Trans. Met. Soc. AIME*, **224**, 416-420 (1962).
85. W. Jander and A. Krieger, "Die Gleichgewichte $\text{Fe}+\text{CoO}=\text{Co}+\text{FeO}$ und $\text{Ni}+\text{CoO}=\text{Co}+\text{NiO}$ im Schmelzflub," *Z. Anorg. Allg. Chem.*, **232**, 39-56 (1937).
86. www.factsage.com. Montreal, 2002.

Table I. Optimized enthalpy, entropy and heat capacity of stoichiometric compounds and model parameters for cobaltowustite and spinel. (J/mol and J/mol·K). (Enthalpies are relative to elements at 298.15 K, entropies are absolute Third law entropies.)

Compounds*	Temperature range (K)	$H_{298.15\text{ K}}^{\circ}$	$S_{298.15\text{ K}}^{\circ}$	C_p
CoO (solid)	298-1600	-237735.0	52.993	$55.383 - 0.0064212T + 7.05602\text{E-}6T^2 + 36800T^2$
	1600-2103	-237808.25	52.936	$58.383 - 0.0104945T + 8.47007\text{E-}6T^2 - 226180T^2$
CoO (liquid)	298-1300	-203885.11	68.050	$55.383 - 0.0064212T + 7.05602\text{E-}6T^2 + 36800T^2$
	1300-3000	-221573.25	41.3762	73.098
Cobaltowustite: CoO-FeO-FeO_{1.5}				
$q_{\text{CoO,FeO}_{1.5}}^{00} = -20920\text{ J/mol}$				
The polynomial “q” parameters are defined in Reference 8.				

(Table I – continued.)

** Spinel: (Co ²⁺ , Co ³⁺ , Fe ²⁺ , Fe ³⁺)[Co ²⁺ , Co ³⁺ , Fe ²⁺ , Fe ³⁺ , Va] ₂ O ₄				
	Temperature range (K)	$H_{298.15\text{ K}}^{\circ}$	$S_{298.15\text{ K}}^{\circ}$	C_p
G_{CH}^*	298-2500	-1072898.0	145.9781	$-218.62 - 20000T^{-1}$
	298-900	-914413.2	109.2860	$262.5 + 0.01T - 2.50E+8T^{-2} + 588.576T^{-0.5}$
G_{CE}^*	900-1200	-916430.9	107.9451	$-764.8517 + 4.453217T - 6.76947E-3T^2 + 3.33123E-6T^3$
	1200-1360	-12520070	-26742.73	$-9138.843 + 4.150808T - 6.842919E+9T^{-2} - 227.2425T^{-0.5}$
	1360-2500	-842277.5	173.1809	$269.40 - 0.015T + 1.0E-5T^2 - 25000T^{-0.5}$

$$I_{\text{CH}} = G_{\text{HH}} + G_{\text{HC}} - 2G_{\text{CH}} = -28289.4 + 11.157T$$

$$\dot{C}_{\text{FC:EH}} = G_{\text{FE}} + G_{\text{CH}} - G_{\text{FH}} - G_{\text{CE}} = 0$$

$$\dot{C}_{\text{FE:FE}} = G_{\text{FF}} + G_{\text{EE}} - G_{\text{FE}} - G_{\text{EF}} = 40000 \quad ***$$

$$\dot{C}_{\text{CE:CE}} = G_{\text{CC}} + G_{\text{EE}} - G_{\text{CE}} - G_{\text{EC}} = 40000 \quad ***$$

$$I_{\text{CE}} = G_{\text{EE}} + G_{\text{EC}} - 2G_{\text{CE}} = 749982.0 \quad ***$$

$$G_{\text{EV}} = 8 G_{\gamma\text{-Co}_2\text{O}_3}^{\circ} - 2RT(5\ln 5 - 6\ln 6) - 5G_{\text{EE}}, \text{ where } G_{\gamma\text{-Co}_2\text{O}_3}^{\circ} = G_{\text{CE}} - G_{\text{CoO}}^{\circ} + 200000.0$$

$$\dot{C}_{\text{CF:CH}} = G_{\text{CC}} + G_{\text{FH}} - G_{\text{CH}} - G_{\text{FC}} = 20920$$

$$\dot{C}_{\text{HC:HE}} = G_{\text{HH}} + G_{\text{CE}} - G_{\text{HE}} - G_{\text{CH}} = -41840$$

$$\dot{C}_{\text{FC:FH}} = G_{\text{FF}} + G_{\text{CH}} - G_{\text{FH}} - G_{\text{CF}} = 0.0$$

$$\dot{C}_{\text{EH:EH}} = G_{\text{EE}} + G_{\text{HH}} - G_{\text{EH}} - G_{\text{HE}} = 0.0$$

Magnetic properties: ****

$$\beta_{\text{CE}} = \beta_{\text{CE}}^i \quad 0.6$$

$$T_{\text{CE}} = T_{\text{CE}}^i \text{ (Néel temperature)} \quad 29.8\text{ K}$$

$$\beta_{\text{CH}} = \beta_{\text{CH}}^i \quad 2.87123$$

$$T_{\text{CH}} = T_{\text{CH}}^i \text{ (Curie temperature)} \quad 784.0\text{ K}$$

$$P \text{ (P factor)} \quad 0.28$$

$$* G = H_{298.15}^{\circ} + \int_{298.15}^T C_p dT - T[S_{298}^{\circ} + \int_{298.15}^T (C_p / T) dT]$$

** Notations F, C, E, H, and V are used for Fe²⁺, Co²⁺, Co³⁺, Fe³⁺ and vacancy, respectively. The Gibbs energies of six end-members (G_{FH} , G_{HF} , G_{FF} , G_{HH} , G_{FV} and G_{HV}) and the corresponding model parameters are given in the previous study.³ The Gibbs energies of two other end-members, G_{CC} and G_{CV} , were defined in the optimization of the CoAl₂O₄ simple spinel and will be reported elsewhere.

*** These parameters were determined from the values recommended by O'Neill and Navrotsky.²⁸

**** β_{CE} and β_{CE}^i are the magnetic moments, and T_{CE} and T_{CE}^i are the Néel temperatures, of hypothetical completely normal and completely inverse Co₃O₄ spinel, respectively (see Reference 3). β_{CH} , β_{CH}^i , T_{CH} and T_{CH}^i are similarly defined for CoFe₂O₄.

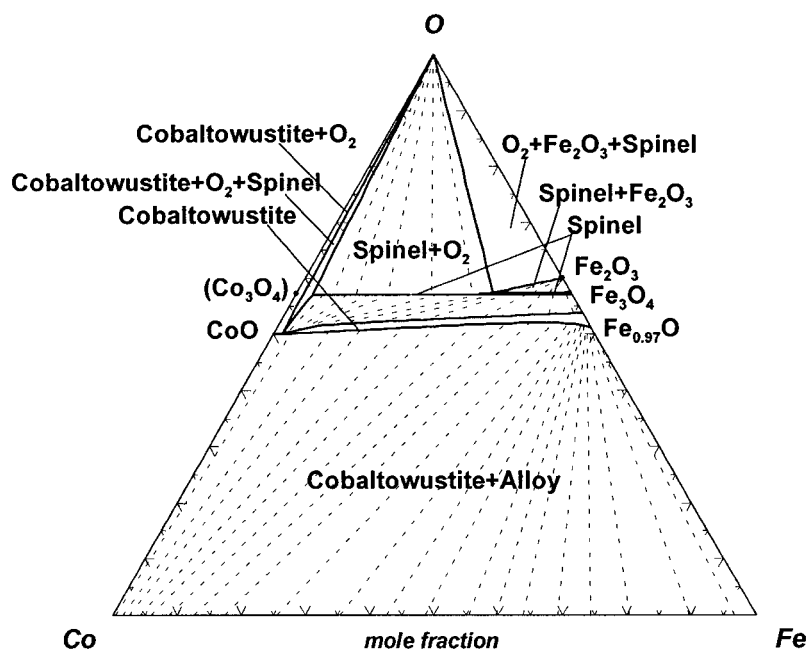


Fig. 1 – Calculated phase diagram of the Fe-Co-O system at 1200°C and $P(\text{O}_2) = 100$ bar.

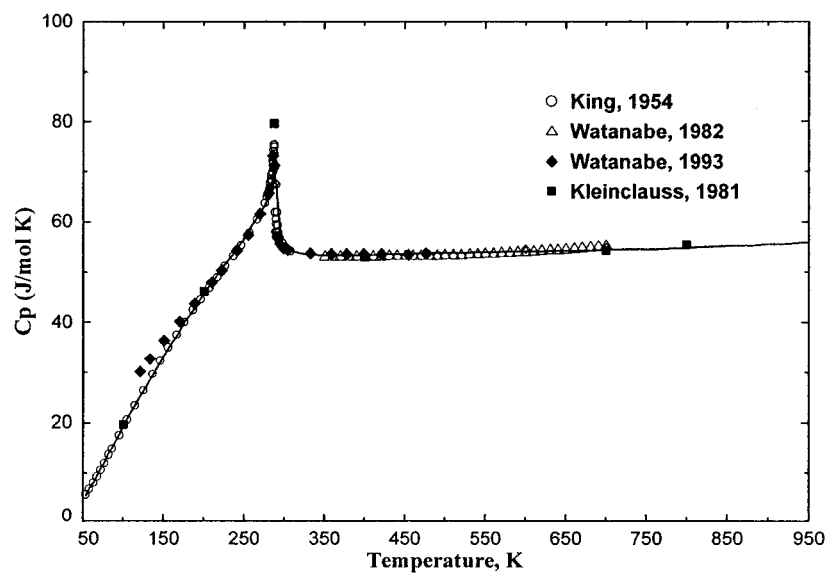


Fig. 2 – Calculated heat capacity of solid CoO.

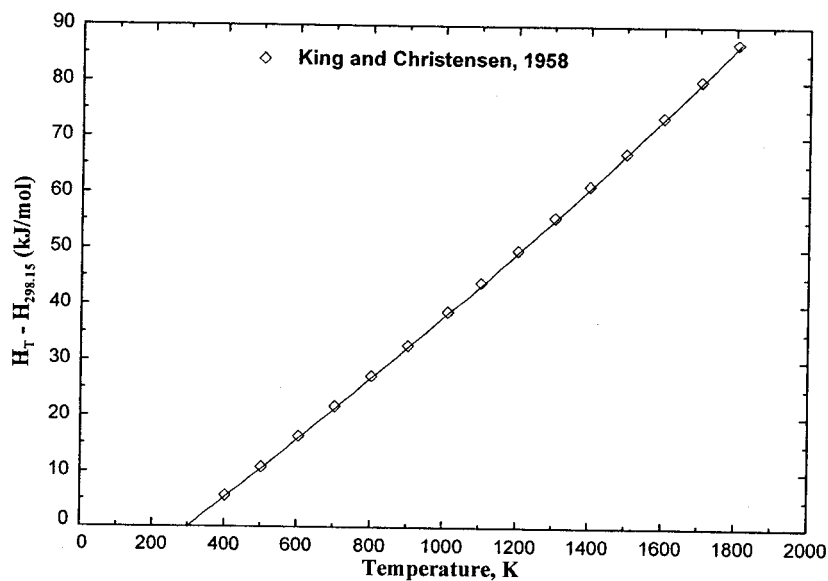


Fig. 3 – Calculated heat content of solid CoO.

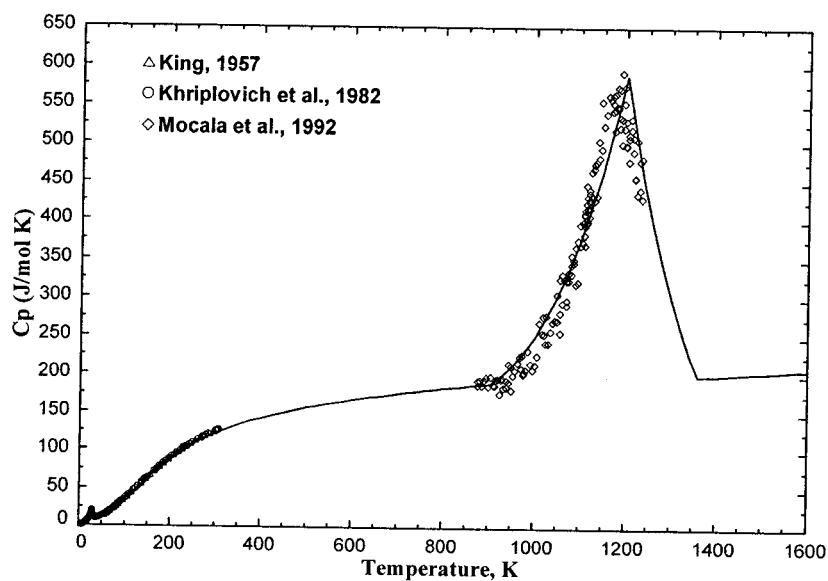


Fig. 4 – Calculated heat capacity of Co_3O_4 spinel. The anomaly at approximately 30 K is an anti-ferromagnetic transition and the anomaly at approximately 1200 K is a transition from the low-spin to the high-spin state of the Co^{3+} cations.

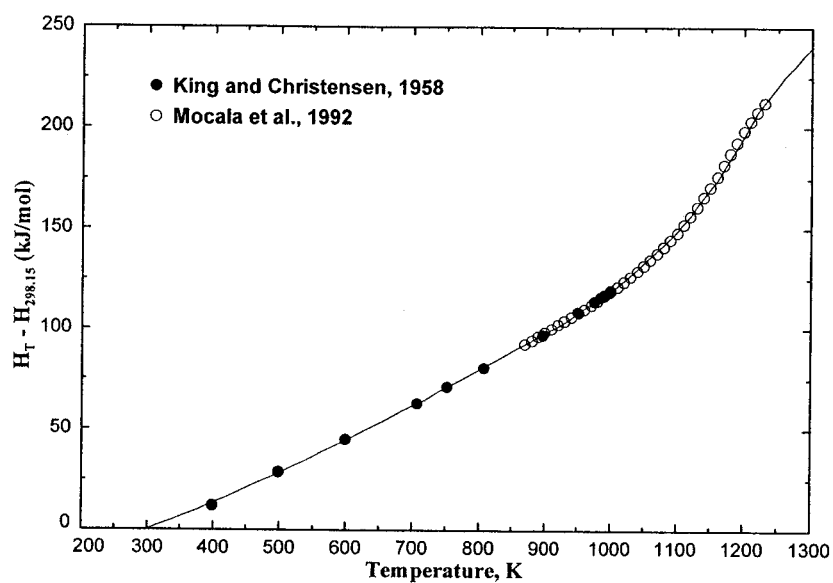


Fig. 5 – Calculated heat content of Co_3O_4 spinel.

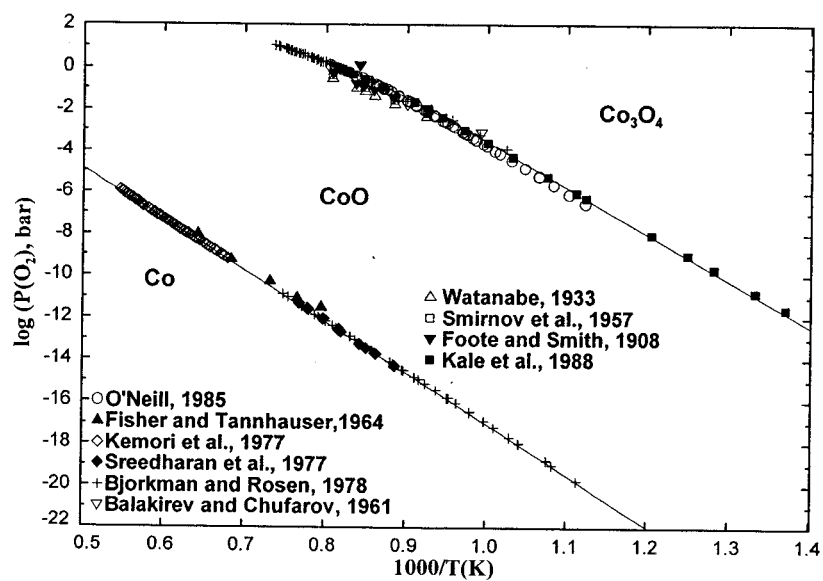


Fig. 6 – Calculated phase diagram of the Co-O system.

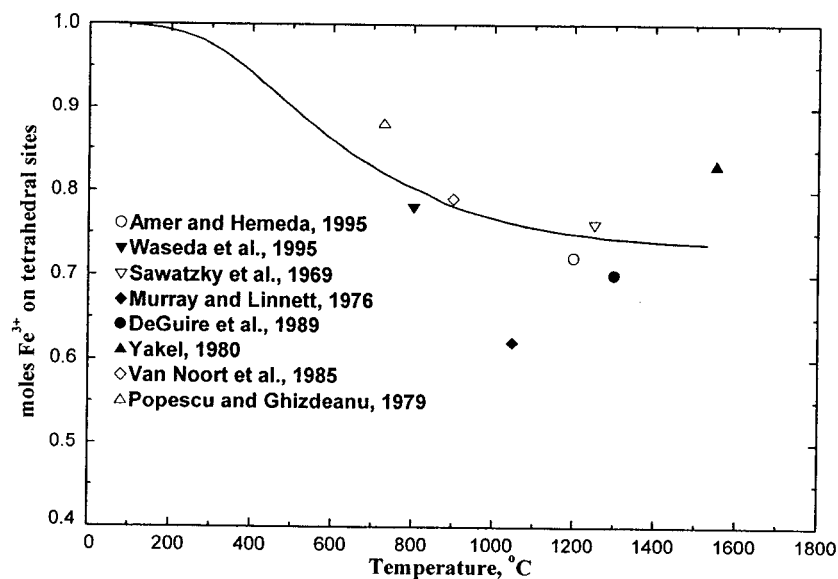


Fig. 7 – Calculated cation distribution in CoFe_2O_4 .

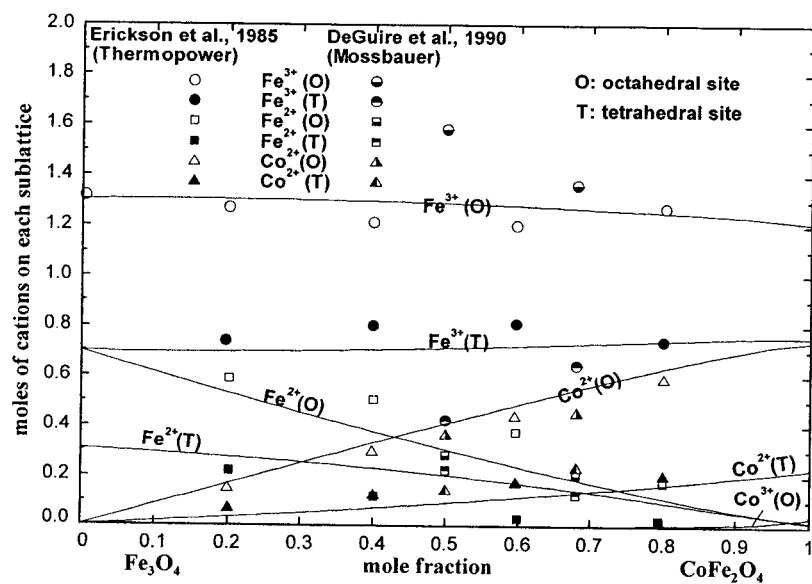


Fig. 8 – Calculated cation distribution in Fe_3O_4 - CoFe_2O_4 spinel solutions saturated with cobaltowustite at 1200°C . Moles of cations on octahedral and tetrahedral sublattices per mole of the spinel solution.

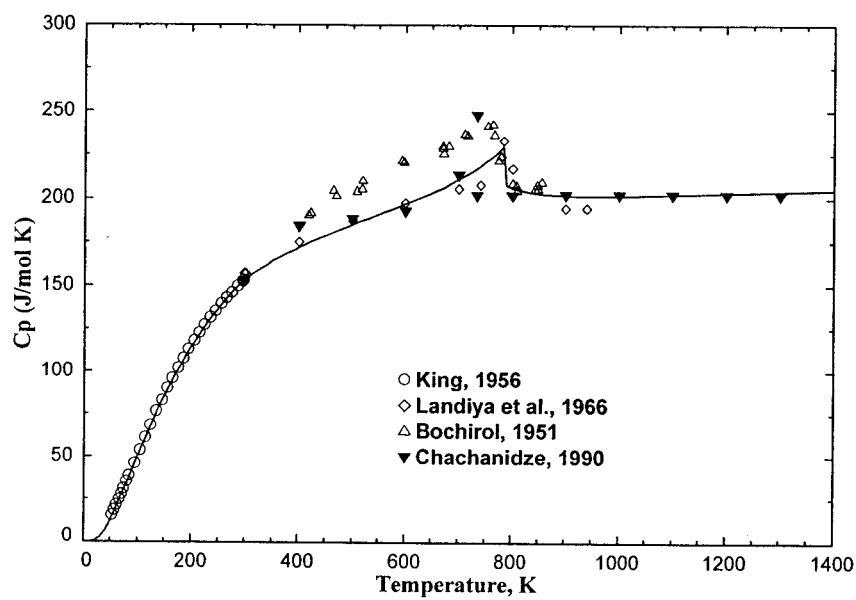


Fig. 9 – Calculated heat capacity of CoFe_2O_4 spinel under the assumption that there is no contribution to C_p from cation redistribution (i. e., that the distribution remains frozen during the measurements).

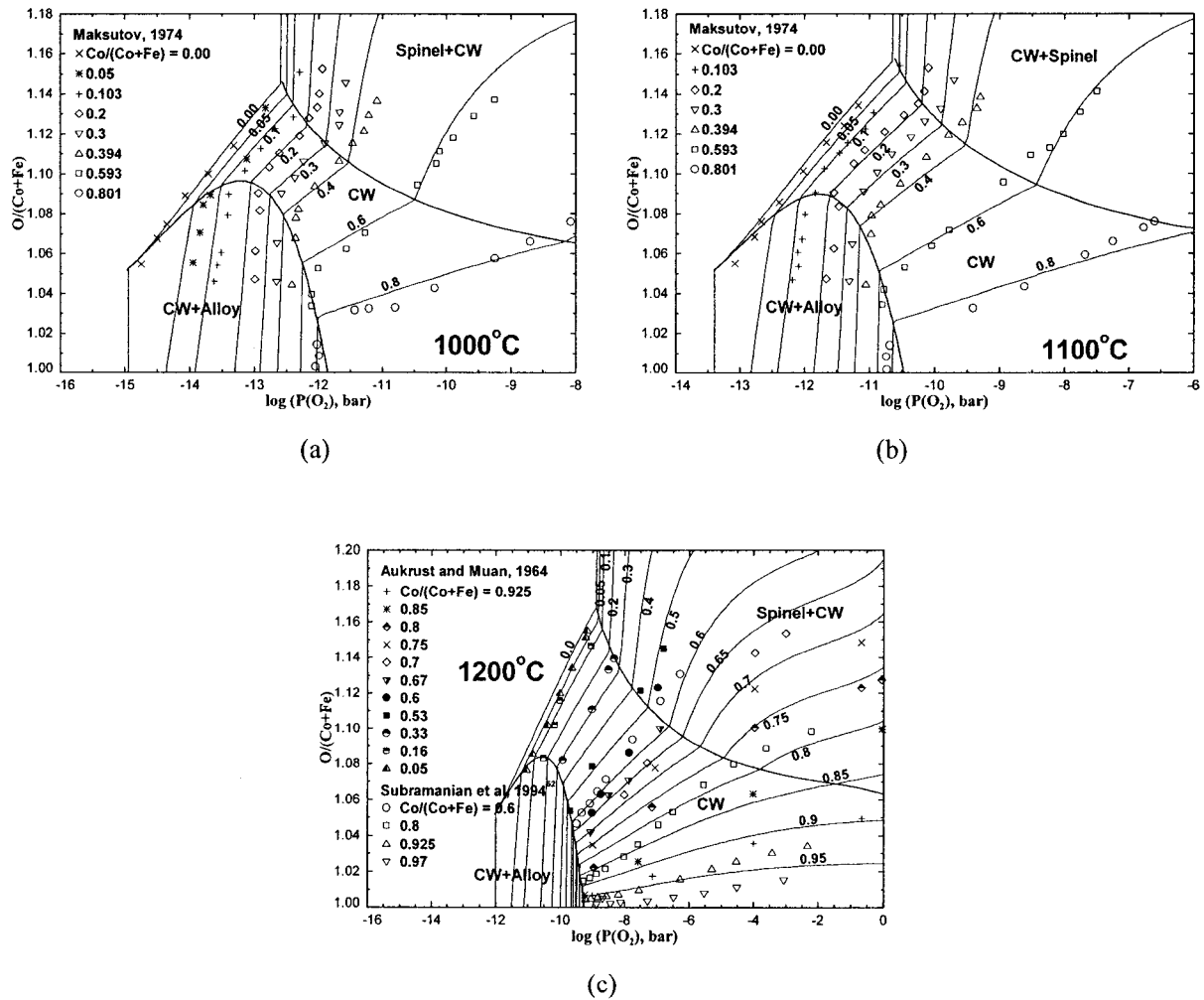


Fig. 10 – Calculated non-stoichiometry, expressed as the molar ratio $O/(Co+Fe)$, in cobaltowustite (CW) as a function of oxygen partial pressure and $Co/(Co+Fe)$ molar ratios. The variation of $O/(Co+Fe)$ in the (CW + Alloy) and (Spinel + CW) two-phase regions is also calculated.

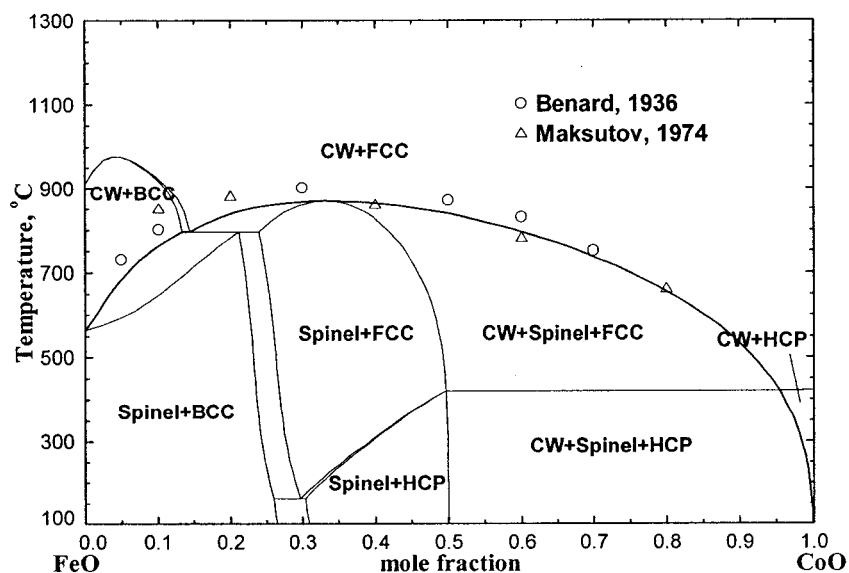


Fig. 11 – Calculated FeO-CoO section of the Fe-Co-O phase diagram. Experimental points represent the onset of decomposition of the cobaltowustite (CW) into spinel and alloy.

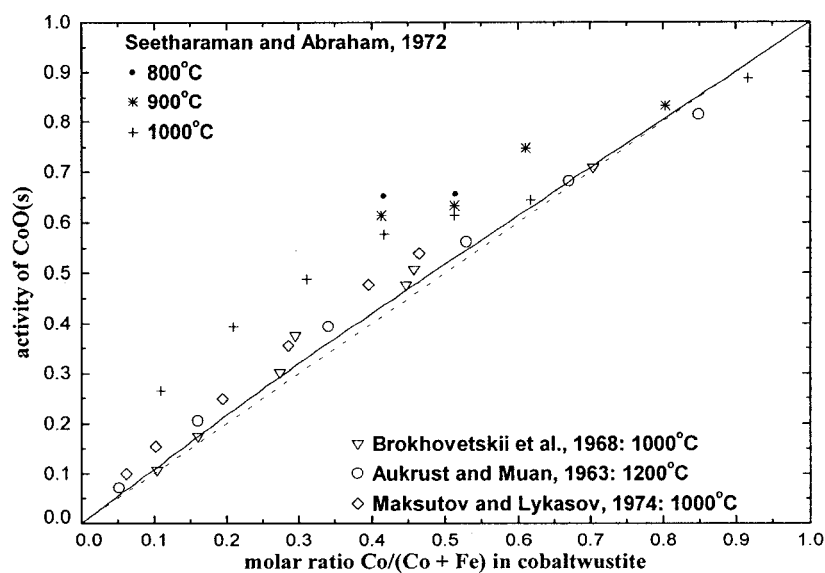


Fig. 12 – Calculated activity of CoO in the cobaltowustite phase, relative to the solid standard state, at saturation with alloy.

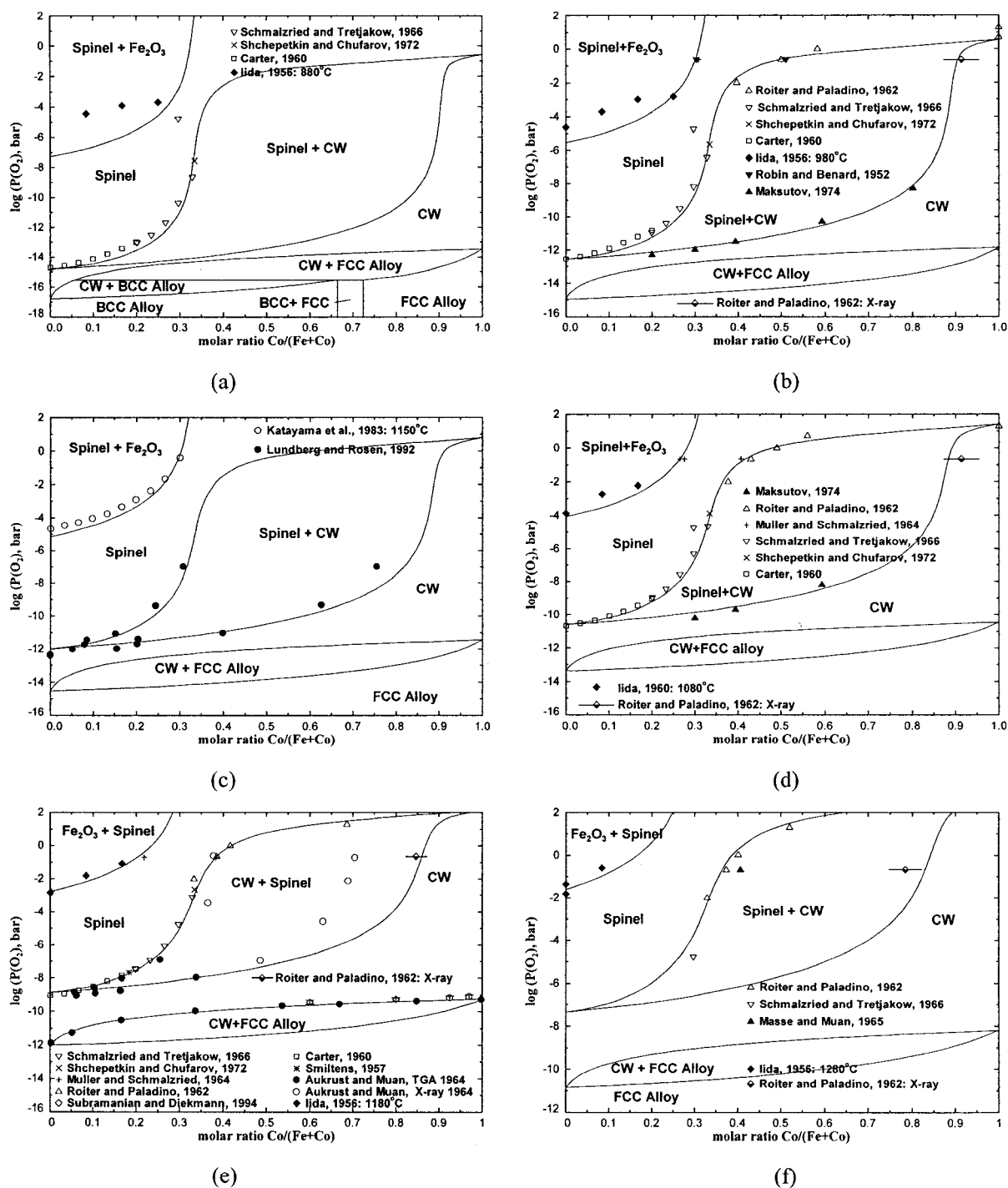


Fig. 13 – Calculated Fe-Co-O phase diagrams at various temperatures. (a) 900°C, (b) 1000°C, (c) 1027°C, (d) 1100°C, (e) 1200°C and (f) 1300°C. CW means cobaltowustite.

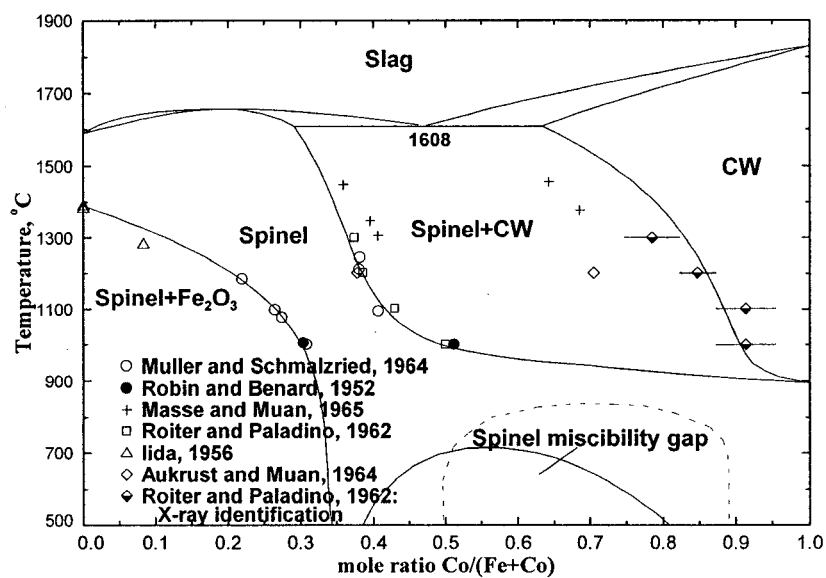


Fig. 14 – Calculated phase diagram of the Fe-Co-O system at air. The dotted line shows the miscibility gap in the spinel phase as reported by Robin and Bernard⁸³. CW means cobaltowustite.

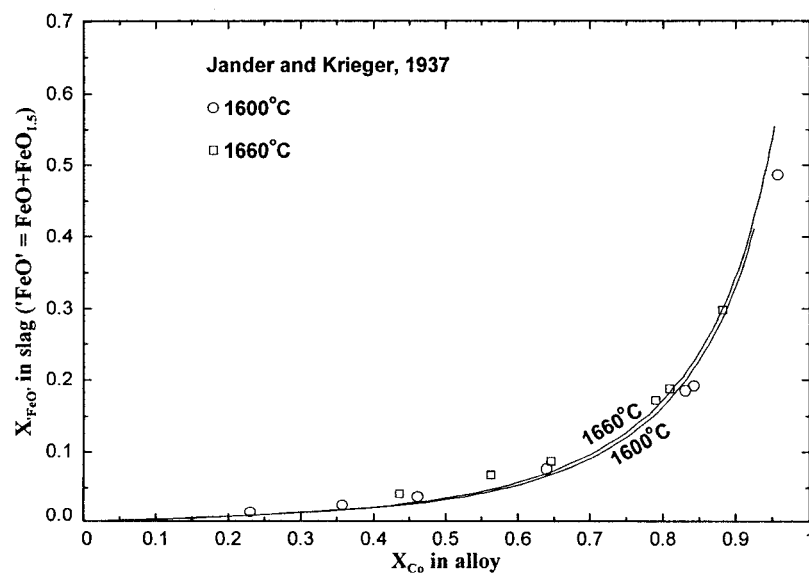


Fig. 15 – Calculated phase equilibria between alloy and slag at 1600° and 1660°C.

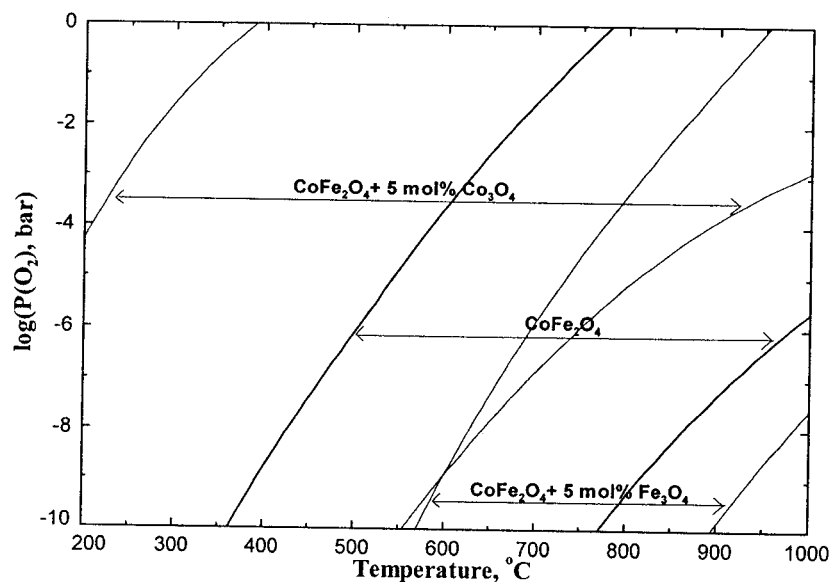


Fig. 16 – Calculated stability range of single-phase CoFe_2O_4 spinel as a function of temperature, oxygen partial pressure and additions. The (spinel + Fe_2O_3) and (spinel + cobaltowustite) two-phase regions are to the left and to the right of the single-phase spinel stability range, respectively.

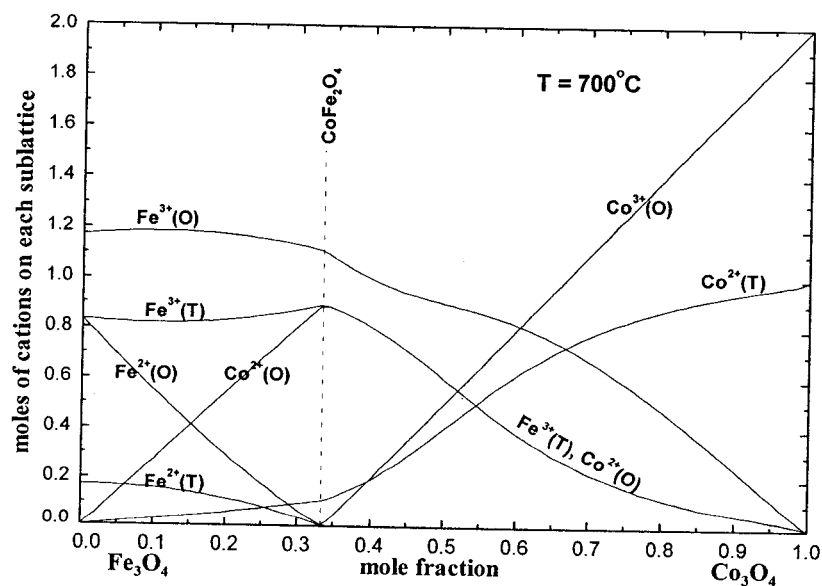


Fig. 17 – Calculated equilibrium cation distribution in Fe_3O_4 - Co_3O_4 spinel solution at saturation with cobaltowustite at 700°C .

Appendix IX

Article :

A Thermodynamic Model for Deoxidation Equilibria in Steel

In-Ho Jung, Sergei A. Decterov and Arthur D. Pelton

Accepted to Metallurgical and Materials Transactions, 2002

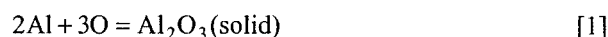
A Thermodynamic Model for Deoxidation Equilibria in Steel

IN-HO JUNG, SERGEI A. DECTEROV, and ARTHUR D. PELTON

For relatively dilute solutions of oxygen and a deoxidizer M (M=Al, Cr, Ca, Mg, ...) in molten Fe, a thermodynamic model is proposed wherein the dissolved species are $\underline{M^*O}$ associates as well as unassociated \underline{M} and \underline{O} atoms. At higher metal concentrations a small amount of $\underline{M_2^*O}$ associates also form. Experimental deoxidation equilibria for 15 deoxidizers M are quantitatively reproduced at all temperatures, with only a constant, temperature-independent and composition-independent parameter for the Gibbs energy of formation of each associate. The deoxidation behavior of Mg and Ca is elucidated for the first time. The parameters are stored in a database which can be used to predict complex deoxidation equilibria in multicomponent steels.

I. INTRODUCTION

THERMODYNAMIC equilibria during the deoxidation of steel are usually treated by the well-known interaction parameter formalism of Wagner.^[1] In Al-deoxidation, for example, for the equilibrium among dissolved \underline{Al} and \underline{O} and pure solid Al_2O_3 :



the equilibrium constant is written as:

$$K_{Al_2O_3} = \frac{1}{(X_{\underline{Al}}^2 \cdot X_{\underline{O}}^3)(f_{\underline{Al}}^2 f_{\underline{O}}^3)} \quad [2]$$

where $X_{\underline{Al}}$ and $X_{\underline{O}}$ are the mole fractions of dissolved aluminum and oxygen, and $f_{\underline{Al}}$ and $f_{\underline{O}}$ are activity coefficients (relative to the infinite dilution standard state) given by:

$$\ln f_{\underline{Al}} = \varepsilon_{\underline{Al}}^{\underline{Al}} X_{\underline{Al}} + \rho_{\underline{Al}}^{\underline{Al}} X_{\underline{Al}}^2 + \varepsilon_{\underline{Al}}^{\underline{O}} X_{\underline{O}} + \rho_{\underline{Al}}^{\underline{O}} X_{\underline{O}}^2 + \rho_{\underline{Al}}^{\underline{Al}, \underline{O}} X_{\underline{Al}} X_{\underline{O}} + \dots \quad [3]$$

$$\ln f_{\underline{O}} = \varepsilon_{\underline{O}}^{\underline{O}} X_{\underline{O}} + \rho_{\underline{O}}^{\underline{O}} X_{\underline{O}}^2 + \varepsilon_{\underline{O}}^{\underline{Al}} X_{\underline{Al}} + \rho_{\underline{O}}^{\underline{Al}} X_{\underline{Al}}^2 + \rho_{\underline{O}}^{\underline{O}, \underline{Al}} X_{\underline{O}} X_{\underline{Al}} + \dots \quad [4]$$

where the ε and ρ coefficients are called first- and second-order interaction parameters. Note that $\varepsilon_{\underline{Al}}^{\underline{O}} = \varepsilon_{\underline{O}}^{\underline{Al}}$. Other interaction parameters may be included in the expansion to account for interactions with other alloying elements.

In order to reproduce the measured data, it is necessary for the cross-interaction parameters $\varepsilon_{\underline{Al}}^{\underline{O}}$, $\rho_{\underline{Al}}^{\underline{O}}$, and $\rho_{\underline{O}}^{\underline{Al}}$ to be very negative in order to account for the very strong attractive interaction between dissolved \underline{Al} and \underline{O} atoms. Furthermore, in order to reproduce the measured data over

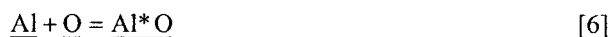
a range of temperature, the interaction parameters must generally have a strong empirical temperature dependence, usually expressed as:

$$\varepsilon = a + b/T \quad [5]$$

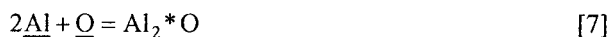
(and $\rho = c + d/T$). By using many empirical parameters, it is often possible to reproduce the measured equilibria over a limited range of temperature and composition. However, the resultant equations extrapolate very poorly outside this range. In the case of very strong deoxidants such as Ca and Mg, the interaction parameter formalism has proven incapable of providing a satisfactory description of the deoxidation equilibria even over the temperature and composition range of the measured data.

The weakness of the classical Wagner formalism lies in the assumption that the dissolved Al and O atoms are independent, randomly distributed particles. The very negative cross-interaction parameters which are required by the model indicate that there is a very strong attractive interaction between Al and O. Therefore, the Al and O atoms should not be independent randomly distributed particles, but should rather exhibit a strong tendency to form dissolved Al^*O "associates" or "molecules."

The following equilibrium among the dissolved associates and dissolved unassociated Al and O atoms may be written:



Because of the mass action law, in dilute solution small associates are much more probable than larger ones. However, at very high aluminum concentrations, some larger Al_2^*O associates may also form:



(Since the total dissolved oxygen content is never large, the concentration of Al^*O_2 associates is always negligibly small.) The total concentration of dissolved oxygen is then given by the sum ($X_{\underline{O}} + X_{\underline{Al^*O}} + X_{\underline{Al_2^*O}}$), where $X_{\underline{O}}$ is

now the mole fraction of dissolved unassociated oxygen, and X_{Al*O} and X_{Al_2*O} are the mole fractions of dissolved associates. Similarly, the total concentration of dissolved aluminum is given by the sum ($X_{Al} + X_{Al*O} + 2X_{Al_2*O}$).

In the present model, these associates are explicitly taken into account.

Equilibrium constants may be written for reactions [6] and [7]:

$$K_{Al*O} = \frac{X_{Al*O}}{f_{Al}(X_{Al} \cdot X_O)} \quad [8]$$

$$K_{Al_2*O} = \frac{X_{Al_2*O}}{f_{Al}^2(X_{Al}^2 \cdot X_O)} \quad [9]$$

where f_{Al} is given simply as:

$$\ln f_{Al} = \varepsilon_{Al}^{Al} X_{Al} \quad [10]$$

That is, only the first-order self-interaction coefficient ε_{Al}^{Al} is required. This is small, and can be obtained from data for the (oxygen-free) Fe-Al binary system. The activity coefficients f_O , f_{Al*O} and f_{Al_2*O} are all assumed to be unity. That is, all interactions between dissolved Al and O are taken into account by the two equilibrium constants K_{Al*O} and K_{Al_2*O} which are the parameters of the new model. Furthermore, it is assumed that $RT \ln K_{Al*O}$ and $RT \ln K_{Al_2*O}$ are both constant and independent of temperature. In the new model, with only these two temperature-independent parameters, it is possible to reproduce the data very well over the entire measured range of composition and temperature for Al deoxidation and, analogously, for Mg, Ca and all other deoxidation equilibria. Furthermore, the equations extrapolate well outside these ranges.

In the present model, the temperature dependence of the measurements is explained as a purely configurational entropy effect, due to the formation of associates, and is reproduced by the temperature-independent (i.e. enthalpic) parameters $RT \ln K_{Al*O}$ and $RT \ln K_{Al_2*O}$. In the Wagner formalism, on the other hand, one is usually obliged to introduce non-configurational entropy effects through the use of unreasonably large empirical temperature-dependent parameters as in Eq.[5]

Calculations using the new model can be performed simply with a hand calculator when the parameters ε_{Al}^{Al} , K_{Al*O} and K_{Al_2*O} are given. Choosing a value of X_{Al} , one first calculates f_{Al} from Eq.[10]. Equation [2] is then solved to give X_O , and finally Eqs.[8] and [9] are solved to

give X_{Al*O} and X_{Al_2*O} . The total dissolved oxygen and aluminum are then given by the sums ($X_O + X_{Al*O} + X_{Al_2*O}$) and ($X_{Al} + X_{Al*O} + 2X_{Al_2*O}$) respectively.

In the following section, the model is developed rigorously for the general case. In subsequent sections, the model is applied to the most important deoxidation systems, and optimized model parameters are derived. In particular, deoxidation equilibria involving Ca and Mg are elucidated for the first time.

II. THE MODEL

This work is an extension of a model described by Bouchard and Bale^[2] and by Heuzey and Pelton^[3] and based upon a suggestion by Blander.^[4]

Consider a ternary liquid solution Fe-M-O, where Fe is the solvent and M is a metal solute. The solution is assumed to contain dissolved unassociated \underline{M} and \underline{O} atoms as well as molecules (associates) $\underline{M*O}$ and, in some systems at the highest concentrations of M, a small amount of $\underline{M_2*O}$ associates. The equilibria among the dissolved associates and the dissolved unassociated \underline{M} and \underline{O} atoms are represented by:

$$\begin{aligned} \underline{M} + \underline{O} &= \underline{M*O} \\ \Delta g_{M*O}^o &= -RT \ln K_{M*O} = g_{M*O}^o - g_M^o - g_O^o \end{aligned} \quad [11]$$

$$\begin{aligned} 2\underline{M} + \underline{O} &= \underline{M_2*O} \\ \Delta g_{M_2*O}^o &= -RT \ln K_{M_2*O} = g_{M_2*O}^o - 2g_M^o - g_O^o \end{aligned} \quad [12]$$

where the g_i^o are standard Gibbs energies in the infinite dilution (Henrian) standard state.

Dissolved species are underlined (\underline{M} and \underline{O}) to distinguish them from the total amount of M and O in solution. Hence, $n_{\underline{M}}$ and $n_{\underline{O}}$ are the numbers of moles of unassociated \underline{M} and \underline{O} atoms, while n_M and n_O are the total numbers of moles of M and O in solution. From mass balance considerations:

$$n_M = n_{\underline{M}} + n_{\underline{M*O}} + 2n_{\underline{M_2*O}} \quad [13]$$

$$n_O = n_{\underline{O}} + n_{\underline{M*O}} + n_{\underline{M_2*O}} \quad [14]$$

Let $n_{Fe} = n_{Fe}$ be the number of moles of solvent. Species mole fractions X_i may be defined as:

$$X_i = n_i / (n_{\underline{M}} + n_{\underline{O}} + n_{\underline{M*O}} + n_{\underline{M_2*O}} + n_{Fe}) \quad [15]$$

($i = \underline{M}, \underline{O}, \underline{M^*O}, \underline{M_2^*O}, \underline{Fe}$), while overall component mole fractions X_i are defined as:

$$X_i = n_i / (n_M + n_O + n_{Fe}) \quad [16]$$

($i = \underline{M}, \underline{O}, \underline{Fe}$). Note that although $n_{Fe} = n_{\underline{Fe}}$, $X_{Fe} \neq X_{\underline{Fe}}$.

The total Gibbs energy of the solution is then given by assuming random mixing of all species:

$$\begin{aligned} G = & (n_{Fe}g_{Fe}^o + n_Mg_M^o + n_Og_O^o + n_{M^*O}g_{M^*O}^o + \\ & n_{M_2^*O}g_{M_2^*O}^o) + RT(n_{Fe}\ln X_{Fe} + n_M\ln X_M + \\ & n_O\ln X_O + n_{M^*O}\ln X_{M^*O} + n_{M_2^*O}\ln X_{M_2^*O}) \\ & + RT(n_{Fe}\ln f_{Fe} + n_M\ln f_M + n_O\ln f_O + \\ & n_{M^*O}\ln f_{M^*O} + n_{M_2^*O}\ln f_{M_2^*O}) \end{aligned} \quad [17]$$

Substitution of Eqs.[11-14] into Eq.[17] yields:

$$\begin{aligned} G = & (n_{Fe}g_{Fe}^o + n_Mg_M^o + n_Og_O^o + n_{M^*O}\Delta g_{M^*O}^o + \\ & n_{M_2^*O}\Delta g_{M_2^*O}^o) + RT\sum n_i\ln X_i + RT\sum n_i\ln f_i \end{aligned} \quad [18]$$

Equation [18] applies in the general case. However, for all systems in the present study, excellent results were obtained by assuming:

$$f_O = f_{M^*O} = f_{M_2^*O} = 1 \quad [19]$$

That is, interaction parameters such as $\varepsilon_M^{M^*O}$, $\varepsilon_M^{M_2^*O}$, etc. for interactions among the various species were found to be unnecessary, as was also the case for ε_O^O . The only excess Gibbs energy terms required were:

$$\ln f_M = \varepsilon_M^M X_M - \frac{1}{2}\varepsilon_M^M X_M^2 \quad [20]$$

$$\ln f_{Fe} = \frac{1}{2}\varepsilon_M^M X_M^2 \quad [21]$$

As discussed by Pelton,^[5-7] this is a modified form of the Wagner formalism in which the final term in Eq.[20] has been included in order to make Eqs.[20, 21] consistent with the Gibbs-Duhem equation and other thermodynamic relationships. Such consistency is not found in the Wagner formalism except at infinite dilution. Note that this modification does not increase the number of parameters.

For all systems Fe-M-O, the only interaction parameter used in the present study was the binary first-order

parameter ε_M^M . The binary parameters ε_M^M and g_M^o are obtained by evaluation/optimization of available data for the oxygen-free Fe-M binary systems. The parameters $\Delta g_{M^*O}^o$ and $\Delta g_{M_2^*O}^o$ are then obtained by evaluation/optimization of available data for the Fe-M-O systems. For all systems studied, temperature-independent (i.e. constant) values of $\Delta g_{M^*O}^o$ and $\Delta g_{M_2^*O}^o$ were found to be sufficient.

For quaternary and higher-order systems Fe-M₁-M₂-...-O, the extension of the model equations is straightforward and will not be given explicitly here. Additional first-order cross-interaction parameters $\varepsilon_{M_1}^{M_2}$ may be required. These may be obtained by evaluation/optimization of data for the oxygen-free Fe-M₁-M₂ systems.

A simple technique of solving the model equations with a hand calculator was described in section I. Calculations for multicomponent Fe-M₁-M₂-...-O systems can be performed similarly. Alternatively, if the model parameters are stored in a computer database then the equations can also be solved by Gibbs energy minimization programs such as are found in standard software packages such as FactSage,^[8] Thermocalc^[9] and MTDATA.^[10] That is, the numbers of associates n_{M^*O} and $n_{M_2^*O}$ at equilibrium are calculated by minimizing G at constant overall composition, subject to the mass balance restrictions of Eqs.[13, 14]:

$$(\partial G / \partial n_{M^*O})_{n_M, n_O, n_{M_2^*O}} = 0 \quad [22]$$

$$(\partial G / \partial n_{M_2^*O})_{n_M, n_O, n_{M^*O}} = 0 \quad [23]$$

Finally, the activities of \underline{M} and \underline{O} can easily be shown to be equal to the activities of \underline{M} and \underline{O} (in all cases relative to the infinite dilution Henrian standard states). Hence:

$$a_M = X_M f_M \quad [24]$$

$$a_O = X_O f_O \quad [25]$$

Activities of \underline{M} and \underline{O} are often reported relative to the 1 weight % standard state. These are related to the activities relative to the Henrian standard state (Eqs.[24, 25]) by:

$$a_i(\text{wt\% std. state}) = \frac{100M_i}{M_{Fe}} a_i(\text{Henrian std. state}) \quad [26]$$

where $i = \underline{O}, \underline{M}$, and where M_i and M_{Fe} are the atomic weights.

III. PARAMETERS FOR BINARY SYSTEMS

The parameters g_M^O , g_O^O and ε_M^M were obtained by evaluation/optimization of experimental data for the binary Fe-M and Fe-O systems. These are listed in Table I. Several of these critical evaluations were performed as part of the present study. Details are given in Appendix I.

IV. EVALUATIONS OF TERNARY FE-M-O SYSTEMS

In all evaluations, the thermodynamic properties (g_i^O) of the pure elements (Fe, M, O₂) and the pure solid oxidation products (Al₂O₃, SiO₂, CaO....) were taken from the FactSage 5.1 database.^[8] For molten oxide inclusions and slags, as well as for solid Fe₃O₄-FeCr₂O₄ and Al₂O₃-Cr₂O₃ solutions, component activities as a function of composition were also obtained from the FactSage 5.1 databases^[8] which have been developed by critical evaluation and modeling of thermodynamic data from the literature.

A. Fe-Al-O System

Several authors^[11-18] have measured the total Al and O contents of liquid Fe in equilibrium with solid Al₂O₃. These "deoxidation equilibria" from several selected authors are shown in Figure 1. Experiments were generally performed in Al₂O₃ crucibles, and Al and O contents were measured by ICP or other techniques. Some authors measured oxygen activities in equilibrium with Al₂O₃ either by equilibration with H₂/H₂O mixtures^[11-12] or by emf techniques.^[13, 15-17] Selected results are shown in Figure 2.

The deoxidation equilibrium may be written as in Eq.[1], with an equilibrium constant as in Eq.[2]. In an ideal Henrian solution of only unassociated Al and O, then, one would expect the oxygen content to decrease continuously as the dissolved Al content increases. This is indeed the case for low Al contents where most of the oxygen is dissolved as free O. However, at higher Al contents, most of the dissolved oxygen is in the form of Al*O associates because the equilibrium constant of reaction [6] is very large, and the principal deoxidation equilibrium becomes:

$$3\text{Al}^*\text{O} = \text{Al}_2\text{O}_3 + \text{Al} \quad [27]$$

$$K = (X_{\text{Al}} \cdot f_{\text{Al}}) / (X_{\text{Al}^*\text{O}}^3 \cdot f_{\text{Al}^*\text{O}}^3)$$

Since f_{Al} and $f_{\text{Al}^*\text{O}}$ are close to or equal to unity, an increase in the total dissolved Al content now results in an increase in $X_{\text{Al}^*\text{O}}$ and thus in an increase in total dissolved oxygen. Hence, a "deoxidation minimum" is observed in the curves of Figure 1. (Note that the axes in Figures 1 and 2 give the total dissolved Al (as $\text{Al} + \text{Al}^*\text{O} + 2\text{Al}_2^*\text{O}$) and, in

Figure 1, the total dissolved oxygen (as $\text{O} + \text{Al}^*\text{O} + \text{Al}_2^*\text{O}$)). Therefore, if the Gibbs energy of formation of the associates is sufficiently negative, a deoxidation minimum will be observed for a deoxidant M whenever the deoxidation product M_xO_y has a ratio $(y/x) > 1$.

Values of $\Delta g_{\text{Al}^*\text{O}}^O$ and $\Delta g_{\text{Al}_2^*\text{O}}^O$ were optimized (Table II) to reproduce the experimental data. The curves in Figures 1 and 2 are calculated from these parameters. Although the parameters are constant, independent of temperature, the temperature dependence of the data is very well reproduced by the model.

It can easily be shown that the assumption of the higher associate Al_2^*O only has a visible effect on the calculated curves when $\log[\text{wt}\% \text{ total Al}] > -0.3$. Even at higher Al concentrations, an acceptable fit can be obtained without considering the formation of Al_2^*O .

Previously, Sigworth and Elliott^[19] modeled this system using Eqs.[3,4] without considering the formation of associates. A very negative parameter $\varepsilon_{\text{Al}}^O$ was required, with a temperature dependence chosen to fit the data. The deoxidation equilibrium at 1600°C, calculated by their model, is shown in Figure 1 by the dashed line. Clearly, their model cannot be extrapolated outside the composition range of the data. On the other hand, with the present model, extrapolations both in composition and temperature are reasonable.

B. Fe-Cr-O System

Similar selected data^[20-28] for deoxidation equilibria in the Fe-Cr-O system are shown in Figures 3 and 4 along with curves calculated from the model with the optimized, temperature-independent values of $\Delta g_{\text{Cr}^*\text{O}}^O$ and $\Delta g_{\text{Cr}_2^*\text{O}}^O$ shown in Table II. In this case, a spinel solution FeCr₂O₄-Fe₃O₄ (rich in FeCr₂O₄) and Cr₂O₃ are the stable deoxidation products at low and high Cr contents respectively. The transition point is calculated at $\log[\text{total wt}\% \text{ Cr}] = 0.65$ (wt% Cr = 4.5) in agreement with the observations (by XRD or EPMA)^[20,24,27,29] which place this point between 2 wt% and 5 wt% Cr.

C. Fe-Mg-O, Fe-Ca-O and Fe-Ba-O Systems

Mg, Ca and Ba are very strong deoxidants. Until now, their deoxidation behavior has never been modeled satisfactorily.

Han et al^[30] and Seo and Kim^[31] equilibrated Fe, initially containing several hundred ppm oxygen and held in an MgO crucible, with Mg vapor (in equilibrium with liquid Mg in a Mo cup at another temperature), all in a sealed Mo chamber. Equilibrium was achieved after several hours. The system was then quenched and the metal was analyzed for dissolved Mg and O. Results are shown in Figure 5. Similar experiments were performed by Ito et al^[32] in open MgO crucibles under Ar with additions of Mg

wrapped in Fe foil. The results are not at all in agreement with those of Han et al^[30] and Seo and Kim.^[31] Since the experiments of Han et al and Seo and Kim were performed in closed crucibles and are in agreement with each other, they have been selected in the present study.

For the Fe-Ca-O system, Seo and Kim^[33] performed similar experiments in closed Mo containers. Gustafsson and Mellberg^[34] and Ototani et al^[35] used open containers, but maintained high Ar pressures to reduce Ca losses. The results of Miyashita and Nishikawa^[36] and of Han et al^[37] may have been influenced by sulfur contamination, while the samples of Ozawa^[38] may have been slightly contaminated by Al. Results from these six studies are shown on Figure 6. Other authors have also reported deoxidation equilibria in this system.^[32,39-40]

Results of Kato et al^[41] for the Fe-Ba-O system are shown in Figure 7. Measurements were made under Ar in CaO crucibles in the presence of BaO. Although Wang et al^[42] reported measurements in sealed Mo containers, the considerable amount of S in their samples may have influenced their results.

Several authors^[30-34,39,41,43-45] have attempted to model the data in Figures 5 to 7 using the interaction parameter formalism (like Eqs.[3, 4]) without considering the formation of associates. Very large negative temperature-dependent first- and second-order parameters ε_M^O , ρ_M^O , $\rho_M^{M,O}$ (M=Mg, Ca, Ba) were used: (for example, $\varepsilon_{Mg}^O = -10000$ to -40000 and $\varepsilon_{Ca}^O = -10000$ to -90000 .) Furthermore, most authors also had to adjust the equilibrium constants K_{MgO} and K_{CaO} for the formation of solid MgO and CaO by two or three orders of magnitude from their literature values in order to fit the data. However Turkdogan^[45] has shown that this is not permissible because the accepted literature values of K_{MgO} and K_{CaO} are quite accurate. The solubility (deoxidation) curves calculated from these models all have strange shapes, some with minima and maxima, and even one in the form of a circle.^[34] The model of JSPS^[44] is the most widely used. The "deoxidation curve" calculated from this model, and reported in the literature, is shown in Figure 6 by the dashed line. However, in Appendix II we show that this curve is actually an unstable solution of the interaction parameter formalism. The true stable solution actually lies at extremely low (< 0.01 ppm) Ca and O contents.

The curves drawn in Figures 5 to 7 were calculated with the present model, with only one assumed associate M^*O (M = Mg, Ca, Ba), with temperature-independent values of $\Delta g_{M^*O}^O$ (Table II). The shape of these curves may be explained as follows. Because $\Delta g_{M^*O}^O$ is very negative, reaction [11] is displaced very strongly to the right. Hence, a solution will contain either dissolved M^*O and O species (but virtually no M species), or dissolved M^*O and M species (but virtually no O species). Suppose we start with Fe containing a high concentration of dissolved oxygen at 1600°C and begin adding Ca (see Figure 6). At first the Ca

reacts with the oxygen to form Ca^*O associates, leaving virtually no free Ca in solution. When the concentration of Ca^*O reaches ~ 17 ppm it attains equilibrium with solid CaO:



As more Ca is added to the metal, it reacts with dissolved oxygen to precipitate CaO; the concentration of dissolved oxygen thus decreases, while the concentration of Ca^*O remains constant (and the concentration of total dissolved Ca remains nearly constant). This results in the nearly vertical section of the deoxidation curve in Figure 6. When the total dissolved oxygen content has been reduced to ~ 5 ppm, the concentrations of free dissolved O and Ca are both extremely low, and Ca^*O associates are virtually the only species in solution. Further addition of Ca thus serves only to increase the free Ca concentration, with virtually no further precipitation of CaO; hence the nearly horizontal section of the curve in Figure 6.

D. Other Fe-M-O Systems (M = V, Ti, Si, Mn, B, Nb, Ta, Ce, La, Zr)

The model was applied to several other Fe-M-O systems. The calculated deoxidation curves are shown in Figure 8 to 20 along with selected experimental data. The optimized temperature-independent model parameters $\Delta g_{M^*O}^O$ and $\Delta g_{M_2^*O}^O$ are listed in Table II.

In the discussion following Eq.[27] it was shown that equilibrium with an M^*O associate can result in a deoxidation minimum (as in Figures 1 and 3) provided that the deoxidation product M_xO_y has a ratio $(y/x) > 1$. It is for this reason that the curves in Figures 5 to 7 (where M=Mg, Ca, Ba) do not exhibit minima. In the Fe-V-O and Fe-Ti-O systems, the deoxidation curves in Figures 8 and 10 exhibit minima at very high metal contents. Since the equilibrium deoxidation products at the highest metal contents are VO or TiO, this would seem to contradict the rule. However, at such high V or Ti contents, the concentrations of V_2^*O and Ti_2^*O associates are large and the principal deoxidation equilibria are:



(where M = V, Ti). Hence, an increase in total dissolved M will result in an increase in M_2^*O content and thus in an increase in total O content.

As shown in Figures 22 and 23 for the Fe-Ce-O system, some authors reported Ce_2O_3 as the equilibrium deoxidation product and some reported CeO_2 . The calculations indicate that Ce_2O_3 is the expected product.

V. MULTICOMPONENT SYSTEMS

The model has been used to predict deoxidation equilibria in multicomponent systems, using only the

binary and ternary parameters listed in Tables I and II along with some first-order cross-interaction parameters $\varepsilon_{M_1}^{M_2}$.

These parameters $\varepsilon_{M_1}^{M_2}$, which can be obtained from evaluation/optimization of the ternary oxygen-free Fe-M₁-M₂ systems, have only a small effect on the equilibria. $\varepsilon_{Al}^{Si} = 13111/T$, $\varepsilon_{Mn}^{Si} = -6153/T$ were taken from JSPS^[44], while $\varepsilon_{Ca}^{Al} = -13072/T$ and $\varepsilon_{Ca}^{Si} = -23220/T$ were optimized in the present study from the data of Sponseller and Flinn^[96] and of Song et al.^[97] All other cross terms $\varepsilon_{M_1}^{M_2}$ were set to zero. In previous studies^[19,44] the parameters $\varepsilon_{M_1}^{M_2}$ were frequently adjusted so as to reproduce measured deoxidation equilibria. With the present model, this is no longer necessary; the deoxidation equilibria in the multicomponent systems are predicted with no additional adjustable parameters.

The equilibria reported by Heinz et al.^[27] for Al-deoxidation of Fe-25%Cr-2%Si-0.7%Mn stainless steels are shown in Figure 28 along with curves calculated by the model. The deoxidation product is an Al₂O₃-Cr₂O₃ solid solution.

Deoxidation equilibria in the Fe-Ca-Al-Si-O system, with the metal in equilibrium at 1600°C with a (53.6wt% CaO - 16.9wt% SiO₂ - 29.5wt% Al₂O₃) liquid slag, as reported by Tamura and Suito^[76] and Cho and Suito,^[77] are shown in Figure 29 along with curves calculated by the model. Agreement is within experimental error limits. Agreement is equally good with similar measurement performed by the same authors with slags of other compositions.

Calculated equilibria for Al-deoxidation of Fe-20%Cr-10%Ni stainless steels are compared with measurements^[78] in Figure 30. The deoxidation product is an Al₂O₃-Cr₂O₃ solid solution. The present associate model was not applied to the Fe-Ni-O system because the tendency to form Ni*O associates is very small. The interaction between dissolved Ni and O was simply modeled with an interaction parameter $\varepsilon_{Ni}^O = 2622/T$ taken from JSPS.^[44] Other reported deoxidation equilibria for Fe-Cr-Ni stainless steels with Al, Cr, Ti, etc. deoxidants were also well predicted by the model.

An inclusion diagram for the Fe-Al-Ca-O system at 1600°C, as calculated by the model, is presented in Figure 31. The curves show iso-oxygen content lines from 5 to 50 weight ppm oxygen. A deoxidation minimum is clearly seen. The equilibrium deoxidation products are also indicated on the diagram. It can be seen that the equilibrium deoxidation product is nearly independent of Al content, depending only on the Ca content. When log[wt% total Ca] > -2.9 (i.e. total Ca > 13ppm), solid CaO is the deoxidation product, and the oxygen content is 5 weight ppm. At higher total Ca contents the oxygen content does not decrease below 5 ppm. This behavior can be understood with reference to Figure 6, where the nearly vertical and nearly horizontal branches of the deoxidation curve occur at ~ 13

ppm Ca and ~ 5 ppm O respectively. Since CaAl₂O₄ melts congruently at ~ 1605°C, a similar diagram calculated above 1605°C would not contain the CaAl₂O₄ region. Similarly, since the CaAl₂O₄-CaAl₄O₇ eutectic temperature is ~ 1595°C, a diagram calculated below 1595°C would not contain the lower "Liquid slag" region. Several authors have measured the line along which solid CaO and liquid slag co-exist as well as the line along which either (slag+CaAl₂O₄) or (slag+CaAl₄O₇) co-exist. Measurements were performed in CaO crucibles in the first case, and Al₂O₃ crucibles in the second case. The data points are plotted on Figure 31. Within the large experimental scatter, these results confirm the model calculations.

VI. DISCUSSION

Available data strongly indicate that metal solutes in molten Fe also form associates M*S and M*N with dissolved sulfur and nitrogen. We are currently applying the present model to these systems.

The present model is actually a simplified limiting case of the more general quasichemical model.^[98] In the more general model, the atoms Fe, M and O all occupy lattice sites and the expansion for the configurational entropy is given by a random distribution of Fe-Fe, M-M, O-O, Fe-M, Fe-O and M-O nearest-neighbor pairs over "pair sites". The parameters of the model are the relative energies of the various pairs. Hence, if the energy of forming M-O pairs is very negative, then their formation is favored. For relatively dilute solutions, and when M-O pair energies are significantly more negative than Fe-O pair energies, the present model can be shown to be a limiting case of the more general model. An advantage of using the more general model is that systems such as Fe-Ni-O, in which Ni-O pair energies are of the same order or weaker than Fe-O pair energies, can be treated by the same model as systems with strong M-O pair energies. The advantage of the present model is its conceptual and calculational simplicity.

In order to permit the prediction of the associate formation energies Δg_{M*O}^o for deoxidizers M for which no or few deoxidation equilibrium data are available, correlations were sought between Δg_{M*O}^o and other data such as the Gibbs energies of formation of the corresponding pure solid or liquid oxides. Surprisingly, the most satisfactory correlation was found with the standard electrode potentials of the metal ions Mⁿ⁺ in aqueous solution as shown in Figure 32. Note that a point for "Fe*O associates" at $\Delta g_{Fe*O}^o = 0$ also falls on the line in Figure 32. No explanation of this unexpected correlation is proposed.

No deoxidation data are available for thorium, which has been proposed as a potential deoxidizer. However, a value of Δg_{Th*O}^o is predicted from Figure 32. This value can be used to calculate a predicted deoxidation curve for the Fe-Th-O system.

The present model is stored as a database of the FactSage software^[8] and can be used together with other FactSage databases for oxides, slags, gases, *etc.*, to calculate complex multiphase, multicomponent equilibria during steelmaking processes.

ACKNOWLEDGMENTS

This project was supported by a CRD grant from the Natural Sciences and Engineering Research Council of Canada in collaboration with the following: INCO, Noranda, Rio Tinto, COMINCO, Alcoa, Dupont, Shell, Corning, Pechiney, Norsk Hydro, Sintef, Schott Glas, St.-Gobain Recherche, Mintek, IIS Technologies.

APPENDIX I

Optimization of Henrian Activity Coefficients and Interaction Parameters in Binary Fe-M Systems

A. Fe-Ba, Fe-Ca and Fe-Mg Systems

These three system were studied in the same laboratory.^[84-86] Sealed Mo crucibles were used, with liquid Fe in a high temperature zone at 1600°C, and liquid Ba, Mg or Ca in a low temperature zone, with saturation of the Fe occurring via vapor transport. Other authors such as Sponseller and Flinn^[96] did not used sealed containers. Results are shown in Figures 33 to 35 along with the optimized curves. In all such curves (in Figures 33 to 44) the intercept at $X_M = 0$ gives the Henrian infinite dilution activity coefficient $\ln \gamma_M^o = \frac{1}{RT} (g_M^o (\text{Henrian std. state}) - g_M^o (\text{Pure element std. state}))$ and the slope is ε_M^M .

In the Fe-Ba and Fe-Ca systems, because of the scatter of the data, the composition dependence of $\ln(P_i/X_i)$ cannot be determined. Hence ε_{Ba}^{Ba} and ε_{Ca}^{Ca} were set to zero. From the experimental points in Figure 35, a least-squares line with slope $\varepsilon_{Mg}^{Mg} = -493$ and intercept at $X_{Mg} = 0$ of 7.35 can be determined. However, this value of ε_{Mg}^{Mg} is so negative as to be unbelievable, the most negative value of ε_M^M reported for any other solute in liquid Fe being $\varepsilon_{Ce}^{Ce} = -16$. Therefore, we set $\varepsilon_{Mg}^{Mg} = 0$ as in the case of the Fe-Ba and Fe-Ca systems.

The optimized values of $\ln \gamma_M^o$ and ε_M^M are shown in Table I. When data were available at only one temperature (as in the case of the Fe-Ba, Fe-Ca and Fe-Mg systems) it was assumed that $RT \ln \gamma_M^o$ is constant; that is, it was assumed that the non-ideality is due entirely to enthalpic effects rather than to non-configurational entropic effects.

Hence, in such cases $\ln \gamma_M^o$ and ε_M^M in Table I are assigned a temperature dependence of $(A/T + 0)$. In the absence of data, this is a better approximation than assuming $\ln \gamma_M^o$ and ε_M^M to be independent of T .

B. Fe-B, Fe-Ce, Fe-Cr, Fe-La, Fe-Nb, Fe-Si, Fe-Ta, Fe-V and Fe-Zr Systems

In the Fe-M systems with $M = B, Ce, Cr, La, Nb, Si, Ta, V$ and Zr , the activities of M in molten Fe-M solutions have been measured by several authors by equilibrating the metal phase with the solid oxide M_xO_y and measuring the oxygen activity either by emf techniques with solid electrolytes, or by equilibration with gaseous mixtures. Selected data are shown in Figures 36 to 44 along with the optimized curves. The optimized parameters $\ln \gamma_M^o$ and ε_M^M are listed in Table I. For internal consistency, the metal activities were calculated from the measured emf's or oxygen pressures using thermodynamic data for the pure oxides from the FactSage database^[8] rather than from the data sources quoted by the various authors.

In the cases of Fe-Nb, Fe-Si and Fe-V, data at temperatures other than 1600°C are also available, and these were used in the optimization, thereby permitting the temperature dependence of the parameters in Table I to be determined. However, only data at 1600°C are shown in Figures 40, 41 and 43.

Although only a first-order interaction parameter ε_V^V was used for the Fe-V system, the evident curvature of the line in Figure 43 results from the final term in Eq.[20]. The curvature of the other lines in Figures 33 to 40 and 44 is not evident because the horizontal axes do not extend to sufficiently high values of X_M .

APPENDIX II

Unstable Solutions of the Interaction Parameter Formalism

Consider the system Fe-M-O where the deoxidation product is MO (eg. $M = Mg, Ca, Ba$). Applying a simple first-order interaction parameter formalism to the solution we have:

$$\ln f_O = \varepsilon_O^M X_M \quad [30]$$

$$\ln f_M = \varepsilon_M^O X_O \quad [31]$$

(where $\varepsilon_O^M = \varepsilon_M^O$ and where ε_O^O and ε_M^M are small and have been ignored). When the melt is in equilibrium with MO, $K_{MO} = (X_M f_M \cdot X_O f_O)^{-1}$ and

$$-\ln K_{MO} = \ln X_M + \ln X_O + \varepsilon_O^M (X_M + X_O) \quad [32]$$

When $K_{MO} \gg 1$ and $\varepsilon \ll 0$, as is the case for a strong deoxidant like Mg or Ca, this equation has two solutions, a stable solution at very low X_M and X_O given by:

$$-\ln K_{MO} \approx \ln X_M + \ln X_O \quad [33]$$

and an unstable solution at higher X_M and X_O .

The curve calculated for the JSPS^[44] model as shown in Figure 6, and as presented in the literature, is the unstable solution.

REFERENCES

1. C. Wagner: *Thermodynamics of Alloys*, Addison-Wesley, Reading, MA, 1962, p. 51.
2. D. Bouchard and C.W. Bale: *J. Phase Equilibria*, 1995, vol. 16, pp. 16-23.
3. M.-C. Heuzey and A.D. Pelton: *Metall. Mater. Trans. B*, 1996, vol. 27B, pp. 810-28.
4. M. Blander: *Private communication*, 1994.
5. A.D. Pelton and C.W. Bale: *Metall. Trans. A*, 1986, vol. 17A, pp. 1211-15.
6. C.W. Bale and A.D. Pelton: *Metall. Trans. A*, 1990, vol. 21A, pp. 1997-2002.
7. A.D. Pelton: *Metall. Mater. Trans. B*, 1997, vol. 28B, pp. 869-76.
8. FactSage: www.factsage.com, Montreal, 2002.
9. Thermocalc: <http://met.kth.se>, Stockholm, 2002.
10. MTDATA: www.npl.co.uk, Teddington, UK, 2002.
11. N.A. Gokcen and J. Chipman: *J. Metals*, 1953, Feb., 173-78.
12. A. McLean and H.B. Bell: *J. Iron Steel Inst.*, 1965, vol. 203, 123-30.
13. R.J. Fruehan: *Metall. Trans.*, 1970, vol. 1, pp. 3403-10.
14. L.E. Rohde, A. Choudhury and M. Wahlster: *Arch. Eisenhüttenw.*, 1971, vol. 42, pp. 165-74.
15. D. Janke and W.A. Fisher: *Arch. Eisenhüttenw.*, 1976, vol. 47, pp. 195-98.
16. D. Janke: *Arch. Eisenhüttenw.*, 1983, vol. 54, pp. 259-66.
17. S. Dimitrov, A. Weyl and D. Janke: *Steel Res.*, 1995, vol. 66, pp. 3-7.
18. J.-D. Seo, S.-H. Kim and K.-R. Lee: *Steel Res.*, 1998, vol. 69, pp. 49-53.
19. G.K. Sigworth and J.F. Elliott: *Met. Sci.*, 1974, vol. 8, pp. 298-310.
20. H.M. Chen and J. Chipman: *Trans. ASM*, 1947, vol. 28, pp. 70-116.
21. E.T. Turkdogan: *J. Iron Steel Inst.*, 1954, vol. 178, pp. 278-83.
22. D.C. Hilty, W.D. Forgeng and R.L. Folkman: *J. Metals*, 1955, Feb. pp. 253-68.
23. J.K. Pargeter: *Canadian Metall. Quarterly*, 1967, vol. 6, pp. 21-37.
24. R.J. Fruehan: *Trans. Metall. Soc. AIME*, 1969, vol. 245, pp. 1215-18.
25. P.A. Cerkasov and W.A. Fisher: *Arch. Eisenhüttenw.*, 1971, vol. 43, pp. 699-702.
26. D. Janke and W.A. Fischer: *Arch. Eisenhüttenw.*, 1976, vol. 47, pp. 147-51.
27. M. Heinz, K. Koch and D. Janke: *Steel Res.*, 1989, vol. 60, 246-54.
28. S. Dimitrov, H. Venz, K. Koch and D. Janke: *Steel Res.*, 1995, vol. 66, pp. 39-43.
29. A. Adachi and N. Iwamoto: *Trans. Iron Steel Inst., Japan*, 1966, vol. 6, pp. 188-95.
30. Q. Han, D. Zhou and C. Xiang: *Steel Res.*, 1997, vol. 68, 9-14.
31. J.-D. Seo and S.-H. Kim: *Steel Res.*, 2000, vol. 71, pp. 101-06.
32. H. Itoh, M. Hino and S. Ban-Ya: *Metall. Mater. Trans. B*, 1997, vol. 28B, 953-56.
33. J.D. Seo and S.H. Kim: *Bull. Kor. Inst. Met. & Mater. (Korea)*, 1999, vol. 12, pp. 402-10.
34. S. Gustafsson and P.O. Mellberg: *Scand. J. Metall.*, 1980, vol. 9, 111-16.
35. T. Ototani, Y. Kataura and T. Degawa: *Trans. Iron Steel Inst., Japan*, 1976, vol. 16, pp. 275-82.
36. Y. Miyashita and K. Nishikawa: *Testu-to-Hagané*, 1971, vol. 57, pp. 1969-75.
37. Q. Han, X. Zhang, D. Chen and P. Wang: *Metall. Trans. B*, 1988, vol. 19B, 617-22.
38. M. Ozawa: The Japan Society for the Promotion of Science, 19th Committee paper No. 9837, Iron Steel Institute of Japan, Tokyo, 1975, p. 6.
39. S. Kobayashi, Y. Omori and K. Sanbongi: *Trans. Iron Steel Inst., Japan*, 1971, vol. 11, 260-69.
40. T. Kimura and H. Suito: *Metall. Trans. B*, 1994, vol. 25B, 33-42.
41. S. Kato, Y. Iguchi and S. Ban-ya: *Testu-to-Hagané*, 1992, vol. 78, pp. 253-59.
42. J. Wang, Q. Han and B. Song: *Acta Metallurgica Sinica*, 1993, vol. 2B, pp. B64-69.
43. M. Nadif and C. Gatellier: *Revue de Metallurgie-CIT*, 1986, vol. 83, pp. 277-94.
44. *Steelmaking Data Sourcebook*, Japan Society for the Promotion of Science, 19th Comm. On Steelmaking, Gordon & Breach Science, New York, NY, 1988.
45. S.-W. Cho and H. Suito: *Iron Steel Inst. Jpn. Int.*, 1994, vol. 34, pp. 265-69.
46. E.T. Turkdogan: *Steel Res.*, 1991, vol. 62, 379-82.
47. J. Chipman and M.N. Dastur: *J. Metals*, 1951, Feb., pp. 111-15.
48. K. Narita and S. Koyama: *Trans. Iron Steel Inst., Japan*, 1969, vol. 9, pp. 53-58.
49. R.J. Fruehan: *Metall. Trans.*, 1970, vol. 1, pp. 2083-88.
50. A. Kontopoulos: Ph.D. dissertation, McMaster Univ., Hamilton, Canada, 1971.
51. D.A.R. Kay and A. Kontopoulos: Chemical metallurgy of iron and steel: proceedings of the International Symposium on Metallurgical Chemistry-Applications in Ferrous Metallurgy (held in the University of Sheffield, 19th-21st July 1971), Iron and Steel Institute, London, 1973, pp. 178-83.
52. Y. Kojima, M. Inouye and J. Ohi: *Arch. Eisenhüttenw.*, 1971, vol. 42, pp. 703-06.

53. H. Chino, Y. Nakamura, E. Tsunetomi and K. Segawa: *Tetsu-to-Hagané*, 1966, vol. 52, pp. s959-966.
54. Y. Kojima, M. Inouye and J. Ohi: *Arch. Eisenhüttenw.*, 1969, vol. 40, pp. 667-71.
55. W.A. Fischer and D. Janke: *Arch. Eisenhüttenw.*, 1971, vol. 42, pp. 691-94.
56. A.M. Smellie and H.B. Bell: *Canadian Metall. Quarterly*, 1972, vol. 11, pp.351-61.
57. D.C. Hilty and W. Crafts: *Trans Metall. Soc. AIME*, 1950, vol. 188, pp. 425-36.
58. N.A. Gokcen and J. Chipman: *J. Metals*, 1952, Feb., pp.171-81.
59. R.J. Fruehan, L.J. Martonik and E.T. Turkdogan: *Trans. Metall. Soc. AIME*, 1969, vol. 245, pp. 1501-09.
60. R.J. Fruehan: *Metall. Trans.*, 1970, vol. 1, pp. 865-70.
61. J. Chipman, J.B. Gero and T.B. Winkler: *J. Metals*, 1950, pp. 341-45.
62. I.A. Novokhatskii and B.F. Belov: *Zh. Fiz. Khim.*, 1970, vol. 44, pp. 2013-17.
63. S. Dimitrov, A. Weyl and D. Janke: *Steel Res.*, 1995, vol. 66, pp. 87-92.
64. Z. Buzek: Chemical metallurgy of iron and steel: Proceedings of the International Symposium on Metallurgical Chemistry-Applications in Ferrous Metallurgy (University of Sheffield, July, 1971), Iron and Steel Institute, London, 1973, pp. 173-77.
65. M. Elle and J. Chipman; *Trans. Met. Soc. AIME*, 1961, vol. 221, pp. 701-03.
66. Y. Sato, K. Suzuki, Y. Omori and K. Sanbongi: *Tetsu-to-Hagané*, 1968, vol. 54, pp. 330-35.
67. W.A. Fischer and D. Janke: *Arch. Eisenhüttenw.*, 1971, vol. 42, pp. 695-98.
68. L. Gu and Z. Tang: *Acta Metallurgica Sinica*, 1985, vol. 21, pp A167-174.
69. S. Wei, S. Zhang, T. Tung and Z. Tang: *Rare Metals*, 1983, vol. 2, pp. 10-20.
70. W.A. Fischer and H. Bertram: *Arch. Eisenhüttenw.*, 1973, vol. 44, pp 87-95.
71. R.J. Fruehan: *Metall. Trans.*, 1974, vol. 5, pp. 345-47.
72. E.B. Teplitskii and L.P. Vladimirov: *Russ. J. Phys. Chem.*, 1972, vol. 46, pp. 762-63.
73. D. Janke and W. A. Fisher: *Arch. Eisenhüttenw.*, 1978, vol. 49, pp. 425-30.
74. Q. Han, X. Feng, S. Liu, H. Hiu and Z. Tang: *Metall. Trans. B*, 1990, vol. 21B, pp. 295-302.
75. E.B. Teplitsky and L.P. Vladimirov: *Izv. Vuz. Chernaya Metall.*, 1973, No.3, pp. 5-7.
76. F. Tamura and H. Suito: *Metall. Trans. B*, 1994, vol. 25B, pp. 235-44.
77. S.-W. Cho and H. Suito: *Iron Steel Inst. Jpn. Int.*, 1994, vol. 34, pp. 177-85.
78. W.A. Fischer and D. Janke: *Arch. Eisenhüttenw.*, 1976, vol. 47(10), pp. 589-94.
79. E. Schurmann, U. Braun and W. Pluschkell: *Steel Res.*, 1998, vol. 69, pp. 355-58.
80. H. Suito, H. Inoue and R. Inoue: *Iron Steel Inst. Jpn. Int.*, 1991, vol. 31, pp. 1381-88.
81. H. Ichihashi and T. Ikeda: Shape Control of Inclusions, Edited by Committee on Non-Inclusion Shape Control, Organization of Joint Society on Iron and Steel Basic Research, Iron Steel Institute of Japan, Toyko, 1984, p. 33.
82. K.-R. Lee and H. Suito: *Metall. Mater. Trans. B*, 1994, vol. 25B, pp. 893-902.
83. CRC Handbook of Chemistry and Physics, Ed. D.R. Lide, 73rd Ed., 1992-1993, CRC Press, Inc., Boca Raton, Florida, 1992.
84. C. Zhang, Q. Han, B. Song and S. Guan: Proceedings of the sixth Japan-China symposium on science and technology of iron and steel, 1992, Chiba, Japan, pp. 18-25.
85. B. Song, Q. Han and X. Zhang: *J. Iron & Steel Res. Int.(China)*, 1996, vol. 3, pp. 11-13.
86. X. Zhang and Q. Han: The 5th China-Japan Symposium on Science and Technology of Iron and Steel. Dec., 1989, Shanghai, pp. 310-18.; X. Zhang and Q. Han: *Acta Metallurgica Sinica*, Series B, 1991, vol. 4, pp. 230-33.; X. Zhang, Q. Han and D. Chen: *Metall. Trans. B*, 1991, vol. 22B, pp. 918-21.
87. R.B. Reese, R.A. Rapp and G.R. St Pierre: *Trans. Metall. Soc. AIME*, 1968, vol. 242, pp. 1719-26.
88. J.M.A. Geldenhuis and R.J. Dippenaar; *Metall. Trans. B*, 1991, vol. 22B, pp. 915-18.
89. P.J. Bowles, H.F. Ramstad and F.D. Richardson: *J. Iron Steel Inst.*, 1964, vol. 202, pp. 113-21.
90. G. Smith and J. Taylor: *J. Iron Steel Inst.*, 1964, vol. 202, pp. 577-80.
91. J. Chipman and R. Baschwitz: *Trans. Met. Soc. AIME*, 1963, vol. 227, p. 473.
92. Syui Tszen-Tszi, A.Yu. Polyakov and A.M. Samarin: *Izv. Akad. Nauk SSSR*, 1961, No. 2, p. 115.
93. M. Ohtani: *Sci. Rep. RITU*, Sendai, Japan, 1955, A7, p. 487.
94. C.W. Weidner, Jr: Ph.D dissertation, Ohio State Univ., Columbus, Ohio, 1971.
95. E. Kato and T. Furukawa: 4th Japan-USSR Joint Symp. on Phys. Chem. of Metall. Proc., Iron Steel Institute of Japan, Toyko, 1973, p. 201.
96. D.L. Sponseller and R.A. Flinn: *Trans. Metall. Soc. AIME*, 1964, vol. 230, pp. 876-88.
97. B. Song, Q. Han, X. Zhang, J. Ji: *J. Univ. of Sci. & Tech. Beijing*, 1993, vol. 15 (special issue for Proc. 1st Academic Conf. RWTH and USTB, 1993, Beijing, China), pp. 95-100.
98. A.D. Pelton and P. Chartrand: *Metall. Mater. Trans. A*, 2001, vol. 33A, 1355-60.
99. D. Bouchard and C.W. Bale: *Metall. Mater. Trans. B*, 1995, vol. 26B, pp. 467-484.
100. SGTE (Scientific Group Thermodata Europe): www.sgte.org, 2002.

Table I. Optimized Henrian activity coefficients and interaction parameters in binary liquid Fe-M systems.

Element	$\ln \gamma_M^o$ *	ϵ_M^M	Pure element standard state	Reference
O	-15280/T+3.5	0	G (0.5 O ₂)	[2]
Al	-7596.7/T+1.2	3802.7/T+0.4	L	[2]
B	10126.4/T-6.948	0	S	This study
Ba	20837.04/T	0	L	This study
Ca	14894.9/T	0	G	This study
Ce	-7103.2/T	-29627.6/T	L	This study
Cr	0	0	S	This study
La	-3380.5/T	0	L	This study
Mg	13774.8/T	0	G	This study
Mn	0	0	L	[99]
Nb	544.6/T	-27404.7/T	S	This study
Ni**	-3320.3/T+1.153	11080.2/T-4.012	L	[100]
Si	-11763.2/T	4026/T+10.25	L	This study
Ta	-2680.1/T	-22788.7/T	S	This study
Ti	-5898.7/T	3467.6/T	L	[99]
V	1579.9/T-2.484	-2768.9/T+4.876	S	This study
Zr	-5619.5/T	0	S	This study

* $RT \ln \gamma_M^o = g_M^o(\text{Henrian Standard State}) - g_M^o(\text{Pure Element Standard State})$

** $\epsilon_{Ni}^{Ni,Ni} = -6659.24/T + 2.5592$

Table II. Optimized energies of associate formation in liquid Fe.

Element	Δg_{M*O}^o J/mol	$\Delta g_{M_2*O}^o$ J/mol
Al	-108614	-179912
B	-33472	-66793
Ba	-240922	
Ca	-305828	
Ce	-192464	
Cr	-41840	-62760
La	-209200	
Mg	-218272	
Mn	-20920	
Nb	-60668	-133888
Si	0	
Ta	-20920	-104600
Ti	-96145	-142256
V	-49371	-104600
Zr	-167360	-251040

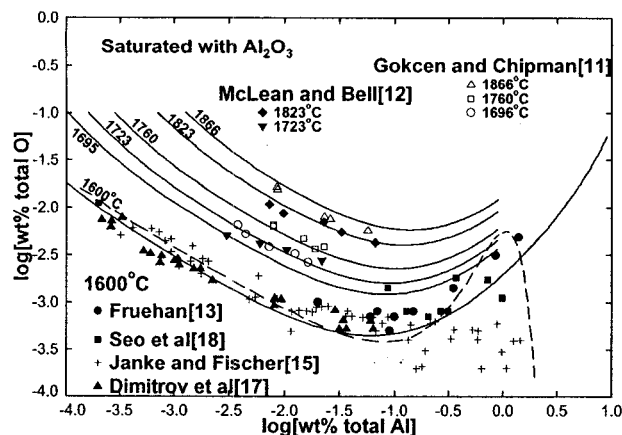


Fig. 1 - Total dissolved oxygen and total dissolved Al contents of liquid Fe in equilibrium with solid Al_2O_3 . Lines calculated from present model. Dashed line calculated from Wagner formalism with parameters of Sigworth and Elliott.^[19]

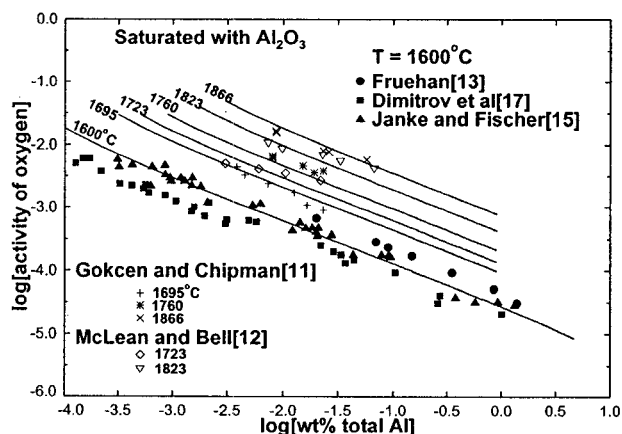


Fig. 2 - Activity of oxygen (weight % standard state) in liquid Fe in equilibrium with solid Al_2O_3 . Lines calculated from model.

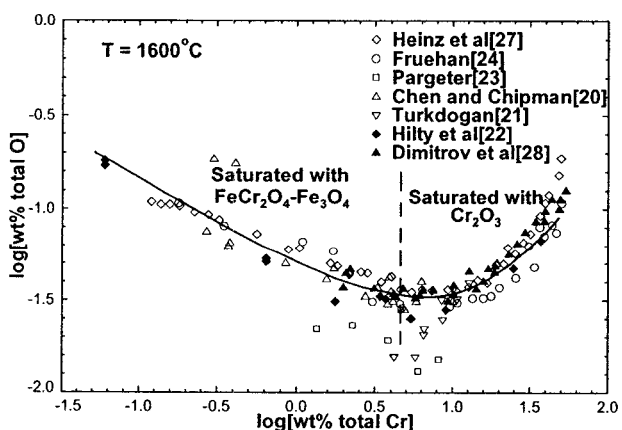


Fig. 3 - Total dissolved oxygen and total dissolved Cr contents of liquid Fe in equilibrium with either $\text{Cr}_2\text{O}_3(\text{s})$ or $\text{FeCr}_2\text{O}_4\text{-Fe}_3\text{O}_4$ solid solution. Lines calculated from model.

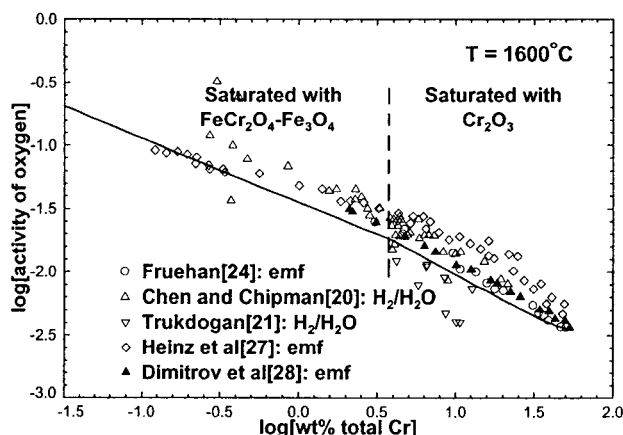


Fig. 4 - Activity of oxygen (weight % standard state) in liquid Fe in equilibrium with either $\text{Cr}_2\text{O}_3(\text{s})$ or $\text{FeCr}_2\text{O}_4\text{-Fe}_3\text{O}_4$ solid solution. Lines calculated from model.

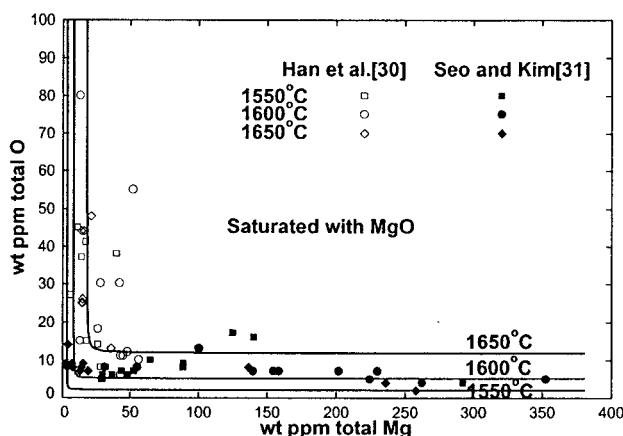


Fig. 5 - Total dissolved oxygen and total dissolved Mg contents of liquid Fe in equilibrium with solid MgO . Lines calculated from model.

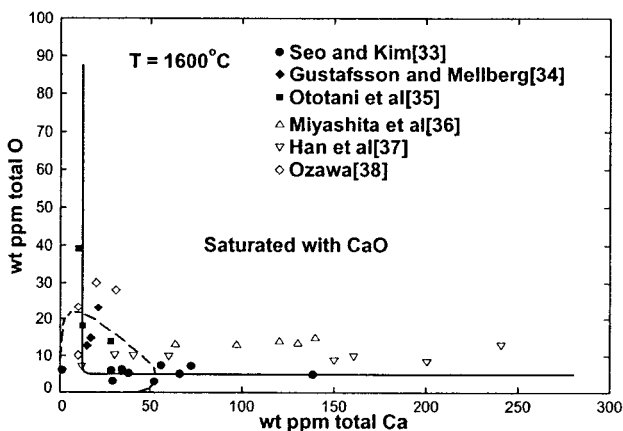


Fig. 6 - Total dissolved oxygen and total dissolved Ca contents of liquid Fe in equilibrium with solid CaO . Lines calculated from present model. Dashed line calculated from Wagner formalism with parameters of JSPS.^[44]

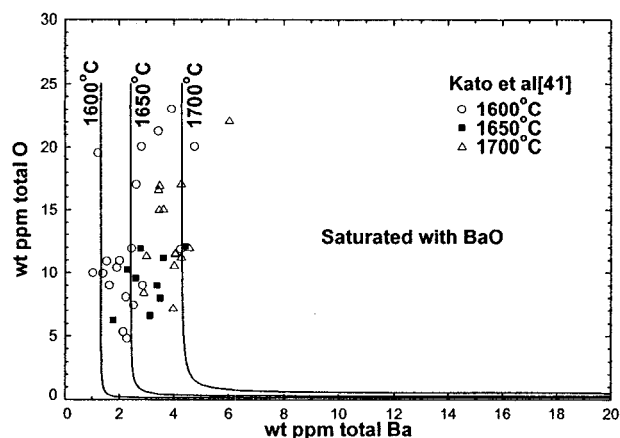


Fig. 7 – Total dissolved oxygen and total dissolved Ba contents of liquid Fe in equilibrium with solid BaO. Lines calculated from model.

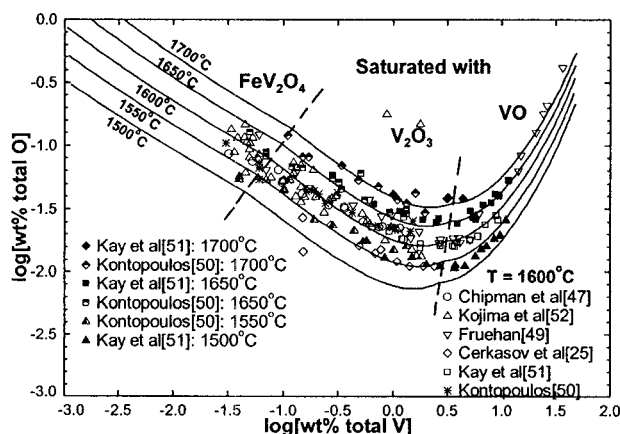


Fig. 8 - Total dissolved oxygen and total dissolved V contents of liquid Fe in equilibrium with either $\text{FeV}_2\text{O}_4(\text{s})$, $\text{V}_2\text{O}_3(\text{s})$ or $\text{VO}(\text{s})$. Lines calculated from model.

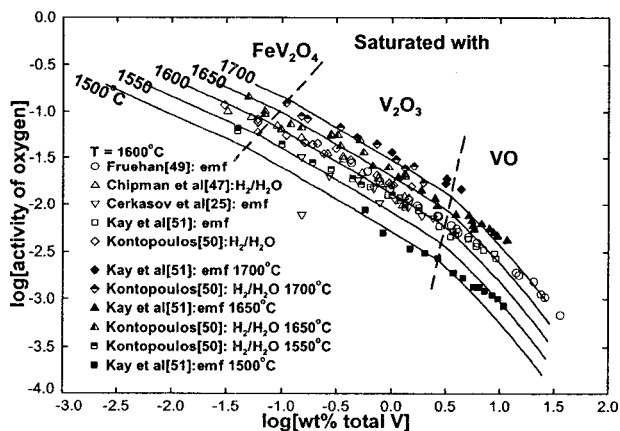


Fig. 9 - Activity of oxygen (weight % standard state) in liquid Fe in equilibrium with either $\text{FeV}_2\text{O}_4(\text{s})$, $\text{V}_2\text{O}_3(\text{s})$ or $\text{VO}(\text{s})$. Lines calculated from model.

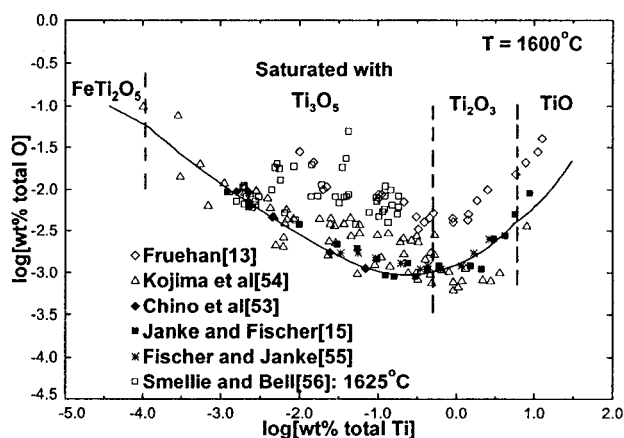


Fig. 10 – Total dissolved oxygen and total dissolved Ti contents of liquid Fe in equilibrium with either $\text{FeTi}_2\text{O}_5(\text{s})$, $\text{Ti}_3\text{O}_4(\text{s})$, $\text{Ti}_2\text{O}_3(\text{s})$ or $\text{TiO}(\text{s})$. Lines calculated from model.

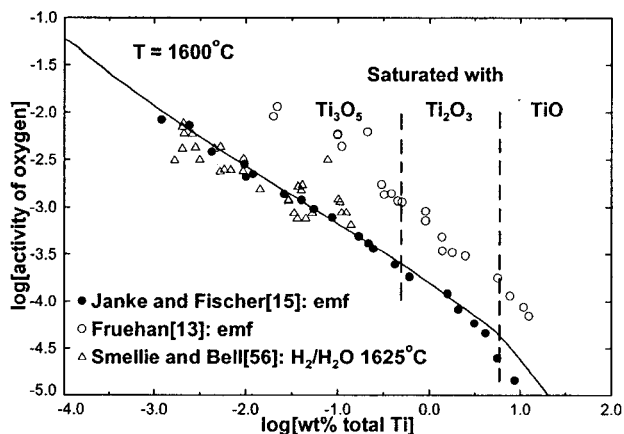


Fig. 11 – Activity of oxygen (weight % standard state) in liquid Fe in equilibrium with either $\text{FeTi}_2\text{O}_5(\text{s})$, $\text{Ti}_3\text{O}_4(\text{s})$, $\text{Ti}_2\text{O}_3(\text{s})$ or $\text{TiO}(\text{s})$. Lines calculated from model.

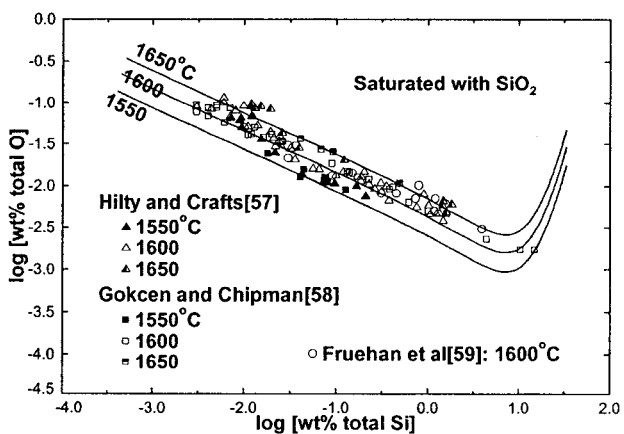


Fig. 12 – Total dissolved oxygen and total dissolved Si contents of liquid Fe in equilibrium with solid SiO_2 . Lines calculated from model.

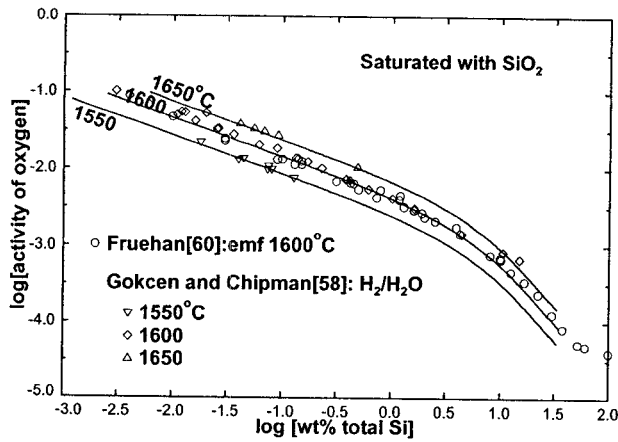


Fig. 13 – Activity of oxygen (weight % standard state) in liquid Fe in equilibrium with solid SiO_2 . Lines calculated from model.

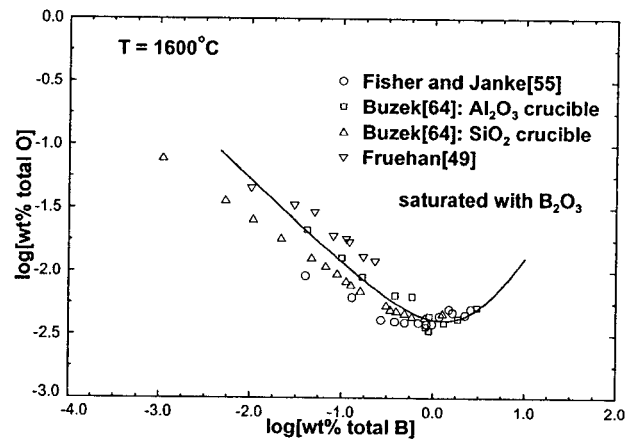


Fig. 16 – Total dissolved oxygen and total dissolved B contents of liquid Fe in equilibrium with solid B_2O_3 . Lines calculated from model.

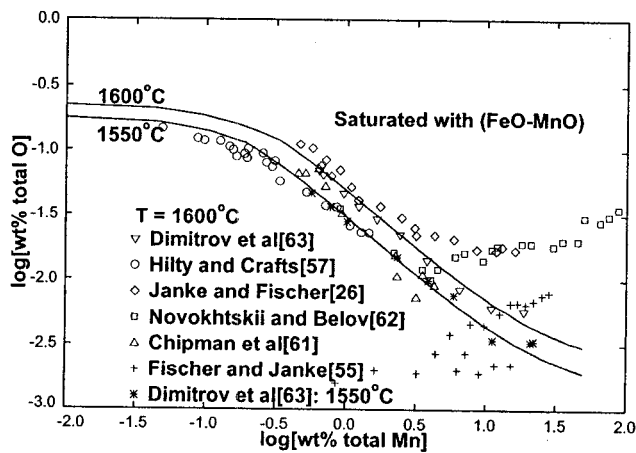


Fig. 14 - Total dissolved oxygen and total dissolved Mn contents of liquid Fe in equilibrium with FeO-MnO solid solution. Lines calculated from model.

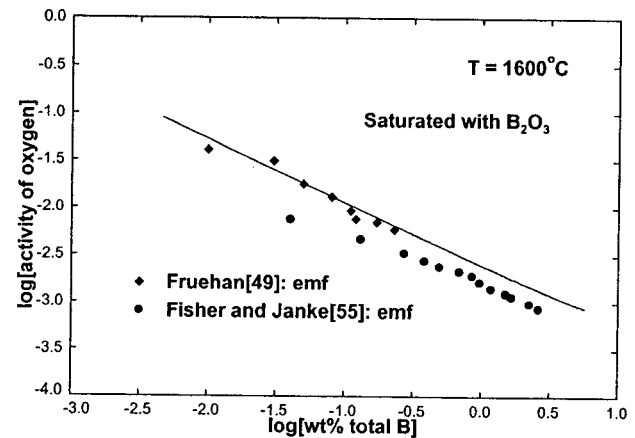


Fig. 17 - Activity of oxygen (weight % standard state) in liquid Fe in equilibrium with solid B_2O_3 . Lines calculated from model.

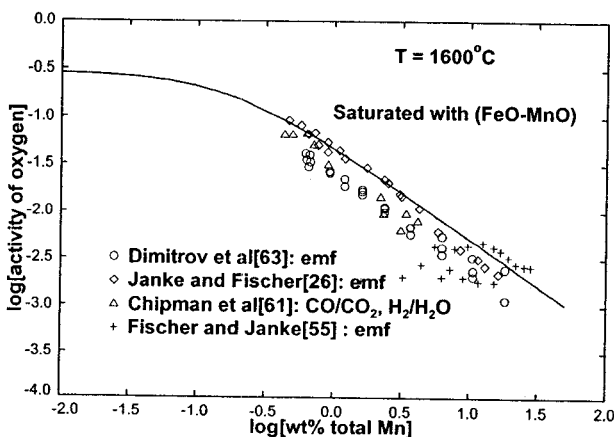


Fig. 15 - Activity of oxygen (weight % standard state) in liquid Fe in equilibrium with FeO-MnO solid solution. Lines calculated from model.

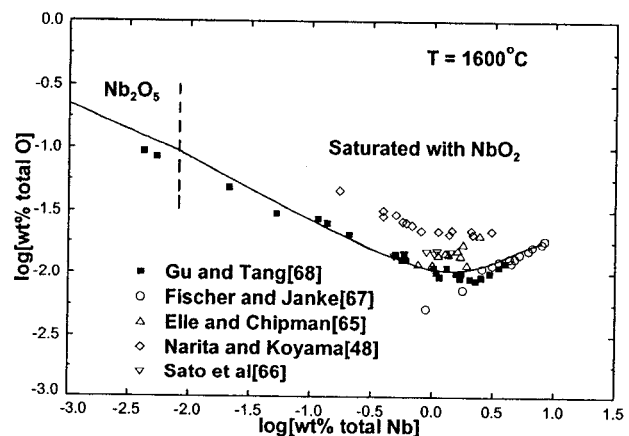


Fig 18 - Total dissolved oxygen and total dissolved Nb contents of liquid Fe in equilibrium with either $\text{Nb}_2\text{O}_5(\text{s})$ or $\text{NbO}_2(\text{s})$. Lines calculated from model.

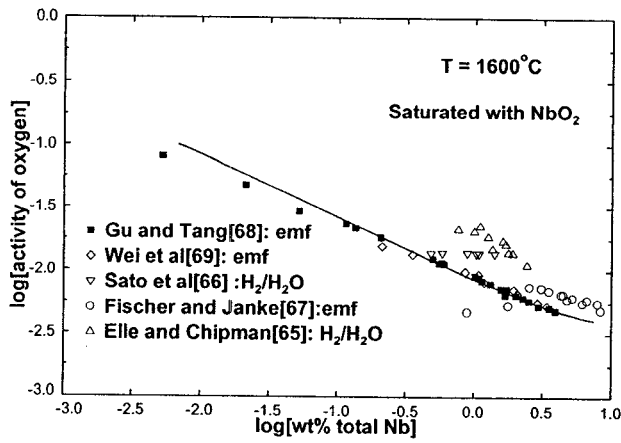


Fig. 19 - Activity of oxygen (weight % standard state) in liquid Fe in equilibrium with $\text{NbO}_2(\text{s})$. Lines calculated from model.

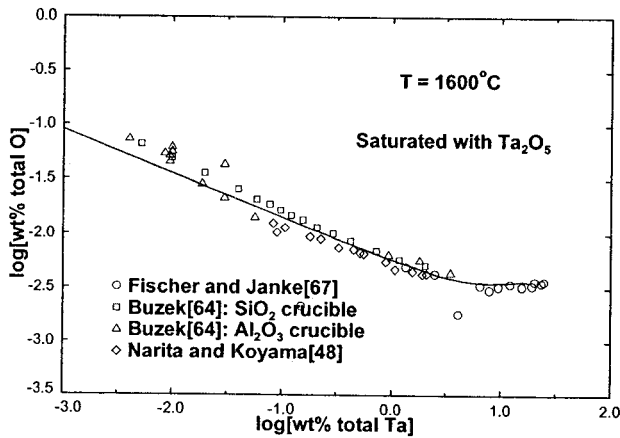


Fig. 20 - Total dissolved oxygen and total dissolved Ta contents of liquid Fe in equilibrium with solid Ta_2O_5 . Lines calculated from model.

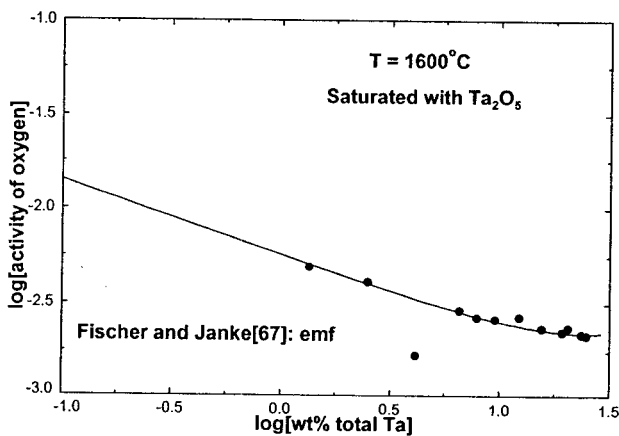


Fig. 21 - Activity of oxygen (weight % standard state) in liquid Fe in equilibrium with solid Ta_2O_5 . Lines calculated from model.

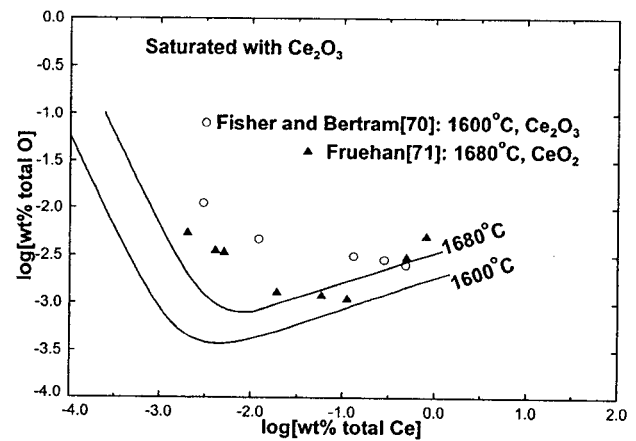


Fig. 22 - Total dissolved oxygen and total dissolved Ce contents of liquid Fe in equilibrium with solid Ce_2O_3 . Lines calculated from model.

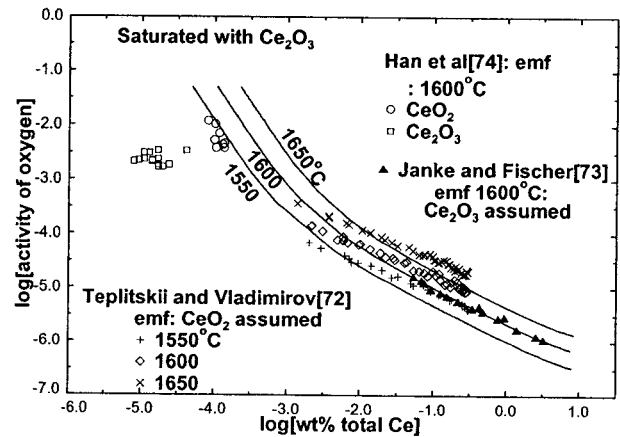


Fig. 23 - Activity of oxygen (weight % standard state) in liquid Fe in equilibrium with solid Ce_2O_3 . Lines calculated from model.

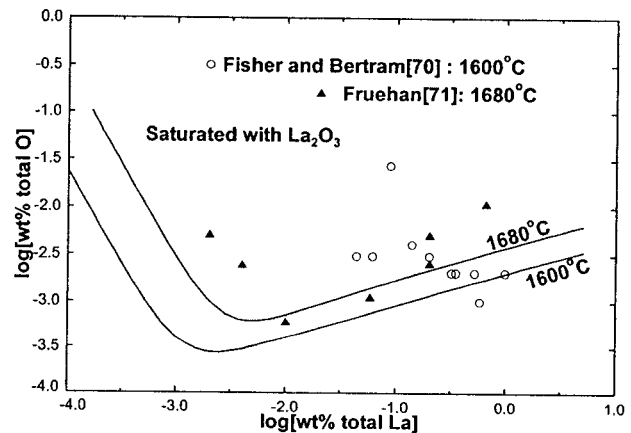


Fig. 24 - Total dissolved oxygen and total dissolved La contents of liquid Fe in equilibrium with solid La_2O_3 . Lines calculated from model.

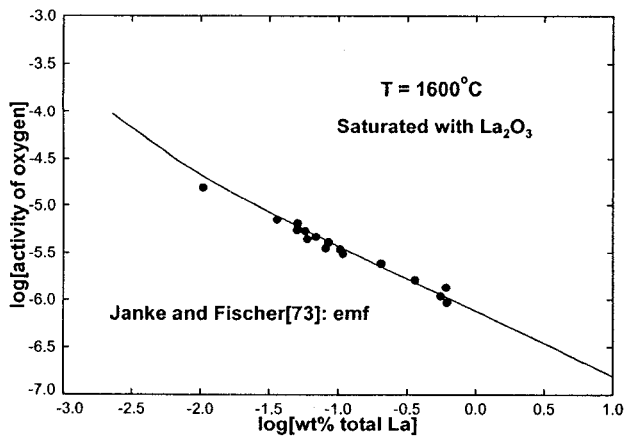


Fig. 25 – Activity of oxygen (weight % standard state) in liquid Fe in equilibrium with solid La_2O_3 . Lines calculated from model.

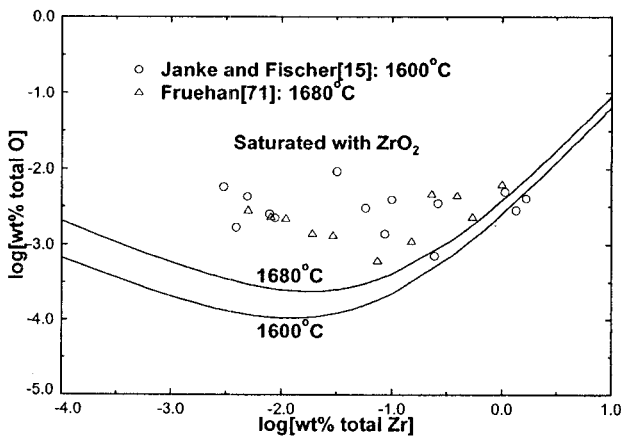


Fig. 26 – Total dissolved oxygen and total dissolved Zr contents of liquid Fe in equilibrium with solid ZrO_2 . Lines calculated from model.

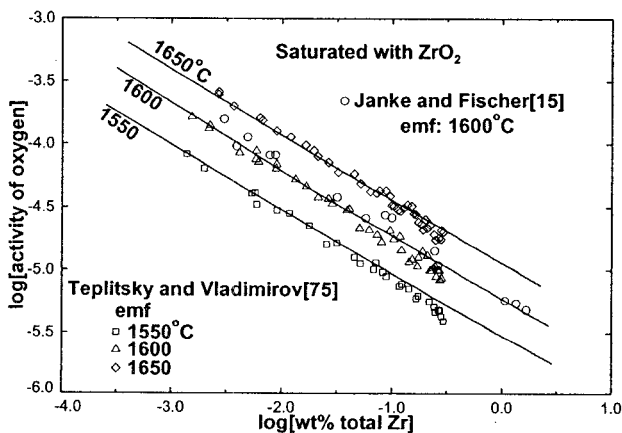


Fig. 27 – Activity of oxygen (weight % standard state) in liquid Fe in equilibrium with solid ZrO_2 . Lines calculated from model.

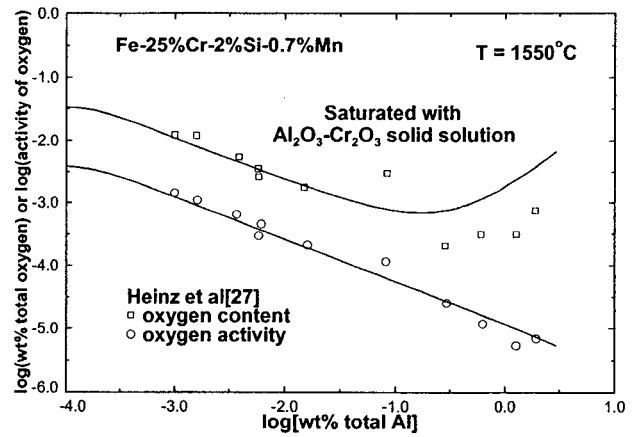


Fig. 28 – Total dissolved oxygen content and activity of oxygen (weight % standard state) and total dissolved Al in liquid Fe-25%Cr-2%Si-0.7%Mn stainless steel in equilibrium with solid Al_2O_3 - Cr_2O_3 solid solutions. Lines predicted from model.

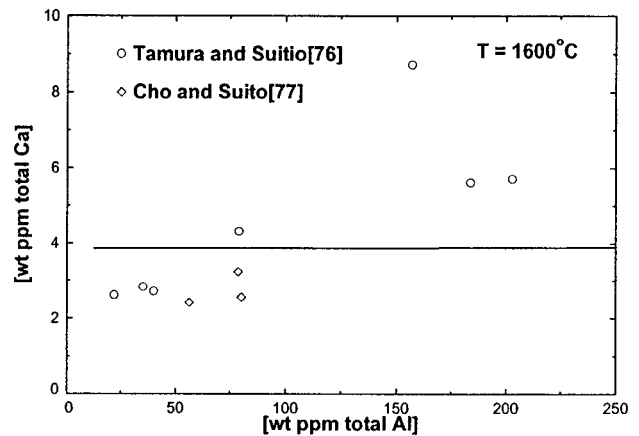


Fig. 29(a) – Total dissolved Ca, Si, Al and O in molten Fe in equilibrium with a (53.6wt% CaO - 16.9wt% SiO_2 - 29.5wt% Al_2O_3) liquid slag. Lines predicted from model.

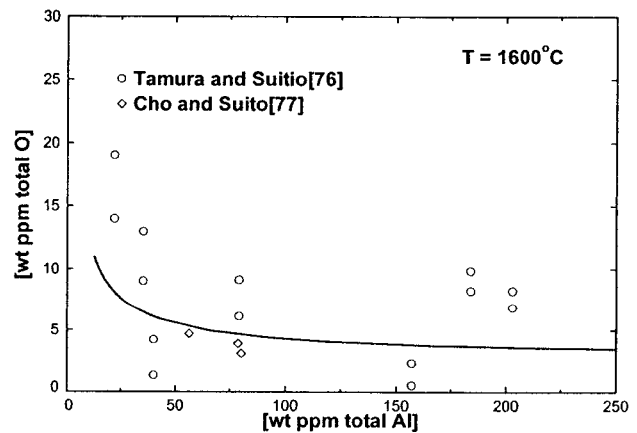


Fig. 29(b) – Total dissolved Ca, Si, Al and O in molten Fe in equilibrium with a (53.6wt% CaO - 16.9wt% SiO_2 - 29.5wt% Al_2O_3) liquid slag. Lines predicted from model.

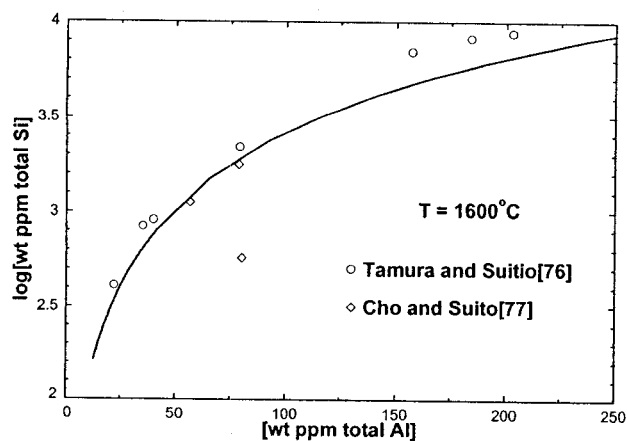


Fig. 29(c) - Total dissolved Ca, Si, Al and O in molten Fe in equilibrium with a (53.6wt% CaO - 16.9wt% SiO₂ - 29.5wt% Al₂O₃) liquid slag. Lines predicted from model.

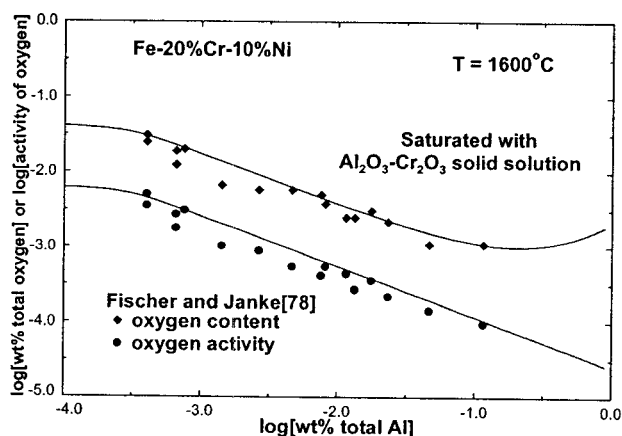


Fig. 30 - Total dissolved oxygen content and activity of oxygen (weight % standard state) and total dissolved Al in liquid Fe-20%Cr-10%Ni stainless steel in equilibrium with solid Al₂O₃-Cr₂O₃ solid solutions. Lines predicted from model.

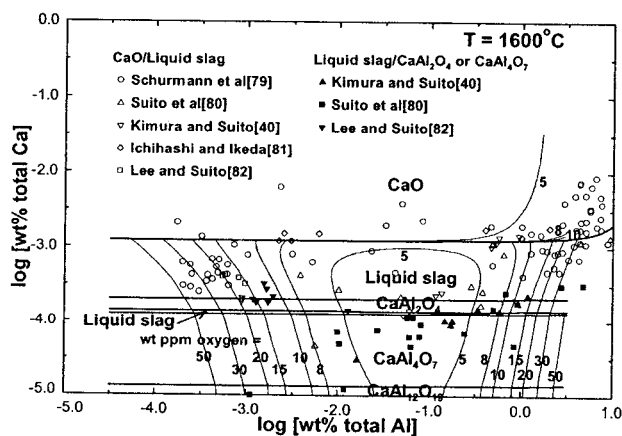


Fig. 31 - Inclusion diagram predicted from model for complex deoxidation with Ca and Al.

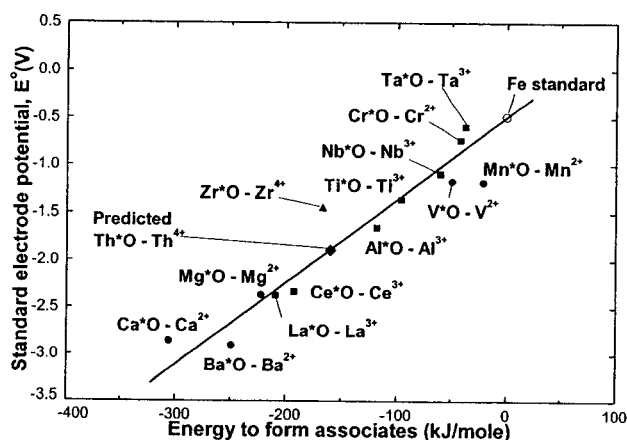


Fig. 32 - Correlation of the energy of formation of M*O associates in liquid Fe ($\Delta G_{M^*O}^\circ$) and the standard electrode potentials^[83] of the ions Mⁿ⁺ in aqueous solution.

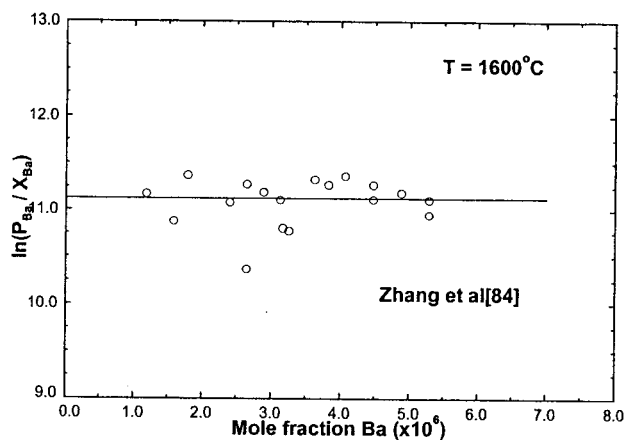


Fig. 33 - Variation of equilibrium Ba partial pressure (bar) with Ba content in molten Fe. Line from model.

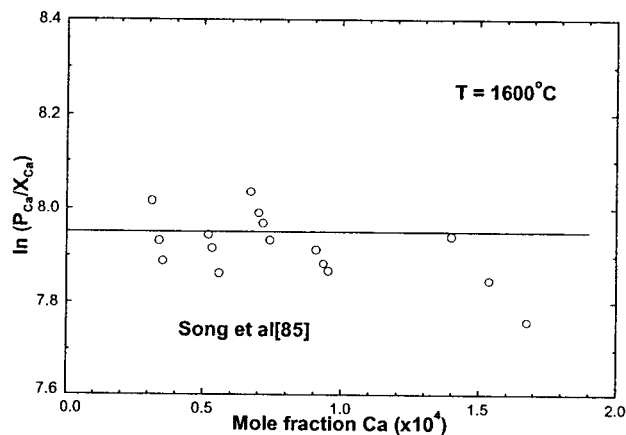


Fig. 34 - Variation of equilibrium Ca partial pressure (bar) with Ca content in molten Fe. Line from model.

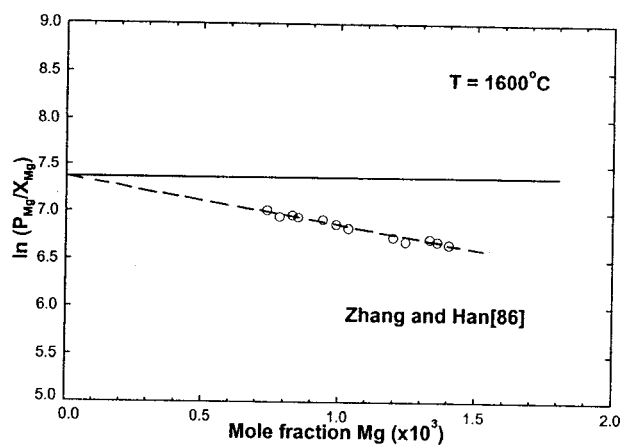


Fig. 35 – Variation of equilibrium Mg partial pressure (bar) with Mg content in molten Fe. Line from model.

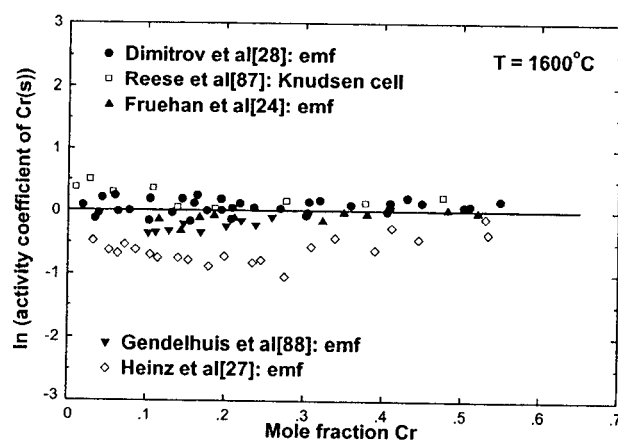


Fig. 38 - Variation of activity coefficient of Cr(s) with Cr content in molten Fe. Line from model.

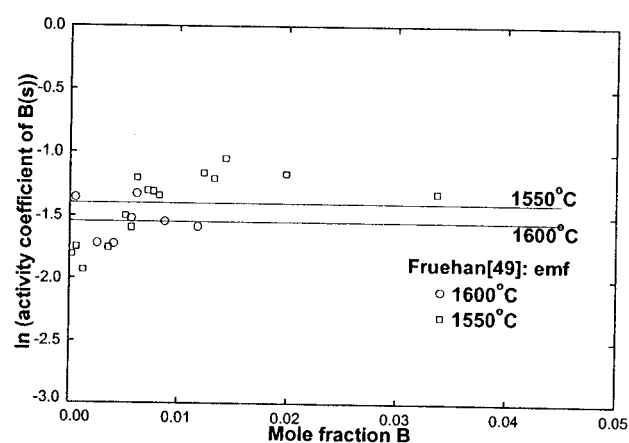


Fig. 36 - Variation of activity coefficient of B(s) with B content in molten Fe. Line from model.

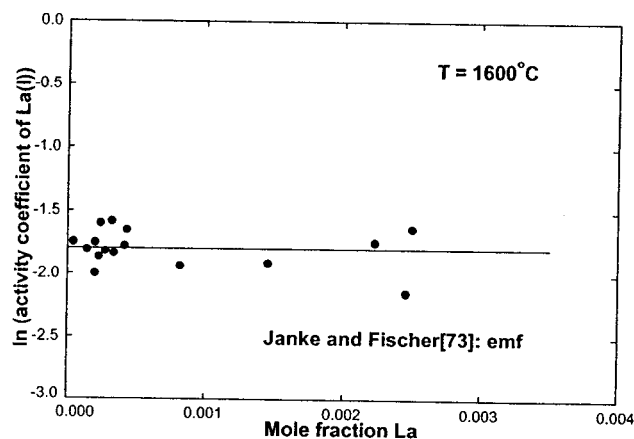


Fig. 39 – Variation of activity coefficient of La(l) with La content in molten Fe. Line from model.

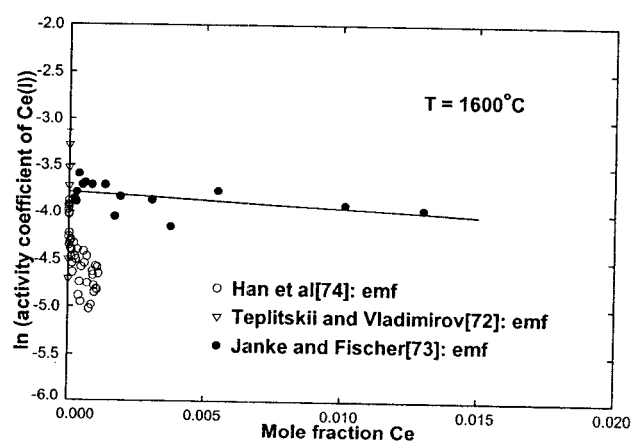


Fig. 37 – Variation of activity coefficient of Ce(l) with Ce content in molten Fe. Line from model.

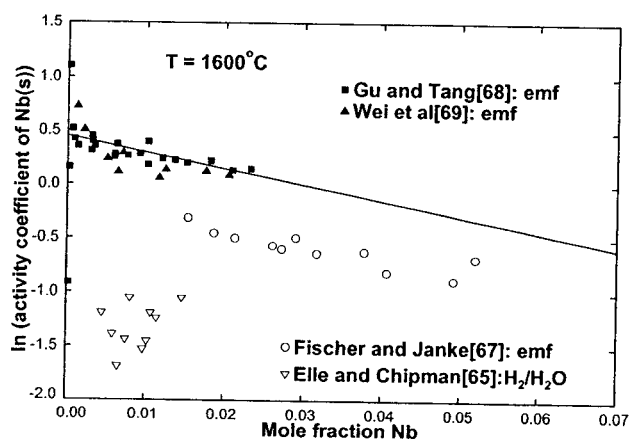


Fig. 40 – Variation of activity coefficient of Nb(s) with Nb content in molten Fe. Line from model.

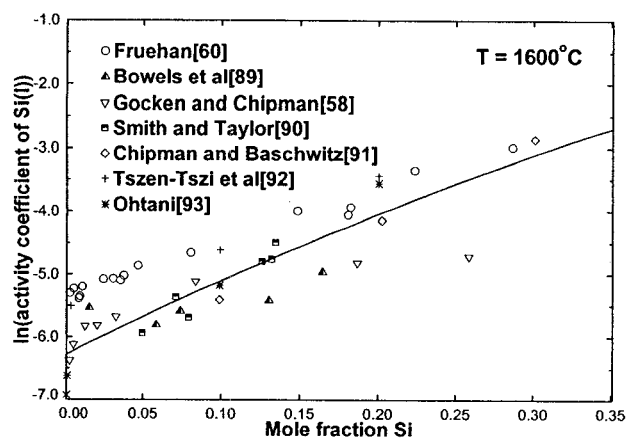


Fig. 41 - Variation of activity coefficient of Si(l) with Si content in molten Fe. Line from model.

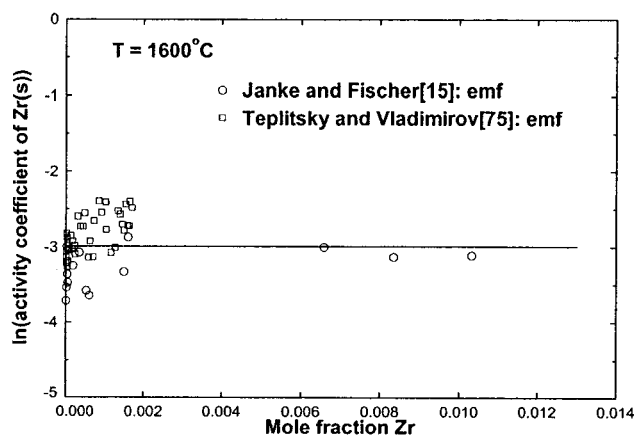


Fig. 44 - Variation of activity coefficient of Zr(s) with Zr content in molten Fe. Line from model.

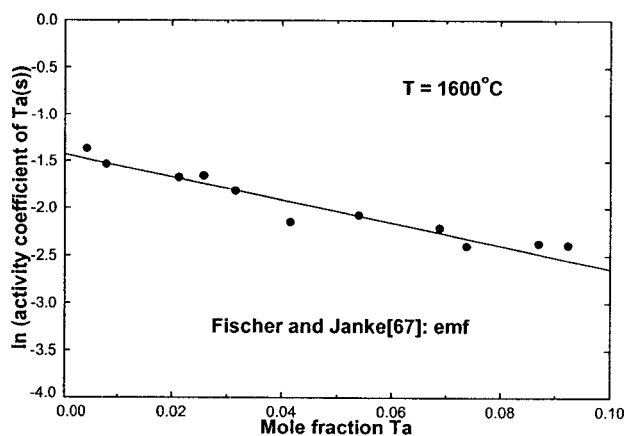


Fig. 42 - Variation of activity coefficient of Ta(s) with Ta content in molten Fe. Line from model.

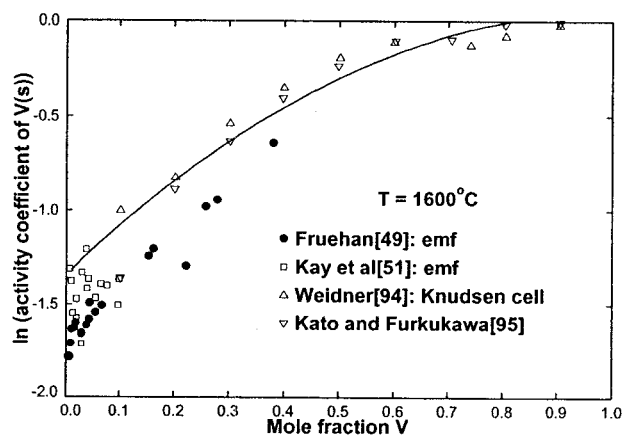


Fig. 43 - Variation of activity coefficient of V(s) with V content in molten Fe. Line from model.

Appendix X

Article :

COMPUTER APPLICATIONS OF THERMODYNAMIC DATABASES TO INCLUSION ENGINEERING

In-Ho Jung, Sergei A. Decterov and Arthur D. Pelton

Submitted to *ISIJ International*, 2003

Computer Applications of Thermodynamic Databases to Inclusion Engineering

In-Ho JUNG, Sergei A. DECTEROV and Arthur D. PELTON

Centre de Recherche en Calcul Thermochimique, École Polytechnique de

Computerized thermodynamic databases for solid and liquid steel, slags and solid oxide solutions, for large numbers of components, have been developed over the last two decades by critical evaluation/optimization of all available phase equilibrium and thermodynamic data. The databases contain parameters of models specifically developed for molten slags; liquid and solid steel; and solid oxide solutions such as spinels. With user friendly software, which accesses these databases, complex equilibria involving slag, steel, inclusions, refractories and gases simultaneously, can be calculated for systems with many components, over wide ranges of temperature, oxygen potential and pressure. In the present article, several case studies will be presented, illustrating applications to complex steelmaking processes such as: Ca injection processes (Fe-Ca-Al-O inclusion diagram), corrosion of refractories, Mn/Si deoxidation, Ti/Al deoxidation (Fe-Al-Ti-O inclusion diagram), spinel formation (Fe-Mg-Al-O inclusion diagram), (Ti,N)(N,C) inclusion formation, oxide metallurgy.

KEY WORDS: thermodynamic databases, inclusion control, inclusion engineering, inclusion diagram, deoxidation, corrosion of refractories, oxide metallurgy, FactSage™.

1. Introduction

Inclusion control is the key to the production of high clean or ultra high clean steel. Inclusions appear in steel at various stages of its production and cause serious problems: nozzle clogging, breakage of steel wire during drawing, hydrogen induced cracking (HIC), low-temperature embrittlement, fatigue failure, degradation of surface quality and so on. Inclusions can be classified into two types: endogenous and exogenous. Endogenous inclusions are mainly formed during the deoxidation process, while exogenous inclusions are caused by slag entrapment, breakdown of refractory materials and reoxidation by air. Moreover, inclusions can be precipitated due to changes of solubility which occur as temperature decreases.

Inclusions can be floated and captured by top slags in secondary steelmaking processes. However, the removal of inclusions is very limited during these processes due to the short process time and to the continuous circulation of liquid steel in the ladle. Therefore, the control of the composition of inclusions has become crucial in modern steelmaking processes. That is, since the presence of inclusions cannot be avoided, it is important to modify their composition to render them less harmful. Because, thermodynamically, the composition of inclusions is very sensitive to the concentrations of even dilute elements dissolved in the steel, accurate thermodynamic data for both steel and inclusions are indispensable to the development of inclusion engineering technology. Moreover, since the inclusions are composed of complex oxides, sulfides and/or nitrides, computer databases and

software are essential to perform useful thermodynamic calculations.

In recent years, thermodynamic modeling has been actively pursued apace with the improvement of computational techniques and software. Based on a proper thermodynamic model for every phase of a given system, all available thermodynamic and phase equilibrium data for a system are critically evaluated simultaneously in order to obtain one self-consistent set of model equations for the Gibbs energies which best reproduce the data for all phases as functions of temperature and composition. This technique has come to be known as thermodynamic "optimization." Where data are lacking for a multicomponent system, the models and optimized model parameters for low-order (binary and ternary) sub-systems can be used to provide good estimates.

In this way, the thermodynamic databases are developed. The databases are then used, along with Gibbs energy minimization software, to calculate the conditions for multicomponent equilibrium.

Thermodynamic databases make it possible to perform versatile thermodynamic calculations within the accuracy of the experimental data even for regions of composition and temperature where no experimental data are available. In the present article, various case studies will be presented in order to demonstrate the versatility and accuracy of commercial thermodynamic databases to calculations of importance to inclusion engineering.

2. Thermodynamic Databases

The selection of proper databases for a given system is a prerequisite for accurate thermodynamic calculations.

The databases must be thermodynamically self-consistent; otherwise very erroneous results can often occur.

The FACT databases¹⁾ for multicomponent oxide, salt, alloy and aqueous solutions have been developed by critical evaluation/optimization over the last 25 years. The databases contain over 4400 compounds and 120 non-ideal multicomponent solution phases. The FACT databases were used for the case studies presented in the present article.

The FACT oxide solution database contains consistently assessed and critically evaluated thermodynamic data for the molten slag phase containing SiO_2 - CaO - MgO - Al_2O_3 - FeO - Fe_2O_3 - MnO - TiO_2 - Ti_2O_3 - CrO - Cr_2O_3 - NiO - CoO - Na_2O - K_2O - B_2O_3 - Cu_2O - S - SO_4 - PO_4 - H_2O - F - Cl and for many extensive ceramic solid solutions containing these components such as spinel, olivine, melilite, monoxide, perovskite, wollastonite, *etc.* The molten slag phase is modeled by the Modified Quasichemical Model,^{2,3)} in which short-range-ordering is taken into account. This model has been recently summarized.^{4,5)} Ceramic solid solutions are mainly modeled in the framework of the Compound Energy Formalism,⁶⁾ taking into account the crystal structure of each solution. For example, the spinel solution is modeled taking into account the distribution of all cations and vacancies over tetrahedral (T) and octahedral (O) sites: $[\text{Fe}^{2+}, \text{Fe}^{3+}, \text{Mg}^{2+}, \text{Al}^{3+}, \text{Cr}^{2+}, \text{Cr}^{3+}]^{\text{T}}(\text{Fe}^{2+}, \text{Fe}^{3+}, \text{Mg}^{2+}, \text{Al}^{3+}, \text{Cr}^{3+}, \text{Va})_2^{\text{O}}\text{O}_4$. The solubilities of S, SO_4 , PO_4 , H_2O , F and Cl in molten slags were modeled by the Blander-Reddy Capacity Model.^{7,8)} In the Blander-Reddy model, dissolved anions such as S^{2-} are assumed to form ideal solutions, substituting for O^{2-} and SiO_4^{4-} anions in the silicate slag. From this simple assumption, sulfide, sulfate, *etc.* solubilities (capacities) can be predicted with good accuracy.⁷⁾ Because the thermodynamic model used for each phase in the database has been chosen with consideration of the actual structure of the phase, the predictive ability is very high for estimating the properties of multicomponent solutions.

Recently, a new FACT database for liquid steel was developed with a new Associate Model⁹⁾ to accurately describe deoxidation phenomena in liquid steel. While the classical Wagner formalism¹⁰⁾ for dilute liquid solutions Fe-M-O assumes that all dissolved elements ($\underline{\text{M}}$ and $\underline{\text{O}}$) exist as separate atoms and are distributed randomly, the Associate Model assumes that dilute elements which have a strong affinity for oxygen dissolve as associated molecules ($\underline{\text{M}^*\text{O}}$), as well as separate atoms ($\underline{\text{M}}$ and $\underline{\text{O}}$), and that all species are distributed randomly. The dissolved species are at equilibrium: $\underline{\text{M}} + \underline{\text{O}} = \underline{\text{M}^*\text{O}}$ with Gibbs energy of this reaction $\Delta g_{\underline{\text{M}^*\text{O}}}$ which is the only model parameter. Furthermore, it has been found⁹⁾ that $\Delta g_{\underline{\text{M}^*\text{O}}}$ is independent of temperature in all cases. The new Associate Model reflects the actual structure of the solution more closely than the classical Wagner formalism and gives a much better description of the configurational entropy. As will be shown below, the observed Ca deoxidation curve (Fe-Ca-O system), which is impossible to explain using the classical Wagner formalism, can be easily reproduced with the

Associate Model with only one temperature-independent model parameter. This database has been developed for all deoxidation systems Fe-M-O ($\text{M} = \text{Ca}, \text{Mg}, \text{Ba}, \text{Al}, \text{Ti}, \text{Cr}, \text{V}, \text{Mn}, \text{Si}, \text{B}, \text{Ce}, \text{Nb}, \text{Zr}, \dots$),⁹⁾ and has high predictive ability for multicomponent systems.

A complete 14-element (Fe-Al-C-Co-Cr-Mn-Mo-N-Nb-Ni-Si-Ti-V-W) FACT database for steel alloys will also soon be available. This database contains fully assessed data for alloy and carbonitride phases: liquid, fcc, bcc, hcp, cementite, laves phase, carbides, sigma phase, *etc.* This database is an updated¹¹⁾ version of the SGTE solution database.¹²⁾ All solutions in the database were developed using the Compound Energy Formalism.

The Gibbs energy minimization software of the FactSage¹⁾ thermochemical computing system was used to perform the thermodynamic calculations in this work. This software can perform equilibrium calculations with up to 32 elements, 30 non-ideal solution phases and an unlimited number of stoichiometric compounds. The FACT databases discussed above are automatically accessed by this user-friendly software. Users can perform complex equilibrium calculations involving simultaneously, slag, steel, inclusions, refractories and gases, for systems with many components, over wide ranges of temperature, oxygen potential and pressure.

3. Sample Applications

3.1. Ca deoxidation: The Fe-Ca-O system

Fig. 1 shows the calculated deoxidation curve in the Fe-Ca-O system at 1600°C compared with experimental data.¹³⁻¹⁸⁾ The curves in Fig. 1 were calculated with the Associate Model with the assumed dissolved associate $\underline{\text{Ca}^*\text{O}}$, with one temperature-independent parameter, $\Delta g_{\underline{\text{Ca}^*\text{O}}}$ for the association reaction $\underline{\text{Ca}} + \underline{\text{O}} = \underline{\text{Ca}^*\text{O}}$.

The shape of the calculated Ca deoxidation curve in Fig. 1 may be explained as follows. Because $\Delta g_{\underline{\text{Ca}^*\text{O}}}$ is very negative, the association reaction is displaced very strongly to the right. Hence, a solution will contain either dissolved $\underline{\text{Ca}^*\text{O}}$ and $\underline{\text{O}}$ species (but virtually no $\underline{\text{Ca}}$ species), or dissolved $\underline{\text{Ca}^*\text{O}}$ and $\underline{\text{Ca}}$ species (but virtually no $\underline{\text{O}}$ species). Suppose we start with Fe containing a high concentration of dissolved oxygen at 1600°C and begin adding Ca. At first the Ca reacts with the oxygen to form $\underline{\text{Ca}^*\text{O}}$ associates, leaving virtually no free $\underline{\text{Ca}}$ in solution. When the concentration of $\underline{\text{Ca}^*\text{O}}$ reaches ~ 17 ppm it attains equilibrium with solid CaO: $\underline{\text{Ca}^*\text{O}} = \text{CaO(s)}$.

As more Ca is added to the metal, it reacts with dissolved oxygen to precipitate solid CaO; the concentration of dissolved oxygen thus decreases, while the concentration of $\underline{\text{Ca}^*\text{O}}$ remains constant (and hence the concentration of total dissolved Ca remains nearly constant). This results in the nearly vertical section of the deoxidation curve in Fig. 1. When the total dissolved oxygen content has been reduced to ~ 5 ppm, the concentrations of free dissolved $\underline{\text{O}}$ and $\underline{\text{Ca}}$ are both extremely low, and $\underline{\text{Ca}^*\text{O}}$ associates are virtually the only species in solution. Further addition of Ca thus serves only to increase the free $\underline{\text{Ca}}$ concentration, with virtually no

further precipitation of CaO; hence the nearly horizontal section of the curve in Fig. 1.

Several authors^{13,14,19-22)} have attempted to model the Ca deoxidation curve using the classical Wagner formalism without considering the formation of associates. Very large negative temperature-dependent first- and second-order interaction parameters $\varepsilon_{\text{Ca}}^{\text{O}}$, $\rho_{\text{Ca}}^{\text{O}}$, $\rho_{\text{Ca}}^{\text{Ca,O}}$ were required. Furthermore, most authors also had to arbitrarily adjust the equilibrium constant K_{CaO} for the formation of solid CaO by two or three orders of magnitude from its literature value in order to fit the data. In the present calculations, this was not necessary, and accepted literature values were used as recommended by Turkdogan.²³⁾ The calculated solubility (deoxidation) curves by other authors all have strange shapes, some with minima and maxima, and even one in the form of a circle.¹⁴⁾ The model of JSPS²¹⁾ is the most widely used; the “deoxidation curve” calculated from this model, and reported in the literature, is shown in Fig. 1 by the dashed line. We have shown⁹⁾ that this is actually an unstable solution of the interaction parameter formalism; the true stable solution actually lies at extremely low (< 0.01 ppm) $\underline{\text{Ca}}$ and $\underline{\text{O}}$ contents. Hence, we believe that the present calculations elucidate the deoxidation behavior of Ca for the first time.

3.2. Modification of solid Al_2O_3 inclusions to liquid CaO- Al_2O_3 inclusions: The Fe-Al-Ca-O system

Solid Al_2O_3 inclusions formed during the Al deoxidation process are not easily removed by floating in the secondary refining process, and thereafter they may degrade the mechanical properties of the steel as well as cause nozzle clogging. In order to reduce these harmful effects, Ca treatment technology is often used, by which solid Al_2O_3 inclusions are modified to less harmful liquid CaO- Al_2O_3 inclusions. The globular liquid inclusions can float more easily to the top slag in the secondary steelmaking process and are less likely to become attached to the nozzle wall. In order to understand the Ca treatment process, an inclusion diagram for the Fe-Al-Ca-O system is essential.

Fig. 2 presents the inclusion diagram for the Fe-Al-Ca-O system at 1600°C calculated using the thermodynamic databases. The equilibrium deoxidation products are also indicated on the diagram and the phase boundaries are represented as heavy lines. Iso-oxygen content lines from 5 to 50 mass ppm oxygen are also plotted. A deoxidation minimum is clearly seen near $\log [\text{mass}\% \text{ Al}] \sim -1.2$ (i.e. $[\text{Al}] \sim 500$ mass ppm). It can be seen that the equilibrium deoxidation product is nearly independent of Al content, depending only on the Ca content. When $\log [\text{mass}\% \text{ total Ca}] > -2.9$ (i.e. total dissolved Ca > 13ppm), solid CaO is the deoxidation product, and the oxygen content is 5 mass ppm. At higher total Ca contents the oxygen content does not decrease below 5 ppm. This behavior can be understood with reference to the Ca deoxidation curve in the Fe-Ca-O system in Fig. 1, where the nearly vertical and nearly horizontal branches of the deoxidation curve occur at ~ 13 mass ppm Ca and ~ 5 mass ppm O respectively.

Since CaAl_2O_4 melts congruently at $\sim 1605^\circ\text{C}$, a similar diagram calculated above 1605°C would not contain the CaAl_2O_4 region. Similarly, since the CaAl_2O_4 - CaAl_4O_7 eutectic temperature is $\sim 1595^\circ\text{C}$, a diagram calculated below 1595°C would not contain the lower “Liquid slag” region. Several authors²⁴⁻²⁸⁾ have measured the line along which solid CaO and liquid slag co-exist as well as the line along which either (slag+ CaAl_2O_4) or (slag+ CaAl_4O_7) co-exist. Measurements were performed in CaO crucibles in the first case, and Al_2O_3 crucibles in the second case. The data points are plotted on Fig. 2. Within the large experimental scatter, these results confirm the model calculations.

The newly calculated inclusion diagram differs significantly from previous diagrams,^{13,29-32)} in which the calculated phase boundaries slope upwards to the right.

The inclusion diagram can be applied to the Ca-treatment for Al_2O_3 solid inclusions. In order to modify the Al_2O_3 inclusions to a liquid CaO- Al_2O_3 phase, at least ~ 2 mass ppm $[\text{Ca}]$ (i.e. $\log [\text{mass}\% \text{ Ca}] \sim -3.7$) is necessary, but the Ca content should be less than ~ 13 mass ppm ($\log [\text{mass}\% \text{ Ca}] \sim -2.9$) to prevent the formation of a solid CaO phase. It should be noted that although the Ca treatment for Al_2O_3 inclusions is useful to prevent nozzle clogging and to absorb inclusions in top slags, the lowest eutectic temperature in the CaO- Al_2O_3 binary oxide system (1413°C) is still much higher than the temperature in the rolling process. Therefore, the CaO- Al_2O_3 inclusions will be solid and undeformable during the rolling process.

3.3. Formation of CaS inclusions during Ca treatment

During the Ca treatment process discussed above, the amount of sulfur in the liquid steel is very important because solid CaS is readily formed. CaS inclusions can be as harmful as solid Al_2O_3 . Therefore, the $[\text{Ca}]/[\text{S}]$ ratio in liquid steel should be controlled precisely.³³⁾

Fig. 3 shows the calculated results for the simulation of CaSi(1:1) wire injection into 100 tonnes of liquid steel (Fe-0.003S-0.05Al in mass%) with suspended Al_2O_3 inclusions. In the calculations, no losses of CaSi (as, for example, by the volatilization of Ca) are assumed. The amount of suspended Al_2O_3 inclusions is set at 100 mass ppm in Fig. 3(a) and 300 mass ppm in Fig. 3(b). As the CaSi wire is injected, initially solid Al_2O_3 is converted to solid $\text{CaAl}_{12}\text{O}_{19}$ and CaAl_4O_7 . Possible solubility of iron in these solids was not considered in the calculations. Thereafter, the liquid oxide inclusions, composed of CaO- Al_2O_3 with a small amount of CaS, are formed. As the amount of CaSi increases further, solid CaS and solid CaO inclusions begin to precipitate and eventually become predominant. In both Fig. 3(a) and Fig. 3(b), CaS is precipitated before CaO. The relative amounts of the solid phases depend on the initial amount of suspended Al_2O_3 inclusions. The more Al_2O_3 is suspended initially, the higher is the CaO/CaS ratio in the final solid inclusions. Clearly, more initial $[\text{S}]$ in the liquid steel will result in the precipitation of CaS at an earlier stage, even before the formation of the CaO- Al_2O_3 liquid if $[\text{S}]$ is large enough.

With the aid of such diagrams, the proper amount of CaSi injection can be calculated, as a function of initial [Al], [S] and suspended Al_2O_3 , in order to form deformable liquid inclusions without forming harmful solid oxide or CaS inclusions.

Clearly, injection of CaSi is also useful for reducing the S content in steel. Calculated diagrams such as Fig. 3 can also be used to determine the minimum [S] contents which can be attained without formation of harmful solid CaS inclusions.

Similar calculations were performed with different sulfur contents in the liquid steel. The initial composition of the steel was fixed as Fe-500[Al]-6[O] + (100 Al_2O_3 inclusions) (in mass ppm) with various initial amounts of [S]. The overall inclusion content was then calculated at 1600°C as increasing amounts of CaSi are added. Fig. 4 shows the calculated trajectories of the overall inclusion composition. Arrows on the figure show the direction of the inclusion composition trajectory during CaSi addition. The general sequence of modifications of Al_2O_3 inclusions during CaSi addition has been shown in Fig. 3. In Fig. 4 the composition of first appearance of CaS or CaO is indicated. When initial [S] = 10 mass ppm, CaO forms prior to CaS, while CaS forms first at all other sulfur contents shown.

Experimental results have been reported³³⁻³⁵⁾ in which some of the trajectories shown in Fig. 4 were followed. It is not possible to compare these results with the calculated trajectories because the initial amounts of suspended Al_2O_3 inclusions were not reported. However, the experimental and calculated trajectories are in satisfactory agreement.

3.4. Effect of Ca treatment on refractories

When Ca treatment is performed in secondary steelmaking processes, the injected CaSi wires not only modify the inclusions but can also react with the refractory linings in the ladle, especially the bottom lining castables, because the CaSi wires are often injected deep into the ladle. Currently, (Al_2O_3 + MgAl_2O_4 spinel) type refractory castables are often used in ladle linings. During Ca treatment, excess Ca can attack the refractories and change their composition.

Fig. 5 shows the calculated compositional changes of bottom lining refractories during CaSi wire treatment at 1600°C. All the Ca injected into the steel was assumed to react with the refractories in the calculation; that is, reaction of Ca with suspended Al_2O_3 inclusions was not considered in the calculations. The CaSi(1:1) was assumed to be injected into 100 tonnes of deoxidized steel (Fe-500[Al]-6[O] in mass ppm) in the ladle at 1600°C, and 200kg (corresponding to a thickness of ~ 2 cm)³⁶⁾ of the bottom lining castables (70mass% Al_2O_3 -30mass% MgAl_2O_4 initially) was assumed to react completely with the injected CaSi wires.

Although the initial refractory composition is 70 mass% Al_2O_3 -30 mass% MgAl_2O_4 at room temperature, this shifts to approximately 50 mass% Al_2O_3 -50 mass% spinel at 1600°C because of the large solubility of Al_2O_3 in the spinel at this temperature. As CaSi is injected, Al_2O_3 in the refractories is first transformed to solid calcium-

aluminates and finally to a liquid phase (26.9 mass% CaO-68.6 mass% Al_2O_3 -4.5 mass% MgO when in coexistence with spinel and CaAl_4O_7).

Of course, the calculations in Fig. 5 represent an unrealistically extreme case of corrosion. In reality the extent of corrosion will be much less because most of the injected Ca will react with suspended Al_2O_3 inclusions and because of kinetic factors. Nevertheless, these calculations show that corrosive attack on ladle lining refractories must be considered in Ca treatment processes.

3.5. Mn/Si deoxidized steel: MnO- Al_2O_3 - SiO_2 inclusions

Mn/Si complex deoxidation is indispensable for the production of high value steel such as tire-cord steel and high-Ni steel (Fe-36%Ni Invar steel) in order to avoid the harmful effects of solid Al_2O_3 inclusions formed during Al deoxidation. Undeformable Al_2O_3 inclusions cause wire breakage during the wire-making process in tire-cord production. Therefore Mn/Si deoxidation, which results in inclusions of low melting temperature, is usually preferred. In actual plant processes, Mn/Si deoxidation usually results in liquid MnO- Al_2O_3 - SiO_2 inclusions as deoxidation products. During the refining stage, these MnO- Al_2O_3 - SiO_2 inclusions may react with CaO-containing top slags to become CaO-MnO- Al_2O_3 - SiO_2 inclusions. In this study, the relationship between the [Mn]/[Si] ratio in the liquid tire-cord steel and the composition of the MnO- Al_2O_3 - SiO_2 inclusions is shown with a view to forming inclusions with low melting temperatures.

Fig. 6 shows the calculated compositional trajectories of the MnO- Al_2O_3 - SiO_2 inclusions for various constant [Mn]/[Si] deoxidant ratios as [Al] is varied in liquid tire-cord steel at 1600°C. (The [C] in tire-cord steel, which is about 0.7 mass%, was ignored in the calculations). The total amount of ([Mn]+[Si]) was set to 1.0 mass% and the calculated phase diagrams at 1600°C and 1200°C are superimposed on the figure. A small amount of Fe_2O_3 (less than 3 mass%) always exists in such inclusions and this was included with MnO (on a molar basis) in Fig. 4. Phase boundaries measured^{37,38)} for various [Mn]/[Si] ratios are also shown in Fig. 4. The agreement with the calculations is excellent.

In Fig. 7 the measured oxygen contents of the steel at equilibrium simultaneously with liquid oxide and a solid oxide (i.e. along the phase boundaries of Fig. 6) are plotted as functions of the [Mn]/[Si] ratio in the steel and are compared to the calculated curves. The experimental results exhibit a large amount of scatter. Agreement between the measurements and the calculations is within the experimental error limits.

The main interest in Mn/Si deoxidation is to maintain the inclusions in the liquid state at the temperature of the wire production process at 1200°C in tire-cord steel. Therefore, the liquidus curve of the MnO- Al_2O_3 - SiO_2 system at 1200°C is superimposed on the diagram in Fig. 6. This permits one to target the appropriate ranges of [Mn]/[Si] ratios to maintain the inclusions in the liquid state at 1200°C.

3.6. Addition of Ti alloying element: Ti/Al deoxidation

Titanium is an alloying element which improves the toughness of steel. Because it is much more expensive than aluminum, it is usually added after Al deoxidation in order to minimize Ti losses through reaction with O . Several authors³⁹⁻⁴¹⁾ have investigated inclusion compositions after Ti/Al deoxidation using sampling techniques, but no comprehensive equilibrium measurements for Ti/Al deoxidation have been conducted. Kunisada *et al.*⁴²⁾ reported that in the case of Ti/Al deoxidation the oxygen content in liquid steel is lower than in the case of Ti deoxidation but is higher than in the case of Al deoxidation; hence, there is no advantage of Ti/Al deoxidation for reducing oxygen content compared with Al deoxidation.

Recently, Gaye *et al.*^{39,43)} calculated an Fe-Al-Ti-O inclusion diagram at 1580°C from their thermodynamic database. They considered Ti_2O_3 , but not Ti_3O_5 , as deoxidation product. However, Ti_3O_5 can also be a deoxidation product under common steelmaking conditions. Furthermore, their diagram shows a region of stability of a liquid oxide phase. However, the eutectic temperature of the Al_2O_3 - TiO_2 phase diagram has been reported⁴⁴⁾ at 1703°C.

Fig. 8 shows our calculated inclusion diagram for the Fe-Al-Ti-O system at 1600°C. Four different stability fields are seen on the diagram. Iso-oxygen content lines are also calculated. In Fig. 8, the experimental results of Ruby-Meyer *et al.*³⁹⁾ are also plotted. These authors observed the variation of Al and Ti concentrations in liquid steel with time after the addition of Ti/Al into liquid steel containing excess oxygen at 1580°C. An initial experimental composition of 0.03mass% $[Al]$ and 0.04mass% $[Ti]$ (marked as the filled triangle in Fig. 8) falls within the Al_2O_3 precipitation region in the calculated diagram. Therefore only Al in the liquid iron will be consumed by reaction with excess oxygen to precipitate Al_2O_3 until the phase boundary is reached at 0.006mass% $[Al]$. Thereafter, Ti will also react to form Ti_3O_5 . Another initial experimental composition of 0.06mass% $[Al]$ and 0.08mass% $[Ti]$ (marked as the filled circle in Fig. 8) falls near the calculated Al_2O_3 / Ti_3O_5 boundary. Therefore, both Al and Ti will react with oxygen to precipitate Al_2O_3 and Ti_3O_5 simultaneously. It can be seen in Fig. 8 that the experimental results in both cases are as predicted from the calculated diagram.

It can also be seen Fig. 8 that there is no advantage to Ti/Al deoxidation over Al deoxidation for reducing oxygen contents except in the very small Al_2TiO_5 region. From the inclusion diagram, it is also possible to calculate the amount of Ti which can be added as an alloying element without wasting it as a deoxidizer. For example, Ti can be added up to 0.66mass% ($\log(\text{mass}\%) = -0.18$) at about 0.05mass% $[Al]$ ($\log(\text{mass}\%) = -1.3$) after Al deoxidation without forming any titanium oxide.

3.7. Spinel formation: The Fe-Al-Mg-O system

Spinel ($MgAl_2O_4$), which has a high melting temperature, is very stable and undeformable. Furthermore, (spinel + corundum) refractories are often used in ladle linings. Therefore, it is important to study the inclusion diagram of the Fe-Al-Mg-O system in order to reduce refractory corrosion as well as to avoid the formation of spinel inclusions.

The calculated inclusion diagram of the Fe-Al-Mg-O system at 1600°C is presented in Fig. 9. Note that spinel is not a stoichiometric compound at 1600°C but rather a solid solution of $MgAl_2O_4$ and Al_2O_3 (containing up to 42 mass% Al_2O_3). As in the diagram for the Fe-Al-Ca-O system (Fig. 2), and for the same reasons, the spinel/MgO and spinel/ Al_2O_3 phase boundaries are almost horizontal up to 0.1mass% total dissolved Al. The Mg deoxidation curve for the Fe-Mg-O system is also very similar to the Ca deoxidation curve in Fig. 1. Matsuno *et al.*⁴⁵⁾ investigated a limited range of the spinel single phase region by analyzing the Al and Mg contents of liquid iron contained in a spinel crucible. Similarly, Itoh *et al.*⁴⁶⁾ measured the positions of the spinel/MgO and spinel/ Al_2O_3 phase boundaries at 1600°C as well as the oxygen contents of the steel along these boundaries.

The calculated spinel/MgO boundary and the experimental data of Itoh *et al.*⁴⁶⁾ are not in good agreement. However, from an assessment⁹⁾ of available data for the Fe-Mg-O deoxidation system it has been shown that the $[Mg]$ concentration in liquid Fe in equilibrium with MgO is about $10^{-3}\text{mass}\%$ which is the position of the calculated boundary in Fig. 9 at low $[Al]$ content. Hence, the data of Itoh *et al.* are not consistent with these data. Possibly, Mg was lost by volatilization during the experiments.

As in the case of Fig. 2, the nearly horizontal calculated phase boundaries in Fig. 9 result from the use of the Associate Model for the molten steel which takes account of the formation of strong Mg^*O associates in solution. Diagrams calculated previously with the classical Wagner formalism showed the boundaries sloping upwards to the right. As in the Fe-Ca-O system discussed above, previous calculations^{13,19,32)} using the Wagner formalism required very large negative temperature-dependent first- and second-order interaction parameters ϵ_{Mg}^O , ρ_{Mg}^O , $\rho_{Mg}^{Mg,O}$. Furthermore, most authors also had to arbitrarily adjust the equilibrium constant K_{MgO} for the formation of solid MgO by several orders of magnitude from its literature value in order to fit the data. In the present calculations, this was not necessary, and accepted literature values were used as recommended by Turkdogan.²³⁾

3.8. Formation of (Ti,Nb)(C,N) inclusions in stainless steel

The control of the nitrogen level in steel is important because it has many harmful (and some beneficial) effects on physical properties and surface characteristics. The addition of Ti to liquid steel has become common practice in order to improve corrosion resistance. Ti can react with

N, C and oxygen to form titanium nitride, carbide, carbo-nitride or oxides. These inclusions may have detrimental effects on properties such as toughness, ductility and weldability and may also result in low surface quality. Ti and Cr have a very strong affinity for N while Ni does not. Because of the affinity of Cr for N, the solubility of N in liquid Fe-18 mass% Cr-8 mass% Ni stainless steel containing 1 mass% Ti is about 160 mass ppm at 1600°C while it is only about 67 mass ppm in pure liquid Fe containing 1 mass% Ti. Once nitrogen is dissolved in liquid stainless steel, it can precipitate later in the solid steel.

Fig. 10 shows the calculated inclusion diagram of Fe-18 mass% Cr-8 mass% Ni-Ti-N-O stainless steel at 1600°C. Iso-oxygen content curves are plotted as thin lines and the stable regions of the (Fe,Ti)N solid solution and Ti_3O_5 and Ti_2O_3 are shown on the diagram. The amount of FeN in the (Fe,Ti)N solid solution is calculated to be about 12 mass% at 0.1 mass% [Ti] and 8 mass% at 1 mass% [Ti]. When the oxygen content is below 19 mass ppm, no titanium oxides are precipitated (deoxidation minimum). Also the calculations show that TiN will never be formed if the [N] content is lower than 160 mass ppm. The calculated inclusion diagram is not significantly changed by including small amounts of [C] (< 0.5mass%) except that carbo-nitride (Fe,Ti)(C,N) is precipitated instead of the nitride.

Fig. 11 presents the results of calculations of the precipitation of carbonitride (Ti,Nb)(C,N) inclusions in solid stainless steel in the temperature range between 1400° and 700°C. The initial steel composition was Fe-16.2 Cr-11.2 Ni-0.04 C-0.8 Mn-0.35 Si-2.7 Mo-0.3 Nb-0.25 Ti-0.05 N in mass%. **Fig. 11(a)** shows the variation of the equilibrium amount of each phase as temperature is decreased, and the corresponding composition of the carbonitride inclusions is presented in **Fig. 11(b)**. Above 1080°C, carbonitride I, composed mainly of TiN and TiC with small amounts of NbN and NbC, is formed, while below this temperature carbonitride II, composed mainly of NbC with small amounts of TiC, is also precipitated. The Fe content in both types of carbonitride inclusions is calculated to be less than 1 mass%. These different types of carbonitride inclusions may have different influences on the phase transformation during heat treatment. These considerations also apply in the case of plain steel.

3.9. Evolution of inclusions during solidification: Oxide metallurgy

Recently the beneficial effects of inclusions on phase transformation behavior has been recognized and termed "oxide metallurgy."^{47,48)} Inclusions can act as intragranular nucleation sites for acicular ferrite, resulting in a reduced grain size and consequently improved physical properties of steel. However the mechanisms of inclusion precipitation are very complex and highly dependent on the composition of the steel matrix. Thermodynamic calculations can aid in understanding the evolution of inclusions formed during casting processes.

Eijk⁴⁹⁾ investigated the inclusions in cast steel which had been deoxidized with Al/Ca and then with Ti. The overall composition was Fe-0.08C-0.08Si-1.55Mn-0.005S-0.002Al-0.003N-0.004O-0.009Ti-0.0007Ca in mass%. The morphology of typical inclusions in the cast steel was examined with EPMA and TEM. The results are shown in **Fig. 12(a)**. In order to understand the origin of these inclusions, an equilibrium calculation for the same composition of steel was performed. **Fig. 12(b)** shows the calculated variation of the equilibrium inclusion composition as the temperature decreases from liquid steel at 1600°C to solid steel at 1250°C.

Based on the thermodynamic calculations, the possible inclusion evolution may be explained as depicted in **Fig. 12(b)**. The CaO- Al_2O_3 solid phase in the inclusion core was most likely formed during initial Al/Ca-deoxidation before Ti was added. When Ti was added, a liquid phase, mainly composed of Ti_2O_3 -MnO- Al_2O_3 , formed around the solid CaO- Al_2O_3 core in a globular shape in the liquid steel. During subsequent solidification, solid MnS precipitated on the surface of the liquid inclusion because of the lower interfacial energy. This will be discussed below. After the precipitation of the solid MnS phase, Ti_3O_5 began to precipitate from the liquid inclusion due to the decreasing solubility of titanium oxide in the molten oxide with decreasing temperature. As temperature decreased further, the remaining liquid phase solidified as an MnO-TiO_x solid. Finally, TiN was precipitated by the diffusion of N from the steel matrix.

According to the thermodynamic calculations, the precipitation of MnS results from the solubility difference of sulfur between liquid steel and solid bcc steel (sulfur is virtually immiscible in the bcc phase) rather than by the precipitation from the liquid inclusion. That is, dissolved sulfur reacts with dissolved Mn in the steel matrix around the inclusions to form MnS on the surface of the inclusion. This results in a so-called "Mn depleted zone" which is observed⁵⁰⁻⁵³⁾ around such inclusions.

Similar thermodynamic calculations for oxide metallurgy have been reported in the literature.⁵⁰⁻⁵³⁾

4. Conclusions

Extensive computerized thermodynamic databases have been prepared for solid and liquid oxide phases and for solid and liquid steel and carbonitride phases. These databases have been developed by critical evaluation of all available thermodynamic and phase diagram data through the use of models appropriate to the structure of each solution. The use of the models permits good estimations to be made of the thermodynamic properties of multicomponent solutions based on the evaluated and optimized model parameters of lower-order (binary and ternary) subsystems. Modern Gibbs energy minimization software is used to access these databases automatically and calculate the conditions for equilibrium in multicomponent, multiphase systems.

Several case studies have been presented in which such calculations are used to elucidate and predict complex equilibria involving inclusion formation at various stages of

steelmaking. The use of thermodynamic calculations can reduce costs and aid in the development of new technology. Furthermore, the combination of thermodynamic calculations and process modeling should result in advances in the automation of steelmaking processes.

Acknowledgements

This project was supported by a CRD grant from the Natural Sciences and Engineering Research Council of Canada in collaboration with the following: INCO, Noranda, Rio Tinto, TeckCominco, Alcoa, Dupont, Shell, Corning, Pechiney, Norsk Hydro, Sintef, Schott Glas, St-Gobain Recherche, Mintek and IIS Materials.

REFERENCES

- 1) FactSage: www.factsage.com, Montreal, (2002).
- 2) A.D. Pelton and M. Blander: *Proc. of the Second International Symposium on Metallurgical Slags and Fluxes*, TMS-AIME, Warrendale, PA, (1984), 281.
- 3) A.D. Pelton and M. Blander: *Metall. Trans. B*, **17B** (1986), 805.
- 4) A.D. Pelton, S.A. Degterov, G. Eriksson, C. Robelin and Y. Dessureault: *Metall. Mater. Trans. B*, **31B** (2000), 651.
- 5) A.D. Pelton and P. Chartrand: *Metall. Mater. Trans. A*, **32A** (2001), 1355.
- 6) M. Hillert, B. Jansson and B. Sundman: *Z. Metallkd.*, **79** (1988), No. 2, 81.
- 7) A.D. Pelton, G. Eriksson and A. Romero-Serrano: *Metall. Trans. B*, **24B** (1993), 817.
- 8) A.D. Pelton: *Glastech. Ber.*, **72** (1999), No. 7, 214.
- 9) I.-H. Jung, S.A. Decterov, and A.D. Pelton: *Metall. Mater. Trans.* (accepted).
- 10) C. Wagner: *Thermodynamics of Alloy*, Addison-Wesley, Reading, MA, (1962), 51.
- 11) P. Spencer, personal communication, (2002).
- 12) Scientific Group Thermochemistry Europe (SGTE), www.sgte.org.
- 13) J.D. Seo and S.H. Kim: *Bull. Kor. Inst. Met. & Mater. (Korea)*, **12** (1999), 402.
- 14) S. Gustafsson and P.O. Mellberg: *Scand. J. Metall.*, **9** (1980), 111.
- 15) T. Ototani, Y. Kataura and T. Degawa: *Trans. Iron Steel Inst., Japan*, **16** (1976), 275.
- 16) Y. Miyashita and K. Nishikawa: *Testu-to-Hagané*, **57** (1971), 1969.
- 17) Q. Han, X. Zhang, D. Chen and P. Wang: *Metall. Trans. B*, **19B** (1988), 617.
- 18) M. Ozawa: *The Japan Society for the Promotion of Science*, 19th Committee paper No. 9837, Iron Steel Institute of Japan, Tokyo, (1975), 6.
- 19) H. Itoh, M. Hino and S. Ban-Ya: *Metall. Mater. Trans. B*, **28B** (1997), 953.
- 20) M. Nadif and C. Gatellier: *Revue de Metallurgie-CIT*, **83** (1986), 277.
- 21) *Steelmaking Data Sourcebook*, Japan Society for the Promotion of Science, 19th Comm. On Steelmaking, Gordon & Breach Science, New York, NY, (1988).
- 22) S.-W. Cho and H. Suito: *ISIJ Int.*, **34** (1994), 265.
- 23) E.T. Turkdogan: *Steel Res.*, **62** (1991), 379.
- 24) E. Schurmann, U. Braun and W. Pluschkell: *Steel Res.*, **69** (1998), 355.
- 25) H. Suito, H. Inoue and R. Inoue: *ISIJ Int.*, **31** (1991), 1381.
- 26) H. Ichihashi and T. Ikeda: *Shape Control of Inclusions*, Edited by Committee on Non Inclusion Shape Control, Organization of Joint Society on Iron and Steel Basic Research, Iron Steel Institute of Japan, Tokyo, (1984), 33.
- 27) K.-R. Lee and H. Suito: *Metall. Mater. Trans. B*, **25B** (1994), 893.
- 28) T. Kimura and H. Suito: *Metall. Trans. B*, **25B** (1994), 33.
- 29) G.M. Faulring and S. Ramalingam: *Metall. Trans. B*, **11B** (1980), 125.
- 30) E.T. Turkdogan: *Second International Conference on Clean Steel*, Balatonfüred, Hungary (1981), 3.
- 31) C. Gatellier, H. Gaye, M. Nadit: *Second International Conference on Clean Steel*, Balatonfüred, Hungary (1981), 31.
- 32) H. Ohta and H. Suito: *Metall. Mater. Trans. B*, **28B** (1997), 1131.
- 33) T.T. Le and M. Ichikawa: *Proceedings of the Second Canada-Japan Symposium on Modern Steelmaking and Casting Techniques*, CIM, Toronto, (1994), 29.
- 34) Y. Higuchi, M. Numata, S. Fukagawa and K. Shinme: *Tetsu to Hagané*, **82** (1996), 671.
- 35) M. Numata, Y. Higuchi and S. Fukagawa: *Tetsu to Hagané*, **84** (1998), 159.
- 36) Rionel Rebouillat: private communication, (2002).
- 37) H. Ohta and H. Suito: *Metall. Mater. Trans. B*, **27B** (1996), 263.
- 38) Y.-B. Kang and H.-G. Lee: unpublished work.
- 39) F. Ruby-Meyer, J. Lehmann and H. Gaye: *CCANMET I*, Lulea (1999), 213; F. Ruby-Meyer, J. Lehmann and H. Gaye: *Scand. J. Metall.*, **29** (2000), 206.
- 40) *POSCO Internal report*, (1995).
- 41) M.-K. Sun: Master Thesis, GSIST, Pohang, Korea (2002).
- 42) K. Kunisada and K. Iwai: *CAMP-ISIJ*, **7** (1994), 1130.
- 43) H. Gaye, J. Lehmann, P. Rocabois, F. Ruby-Meyer: *Proceedings of the 6th International Conference on Molten Slags, Fluxes and Salts*, Stockholm, Sweden-Helsinki, Finland, (2000).
- 44) D. Goldberg: *Rev. Int. Hautes Temp. Refract.*, **5** (1968), 181.
- 45) H. Matsuno, Y. Kikuchi and Y. Kawai: *Report in the Subcommittee of Nonmetallic Inclusion in Steel*, 19th Committee on Steelmaking, Japan Society for Promotion of Science, 4 (1991), 31.
- 46) H. Itoh, M. Hino and S. Ban-Ya: *CAMP ISIJ*, **7** (1994), 38.; H. Itoh, M. Hino and S. Ban-Ya: *CAMP ISIJ*, **8** (1995), 75.; H. Itoh, M. Hino and S. Ban-Ya: *Tetsu to Hagané*, **84** (1998), 85.
- 47) J. Takamura and S. Mizoguchi: *Proc. 6th Iron and Steel Congress*, Vol. 1, ISIJ, Tokyo, (1990), 591.
- 48) S. Ogibayashi, K. Yamaguchi, M. Hirai, H. Goto, H. Yamaguchi and K. Tanaka: *Proc. 6th Iron and Steel Congress*, Vol. 1, ISIJ, Tokyo, (1990), 612.
- 49) C. Van Der Eijk: Ph.D. Dissertation, NTNU, Trondheim, Norway (1999).
- 50) H.S. Kim, H.-G. Lee and K.-S. Oh: *Metals and Materials (Korea)*, **6** (2000), 305.
- 51) H.S. Kim, H.-G. Lee and W.-K. Jung: *ISIJ Int.*, **40**(supplement) (2000), 82.
- 52) H.S. Kim, H.-G. Lee and K.-S. Oh: *Metall. Mater. Trans. A*, **32A** (2001), 1519.
- 53) J.-S. Byun, J.-H. Shim, Y.W. Cho and D.N. Lee: *Acta mater.*, in press.

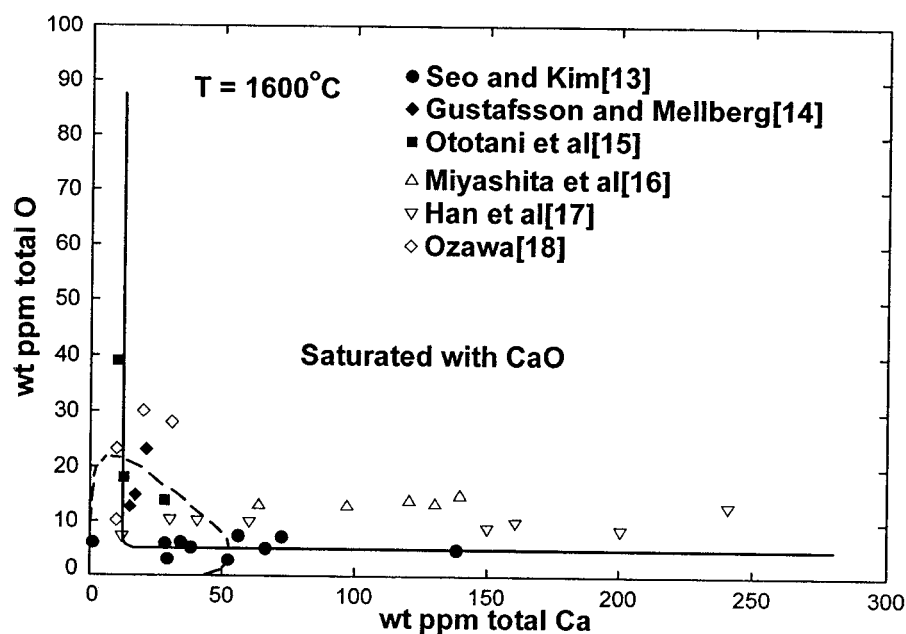


Fig. 1. Total dissolved oxygen and total dissolved Ca contents of liquid Fe in equilibrium with solid CaO. Lines calculated from database with the Associate Model.⁹⁾ Dashed line calculated from Wagner formalism with parameters of JSPS.²¹⁾

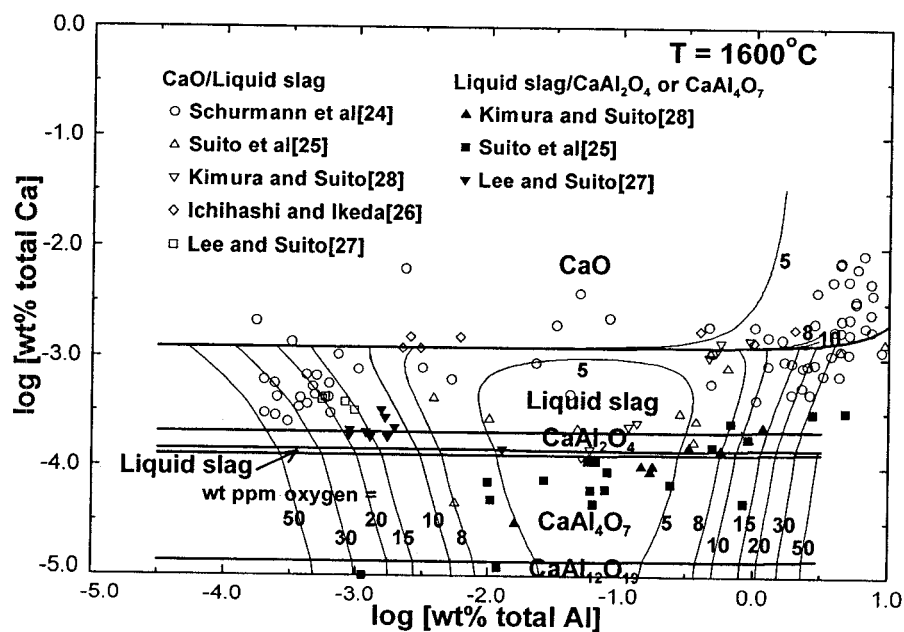
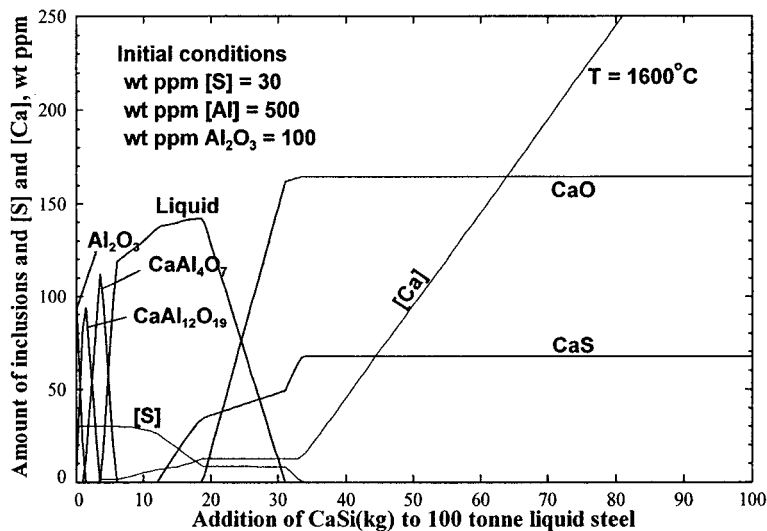
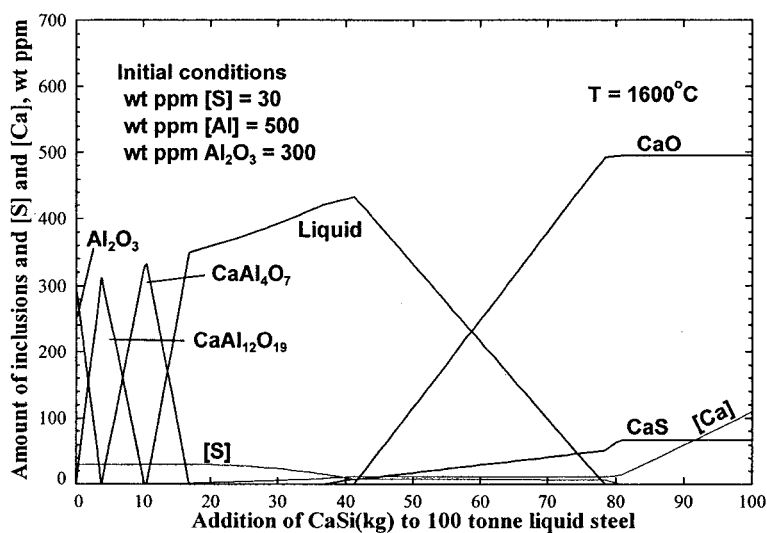


Fig. 2. Calculated inclusion diagram for complex deoxidation with Ca and Al showing total dissolved oxygen content of liquid steel and equilibrium deoxidation products as functions of total dissolved Ca and Al.



(a)



(b)

Fig. 3. Modification of Al_2O_3 inclusions and variation of total dissolved [Ca] and [S] content of steel with CaSi injection into 100 tonnes of Al deoxidized liquid steel containing sulfur at 1600°C. (a) Initial steel: [S]=30ppm, [Al]=500ppm and Al_2O_3 =100ppm; (b) Initial steel: [S]=30ppm, [Al]=500ppm and Al_2O_3 =300ppm.

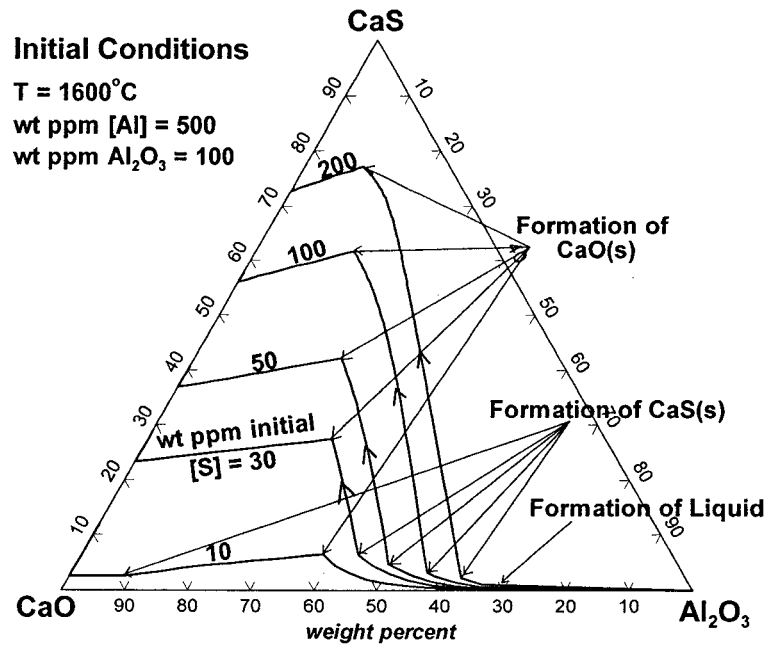


Fig. 4. Calculated overall compositional trajectories of inclusions during the modification of Al_2O_3 inclusions with CaSi injection into Al-deoxidized liquid steel containing various initial sulfur contents at 1600°C . Initial steel: $[\text{Al}] = 500 \text{ mass ppm}$ and $\text{Al}_2\text{O}_3 = 100 \text{ mass ppm}$.

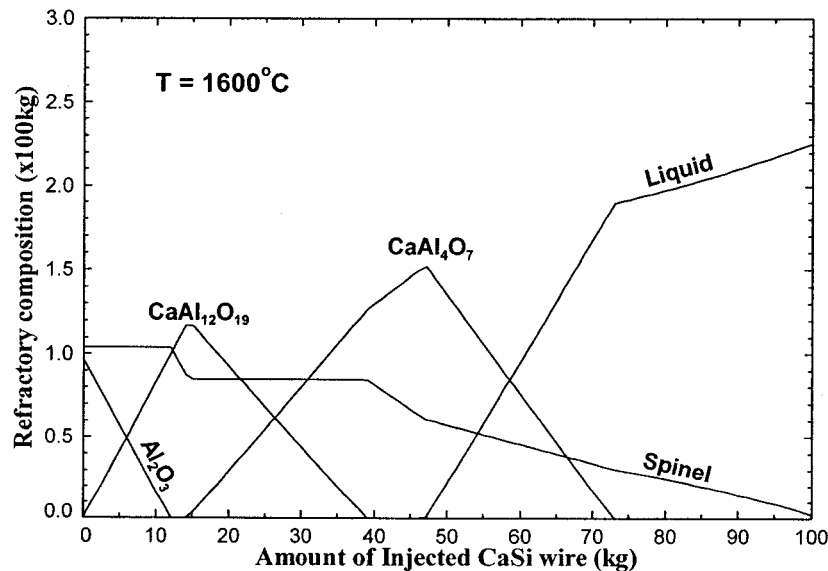


Fig. 5. Calculated compositional change of refractories during CaSi injection at 1600°C . Initial refractory: 200kg of 70mass% Al_2O_3 + 30mass% MgAl_2O_4 . Steel: 100 tonnes of Fe-0.05mass% $[\text{Al}]$ -0.0006mass% $[\text{O}]$. Complete reaction is assumed. No reaction between CaSi and Al_2O_3 inclusions is assumed.

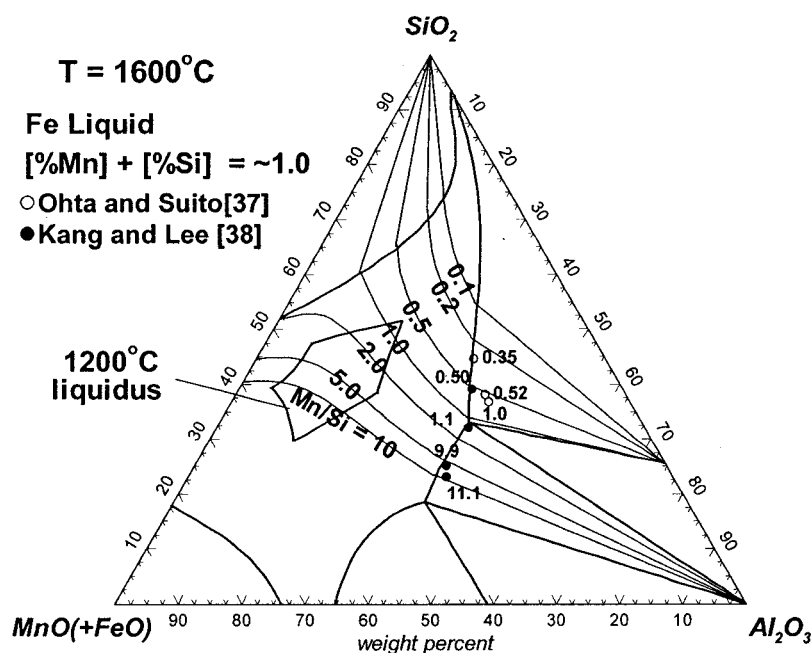


Fig. 6. Calculated compositional trajectories of MnO-Al₂O₃-SiO₂ inclusions in equilibrium with liquid Fe containing various dissolved [Mn]/[Si] weight ratios and a total dissolved ($\text{Mn} + \text{Si}$) content of 1.0 mass% at 1600°C. Experimental^{37,38)} [Mn]/[Si] ratios at alumina or mullite saturation are shown beside each experimental point. The calculated liquidus curves at 1600°C and 1200°C are also shown.

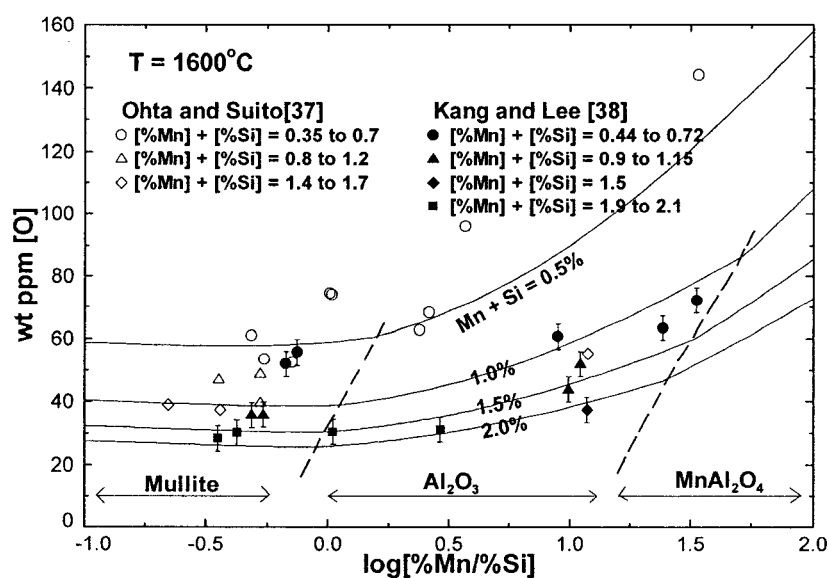


Fig. 7. Calculated oxygen content versus dissolved [Mn]/[Si] weight ratio at various total dissolved ($\text{Mn} + \text{Si}$) contents in liquid Fe in equilibrium with liquid MnO-Al₂O₃-SiO₂ inclusions saturated with MnAl₂O₄, Al₂O₃, or mullite at 1600°C.

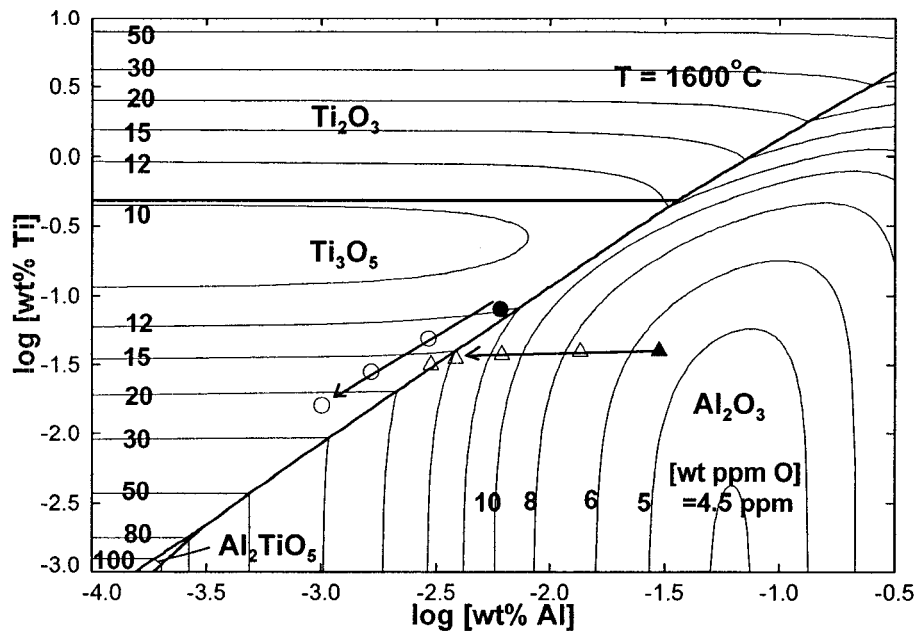


Fig. 8. Calculated inclusion diagram of the Fe-Al-Ti-O system at 1600°C. Experimental data from Ruby-Meyer *et al.*³⁹⁾ at 1580°C (filled symbols are initial compositions and open symbols are measured compositions with time.)

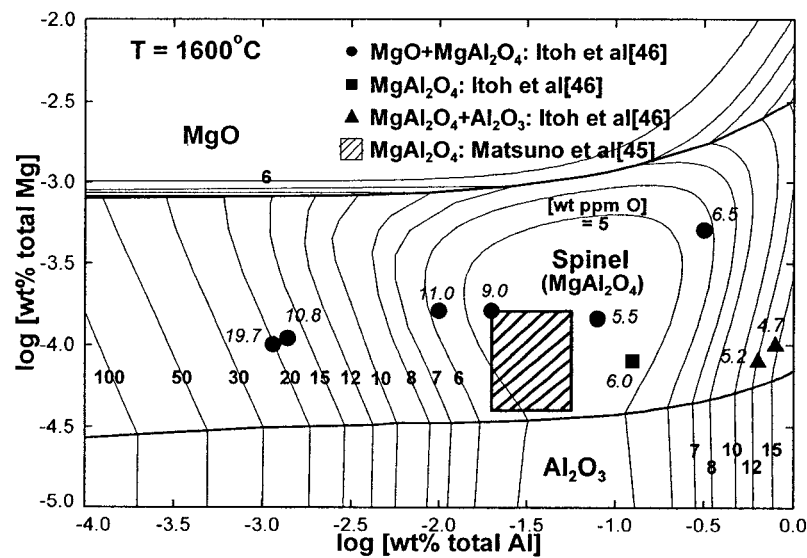


Fig. 9. Calculated inclusion diagram of the Fe-Al-Mg-O system at 1600°C. (Numbers in italics are measured oxygen contents.)

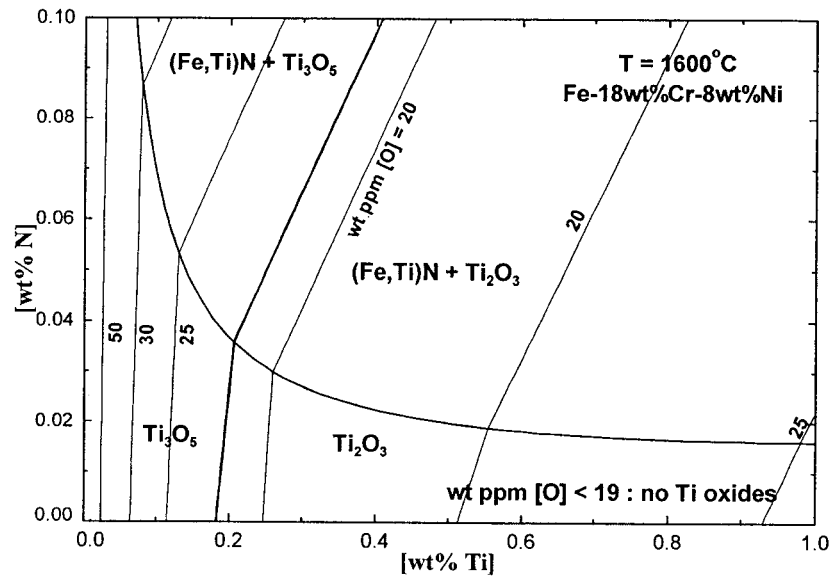
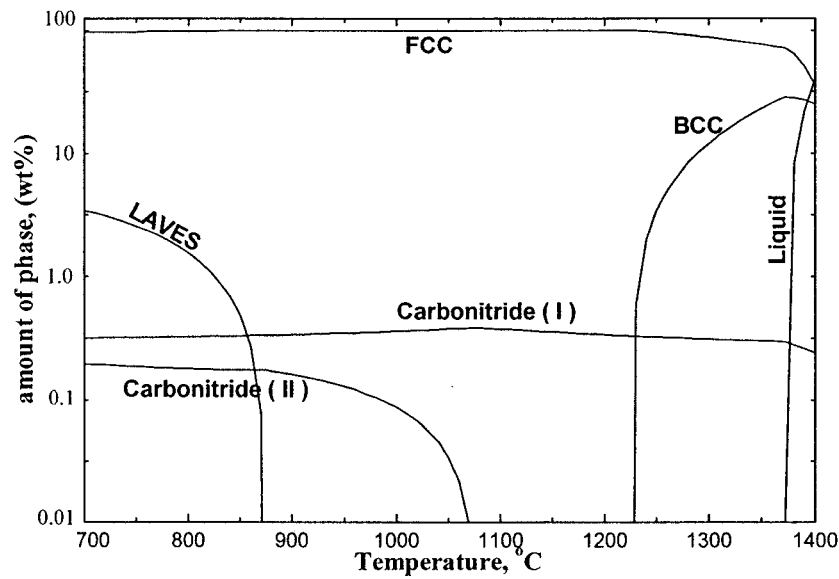
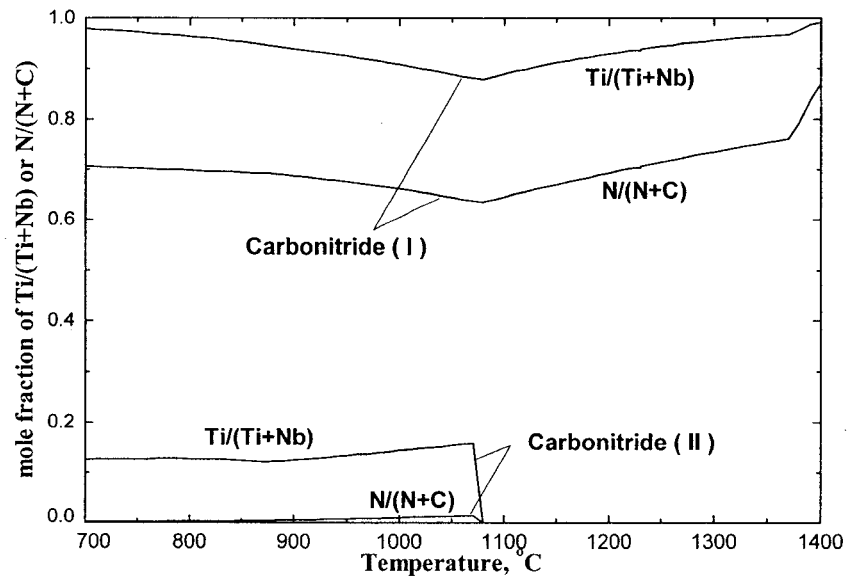


Fig. 10. Calculated inclusion diagram in the Fe-18mass% Cr-8mass% Ni-Ti-N-O system at 1600°C.



(a)



(b)

Fig. 11. Calculated precipitation of (Ti,Nb)(C,N) inclusion from stainless steel during the rolling process. Initial steel composition: Fe-16.2Cr-11.2Ni-0.04C-0.8Mn-0.35Si-2.7Mo-0.3Nb-0.25Ti-0.05N in mass%. (a) Variation of amount of each phase, (b) Composition of the carbonitride inclusions.

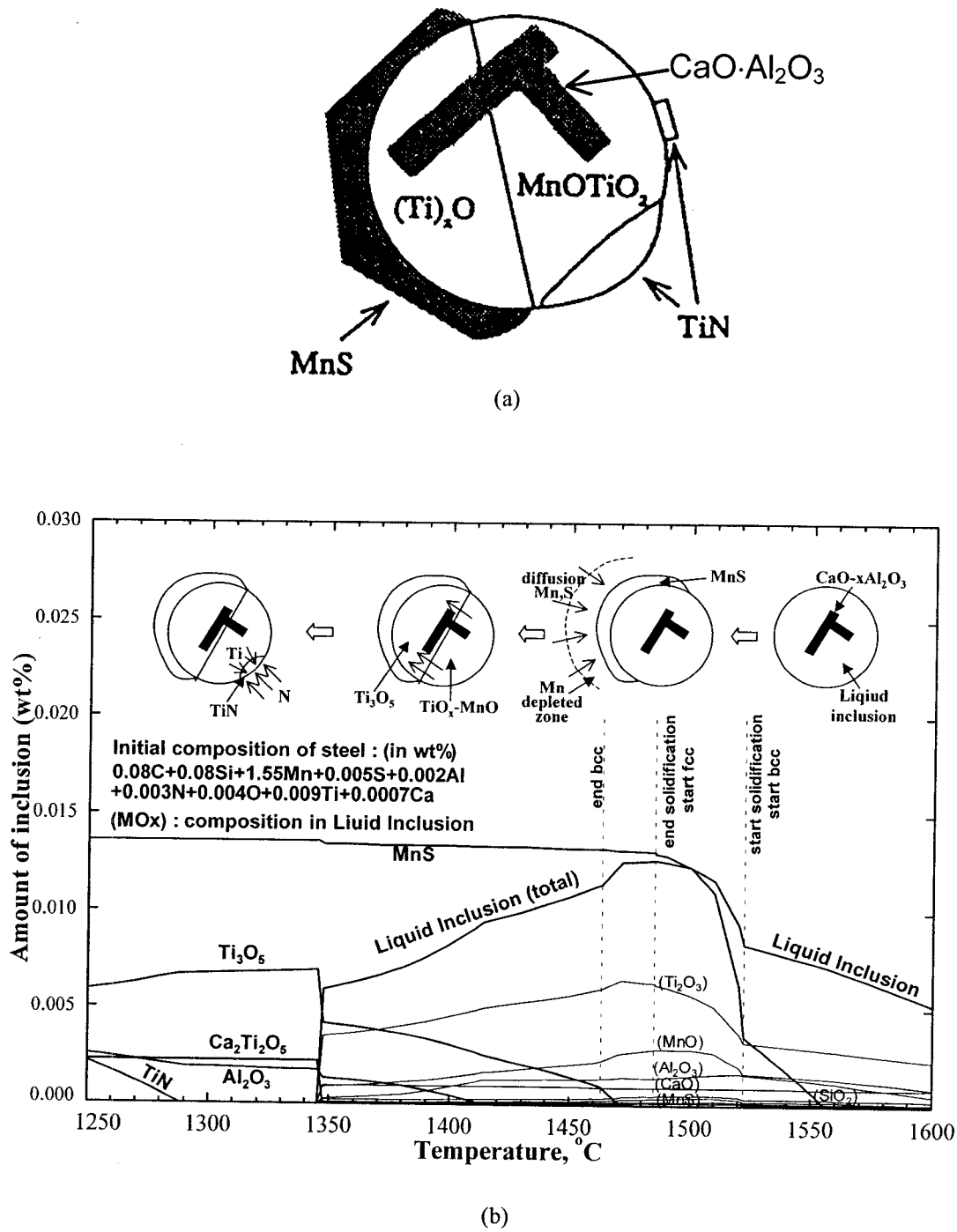


Fig. 12. The evolution of inclusions during the casting process for steel of initial composition: Fe-0.08C-0.08Si-1.55Mn-0.005S-0.002Al-0.003N-0.004O-0.009Ti-0.0007 Ca in mass%. (a) Inclusion morphology observed by Eijk⁴⁹⁾ (b) Calculated inclusion composition as temperature decreases from 1600°C to 1250°C, and a possible inclusion formation mechanism.

Appendix XI

Compound Energy Formalism (CEF)

Compound Energy Formalism

The Compound Energy Formalism (CEF) was advanced by Hillert *et al.* (1988).

For solution phases with two or more sublattices it is natural to regard stoichiometric compounds rather than elements as the components. For a phase $(A,B)_a(C,D)_c$ one would have the four component compounds A_aC_c , A_aD_c , B_aC_c and B_aD_c . It is thus natural to represent the Gibbs energy of such a phase with reference to the Gibbs energies of these “end-member” compounds in pure form. These may be denoted by G_{AC} , G_{AD} , G_{BC} and G_{BD} if the stoichiometric numbers are omitted. However, there is a problem because an average composition can be obtained by mixing three of the compounds and if all four are used their amounts are not uniquely defined. This problem has been solved by the adoption of a mathematical model which is based on the use of site fractions, i.e. mole fractions defined for each sublattice. In the case of the $(A,B)_a(C,D)_c$ solution, the Gibbs energy of a reciprocal solution per formula unit can be expressed:

$$G^m = Y'_A Y''_C G_{AC} + Y'_A Y''_D G_{AD} + Y'_B Y''_C G_{BC} + Y'_B Y''_D G_{BD} \\ + aRT(Y'_A \ln Y'_A + Y'_B \ln Y'_B) + cRT(Y''_C \ln Y''_C + Y''_D \ln Y''_D) + G^E \quad (1)$$

where Y'_i and Y''_j represent the site fractions of constituents i and j on the first and second sublattices. Clearly, the logarithmic terms come from the entropy of mixing under the assumption of random mixing within each sublattice. The first four terms can be rationalized on the assumption of random mixing if it is assumed that all nearest-neighbors to an atom are situated on the other sublattice and, furthermore, that the nearest neighbor bond energies are constant. Finally, the last term is an excess Gibbs energy which, to the first approximation, results from interactions between second-nearest-neighbor atoms or ions on the same sublattice. Recognizing that these

interaction energies may depend on which species occupies the other sublattice, the following expression was proposed.

$$G^E = Y_A' Y_B' Y_C'' L_{AB;C} + Y_A' Y_B' Y_D'' L_{AB;D} + Y_A' Y_C'' Y_D'' L_{A;CD} + Y_B' Y_C'' Y_D'' L_{B;CD} \quad (2)$$

where $L_{ij;k}$ and $L_{k;ij}$ are the interaction energies between species i and j on one sublattice when the other sublattice is occupied solely by k . The L parameters can be constant interaction energies or can be treated as dependent on composition. Usually the compositional dependence of the L parameters is expressed using Redlich-Kister polynomials.

In some cases, G_{ij} of an “end-member” may represent the Gibbs energy of a real stoichiometric compound. In other cases, no real compound “ ij ” exists and the G_{ij} thus become the parameters of the model which are related to interactions between the species on the different lattices.

The formalism can be easily extended to multicomponent systems and to solutions with many sublattices. The Compound Energy Formalism has been widely used to describe the Gibbs energies of metallic alloy phases.

This formalism is often called the Compound Energy Model. However, this is not a model but a mathematical formalism. Within the framework of the CEF, many different models can be developed by combining with structural concepts. One of the most important criteria in distinguishing the models is the way of defining the Gibbs energies of hypothetical end-member components. Different ways of treating these Gibbs energies can eventually result in completely different predictions in multicomponent solutions.

Appendix XII

Interpolation Techniques

Interpolation techniques

In order to estimate the thermodynamic properties of ternary or multicomponent systems, the binary model parameters and ternary model parameters can be interpolated based on several “geometric” models. This has been reviewed by Chartrand and Pelton (2000) and Pelton (2001).

The molar excess Gibbs energy of a binary 1-2 solution is often expressed as

$$G_{12}^E = \alpha_{12} X_1 X_2 \quad (1)$$

The term α_{12} is often expanded as a polynomial in the mole fractions:

$$\alpha_{12} = \sum_{i \geq 0} \sum_{j \geq 0} q_{12}^{ij} X_1^i X_2^j \quad (2)$$

where the q_{12}^{ij} are empirical coefficients which may be temperature dependent. Of course, the equivalent fraction Y_1 and Y_2 can be used instead of X_1 and X_2 when the Modified Quasichemical Model is used. Equation (2) is frequently re-arranged into “Redlich-Kister” form:

$$\alpha_{12} = \sum_{i \geq 0} {}^i L_{12} (X_1 - X_2)^i \quad (3)$$

Clearly, the set of coefficients q_{12}^{ij} can be calculated from the set of ${}^i L_{12}$ and vice versa.

Extension to ternary solutions

For ternary systems, several “geometric” models may be proposed. Some of these are illustrated in Figure 1. In each model, G^E in the ternary solution at a composition point p is estimated from the excess Gibbs energies in the three binary subsystems at points a , b and c by the equation:

$$G^E = \alpha_{12(a)} X_1 X_2 + \alpha_{23(b)} X_2 X_3 + \alpha_{31(c)} X_3 X_1 + (\text{ternary terms}) \quad (4)$$

where $\alpha_{12(a)}$, $\alpha_{23(b)}$ and $\alpha_{31(c)}$ are the binary “ α -functions” evaluated at points a , b and c . The “ternary terms” are polynomial terms which are identically zero in the three binary subsystems. The empirical coefficients of the ternary terms may be chosen in order to fit ternary experimental data. However, these ternary coefficients should be small.

If, at a given temperature, all three binary α -functions are constant (regular solution), independent of composition, then all geometric models are clearly identical. The Kohler and Muggianu models in Figures 1 (a) and (c) are “symmetric” models, whereas the Kohler/Toop and Muggianu/Toop models in Figures 1 (b) and (d) are “asymmetric” models inasmuch as one component (component 1 in Figure 1 (b) and (d)) is singled out. In these two asymmetric models, α_{12} and α_{31} are assumed to be constant along lines where X_1 is constant. That is, replacing component 2 by component 3 is assumed to have no effect on the energy, α_{12} , of forming (1-2) nearest-neighbor pairs, and similarly for (3-1) pairs. An asymmetric model is thus more physically reasonable than a symmetric model if components 2 and 3 are chemically similar while component 1 is chemically different. For example, the slags in the SiO_2 -CaO-MgO, Al_2O_3 -CaO-MgO, *etc.* systems are well described by this asymmetric model shown in Figure 1(b) (where SiO_2 and Al_2O_3 are the asymmetric components in each system). Solid solutions such

as Fe_2O_3 -FeO-MgO monoxide are also well fitted by the same model (Fe_2O_3 as asymmetric component).

When G^E is large and α_{12} and α_{31} depend strongly on composition, a symmetric and an asymmetric model will give very different results. In the FactSage thermodynamic software (FactSage, 2002), any kind of interpolation technique is now permitted for each subsystem in order to maximize the ability to estimate the Gibbs energy of ternary or multicomponent solutions from the optimized parameters of low-order systems.

In equation (4), when the Kohler approximation is chosen for the 1-2 subsystem, then the α_{12} can be written:

$$\alpha_{12} = \sum_{i \geq 0} \sum_{j \geq 0} q_{12}^{ij} \left(\frac{X_1}{X_1 + X_2} \right)^i \left(\frac{X_2}{X_1 + X_2} \right)^j : \text{Kohler-type} \quad (5)$$

Instead, if the Toop-type approximation is chosen for the 1-2 subsystem, then the α_{12} can be written:

$$\alpha_{12} = \sum_{i \geq 0} \sum_{j \geq 0} q_{12}^{ij} X_1^i (1 - X_1)^j : \text{Toop-type} \quad (6)$$

Finally, if α_{12} is approximated by a Muggianu-type approximation, then:

$$\alpha_{12} = \sum_{i \geq 0} \sum_{j \geq 0} q_{12}^{ij} \left(\frac{1 + X_1 - X_2}{2} \right)^i \left(\frac{1 - X_1 + X_2}{2} \right)^j : \text{Muggianu-type} \quad (7)$$

The corresponding Redlich-Kister polynomial expression for α_{12} in each case is given by Pelton (2001).

Extension to multicomponent solutions

In order to estimate the excess Gibbs energy in a multicomponent solution of $N > 3$ components, Chartrand and Pelton (2000) and Pelton (2001) devised a rational method of extending the Kohler-Toop-Muggianu geometric formalism to N -component systems.

When any of the Kohler-Toop-Muggianu geometric approximations can be chosen for a binary sub-system, 64 different geometric model become possible for a ternary solution. Therefore a rational method of extending these approximations to multicomponent solutions should be devised.

Consider a 5-component system in which a choice of models for the ternary subsystems has been made as illustrated in Figure 2. For instance, the α_{12} function is given in the 1-2-3 system by a Toop-type approximation at constant X_2 , in the 1-2-4 system by a Toop-type approximation at constant X_1 , and in the 1-2-5 system by a Kohler-type approximation...

A new composition variable can be defined:

$$\xi_{ij} = X_i + \sum_k X_k \quad (8)$$

where the summation is over all components k of i - j - k ternary solutions in which α_{ij} is given by a Toop-type approximation along lines of constant X_j . In the example of Figure 2:

$$\begin{aligned} \xi_{12} &= X_1 + X_3 & \xi_{21} &= X_2 + X_4 \\ \xi_{13} &= X_1 & \xi_{31} &= X_3 + X_4 \end{aligned}$$

$$\begin{aligned}
\xi_{14} &= X_1 & \xi_{41} &= X_4 + X_2 + X_3 + X_5 \\
\xi_{15} &= X_1 & \xi_{51} &= X_5 + X_4 \\
\xi_{23} &= X_2 & \xi_{32} &= X_3 + X_1 \\
\xi_{24} &= X_2 + X_3 & \xi_{42} &= X_4 \\
\xi_{25} &= X_2 & \xi_{52} &= X_5 \\
\xi_{34} &= X_3 & \xi_{43} &= X_4 + X_2 + X_5 \\
\xi_{35} &= X_3 + X_2 & \xi_{53} &= X_5 + X_4 \\
\xi_{45} &= X_4 & \xi_{54} &= X_5
\end{aligned} \tag{9}$$

The significance of these variables is as follows. The choice of a Toop-type approximation for α_{12} in the 1-2-3 and 1-2-4 subsystems means that α_{12} , the energy of forming (1-2) nearest-neighbor pairs, is assumed to remain constant as component 1 is replaced by component 3 in the 1-2-3 ternary system and as component 2 is replaced by component 4 in the 1-2-4 system. Hence, in the multicomponent system it is reasonable to assume that α_{12} should remain constant at constant $\xi_{12} = X_1 + X_3$ and at constant $\xi_{21} = X_2 + X_4$ when all other mole fractions (X_5 in this case) are held constant. Similarly, α_{31} should remain constant at constant $\xi_{13} = X_1$, and at constant $\xi_{31} = X_3 + X_4$ when X_2 and X_5 are held constant; and similarly for the other α_{ij} functions.

Finally, for the general case of an α_{ij} -function which may be given by Kohler-, Muggaianu- and Toop-type approximations in the ternary subsystems, another new function can be defined as:

$$\sigma_{ij} = \sigma_{ji} = 1 - \sum_k X_k \tag{10}$$

where the summation is over all components k of ternary subsystems $i-j-k$ in which α_{ij} is given by a Kohler-type approximation. In the example in Figure 2:

$$\begin{aligned}
 \sigma_{12} &= 1 - X_5 & \sigma_{24} &= 1 - X_1 - X_5 \\
 \sigma_{13} &= 1 & \sigma_{25} &= 1 - X_1 \\
 \sigma_{14} &= 1 & \sigma_{34} &= 1 \\
 \sigma_{15} &= 1 - X_2 & \sigma_{35} &= 1 \\
 \sigma_{23} &= 1 - X_4 - X_5 & \sigma_{45} &= 1 - X_1 - X_3
 \end{aligned} \tag{11}$$

Then, α_{ij} can be written by replacing X_i and X_j in equation (2) by the functions

$\left(1 + \frac{\xi_{ij} - \xi_{ji}}{\sigma_{ij}}\right)/2$ and $\left(1 + \frac{\xi_{ji} - \xi_{ij}}{\sigma_{ij}}\right)/2$ respectively. That is, for the case of α_{12} :

$$\alpha_{ij} = \sum_{i \geq 0} \sum_{j \geq 0} q_{12}^{ij} \left(\frac{1 + \frac{\xi_{12} - \xi_{21}}{\sigma_{12}}}{2} \right)^i \left(\frac{1 + \frac{\xi_{21} - \xi_{12}}{\sigma_{12}}}{2} \right)^j \tag{12}$$

These general expressions reduce to the correct expressions for α_{ij} in all ternary subsystems.

Ternary terms

If ternary terms in equation (4) are introduced, a function of

$$q_{123}^{ijk} X_1^i X_2^j X_3^k \quad (13)$$

where $i \geq 0, j \geq 0$ and $k \geq 0$ and q_{123}^{ijk} is an empirical coefficient, is generally used. However, such terms have little theoretical justification. For extending these ternary terms into the N-component system, the following procedure (Pelton, 2001) is used:

- (1) If α_{12} in the 1-2-3 system is given by a Kohler-type or a Muggianu-type approximation, then the following ternary terms may be included:

$$X_1 X_2 \left[q_{12(3)}^{ijk} \left(\frac{1 + \frac{\xi_{12} - \xi_{21}}{\sigma_{12}}}{2} \right)^i \left(\frac{1 + \frac{\xi_{21} - \xi_{12}}{\sigma_{12}}}{2} \right)^j X_3 (1 - \xi_{12} - \xi_{21})^{k-1} \right] \quad (14)$$

- (2) If α_{12} in the 1-2-3 system is given by a Toop-type approximation along lines of constant X_1 , then the following ternary terms may be included:

$$X_1 X_2 \left[q_{12(3)}^{ijk} \left(\frac{1 + \frac{\xi_{12} - \xi_{21}}{\sigma_{12}}}{2} \right)^i \left(\frac{1 + \frac{\xi_{21} - \xi_{12}}{\sigma_{12}}}{2} \right)^j \frac{X_3}{\xi_{21}} \left(1 - \frac{X_2}{\xi_{21}} \right)^{k-1} \right] \quad (15)$$

All these interpolation techniques presently coded in the FactSage software (FactSage, 2002).

In this Appendix, the equations have been developed for interpolating the excess model parameters q_{ij} and $q_{ij(k)}$ when G^E is expanded as a polynomial. In the case of the Modified Quasichemical Model, similar equations apply to interpolating the ω_{ij} and $q_{ij(k)}$ model parameters.

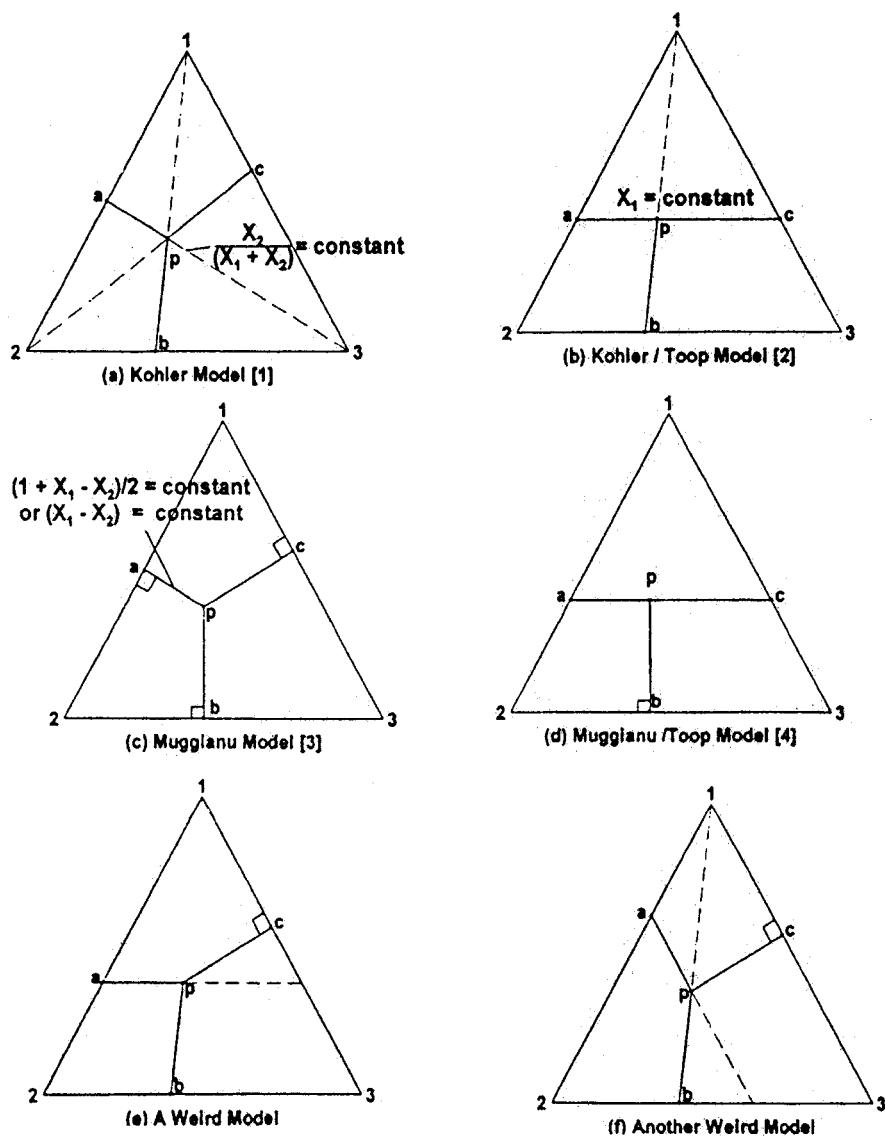


Figure 1: Some “geometric” models for estimating ternary thermodynamic properties from optimized binary data (after Pelton, 2001).

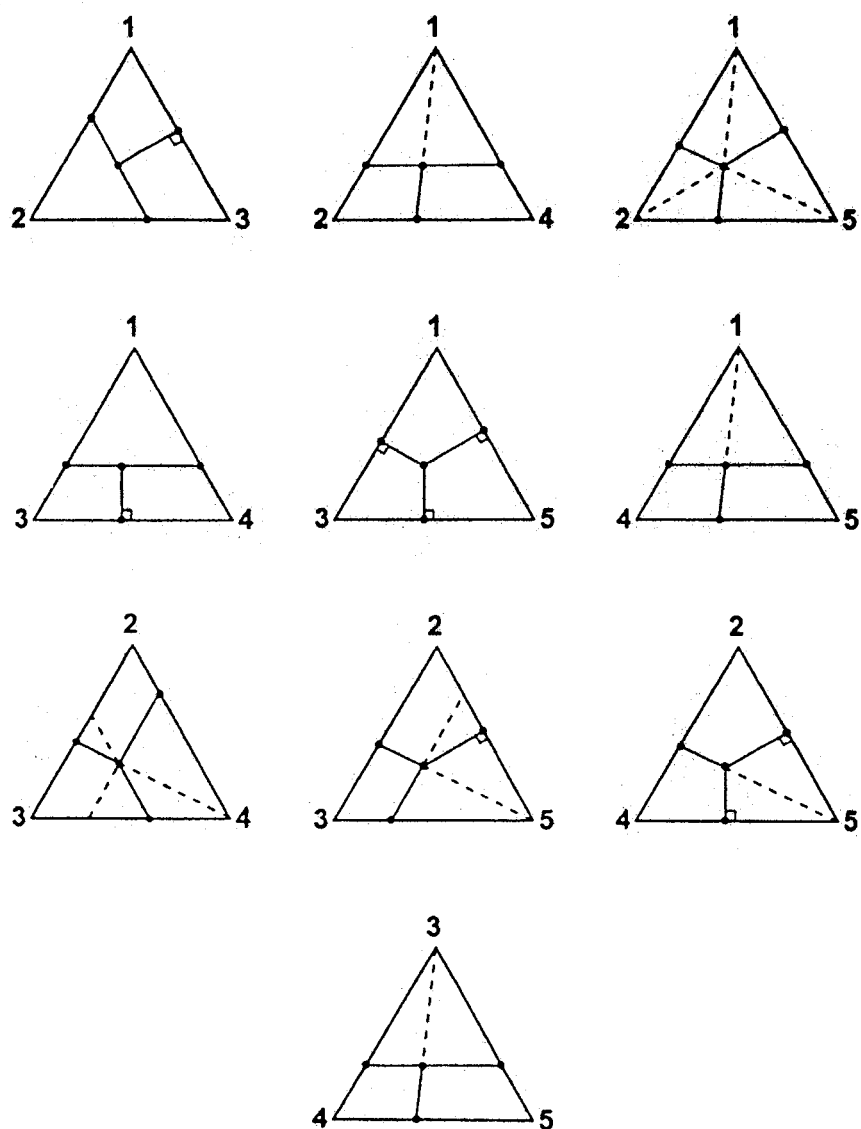


Figure 2 : 5-component solution showing the geometric models chosen for all ternary subsystems (after Pelton, 2001).